A novel Lagrangian-based method for the deconvolution of electron energy-loss spectra

Dissertation

zur Erlangung des Grades
Doktor der Naturwissenschaften
– Dr. rer. nat. –

angefertigt am
Department für Physik
der Fakultät für Naturwissenschaften
der Universität Paderborn

von
Christian Zietlow
geb. am 15. Mai 1992 in Bad Oldesloe

eingereicht
am
15. Juli 2025

Erstgutachter : Prof. Dr. Jörg K. N. Lindner, Universität Paderborn
Zweitgutachter : Prof. Dr. Arno Schindlmayr, Universität Paderborn

Datum der Disputation: 6. November 2025

Kurzzusammenfassung

Elektronenenergieverlustspektroskopie (engl. EELS) ist eine fortgeschrittene Analysemethode der Transmissionselektronenmikroskopie, die auf atomarer Ebene Einblicke in Materialcharakteristika wie bspw. Eigenschaften des Elektronensystems oder der Materialzusammensetzung erlaubt. Die Genauigkeit jeder EELS-Analyse ist jedoch fundamental durch Rauschen und Unschärfe begrenzt.
Diese Thesis beschreibt solche Rauschphänomene im Detail. Vor allem bei strahlempfindlichen Materialien, die kurze Bestrahlzeiten erfordern, aber auch bei Elektron-Materie-Wechselwirkungen mit geringer Auftrittshäufigkeit, ist eine solche Beschreibung notwendig, da das Rauschen solche Messungen dominiert. Zusätzlich spielen Korrelationen des Rauschens eine Rolle, die durch Faltung des verrauschten Signals mit der Punktspreizfunktion des Detektors entstehen und die sowohl theoretisch als auch experimentell beschrieben werden. Methoden zur Messung der wichtigsten Rauschparameter bei typischen Detektorsystemen werden vorgestellt und erlauben es, das Rauschmodel auf jeden beliebigen EELS-Detektor anzupassen.
Eine neue Entfaltungsmethode wird vorgeschlagen, die EELS-Messungen schärft und entrauscht. Die Wirksamkeit dieser Methode wird an Simulations- und Experimentaldaten dargelegt. Hierbei wird gezeigt, dass die neue Methode signifikant bessere Ergebnisse liefert, als bisherige und somit eine Analyse von Messdaten auf einem Level ermöglicht, das die Möglichkeiten der Elektronenmikroskopie deutlich erweitert.

Abstract

Electron energy-loss spectroscopy (EELS) is an advanced analytical technique in transmission electron microscopy, as it provides insights into material characteristics, such as electronic properties or elemental composition, at the atomic scale. The precision of every EELS analysis, however, is inherently limited by noises and blur. This thesis offers a comprehensive understanding of the noise, which is particularly valuable at low dwell times necessary for beam sensitive materials and for electron-matter interactions with low frequency of occurrence, where the noise dominates the measurement. Additionally, correlations encountered in the noise of an EELS measurement are described from both a theoretical and experimental perspective. These correlations are caused by a convolution of the noisy signal with the detector point spread function. Methods for characterizing key noise parameters of typical detectors are described, allowing the noise model to be tailored to any EELS detector. Ultimately, a novel deconvolution method enabling significant sharpening and denoising of EELS measurements is introduced and demonstrated. Its efficiency is further validated on both simulation and experimental data. The described advancement offered by the proposed deconvolution method enables the extension of current electron microscope capabilities, facilitating analysis that would be unfeasible with existing deconvolution techniques.

Contents

Chapter 1

Introduction

Electron microscopy serves as a gateway to the nanoworld, allowing the visualization and analysis of structures down to the atomic or even the sub-atomic level [1–5]. As a versatile tool for material characterization, electron microscopy has become an indispensable technique for analyzing semiconductor materials and beyond [6]. The production of computer chips, for instance, relies heavily on the regular compositional analysis of transistors [6–8]. Considering that modern transistors consist of layers that are only a few nanometers thick [9, 10], precise composition analysis at the atomic scale is essential to ensure optimal function [11, 12].

Typically, such measurements are conducted in modern aberration-corrected transmission electron microscopes (TEM), which can readily achieve the spatial resolution necessary to observe the atomic structure of materials. In addition, TEM enables the employment of a multitude of analytical characterization techniques, including energy-dispersive X-ray spectroscopy (EDS) and electron energy-loss spectroscopy (EELS) [5], both of which allow for determining the elemental compositions. Beyond this, EELS also has the benefit of providing additional insights into the plasmonic properties of a specimen, the band structure, the phononic system, and even the bonding states of atoms within the specimen. Due to the ability to probe the band structure, EELS allows to investigate the optical properties of small objects by reconstructing the complex optical permittivity through Kramers-Kronig analysis [13, 14] of the energy-loss signal [15].

The optical permittivity, for example, plays a crucial role in the design and performance of nanolasers and waveguides, which are essential components of photonic integrated circuits. In these components, the reflections at the interface between the structure and its surroundings are critical, as they govern the wave transport and modal behavior within the material [16, 17].

One of the drawbacks of EELS is that these measurements are strongly impacted by noise due to the low probability of occurrence of many electron-specimen interactions of interest. These low probabilities, in turn, translate into low-intensity EEL signals, which are often superimposed by higher-intensity background signals. One example of such a background signal is directly related to the zero-loss peak (ZLP), which is by far the most intense feature of an EEL spectrum. This peak results from beam electrons transmitting through a specimen without losing energy. In contrast, signal features resulting from energy-losses related to the band structure of the specimen material remain comparatively small. Due to the low energy-losses related to optical transitions, these peaks are situated right next to the ZLP and thus become superimposed by the right-hand side tail of it. This tail forms a background signal, which often is larger in magnitude than the loss-features related to optical transitions. Due to the quantized nature of beam electrons, both background signal and energy-loss signal are inherently subject to Poisson noise. This results in the two noise levels adding up, such that the desired information about the material's band gaps is often distorted and not easily accessible.

Noise, in particular, is also a problem for beam-sensitive materials that are prone to degradation and therefore require low beam exposure. While reducing acquisition times increases the likelihood of measuring undamaged materials [18–20], it also leads to extremely low signal-to-noise ratios. As a result, obtaining reliable EELS measurements on intact structures under these noisy conditions is challenging [21], especially in the research of biological and polymer specimen [22–26].

In addition to being obscured by noise, EEL spectra are inevitably convolved with the energy characteristics of the impinging electron beam and the detector's point spread function (PSF) [5, 27]. These contributions cause blurring of the EEL spectra. As blur reduces the energy resolution of the measurement, it is commonly removed through post-processing methods like deconvolution [27]. During the work on this thesis, it became apparent that current noise models used for EELS detectors are inadequate and only partially account for the noises faced in such measurements. Since deconvolution methods rely on precise noise models, a discrepancy between existing noise models and actual noise statistics hinders the effectiveness of deconvolution and significantly compromises quantitative analyses.

The first objective of this thesis is therefore to develop a comprehensive noise model that accounts for the whole signal detection process and accurately captures the noise characteristics encountered in TEM. To achieve this goal, this thesis presents simple and practical methods to determine the key noise parameters, allowing the proposed noise model to also be tailored to the specific requirements of EELS. While primarily focusing on detectors employed in TEM, this noise model may also prove useful for medical imaging, which often relies on a similar type of detector. Due to the generality of the principles, the noise model is – in large parts – applicable to other array detectors, such as common-use CCD or CMOS cameras. By providing a clear description, this thesis enables researchers to implement and adjust the noise model to their respective experimental setups under a variety of different detectors.

The noise model developed in this thesis also enables the characterization of uncertainties associated with imaging on these detectors, both generally and specifically in the context of EELS measurements. The determination of such uncertainties is crucial for scientific research, as they decisively determine the quality of an experiment and, more importantly, the meaningfulness of results.

Building on the proposed noise model, the second objective of this thesis is to develop an improved deconvolution method that outperforms existing methods in terms of accuracy. This novel deconvolution method is designed to address the aforementioned challenges: It shall effectively reduce noise, thereby enabling shorter exposure times to minimize material degradation; and shall further enhance energy resolution, allowing for the recovery of finer features in EEL spectra. Due to its straightforward implementation as a post-processing step, this deconvolution method is intended to facilitate advancement of current research in the field by improving the data. This thesis demonstrates both theoretically and experimentally that the proposed noise model and the deconvolution method are applicable to current generations of detectors. Given the universality of the underlying principles, it is anticipated that the derived formulas will remain valid and applicable for future generations of detectors, thereby benefiting ongoing research endeavors.

In order to prove that the deconvolution method enhances real measurement EELS data in a way that, in some cases, makes reasonable evaluation possible in the first place, a Janus nanoparticle consisting of two sides of different metals was fabricated and analyzed for its energy-losses induced by plasmonic resonances. Such Janus particles are hardly covered in current literature with respect to their surface plasmons, especially in EELS measurements. A very recent example of literature on Janus surface plasmons is [28] – however, there is not much more to be found in that regard.

In view of the work's broad applicability, the findings of this thesis have been published in four research articles, which are part of this manuscript. To aid understanding of this thesis' contributions to electron microscopy and EELS, the subsequent chapters offer an overview of transmission electron microscopy, electron energy-loss spectroscopy, and other relevant characterization techniques employed in this thesis, as well as a concise introduction to the underlying principles of plasmonics.

Chapter 2

Plasmonic nanoparticles

As this thesis investigates plasmonic nanoparticles, a profound understanding of their properties is necessary. This chapter aims at explaining the basic concept of plasmons and the use-cases of plasmonic Janus structures, emphasizing their importance. To enable reproducible production of such particles, their fabrication process is explained in detail. During this thesis, a corresponding particle simulation tool was developed as well, since it is highly desirable to simulate these particles. Having simulated nanoparticles, closely resembling the fabricated ones, allows for more advanced plasmonic simulations. These, in turn, allow the design and fine-tuning of particles to achieve specific plasmonic characteristics for optimal behavior in subsequent applications – prior to fabrication. Additionally, this approach enables the cross-checking of EELS measurement results with the relevant simulation data facilitating the interpretation of plasmonic features.

2.1 Plasmons

Both electrons and nuclei respond to applied electromagnetic fields and are therefore influenced by external radiation, such as light. However, due to their significantly larger mass, nuclei are unable to keep pace with the electrons in high-frequency fields. This disparity in inertia leads to a collective charge separation within a material in the presence of high-frequency fields, resulting in an oscillating state of polarization. This polarized state can be treated as a quasi-particle, known as a *plasmon* [29, 30].
Plasmonics play a crucial role in metals [31, 32], although they also occur, albeit with reduced intensity, in semiconductors. The low electronegativity of metal atoms leads to a state where the valence electrons become delocalized, forming an electron gas between the ionized atomic cores. This state resembles a plasma, hence the term plasmon. Due to the overlap of valence and conduction bands or, in the case of monovalent metals, a partially filled valence band, electrons can acquire arbitrarily small energy increments, enabling energy to readily propagate throughout the system via a collective movement of the electrons. As charge accumulates at the opposing surfaces, a restoring electric field is generated within a particle, ultimately resulting in a harmonic oscillation of the electronic system. Due to scattering with the atom hulls and with other electrons, the motion is damped. According to the Lorentz-Drude model, the equation of motion can be written as [29]:

$$m_e^* \ddot{\vec{X}}(\vec{r},t) + m_e^* \gamma \dot{\vec{X}}(\vec{r},t) + m_e^* \Omega_0^2 \vec{X}(\vec{r},t) = -e\vec{E}_{\text{ext}}(\vec{r},t) \ , \tag{2.1}$$

with the effective electron mass m_e^*, the elementary charge e, and the damping coefficient γ. The resonant frequency for the electrons bound to the nucleus (similar to the spring in a harmonic oscillator) is denoted as Ω_0 and the periodic external electrical field is given as $\vec{E}_{\text{ext}}(\vec{r},t) = E_{0,\text{ext}} \cdot e^{i\left(\vec{k}\cdot\vec{r}-\omega t\right)}$ at the time t on position $\vec{r}$, with an amplitude of $E_{0,\text{ext}}$, a wave vector $\vec{k}$ and an angular frequency of ω.

This results in the solution [29]:

$$\vec{X}(t) = \frac{e}{m_e^*} \frac{\vec{E}_{\text{ext}}(\vec{r}, t)}{\omega^2 + i\gamma\omega - \Omega^2} \,. \tag{2.2}$$

The corresponding energy of the plasmon E_{Plasm} and its frequency ω_{Plasm} are then given as [29]:

$$E_{\text{Plasm}} = \hbar \cdot \omega_{\text{Plasm}} \quad \text{and} \quad \omega_{\text{Plasm}} = \sqrt{\frac{n_e\, e^2}{m_e^* \varepsilon_0}} \,, \tag{2.3}$$

with the conduction electron density n_e and the permittivity of free space ε_0.
However, this oscillator is not only characterized by the effective mass of the electron and the electron density, but also by the particle's geometry and size [30]. Two distinct types of plasmons can be identified: the *bulk* and the *surface plasmons*. Bulk plasmons oscillate throughout the material, while surface plasmons are confined to and propagate along the surface of metallic or semiconductor structures. Typically, plasmon energies range from a few eV for surface plasmons up to several tens of eV for bulk plasmons.
Particularly in metallic nanostructures, which exhibit a high surface-to-volume ratio, surface-bound plasmons play a significant role. Here, electric fields can penetrate the entire volume of the particle, affecting the whole electronic system. The distinction between surface and volume becomes increasingly blurred. Stable resonant oscillations emerge that are characteristic of *localized surface plasmons*. Notably, for smaller particles, the localized surface plasmons shift towards higher energies – a phenomenon known as the *confinement effect* [33].
Plasmons can be excited not only by light but also by beam electrons in a TEM and are therefore observable with EELS [34–37]. Hence, scanning TEM allows for the spatially resolved excitation of plasmons in individual nanoparticles. In this context, it is important to consider the differential scattering cross-section of the beam electrons with plasmons, since strong forward scattering increases the likelihood of measuring plasmon interactions in the direct beam path with which the EELS spectrometer is typically aligned. The scattering cross-section can be expressed as [3]:

$$\frac{d\sigma}{d\Omega} = \frac{1}{2\pi a_0} \left(\frac{\theta_E}{\theta^2 + \theta_E^2} \right) \quad \text{, with} \quad \theta_E = \frac{E_{\text{Plasm}}}{E_0} \,, \tag{2.4}$$

with the Bohr radius a_0, the scattering angle θ, the characteristic scattering angle θ_E, the kinetic energy of the electron E_0, and the plasmon energy E_{Plasm}.
Given that the kinetic energy of the beam electrons used in this thesis is 200 keV, which by far exceeds typical plasmon energies in the order of a few to a few tens of eV, strong forward scattering is expected according to Eq. 2.4 [3]. Therefore, the path of the beam electrons remains rather unchanged under plasmon scattering, making an EELS setup employed in the direct beam path a suitable tool for plasmon analysis.

2.2 Metallic Janus-nanoparticles

In this thesis, plasmonic Janus nanoparticles are of special interest. The terminus *Janus* refers to the two-faced roman god Janus and just like the god, these particles compose of two or more distinct solid-state materials.
Janus nanoparticles, such as cobalt-gold (Co-Au) or iron-gold (Fe-Au) coated polystyrene nanodome-particles, have proven to be good nanoheaters that can be utilized for photothermal therapies [38, 39] like optical hyperthermia for cancer treatments or temperature-activated drug delivery. These nanoheaters exploit the light-absorbing properties in the near infrared (NIR) spectrum of gold on the one hand. On the other hand, the magnetic properties of the iron or cobalt parts allow for interactions with a low AC magnetic field to measure viscosity-dependent rotation dynamics of the nanodomes, which in turn provide information about the local temperature [38]. This enables a precise tuning and controlling of temperature, which is crucial to avoid damaging healthy tissue [38, 39]. Hence, these plasmonic properties are highly relevant for medical applications [40–43].
A very interesting application is the usage of such Janus nanoparticles as optical nanomotors. When a silica sphere with a gold half-cap is illuminated by a plane wave, these particles tend to rotate indefinitely as long as they are illuminated [44, 45]. Hence, these particles could, for example, be the heart of a drive for nanorobots [45]. Even more interesting is the idea that these particles can be guided by switching the frequency of the light. This behavior was shown to occur when two caps with different materials are employed, i.e. with a gold face and a titanium-nitride face, instead of just half-capping the surface [46]. These kinds of particle use thermophoretic drift as the propulsion mechanism.
Janus particles consisting of a gold (Au) and a platinum (Pt) side are especially interesting, as both combine plasmonic properties with high bio-compatibility. It was shown that these particles exhibit self-propulsion properties by exploiting electrophoresis, however, this mechanism still requires some kind of fuel such as hydrogen peroxide [47].

Such Au-Pt Janus nanoparticles were investigated with respect to their plasmonic properties. However, the noisiness of the EELS measurements and the width of the energy distribution of the microscope employed in this thesis made it hard to impossible to properly investigate these structures. Therefore, it was necessary to use the novel deconvolution method on these measurements to make evaluation of these particles possible. The results are shown in the publication in Appendix D alongside the definition of the deconvolution method.

The Au-Pt Janus particles were fabricated with the technique of double-angle resolved nanosphere lithography [48–50]. While this technique is not the most precise method with respect to the size and shape of the particles, it is very cost-efficient and capable of patterning substrates in the order of several cm^2 with a high density of such structures. Since the nanoparticles are evaluated in the TEM, it is desirable to have such a dense population of particles to make sure to catch as many structures as possible. This is because TEM evaluation requires extensive preparation to create ultra-thin specimens and also because TEM limits the effectively usable specimen size to only a few hundreds of μm^2. For specimens patterned by nanosphere lithography (NSL) techniques, this corresponds to several thousands of observable nanoparticles. Therefore, NSL provides an ideal tool for fabricating such particles for the TEM. In the following sections, this method of creating nanoparticles will be explained in detail.

2.2.1 Fabrication of the nanomask

The Janus particles investigated in this thesis were fabricated by employing nanosphere lithography. Just as the name suggests, the process of nanosphere lithography (NSL) [48, 49] requires a nanosphere mask to begin with. Such a nanosphere mask can be produced by utilizing the doctor blade technique [55, 56]. For this purpose, a large number of nanospheres is provided in a suspension, which is deposited on a substrate. For the nanomasks used in this thesis, an aqueous suspension of polystyrene nanospheres with a diameter of 750 nm was drop-coated on a Si[100]-substrate. This suspension is subsequently spread-out by a doctor blade that is linearly moved relative to the substrate, as depicted in Fig. 2.1(a). During this procedure, a meniscoid triple-phase boundary is formed between substrate, doctor blade, and surrounding atmosphere, which follows the relative movement of the doctor blade due to evaporation of the suspension liquid [51, 56]. As a consequence of capillary forces between neighboring nanospheres and the moving meniscus, the nanospheres self-organize into an energetically favorable order: a hexagonal close-packing of spheres. This constitutes a closed nanomask with triangularly shaped openings between each three neighboring spheres, which can be used as apertures for the NSL process [51].
The quality of such nanomasks depends on multiple factors, such as humidity, temperature, relative velocity of the doctor blade to the substrate, surface energy of the substrate, concentration of nanospheres in the suspension, diameter and diameter distribution of the nanospheres, material of the nanospheres, composition of the suspension liquid and many more. However, once a stable set of parameters is found, depending on the current conditions, rather large nanomask-monolayers – in the order of cm^2 – can

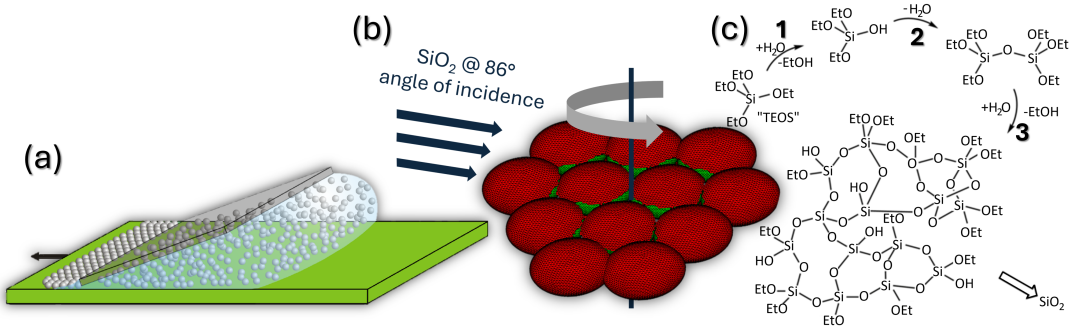

Fig. 2.1: **(a)** Schematic of the doctor blade technique (from [51]) to create a monolayer of nanospheres (white) in a hexagonally closed-packed order on a substrate (green). The arrow shows the direction of movement of the substrate relative to the doctorblade (transparent grey). A triple-phase boundary forms at the left side of the doctor blade between liquid (transparent blue), the substrate, and the surrounding atmosphere. Due to capillary effects of the nanospheres and the evaporation of the liquid, the nanospheres order at the boundary per self-organization and form a nanosphere mask that can further be modified for nanosphere lithography. **(b)** After creating the nanomask, 15 nm of SiO_x is deposited via electron beam physical vapor deposition (EBPVD) on top of the spheres at an 86° angle relative to the surface normal of the substrate, as indicated by the arrows. This angle is chosen such that SiO_x is only deposited on top of the spheres, but not onto the substrate. During the EBPVD process, the substrate is rotated at 15 rpm for several minutes to create a homogeneous coating from all sides. This results in a cap coating (red) of the central spheres (green) with an average thickness of approximately 3 – 4 nm, as simulated by a ray-tracing algorithm [52]. **(c)** Simplified representation of the Stöber process (from [53]). In a first step, a TEOS molecule reacts with a water molecule and is hydrolyzed as a result. This reaction produces ethanol (EtOH) and a mixture of ethoxysilanols, such as the depicted $Si(OEt)_3OH$. In a second step, the ethoxysilanols condense with a loss of water and form increasingly bigger cross-linked structures by repeating the first two steps over and over again in step 3 [54]. This procedure results in the formation of a large structure that eventually translates into a SiO_x layer growth reducing the aperture size of the nanomask.

be formed with millions to billions of apertures [51, 55]. However, to effectively *draw* well-defined particles with these apertures, their diameter must partially be closed [57]. Such a method was proposed in [58] and utilizes the Stöber process [59] to chemically deposit material on top of a nanomask-layer, controlledly closing the apertures in a couple of hours.

The Stöber process [59] characterizes the growth of silica nanospheres forming in a mixture of tetraethylorthosilicate (TEOS) and an alcoholic solution, as depicted in Fig. 2.1(c). This process is catalyzed by increasing the pH of the solution by e.g. adding ammonia; details of the Stöber process are found in [54, 59]. Important, however, is that this process can also be used to create layer-growth at SiO_x surfaces by slowing down the process via adjusting the pH value of the solution.

As the Stöber process does not work on regular polystyrene nanospheres, coating these with a SiO_x-layer previous to the Stöber process is mandatory. To apply this coating to the spheres, the electron beam physical vapor deposition (EBPVD) process was employed at an incident angle of $86°$ relative to the surface normal of the substrate. Due to the high angle, the SiO_x is only deposited on top of the spheres, as shown in the simulation in Fig. 2.1(b), but not onto the substrate. To create a homogeneous layer, the sample is constantly rotated during evaporation. This method provides good results for subsequent mask modifications with the Stöber process.

When applying the Stöber process to such modified spheres, a radial growth on top of the coatings is observed, shrinking the openings between spheres to provide smaller apertures for the lithography process. This procedure was implemented in [52] and presented in [60]. One of the obtained results is shown in Fig. 2.2, where the shrinking of aperture size is illustrated in the upper row as a function of the Stöber process duration. The lower row shows the vertical projection of gold onto the substrate via EBPVD, resulting in a nanoparticle capturing the corresponding apertures shape and size. Subsequently, the nanomask was removed in a tetrahydrofuran (THF) bath, dissolving the polystyrene nanospheres.

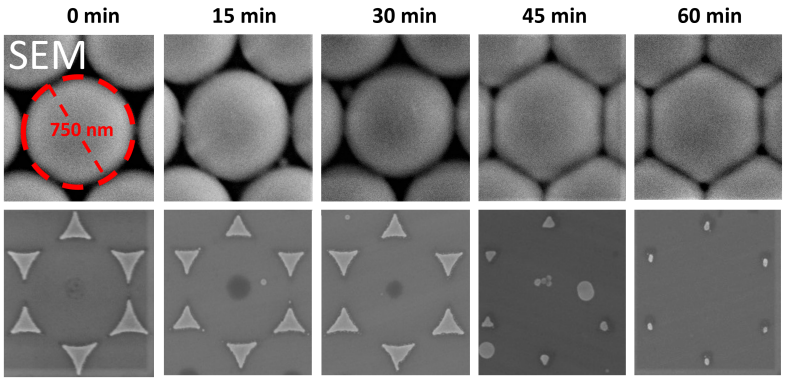

Fig. 2.2: SEM images (from [60]) showing a time series of the mask modification by the Stöber process. The used nanospheres had a diameter of 750 nm, were coated with SiO_x, according to Fig. 2.1(b), and subsequently were submersed into a Stöber solution bath for an increasing time duration. As a consequence, they are closed to an increasing degree. The upper row depicts the closing of the polystyrene nanosphere mask in the course of time. The lower row shows the vertical projection of a 4 nm titanium (Ti) adhesion layer followed by 20 nm of Au onto the substrate via EBPVD. Hence, the dimensions of the resulting gold nanoparticles correspond to those apertures shown in the upper row and are much easier to evaluate than the apertures themselves. This is because the visual aperture size of the nanomask strongly depends on the contrast settings of the SEM, whereas the visual particle size of the gold nanoparticles is considerably less influenced by this parameter. After the EBPVD process, the nanomask was removed in a tetrahydrofuran (THF) bath, which dissolved the polystyrene nanospheres. Therefore, only the gold structures visibly remain on the substrate.

Both upper and lower row images were measured using a scanning electron microscope (SEM).
In Fig. 2.3(a) the mean aperture size is provided as a function of the Ströber process duration. The aperture size is characterized by the height of the projected triangular shaped gold structure in the lower row of Fig. 2.2, as indicated by the inset in (a). Evaluation of such metallic nanoparticles provides better contrasts than directly measuring the apertures and therefore improves overall evaluation.
To facilitate the application of the mask modification process, linearity of the aperture closing is desirable. Therefore, the Stöber solution is exchanged after 30 min to mitigate effects of the decrease of TEOS concentration. Fortunately, this exchange of solutions also eliminates the small silicon nanospheres that form as an undesirable by-product of the Stöber process and could clog the nanomask apertures. The exchange of the liquids is indicated by the blue dotted line.
Eventually, the aperture size distributions corresponding to several Stöber process durations were evaluated by determining sizes of several gold particles, such as the ones shown in the lower row of Fig. 2.2. The resulting size distributions are shown in Fig. 2.3(b) and were fitted by log-normal distributions allowing for a rough statement about the homogeneity of the process [60]. In general, the FWHMs of the corresponding distributions are in the order of a few tens of nanometers.
While these results definitely leave room for improvements, it is to note that minor deviations of the spheres position relative to the regular nanosphere-lattice position as well as small differences in the diameter of the nanospheres contribute to the FWHM of the particle size distribution and lead to obvious deviations to the fit. These contributions are unavoidable. However, with increasing progress of the mask closing procedure, these deviations become smaller with the closing of the aperture, as is apparent from Fig. 2.3(b). The reason for this behavior may at least partially be attributed to geometric reasons. Since the deviation in sphere position was already present during the deposition of the SiO_x coating, all spheres constituting the aperture are less shadowed by the respective other two spheres during this process. This results in a coating that penetrates deeper into the aperture relative to that of regular sized apertures. This reduces the overall distance for closing the aperture, effectively compensating at least in partial for the increased distance from the deviation.

All in all, the results achieved are sufficient for the general process of *drawing* Janus particles.

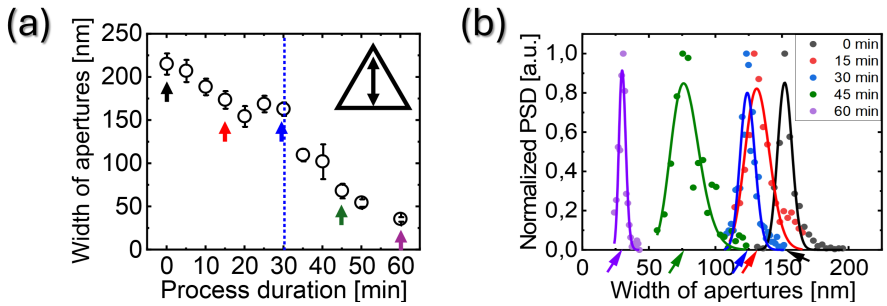

Fig. 2.3: **(a)** Closing of the triangular apertures as a function of time, determined by the triangle height, as depicted in the inset. The blue dotted line indicates an exchange of the Stöber solution to reduce the deposition of SiO_x particles nucleated in the solution and to linearize aperture closing. The colored arrows indicate the aperture sizes that were further evaluated with respect to their particle size distribution (PSD). These selected distributions are shown in **(b)**, where the PSDs are normalized to the maximum number of counted particle sizes after 0 – 60 min in the Stöber solution, following a log-normal model. The colored arrows in the graph indicate the maximum position of the PSD and correspond to the values indicated by the same colored arrows in (a). Further explanations of the results are provided in [52].

2.2.2 Double-angle resolved nanosphere lithography

After the mask modification process, which defines the aperture size of the nanomask, material can be deposited through the nanomask by an EBPVD process [61]. By tilting the sample by an angle θ and rotating the sample by an angle φ, the aperture of the nanomask is projected onto different positions of the sample [50], visualized in Fig. 2.4(a). This process can be controlled in a sufficiently smooth manner with stepper motors, allowing to *draw* well-defined nano structures having a *pencil width* determined by the aperture. Therefore, double-angle resolved NSL allows fabrication of billions of nano-objects in parallel [51]. As several crucibles with the different materials are provided in a revolver setup in the vacuum chamber, switching materials is possible without breaking the vacuum. In Fig. 2.4(b), a substrate was patterned with elongated gold-platinum Janus nanostructures.
Due to mask clogging caused by the deposited material, the aperture size reduces by approximately twice the thickness of the deposited material. This is because the material is deposited to all sides of the aperture, closing it along the surface normals of all spheres by the thickness of the deposited material, respectively. Hence, depositing 15 nm of a material results in a clogging of the aperture by 30 nm.

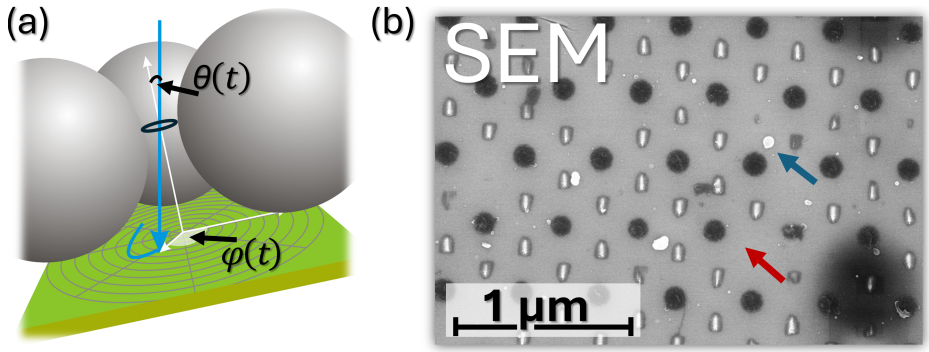

Fig. 2.4: **(a)** Schematic of the projection of material through a nanomask aperture onto a substrate via EBPVD (from [51]). Due to adjustments of a tilting angle θ relative to the surface normal (white) of the sample (green) and by a rotation of an angle φ, different positions on a substrate can be targeted, as indicated by the blue arrow. When these angles are continuously changed, i.e. $\theta \rightarrow \theta(t)$ and $\varphi \rightarrow \varphi(t)$, throughout the EBPVD process, material can be deposited in a way that resembles a *drawing* of particles, indicated by the blue path on the substrate. Due to the hexagonal structure of the nanomask, each nanosphere is surrounded by six apertures, which all contribute to the patterning of the substrate. In **(b)**, a SEM image of such a patterned substrate is shown after the mask removal in a THF bath. A chromium (Cr) adhesion layer having an average thickness of 3.5 nm (15 nm in total deposited material) was deposited at an angle between $\varphi = \pm 5^\circ$ and $\theta \approx \pm 10^\circ$ prior to the fabrication of the particle. This results in rectangular adhesion patches that are slightly broader than the particles to be fabricated thereon. Afterwards, the substrate was tilted from $\theta = 0^\circ$ to $\theta \approx \pm 10^\circ$ during the EBPVC process, positive tilt for the gold side and negative tilt for the platinum side, all while the rotation angle remained $\varphi = 0^\circ$. During this process, the evaporation material was switched from gold to platinum five times, with a total deposition of 7.5 nm for each material and each run, respectively. This results in 120 nm long boat-like structures consisting of equally sized portions of gold and platinum. The evaporation process was performed in vacuum with the pressure being in the order of approximately 10^{-4} to 10^{-5} mbar, depending on the deposited material. The process was initiated on a nanosphere mask with aperture sizes of 120 nm, which are subsequently reduced to 90 nm during the deposition of the adhesion layer, visible as the size of the particles deposited afterwards. It is apparent that some very small residual SiO_x nanospheres, formed during the Stöber process, adhere to the substrate, as indicated by the blue arrow. These particles sometimes clog the mask apertures as well, leading to vacant patterning spots. As an example, one of these spots is highlighted by the red arrow. In the SEM image, the former sites of the nanospheres are indicated by the dark circular spots on the substrate, whereas the nanostructures and the residual SiO_x nanospheres appear much brighter.

2.2.3 Simulation of nanoparticles

When having such a versatile technique to *draw* nanoparticles, it is desirable to design the particles upfront before fabrication. Therefore, it is important to get an impression on how the final particles will look like. Since EBPVD is performed in vacuum, the evaporated atoms of the target material are expected to move in straight lines, with only the nanomask blocking the path to the substrate. This can be reproduced in a ray-tracing simulation, such as the one outlined in [57], where both the substrate and the nanospheres are modeled by a grid consisting of a triangle mesh with vertices and faces therebetween, as can be seen from the simulated nanospheres in Fig. 2.5(a). By checking if a ray can escape a given vertex of the plane substrate without hitting the spheres [62], one can map the positions where material is deposited. A vertex, where material is deposited, is then modified in its position by moving it along the averaged surface-normal direction of its surrounding faces by a margin that corresponds to the height of the deposited layer. As material is not only deposited to the substrate but is also deposited on the spheres, the vertices of the nanospheres are also modified according to the above-described method.
As the material is deposited to both substrate and spheres simultaneously in the real process, a similar effect can be modeled in the simulation by incrementing the layer thickness by only a fraction of the desired final thickness, while adding the material to both substrate and spheres during several iteration steps. This increasingly clogs the virtual nanomask similarly to the real one [51]. Such a clogged nanomask as a result of an EBPVD process is shown in Fig. 2.5(a). Since the aperture size diminishes during the EBPVD process, less and less material is deposited to the substrate. This results in a tapering of the nanoparticle to the top. Since the projection of the aperture corresponds to a triangle moving across the substrate, each *drawn* particle will also inherit this trait from the aperture. Therefore, the path defining the final shape of the particle will always appear convolved with a triangle.
In the experimental setup, any target material in a crucible has a certain lateral expansion. Therefore several solid angles may contribute to the particle formation. Since both, the diameter of the crucible and its distance to the substrate in the EBPVD chamber are known, this information can be used to calculate

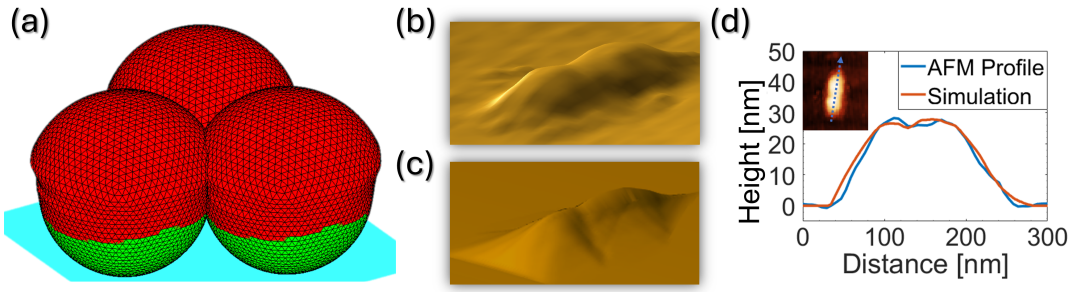

Fig. 2.5: **(a)** A simulated mask (green) covered with metal (red). The black triangular mesh represents the boundaries of the green and red faces. A vertex is defined as the central point of six adjacent triangles. The initial spheres, before the simulated EBPVD process, correspond to the three central spheres of Fig. 2.3(b), with the Stöber process being modeled by an additional radial layer growth on top of the spheres. In **(b)** an example of an Au-Pt Janus particle, fabricated using a 120 nm wide mask aperture, is provided as a 3D map of an AFM measurement and is shown alongside **(c)** the corresponding ray-tracing simulation. Both appear similar in shape, however, the flanks of both particles do not seem to match quite well. **(d)** Comparison of height profiles extracted from the AFM image and the corresponding simulation along the long axis of the particle. This axis is indicated by the blue arrow in the inset, which, in turn, shows the vertical projection of the AFM image provided in (b).

a maximum and minimum solid angle that can possibly contribute to particle formation. This effect can be modeled in the simulation by testing several solid angles aside from a central position defined by θ and φ. In the algorithm designed for this thesis, these penumbra angles are circularly arranged within two sets of eight angles in a distance of $0.1°$ and $0.2°$, respectively, to the central orientation.
Since more solid angles contribute to material deposition in the middle of the aperture's projection than solid angles contribute to the boundary portion, where most of the rays are blocked by the spheres, this results in a penumbra effect at the borders of the particle with material deposition fading out.
To demonstrate the effectiveness of the simulation, a comparison is provided between a real gold-platinum Janus nanoparticle measured in an atomic force microscope (AFM), depicted in Fig. 2.5(b), and the corresponding simulation of the same particle, depicted in Fig. 2.5(c). While it is evident that the flanks of both particles differ, the height profiles of the particles along the longer axis shown in (d) match quite well. The differences of the flanks may be attributed to the real particle minimizing surface energies and tensions, which leads to a selective grain growth. This phenomenon leads to a rounder shape of the central portion of the particle, as observable in Fig. 2.5(b).
All of the above-described is implemented into the ray-tracing simulation program *Lithogram*. This program was originally developed in [51] and was massively modified in the course of this thesis to improve the algorithm and to adapt it to the requirements of the Stöber mask modification process. Via the tool *EELS-Simulator* that was also developed during the course of this thesis, these simulated particles can further be transferred into the *MNPBEM-toolbox* [63] as an input.
This toolbox was initially published in 2012 and updated in 2017. It allows to simulate the plasmonic behavior of metal nanoparticles, as one could observe it by STEM-EELS plasmonic mapping. It is intended to solve Maxwell's equations for typical dielectric environments, i.e. the vacuum necessary for EELS, where nanoparticles with homogeneous and isotropic dielectric functions are separated by abrupt interfaces. Hence, the abbreviation *MNPBEM* stands for **M**etallic **N**ano**P**article **B**oundary **E**lement **M**ethod and describes the simulation method. Over the years, the MNPBEM-toolbox has become one of the preferred tools for simulating EEL signals for plasmonic particles and is cited over a thousand times in recent literature.

Both, the ray-tracing software *Lithogram* as well as the software to implement the nanoparticles into the MNPBEM-toolbox, the *EELS-Simulator*, are provided on a USB drive attached to the back cover of this thesis.

Chapter 3

Transmission electron microscopy (TEM)

This chapter aims to explain the principles of transmission electron microscopy and related analytical characterization techniques employed in this thesis. Particular emphasis is placed on electron energy-loss spectroscopy, which is the main analytical technique this thesis seeks to improve by the proposed deconvolution method.

3.1 The transmission electron microscope

The transmission electron microscope (TEM) utilizes electrons that pass through the specimen with minimal interaction and hence experience only little to no elastic or inelastic scatter events. In TEM, the specimen must be exceptionally thin (< 100 nm) and the electrons must possess a sufficiently high energy of usually 30 – 300 keV to guarantee electron transparency. The TEM employed in this thesis, the *JEOL JEM-ARM200F*, which is schematically depicted in Fig. 3.1, has an optimized energy range of 60 – 200 keV.
Modern transmission electron microscopes typically feature two primary operating modes, the *TEM mode* and the *scanning-TEM (STEM) mode*. In both modes, the beam is formed by a system of electromagnetic lenses, referred to as the first and second condenser lenses and is projected through an aperture. However, systems employing more than these two condenser lenses are also possible.
Fundamentally, it is impossible to create perfect rotationally symmetrical electromagnetic lenses in particle physics. This results in beam shapes that are inherently subject to spherical aberrations and aberrations of higher orders. To overcome these limitations, a sophisticated electron optical system is employed, the C_s-corrector, combining multiple adapter and transfer lenses with two hexapole lenses. This system corrects for spherical aberrations (denoted as C_s), but at the cost of introducing six-fold astigmatism and higher-order aberrations [64–66]. These higher order lens errors, however, are of minor impact compared to the spherical aberrations. Therefore, employing a C_s-corrector, like the TEM used in this thesis, allows for smaller probe sizes, consequently enhancing the image resolution.
In TEM mode, a parallel electron beam illuminates a large area of the specimen. The image of this specimen is then produced in the image plane of the objective lens followed by intermediate and projector lenses and finally captured by a detector. In STEM mode, the beam is focused to form a convergent probe that samples the specimen in a raster pattern. In contrast to TEM mode, where all pixels of the image are captured in parallel, the image in STEM mode consists of a sequence of point measurements that constitute the pixels of the image. Due to the difference in image acquisition, both modes provide distinct characterization techniques, enabling the resolution of various specimen characteristics.
For example, as TEM employs a parallel incident beam, the Bragg diffraction enhances or decreases the image intensity of grains with a specific crystalline orientation. Therefore, TEM readily allows for the distinction of different crystalline orientations. By orienting the specimen in a certain crystalline orientation, individual domains and grain boundaries can be analyzed in detail. Further, selected diffraction spots, which correspond to a specific crystalline orientation, can be blocked in the back focal plane of the objective lens. As a consequence, grains with this crystalline orientation appear dark

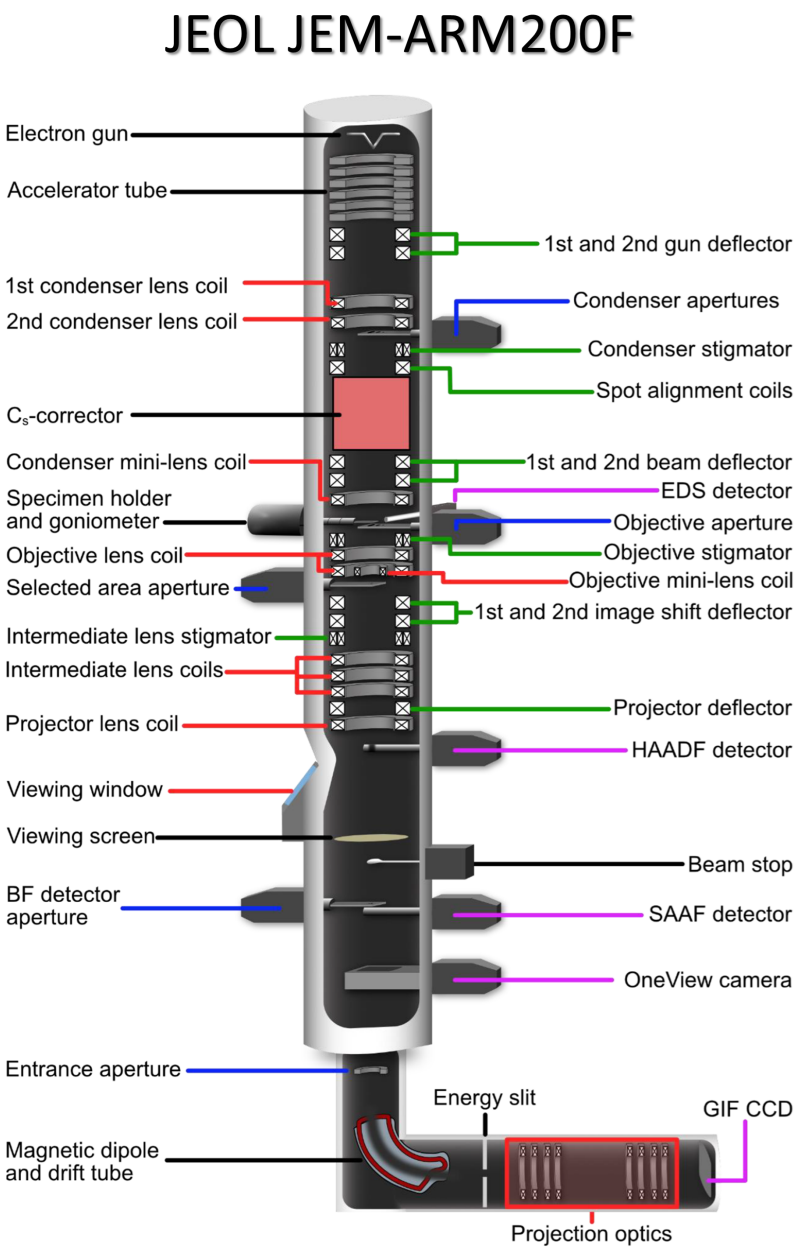

Fig. 3.1: Schematic illustration of the JEOS-JEM-ARM200F transmission electron microscope with a $90°$-post-column *Gatan imaging filter system (GIF) Quantum ER* spectrometer attached (from [67], further descriptions about the microscope are found there as well). In TEM mode, the specimen is illuminated by a parallel beam, and in STEM mode, the beam is focused into a sharp probe that is raster-scanned over the specimen using beam deflection coils. Notably, the electron microscope employed in this study features a C_s-corrector for STEM-mode, which utilizes a system comprising adapter lenses, transfer lenses, and hexapole lenses to minimize higher-order aberrations in the electron beam shape. In TEM, the parallel beam is then focused by the imaging system, comprising pre- and post-field objective lenses and is finally projected onto a detector, which measures the image. In contrast, STEM images are composed of pixels that represent the measured intensity of a given position in the raster-pattern. This intensity is often measured by annular dark field detectors, such as the one displayed in Fig. 3.2, which capture the beam electrons scattered at an angle and leave the optical axis of the direct beam path. For EELS measurements, the beam is further directed into the GIF spectrometer attached to the end of the column. This spectrometer is further explained in Sec. 3.2.1.

in the resulting image. The likelihood of scattering events increases with higher atomic numbers of the specimen material and its thickness, beside other factors [5, 27]. Consequently, the intensity in a bright-field TEM image decreases as beam electrons scatter out of the optical axis of the direct beam path, enabling the differentiation of structures. The term *bright-field* refers to an image formation technique that collects incident beam electrons transmitting through the specimen without deviating much from the optical axis of the direct beam path [3]. This is in contrast to *dark-field* imaging, which explicitly uses scattered beam electrons that deviate from the optical axis [3].
In STEM, the beam only interacts with a localized region of the specimen, corresponding to the spot size on the specimen. This enables to link signals to their point of origin, whereas in TEM mode, spatial information is convolved with contributions from all other specimen positions due to scattering. Consequently, STEM offers precisely localized information in terms of signal collection, but its pixel-by-pixel image formation process makes it slower. To compensate for the slower acquisition, often a lower number of pixels per image is chosen or, alternatively, the pixel dwell time is reduced. However, this results in images that are more susceptible to noise, as either the sampling of features is performed by less pixels or the signal strength per pixel is diminished – both approaches result in a reduced image statistics.
In STEM, differences in atomic number and thickness variations are observable as well, for the same reasons as were explained for TEM imaging. However, due to the ability to correlate signal strength to specimen position, STEM enables the measurement of signals of different scattering solid angles using annular detectors. Consequently, multiple types of information can be extracted simultaneously using bright-field and dark-field imaging techniques [1, 3]. This enables a further quantitative investigation of the signal to gain insight into the interactions within the specimen. The following sections describe the key STEM techniques employed in this thesis.

3.1.1 Annular dark-field imaging (ADF)

Annular dark-field (ADF) imaging is a technique widely used in STEM. The signal is acquired using an annular detector located around the electron beam, which detects electrons scattered out of the direct beam (see Fig. 3.2). As only scattered electrons are detected, ADF imaging offers the advantage of being employed simultaneously with other techniques, such as bright-field imaging or EELS, that use the direct beam. Since ADF detectors collect electrons scattered at an angle, the primary contrast mechanism again relates to the atomic number of specimen constituents and their projected thickness [5, 68], as explained in the last section. Consequently, materials with higher atomic numbers or thicker regions of the specimen generate higher image intensity in the dark field compared to lighter or thinner materials. In this thesis, gold and platinum nanostructures are investigated for their plasmonic resonances. Due to the high atomic number of gold and platinum compared to the silicon substrate, ADF contrasts are generally high in such specimens, making ADF an adequate tool for locating these structures. Furthermore, this technique enables the visualization of thickness gradients in the silicon substrate, allowing for the qualitative distinction between thinner and thicker regions, which is crucial for subsequent EELS characterization.

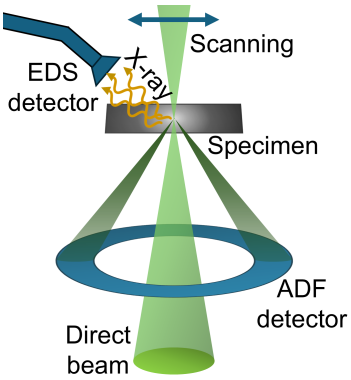

Fig. 3.2: Schematic illustration (according to [5]) of the annular dark field (ADF) and energy-dispersive X-ray spectroscopy (EDS) detector arrangement. Note that no pre- and post-specimen lenses are displayed in the sketch. In STEM mode, the direct beam (light green) is scanned across the specimen (grey) in a raster pattern. As the beam electrons interact with the specimen, some electrons of the specimen's atoms are excited to higher energy states. Upon relaxing, they emit characteristic X-rays (yellow) that can be detected by the EDS detector. Due to scattering, the beam electrons disperse into various solid angles, where the lowest angles relative to the incident direction contribute to the direct beam intensity. These electrons can be further analyzed using EELS. The electrons experiencing higher scattering angles (dark green) are detected by the ADF detector.

3.1.2 Energy dispersive X-ray spectroscopy (EDS)

Energy-dispersive X-ray spectroscopy (EDS) is an analytical technique commonly used in TEM and STEM mode to characterize the elemental composition of structures of interest. It relies on inelastic electron-matter interactions within the specimen, which result in X-rays of characteristic energies that can be assigned to specific elements. A good overview of the technique is given in [5, 27] and a schematic of the experimental setup for STEM is provided in Fig. 3.2. There, it is illustrated that the EDS detector is moved close to the specimen to maximize the solid angle at which characteristic X-rays can be detected. Since the probe position is precisely known in STEM, a quantitative analysis of the X-ray spectrum reveals the material composition of structures at each pixel leading to elemental maps. By assigning different colors to each element, this method provides a quick and comprehensive overview of the material composition.

3.2 Electron energy-loss spectroscopy (EELS)

One of the key analytical techniques in transmission electron microscopy is *electron energy-loss spectroscopy (EELS)*, which resolves the energy losses of the electrons that have passed through and interacted with a specimen. By employing this technique, an intensity spectrum is recorded as a function of the energy-loss of the beam electrons. Often, these losses are directly related to inelastic scattering events with the specimen material. Since these interactions lead to specific energy-losses, this technique enables to identify the corresponding interactions. This enables the deduction of elemental composition, bonding states, and resonant interactions of the specimen with light, for example.
As this thesis deals with the noises expected in EELS and aims to improve related post-processing deconvolution methods, further explanations are provided subsequently.

3.2.1 Measurement technique for EELS

All EELS measurements performed in this work were conducted using a so-called $90°$-post-column energy filter mounted underneath the (S)TEM column, as depicted in Fig. 3.1. For EELS, all detectors that sit on the optical axis of the (S)TEM and block the direct beam are retracted. The post-specimen electron wave is projected by means of the objective lens and a system of imaging lenses onto a magnetic prism deflecting the beam by $90°$ via the Lorentz force. As the Lorentz force depends on the velocity of particles, different deflection angles occur between electrons that have experienced different energy-losses in the specimen due to elastic scattering. This can be exploited through the use of *energy-filtered TEM spectral imaging (EFTEM-SI)* or *STEM spectral imaging (STEM-SI)* techniques. In the experimental setup used, both techniques are realized in a *Gatan imaging filter system (GIF) Quantum ER*, which is well-described in [69] and depicted in Fig. 3.3(a). To enable imaging, the GIF column contains a complex set of quadrupole and hexapole lenses. These lenses either project the incident beam electrons as a spectrum, in the case of STEM-SI, or as an image, for EFTEM-SI, onto the EELS detector. For the latter case of EFTEM-SI, the image is only formed from incident beam electrons that have passed a slit in the energy dispersive plane of the spectrometer, thereby filtering for electrons having experienced a specific range of energy-losses. A good overview on both techniques is found in [27, 70, 71]. However, a brief summery is provided subsequently for the understanding of this thesis.

EFTEM-SI describes an EELS measurement in TEM-mode, where a broad electron beam with homogeneous intensity distribution is illuminating the specimen. A slit is inserted in the beam path of the GIF, which selects the electrons of a desired energy range and discards the others. To collect an image for several consequent energy-losses, a drift-tube voltage in the spectrometer is incremented step by step, such that the selected loss-energy changes accordingly. As a result, only those electrons with the selected energy range contribute to the image formation on a detector at the end of the GIF column. Measuring with this technique results in a 3D data cube, consisting of multiple 2D maps of the structure at different energy-losses (see Fig. 3.3(b)). These maps are subsequently concatenated into a third dimension, providing spectral information about the energy-losses. Since this technique acquires all electrons of the same energy-loss for the entire image in parallel, many pixels contribute to the image formation here. This results in a high sampling of lateral features with many pixels. In contrast, the spectral resolution is severely limited by the width of the energy selective slit and the dispersion of the spectrometer (in the order of 1 – 5 eV) resulting in a low sampling of spectral features. EFTEM-SI is therefore the preferred method when investigating larger sample areas. It is also preferred for beam sensitive materials, since the beam can easily be broadened reducing its current density.

STEM-SI describes an EELS measurement in STEM-mode. In contrast to EFTEM-SI, the energy-filter slit is removed. At any given specimen position, all electrons are dispersed by their respective energy-losses and are recorded simultaneously as a spectrum by the detector. Multiple EEL spectra at different specimen position can spatially be concatenated to form a 3D data cube (see Fig. 3.3(c)), the so-called *EELS map*. Here, the sampling of spectral features is relatively high, as many pixel columns contribute to the formation of the spectrum. In contrast, the spatial sampling is often limited due to time constraints of the overall acquisition process, which is inherently slow for STEM measurements, as explained in the last section. Spacial sampling is therefore rather low compared to EFTEM-SI. The time constraints usually

comes from the accumulation of contamination on top of the specimen. These result in undesirable distortions of the EEL signal for increasing acquisition times [73]. Also, beam damage may play a role for sensitive materials since the beam is quite intense due to the requirement of a tiny probe size. Further relevant factors limiting acquisition times are the increasing energy drifts and instabilities of the electron beam. Therefore, data cubes rarely contain more than 100×100 spectra in the lateral dimensions. Due to the low spatial sampling of feature, EELS maps acquired with this technique are particularly susceptible to noise, which obscures measurements and makes proper analysis particularly challenging to conduct. Especially for finer features of interest, which consist of very few data points, this is a challenging problem, as they may completely be hidden within the noise. However, the increased spectral sampling makes STEM-SI the preferred choice for measuring subtle spectral changes, which are necessary for determining chemical bonding states or optical properties via Kramers-Kronig analysis.

This thesis primarily focuses on EELS measurements conducted in STEM-mode, i.e. STEM-EELS and STEM-SI measurements, which are subsequently referred to as *EELS maps*.

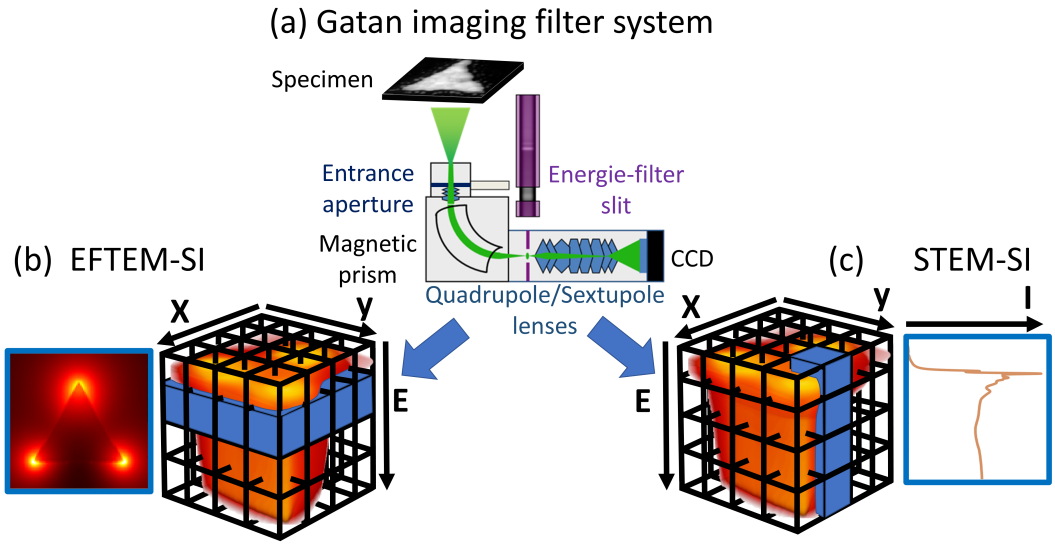

Fig. 3.3: **(a)** Schematic of the *Gatan imaging filter (GIF)* system (from [72]). The transmitted beam (green) from the specimen passes through the entrance aperture (a width of 5 mm was used in this thesis) and is dispersed into different loss-energies by a magnetic prism. In EFTEM-SI, a precise drift tube voltage is applied to the beam electrons before passing the prism. These electrons are subsequently filtered by the energy slit (purple), which selects for the electrons of a specific energy range while discarding all others. By tuning the drift tube voltage, a slight increase in beam electron velocity is achieved, which results in a change of deflection angle. Thereby, electrons having experienced a different energy-loss are selected by the energy slit. This results in energy-filtered images, which are sequentially recorded by a CCD sensor (black) after being magnified and focused by a lens system (blue). In STEM-SI, instead of focusing a whole image, only the small beam is transmitted through the entrance aperture, dispersed by the magnetic prism, and recorded as a spectrum on the detector as a sequence of beam positions. In both cases, **(b)** EFTEM-SI and **(c)** STEM-SI, a 3D data cube is formed as a result, which consists of multiple voxels. The black grid shows the individual voxels of the low-loss EELS data cube of a simulated triangular gold nanoparticle from the MNPBEM-toolbox [63]. It can be seen that in (a) EFTEM-SI, the data cube is acquired as a sequence of concatenated slices (blue x-y slice). Red and yellow colors indicate the lower and higher amplitude regions of the loss intensity. Since the data cube in (b) STEM-SI is generated using a focused electron beam, which is scanned in x-y-direction across the specimen, the data cube is acquired as a sequence of laterally merged EEL spectra, represented by the blue voxel stack, where the intensities are given as counts in a spectrum. Both the EELS slice and EEL spectrum are shown as examples alongside their respective data cubes.

3.2.2 Scintillation based-CCD detectors

The *US1000FT-XP 2* employed in the GIF that was used for the measurements of this thesis is a so-called *scintillation-based CCD detector*. This type of detector is frequently used in EELS and is schematically depicted in Fig. 3.4. In general, such a detector composes of three main layers, a scintillation layer, a fiber optics, and a CCD sensor, as shown in Fig. 3.4(a), all of which are glued together.
Upon impact of incident beam electrons, the scintillation layer generates a multitude of photons, typically in the order of several hundreds to thousands of photons per incident beam electron. These photons are then guided by the fiber optics to the CCD sensor. In this setup, the fiber optics ensures sharp images by effectively coupling the scintillation layer to the CCD sensor. It further shields the CCD from bremsstrahlung created in the scintillation layer due to the deceleration of incident beam electrons.
In the CCD sensor, the photons create charge carriers. These are subsequently read-out by the analogue-to-digital converter (ADC), which converts the signal into counts that are output as a result. Since several counts are registered per incident beam electron hitting the scintillation layer, the measured signal from the CCD is amplified by a *gain factor*, which is in the order of the order of 10 – 20, as shown in the publication in Appendix A. It is apparent that this number is drastically reduced compared to the initial number of generated photons in the scintillation layer. The reason for this discrepancy is that many photons are lost through internal reflections and light scattering, such that they do not even reach the fiber optics in the first place let alone reach the CCD sensor.
CCD sensors consist of an array of pixels that are construed as metal–oxide–semiconductor (MOS) capacitors [74]. As photons with sufficient energy hit the pixel array, electron-hole pairs form as a result of the photoelectric effect. This generation of charge carriers is largely proportional to the light intensity. However, not every photon is transformed into such charge carriers and therefore a proportionality factor is introduced, which is called the *quantum efficiency* [75]. By applying a voltage to the capacitors, charge

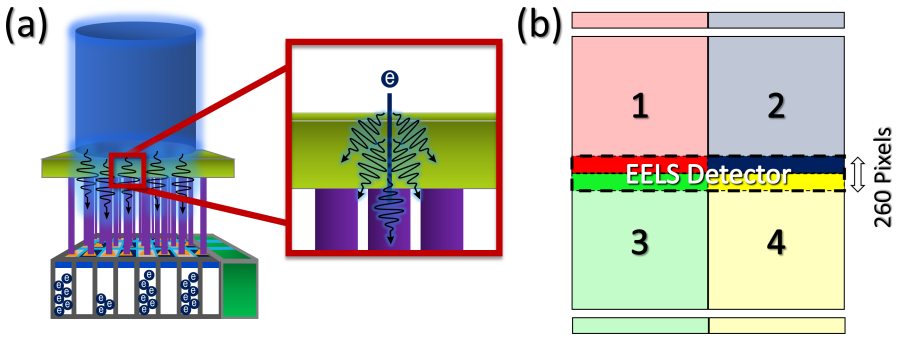

Fig. 3.4: **(a)** Schematic of the scintillation-based detector (from the publication in Appendix A) with the incident electron beam (blue), the fluorescent scintillation layer (green) generating optical photons, and the fiber optic (purple) connecting the fluorescence layer to the CCD sensor. The CCD reconverts the optical photons in charge carriers and with the analog-digital-converter (dark green) into counts. The red box shall point out, that several photons are generated per incident electron and spread across the fluorescence layer. **(b)** Schematic of the US1000FT-XP 2 detector (from the publication in Appendix B). Four distinct detector segments can be identified, labeled 1 – 4, of which only a narrow portion is used for EEL signal detection, as indicated by the colored boxes in the middle of the detector segments. The shaded areas are discarded. The inner region is 260×2048 pixels. All rows of a detector column get summed up to form EEL channels. The detector segments are connected to their respective analogue-to-digital converters (ADC), indicated by the small boxes near the detector.

carriers are separated by the resulting electric field. Subsequently, the electrons are trapped within a potential well due to an insulating layer blocking the path to the anode, while the holes are depleted from that very region due to the applied electrical field, reducing the probability of recombination[74, 75]. Since the potential wells are finite, some of the trapped electrons may diffuse to neighboring pixels. This results in a spreading-out of the signal recorded in each and every pixel of the array. Typically, this effect is modeled by the convolution of a measured signal with a detector *point spread function (PSF)* [76]. For scintillation-based CCD detectors, this PSF also incorporates the spreading-out of the signal due to scattering processes in the scintillation layer and the transport within the fiber optics.
Eventually, the charge carriers in the pixel array are transported via shift registers to the ADC, which converts the charges into an output voltage that translates into a certain number of counts. To optimally use the detectors bandwidth, it is beneficial to only have a positive number of counts [75]. Therefore, a DC offset voltage, the so-called *bias voltage*, is applied to the pixels to ensure positive values during readout [75]. Further information about the functioning of CCD sensors are found as well in [74, 75].
To increase readout speeds, the *US1000FT-XP 2* detector is composed of four individual detector segments, each having a separate ADC, as schematically shown in Fig. 3.4(b). EEL signals are exclusively measured in the middle area of these quadrants while all other pixel values outside of this region are discarded. This helps optimizing signal-to-noise ratios and further optimizes readout times.
Since every pixel is subject to readout noise, as a consequence of the circuitry of the ADC, discarding the unused pixels helps to reduce the overall noise level of the spectrum. This is because eventually, the pixels of the EELS region are summed up column-wise to create an EEL spectrum.
The present segmentation also allows for *Dual-EELS* measurements. In Dual-EELS, a first part of the spectrum, usually the ZLP region including the low-energy losses is projected at the upper half of the EELS region (quadrants 1 and 2 of Fig. 3.4(b)), while typically a part of the high-loss spectrum, including, for example, core-loss edges of specific elements, is projected onto the lower half of the EELS region (quadrants 3 and 4 of Fig. 3.4(b)). Therefore, this technique enables the simultaneous acquisition of two different parts of the spectrum with different exposure times on a single detector.
The different parts of the EEL spectrum, including the most significant features, are subject of the next section.

3.2.3 The features of EEL spectra

The most straightforward way to understand EELS is to examine an exemplary EEL spectrum (see Fig. 3.5) and systematically analyze the scattering processes that contribute to specific energy intervals and the corresponding peaks within them.

The energy gain region ($E < 0$ eV) is situated immediately adjacent to the zero-loss peak on the negative side of the loss spectrum, which corresponds to energy gains. The energy gains of the beam electrons are primarily caused by phonon interactions [77], which are quantized lattice vibrations. As a result, the energy gain is typically confined to a narrow interval between zero and a few negative meV. In general, energy gains are of minor interest and are usually superimposed by and obscured within the intense and broad zero-loss peak in most microscopes [77]. Consequently, the energy gain interval preceding the zero-loss peak is dominated by the tail of the ZLP plus detector noise.

The zero-loss-peak (ZLP)($E = 0$) is the strongest peak to encounter in the EEL spectrum of any material (see Fig. 3.5). It contains all electrons that were transmitted or elastically scattered without energy-loss. Theoretically, the ZLP would be expected to have a delta peak shape, but due to quantum uncertainty and thermal energies, the electrons emitted by the electron gun have a range of kinetic energies. Since the transmission electron microscope used in this thesis employs a *cold field emission gun (cFEG)*, the ZLP intensity distribution can be modeled using the Fowler-Nordheim equation, which provides the distribution of the beam current of a cold field emitter j_{FEG} as a function of the electron energies E. It equates as [5]:

$$\frac{dj_{\mathrm{FEG}}}{dE} = \frac{4\pi\, m\, e^3}{h^3}\, d^2 \exp\left(-\frac{2\, \upsilon(y)\ \phi}{3\, t(y)\ d}\right) \cdot \frac{\exp\left(\frac{E}{d}\right)}{1+\exp\left(\frac{E}{k_B T}\right)}\,, \tag{3.1}$$

$$\text{with } d = \frac{h\, F}{4\pi\, t(y)\, \sqrt{2\, m\, e\, \phi^3}}\,,$$

where m is the mass of the electron, e is the charge of the electron, h is the Planck constant, d is a measure for the internal energy of the material dependent on the enhanced extraction voltage F at the sharp emitter tip, k_B is the Boltzmann constant, and T is the temperature of the emitter. The work function of the emitter material is given as ϕ, y is the relative decrease of the potential energy due to the applied field, and $\upsilon(y)$ and $t(y)$ are slowly varying functions describing correction factors for the Schottky-Nordheim barrier, which hinders the electrons to escape the tip of the cFEG.
This energy characteristic of the probe and further distortions induced by misalignment and residual lens aberrations of the spectrometer's electron optics (see Fig. 3.3(a)) result in an asymmetrically broadened peak, which is observable in Fig. 3.5(a). Subsequently upon detection, this ZLP is also subject to broadening by the detector point spread function, as explained in the last section.
Having a good approximation of the ZLP is important for post-processing techniques, since the ZLP must be removed prior to for deconvolution (see the publication in Appendix D). Methods of approximating the ZLP of a measurement include fitting some distribution functions [78–81] to the ZLP. Also approaches like mirroring its left-hand side ($\Delta E < 0$) to the right hand side ($\Delta E > 0$) have been employed, since the right-hand side contains valuable information that should not be removed. Further information about the precise modeling of the ZLP's intensity distribution can also be found in [5]. However, all of the above-explained contributions to the ZLP can altogether be measured in vacuum without specimen in the beam path. This vacuum ZLP measurement provides an easy way to capture the ZLP without specimen characteristics distorting it. In contrast, utilizing a Nordheim-Fowler fit leads to discrepancies to the actual ZLP that are observable in Fig. 3.5 and most likely result from the above-mentioned misalignments and residual lens aberrations of the spectrometer.
Therefore, the vacuum ZLP was always measured before and right after conducting the actual EELS measurements. In contrast to all the other methods to model the ZLP, the direct measurement of the vacuum ZLP provided the most reliable results for the experimental EELS setup employed in this thesis. To get a good signal statistics of the vacuum ZLP, several ZLPs are energy aligned and averaged. This vacuum ZLP may subsequently also be fitted to each of the specimen's spectra individually (by minimizing the *mean squared error* (MSE) as a measure for the distance between both curves) in order to subtract it from the spectrum. This procedure is necessary for deconvolution to avoid artifacts of the deconvolution results, as will be fully explained in the publication in Appendix D.

The low-loss region ($E \leq 50$ eV) of the EEL spectrum contains information about the inelastic scattering at phonons, inter- and intraband transitions, as well as the surface and bulk plasmonic peaks, most of which are superimposed to the tails of the ZLP. Notably, all data are convolved with the distribution of the vacuum zero-loss peak. As a result, all the signals are broadened, leading to a loss of spectral resolution. To remove this blur, deconvolution with the vacuum ZLP is necessary.
For very fast electrons, an additional energy-loss mechanism occurring in the low-loss region is worth mentioning: Cherenkov radiation [82–84]. As electrons travel through a material with a velocity higher than the phase velocity of light in that medium, Cherenkov radiation is emitted with the energy distribution:

$$\frac{d^2E}{dx\,d\omega} = \frac{q^2}{4\,\pi} \cdot \mu\,(\omega)\, \cdot x \cdot \omega \cdot \left(1 - \frac{c^2}{v^2\,n^2(\omega)}\right)\,, \tag{3.2}$$

where x is the unit length traveled, ω is the frequency of the emitted light, $\mu(\omega)$ is the permeability of the material, $n(\omega)$ is the index of refraction, q is the particle charge, v is the velocity of the incident electron, and c is the speed of light.
Cherenkov radiation is expected in the EELS measurements conducted in this thesis, since the silicon substrates used for carrying nanostructures exhibited a thickness of approximately 100 nm after the TEM preparation, as will be explained in the publication in Appendix D. Therefore, it is standing to reason that Cherenkov radiation is observed. Usually, the energy of Cherenkov radiation is below 10 eV [84].

The high-loss region ($E \geq 50$ eV) contains information about the elemental composition of the specimen and bonding states of its constituents, because the electron beam excites and ionizes atoms or molecules of the specimen material. The high-loss region also contains background signals from the plasmon tails, the X-ray continuum, and lower energy core-edges. These background signals can be subtracted using an inverse power law fit [27, 85]:

$$J\,(E) = A \cdot E^{-r}\,, \tag{3.3}$$

where A is a scaling coefficient, E is the loss-energy, and r is the slope exponent. Features of the high-loss region are also convolved with both the vacuum ZLP and the features in the low-loss energy range, particularly in thick specimens.

As a concise overview, the most important energy intervals and their respective characteristic interaction are listed in Tab. 3.1.

Interval/Feature	Energy range
Energy gain region	< 0 eV
ZLP	0 eV
Low-loss region	0 – 50 eV
Optical transitions	0.1 – 5 eV
Cherenkov radiation	< 10 eV
Surface plasmons	0.1 – 5 eV
Bulk plasmons	10 – 50 eV
High-loss region	>50 eV
Composition	> 50 eV
Bonding states	> 50 eV

Tab. 3.1: Table containing the most important energy intervals with their corresponding interactions. Since the intervals are used for structuring the EEL spectrum, these are indicated in bold.

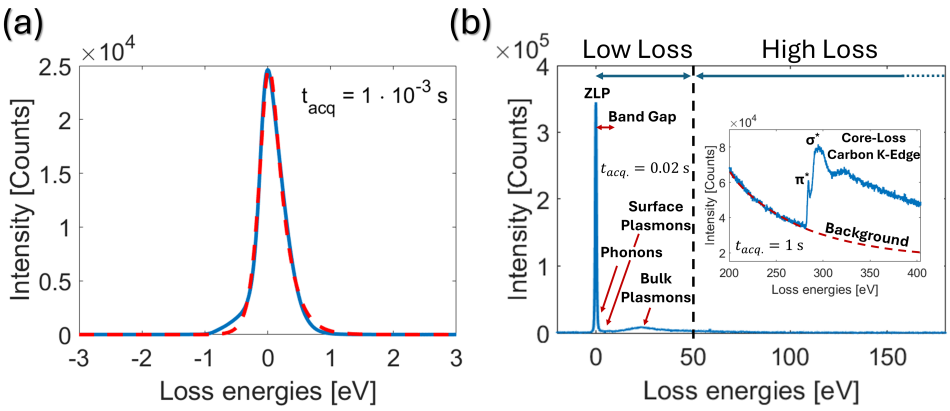

Fig. 3.5: **a)** Zero-loss peak (ZLP) measured in vacuum as an average across 30 individual measurements with an acquisition time of $t_{acq} = 1 \cdot 10^{-3}$ s per spectrum. It is apparent that the measured ZLP (blue line) is asymmetric and appears skewed to the left side. The reason for this is mainly given by the projection of the ZLP onto the detector by the spectrometer optics (see Fig. 3.3(a)), which induces a slight twist to the ZLP relative to the pixel array orientation, beside many other distortions (see publication in Appendix B for more information). Therefore, while the fundamentals of the ZLP may be described by the Nordheim-Fowler distribution in Eq. 3.2, fitting it (red dashed line) to the ZLP results in discrepancies between both curves that are particularly pronounced in the tails of the ZLP, which superimpose the band gap losses and surface plasmonic peaks. **b)** Measured EEL spectrum of a FeCo specimen contaminated with carbon, which was acquired using a Dual-EELS setup, as explained in the last section. The first spectrum, comprising the low-loss energies from 0 to 50 eV, was recorded with an acquisition time of $t_{acq.} = 0.02$ s. The second spectrum, shown as the inset, comprises part of the high-loss energies from 200 up to 400 eV and was recorded with an acquisition time of $t_{acq.} = 1$ s. Per convention, the EEL spectrum is distinguished into two parts: the low-loss region (< 50 eV), indicated by the vertical dotted line, and the high-loss region (> 50 eV). In the low-loss region, the most intense peak is the zero-loss peak (ZLP). The tail of the ZLP superimposes the phonons (typically in the range of a few to a few hundred meV) and the optical transitions (typically $0.1 - 5$ eV). Surface plasmons are typically found in the range of a few eV, while bulk plasmons are found in the range of $10 - 50$ eV. Usually, the bulk plasmonic features are second in intensity right after the ZLP. In the high-loss region, information is found about the chemical composition, the bonding states, and about the inner electrons of the atoms. In this example, the K-edge of carbon is shown. Within this structure, finer details are observed, where the peak at 284 eV is linked to the π^* molecular orbital and the broader peak at 295 eV can be attributed to the σ^* orbital. The overall spectrum appears similar to the results in [86], indicating a thin layer of amorphous carbon. It is apparent that the carbon K-edge is situated on top of a power-law background (see Eq. 3.3), which typically forms from the plasmon tails, the X-ray continuum, or lower energy core edges.

Chapter 4

The current state-of-the-art

Throughout the last chapters, it was outlined that transmission electron microscopy and the EELS technique are fundamental tools in researching various aspects of nano-materials and biological specimen. It was further described that these kinds of measurements are often hard or even impossible to conduct because of the beam sensitivity of such materials and a poor imaging statistics as a result thereof. This, in turn, leads to measurements that are drowned in noise and become uninterpretable.
This thesis aims at significantly improving such measurements by utilizing their inherent noise statistics in order to restore the underlying signals. To understand the significance of the advancements presented in this thesis, it is necessary to define the current state-of-the-art for the main developments of this work. The following sections are intended to provide a brief introduction to the currently used noise models in transmission electron microscopy and EELS. In defining both, it will become apparent that the currently used mathematical models are insufficient for this purpose and do not adequately describe the actual occurring noises.
Further, an introduction of the Richardson-Lucy deconvolution algorithm will be given, which has seen widespread adoption in EELS [27]. However, since this algorithm relies on these imprecise noise models, it is limited in its ability to improve actual EELS measurements.
It is therefore the task of the following sections to highlight the disadvantages of the current models and deconvolution algorithms in order to provide, within the publications, new approaches to overcome these issues.

4.1 Noise models in TEM

Every measurement is subject to noise. Cases in which noise becomes dominant commonly occur in measurements with limited acquisition time due to sensitive materials or short-lived dynamic processes. In these cases, there are too few interactions to properly determine important characteristics or to distinguish changes. This problem is often exacerbated when features of interest are sampled with only a few data points in a measurement. This often occurs in spectroscopic measurements, such as EELS (see the explanation in Sec. 3.2.1). Due to these limitations, noise can obscure measurements to the extent that they become uninterpretable to the eye.
Having capable post-processing techniques at hand to reduce noise may therefore be a game changer for such experiments, as these techniques would allow to evaluate interactions that previously were impossible to observe. These methods, however, require a precise noise model as their foundation in order to distinguish signal from noise.
Noise models currently used in transmission electron microscopy and especially in EELS only account for part of the noise and are mainly limited to Poisson noises arising from the quantized nature of electrons. This simplistic description, however, does neither account for interactions in the detector, altering the image statistics, nor for the readout noises.
In the following sections, the fundamental noise statistics occurring in EELS will briefly be introduced and the shortcomings of current noise models will be discussed.

4.1.1 Noise fundamentals

Noise follows strict statistical principles that one can utilize to describe it. This section deals with the most common sorts of noise – Gaussian and Poisson noise, their statistical distribution and their origin.

Gaussian noise

The normal distribution or Gaussian noise, named after Carl Friedrich Gauss, has the probability density function [87]:

$$\mathcal{N}(n) = \frac{1}{\sigma\sqrt{2\pi}} \exp\left\{-\frac{(n-\mu)^2}{2\sigma^2}\right\} , \tag{4.1}$$

which is described by μ the mean value of a signal and σ its standard deviation, wherein n represents a number of counts to which a probability is assigned. This means that any measurement of a variable influenced by this kind of noise will result in a value that is distributed most likely in the interval of σ around the *true* mean value of a signal μ. The special case, in which series of measurements are statistically independent and identically distributed at any given pair of times, is called white Gaussian noise. These properties make Gaussian noise an additive noise, which means that it is uniformly distributed and independent of the signal strength. It thus forms a background to the signal. In modern experimental setups, this type of noise is often induced by CCD sensor readouts as a consequence of the electrical circuitry and the analogue-to-digital converters (ADC) that transform charge carriers in the CCD pixels into digital counts. Gaussian readout noise is therefore also encountered in presently used TEM detectors [27, 88].

Poisson noise

Poisson noise, named after the mathematician Siméon Denis Poisson, originates in the discrete nature of charges and photons. The Poisson distribution is defined as [89, 90]:

$$\mathcal{P}(S = n) = \frac{\hat{S}^n\, e^{-\hat{S}}}{n!} . \tag{4.2}$$

In contrast to Gaussian noise, this probability distribution depends on the expected number of counts of the signal $\hat{S}$. It assigns a probability to measuring a certain number of counts $n \in \mathbb{N}_0$ having the signal S. An important characteristic of the Poisson distribution is that the expected number of counts of the signal $\hat{S}$ equals the variance σ^2 of the distribution. This means that the Poisson noise is directly incorporated into the signal, as it depends on its strength. It is therefore fundamentally different from Gaussian noise, which is independent of the signal. In the case of only a few counts, both statistics differ significantly, however, in the case of a higher number of counts $\hat{S} > 40$, the shape of the Poisson distribution approaches that of a Gaussian.

4.1.2 Noises in TEM imaging

In the context of measuring signals on a CCD detector, the signal is typically subject to Poisson noise arising from the quantized nature of photons or electrons. Additionally, the measurement process on a detector introduces Gaussian readout noise. Consequently, the overall noise distribution is more accurately characterized by Poisson-Gaussian noise mixed statistics than by either of the individual components.
Due to heat generated during device operation, thermal excitons form, offsetting pixel values locally, even in the absence of incoming signals. This phenomenon can be described by so-called *dark currents* that increase with time. Consequently, a dark current background image ξ_{DF}, often called *dark frame*, with corresponding acquisition time must be subtracted from a measurement image ξ to correct these offsets for a dark-frame corrected measurement $\xi_{DF,Corr}$, which is given as:

$$\xi_{DF,Corr} = \xi - \xi_{DF} \ . \tag{4.3}$$

Specifically in scintillation-based CCD detectors that are often employed in electron microscopy, gain factors alter the noise statistics significantly. As explained in Sec. 3.2.2, these gains are primarily introduced by the scintillation layer that converts incident beam electrons to multiple photons. Subsequently, these gains are reduced by the fiber optics, as photons are lost due to internal scattering at the interfaces of the layers and due to waveguiding. Eventually, some of the photons are not detected by the CCD, due to limitations in quantum efficiency. Therefore, the pure Poisson noise statistics from Eq. 4.2 is not applicable, but is rather changed into a super-Poisson distribution. Additionally to this change in Poisson statistics, scintillation-based CCD have a significant point spread function, as explained in Sec. 3.2.2. In combination with the large gain, the PSF inevitably leads to correlations within the Poisson noise that must be regarded for a sufficient noise model. These changes of Poisson statistics are detailed in the publication in Appendix A.
Moreover, due to the manufacturing process of these multi-layered detectors, thickness variations in the scintillation layer may occur in addition to other inhomogeneities, thereby locally altering the gain and consequently creating image artifacts. This problem can be mitigated by employing a gain reference image ξ_{Ref}, which is typically acquired under conditions of homogeneous illumination, where the only variations to be expected come from the detector itself. This includes capturing a so called *bright frame* image ξ_{BF}, which is dark-frame corrected, and then divided by its corrected mean intensity level I. Therefore, the gain reference ξ_{Ref} is given as:

$$\xi_{Ref} = \frac{\xi_{BF} - \xi_{DF}}{I} \ . \tag{4.4}$$

This gain reference captures all of these gain variations. By subsequently dividing acquired images by such a gain reference ξ_{Ref}, any artifacts due to sensitivity variations of the CCD are removed from the measurement:

$$\xi_{Corr} = \frac{\xi - \xi_{DF}}{\xi_{ref}} \ . \tag{4.5}$$

However, it should be noted that this procedure does also result in a change of the image statistics.
Additional effects that alter the noise statistics are found in the pixels of the detection system, which

are limited in their ability to capture and retain charge carriers. This results in non-linearities occurring as the number of counts increases, primarily due to the difficulty of generating new charge carriers as the accumulation of charge within the pixel proceeds. This charge accumulation also facilitates charges escaping the very pixel they are stored in [76]. Such redistribution processes, however, broaden the PSF of the detector with increasing signal strength altering – again – the noise statistics.

4.1.3 Noises of EEL spectra

In the above paragraphs, it is laid-out that even for routine TEM images a rudimentary Poisson noise model may prove inadequate to describe the image statistics of the corrected images, as they are frequently employed in the domain of transmission electron microscopy.
In EELS, spectra are calculated by summing up pixel intensities from the columns of a CCD sensor. As an extension to single EEL spectra, EELS map measurements allow to probe specimen structures of interest in a raster pattern. Here, multiple spectra are successively acquired allowing to visualize the lateral distribution of energy-losses, i.e. the lateral distributions of plasmonic modes of a metal nanoparticle.
However, the conversion from 2D images into 1D spectra alters the signal statistics of EELS and EELS maps by partially reversing correlations of the signal caused by the detector PSF. This summation leads to a new detector PSF Ω_D for EEL spectra. Additionally, EEL signals are convolved by the energy distribution of the electron gun Ω_E and the projection of the magnetic lens system of the spectrometer onto the detector Ω_{STEM}.
It is evident that these convolution processes impose limitations on the energy resolution of the measurement. To address this, deconvolution is employed as a reversal of the convolution process to restore the original information.
Specifically in EELS map measurements, the sequential acquisition process of spectra permits beam current deviations and energy drifts between individual spectra, thereby increasing the noise level. Corrections for the deviations in beam current can be achieved through normalization of the spectra to the sum of all its counts. Realignments of the position of the ZLP are employed to address energy drifts. However, it should be noted that both of these methods alter the noise statistics of the measurement, as shown in the publication in Appendix B.
It is apparent that even a noise model adapted to the conditions of a scintillation-based CCD detector, as previously outlined, is significantly different from the noises that must be considered when conducting EELS and in particular EELS map measurements.
At this point, it may be recognized that defining a proper noise model involves considering many noise contributions and many interconnections thereof. In order to quantify the individual noise contributions, they must be regarded in isolation as good as possible to check the foundations of such a noise model. Eventually, such a noise model must be made applicable to users. It is not sufficient to merely identify each individual contribution to the noise; it is equally essential to facilitate quantifying these contributions on every detector. To make such a noise model applicable, a straightforward methodology for measuring the most significant noise parameters is essential. This methodology is outlined in the publication in Appendix B.

4.1.4 Current noise models employed in EELS

In view of the above, it can be deduced that no satisfactory noise model currently exists for either scintillation-based CCD detector images, or EEL spectra, let alone EELS maps. Nevertheless, several authors have described aspects of the aforementioned noise model [91–93].
Verbeeck and Bertoni [93] concentrate on the aspects of correlation of the noise, which is a consequence of the scattering processes in the scintillation layer and the associated gain. In their publication, they describe the implications of this for the likelihood approach, which constitutes an essential approach for deconvolution. Numerous findings and descriptions from Verbeeck and Bertoni have been incorporated into the publications of this thesis. Notably, the description of correlations by Pearson coefficients provided a significant foundation for incorporating them in a noise model. While these findings have offered valuable insight and form part of the foundation on which the present noise model is based, Verbeeck and Bertoni never demonstrated how to interconnect their findings. For instance, they speak of noise smoothing by a convolution with a PSF, but do not describe mathematically how to quantify this smoothing.
Meyer and Kirkland [91, 92] also investigated scintillation-based CCD detectors with respect to the scattering processes within the scintillation layer. They described the modulation transfer function (MTF) as well as the detective quantum efficiency (DQE). Conceptually, the MTF describes the spatial frequencies contributing to the image formation and is therefore a measure for the contrast of an imaging system. The MTF is closely related to the point spread function. The DQE, in contrast, describes a measure similar to the signal-to-noise ratio (SNR) but for the spatial frequencies contributing to the image. The approach of Meyer and Kirkland is purely based on statistics and Monte-Carlo simulations. While having a profound mathematical concept of the interactions of the beam electrons with the scintillation layer is very important for the understanding of the noise, the approach does not provide concepts on how to incorporate the results into an applicable noise model. The derived formulas lack being easily incorporated into a noise model that allows, for example, deconvolution. However, they describe the measurement of the MTF by employing the noise method, which involves analyzing the noise of homogeneously illuminated detectors. This method provides the basis for employing the auto-correlation to gather the Pearson coefficients of the noise, as shown in the publication in Appendix A.

It is evident that both descriptions of noise rather focus on statistical aspects of the noise, while neither Verbeeck and Bertoni nor Meyer and Kirkland aim to validate their findings by measurements. This, in turn, constitutes an important element of the approach adopted in the publications of this thesis. The present thesis adopts an integrated approach that combines statistics and experimental measurement, which facilitates the identification of the most significant noise contributions and their quantification. Consequently, the proposed noise model is well-suited for application to real measurements and extends existing noise models by also incorporating image corrections, such as the application of a gain reference to account for channel-to-channel gain variations [94], into the image statistics.
In practical measurements, several additional factors must also be considered. For instance, detector non-linearities and saturation effects become increasingly significant as the number of counts per pixel rises [95]. These issues are particularly relevant when analyzing high-intensity features, such as the ZLP. Appropriate non-linearity correction procedures can be applied to restore the original relative intensities between spectral features, which is essential for accurate quantitative EELS analysis. Furthermore,

energy drifts and beam intensity deviation can occur between the acquisition of individual spectra within an EELS map and must also be corrected to ensure data consistency.
A common characteristic of all these correction procedures is their reliance on empirical measurements to characterize detector-related effects. However, the process of determining these corrections introduces its own uncertainties, which must be quantified using statistical methods. These uncertainties significantly alter the noise characteristics of the acquired data. By adopting an integrated approach, it becomes possible to both mathematically describe and experimentally assess these uncertainties. This, in turn, enables the development of improved correction strategies through the implementation of novel methods, which are proposed in the publications of this thesis.

4.2 Deconvolution techniques employed in EELS

In the following, the two main deconvolution techniques currently used in EELS, the Fourier-ratio method and the Richardson-Lucy algorithm, are described. Although the Fourier-ratio method does not incorporate any noise statistics, it is the simplest and most direct form of deconvolution and therefore serves as an easy introduction into the topic. The drawback of this method is directly related to the lack of noise incorporation, which is why this method is very limited in its application. For a reader without a mathematical background in the art of deconvolution, the relationship between noise and insufficient deconvolution may be unclear. Therefore, this section explains how noise affects deconvolution.
As the second, and by far most prominent, deconvolution method employed in EELS, this section introduces the Richardson-Lucy algorithm. Unlike the Fourier-ratio deconvolution, which does not depend on any noise statistics, the Richardson-Lucy algorithm is deeply embedded in (pure) Poisson noise statistics, from which it is directly derived.
It is therefore readily apparent from the last section that both deconvolution methods fail to incorporate the real noise statistics faced in EELS. As a consequence, both methods tend to diverge before reaching their full potential, limiting their success in enhancing EELS measurements.

4.2.1 Fourier-ratio method

The *Fourier-ratio method (FR)*, or inverse filtering, provides the easiest approach to deconvolution. All energy-losses of an EEL spectrum are measured using the same probe, the vacuum ZLP, as explained in Sec. 3.2.3. Hence, the measured spectrum $\xi(E)$ appears as a convolution between the *true* underlying spectrum $\hat{S}(E)$ and the vacuum ZLP $\Omega(E)$. According to the convolution theorem, this convolution can be described as a simple multiplication in Fourier space:

$$\begin{aligned} \xi(E) &= \Omega(E) \otimes \hat{S}(E) \\ &= \mathcal{F}^{-1}\left\{\mathcal{F}\left[\Omega(E)\right] \cdot \mathcal{F}\left[\hat{S}(E)\right]\right\}, \end{aligned} \tag{4.6}$$

where $\otimes$ denotes the convolution operator, $\mathcal{F}$ denotes the Fourier transform, and $\mathcal{F}^{-1}$ its inverse. Rearranging yields the direct deconvolution procedure of the Fourier-ratio method [27]:

$$\begin{aligned} & \mathcal{F}\big[\xi\,(E)\,\big] = \mathcal{F}\big[\Omega\,(E)\,\big] \cdot \mathcal{F}\big[\hat{S}\,(E)\,\big] \\ \Rightarrow \quad & \xi\,(\omega) \;=\; \Omega\,(\omega) \;\cdot\; \hat{S}\,(\omega) \\ \Rightarrow \quad & \hat{S}\,(E) \;=\; \mathcal{F}^{-1}\left[\frac{\xi\,(\omega)}{\Omega\,(\omega)}\right] \quad , \end{aligned} \tag{4.7}$$

where ω describes the frequencies of the EEL spectrum in Fourier space. Theoretically, this deconvolution method would eliminate the energy distribution of the vacuum ZLP, including its asymmetries and tails, from the measured data [96]. As a consequence, this operation should yield a spectrum with perfect energy resolution, if there was no noise $N(E)$ in the spectrum. In practice, however, noise is an inherent property of the measurement. Hence, the above formula needs to be rewritten:

$$\begin{aligned} & \xi\,(\omega) \;=\; \Omega\,(\omega) \cdot \hat{S}\,(\omega) + N\,(\omega) \\ \Rightarrow \quad & \frac{\xi\,(\omega)}{\Omega\,(\omega)} = \hat{S}\,(\omega) + \tfrac{N(\omega)}{\Omega(\omega)} \,, \end{aligned} \tag{4.8}$$

such that the noise term $N(E)$ is eventually divided by the vacuum ZLP $\Omega(E)$. As in general $\Omega(\omega) \to 0$ for higher frequencies, this procedure amplifies high-frequency noise due to the division of higher Fourier coefficients, resulting in the entire spectrum being dominated by noise in real space.
Usually this effect can be reduced by (re-)convolving the spectrum with a Gaussian mollifier $G\,(E)$ that has the same FWHM as the ZLP, damping these high frequencies again [27]:

$$\hat{S}\,(E) = \mathcal{F}^{-1}\left[G\,(\omega) \cdot \frac{\xi\,(\omega)}{\Omega\,(\omega)}\right] \,, \tag{4.9}$$

yet largely removing asymmetries from the ZLP. This re-convolution, however does not increase the energy resolution of the data, as the mollifier again broadens the data to the previous extend. If the FWHM of the Gaussian is chosen smaller than that of the ZLP, the spectrum can be sharpened compared to the original data, but with the drawback of increased noise content [96].

In conclusion, the direct deconvolution procedure provided by the Fourier-ratio method is limited in sharpening the energy resolution due to the large amplification of noise for reasonably small resolution improvements.

4.2.2 Richardson-Lucy algorithm (RLA)

Another approach for deconvolution employs statistics to formulate a substantiated estimate of the *real* spectrum. The objective is to ascertain a spectrum, that, obscured by the ZLP, yields a result that is consistent with the observed measurement data. This approach has the advantage of not utilizing a direct inversion as in the Fourier-ratio of the last section. Thereby, this approach minimizes the amplification of noises.

According to Bayes theorem [97], the conditional probability density relationship is given by:

$$P\left(A \,|\, B\right) = \frac{P\left(B \,|\, A\right)\, P\left(A\right)}{P\left(B\right)}\,, \tag{4.10}$$

with the probability $P(A \,|\, B)$ that the underlying signal A is observed, given that the noisy spectrum B has been measured, the prior probability $P(A)$ that the underlying signal A has occurred, $P(B)$ is the probability of obtaining the noisy spectrum B and $P(B \,|\, A)$ is the probability of measuring the noisy spectrum B given that the underlying signal A is observed. This equation can be used to find an estimate $\hat{S}_{\mathrm{RLA}}(E)$ for the *true* spectrum $\hat{S}(E)$, such that $\hat{S}_{\mathrm{RLA}}(E) \approx \hat{S}(E)$. In order to compare this estimate with the acquired data $\xi(E)$, it must be blurred with the convolution kernel $\Omega(E)$, such that it can resemble the measurement $\xi(E)$. Accordingly, one finds $\hat{S}_{\Omega,\mathrm{RLA}}(E) = \Omega(E) \otimes \hat{S}_{\mathrm{RLA}}(E)$, such that $\hat{S}_{\Omega,\mathrm{RLA}}(E) \approx \xi(E)$. Applying the above to Bayes theorem yields:

$$P\left(\hat{S}_{\Omega,\mathrm{RLA}}\left(E\right) \,|\, \xi\left(E\right)\right) = \frac{P\left(\xi\left(E\right) \,|\, \hat{S}_{\Omega,\mathrm{RLA}}\left(E\right)\right)\, P\left(\hat{S}_{\Omega,\mathrm{RLA}}\left(E\right)\right)}{P\big(\xi\left(E\right)\big)}\,, \tag{4.11}$$

where $P\Big(\hat{S}_{\Omega,\mathrm{RLA}}\left(E\right)\Big)$ is called the *Bayesian prior*. The probability of measuring a spectrum $P(\xi\left(E\right))$ is considered a constant value with no effect on the maximization process and thus is being ignored, as will be shown subsequently. By maximizing the right side of the equation, the most likely estimate of the true loss probabilities can be found via the *maximum likelihood (ML)* approach:

$$\mathrm{ML}\left(\hat{S}_{\Omega,\mathrm{RLA}}\left(E\right)\right) = \underset{\hat{S}_{\Omega,\mathrm{RLA}} \,\in\, \Theta}{\arg\max} \left[P\left(\xi\left(E\right) \,|\, \hat{S}_{\Omega,\mathrm{RLA}}\left(E\right)\right)\right], \tag{4.12}$$

with Θ denoting the discrete parameter space of $E = [E_1\,,\, E_2\,,\, \ldots\,,\, E_k]$ with k energy channels of the spectrometer. The ML solution is valid if a uniform probability density for $P\Big(\hat{S}_{\Omega,\mathrm{RLA}}\left(E\right)\Big)$ is given [98]. By approximating the noise statistics of acquiring an EEL spectrum as a Poisson distribution, the probability $P\Big(\xi\left(E\right) \,|\, \hat{S}_{\Omega,\mathrm{RLA}}(E)\Big)$ can be written as [99]:

$$P\left(\xi\left(E\right) \,|\, \hat{S}_{\Omega,\mathrm{RLA}}\left(E\right)\right) = \prod_{i=1}^{k} \left[\frac{\big[\hat{S}_{\Omega,\mathrm{RLA}}\left(E_i\right)\big]^{\xi(E_i)} \exp\Big\{-\big[\hat{S}_{\Omega,\mathrm{RLA}}\left(E_i\right)\big]\Big\}}{\xi\left(E_i\right)!}\right]. \tag{4.13}$$

By comparing this equation with the Poisson distribution from Eq. 4.2, it can be stated that the mean value of the signal is given by the convolved estimate $\lambda = \hat{S}_{\Omega,\mathrm{RLA}}(E) = \hat{S}_{\mathrm{RLA}}(E) \otimes \Omega(E)$ and that the counts are given by the measured signal $n = \xi(E)$. For a sufficient minimization to be solved, the maximum likelihood approach from Eq. 4.12 must be rewritten. Maximizing the probability of the whole spectrum is equal to minimizing the same probability multiplied by minus one. Therefore, Eq. 4.13 can be rewritten as [99]:

$$-\ln\left[P\left(\xi\left(E\right) \,|\, \hat{S}_{\Omega,\mathrm{RLA}}\left(E\right)\right)\right] = \sum_{i=1}^{k} \Big[-\xi\left(E_i\right) \ln\big[\hat{S}_{\Omega,\mathrm{RLA}}\left(E_i\right)\big] + \hat{S}_{\Omega,\mathrm{RLA}}\left(E_i\right) + \ln\big[\xi\left(E_i\right)!\big]\Big]\,, \tag{4.14}$$

$$G_P\left(\xi\left(E\right) \,|\, \hat{S}_{\Omega,\mathrm{RLA}}\left(E\right)\right) = \sum_{i=1}^{k} \Big[-\xi\left(E_i\right) \ln\big[\Omega\left(E_i\right) \otimes \hat{S}_{\mathrm{RLA}}\left(E_i\right)\big] + \Omega\left(E_i\right) \otimes \hat{S}_{\mathrm{RLA}}\left(E_i\right)\Big]\,, \tag{4.15}$$

where the functional $G_P\Big(\xi\,(E)\mid\hat{S}_{\Omega,\mathrm{RLA}}(E)\Big)$ is chosen to be the negative natural logarithm of the probability $P\Big(\xi\,(E)\mid\hat{S}_{\Omega,\mathrm{RLA}}(E)\Big)$. This can be done, because logarithms are strictly monotonic functions that preserve the minimum. Further, the $\ln\left[\xi(E_i)\,!\right]$ term can be neglected, as it does not depend on $\hat{S}_{\mathrm{RLA}}(E_i)$ and therefore plays no further role in the subsequent minimization step. Since $G_P\Big(\xi(E)\mid\hat{S}_{\Omega,\mathrm{RLA}}(E)\Big)$ is convex in $\hat{S}_{\mathrm{RLA}}(E)$, as one might easily imagine by flipping a Poisson distribution (see Eq. 4.2) upside down, the minimum can be found via derivation:

$$\frac{\partial}{\partial\hat{S}_{\mathrm{RLA}}}\,G_P\left(\xi\,(E)\mid\hat{S}_{\Omega,\mathrm{RLA}}\,(E)\right)=0\,, \tag{4.16}$$

$$\Rightarrow\qquad\left[\frac{\xi\,(E)}{\Omega\,(E)\otimes\hat{S}_{\mathrm{RLA}}\,(E)}\otimes\Omega^{T}\,(E)\right]=1\,, \tag{4.17}$$

with the adjoint operator $\Omega^T(E)$, or complex conjugate in Fourier space, which in this real positive case equals the flipped distortion function $\Omega^T(E)=\Omega(-E)$. Multiplying both sides by $\hat{S}_{\mathrm{RLA}}(E)$ and using Picard iteration [100] leads to the *Richardson-Lucy algorithm (RLA)* [101, 102]:

$$\hat{S}^{k+1}_{\mathrm{RLA}}\,(E)=\hat{S}^{k}_{\mathrm{RLA}}\,(E)\cdot\left[\frac{\xi\,(E)}{\Omega\,(E)\otimes\hat{S}^{k}_{\mathrm{RLA}}\,(E)}\otimes\Omega\,(-E)\right]\,, \tag{4.18}$$

with the k-th iteration $\hat{S}^k_{\mathrm{RLA}}(E)$ and $\hat{S}^0_{\mathrm{RLA}}(E)=\xi\,(E)$ as the initial guess or starting point of the iteration. The RLA sharpens the energy resolution [103, 104] and works equivalently to the Fourier-ratio method [96]. Because EEL signals are always meant to be positive, it would be beneficial, if the results obtained from this method were positive as well. This is indeed a big advantage of the RLA compared to direct inversions like the Fourier-ratio method, since it ensures the non-negativity of the result for positive inputs $\Omega(E)>0$ and $\xi(E)>0$ [105].

4.2.3 Insufficiency of current deconvolution techniques

A review of the preceding sections reveals that commonly employed deconvolution methods in EELS often fail to account for the actual noise statistics inherent of the measurements – or, in some cases, neglect noise considerations entirely.

Not incorporating noise into the deconvolution process results in a substantial amplification of the noise, as shown in Eq. 4.8. In an attempt to smooth these noises to an acceptable level, mollifiers must be employed. However, this smoothing process imposes strict limitations on the method's ability to accurately reconstruct sharp spectral features. Given that the approach fails to sufficiently mitigate noise and falls short in accurately recovering spectral detail, it places the user in a particularly challenging position, forced to compromise between two suboptimal outcomes. The user is presented a dilemma and may decide whether a higher noise level or reduced deconvolution is more suitable.

Deconvolution methods that incorporate noise modeling offer a significantly more robust alternative. This is likely one of the key reasons why the RLA has gained widespread adoption over the past decades. However, the RLA relies on the assumption that the measured EELS data is fully described by the pure Poisson noise statistics it was derived from, as shown in the last section. The assumption of pure Poisson noise, however, has been undoubtedly disproven by various authors [91–95] and also by the

publications of this thesis in particular. These findings demonstrate that the noise characteristics in EELS measurements deviate from pure Poisson behavior, thus calling into question the validity of applying the RLA without further modification or correction.

One consequence of this mismatch between the assumed and the actual noise statistics is the amplification of noise during the iterative deconvolution process, typically emerging at an unpredictable iteration step [105]. A recent mathematical study even goes one step beyond and indicates that the RLA is doomed to amplify noises even for data adhering to the pure Poisson noise statistics [106]. As a consequence, a common strategy to mitigate this effect is the early termination of the RLA after about 15 iterations. This premature stopping, however, inevitably constrains the algorithm's capacity to reach its full deconvolution potential and results in a substantial reduction in its ability to enhance spectral sharpness.

It is therefore desirable to develop a method that can be readily adapted to more accurate noise models, tailored to the specific characteristics of individual EELS detectors, and that operates deterministically based on mathematically rigorous and verifiable assumptions in order to improve EELS measurements. Such a method can be constructed based on the *Alternating Direction Method of Multipliers (ADMM)* [107], as shown in the publication in Appendix C. A key advantage of ADMM resides in its ability to solve a broad class of optimization problems formulated through Lagrangian functions. Its flexibility makes it particularly well-suited for adaptation to the specific requirements of EELS, including the incorporation of complex noise models and detector-specific characteristics.

Since this class of algorithms has been proven to converge under broad conditions [107], it offers a resolution to the dilemma inherent of conventional deconvolution approaches by enabling iteration until an optimal and stable solution is obtained. As is shown in the publication in Appendix D, the results achieved with this method are significantly improved compared to those of the RLA.

Nevertheless, the Nyquist–Shannon sampling theorem [108, 109] imposes a fundamental mathematical constraint on the ability of any method to fully restore data at perfect resolution. According to this theorem, accurate reconstruction of features is only possible if the sampling rate is at least twice the highest frequency present in the signal. In frequency domain, convolution with a broad kernel acts as a low-pass filter, suppressing high-frequency components of the data. Conversely, noise introduces a background in frequency domain. If a frequency is obscured by this noise background, it cannot contribute to the reconstruction of the original data, leading to a loss of features.

These fundamental limitations also extend to methods based on artificial intelligence (AI) or machine learning (ML) at least insofar as such methods are expected to meet basic scientific standards. In particular, the validity of results must be grounded in the measured data itself, rather than relying on algorithmic inference of features that fall below the threshold of statistical significance. Given that the proposed deconvolution method follows a desirable deterministic and mathematically rigorous approach, the method proposed in this thesis may also serve as a valuable benchmark for validating or training AI and ML models, ensuring that they adhere to these scientific principles.

Chapter 5

Summary of the publications and the thesis

This thesis presents a unified noise model for detectors employed in transmission electron microscopy, which is rigorously derived and validated. It also demonstrates methods for determining and measuring the most critical noise parameters. Such a noise model is crucial, as it serves as a basis for post-processing methods like deconvolution, which is frequently applied to measured data in order to improve spectral resolution. The proposed algorithm achieves a significant reduction in the noise level of EELS measurements, while also removing the blur caused by the energy characteristics of the probe and the detector PSF. This enables the analysis of measurements with shorter acquisition times, while maintaining an improved overall signal-to-noise ratio. The first two publications establish the foundational aspects of the noise model, while the latter two publications examine the mathematical properties of the deconvolution method, both in general terms and in the context of its application to EELS data. In more detail:

The first publication titled *An applied noise model for scintillation-based CCD detectors in transmission electron microscopy* in *Scientific Reports*, **15** (2025) (see Appendix A) presents a foundational statistical noise model for scintillation-based CCD detectors, which are widely employed in the acquisition of TEM images and EEL spectra. This publication demonstrates the types of noises that occur on such detectors and examines the impact of detector calibrations, such as gain normalization and non-linearity corrections, on the noise statistics. A mathematical model for image acquisition on these detectors is derived and experimentally validated. Particular emphasis is placed on measuring the most critical noise parameters for these detectors, enabling the proposed noise model to be tailored to each individual detector. Additionally, the signal correlation effects induced by the detector point spread function (PSF) are examined, and their implications for detector binning are demonstrated. In summary, this publication proposes a novel method for determining the point spread function of scintillation-based CCD detectors, which are often employed in transmission electron microscopy. The degree of noise smoothing expected from convolution of the signals with this PSF is mathematically described and made quantifiable. Methods for improving gain non-linearity corrections are proposed. Uncertainties related to corrective measures, such as the use of a gain reference are derived and straightforward methods are proposed to measure them.

A subsequent publication titled *An applied noise model for low-loss EELS maps* in *Ultramicroscopy*, **270** (2025) (see Appendix B) builds upon the initial noise model by extending it to EEL spectra and EELS maps. In the context of EELS, a 2D signal confined to a small area of the detector is integrated to produce a 1D spectrum. The integration of the signal significantly alters the correlation effects arising from the point spread function (PSF) of the detector, thereby changing the noise properties relative to the 2D signals. In the case of EELS maps, energy drifts are anticipated to occur between the sequentially acquired EEL spectra. The publication therefore examines various energy-alignment strategies and assesses the effect of these realignments on the overall noise statistics. In summary, it is demonstrated how the 2D detector point spread function of the previous publication translates into a 1D point spread function for spectroscopic measurements such as EELS. Uncertainties related to intensity normalization of the spectrum and uncertainties related to various energy-alignment techniques are derived and made quantifiable.

The third publication titled *ADMM-TGV image restoration for scientific applications with unbiased parameter choice* in *Numerical Algorithms*, **97** (2024) (see Appendix C) addresses optimization problems related to the alternating direction method of multipliers (ADMM) algorithm. The ADMM algorithm serves as the basis for the proposed EELS deconvolution method, enabling the minimization of Lagrangian functions that formulate the deconvolution problem. The primary focus of this publication is the development of an algorithm that operates independently of user inputs, relying solely on the mathematical properties of the algorithm and measured noise parameters of the detector. A mathematical derivation for the selection of penalty and regularization parameters is presented, which allows for optimal deconvolution results, unbiased by the user, when employing the proposed algorithm. The effectiveness of the proposed selection methods is demonstrated using test images that are commonly deployed in the image processing literature. As the derived algorithms are of wider interest there, the use of these images facilitates comparability with other results in the literature and thus promotes a general understanding of the algorithms' capabilities. Examples of how the algorithm improves transmission electron microscopy images are provided to illustrate the broad applicability of the algorithm. In summary, a novel method is proposed to guarantee the convergence of ADMM algorithms employed in image post-processing to desirable results, eliminating the need for manual selection of essential parameters that determine both convergence properties and the quality of the deconvolution outcome.

The fourth publication titled *An unbiased ADMM-TGV algorithm for the deconvolution of STEM-EELS maps* in *Ultramicroscopy*, **275** (2025) (see Appendix D) presents the derivation of the actual deconvolution method for EELS maps. By integrating the findings from the three preceding publications, the noise models developed in the publications in Appendix A and Appendix B, along with the unbiased parameter selection methods from the publication in Appendix C, are leveraged to establish an objective algorithm that can be adapted for use with any EELS detector. The superiority of the algorithm over commonly used techniques, such as the Richardson-Lucy algorithm (RLA), is demonstrated. It is shown that post-processing EELS data using the proposed method reveals previously obscured plasmonic features within plasmon measurements on a Janus-particle. In summary, a new deconvolution method for EELS is presented that outperforms the widely used and commonly employed Richardson-Lucy algorithm by 60% in terms of the mean squared error (MSE). This distance was measured between the simulated ground truth data and the deconvolution outcome of the same dataset, which was treated with blur and noise according to the noise parameters determined for the EELS detector used in this thesis. It is demonstrated that the deconvolution method works for experimental data as well. Here, it is explicitly shown that this novel method makes evaluation of plasmonic modes of metallic nanoparticles possible, which could otherwise not be distinguished with the employed microscope using the wide-spread RLA deconvolution method. These recovered modes were cross-checked with simulation data and verified. Eventually, this new deconvolution method was used to analyze the plasmonic modes of a Janus particle consisting of gold and platinum.

All datasets associated with the publications, along with the evaluation and deconvolution software, are provided on a USB drive attached to the back cover of this thesis. The core software tools, specifically those used for noise parameter evaluation and the implementation of the deconvolution algorithm, have also been uploaded as part of the supplementary materials of the related publications and are accessible

to everyone through the journal websites. To further facilitate a broad distribution of the code, copies of the algorithms were uploaded to Mathworks, which is the primary source for users to search for Matlab related scripts:

- https://www.mathworks.com/matlabcentral/fileexchange/180009-noise-evaluation-in-transmission-electron-microscopy-tem
- https://www.mathworks.com/matlabcentral/fileexchange/159873-automated-admm-tgv-denoising-deconvolution-for-images
- https://www.mathworks.com/matlabcentral/fileexchange/181166-admm-tgv-deconvolution-algorithm-for-stem-eels-maps

All codes have been made freely available under a CC-BY 4 license or similar conditions.

On the USB drive, four programs are found that were improved or developed bottom-up during the work on this thesis:

- *Lithogram* – A software tool for raytracing simulations to model the EBPVD process for the fabrication of nanoparticles in double-angle resolved nanosphere lithography. This software tool was improved during this thesis and also contains the motor control for providing the correct angles for the fabrication of the nanoparticles during the EBPVD process.
- *EELS-Simulator* – A software tool that was developed during this thesis to transfer the simulated nanoparticles from the Lithogram software into the MNPBEM toolbox [63] in order to create the simulation of a plasmon related EEL signals.
- *Sim-Noiser* – A software tool that was developed during this thesis to add blur and noise to the simulated EEL signal from the MNPBEM toolbox according to the measured blur and noise parameters of the employed EELS detector. This software also contains the ADMM-TGV and RLA deconvolution methods in order to compare their results to the underlying ground truth signal.
- *EELS-Analyzer* – A software tool that was developed during this thesis and is intended to facilitate the analysis of experimental EELS data, including the application of the non-linearity correction method proposed in the publication in Appendix A, the energy-alignment method proposed in the publication in Appendix B, the intensity normalization, the ZLP subtraction, the deconvolution with the proposed ADMM-TGV deconvolution method proposed in the publication in Appendix D, and the visualization of EELS data cubes as spectra and slices, respectively.

In conclusion, the present thesis presents novel approaches to achieving the objectives stated in the introduction. Detailed noise models are hereby presented for TEM and particularly for EELS, both of which accurately capture the noises encountered in these types of measurements. On the basis of these noise models, a novel deconvolution method for EELS and EELS maps is proposed that verifiably outperforms currently available techniques in terms of accuracy.

Bibliography

[1] EGERTON, R. F.: *Physical Principles of Electron Microscopy: An Introduction to TEM, SEM, and AEM*. New York, NY : Springer, 2005. – ISBN 0–387–25800–0.

[2] REIMER, L. ; KOHL, H.: *Springer Series in Optical Sciences*. Bd. 36: *Transmission Electron Microscopy: Physics of Image Formation*. 5. ed. New York, NY : Springer, 2008. – ISBN 978–0–387–40093–8.

[3] WILLIAMS, D. B. ; CARTER, C. B.: *Transmission Electron Microscopy: A textbook for materials science*. 2. ed. New York : Springer, 2009. – ISBN 978–0–387–76500–6.

[4] PENNYCOOK, S. J. ; NELLIST, P. D.: *Scanning Transmission Electron Microscopy*. New York, NY : Springer New York, 2011. – ISBN 978–1–4419–7199–9.

[5] CARTER, C. B. ; WILLIAMS, D. B.: *Transmission Electron Microscopy: Diffraction, Imaging, and Spectroscopy*. Cham : Springer International Publishing, 2016. – ISBN 978–3–319–26649–7.

[6] RAI, R. S. ; SUBRAMANIAN, S.: Role of transmission electron microscopy in the semiconductor industry for process development and failure analysis. In: *Progress in Crystal Growth and Characterization of Materials* 55 (2009), Nr. 3-4, S. 63–97. http://dx.doi.org/10.1016/j.pcrysgrow.2009.09.002.

[7] YU, B. C. ; SUN, M. ; PAN, R. H. ; TIAN, J. M. ; ZHENG, F. Y. ; HUANG, D. ; LYU, F. J. ; ZHANG, Z. T. ; LI, J. J. ; CHEN, Q. ; LI, Z. H.: Semi-custom methodology to fabricate transmission electron microscopy chip for in situ characterization of nanodevices and nanomaterials. In: *Science China Technological Sciences* 65 (2022), Nr. 4, S. 817–825. http://dx.doi.org/10.1007/s11431-021-1980-1.

[8] NGUYEN, L.: *First semi standard for electron microscopy workflows*. https://www.semi.org/en/standards-watch/first-tem-lamella-carrier-standard-2019. Version: 2019.

[9] SAMSUNG: *Samsung begins chip production using 3 nm process technology with GAA architecture*. https://news.samsung.com/global/samsung-begins-chip-production-using-3nm-process-technology-with-gaa-architecture. Version: 2022.

[10] TSCM: *TSMC holds 3 nm volume production and capacity expansion ceremony, marking a key milestone for advanced manufacturing*. https://pr.tsmc.com/english/news/2986. Version: 2022.

[11] WANG, B. ; ISLAM, Z. ; HAQUE, A. ; CHABAK, K. ; SNURE, M. ; HELLER, E. ; GLAVIN, N.: In situ transmission electron microscopy of transistor operation and failure. In: *Nanotechnology* 29 (2018), Nr. 31, S. 31LT01. http://dx.doi.org/10.1088/1361-6528/aac591.

[12] ADABIFIROOZJAEI, E. ; RASTKERDAR, E. ; NEMOTO, Y. ; NAKAYAMA, Y. ; NISHIMIYA, Y. ; FRONZI, M. ; YAO, Y. ; NGUYEN, M. T. ; MOLINA-LUNA, L. ; SUZUKI, T. S.: In-situ scanning transmission electron microscopy study of Al-amorphous SiO2 layer-SiC interface. In: *Journal of Materials Science* 58 (2023), Nr. 6, S. 2456–2468. http://dx.doi.org/10.1007/s10853-023-08186-z.

[13] KRAMERS, H. A.: La diffusion de la lumiere par les atomes. In: *Atti Cong. Intern. Fisici, (Transactions of Volta Centenary Congress) Como* (1927), Nr. 2.

[14] KRONIG, R. d. L.: On the Theory of Dispersion of X-Rays. In: *Journal of the Optical Society of America* 12 (1926), Nr. 6, S. 547. http://dx.doi.org/10.1364/JOSA.12.000547.

[15] GARCÍA DE ABAJO, F. J.: Optical excitations in electron microscopy. In: *Reviews of Modern Physics* 82 (2010), Nr. 1, S. 209–275. http://dx.doi.org/10.1103/RevModPhys.82.209.

[16] CHANG, S.-W. ; LIN, T.-R. ; CHUANG, S. L.: Theory of Plasmonic Fabry-Perot Nanolasers. In: *Optics Express* 18 (2010), Nr. 14, S. 15039. http://dx.doi.org/10.1364/OE.18.015039.

[17] DI GIULIO, V. ; AKERBOOM, E. ; POLMAN, A. ; GARCÍA DE ABAJO, F. J.: Toward Optimum Coupling between Free Electrons and Confined Optical Modes. In: *ACS Nano* 18 (2024), Nr. 22, S. 14255–14275. http://dx.doi.org/10.1021/acsnano.3c12977.

[18] HAYWARD, S. B. ; GLAESER, R. M.: Radiation damage of purple membrane at low temperature. In: *Ultramicroscopy* 04 (1979), Nr. 2, S. 201–210. http://dx.doi.org/10.1016/S0304-3991(79)90211-0.

[19] EGERTON, R. F. ; LAZAR, S. ; LIBERA, M.: Delocalized radiation damage in polymers. In: *Micron* 43 (2012), Nr. 1, S. 2–7. http://dx.doi.org/10.1016/j.micron.2011.05.007.

[20] LEIJTEN, Z. J. W. A. ; KEIZER, A. D. A. ; WITH, G. de ; FRIEDRICH, H.: Quantitative Analysis of Electron Beam Damage in Organic Thin Films. In: *The journal of physical chemistry. C* 121 (2017), Nr. 19, S. 10552–10561. http://dx.doi.org/10.1021/acs.jpcc.7b01749.

[21] LIBERA, M. R. ; EGERTON, R. F.: Advances in the Transmission Electron Microscopy of Polymers. In: *Polymer Reviews* 50 (2010), Nr. 3, S. 321–339. http://dx.doi.org/10.1080/15583724.2010.493256.

[22] VELAZCO, A. ; BÉCHÉ, A. ; JANNIS, D. ; VERBEECK, J.: Reducing electron beam damage through alternative STEM scanning strategies, Part I: Experimental findings. In: *Ultramicroscopy* 232 (2022), S. 113398. http://dx.doi.org/10.1016/j.ultramic.2021.113398.

[23] ILETT, M. ; S'ARI, M. ; FREEMAN, H. ; ASLAM, Z. ; KONIUCH, N. ; AFZALI, M. ; CATTLE, J. ; HOOLEY, R. ; RONCAL-HERRERO, T. ; COLLINS, S. M. ; HONDOW, N. ; BROWN, A. ; BRYDSON, R.: Analysis of complex, beam-sensitive materials by transmission electron microscopy and associated techniques. In: *Philosophical transactions A* 378 (2020), Nr. 2186, S. 20190601. http://dx.doi.org/10.1098/rsta.2019.0601.

[24] DANG, Z. ; LUO, Y. ; WANG, X.-S. ; IMRAN, M. ; GAO, P.: Electron-beam-induced degradation of halide-perovskite-related semiconductor nanomaterials. In: *Chinese Optics Letters* 19 (2021), Nr. 3, S. 030002. http://dx.doi.org/10.3788/COL202119.030002.

[25] BUBAN, J. P. ; RAMASSE, Q. ; GIPSON, B. ; BROWNING, N. D. ; STAHLBERG, H.: High-resolution low-dose scanning transmission electron microscopy. In: *Journal of Electron Microscopy* 59 (2010), Nr. 2, S. 103–112. http://dx.doi.org/10.1093/jmicro/dfp052.

[26] ORTEGA, E. ; JONGE, N. de: Analysis of the Dose-Limited Spatial Resolution in Transmission Electron Microscopy. In: *Microscopy and Microanalysis* 26 (2020), Nr. S2, S. 1216–1217. http://dx.doi.org/10.1017/S1431927620017365.

[27] EGERTON, R. F.: *Electron Energy-Loss Spectroscopy in the Electron Microscope*. 3. ed. Boston, MA : Springer Science+Business Media LLC, 2011. – ISBN 978–1–4419–9582–7.

[28] KHSHANOVSKA, O. ; KRYSHTAL, A.: Valence EELS study of the composition of a liquid phase in a Janus Sn-Ge nanoparticle over a temperature range of 250-750 °C. In: *Ultramicroscopy* 276 (2025), S. 114199. http://dx.doi.org/10.1016/j.ultramic.2025.114199.

[29] MAIER, S. A.: *Plasmonics: Fundamentals and Applications*. New York, NY : Springer, 2007. – ISBN 0–387–33150–6.

[30] BRONGERSMA, M. L. ; KIK, P. G.: *Springer Series in Optical Sciences*. Bd. 131: *Surface plasmon nanophotonics*. Dordrecht : Springer, 2007. – ISBN 978–1–4020–4349–9.

[31] HOLGATE, S. A.: *Understanding Solid State Physics*. Boca Raton, Fla. : CRC Press, 2010. – ISBN 978–0750309721.

[32] RAZEGHI, M.: *Fundamentals of Solid State Engineering*. 4th ed. 2019. Cham : Springer International Publishing, 2019. – ISBN 978–3319757087.

[33] ZAPATA-HERRERA, M. ; FLÓREZ, J. ; CAMACHO, A. S. ; RAMÍREZ, H. Y.: Quantum Confinement Effects on the Near Field Enhancement in Metallic Nanoparticles. In: *Plasmonics* 13 (2018), Nr. 1, S. 1–7. http://dx.doi.org/10.1007/s11468-016-0476-y.

[34] MKHOYAN, K. A. ; BABINEC, T. ; MACCAGNANO, S. E. ; KIRKLAND, E. J. ; SILCOX, J.: Separation of bulk and surface-losses in low-loss EELS measurements in STEM. In: *Ultramicroscopy* 107 (2007), Nr. 4-5, S. 345–355. http://dx.doi.org/10.1016/j.ultramic.2006.09.003.

[35] KOH, A. L. ; BAO, K. ; KHAN, I. ; SMITH, W. E. ; KOTHLEITNER, G. ; NORDLANDER, P. ; MAIER, S. A.; MCCOMB, D. W.: Electron energy-loss spectroscopy (EELS) of surface plasmons in single silver nanoparticles and dimers: influence of beam damage and mapping of dark modes. In: *ACS Nano* 3 (2009), Nr. 10, S. 3015–3022. http://dx.doi.org/10.1021/nn900922z.

[36] BOSMAN, M. ; YE, E. ; TAN, S. F. ; NIJHUIS, C. A. ; YANG, J. K. W. ; MARTY, R. ; MLAYAH, A. ; ARBOUET, A. ; GIRARD, C. ; HAN, M.-Y.: Surface plasmon damping quantified with an electron nanoprobe. In: *Scientific Reports* 3 (2013), S. 1312. http://dx.doi.org/10.1038/srep01312.

[37] RAZA, S. ; ESFANDYARPOUR, M. ; KOH, A. L. ; MORTENSEN, N. A. ; BRONGERSMA, M. L. ; BOZHEVOLNYI, S. I.: Electron energy-loss spectroscopy of branched gap plasmon resonators. In: *Nature Communications* 7 (2016), S. 13790. http://dx.doi.org/10.1038/ncomms13790.

[38] LI, Zhi ; LOPEZ-ORTEGA, Alberto ; ARANDA-RAMOS, A. ; TAJADA, J.. L. ; SORT, J. ; NOGUES, C. ; VAVASSORI, P. ; NOGUES, J. ; SEPULVEDA, B.: Simultaneous Local Heating/Thermometry Based on Plasmonic Magnetochromic Nanoheaters. In: *Small* 14 (2018), Nr. 24, S. 1800868. http://dx.doi.org/10.1002/smll.201800868.

[39] LI, Z. ; ARANDA-RAMOS, A. ; GÜELL-GRAU, P. ; TAJADA, J. L. ; POU-MACAYO, L. ; LOPE PIEDRAFITA, S. ; PI, F. ; ROCA, A. G. ; BARÓ, M. D. ; SORT, J. ; NOGUÉS, C. ; NOGUÉS, J. ; SEPÚLVEDA, B.: Magnetically amplified photothermal therapies and multimodal imaging with magneto-plasmonic nanodomes. In: *Applied Materials Today* 12 (2018), S. 430–440. http://dx.doi.org/10.1016/j.apmt.2018.07.008.

[40] GAO, Z. ; YE, H. ; TANG, D. ; TAO, J. ; HABIBI, S. ; MINERICK, A. ; TANG, D. ; XIA, X.: Platinum-Decorated Gold Nanoparticles with Dual Functionalities for Ultrasensitive Colorimetric in Vitro Diagnostics. In: *Nano Letters* 17 (2017), Nr. 9, S. 5572–5579. http://dx.doi.org/10.1021/acs.nanolett.7b02385.

[41] AIOUB, M. ; PANIKKANVALAPPIL, S. R. ; EL-SAYED, M. A.: Platinum-Coated Gold Nanorods: Efficient Reactive Oxygen Scavengers That Prevent Oxidative Damage toward Healthy, Untreated Cells during Plasmonic Photothermal Therapy. In: *ACS Nano* 11 (2017), Nr. 1, S. 579–586. http://dx.doi.org/10.1021/acsnano.6b06651.

[42] STAVROPOULOU, A. P. ; THEODOSIOU, M. ; SAKELLIS, E. ; BOUKOS, N. ; PAPANASTASIOU, G. ; WANG, C. ; TAVARES, A. ; CORRAL, C. A. ; GOURNIS, D. ; CHALMPES, N. ; GOBBO, O. L. ; EFTHIMIADOU, E. K.: Bimetallic gold-platinum nanoparticles as a drug delivery system coated with a new drug to target glioblastoma. In: *Colloids and Surfaces B: Biointerfaces* 214 (2022), S. 112463. http://dx.doi.org/10.1016/j.colsurfb.2022.112463.

[43] MOLLANIA, H. ; OLOOMI-BUYGI, M. ; MOLLANIA, N.: Catalytic and anti-cancer properties of platinum, gold, silver, and bimetallic Au-Ag nanoparticles synthesized by Bacillus sp. bacteria. In: *Journal of Biotechnology* 379 (2024), S. 33–45. http://dx.doi.org/10.1016/j.jbiotec.2023.11.007.

[44] ILIC, O. ; KAMINER, I. ; ZHEN, B. ; MILLER, O. D. ; BULJAN, H. ; SOLJAČIĆ, M.: Topologically enabled optical nanomotors. In: *Science Advances* 3 (2017), Nr. 6, S. e1602738. http://dx.doi.org/10.1126/sciadv.1602738.

[45] DING, H. ; KOLLIPARA, P. S. ; KIM, Y. ; KOTNALA, A. ; LI, J. ; CHEN, Z. ; ZHENG, Y.: Universal optothermal micro/nanoscale rotors. In: *Science Advances* 8 (2022), Nr. 24, S. eabn8498. http://dx.doi.org/10.1126/sciadv.abn8498.

[46] ILIC, O. ; KAMINER, I. ; LAHINI, Y. ; BULJAN, H. ; SOLJAČIĆ, M.: Exploiting Optical Asymmetry for Controlled Guiding of Particles with Light. In: *ACS Photonics* 3 (2016), Nr. 2, S. 197–202. http://dx.doi.org/10.1021/acsphotonics.5b00605.

[47] MORAN, J. L. ; POSNER, J. D.: Phoretic Self-Propulsion. In: *Annual Review of Fluid Mechanics* 49 (2017), Nr. 1, S. 511–540. http://dx.doi.org/10.1146/annurev-fluid-122414-034456.

[48] HAYNES, C. L. ; VAN DUYNE, R. P.: Nanosphere Lithography: A Versatile Nanofabrication Tool for Studies of Size-Dependent Nanoparticle Optics. In: *The Journal of Physical Chemistry B* 105 (2001), Nr. 24, S. 5599–5611. http://dx.doi.org/10.1021/jp010657m.

[49] COLSON, P. ; HENRIST, C. ; CLOOTS, R.: Nanosphere Lithography: A Powerful Method for the Controlled Manufacturing of Nanomaterials. In: *Journal of Nanomaterials* (2013), Nr. 1. http://dx.doi.org/10.1155/2013/948510.

[50] BRODEHL, C. ; GREULICH-WEBER, S. ; LINDNER, J. K. N.: Fabrication of tailored nanoantennas on large areas for plasmonic devices. In: *Materials Today: Proceedings* 4 (2017), S. S44–S51. http://dx.doi.org/10.1016/j.matpr.2017.05.009.

[51] BRODEHL, C.: *Großflächige Herstellung von maßgeschneiderten Nanopartikeln für plasmonische Anwendungen*, Universität Paderborn, Dissertation, 2019. http://dx.doi.org/10.17619/UNIPB/1-765.

[52] WESSEL, C. L.: *Entwicklung eines chemischen Depositionsprozesses zur Modifikation kolloidaler Nanokugelmasken*, Universität Paderborn, Bachelorthesis, 2022.

[53] SMOKEFOOT: *SolGelCartoon.png*. https://commons.wikimedia.org/wiki/File:SolGelCartoon.png. Version: 2022.

[54] VAN BLAADEREN, A. ; VAN GEEST, J. ; VRIJ, A.: Monodisperse colloidal silica spheres from tetraalkoxysilanes: Particle formation and growth mechanism. In: *Journal of Colloid and Interface Science* 154 (1992), Nr. 2, S. 481–501. http://dx.doi.org/10.1016/0021-9797(92)90163-G.

[55] YANG, H. ; JIANG, P.: Large-scale colloidal self-assembly by doctor blade coating. In: *Langmuir* 26 (2010), Nr. 16, S. 13173–13182. http://dx.doi.org/10.1021/la101721v.

[56] RIEDL, T. ; LINDNER, J. K. N.: Automated SEM Image Analysis of the Sphere Diameter, Sphere-Sphere Separation, and Opening Size Distributions of Nanosphere Lithography Masks. In: *Microscopy and Microanalysis* 28 (2022), Nr. 1, S. 185–195. http://dx.doi.org/10.1017/S1431927621013866.

[57] BRODEHL, C. ; GREULICH-WEBER, S. ; LINDNER, J. K. N.: An Algorithm for Tailoring of Nanoparticles by Double Angle Resolved Nanosphere Lithography. In: *MRS Proceedings* 1748 (2015). http://dx.doi.org/10.1557/opl.2015.77.

[58] VOSSEN, D. L. J. ; PENNINKHOF, J. J. ; VAN BLAADEREN, A.: Chemical modification of colloidal masks for nanolithography. In: *Langmuir* 24 (2008), Nr. 11, S. 5967–5969. http://dx.doi.org/10.1021/la703847p.

[59] STÖBER, W. ; FINK, A. ; BOHN, E.: Controlled growth of monodisperse silica spheres in the micron size range. In: *Journal of Colloid and Interface Science* 26 (1968), Nr. 1, S. 62–69. http://dx.doi.org/10.1016/0021-9797(68)90272-5.

[60] ZIETLOW, C.. ; WESSEL, C. L. ; LINDNER, J. K. N.: Modification of self-organized nanosphere lithography masks using the Stoeber process. In: *14th Int. ICPAM Conf.* (2022), S. 275–277.

[61] AWAN, T. I. ; BASHIR, A. ; TEHSEEN, A.: *Chemistry of Nanomaterials: Fundamentals and Applications*. Amsterdam and Kidlington, Oxford and Cambridge, MA : Elsevier, 2020. – ISBN 978–0–12–818908–5.

[62] MÖLLER, T. ; TRUMBORE, B.: Fast, Minimum Storage Ray-Triangle Intersection. In: *Journal of Graphics Tools* 2 (1997), Nr. 1, S. 21–28. http://dx.doi.org/10.1080/10867651.1997.10487468.

[63] HOHENESTER, U. ; TRÜGLER, A.: MNPBEM – A Matlab toolbox for the simulation of plasmonic nanoparticles. In: *Computer Physics Communications* 183 (2012), Nr. 2, S. 370–381. http://dx.doi.org/10.1016/j.cpc.2011.09.009.

[64] HAIDER, M. ; ROSE, H. ; UHLEMANN, S. ; KABIUS, B. ; URBAN, K.: Towards 0.1 nm resolution with the first spherically corrected transmission electron microscope. In: *Journal of Electron Microscopy* 47 (1998), Nr. 5, S. 395–405. http://dx.doi.org/10.1093/oxfordjournals.jmicro.a023610.

[65] MÜLLER, H. ; UHLEMANN, S. ; HARTEL, P. ; HAIDER, M.: Advancing the hexapole Cs-corrector for the scanning transmission electron microscope. In: *Microscopy and Microanalysis* 12 (2006), Nr. 6, S. 442–455. http://dx.doi.org/10.1017/S1431927606060600.

[66] HAIDER, M. ; HARTEL, P. ; MÜLLER, H. ; UHLEMANN, S. ; ZACH, J.: Information transfer in a TEM corrected for spherical and chromatic aberration. In: *Microscopy and Microanalysis* 16 (2010), Nr. 4, S. 393–408. http://dx.doi.org/10.1017/S1431927610013498.

[67] BÜRGER, J.: *Contributions to differential phase contrast imaging*, Universität Paderborn, Dissertation, 2024. http://dx.doi.org/10.17619/UNIPB/1-1985.

[68] NELLIST, P. D. ; PENNYCOOK, S. J.: The principles and interpretation of annular dark-field Z-contrast imaging. Version: 2000. http://dx.doi.org/10.1016/S1076-5670(00)80013-0. In: ACADEMIC PRESS (Hrsg.): *Advances in Imaging and Electron Physics* Bd. 113. Elsevier, 2000.

[69] GUBBENS, A. ; BARFELS, M. ; TREVOR, C. ; TWESTEN, R. ; MOONEY, P. ; THOMAS, P. ; MENON, N. ; KRAUS, B. ; MAO, C. ; MCGINN, B.: The GIF Quantum, a next generation post-column imaging energy filter. In: *Ultramicroscopy* 110 (2010), Nr. 8, S. 962–970. http://dx.doi.org/10.1016/j.ultramic.2010.01.009.

[70] SCHAFFER, B. ; KOTHLEITNER, G. ; GROGGER, W.: EFTEM spectrum imaging at high-energy resolution. In: *Ultramicroscopy* 106 (2006), Nr. 11-12, S. 1129–1138. http://dx.doi.org/10.1016/j.ultramic.2006.04.028.

[71] WU, Y. ; LI, G. ; CAMDEN, J. P.: Probing Nanoparticle Plasmons with Electron Energy Loss Spectroscopy. In: *Chemical Reviews* 118 (2018), Nr. 6, S. 2994–3031. http://dx.doi.org/10.1021/acs.chemrev.7b00354.

[72] GATAN: *Gatan Imaging Filter Quantum ER*. https://www.gatan.com/techniques/spectrum-imaging.

[73] MCGILVERY, C. M. ; GOODE, A. E. ; SHAFFER, M. S. P. ; MCCOMB, D. W.: Contamination of holey/lacey carbon films in STEM. In: *Micron* 43 (2012), Nr. 2-3, S. 450–455. http://dx.doi.org/10.1016/j.micron.2011.10.026.

[74] NAKAMURA, J. (Hrsg.): *Image Sensors and Signal Processing for Digital Still Cameras*. Boca Raton, Fla. : Taylor & Francis, 2006. – ISBN 0–8493–3545–0.

[75] MURPHY, D. B. ; DAVIDSON, M. W.: *Fundamentals of Light Microscopy and Electronic Imaging*. 2. ed. Hoboken, NJ : Wiley-Blackwell, 2013. – ISBN 978–0–471–69214–0.

[76] ASTIER, P. ; ANTILOGUS, P. ; JURAMY, C. ; LE BRETON, R. ; LE GUILLOU, L. ; SEPULVEDA, E.: The shape of the photon transfer curve of CCD sensors. In: *Astronomy & Astrophysics* 629 (2019), S. A36. http://dx.doi.org/10.1051/0004-6361/201935508.

[77] EGOAVIL, R. ; GAUQUELIN, N. ; MARTINEZ, G. T. ; VAN AERT, S. ; VAN TENDELOO, G. ; VERBEECK, J.: Atomic resolution mapping of phonon excitations in STEM-EELS experiments. In: *Ultramicroscopy* 147 (2014), S. 1–7. http://dx.doi.org/10.1016/j.ultramic.2014.04.011.

[78] STÖGER-POLLACH, M.: Optical properties and bandgaps from low loss EELS: pitfalls and solutions. In: *Micron* 39 (2008), Nr. 8, S. 1092–1110. http://dx.doi.org/10.1016/j.micron.2008.01.023.

[79] RAFFERTY, B. ; PENNYCOOK, S. J. ; BROWN, L. M.: Zero loss peak deconvolution for bandgap EEL spectra. In: *Journal of Electron Microscopy* 49 (2000), Nr. 4, S. 517–524. http://dx.doi.org/10.1093/oxfordjournals.jmicro.a023838.

[80] VAN BENTHEM, K. ; ELSÄSSER, C. ; FRENCH, R. H.: Bulk electronic structure of SrTiO3: Experiment and theory. In: *Journal of Applied Physics* 90 (2001), Nr. 12, S. 6156–6164. http://dx.doi.org/10.1063/1.1415766.

[81] GRANERØD, C. S. ; ZHAN, W. PRYTZ, Ø.: Automated approaches for band gap mapping in STEM-EELS. In: *Ultramicroscopy* 184 (2018), Part A, S. 39–45. http://dx.doi.org/10.1016/j.ultramic.2017.08.006.

[82] CHERENKOV, P. A.: Visible emission of clean liquids by action of γ-radiation. In: *Journal of Physics D: Applied Physics* 93 (1967), Nr. 10, S. 385–388. http://dx.doi.org/10.3367/UFNr.0093.196710n.0385.

[83] STÖGER-POLLACH, M. ; FRANCO, H. ; SCHATTSCHNEIDER, P. ; LAZAR, S. ; SCHAFFER, B. ; GROGGER, W. ; ZANDBERGEN, H. W.: Cerenkov losses: a limit for bandgap determination and Kramers-Kronig analysis. In: *Micron* 37 (2006), Nr. 5, S. 396–402. http://dx.doi.org/10.1016/j.micron.2006.01.001.

[84] MENG, Q. ; WU, L. ; XIN, H. L. ; ZHU, Y.: Retrieving the energy-loss function from valence electron energy-loss spectrum: Separation of bulk-, surface-losses and Cherenkov radiation. In: *Ultramicroscopy* 194 (2018), S. 175–181. http://dx.doi.org/10.1016/j.ultramic.2018.08.014.

[85] FUNG, K. L. Y. ; FAY, M. W. ; COLLINS, S. M. ; KEPAPTSOGLOU, D. M. ; SKOWRON, S. T. ; RAMASSE, Q. M. ; KHLOBYSTOV, A. N.: Accurate EELS background subtraction - an adaptable method in MATLAB. In: *Ultramicroscopy* 217 (2020), S. 113052. http://dx.doi.org/10.1016/j.ultramic.2020.113052.

[86] CASCIARDI, S. ; SISTO, R. ; DIOCIAIUTI, M.: The Analytical Transmission Electron Microscopy: A Powerful Tool for the Investigation of Low–Dimensional Carbon Nanomaterials. In: *Journal of Nanomaterials* 2013 (2013), Nr. 1. http://dx.doi.org/10.1155/2013/506815.

[87] ROSS, S. M.: *Introduction to Probability Models*. 13th Edition. San Diego, CA and London : Academic Press, 2024. – ISBN 9780443187612.

[88] ZUO, J. M. ; SPENCE, J. C. H.: *Advanced Transmission Electron Microscopy: Imaging and Diffraction in Nanoscience*. New York : Springer, 2017. – ISBN 978–1–4939–6607–3.

[89] LEMONS, D. S.: *An Introduction to Stochastic Processes in Physics*. Baltimore, Md. and London : Johns Hopkins University Press, 2002. – ISBN 978–0801868665.

[90] RÉFRÉGIER, P.: *Noise Theory and Application to Physics: From Fluctuations to Information*. New York, NY : Springer, 2004 (Advanced Texts in Physics). – ISBN 978–0387225265.

[91] MEYER, R. R. ; KIRKLAND, A. I.: The effects of electron and photon scattering on signal and noise transfer properties of scintillators in CCD cameras used for electron detection. In: *Ultramicroscopy* 75 (1998), Nr. 1, S. 23–33. http://dx.doi.org/10.1016/S0304-3991(98)00051-5.

[92] MEYER, R. R. ; KIRKLAND, A. I.: Characterisation of the signal and noise transfer of CCD cameras for electron detection. In: *Microscopy research and technique* 49 (2000), Nr. 3, S. 269–280. http://dx.doi.org/10.1002/(SICI)1097-0029(20000501)49:3<269::AID-JEMT5>3.0.CO;2-B.

[93] VERBEECK, J. ; BERTONI, G.: Model-based quantification of EELS spectra: treating the effect of correlated noise. In: *Ultramicroscopy* 108 (2008), Nr. 2, S. 74–83. http://dx.doi.org/10.1016/j.ultramic.2007.03.004.

[94] PLOTKIN-SWING, B. ; CORBIN, G. J. ; CARLO, S. de ; DELLBY, N. ; HOERMANN, C. ; HOFFMAN, M. V.; LOVEJOY, Tracy C. ; MEYER, C. E. ; MITTELBERGER, A. ; PANTELIC, R. ; PIAZZA, L. ; KRIVANEK, O. L.: Hybrid pixel direct detector for electron energy loss spectroscopy. In: *Ultramicroscopy* 217 (2020), S. 113067. http://dx.doi.org/10.1016/j.ultramic.2020.113067.

[95] CRAVEN, A. J. ; SALA, B. ; MACLAREN, D. A. ; MCFADZEAN, S. ; SCHAFFER, B. ; MACLAREN, I.: Splicing dual-range EELS spectra: Identifying and correcting artefacts. In: *Ultramicroscopy* 272 (2025), S. 114135. http://dx.doi.org/10.1016/j.ultramic.2025.114135.

[96] WANG, F. ; EGERTON, R. F. ; MALAC, M.: Fourier-ratio deconvolution techniques for electron energy-loss spectroscopy (EELS). In: *Ultramicroscopy* 109 (2009), Nr. 10, S. 1245–1249. http://dx.doi.org/10.1016/j.ultramic.2009.05.011.

[97] BAYES, T.: LII. An essay towards solving a problem in the doctrine of chances. By the late Rev. Mr. Bayes, F. R. S. communicated by Mr. Price, in a letter to John Canton, A. M. F. R. S. In: *Philosophical Transactions of the Royal Society of London* 53 (1763), S. 370–418. http://dx.doi.org/10.1098/rstl.1763.0053.

[98] EGIAZARIAN, K. ; CAMPISI, P.: *Blind Image Deconvolution: Theory and Applications*. Boca Raton : CRC Press, 2007. – ISBN 978–0849373671.

[99] DEY, N. ; BLANC-FERAUD, L. ; ZIMMER, C. ; ROUX, P. ; KAM, Z. ; OLIVO-MARIN, J.-C. ; ZERUBIA, J.: Richardson-Lucy algorithm with total variation regularization for 3D confocal microscope deconvolution. In: *Microscopy Research and Technique* 69 (2006), Nr. 4, S. 260–266. http://dx.doi.org/10.1002/jemt.20294.

[100] ISAACSON, E. ; KELLER, H. B.: *Analysis of Numerical Methods*. New York, NY : Dover, 1994 http://www.loc.gov/catdir/description/dover031/94007740.html. – ISBN 0–486–68029–0.

[101] RICHARDSON, W. H.: Bayesian-Based Iterative Method of Image Restoration*. In: *Journal of the Optical Society of America* 62 (1972), Nr. 1, S. 55. http://dx.doi.org/10.1364/JOSA.62.000055.

[102] LUCY, L. B.: An iterative technique for the rectification of observed distributions. In: *The Astronomical Journal* 79 (1974), S. 745. http://dx.doi.org/10.1086/111605.

[103] BELLIDO, E. P. ; ROSSOUW, D. ; BOTTON, G. A.: Toward 10 meV electron energy-loss spectroscopy resolution for plasmonics. In: *Microscopy and Microanalysis* 20 (2014), Nr. 3, S. 767–778. http://dx.doi.org/10.1017/S1431927614000609.

[104] EGERTON, R. F. ; WANG, F. ; MALAC, M. ; MORENO, M. S. ; HOFER, F.: Fourier-ratio deconvolution and its Bayesian equivalent. In: *Micron* 39 (2008), Nr. 6, S. 642–647. http://dx.doi.org/10.1016/j.micron.2007.10.004.

[105] EGERTON, R. F. ; QIAN, H. ; MALAC, M.: Improving the energy resolution of X-ray and electron energy-loss spectra. In: *Micron* 37 (2006), Nr. 4, S. 310–315. http://dx.doi.org/10.1016/j.micron.2005.11.005.

[106] LIU, Y. ; PANEZAI, S. ; WANG, Y. ; STALLINGA, S.: Noise amplification and ill-convergence of Richardson-Lucy deconvolution. In: *Nature Communications* 16 (2025), Nr. 1, S. 911. http://dx.doi.org/10.1038/s41467-025-56241-x.

[107] BOYD, S. ; PARIKH, N. ; CHU, E. ; PELEATO, B. ; ECKSTEIN, J.: Distributed Optimization and Statistical Learning via the Alternating Direction Method of Multipliers. In: *Foundations and Trends® in Machine Learning* 3 (2010), Nr. 1, S. 1–122. http://dx.doi.org/10.1561/2200000016.

[108] NYQUIST, H.: Certain Topics in Telegraph Transmission Theory. In: *Transactions of the American Institute of Electrical Engineers* 47 (1928), Nr. 2, S. 617–644. http://dx.doi.org/10.1109/T-AIEE.1928.5055024.

[109] SHANNON, C. E.: Communication in the Presence of Noise. In: *Proceedings of the IRE* 37 (1949), Nr. 1, S. 10–21. http://dx.doi.org/10.1109/JRPROC.1949.232969.

Appendix A

An applied noise model for scintillation-based CCD detectors in transmission electron microscopy

scientific reports

Check for updates

OPEN

An applied noise model for scintillation-based CCD detectors in transmission electron microscopy

Christian Zietlow✉ & Jörg K. N. Lindner

Measurements in general are limited in accuracy by the presence of noise. This also holds true for highly sophisticated scintillation-based CCD cameras, as they are used in medical applications, astronomy or transmission electron microscopy. Further, signals measured with pixelated detectors are convolved with the inherent detector point spread function. The Poisson noise, arising from the quantized nature of the beam electrons, gets correlated by this convolution, which allows to reconstruct the detector PSF based on the Wiener–Khinchin theorem and the Pearson correlation coefficients under homogeneous illumination conditions. However, correlation also has a strong impact on the noise statistics of basic operations like the binning of signals, as it is usually done in electron energy-loss spectroscopy. Thus, this paper aims to give an insight into the different noise contributions occurring on such detectors, into their underlying statistics and their correlation. Detectors usually suffer from gain non-linearities and quantum efficiency deviations, which must be corrected for optimal results. All these operations influence the noise and are influenced by it, vice versa. In this work, we mathematically describe all these changes and show them experimentally. Methods on how to measure individual noise and correlation parameters are described allowing readers to implement routines for finding them. Sufficient knowledge on the noise of a measurement is not only crucial for classifying its quality and meaningfulness, but also allows for better post-processing operations like deconvolution, which is a common practice in spectroscopy to enhance signals.

Keywords Noise model, Scintillation detector, Electron microscopy, Non-linearity correction, Brighter-fatter effect, Point spread function

Every measurement is subject to noise. The most prominent ones for electron microscopy and especially transmission-electron-microscopy (TEM) certainly are Poisson noise, arising from the quantized signal itself[1,2], and Gaussian read-out noise from the detector electronics[3,4]. Further, gains that influence the Poisson noise are generated by the parts of the scintillation-based detector[5] and differences in quantum efficiency between pixels on the detector[6,7] alter the noise. Correlation effects between pixels caused by the point spread function (PSF) of the detector and mathematical operations in order to correct the signal from detector artifacts further complicate the above mentioned signal alterations. To top it all of, the detector suffers from non-linearities with increasing signal strength.

To an operator, who does not have year-long experience in the subject of noise and statistics, noise statistics in general looks confusing and overwhelming. However, understanding the noise helps to interpret artifacts in the data, helps designing measurement conditions under which certain effects become visible and helps manufacturers to improve their detectors and image acquisition in the first place. Having a valid noise model also allows for modern denoising or deconvolution techniques, which improve the evaluation or make it even possible to evaluate sensitive materials such as organic or biological materials that degrade at very short exposure times in an electron microscope[8–12]. Thus, there is a broad and interdisciplinary need for algorithms in TEM, which require such a noise model. In[13], we have shown how to design and use ADMM algorithms for denoising and deconvolution in a scientific context, such that they operate unbiased by the user and purely on the measurable noise parameters of a detector and a suitable noise model. Scintillation-based CCD detectors are not limited to electron microscopy, they have use-cases in X-ray detection for astronomy[14], nuclear physics[15] as well as in medicine[16–20]. Since the detector architecture uses a CCD, the noise model that we will derive in the following is in large parts valid for general CCD cameras as well.

Nanopatterning-Nanoanalysis-Photonic Materials Group, Department of Physics, Paderborn University, Warburgerstr. 100, 33098 Paderborn, Germany. ✉email: christian.zietlow@upb.de

A 'rather complex' statistical framework is needed to describe the noise and all the alterations of measurements on such a detector. Such frameworks can be found in the references[21,22] and especially in[23]. A typical TEM user, however, may not want to deal with all contributions to the statistics of his detector. Here, we would like to focus on such contributions that are relevant or may appear relevant for the usage of a scintillation-based CCD camera attached to a TEM. Further, a typical TEM user cannot open a CCD detector without the risk of damaging it immediately. This restricts the ability to analyze the detector layers in detail. Thus, many of the parameters such as coupling efficiencies, gains, input and output quanta needed to utilize noise models for cascaded systems from Rabbani[24] or Cunningham[25] are not directly accessible. While these are sophisticated statistical descriptions, they cannot easily be applied in practical TEM work.

This paper presents a novel approach to understanding detector noise, one that integrates both theoretical and experimental perspectives to provide a comprehensive framework for noise analysis. Unlike previous studies, which often focus on either theoretical models or experimental measurements, our work seeks to bridge the gap between these two approaches. By identifying the most significant noise contributions relevant to experimentalists, we aim to develop a coherent theoretical framework that can be applied to real-world detectors.

This article starts with a general analysis of key noise sources, such that our approach can be used even with limited statistical expertise. By presenting a comprehensive treatment of the subject, we hope to facilitate a deeper understanding of the overall framework, highlighting the interconnectedness of all components and providing a cohesive framework for noise analysis.

While this paper may be lengthy and detailed, we believe that its comprehensive nature is essential for providing a thorough understanding of detector noise. By integrating theoretical and experimental perspectives, we aim to provide a valuable resource for experimentalists seeking to optimize their detectors and minimize the impact of noise on their measurements.

It is clear that this paper simplifies the vast body of statistical work on noise analysis, which spans thousands of pages of published research. To develop a practical model that can be applied under common conditions, we must identify useful approximations that enable us to isolate and separate the different noise components, allowing us to validate our model through straightforward measurements.

In statistical analysis, the reference frame in which noise is determined is crucial. The measurements proposed in this paper to quantify noise are no exception, and therefore, we strive to provide precise descriptions of our experimental methodology. By doing so, we aim to ensure that our results are reliable and reproducible, and that our model can be applied in real-world scenarios.

First of all, the general architecture of the detector is needed. In our setup, we use the *US1000FT-XP 2* detector installed in a *Gatan GIF Quantum ER* image filter[26], which is shown schematically in Fig. 1a. The analysis of this detector is the basis that we will use to evaluate our noise model. The scintillation-based detector mainly consists of three layers: a fluorescence layer, that converts incident electrons into photons; a fiber optic, which guides the photons to a CCD camera; and the CCD camera itself, converting photons into charge carriers. Such systems were statistically analyzed e.g. by Cunningham et al.[25,27]. As shown in Fig. 1b, the CCD camera consists of four segments with respectively 1024 times 1024 pixels, connected to separate read-out ports, where the charge carriers are converted into counts via analogue-digital-converters (ADC). The segmentation increases read-out speeds, but comes at the cost of having different noise properties, which must be regarded individually. In the

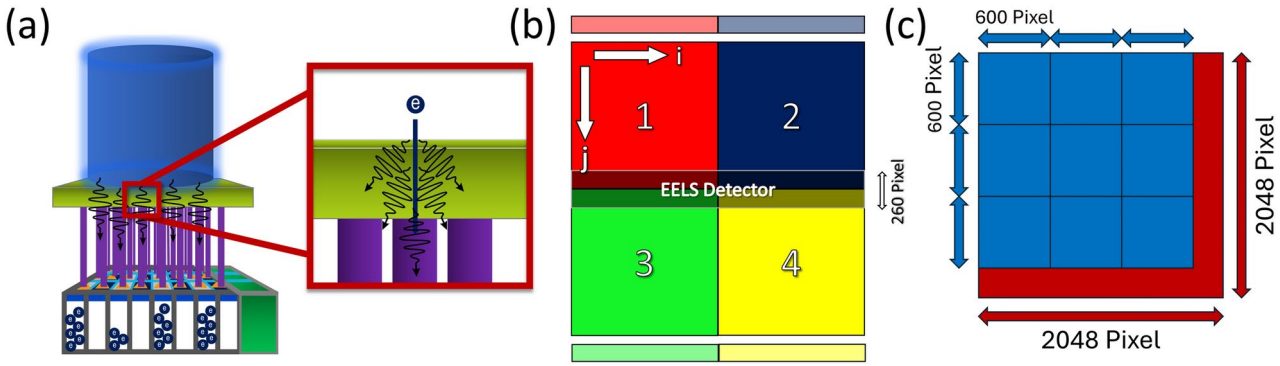

Fig. 1. (**a**) Schematic of the scintillation-based detector with the incident electron beam (blue), the fluorescent scintillation layer (green) generating optical photons and the fiber optic (purple) connecting the fluorescence layer with the 2D CCD detector, which reconverts the optical photons in charge carriers and with the analog-digital-converter (dark green) into counts. The red box shall point out, that several photons are generated per incident electron and spread across the fluorescence layer. (**b**) Schematic of the *US1000FT-XP 2* from *Gatan*[26] with 4-port read-out electronics indicated. The respective ADC ports are shown in faded colors above or below the segments. We define the respective column of the CCD to be indicated by the index *i* and the respective row of the detector by the index *j*. The region for EELS detection is located in the middle of the detector spanning across all four segments with 260 pixels in height. (**c**) Schematic for an exemplary 600 times 600 pixel binning on a 2048 times 2048 pixel detector, where the blue boxes represent the binned pixels and the red regions represent the rest that cannot fully be binned into a 600 times 600 pixel. One can easily see, that for a 2048 times 2048 pixel detector, binning with a number that contains a prime factor unequal to two leads to leftover pixels.

image filter, the CCD camera is used for both, recording images and spectra. By guiding the electron beam through a series of magnets, the electrons disperse with respect to their kinetic energy allowing to investigate energy losses induced by a specimen. Dispersing the beam in TEM mode is called energy-filtered TEM (EFTEM) and for scanning electron transmission microscopy (STEM) this method is referred to as electron-energy loss spectroscopy (EELS). The features of such loss spectra are of special interest, as they allow to determine e.g. the elemental composition of a given material or to analyze its electronic structure including light-matter interactions. In the middle of the detector, the EELS signal is measured and then summed across all rows j to convert a 2D image into a 1D spectrum. We indicated the region on the detector in Fig. 1b, where a typical EELS signal is measured. This measuring process with the CCD introduces a further spreading of the signal, leading to correlations, which was analyzed e.g. by Stierstorfer et al.[28]. Eventually, the summation process can be seen as a post-binning of the image. So, for a full analysis of the noise model useful for both TEM and STEM mode, it is necessary to understand the impact of binning. It is obvious that there are leftover pixels for any binning number containing a prime factor that is unequal to two, considering the analysis of the full 2048 times 2048 pixel detector. A schematic of such a binning is shown as an example in Fig. 1c.

In general, all scintillation-based CCD detectors are quite similar in their design, with the devil being in the 'details'. There are detectors employing less segments or a lens optics instead of fiber optics. This however does not change the general noise model but only the extend of contributing factors.

In this paper, we focus on the transmission electron microscopy (TEM) mode and give a short outlook on the impact of those findings for STEM-EELS. It is crucial for the measurement of noises to perform measurements without a specimen in the beam path to minimize variations of the signal due to external factors other than noises. This is why we performed all noise measurements in vacuum. The principles of the noise model found here can be applied to any signals acquired from structures of interest.

This paper is organized as follows: following this introduction, "Section Fundamentals of different noise statistics" provides an overview of the statistical formulas and mathematical principles exploited in this paper. This section serves as a reference, to which we will frequently refer during the derivation of our noise model in "Section The noise model". In this section, we present the proposed noise model, which encompasses the mathematical description of the image acquisition process and the various image corrections required to address deviations and non-linearities in the scintillation-based CCD detector, as well as their influence on the noise model. Additionally, we demonstrate how binning, a crucial step in the formation of EEL spectra, affects correlations and gain in the data. In "Section Evaluation of the noise model", we describe the procedure for measuring the parameters of the proposed noise model and experimentally validate the mathematical expressions. Moreover, we outline the process for acquiring the necessary detector corrections and present a method for determining the detector PSF. In "Section Theoretical considerations on STEM-EELS measurements", we examine the implications of our findings for EEL spectra, and "Section Conclusions presents a comprehensive discussion of the overall results and conclusions.

Fundamentals of different noise statistics

Noise is a stochastic process, allowing for a description in a general statistical framework, even though knowing its exact representation in the data is impossible. This publication aims to provide a comprehensive understanding of the fundamental properties of noise in data generated by scintillation-based CCDs. To establish a solid foundation for our discussion, we briefly outline the underlying mathematical principles in the following sections. In "Sections Gaussian noise" and "Poisson noise", we introduce the respective probability distributions and examine their behavior under various mathematical operations that are essential for developing the noise model. "Section Noise correlation effects" delves into the impact of correlations on the measured sample standard deviation, a crucial aspect for our analysis. Finally, in "Section Noise and convolution", we explore the effects of convolutional operations on the noise, providing a thorough understanding of this critical component of the noise model.

Gaussian noise

The most commonly known statistics describing noise in signal processing certainly is the Gaussian distribution. Coming from statistical independent random processes, it can be described with the probability density function (PDF) $\mathcal{N}$[29]:

$$\mathcal{N}\left[J(X)=n\,,\,\mu\,,\,\sigma^2\right]=\frac{1}{\sqrt{2\pi\sigma^2}}\cdot\exp\left\{-\frac{(n-\mu)^2}{2\sigma^2}\right\}\,, \tag{1}$$

with the mean value μ and the variance σ^2. In general, the normal distribution gives the probability to measure n noise counts as a result of a measurement J of a random and thus independent variable X, which, in our case, might be a pixel number.

To shorten notation, we will use $\mathcal{N}\left[\mu\,,\,\sigma^2\right]$ as a representation of the above described measurement.

Working with Gaussian distributions requires several important mathematical operations, such as addition, subtraction, multiplication and so on. These operations change the mean value and variance to different extents, but fortunately most are commonly found in standard text books of statistics for students. For our work, we need the following operations for our noise model:

Adding two or more independent random variables X_w leads to the addition of their mean values and their variances. The resulting distribution also corresponds to a Gaussian distribution[30]. Adding Gaussian distributions is also equal to convolving them[31,32]:

$$\sum_{w=1}^{W} X_w = X_1 \otimes X_2 \otimes \cdots \otimes X_W = \sum_{w=1}^{W} \mathcal{N}\left[\mu_w\,,\,\sigma_w^2\right] = \mathcal{N}\left[\sum_{w=1}^{W}\mu_w\,,\,\sum_{w=1}^{W}\sigma_w^2\right]\,, \tag{2}$$

where $\otimes$ is the convolution operator.

The multiplication of a Gaussian distributed variable X by a constant c is given as[29]:

$$cX = \mathcal{N}\left[c\mu\,,\,c^2\sigma^2\right]\,, \tag{3}$$

where it is important to note that the factor c appears squared in the variance.

The distribution f_Z of the product of two uncorrelated random variables $Z = XY$ with the expectation value $E(Z)$ and variance $\mathrm{VAR}(Z)$ are given as[33]:

$$f_Z(z) = \int_{-\infty}^{\infty} \frac{1}{|x|}\, f_X(x)\; f_Y(z/x)\; dx \qquad , \tag{4}$$

$$E(Z) = E(X)\cdot E(Y) \qquad , \tag{5}$$

$$\mathrm{VAR}(Z) = \left(\sigma_X^2 + \mu_X^2\right)\cdot\left(\sigma_Y^2 + \mu_Y^2\right) - \mu_X^2\mu_Y^2\,, \tag{6}$$

with the respective probability density functions $f_X(x)$ and $f_Y(y)$. Here, x, y and z denote the position in the distribution. Note that the resulting distributions are still quite elaborate and often result in infinite sums. Simplifications of these exact representations are a current topic of research[34].

For the ratio of a random variable $1/X$, one can utilize Díaz-Francés et al.[35] who showed that the ratio with a Gaussian can be approximated by a normal distribution, if the denominator is closely distributed about its mean value:

$$\mathcal{N}\left[\mu,\sigma^2\right]^{-1} \approx \mathcal{N}\left[\mu^{-1},\frac{\sigma^2}{\mu^4}\right]\,. \tag{7}$$

Poisson noise

Another important process occurring as a consequence of the discrete nature of photons or electrons is the Poisson process. Similar to tossing a coin, there are only two possible outcomes: measuring or not measuring an event. This leads to a PDF that is slightly skewed towards higher counts[32,36]:

$$\mathscr{P}\left[J\left(\hat{S}\right) = n\right] = \frac{\hat{S}^{\,n}}{n!}\exp\left\{-\hat{S}\right\}\,, \tag{8}$$

with the probability $\mathscr{P}$ to measure n counts of a signal S with its expectation value $E[S] = \hat{S}$ and J again denoting the measurement. We shorten the notation to $\mathscr{P}\left[\hat{S}\right]$. For a sufficiently high count regime, the Poisson distribution converges to the Gaussian distribution, with both the mean value and the variance equal to the expectation value[36]:

$$\lim_{\hat{S}\to\infty}\mathscr{P}\left[\hat{S}\right] \approx \mathcal{N}\left[\hat{S}\,,\,\hat{S}\right]\,. \tag{9}$$

In fact, a main characteristic of the Poisson distribution is that the noise variance always equals the expectation value of the signal $\sigma^2 = \mu$[36].

The summation rule for Poisson distributions is given as[31,36]:

$$\sum_{w}\mathscr{P}\left[\hat{S}_w\right] = \mathscr{P}\left[\sum_{w}\hat{S}_w\right]\,, \tag{10}$$

where the sum of Poisson distributions equals the Poisson distribution of the sum of the expectation values. Subtracting Poisson distributions in contrast leads to the Poisson-difference distribution, also known as Skellam distribution[37]:

$$\mathscr{S}\left[J\left(\hat{S}_1\right) - J\left(\hat{S}_2\right) = n\,,\hat{S}_1,\hat{S}_2\right] = \exp\left\{-\left(\hat{S}_1+\hat{S}_2\right)\right\}\left(\frac{\hat{S}_1}{\hat{S}_2}\right)^{n/2}\mathscr{I}_{|n|}\left(2\sqrt{\hat{S}_1\cdot\hat{S}_2}\right)\,, \tag{11}$$

with $\mathscr{I}_{|n|}(x)$ denoting the modified Bessel function of the first kind and $\hat{S}_{1,2}$ the expectation values of $S_{1,2}$. For a shorter notation, we will write $\mathscr{S}\left[\hat{S}_1,\hat{S}_2\right]$.

Multiplying a Poisson distributed signal S^* with a gain factor g, such that $S = g\cdot S^*$, leads to the distribution[38–40]:

$$g \cdot \mathscr{P}\left[\hat{S}^*\right] = g \cdot \mathscr{P}\left[\frac{\hat{S}}{g}\right] = \mathscr{P}_g\left[\hat{S}\right] \quad \text{, with} \quad \mathscr{P}_g\left[\hat{S}\right] = \frac{\left(g^{-1} \cdot \hat{S}\right)^{g^{-1} \cdot n}}{\Gamma\left[g^{-1} \cdot n + 1\right]} \exp\left\{-g^{-1} \cdot \hat{S}\right\} \ , \tag{12}$$

which is denoted as the super-Poisson distribution for $g > 1$ and as sub-Poisson distribution for $g < 1$[40,41]. Here, the multiplication of the signal is comparable to Eq. 3, as it shifts the mean value of the distribution and changes its variance accordingly. To complete the trio, we will refer to the Poisson distribution as the true-Poisson distribution for the case $g = 1$ in the following. This formula is valid for deterministic gains, where each incident electron generates the exact same number of photons. However, this would only allow for *n*-values, which are a multiple of *g*, and integer values of *g*. Usually, this is not the case for scintillation-based detectors, as the generation of photons from beam electrons is a statistical process itself and may vary for each incident electron[25]. Thus, we consider the gain of the detector to be the mean value of said generation process. This definition allows the gain to be a fractional number. As a consequence, in the above formula, we have replaced the factorial by the gamma function $\Gamma[\cdot]$ to account for non-integer values within the argument, as $n! = \Gamma[n+1]$. It is obvious that the above scaled Poisson distribution is a simple approximation to the true distribution[42], but we found it to work quite well for us. A description of the true distribution is found in e.g.[25], but its description is much more complex and requires many input parameters that are usually not directly measurable on a detector, as mentioned in the introduction.

Noise correlation effects

So far, the above noise distributions assume the noise to be independently distributed. However, in a detector this is rarely the case. Thus we need to explain the impact of correlation on the variance of the noise distributions.

To differentiate the variance measured within a single frame σ^2_{SF}, which is subject to correlation effects, from the variance of a single pixel across many frames σ^2, which we consider independent and thus 'true', we use different variables for them. This differentiation is important as the expected variances of both are not equal under the premise of correlation. In the experimental section of this work, we mainly determine the variances within a single frame σ^2_{SF} and thus need to elaborate on the implications that this frame of reference offers.

The definition for the variance is given as[30,32]:

$$\sigma^2 = E\left[S^2\right] - E\left[S\right]^2 = E\Big[\, S - E\left[S\right] \,\Big]^2 \ , \tag{13}$$

with the expectation value $E[S]$ of a random variable *S*, that in our case could be a signal. For a finite number of pixels in a detector and a homogeneous signal, where all expectation values are equal $E[S] = E[s_{i,j}]$, the true variance is unknown but can be estimated using:

$$\sigma^2_{SF} = E\left[s_{i,j} - \frac{1}{MN} \sum_{m^*=1}^{M} \sum_{n^*=1}^{N} s_{m^*,n^*} \right]^2 \ , \tag{14}$$

with the value of a pixel $s_{i,j}$ and the latter term describing the mean value of all pixels with the double sum across all indices. Here, $i \in [1, \ldots, N]$ describes the position in the row, and $j \in [1, \ldots, M]$ describes the position in the column. By replacing $s_{i,j}$ with the difference between pixel and its expectation value $ds_{i,j} = s_{i,j} - E[s_{i,j}]$ in the above expression, we obtain[43]:

$$\sigma^2_{SF} = E\left[ds_{i,j} - \frac{1}{MN} \sum_{m^*=1}^{M} \sum_{n^*=1}^{N} ds_{m^*,n^*} + E\left[s_{i,j}\right] - \frac{1}{MN} \sum_{m^*=1}^{M} \sum_{n^*=1}^{N} E\left[s_{m^*,n^*}\right] \right]^2 \ , \tag{15}$$

where the first two terms describe deviations of the variance of a given pixel from the mean variance of the detector. The latter terms vanishes, if the signal is homogeneous, since the expectation value for all *s* is identical in this specific case. Utilizing Eq. 13 leads to[43]:

$$\begin{aligned} \sigma^2_{SF} &= E\left[ds^2_{i,j}\right] - E\left[\frac{1}{M \cdot N} \cdot \sum_{m^*=1}^{M} \sum_{n^*=1}^{N} ds_{m^*,n^*} \right]^2 \\ &= \sigma^2 - \frac{1}{(MN)^2} \cdot \sum_{m^*=1}^{M} \sum_{n^*=1}^{N} \sum_{p=1}^{M} \sum_{q=1}^{N} E\left[ds_{m^*,n^*} \cdot ds_{p,q}\right] \ , \end{aligned} \tag{16}$$

where $E\left[ds^2_{i,j}\right] = \sigma^2$ gives the expectation value of the variance of a given pixel, which is the true uncertainty of the data. The latter term describes the mean covariance of all pixels, with the covariance defined as[32]:

$$\operatorname{cov}\left[s_{m^*,n^*}\,,\, s_{p,q}\right] = E\Big[\underbrace{\left(s_{m^*,n^*} - E\left[s_{m^*,n^*}\right]\right)}_{= ds_{m^*,n^*}} \cdot \underbrace{\left(s_{p,q} - E\left[s_{p,q}\right]\right)}_{= ds_{p,q}} \Big] \ . \tag{17}$$

As the noise is homogeneously distributed across the detector, the covariance $\mathrm{cov}\left[s_{m^*,n^*},\, s_{p,q}\right]$ only depends on the horizontal and vertical separation $m = p - m^*$ and $n = q - n^*$, respectively, and not on the individual pixel $\mathrm{s}_{i,j}$. Often, *m* and *n* are referred to as horizontal and vertical lag. We can thus simplify:

$$\begin{aligned} \mathrm{cov}\left[s_{m^*,n^*},\, s_{p,q}\right] &= \mathrm{cov}\left[s_{m^*,n^*},\, s_{m^*,n^*}\right] \cdot \rho_{m,\,n} \\ &= \sigma^2 \cdot \rho_{m,\,n} \end{aligned} \quad , \text{with} \quad \begin{aligned} \rho_{m,\,n} &= \frac{\mathrm{cov}\left[s_{m^*,n^*},\, s_{m^*+m,\,n^*+n}\right]}{\mathrm{cov}\left[s_{m^*,n^*},\, s_{m^*,n^*}\right]} \\ &= \frac{\mathrm{cov}\left[s_{m^*,n^*},\, s_{m^*+m,\,n^*+n}\right]}{\sigma^2} \end{aligned} , \tag{18}$$

where $\rho_{m,n}$ are the Pearson correlation coefficients[44], describing the autocovariance function of two pixels in the data set. In order to calculate the variance within the single frame, we need to combine Eq. 16 with Eq. 18. However, two double sums are hard to handle and thus we need a simpler solution. For the values $n^* = 1$ and $q = 1$(thus $n = 0$) within the total sum, we obtain:

$$\sum_{m^*=1}^{M}\sum_{p=1}^{M} E\left[ds_{m^*,1} \cdot ds_{p,1}\right] = \sigma^2 \cdot \sum_{m^*=1}^{M} \rho_{1-m^*,0} + \rho_{2-m^*,0} + \cdots + \rho_{M-m^*,0} = \sum_{m=-(M-1)}^{M-1} (M - |m|) \cdot \rho_{m,0} \,. \tag{19}$$

It can easily bee seen that by increasing m^* from 1 to *M*, $\rho_{0,0}$ is contained *M* times within the sum. We further find $\rho_{1,0}$ and $\rho_{-1,0}$ to be contained $(M-1)$ times, $\rho_{2,0}$ and $\rho_{-2,0}$ $(M-2)$ times and so on, until we obtain $\rho_{M-1,0}$ and $\rho_{-(M-1),0}$ only once. Repeating this pattern for all the other values of n^* and *q* to complete the two double sums in Eq. 16, leads to:

$$\sigma_{SF}^2 = \sigma^2 \cdot \left(1 - \frac{1}{(M \cdot N)^2} \sum_{m=-(M-1)}^{M-1} \sum_{n=-(N-1)}^{N-1} (M - |m|) \cdot (N - |n|) \cdot \rho_{m,\,n}\right) \,, \tag{20}$$

where $\rho_{m,\,n} \in [-1, 1]$ ranges from -1, in case of total anti-correlation, through 0, for uncorrelated data, to 1, for total correlation of the data[32]. Naturally, a given pixel is always totally correlated with itself, so $\rho_{0,0} = 1$. In a case with uncorrelated noise between pixels, all other coefficients are zero $\rho_{m,\,n} = 0$. By simplifying and rearranging the sample variance is revealed[45]:

$$\begin{aligned} \sigma^2 &= \frac{MN}{M \cdot N - 1} \cdot \sigma_{SF}^2 \\ &= \frac{1}{M \cdot N - 1} \cdot \sum_{i=1}^{M}\sum_{j=1}^{N} E\left[s_{i,j} - \frac{1}{MN}\sum_{m^*=1}^{M}\sum_{n^*=1}^{N} s_{m^*,n^*}\right]^2 \,, \end{aligned} \tag{21}$$

by utilizing Eq. 14. In a case of total anti-correlation, where all other coefficients $\rho_{m,\,n} = -1$, the single frame variance $\sigma_{SF}^2 \to 2\sigma^2$ approaches twice the true variance, as the number of pixels increases. Conversely, in case of total correlation of the data, with all $\rho_{m,\,n} = 1$, Eq. 20 equals zero as a logical consequence. Per definition all pixels must have the same value in this case. We can thus establish, that correlated data exhibits a smaller variance than uncorrelated data and that anti-correlation leads to higher measured sample variances.

Considering all of the above, we can define a factor β_{corr} that accounts for the change in the sample variance due to correlation:

$$\beta_{corr} = \frac{MN}{MN - 1} \cdot \left(1 - \frac{1}{(M \cdot N)^2} \sum_{m=-(M-1)}^{M-1} \sum_{n=-(N-1)}^{N-1} (M - |m|) \cdot (N - |n|) \cdot \rho_{m,n}\right) \,, \tag{22}$$

with $\beta_{corr} \in [0,\, 2]$. It can easily be seen that for large sets of pixels $\beta_{corr} \to 1$ and thus the influence of correlation decreases. With the newly defined β_{corr}, we can rewrite Eq. 20 to:

$$\beta_{corr} \cdot \sigma^2 = \frac{1}{M \cdot N - 1} \sum_{i=1}^{M}\sum_{j=1}^{N} E\left[s_{i,j} - \frac{1}{MN}\sum_{m^*=1}^{M}\sum_{n^*=1}^{N} s_{m^*,n^*}\right]^2 \,. \tag{23}$$

where it can be seen that the measured variance within a single frame changes with correlation.

Correlation indicates a common process that links both variables. It thus does not influence the shape of a Gaussian or a Poisson distribution, except for their variance:

$$\mathcal{N}\left[\mu\,,\, \sigma^2\right] \overset{Correl.}{\longrightarrow} \mathcal{N}\left[\mu\,,\, \beta_{corr} \cdot \sigma^2\right] \quad \text{and} \quad \mathscr{P}\left[\hat{S}\right] \overset{Correl.}{\longrightarrow} \mathscr{P}_{\beta_{corr}}\left[\hat{S}\right] \,. \tag{24}$$

For the true-Poisson distribution this necessarily leads to a sub-Poisson distribution for correlation or a super-Poisson in case of anti-correlation. This means that correlation of the signal acts like an additional gain-factor on the Poisson distribution, when considering the noise inside an image. In contrast, the statistics of a single pixel in

a series of measurements is not altered. This is for instance the case for EELS-mapping, where a series of spectra is taken on the same detector.

Correlation also drastically changes the addition of correlated random variables. Adding pixels of a detector, e.g. by binning, leads to a reduction of the pixel-set, but also to additions within the Pearson correlation coefficients as shown schematically in Fig. 2. Under the influence of correlation, Eq. 2 changes into[32]:

$$\sum_{w=1}^{W} \mathcal{N}\left[\mu_w\,,\,\sigma_w^2\right] = \mathcal{N}\left[\sum_{w=1}^{W}\mu_w\,,\,\sum_{w=1}^{W}\sum_{w^*=1}^{W}\mathrm{cov}\left[S_w, S_{w^*}\right]\right]\,, \tag{25}$$

in the general case, where the covariances between variables add to the total variance. Under the assumption that all pixels have the same variance and the same expectation value, we can state for a detector:

$$\begin{aligned}\sum_{h=1}^{H}\sum_{v=1}^{V}\mathcal{N}\left[\mu_{h,v},\,\sigma_{h,v}^2\right] &= \mathcal{N}\left[\sum_{h=1}^{H}\sum_{v=1}^{V}\mu_{h,v},\,\sigma^2\cdot\rho_{0,0}^{bin,*}\right] \quad\text{, with}\\ \rho_{0,0}^{bin,*} &= \sum_{h=-(H-1)}^{H-1}\;\sum_{v=-(V-1)}^{(V-1)}(H-|h|)\,(V-|v|)\cdot\rho_{h,v}\,,\end{aligned} \tag{26}$$

with the summation being limited by the number of available pixels $H \in [1, M]$ and $V \in [1, N]$. In general, the new Pearson coefficients $\rho_{m,n}^{bin}$ of a system after vertical summation of V rows and horizontal summation of H columns are given as:

$$\rho_{m,n}^{bin} = \frac{\sum_{h=-(H-1)}^{H-1}\sum_{v=-(V-1)}^{V-1}(H-|h|)\,(V-|v|)\cdot\rho_{H\cdot m+h,V\cdot n+v}}{\rho_{0,0}^{bin,*}}\,, \tag{27}$$

where the central Pearson correlation coefficient is always defined as $\rho_{0,0}^{bin} = 1$.

The Wiener–Khinchin theorem[46,47] states that the autocovariance function K of a random process and the power spectral density (PSD) form a Fourier-transform pair, which allows to determine all the Pearson coefficients $\rho_{n,m}$ of an image ξ by normalizing with respect to the maximum entry:

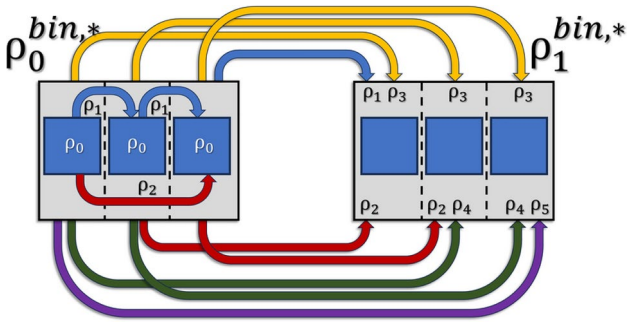

Fig. 2. This schematic shows six pixels (blue) in a row, out of which the first three are binned into one pixel (grey). The same is done for the next three pixels. The indices of the Pearson correlation coefficient denote the distance between correlated pixels, thus one can easily count the amount of possible distances within a new or between new, added up pixels. By adding three neighboring pixels (blue) on the left side, one can see that the $\rho_0^{bin,*}$-coefficient of the new pixel (grey) must incorporate 3 times the ρ_0-coefficient, 2 times the ρ_1-coefficient, and once the ρ_3-coefficient. The correlations, expressed by their Pearson correlation coefficients, are indicated with a blue arrow for next neighbors, with a red arrow for the second next neighbors as well as yellow, green and purple for the more distant neighbors. Note that the distance between pixels works in both ways, so the negatively numbered Pearson correlation coefficients ρ_{-1} and ρ_{-2} must be added to the respective new coefficient in equal number as their positive counterparts. ρ_0, indicated in white, is the correlation of a pixel with itself and is thus defined as 1. Now, the correlation between the binned pixels is of interest. On the right side the new $\rho_1^{bin,*}$-coefficient must inherit 3 times the ρ_3-coefficient, 2 times the ρ_2-coefficient, and once the ρ_1-coefficient of the unbinned pixels. Additionally, one obtains 2 times the ρ_4-coefficient and once the ρ_5 -coefficient. So, when binning w pixels, one sees that this requires $2w - 1$ additions of the Pearson correlation coefficients of the former system. These principles extend on higher and on negative new coefficients. Now, $\rho_0^{bin,*}$ gives the multiplicand for the old true variance σ^2 to form the new $\sigma_{true,bin}^2$. Normalizing all new coefficients by $\rho_0^{bin,*}$ gives the nth Pearson correlation coefficient ρ_n^{bin} of the new system, with which a new β_{corr}^{bin} can be calculated using Eq. 22.

$$\rho(\xi) = \frac{K(\xi)}{\sigma^2} = \frac{\mathscr{F}^{-1}[PSD(\xi)]}{\max\{\mathscr{F}^{-1}[PSD(\xi)]\}} \quad , \text{with} \quad PSD(\xi) = \frac{\left|\mathscr{F}\left[\xi - \frac{1}{N\cdot M}\sum_{i=1}^{M}\sum_{j=1}^{N}\xi_{i,j}\right]\right|^2}{N\cdot M} \ , \tag{28}$$

where $\mathscr{F}[\cdot]$ and $\mathscr{F}^{-1}[\cdot]$ denote the 2D Fourier transform and its inverse, while $|\cdot|$ denotes the absolute value. Autocovariance and autocorrelation are two terms that are often used synonymously[48]. However, the autocovariance function $K(\xi)_{x,y,x',y'}$ between the positions (x, y) and (x', y') equals the autocorrelation function $R_{x,y,x',y'}(\xi)$ with the mean values of both positions multiplied and subtracted[49]:

$$K_{x,y,x',y'}(\xi) = R_{x,y,x',y'}(\xi) - \mu_{x,y}(\xi)\,\mu_{x',y'}(\xi) \ . \tag{29}$$

Noise and convolution

So far, we have described the fundamentals of different noise distributions and how performing mathematical operations with them changes their respective distributions. We further discussed, how correlation changes the measured variances within a single frame and the resulting variances, when adding variables. What we have not discussed yet, is how convolution changes the noise on a detector.

From a mathematical perspective, convolution and cross-correlation are closely related, with the only difference being the direction with which the kernel is applied[50]. Revisiting the last section, autocorrelation is nothing else than cross-correlation between a signal and itself[50,51]. In discrete form, convolution and cross-correlation are given as[51]:

$$[f\otimes g]_{m,n} = \sum_{m^*=-\infty}^{\infty}\sum_{n^*=-\infty}^{\infty} f_{m-m^*,\,n-n^*}\,g_{m^*,\,n^*} \qquad \text{and} \qquad [f\star g]_{m,n} = \sum_{m^*=-\infty}^{\infty}\sum_{n^*=-\infty}^{\infty} \overline{f_{m^*-m,\,n^*-n}}\,g_{m^*,\,n^*} \ , \tag{30}$$

where $\overline{f_{m^*-m,\,n^*-n}}$ denotes the complex conjugate of $f_{m^*-m,\,n^*-n}$. If f and g are Hermitian, both convolution and cross-correlation are equal $[f\otimes g]_{m,n} = [f\star g]_{m,n}$[51,52]. Knowing this and considering the last section, where we discussed the Pearson correlation coefficients, the idea is obvious that correlation and convolution are closely related. And indeed, one can show how convolutions changes the power spectral density of the noise, which is greatly explained in i.e. reference[21]. In this section, we will elaborate on this and try to summarize the most important points.

Since the convolution process satisfies the distributive property[50], we can separate a given signal S into a pure-signal $\hat{S}$ and a pure-noise component. Approximating the Poisson distribution by a Gaussian $\mathscr{N}\left[0,\sigma_S^2\right]$ and convolving, leads to both the signal and the noise being convolved with the same kernel Ω^*:

$$\Omega^*\otimes(\hat{S}+\mathscr{N}\left[0,\sigma_S^2\right]) = \Omega^*\otimes\hat{S} + \Omega^*\otimes\mathscr{N}\left[0,\sigma_S^2\right] \ . \tag{31}$$

From this point on, we focus on the noisy part of the equation and set aside the convolved signal. Considering a homogeneous signal, the Poisson noise σ_S is evenly distributed. We can split the convolution into a gain g and a normalized kernel Ω, which we apply on the noise. For noise smoothing to occur by convolution, a scattering process is needed that generates multiple particles per incident electron, with $g \gg 1$, enabling them to distribute laterally while remaining correlated due to their common origin. This criterion is more than fulfilled for the TEM, as every incident beam electron creates a cloud of hundreds to thousands of photons in the scintillation layer.

In contrast, a smoothing of the noise would not be possible if only one photon was created[24,25]. In this case, some lateral deviation from the designated path would indeed lead to image blurring, but not affect the noise at all. Further, Cunningham et al.[25] pointed out that the conversion gain from electrons to photons is a statistical process itself and thus subject to variations, which they described as Poisson distributed. For lower gains, Eq. 12 must be altered by an noise excess term[25] to account for the correct noise variance. Thus, we need to consider a high conversion gain such that the overall influence of these deviations is small for a sufficient approximation.

Given every pixel of this image is a representation drawn from the noise distribution $\zeta_{i,j} \in \mathscr{N}\left[0,\sigma_S^2\right]$, we can write:

$$\Omega^*\otimes\zeta = g\cdot\Omega\otimes\zeta \qquad \text{, with} \qquad g = \sum_{m,n}^{M,N}\Omega^*_{m,n} \quad \text{and} \quad \Omega = \frac{\Omega^*}{g} \ . \tag{32}$$

Autocorrelation yields the Pearson coefficients, as described in the previous section, multiplied by the variance. It is defined as the cross-correlation of a signal with itself. So, the autocorrelation function of convolved noise is given as:

$$\left[g\cdot\Omega\otimes\zeta\star g\cdot\Omega\otimes\zeta\right]_{m,n} = g^2\cdot\left[\Omega\star\Omega\otimes\zeta\star\zeta\right]_{m,n} \ , \tag{33}$$

where we use the associative property for a scalar multiplication[50] and Eq. 3 for the gain g. Further, we can rearrange the equation, in case both Ω and the distribution of noise in the image are Hermitian, due to the associative property of the convolution[50]. Scattering processes are of symmetrical nature and the detector inherits a x-/y- symmetry of the detector-pixels, thus we can assume that Ω is in close approximation to being

symmetric with respect to its main diagonal. Additionally, we can assume that all elements $\Omega_{m,n} \in \mathbb{R}$, which then satisfies a Hermitian matrix.

In case the noise is uncorrelated, the autocovariance function yields the Pearson correlation coefficients multiplied by the variance of the image σ_S^2. The Pearson correlation coefficients can be written as a Dirac delta functional $\rho_{m,n} = \delta_{m,n}$, as only the $\rho_{0,0} = 1$. The only functional H obeying $[H \star H]_{m,n} = \delta_{m,n}$ is again a Dirac delta functional, which also satisfies a Hermitian matrix:

$$g^2 \cdot \left[\Omega \star \Omega \otimes \zeta \star \zeta\right]_{m,n} = g^2 \cdot \left[\Omega \star \Omega \otimes \delta \cdot \sigma_S^2\right]_{m,n} = g^2 \sigma_S^2 \cdot [\Omega \star \Omega]_{m,n} \ , \tag{34}$$

where the convolution with δ gives the original expression. The equation can be rewritten:

$$g^2 \sigma_S^2 \cdot [\Omega \star \Omega]_{m,n} = g^2 \sigma_S^2 \cdot [\Omega \otimes \Omega]_{m,n} \ . \tag{35}$$

We see, that the autocorrelation takes the shape of the convolution kernel convolved with itself. Considering a process with a sufficiently high gain, we see that convolving noise with a kernel broader than a Dirac delta peak δ leads to a reduction of the central element $[\Omega \otimes \Omega]_{0,0} \leq 1$. Since autocorrelation gives the Pearson coefficients and their central element is defined as $\rho_{0,0} = 1$, we need to rescale it to 1:

$$g^2 \sigma_S^2 \cdot [\Omega \otimes \Omega]_{0,0} \frac{[\Omega \otimes \Omega]_{m,n}}{[\Omega \otimes \Omega]_{0,0}} = g^2 \cdot \sigma_S^2 \cdot \beta_{conv} \cdot \rho_{m,n} \quad \text{, with} \quad \rho_{m,n} = \frac{[\Omega \otimes \Omega]_{m,n}}{[\Omega \otimes \Omega]_{0,0}} \ , \tag{36}$$

by introducing a smoothing factor β_{conv} for the correlation, given as:

$$\beta_{conv} = [\Omega \otimes \Omega]_{0,0} = \left(\sum_{m=-(M-1)}^{M-1} \sum_{n=-(N-1)}^{N-1} \frac{[\Omega \otimes \Omega]_{m,n}}{[\Omega \otimes \Omega]_{0,0}} \right)^{-1} = \left(\sum_{m=-(M-1)}^{M-1} \sum_{n=-(N-1)}^{N-1} \rho_{m,n} \right)^{-1} \ , \tag{37}$$

where $\beta_{conv} \in [0, 1]$. We obtain a new variance $\sigma^2_{\Omega \otimes S} = \beta_{conv} \cdot \sigma_S^2$ for the convolved signal, which is reduced compared to the original.

Again, regarding Eq. 33 for the case the noise is somehow correlated, we obtain the Pearson correlation coefficients to be Hermitian as a result of the autocorrelation function[51]. By utilizing the associative property of the convolution[50], the equation can be rewritten as:

$$\sigma_S^2 \cdot \rho_{m,n} = \sigma_S^2 \cdot [\Omega_1 \otimes \Omega_0 \otimes \delta \star \Omega_1 \otimes \Omega_0 \otimes \delta]_{m,n} = \sigma_S^2 \cdot [\Omega \otimes \Omega]_{m,n} \quad \text{, with} \quad \Omega = \Omega_0 \otimes \Omega_1 \ . \tag{38}$$

We have shown that the convolution of a signal S with a kernel Ω leads to a gain g, a smoothing factor β_{conv} reducing the variance of the signal σ_S, and to correlation, which further smoothens the variance with a factor β_{corr}, if measured within the same image (see Eq. 22). In Eq. 31, we approximated the Poisson distribution by a Gaussian to separate noise and signal. We need to reassemble both again in order to determine the effect of convolution on the Poisson distribution. Considering that the noise inherently follows the signal, due to the quantized nature of the electron, and a gain combined with a convolution changes the expected variance, we can state that convolution leads to a super- or sub-Poisson distribution, depending on the gain and the smoothing factor. Again, for a Poisson distributed signal $\hat{S}^*$ and an unnormalized convolution kernel $\Omega^* = g \cdot \Omega$, with $S = g \cdot S^*$, we obtain:

$$\Omega^* \otimes \mathscr{P}\left[\hat{S}^*\right] = \Omega \otimes \mathscr{P}_g\left[\hat{S}\right] = \mathscr{P}_{g \cdot \beta_{conv} \cdot \beta_{corr}}\left[\Omega \otimes \hat{S}\right] \quad \text{, given that} \quad g \gg 1 \ , \tag{39}$$

as multiple particles are needed as a result of a scattering event to spread out.

Owing to the similarity between correlation and convolution, one can determine the PSF, or in other words the convolution kernel, of the entire detector with all its complex architecture as the inverse Fourier transform of the square root of the PSD function Eq. 28:

$$\Omega = \mathscr{F}^{-1}\left[\left(\mathscr{F}\left[\rho\left(\xi\right)\right]\right)^{1/2}\right] \ . \tag{40}$$

So, if the signal convolved with the detector PSF $\Omega \otimes \hat{S}$ is sufficiently known, e.g. homogeneously distributed, the mean value of every pixel can be subtracted from a noisy image, following Eq. 28, and the detector PSF can easily be found hidden within the noise. Later in this paper, we will show how this is done under experimental conditions.

However, summing the Pearson coefficients of a stationary process ρ^*, such as found on a CCD, eventually yields zero[53]:

$$\sum_{m=-(M-1)}^{M-1} \sum_{n=-(N-1)}^{N-1} \rho^*_{m,n} = 0 \ . \tag{41}$$

Unfortunately, this leads to an underestimation of the higher coefficients and even produces negative coefficients, such that the above equation is satisfied.

Now, that we have outlined the mathematical and statistical principles, we can apply them to a real detector to develop a valid noise model.

The noise model

As is shown in the following, the acquisition of images with a scintillation-based CCD detector like the *US1000FT-XP 2* detector employed in the *'Gatan Image Filter (GIF) Quantum ER'* is a rather complex process. In these detectors, several transformation processes, from electrons to photons to excitons to counts, are necessary to gather an image. Starting with a general description of different types of noises and their origins, the following section will guide through the acquisition process of the camera itself and the mathematical description of the noises connected to it. Usually these images are further processed to improve the quality of data. Gain normalization and dark frame subtractions are standard procedures to clear the images of detector induced artifacts. Pixel binning and summations of the 2D images to individual spectra, like in EELS, are done to improve the visual understanding of the data, to reduce storage space and processing time - but all these procedures change the noise level and the corresponding noise distribution. To describe all these processes mathematically, we need a lot of different variables. We found it helpful to have a list, where all following variables are explained briefly, to increase the readability of the paper. This list can be found in the supplementary information.

To facilitate understanding of the noise model, we provide a flow chart of the image acquisition process in Fig. 3, serving as a guide for the reader throughout this paper.

Our experimental setup consists of a *'JEOL JEM-ARM200F'* microscope, with no specimen in the beam path, as we focus on noise analysis. The beam is directed into the GIF camera, where it interacts with a scintillation layer, converting the incident electrons into photons. These photons are subsequently transmitted through fiber optics to a CCD camera. In "Section Signal and detector noise", we discuss beam correlations and demonstrate how convolution with the detector's point-spread function (PSF) affects the resulting Pearson correlation coefficients of this correlation phenomenon. We also introduce multiple gain factors associated with individual detector layers and the corresponding smoothing factors arising from convolution operations. A simple mathematical framework is provided to describe detector deviations and non-linearities, which require corrections. Furthermore, we identify and describe various components of detector noise.

Subsequently, the detector characteristics are removed through multiple post-processing steps, which are implemented in software and affect both signal and detector noises. We begin by examining the impact of background subtraction on detector noise in "Section Dark frame subtraction". Next, we describe the formation of a gain reference image in "Section The acquisition of a gain reference", which is crucial for determining the uncertainty associated with such a measurement. In "Section The application of a gain reference", we discuss how the application of the gain reference alters both signal and detector noises. Furthermore, we address the non-linearity effects of the camera, which must be incorporated into the noise model. In "Section Gain non-linearities", we explain how to include these corrections and demonstrate their impact on signal and detector

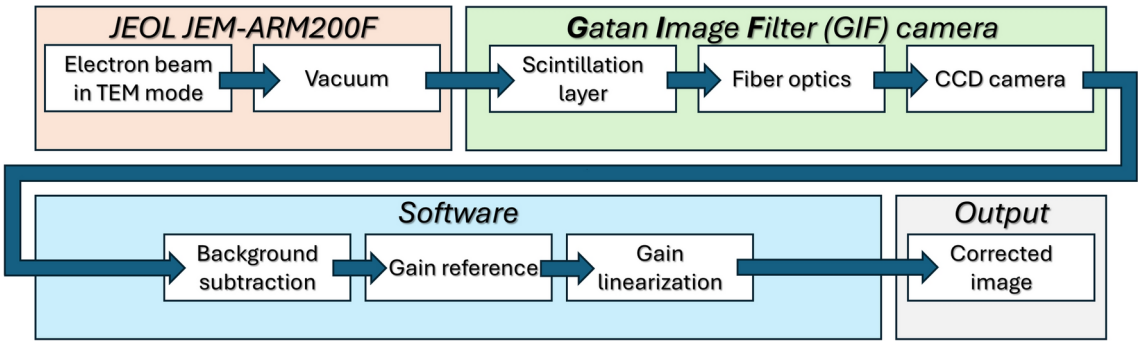

Fig. 3. Schematic flow chart of the image acquisition process. Our experimental setup utilizes a *'JEOL JEM-ARM200F'* transmission electron microscope with no specimen within the beam path, since we are only interested in the image noises. The microscope constitutes the initial stage of the image acquisition process (depicted in orange). The image acquisition process then splits into two primary components, the detector hardware, comprising the *'Gatan Image Filter (GIF) Quantum ER'* camera, which generates the raw image data (indicated in green); and the subsequent software post-processing (depicted in blue). The combination of hardware and software components ultimately yields the corrected image as output (depicted in gray). The hardware component can be further divided into three distinct detector layers: First, the scintillation layer, where incident beam electrons are converted into photons. Second, the fiber optics system, which guides these photons to the subsequent layer. Third, the CCD camera, where the photons are converted into excitons and ultimately into counts. Following the hardware processing, the software post-processing corrects for offsets in the image by subtracting a background frame. To compensate for quantum deviations, the resulting image is then multiplied by a gain reference acquired under homogeneous illumination conditions prior to the experiment. Finally, the counts are corrected via gain linearization, which accounts for the non-linear behavior of the CCD detector with increasing count numbers.

noises. Notably, the non-linearity correction must be applied not only to the measurement data but also to the gain reference, as it is also acquired using a non-linear detector. Additionally, we discuss the brighter-fatter effect, a phenomenon that alters the width of the detector's point-spread function (PSF) with increasing signal strength, driven by charge diffusion processes in the CCD camera. This effect is considered essential in our noise model.

As binning of multiple detector pixels is a commonly employed feature, we examine its impact on correlation, detector PSF, signal, and detector noises in "Section Binning of the detector".

A comprehensive understanding of the individual noise processes is essential for describing the entire image formation process. Therefore, we will provide a detailed outline of the complete noise model in the subsequent sections, following the framework described above. This thorough explanation will facilitate a deeper understanding of the complex interactions between various noise components and their effects on the imaging process.

Signal and detector noise

Due to the quantization of electrons, the probability of measuring an electron leaving the electron gun in a given time interval can be modeled as a pure-Poisson distribution $\mathscr{P}\left[\hat{S}_{src,el}\right]$ (see Eq. 8). However, during the acceleration phase, Coulomb forces between beam electrons cause spacio-temporal correlations in the electron beam[54,55], such that the electron beam is correlated within itself to some degree. This depends on beam currents and the correlation time, within which consecutively emitted electrons are correlated. Indeed, these beam correlations are quite important for the measurements and necessary to regard, as will be shown later in this paper. By broadening the beam in TEM mode, the electrons from the electron gun, which can be modeled as a point-source, are deflected with a kernel Ω^*_{TEM} to form a disc. It is thus symmetric, which allows us to interchangeably use convolution and autocorrelation. Since the uncorrelated electrons are independent, the Poisson statistics is not affected by the deflection, which is represented by the convolution being applied inside the Poisson term $\mathscr{P}\left[\Omega^*_{TEM} \otimes \hat{S}_{src,el}\right]$. This changes for the correlated electrons, for which the convolution acts on the Poisson term itself $\Omega^*_{TEM} \otimes \mathscr{P}\left[\hat{S}_{src,el}\right]$, since the electrons are influenced by the previous ones. We obtain the electron beam for the TEM mode B_{TEM} consisting of both, correlated and uncorrelated electrons hitting the fluorescence layer of the CCD as:

$$B_{TEM} = p \cdot \left(\Omega^*_{TEM} \otimes \mathscr{P}\left[\hat{S}_{src,el}\right]\right) + (1-p) \cdot \mathscr{P}\left[\Omega^*_{TEM} \otimes \hat{S}_{src,el}\right] \quad , \tag{42}$$

where p gives the probability for correlated electrons within the beam. The broadening of the point-source to a parallel beam happens without additional gain. However, since we are interested in the broadened signal rather than the total beam intensity we define Ω^*_{TEM} to have the height of one, indicated by $*$. This is in contrast to all following convolutions, which are normalized to the sum of all entries. For this type of signal, we obtain the Pearson correlation coefficients following Eq. 36 as:

$$\begin{aligned} \rho_{TEM,m,n} &= \left[(p \cdot \Omega^*_{TEM} + (1-p) \cdot \delta) \otimes (p \cdot \Omega^*_{TEM} + (1-p) \cdot \delta)\right]_{n,m} \\ &\approx \left[p^2 \cdot \Omega^*_{TEM} \otimes \Omega^*_{TEM} \; + \; 2 \cdot p \cdot (1-p) \cdot \Omega^*_{TEM} + (1-p)^2 \cdot \delta\right]_{n,m} \quad , \end{aligned} \tag{43}$$

where δ is the Dirac delta, since the Poisson distributions of the uncorrelated electrons is unchanged by the beam deflection. For a sufficiently large beam disc Ω^*_{TEM} with respect to the detector, we can approximate the first term as a constant.

In the fluorescence layer of the detector, every incident electron produces a cascade of photons (see Fig. 1a). The generation of photons in the scintillation layer is rather complex, as multiple factors like thickness, reflections at the scintillator interface and scattering events, defects, etc. influence the electron path and thus shape the signal locally[1,6]. Verbeeck and Bertoni[5] pointed out that under the assumption of a rather homogeneous fluorescence layer, this is negligible. Following Eq. 39, this process can be modeled as another convolution of the electron beam B_{TEM} with a kernel Ω_{fl} and with a fluorescence gain $g_{fl} \gg 1$. This convolution affects both the Poisson statistics of the correlated and the uncorrelated electrons, since all electrons produce multiple photons, which are then spread by the convolution. This leads to a smoothing of the noise, as was shown in "Section Noise and convolution". With $S_{el} = \Omega^*_{TEM} \otimes S_{src,el}$, we obtain:

$$\begin{aligned} g_{fl} \cdot \Omega_{fl} \otimes B_{TEM} = \mathscr{P}_{g_{fl} \cdot \beta_{fl} \cdot \beta_{TEM}} \left[\Omega_{fl} \otimes \hat{S}_{el}\right] \quad &, \text{with} \quad \beta_{TEM} = \beta_{TEM,conv} \cdot \beta_{TEM,corr} \\ &\text{and} \quad \beta_{fl} \;\; = \beta_{fl,conv} \;\; \cdot \beta_{fl,corr} \quad . \end{aligned} \tag{44}$$

As a result, we obtain a smoothing of the variance as described in Eqs. 37 and 22, which depends on the Pearson correlation coefficients. This smoothing of the noise by $\beta_{TEM,conv}$ and $\beta_{TEM,corr}$ as well as $\beta_{fl,conv}$ and $\beta_{fl,corr}$ is the one mentioned by several authors[5,6]. Every following spreading of the correlated signal will thus add on the PSF applied to the signal, as well as on the smoothing of the formerly true-Poisson noise, which changes into a super-Poisson distribution, as the gain g_{fl} by far exceeds the smoothing.

After the fluorescence layer, the created photons are guided by the fiber optic, which absorbs or loses some of the photons, indicating a second gain $g_{opt} < 1$ and an additional PSF Ω_{opt}. The photons finally arrive at the CCD camera and are absorbed and converted back into charge carriers. As not every photon creates an exciton, this leads to a third gain $g_{CCD} < 1$, also known as the Fano factor[40,41]. Obviously, the wells of the pixels are finite, thus creating a third PSF for the actual CCD camera Ω_{CCD}. Implementing all these considerations into

a formula, leads to a convolution of the detector kernel Ω_d with the different Poisson noise distributions of the electron beam B_{TEM}:

$$g_d \cdot \Omega_d \otimes B_{TEM} = \mathscr{P}_{\beta_{conv}\cdot\beta_{corr}\cdot g_d}\left[\Omega_d \otimes \hat{S}_{el}\right] \quad \text{, with} \quad \Omega_d = \Omega_{fl} \otimes \Omega_{opt} \otimes \Omega_{CCD} \ . \tag{45}$$

So a total detector gain value $g_d = g_{fl} \cdot g_{opt} \cdot g_{CCD}$ is obtained for the system as well as a smoothing factor for the convolution $\beta_{conv} = \beta_{TEM,conv} \cdot \beta_{fl,conv} \cdot \beta_{opt,conv} \cdot \beta_{CCD,conv}$ and a smoothing factor for the correlation $\beta_{corr} = \beta_{TEM,corr} \cdot \beta_{fl,corr} \cdot \beta_{opt,corr} \cdot \beta_{CCD,corr}$ altering the noise. We combine both to a total smoothing factor $\beta = \beta_{conv} \cdot \beta_{corr}$ for shorter notation. As a result of Eq. 38, we can simplify the individual convolution kernels of the layers to a combined kernel for the entire detector.

Correspondingly, we obtain the Pearson correlation coefficients of the image formation change from Eq. 43 into:

$$\rho_{m,n} \approx \left[\Omega_d^* \otimes \Omega_d^* \otimes \left(p^2 \cdot \Omega_{TEM}^* \otimes \Omega_{TEM}^* + 2 \cdot p \cdot (1-p) \cdot \Omega_{TEM}^* + (1-p)^2 \cdot \delta\right)\right]_{n,m} \ , \tag{46}$$

where Ω_d^* describes the detector PSF normalized to the height of one. The convolution with a rather constant first term again yields a constant.

The gain acts as a conversion factor from incident beam electrons to charge carriers in the detector, with the detector signal given as $S_d = g_d \cdot S_{el}$. In a real-world system, quantum efficiencies vary in the fluorescence layer as well as in the CCD detector. Assuming that the direct path, rather than internal reflections, predominantly contributes to the intensity of a given detector pixel (i,j) and the others are negligible, the total gain can be written as an unknown distribution $\mathscr{X}$ varying around the mean value of all gains $G_{d,i,j} = g_d \cdot \frac{\mathscr{X}[g]_{i,j}}{g_d} = g_d \cdot \mathscr{X}\left[\bar{g}\right]_{i,j}$, with $\mathscr{X}\left[\bar{g}\right]_{i,j} \in [0,\infty)$. The quantum efficiency variations are fixed and therefore are commonly referred to as fixed-pattern-noise[56,57]. This leads to the overall probability to measure n signal counts in a detector pixel:

$$\begin{aligned}\mathscr{P}_{\beta\cdot G_{d,i,j}}\left[\Omega_d \otimes \hat{S}_{el}\right]_{i,j} &\approx \frac{\left(g_d^{-1}\cdot\mathscr{X}\left[\bar{g}\right]_{i,j}^{-1}\cdot\left[\Omega_d\otimes\hat{S}_d\right]_{i,j}\right)^{g_d^{-1}\mathscr{X}\left[\bar{g}\right]_{i,j}^{-1}\beta^{-1}\cdot n}}{\left(g_d^{-1}\cdot\mathscr{X}\left[\bar{g}\right]_{i,j}^{-1}\cdot\beta^{-1}\cdot n\right)!}\exp\left\{-g_d^{-1}\cdot\mathscr{X}\left[\bar{g}\right]_{i,j}^{-1}\cdot\beta^{-1}\cdot n\right\} \\ &= g_d\cdot\mathscr{X}\left[\bar{g}\right]_{i,j}\cdot\beta\cdot\mathscr{P}\left[\frac{\left[\Omega_d\otimes\hat{S}_d\right]_{i,j}}{g_d\cdot\mathscr{X}\left[\bar{g}\right]_{i,j}\cdot\beta}\right]\end{aligned} \ , \tag{47}$$

which can be rescaled to a pure-Poisson distribution by factoring the gains and β out (see Eq. 12). Taking into account the simplification that only the direct path contributes to the signal, we use the approximate sign.

Operating a CCD camera always produces heat, and even if the camera is cooled, this thermal energy is likely to produce excitons in the course of the acquisition time t_{acq}. The generation of these is known to produce dark currents I_{dark} and the longer the acquisition time, the higher is the accumulated charge and thus the offset $\mu_{therm} = I_{dark} \cdot t_{acq}$ in charge[7]. These dark currents are especially favored by certain defects within the material[58], which are not uniformly distributed across the CCD array, leading to another unknown distribution $\Upsilon[\mu_{therm}]_{i,j}$ for the conversion of thermal energy into excitons. Owing to the quantized nature of charge, these thermal excitons further add Poisson noise[6,7,59].

Finally, charges are converted into counts by the analog-digital-converter (ADC). This process is widely known to add further Gaussian distributed read-out noise to a measurement[6,7,60]. The Gaussian distribution is given in Eq. 1. To avoid negative counts, an external bias voltage offsets the read-out process[61]. Fluctuations of bias in between rows occur as row artifacts. We also consider these to be Gaussian distributed, with the mean value of the respective row $\mu_{row,j}$ and the variance σ_{read}^2 of the read-out noise. Here, the mean value itself varies from row to row with $\mathscr{N}\left[\bar{\mu}_{read},\, \sigma_{row}^2\right]$. Combining both, the read-out noise can be written as $\mathscr{N}\left[\bar{\mu}_{read}\,,\, \sigma_{read}^2 + \sigma_{row,j}^2\right]$.

With a conversion gain g_c from charge carriers to counts, a total mean gain $g = g_c \cdot g_d$ and a total varying gain $G_{i,j} = g \cdot \mathscr{X}\left[\bar{g}\right]_{i,j}$ can be found. The signal in counts is then given as $S_c = g_c \cdot S_d = g \cdot S_{el}$, where S_{el} gives the electron signal of the beam and S_d gives the detector charge carriers.

However, the gain of the pixels is not a constant, but changes with the intensity due to saturation effects besides other non-linearities[61,62]. As a pixel can be seen as a capacitor, higher levels of accumulated charge restrain the probability of creating additional excitons, thereby decreasing the overall gain. So, the gain of the system does not only depend on the camera system itself, but also on the level of the acquired signal, thus $\mathscr{X}\left[\bar{g}\right]_{i,j} \to \mathscr{X}\left[\bar{g}(S_{el})\right]_{i,j}$.

Considering all of the above, we can express the image formation process of the image ξ as follows:

$$\xi_{i,j} \approx g\cdot\mathscr{X}\left[\bar{g}\left(\Omega_d\otimes\hat{S}_{el}\right)\right]_{i,j}\cdot\beta\cdot\mathscr{P}\underbrace{\left[\frac{\left[\Omega_d\otimes\hat{S}_{el}\right]_{i,j}}{\beta}\right]}_{=\frac{\left[\Omega_d\otimes\hat{S}_c\right]_{i,j}}{g\cdot\mathscr{X}\left[\bar{g}(S_c)\right]_{i,j}\cdot\beta}} + g_c\cdot\left(\mathscr{P}\left[\Upsilon[\mu_{therm}]_{,i,j}\right] + \mathscr{N}\left[\bar{\mu}_{read}\,,\,\sigma_{read}^2+\sigma_{row,j}^2\right]\right) \ , \tag{48}$$

assuming homogeneous read-out noise across the CCD camera and an additional noise term in the vertical and only in the vertical direction of the image columns i, as it is fixed per row j. Using the convolution of noise Eq. 2,

we can write the total noise as the sum of the individual noise distributions. It is important to note that the values for $\bar{\mu}_{read}$, σ_{read}, σ_{row} and μ_{therm} vary between detector segments, as each segment has its own ADC (see Fig. 1b). In the following, we will abbreviate $\hat{S}_{\Omega,el} = \left[\Omega_d \otimes \hat{S}_{el}\right]$ to shorten notation.

We consider this image formation as the general case for our detector for measurements in TEM mode and under reserve for STEM mode, which we will elaborate on later.

Processing operations

We have described the image formation process for a measurement on a typical scintillation-based CCD detector, but often the quality of the acquired images is enhanced by techniques, such as background subtractions, applying gain references or gain non-linearity corrections. All these corrections do influence the noise in the corrected images, which is the subject of this section.

Dark frame subtraction

To clear an image from the offset and additional dark currents, a second image is acquired with a closed shutter $\hat{S}_{el} = 0$, the so-called dark frame. This dark frame is then subtracted from the original image[6,7] (see Fig. 4a,b), leading to:

$$\xi_{DS,i,j} = \xi_{i,j} - \xi_{dark,i,j} \quad \text{, with} \quad \xi_{dark,i,j} = g_c \cdot \left(\mathscr{P}\left[\Upsilon[\mu_{therm}]_{i,j} \right] + \mathscr{N}\left[\bar{\mu}_{read},\, \sigma^2_{read} + \sigma^2_{row,j} \right] \right) . \tag{49}$$

Since both measurements are uncorrelated, the summation rule Eq. 2 can be utilized for the Gaussian distributed parts of Eq. 48. This increases read-out and row noise, but clears the image from the read-out offset $\bar{\mu}_{read}$. Further, subtracting Poisson distributions leads to a Skellam distribution (see Eq. 11) for the thermal noise. So, the image formation for a dark frame subtracted image is given as:

$$_{DS,i,j} \approx g \cdot \mathscr{X}\left[\bar{g}\left(\hat{S}_{\Omega,el} \right) \right]_{i,j} \cdot \beta \cdot \mathscr{P}\left[\frac{\hat{S}_{\Omega,el,i,j}}{\beta} \right] + g_c \cdot \left(\mathscr{S}\left[0\,,\, \Upsilon\left[\hat{\mu}_{therm} \right]_{i,j}\,,\, \Upsilon\left[\hat{\mu}_{therm} \right]_{i,j} \right] + \mathscr{N}\left[0\,,\, 2\sigma^2_{read} + 2\sigma^2_{row,j} \right] \right) , \tag{50}$$

where the dark frame subtracted image $\xi_{DS,i,j}$ provides the counts of every pixel cleared by the offset.

Since the noise contribution of dark currents in a cooled CCD is rather small and the zero centered Skellam distribution with $S_1 = S_2$ is symmetric, it can be (and usually is) approximated by a Gaussian distribution. Since $\Upsilon[\mu_{therm}]_{i,j}$ is further assumed to be rather homogeneously distributed across the CCD, this yields:

$$\xi_{DS,i,j} \approx g \cdot \mathscr{X}\left[\bar{g}\left(\hat{S}_{\Omega,el} \right) \right]_{i,j} \cdot \beta \cdot \mathscr{P}\left[\frac{\hat{S}_{\Omega,el,i,j}}{\beta} \right] + \mathscr{N}\left[0\,,\, 2\sigma^2_{read} + 2\sigma^2_{row,j} + 2\sigma^2_{therm} \right] , \tag{51}$$

with $\sigma^2_{therm} = g_c \cdot \mu_{therm}$ depending on the dark current μ_{therm}. The factor of 2 reflects the fact that two images are subtracted from each other. However, it shall be noted that the Skellam distribution has larger tails than the Gaussian distribution. $\Upsilon[\mu_{therm}]_{i,j}$ might also deviate locally due to the construction of the CCD, but as the noise contribution is generally low, the effect is negligible. To clear notation, in the following read-out, row and thermal noises will be referred to as 'detector noise':

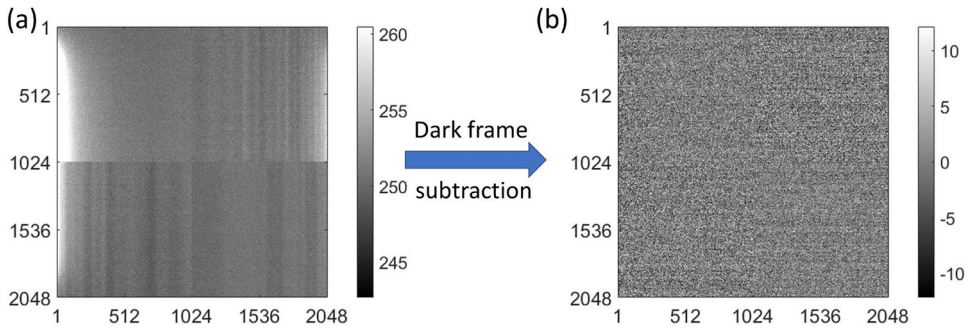

Fig. 4. (**a**) Bias frame averaged across 30 unprocessed images without signal at zero exposure time. It can be seen that the image is offsetted by $\mu \approx 252$ counts indicated by the grey value in between a 5σ range displayed. Further, brighter areas can be spotted on the detector, where dark currents σ_{therm} are increased and vertical columns are visible, where the Ohmic resistance changes currents. The four quadrants can be seen at their boundaries, where image features are interrupted. (**b**) After subtracting an image without signal, the result appears without offset, brighter areas are cleared and the image in general has fewer features than before subtraction. Horizontal lines become visible, where the bias of the entire line varies between read-out, because image variation in general decreases. Most of the image variation now is given by the read-out noise σ_{read} changing between pixels on top of the row noise $\sigma_{row,j}$. This procedure of getting from (a) to (b) is referred to as 'dark frame subtraction'.

$$\sigma_d^2 = \sigma_{read}^2 + \sigma_{row,j}^2 + \sigma_{therm}^2 \ . \tag{52}$$

The acquisition of a gain reference

Detectors are often calibrated with respect to their gain distribution to compensate for variations in the quantum efficiency at each pixel. Generally, the gain reference[6,7] is acquired with high counts and a uniform signal across the detector, which can easily be achieved in TEM mode by expanding the beam. The resulting signal frame image $\xi_{ref,SF}$ is then dark frame subtracted by a dark frame image $\xi_{ref,DF}$ and divided by the mean value of the image. The gain reference image formation of a scintillation-based CCD detector thus can be modeled as:

$$\xi_{ref,i,j} \approx \frac{\mathscr{X}\left[\bar{g}(S_{ref})\right]_{i,j} \cdot g \cdot \beta \cdot \mathscr{P}\left[\frac{\hat{S}_{ref}}{\beta}\right] + \mathscr{N}\left[0\,,\,2\sigma_d^2\right]}{g \cdot \bar{S}_{ref}} \ , \tag{53}$$

with the convolution of a homogeneous electron signal $\Omega_d \otimes \hat{S}_{ref} = \hat{S}_{ref}$ having no significant effect other than for correlation and noise smoothing as described in "Sections Noise correlation effects" and "Noise and convolution". The noise term $\mathscr{N}\left[0,\,2\sigma_d^2\right]$ describes the dark frame subtracted detector noise. The denominator is given by the mean value of the reference signal $\bar{S}_{ref} \to \hat{S}_{ref}$ approaching its expectation value for large enough pixel sets and a high reference signal. Both assumptions hold for typical CCD cameras and gain calibration procedures. To mitigate the impact of saturation on deviations in the quantum efficiencies, this procedure is performed at ~1/10 of the maximum count. As some pixels generate more counts per incident electron than others, they saturate faster, which leads to an underestimation of the quantum deviations at lower signal strengths. To maintain high signal strength, *w* images can be added up, increasing the signal but also the noises:

$$\xi_{ref,i,j} \approx \frac{\mathscr{X}\left[\bar{g}\left(\hat{S}_{ref}\right)\right]_{i,j} \cdot g \cdot \beta \cdot \mathscr{P}\left[\frac{\sum_w \hat{S}_{ref}}{\beta}\right] + \mathscr{N}\left[0\,,\,2\sum_w \sigma_d^2\right]}{g \cdot \sum_w \hat{S}_{ref}} \ , \tag{54}$$

according to the summation rules for Gaussian and Poisson distributions in Eqs. 2 and 10. Further, we can approximate $\mathscr{X}\left[\bar{g}(S_{ref})\right]_{i,j} \to \mathscr{X}\left[\bar{g}\left(\hat{S}_{ref}\right)\right]_{i,j}$ as the signal approaches its expectation value $S_{ref} \to \hat{S}_{ref}$ across several measurements *w*. The overall probability to measure a gain reference that resembles the quantum efficiency differences $\mathscr{X}\left[\bar{g}\left(\hat{S}_{ref}\right)\right]_{i,j}$ is given as the convolution (see Eq. 2) of the Poisson distribution with the normal distributed part:

$$\Pr\left[\xi_{ref,i,j} = \mathscr{X}\left[\bar{g}\left(\hat{S}_{ref}\right)\right]_{i,j} \cdot \zeta_{ref,i,j}\right] \approx \mathscr{X}\left[\bar{g}\left(\hat{S}_{ref}\right)\right]_{i,j} \cdot \frac{g \cdot \beta \cdot \mathscr{P}\left[\frac{\sum_w \hat{S}_{ref}}{\beta}\right] \otimes \mathscr{N}\left[0\,,\,2 \cdot \sum_w \sigma_d^2\right]}{g \cdot \sum_w \hat{S}_{ref}} \ . \tag{55}$$

As for high signals, the Poisson distribution is in good approximation equal to the normal distribution (see Eq. 9). It can be rewritten:

$$\Pr\left[\xi_{ref,i,j} = \mathscr{X}\left[\bar{g}\left(\hat{S}_{ref}\right)\right]_{i,j} \cdot \zeta_{ref,i,j}\right] \approx \mathscr{X}\left[\bar{g}\left(\hat{S}_{ref}\right)\right]_{i,j} \cdot \frac{g \cdot \beta \cdot \mathscr{N}\left[\frac{\sum_w \hat{S}_{ref}}{\beta}\,,\,\frac{\sum_w \hat{S}_{ref}}{\beta}\right] \otimes \mathscr{N}\left[0\,,\,2 \cdot \sum_w \sigma_d^2\right]}{g \cdot \sum_w \hat{S}_{ref}} \ . \tag{56}$$

Again, by utilizing the convolution rules of two Gaussian distributions Eq. 2 and the multiplication by a constant in Eq. 3, this allows to simplify the resulting normal distribution to:

$$\begin{aligned} \Pr\left[\xi_{ref,i,j} = \mathscr{X}\left[\bar{g}\left(\hat{S}_{ref}\right)\right]_{i,j} \cdot \zeta_{ref,i,j}\right] &\approx \mathscr{X}\left[\bar{g}\left(\hat{S}_{ref}\right)\right]_{i,j} \cdot \mathscr{N}\left[1,\,k_{ref,i,j}^2\right] \quad \text{, with} \\ k_{ref,i,j}^2 &= \frac{\sum_w g^2 \cdot \beta \cdot \hat{S}_{ref} + 2 \cdot \sum_w \sigma_d^2}{\left(g \cdot \sum_w \hat{S}_{ref}\right)^2} \quad , \end{aligned} \tag{57}$$

where the measured signal in counts is given as $\hat{S}_{ref,c} = g \cdot \hat{S}_{ref}$. Further, by approximating the local $k_{ref,i,j} \approx k_{ref}$ by their overall mean value and by taking the inverse distribution, following Eq. 7, we obtain:

$$\xi_{ref,i,j}^{-1}\left(\hat{S}_{ref}\right) = \mathscr{X}\left[\bar{g}\left(\hat{S}_{ref}\right)\right]_{i,j}^{-1} \cdot \zeta_{ref,i,j}^{-1} \quad \text{, with} \tag{58}$$

$$\zeta_{ref,i,j}^{-1} \in \mathscr{N}\left[1,\,k_{ref}^2\right] \in [0,\,\infty) \quad , \tag{59}$$

where $\zeta_{ref,i,j}^{-1}$ is the actual representation of the normal distribution and k_{ref} describes the uncertainty of the gain reference. This gain reference (see Fig. 5) can now be applied to individual images via multiplication, which is faster in processing as divisions. It is important to note that the gain reference is acquired across all detector

segments altogether and it is to be assumed that the real gain of each quadrant slightly differs from the others. This results in slightly different *k*-values for any subset of pixels differing from the full detector, as it is the case for EELS in particular. At this point, the acquired gain reference is only valid for a specific intensity $\hat{S}_{ref}$, as deviating from this intensity necessarily shifts the individual gain values for all pixels due to the non-linearity of the detector.

The application of a gain reference

Now, that a suitable gain reference has been found, it needs to be applied to images. In general, applying the gain reference frame results in ratio distributions, whose probability density functions are complicated and for which the standard deviation is not always defined. For sufficiently low values of k_{ref}, which is a basic requirement of a good gain reference, Eq. 7 is valid and the overall Gaussian of the multiplicand becomes quite narrow. So narrow that is does not change the overall shape of the respective noise distribution significantly, except for slightly broadening its variance.

With the above considerations, a gain reference like the one displayed in Fig. 5 can be applied to dark frame subtracted images (see Eq. 51), which leads to the gain normalized image ξ^*, given as:

$$\xi^*_{i,j} = \xi_{DS,i,j} \cdot \xi^{-1}_{ref,i,j}\left(\hat{S}_{ref}\right) \approx \frac{\mathscr{X}\left[\bar{g}(S_{\Omega,el})\right]_{i,j}}{\zeta_{ref,i,j} \cdot \mathscr{X}\left[\bar{g}\left(\hat{S}_{ref}\right)\right]_{i,j}} \cdot g \cdot \beta \cdot \mathscr{P}\left[\frac{\hat{S}_{\Omega,el,i,j}}{\beta}\right] + \frac{\mathscr{N}\left[0\,,\,2\sigma_d^2\right]}{\xi_{ref,i,j}\left(\hat{S}_{ref}\right)}\,, \quad (60)$$

with ζ^{-1}_{ref} describing the 'new' fixed-pattern noise induced by gain normalization, whereas the gain reference is printed into the background noise of the detector.

To see how the application of the gain reference influences the different noises, we separate the above equation into two separate parts, the Poisson distributed signal part and the Gaussian distributed detector noise part. Starting with the influence on the Gaussian distributed detector noises of Eq. 60, we can assume a rather homogeneous distribution of the quantum efficiencies across the detector and roughly approximate $\xi^{-1}_{ref} \approx \mathscr{N}\left[\phi^{-1}_{ref}\,,\,\frac{\sigma^2_{ref}}{\phi^4_{ref}}\right]$, with $\sigma^2_{ref} \approx \sigma^2_{QE} + k^2_{ref}$. Here, ϕ^{-1}_{ref} is the mean value of the inverse gain reference of each specific segment (see Fig. 5). Due to inhomogenieties in the distribution of the gains, these mean values slightly differ from one. The detector noises are given as Eq. 52. From Eq. 6 follows that:

$$\xi^{-1}_{ref} \cdot \mathscr{N}\left[0\,,\,2\sigma_d^2\right] \approx \mathscr{N}\left[0\,,\,\left(\phi^{-2}_{ref} + \frac{\sigma^2_{ref}}{\phi^4_{ref}}\right) \cdot 2\sigma_d^2\right]\,, \quad (61)$$

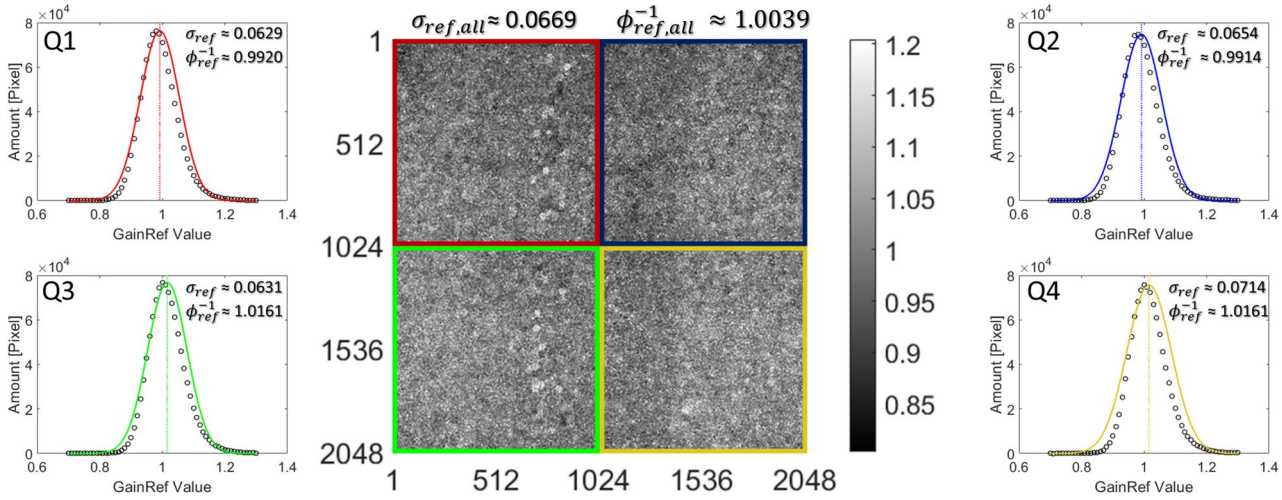

Fig. 5. Gain reference of our *US1000FT-XP 2* detector in the middle, acquired by adding up 30 images under homogeneous illumination conditions in TEM mode and then subtracting 30 dark frame images with the same exposure of $t \approx 0.85\,\mathrm{s}$. The mean intensity of each image was targeted at $\hat{S}_{ref} \approx 7050$ counts. Due to differences in the glue and the fluorescence layer in the manufacturing, the gain reference shows stripes superimposed to artifacts from the fiber optics. The gain reference is surrounded by the individual frequency distributions of the gain values in the four detector quadrants Q1-Q4, where each dot represents an interval of 0.01 around its center. Since the gain reference normalizes with respect to all quadrants, the respective mean values of the quadrants differ from 1. The standard deviations $\sigma \approx 0.067$ are similar for all quadrants indicating a rather homogeneous gain distribution across the detector, however the aforementioned stripes and artifacts lead to small differences. Overall, the gain distributions are slightly skewed to the right for all quadrants, as a result of the inversion. Therefore, the overall mean of the inverse gain reference differs slightly from 1 (see Eq. 7).

for each of the four quadrants.

Now, that the effect of the gain reference on the detector noise has been shown, it is to show how it influences the signal noise of Eq. 60. Assuming, for a moment, that the measured image intensity is in close proximity to the image intensity of the gain reference, we can approximate $\mathscr{X}_{R,i,j} = \frac{\mathscr{X}[\bar{g}(S_{\Omega,el})]_{i,j}}{\mathscr{X}[\bar{g}(\hat{S}_{ref})]_{i,j}} \approx 1$. We will further elaborate on this term in the next section. Thus, we are left with:

$$\mathscr{X}_{R,i,j} \cdot \zeta_{ref,i,j}^{-1} \cdot g \cdot \beta \cdot \mathscr{P}\left[\frac{\hat{S}_{\Omega,el,i,j}}{\beta}\right] = \mathscr{X}_{R,i,j} \cdot \mathscr{N}\left[1\,,\, k_{ref}^2\right] \cdot g \cdot \beta \cdot \mathscr{P}\left[\frac{\hat{S}_{\Omega,el,i,j}}{\beta}\right] \,. \tag{62}$$

By utilizing the Gaussian approximation of the Poisson distribution (see Eq. 9) and the multiplication of distributions (see Eq. 6) it can be shown that:

$$\mathscr{N}\left[1\,,\, k_{ref}^2\right] \cdot g \cdot \beta \cdot \mathscr{P}\left[\frac{\hat{S}_{\Omega,el,i,j}}{\beta}\right] \approx g \cdot \beta \cdot \mathscr{P}\left[\frac{\hat{S}_{\Omega,el,i,j}}{\beta}\right] + \mathscr{N}\left[0\,,\, k_{ref}^2 \cdot \left(g^2 \cdot \hat{S}_{\Omega,el,i,j}^2 + g^2 \cdot \beta \cdot \hat{S}_{\Omega,el,i,j}\right)\right] \,, \tag{63}$$

i.e. the multiplication by the gain reference deviates the expectation value and the variance $\hat{S}_{el}$ of the Poisson distribution by its variance k_{ref}^2. Combining the results of Eqs. 61 and 63, we can rewrite Eq. 60 as:

$$\xi_{i,j}^* \approx \mathscr{X}_{R,i,j} \cdot g \cdot \beta \cdot \mathscr{P}\left[\frac{\hat{S}_{\Omega,el,i,j}}{\beta}\right] + \mathscr{N}\left[0\,,\, \mathscr{X}_{R,i,j}^2 \cdot k_{ref}^2 \cdot \left(g^2 \cdot \hat{S}_{\Omega,el,i,j}^2 + g^2 \cdot \beta \cdot \hat{S}_{\Omega,el,i,j}\right)\right] + \mathscr{N}\left[0\,,\, 2{\sigma_d^*}^2\right] \,, \tag{64}$$

with the gain normalized detector noise:

$${\sigma_d^*}^2 = \left(\phi_{ref}^{-2} + \frac{\sigma_{ref}^2}{\phi_{ref}^4}\right) \cdot \sigma_d^2 \,, \tag{65}$$

where ϕ is the mean value of the respective quadrant varying the detector noises between quadrants and σ_{ref} is the standard deviation of the acquired gain reference frame.

To make the gain reference independent of the signal strength of the measurement, saturation and other non-linearity effects must be corrected for in both gain reference and signal.

Gain non-linearities

Often, images cover a large dynamic range. Especially in measurements like EELS, we obtain very high intensities in the zero-loss peak (ZLP) and comparably small signals of interest. To gather enough statistic for the signals, the ZLP often reaches into the domain, where saturation effects beside other non-linearities are observed. This leads to deviations between the original and the measured signal intensity. Also, the gain reference, to this point, is only valid for a limited range around the target intensity it was acquired with. Especially for EELS, this is undesirable, as the gain reference is only valid for a small portion of the signal. Thus, it is important to find a general correction for the detector, which linearizes the gain throughout the entire dynamic range.

Adjusting the gains to counteract non-linearities generally changes the noise. To see the actual effects, we need to reconsider Eq. 64, especially with respect to $\mathscr{X}_{R,i,j}$. Due to differences in the thickness in the fluorescence layer and different quantum efficiencies, some pixels collect more charge than others. Considering a large range of signals, some pixels saturate more than others, which leads to deviations between the gain reference and the actual gain distribution represented in another experiment. So, not only the actual measurement but also the gain reference must be corrected for non-linearities. To compensated with an unknown factor $g_{lin,i,j}$, defined to removes the dependency of the gain on the signal level $\hat{S}$, linearizing the gain for the entire dynamic range, we must rescale the intensity of every pixel by its non-linearity correction function. We obtain:

$$\mathscr{X}_{R,i,j} = \frac{\mathscr{X}\left[g_{lin}(S_{\Omega,el}) \cdot \bar{g}(S_{\Omega,el})\right]_{i,j}}{\mathscr{X}\left[g_{lin}\left(\hat{S}_{ref}\right) \cdot \bar{g}\left(\hat{S}_{ref}\right)\right]_{i,j}} = \frac{\mathscr{X}\left[\bar{g}\right]_{i,j}}{\mathscr{X}\left[\bar{g}\right]_{i,j}} = 1 \,. \tag{66}$$

Assuming that the gain deviations inside the CCD are much smaller than in the fluorescence layer and fiber optics, we can approximate the linearization correction g_{lin} to be equal for all pixels. We thus obtain a mean photon transfer curve (PTC) for the entire detector as the inverse of g_{lin}.

Usually, non-linearities of the detector gain are fitted by a second or third order polynomial as a function of signal strength $g\left(\hat{S}_c\right) = g \cdot \left(\hat{S}_c - x_1 - x_2 \cdot \hat{S}_c^2 - x_3 \cdot \hat{S}_c^3\right)$[63]. Here, the coefficients $x_{1,2,3}$ represent the fit parameters. As the signal is subject to different noises, it is better described with the measurement $\xi_{i,j}$ instead of $\hat{S}$, such that a correction factor is given as:

$$g_{lin}(\xi_{i,j}) = \frac{g \cdot \xi_{i,j}}{g \cdot \left(\xi_{i,j} - x_1 - x_2 \cdot \xi_{i,j}^2 - x_3 \cdot \xi_{i,j}^3\right)} \,. \tag{67}$$

Note that this correction applies to the original measurement without background subtraction, since the offset must be considered for the correct total count.

As the correction factor is obtained by fitting measurements, it is again subject to deviations between fit and the actual gains. Particularly, as the saturation may vary from pixel to pixel. Based on the previous argumentation in this work, it can easily be anticipated that these deviations in the gain appear squared in the noise, which consequently leads to second and forth order terms connected to the Poisson term and to forth and eighth order deviations in the Gaussian term connected to the deviations induced by the gain reference. To maintain reasonably clear noise model, we only consider a second order term and neglect the higher ones. Note however that these deviation of the gain linearization k_{lin}^2 do not add (much) to the image volatility per se. They rather alter the linearity of the gain throughout the dynamic range. So, it depends on the difference between intensities that are compared. For normal imaging as well as for EELS, k_{lin}^2 can be neglected and the corresponding noise term is well below the Poisson noise, as we will see later. However, we require this term for a precision analysis for the binning of detector noises, where it will appear as a small offset to the uncertainty of the gain reference. This is the sole reason for its inclusion here.

For a gain normalized and non-linearity corrected image $\xi^{corr} = \frac{g_{lin}(\xi)\cdot\xi_{DS}}{g_{lin}(\xi_{ref,org})\cdot\xi_{ref}}$, where $\xi_{ref,org}$ denotes the original measurements used for the gain reference and ξ_{DS} is the dark frame subtracted image from Eq. 51, we can write instead of Eq. 64:

$$\xi_{i,j}^{corr} \approx g\cdot\beta\cdot\mathscr{P}\left[\frac{\hat{S}_{\Omega,el,i,j}}{\beta}\right] + \mathscr{N}\left[0,\, k^2\cdot g^2\cdot\hat{S}_{\Omega,el,i,j}^2 + k^2\cdot g^2\cdot\beta\cdot\hat{S}_{\Omega,el,i,j}\right] + \mathscr{N}\left[0,\, 2\sigma_{d,corr}^2\right] \quad \text{, with} \tag{68}$$

$$\sigma_{d,corr}^2 \approx \bar{g}_{lin}^2\cdot\sigma_d^{*\,2} \qquad \text{and} \qquad \bar{g}_{lin} = \frac{1}{NM}\sum_{i,j} g_{lin,i,j} \qquad \text{as well as} \qquad k^2 = k_{ref*}^2 + k_{lin}^2\,, \tag{69}$$

where the factor k includes the uncertainties of the non-linearity corrected gain reference k_{ref*} and the deviation of the gain linearization k_{lin}. We utilized Eq. 6 for the multiplication of $\sigma_{d,corr}^2$ from Eq. 65 with g_{lin}. For the latter, we neglected the contribution of its variance term, since it depends on the distribution of the signal and the overall influence is estimated to be quite small.

Another effect, known as 'brighter-fatter effect'[64,65], describes the increase in the detector PSF with increasing signal $\Omega \to \Omega\,(S)$ due to diffusion of charge carriers between pixels. This effect leads to the observation that brighter objects appear larger on the CCD than darker objects, despite being the same size. Following Eq. 37, describing the smoothing of the noise due to convolution β_{conv}, and Eq. 22, describing the smoothing of the noise due to correlation β_{corr}, a broader PSF leads to a reduction of the variance described by the smoothing factor $\beta = \beta_{conv}\cdot\beta_{corr}$ and thus to the observation of a reduced smoothed gain $\beta\cdot g$. Thus, we must rewrite the smoothing factor $\beta \to \beta(S)$. This effect is reported to be reduced by binning or summation of neighboring pixels[64], such as it is the case for EEL-spectra in one dimension. As it is impossible to differentiate the gain from the smoothing within this experimental setup, we speak of a smoothed gain here.

We neglect the additional convolution for simplicity, but describe the effect on the noise by:

$$\xi_{i,j}^{corr} \approx g\cdot\beta\cdot\beta_{BF}\cdot\mathscr{P}\left[\frac{\hat{S}_{\Omega,el,i,j}}{\beta\cdot\beta_{BF}}\right] + \mathscr{N}\left[0\,,\, k^2\cdot g^2\cdot\hat{S}_{\Omega,el,i,j}^2 + k^2\cdot g^2\cdot\beta\cdot\beta_{BF}\cdot\hat{S}_{\Omega,el,i,j}\right] + \mathscr{N}\left[0\,,\, 2\sigma_{d,corr}^2\right]\,. \tag{70}$$

As we will show in the following evaluation, the additional convolution induced by the brighter-fatter effect is rather small. It is negligible, even in high-count regimes, where the effect is most pronounced. Its impact on the variance, however, is important when measuring non-linearity effects with the signal-to-variance method. It must be corrected for in order to obtain the valid non-linearity correction $g_{lin}(\xi_{i,j})$[63].

Binning of the detector

Detector binning is often employed to reduce detector noises. When binning the detector, two or more neighboring pixels are transferred to the ADC and are cumulatively read out, causing the binned pixels to appear as one. Relative to signal strength, the detector noises are reduced by binning.

However, due to correlation effects the signal noises change. This is the reason why manufacturers like *Gatan* acquire a set of different gain references for the most important binning settings. To maintain consistency, we focus on post-binning of the images, like it is performed for e.g. EELS measurements. In contrast to regular binning, post-binning does not reduce detector noises, but it alters the signal noise in the same manner as the regular binning.

Following Eq. 70, vertically summing V pixel along the columns and horizontally summing H pixel along the rows, can be written as:

$$\xi_{Bin,H,V}^{corr} \approx \sum_{i,j}^{H,V}\left(g\cdot\beta\cdot\beta_{BF}\cdot\mathscr{P}\left[\frac{\hat{S}_{\Omega,el,i,j}}{\beta\cdot\beta_{BF}}\right] + \mathscr{N}\left[0\,,\, \underbrace{k^2\cdot g^2\cdot\hat{S}_{\Omega,el,i,j}^2}_{1.} + \underbrace{k^2\cdot g^2\cdot\beta\cdot\beta_{BF}\cdot\hat{S}_{\Omega,el,i,j}}_{2.} + \underbrace{2\sigma_{d,corr}^2}_{3.}\right]\right)\,. \tag{71}$$

Again, we can separate the noise into different parts and treat the summations independently.

Utilizing the addition of Poisson distributions (see Eq. 10) on the first part of Eq. 71 leads to:

$$\sum_{i,j}^{H,V} g\cdot\beta\cdot\beta_{BF}\cdot\mathscr{P}\left[\frac{\hat{S}_{\Omega,el,i,j}}{\beta\cdot\beta_{BF}}\right] = g\cdot\beta_{H,V}\cdot\beta_{BF,H,V}\cdot\mathscr{P}\left[\frac{\sum_{i,j}^{H,V}\hat{S}_{\Omega,el,i,j}}{\beta_{H,V}\cdot\beta_{BF,H,V}}\right]\,, \tag{72}$$

with the column- and row-wise addition of the signal removing some of the noise correlation induced by the detector PSD. This leads to a reduced smoothing factor $\beta_{H,V} = \beta_{conv,H,V} \cdot \beta_{corr,H,V}$, where H and V denote the summed pixels or binning values in the respective direction. As described in Eq. 36, convolution leads to correlation, which can be described by the Pearson correlation coefficients. According to Eqs. 26 and 27, these coefficients change under summation. The smoothing due to the convolution β_{conv} changes according to Eq. 37, as part of the convolution is removed by summation. Further, the smoothing due to correlation β_{corr} changes according to Eq. 22. As a result, we obtain a change for the smoothing factor $\beta_{H,V}$. The same happens to the brighter-fatter smoothing $\beta_{BF,H,V}$.

Summing up the variations of the signal introduced by the fixed-pattern noise of the gain reference (see Eq. 71 1.), however, is more complex, since the column distribution is lost by that summation. As the signal is not uniformly distributed across a given pixel column or row, some pixels contribute more to the signal than others. To address this this, we introduce a distribution factor $\alpha_{H,V}$. Since k^2 can be assumed to be rather homogeneously distributed across the detector, every pixel adds a fraction of k^2 equal to its contribution to the overall signal. So, we can sum up the fist part of the normal distribution of Eq. 71 1. as following:

$$\sum_{i,j}^{H,V} k^2 \cdot g^2 \cdot \hat{S}^2_{\Omega,el,i,j} = k^2 \cdot g^2 \cdot \sum_{i,j}^{H,V} \hat{S}^2_{\Omega,el,i,j} = \alpha_{H,V} \cdot \underbrace{\left(k^2_{ref^*,H,V} + k^2_{lin}\right)}_{=k^2_{H,V}} \cdot g^2 \cdot \left(\sum_{i,j}^{H,V} \hat{S}_{\Omega,el,i,j}\right)^2 \quad \text{, with} \tag{73}$$

$$\alpha_{H,V} = \sum_{i,j}^{H,V} \left(\frac{\hat{S}_{\Omega,el,i,j}}{\sum_{i,j}^{H,V} \hat{S}_{\Omega,el,i,j}} \right)^2 \quad . \tag{74}$$

Under typical conditions, the image signal can be considered rather similar between neighboring pixels and for small binning values, allowing us to often neglect $\alpha_{H,V} \approx 1$. However, for large binning values, as required for EELS, $\alpha_{H,V}$ must be taken into consideration.

As the measurement of the non-linearity corrected gain reference $k^2_{ref*} \rightarrow k^2_{ref^*,H,V}$ is also correlated, due to beam correlations and the detector PSF, the same procedure as for the Poisson part has to be applied here, too. Taking a look into Eq. 57 reveals that $k^2_{ref,H,V}$ needs an update for the change in the smoothing factor $\beta = \beta_{conv} \cdot \beta_{corr}$, but we observe a change in the expectation value of the non-linearity corrected reference signal $\hat{S}^*_{ref}$ as well, due to the summation of pixel intensities during binning. We obtain:

$$k^2_{ref^*,H,V} = \frac{\sum_w g^2 \cdot \beta_{H,V} \cdot \sum_{i,j}^{H,V} \hat{S}^*_{ref} + 2 \cdot \sum_w \sum_{i,j}^{H,V} \bar{g}^2_{lin} \cdot \sigma^2_d}{\left(g \cdot \sum_w \sum_{i,j}^{H,V} \hat{S}^*_{ref}\right)^2} \quad , \tag{75}$$

for the binned uncertainty of the non-linearity corrected gain reference, where $\bar{g}_{lin}$ is the mean value of the linearization factor $g_{lin,i,j}$, as shown in Eq. 69.

The factor k_{lin} giving the uncertainty of the linearization correction, however, remains unchanged under summation and thus we obtain $k^2_{H,V}$ as defined above.

Similar changes can be found in the summation of the second part of the normal distribution in Eq. 71 2., which describes the variation of the Poisson noise by the fixed-pattern noise of the gain reference, which is given as:

$$\sum_{i,j}^{H,V} k^2 \cdot \beta \cdot \beta_{BF} \cdot g^2 \cdot \hat{S}_{\Omega,el,i,j} = k^2_{H,V} \cdot g^2 \cdot \beta_{H,V} \cdot \beta_{BF,H,V} \cdot \sum_{i,j}^{H,V} \hat{S}_{\Omega,el,i,j} \quad . \tag{76}$$

The distribution factor $\alpha_{H,V}$ is not required here, since the noise is independent of the distribution of the signal, but just a mere variation of the Poisson noise.

The summation of the detector noise $\sigma_{d,corr}$ in the last part of the normal distribution of Eq. 71 3. is straightforward following Eq. 69, which describes the non-linearity corrected, gain normalized detector noise, and the summation rule of Eq. 25.

Combining the results of the summation of the Poisson noises in Eq. 72, the summation of the signal variation in Eq. 73 and the Poisson noise variation by the gain reference in Eq. 76, along with the addition of detector noises, the vertically binned image and its noises are given as:

$$\begin{aligned} \xi^{corr}_{Bin,H,V} &\approx g \cdot \beta_{H,V} \cdot \beta_{BF,H,V} \cdot \mathscr{P}\left[\frac{\sum_{i,j}^{H,V} \hat{S}_{\Omega,c,i,j}}{g \cdot \beta_{H,V} \cdot \beta_{BF,H,V}}\right] + \mathscr{N}\left[0, \sigma^2_{Bin,H,V}\right] \quad \text{, with} \\ \sigma^2_{Bin,H,V} &= \underbrace{\alpha_{H,V} \cdot k^2_{H,V} \cdot \left(\sum_{i,j}^{H,V} \hat{S}_{\Omega,c,i,j}\right)^2}_{1.} + \underbrace{k^2_{H,V} \cdot g \cdot \beta_{H,V} \cdot \beta_{BF,H,V} \cdot \sum_{i,j}^{H,V} \hat{S}_{\Omega,c,i,j}}_{2.} + \underbrace{2 \sum_{i,j}^{H,V} \sigma^2_{d,corr}}_{3.} \quad , \end{aligned} \tag{77}$$

where we convert the signal back to counts $\hat{S}_{\Omega,c} = g \cdot \hat{S}_{\Omega,el}$, as this is how the microscope presents the results. Note that the row noise $\sigma_{row,j}$ contained in $\sigma_{d,corr}$ is constant along the rows and thus adds up quadratically.

We consider this our noise model for TEM measurements under binning, from which we obtain the noise model of a regular image for $H = 1$ and $V = 1$. For the sake of clarity, we provide a concise summary of the involved variables. g is the overall gain of the detector, which encompasses the gain of the fluorescence layer $g_{fl} > 1$, the gain of the fiber optics $g_{opt} < 1$, the gain of the CCD detector $g_{CCD} < 1$, and a conversion gain g_c into counts. Due to the broadening of the signal by the detector PSF, the Poisson noise is smoothed and therefore reduced by a smoothing factor β. This factor incorporates the smoothing of the noise by the convolution with the detector PSF β_{conv} and smoothing that occurs by the effect of the correlation β_{corr} induced by this convolution. Since the width of the detector PSF increases with signal strength, known as the brighter-fatter effect, we observe a variation of the smoothing that is accounted for by β_{BF}. As convolutional effects are mitigated by binning, both β and β_{BF} are functions of the binning values in the horizontal H and vertical directions V. The expectation value of the signal $\hat{S}_\Omega$ convolved with the detector PSF Ω in counts c on the position (i, j), is summed through binning. To recover the original Poisson distribution $\mathscr{P}$ of the signal, it is rescaled by the smoothed gain. Furthermore, we identify three Gaussian distributed $\mathscr{N}$ noise contributions: 1. The variation of the signal due to the uncertainty of the gain reference $k_{H,V}$ which is influenced by the binning values and the signal distribution factor $\alpha_{H,V}$, given by Eq. 74. 2. The variation of the Poisson noise resulting from the uncertainty of the gain reference. 3. The detector noise, characterized by the variance σ_d, which is modified by the application of the gain reference and gain-linearization. A factor of 2 arises from the subtraction of a background frame.

In general, EFTEM does not act like an additional convolution on the image and the noise. As the signal is splitted into the respective electron-energy loss energies for EFTEM, we discard most of the incident electrons, changing the effective beam current and thus the beam correlation probability p (see Eq. 43). Without further changes to the noise model, the smoothing factor β would need a reevaluation. In contrast, STEM-EELS measurements are convolved with the characteristics of the energy distribution of the beam, as we will discuss later. Note that depending on how one looks at the noise, either with respect to the noise within the image or between consecutive images, the correlation smoothing factor β_{corr}(see Eq. 22) must be regarded or discarded as a component of the smoothing factor $\beta = \beta_{conv} \cdot \beta_{corr}$. In general, we can state that the overall uncertainty of the measurement is given by not considering the smoothing factor for the data correlation β_{corr}, whereas considering it describes the volatility of the noise of an image. This is of special interest for a series of consecutive EFTEM images or for EELS mapping.

Evaluation of the noise model

To validate the proposed noise model, we will demonstrate how the detector and signal noises behave under various operations and provide the methodology for measuring the required parameters and factors. For clarity, we have divided the following section into three main parts: the detector noises, the noises connected to the signal, and measuring the detector PSF.

In "Section Detector noise", we describe a method for removing cosmic rays and other artificial spike signals from the data. This is followed by an analysis of the various components of detector noise, including their time dependency and correlations, and how post-processing operations, such as applying the gain reference, affect these contributions. Additionally, we examine the effects of binning on the detector noises in "Section Binning of detector noises".

In "Section Signal and fixed-pattern noise", we present a detailed analysis of the noises connected to the signal. This includes the acquisition of the gain reference and the fixed-pattern noises arising from the uncertainty associated with its measurement in "Section The fixed-pattern noise of the gain reference". Additionally, we provide an in-depth examination of the brighter-fatter effect in "Section The brighter-fatter effect", including a method for determining its impact on measurements. We also investigate the non-linearity effect of the detector gain with increasing signal strength in "Section Correction of gain non-linearities", highlighting the importance of accounting for the brighter-fatter effect in order to achieve a proper correction. Furthermore, we examine the effects of binning on signal noise and the uncertainty of the gain reference in "Section Binning of signal and fixed-pattern noises".

Finally, in "Section Beam correlations and the reconstruction of the detector PSF", we describe a method for determining the detector point spread function using the signal noise, providing a comprehensive understanding of the detector's behavior.

Detector noise

For the evaluation of the different detector noises, images were acquired with zero emission and thus with no signal measured on the detector. Since unprocessed images do inherit a certain structure (see Fig. 4a), the following argumentation builds upon dark frame subtracted images that are much more homogeneous. However, it has to be considered that subtracting two images doubles the variance. All images were cleared of external counting events such as cosmic rays that accumulate over time (see Fig. 6a). These events appear as spikes in the image and can be detected as pixels leaving a 5σ distance around the mean value of the image (see Fig. 6b). Since a subtracted dark frame can also contain cosmic rays, the distance is applied to both sides of the mean. The images were further separated into fractions of read-out noise σ_{read} and thermal noise σ_{therm}(see Fig. 6c) as well as row noise $\sigma_{row,j}$ that occurs as row artifacts (see Fig. 6d). As the thermal noise is influenced by the temperature of the detector, we cooled it to $T_{Detector} \approx -20^\circ$ C. By calculating the mean value of the respective row, it can be observed that the row artifacts seem to be Gaussian distributed around integers (see Fig. 7b). Considering the standard deviation of the mean, the Gaussian can fully be described by the read-out

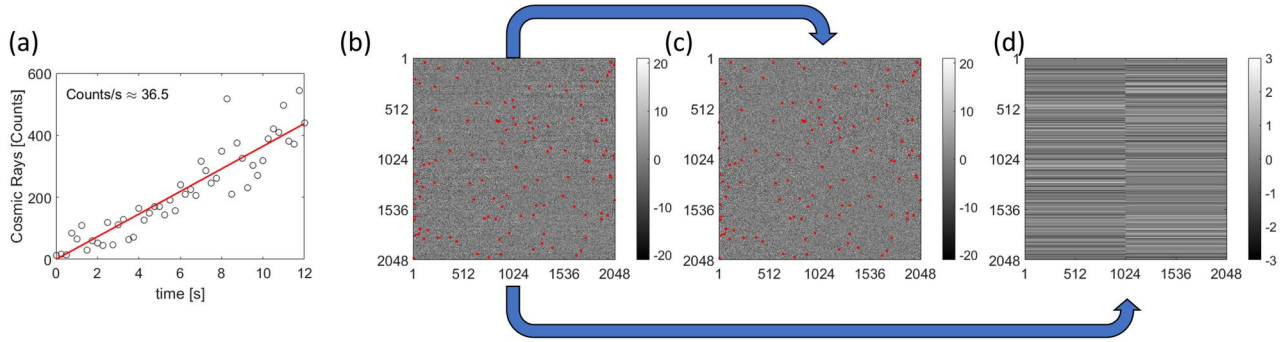

Fig. 6. (**a**) The graph shows the cosmic ray count to increase linearly over time at a rate of approximately 36.5 counts/s. Cosmic rays are found as events that are outside by a 5σ distance to the mean value of the image and are excluded from the noise statistics. In (**b**) an exemplary dark frame subtracted image ξ_{DS} with an acquisition time of $t_{acq} = 4.75$ s is shown with the cosmic rays removed (marked as red patches). To make them visible to the eye, the dots are exaggerated as 10 times 10 pixel patches. The image was used as acquired by the *Gatan* software. By calculating the mean value of each quadrants detector rows, the image can then be separated into fast changing (**c**) read-out σ_{read} and thermal noise σ_{therm} as well as the slow changing (**d**) row noise $\sigma_{row,j}$ occurring as row artifacts. The images are displayed as a 5σ range around their mean.

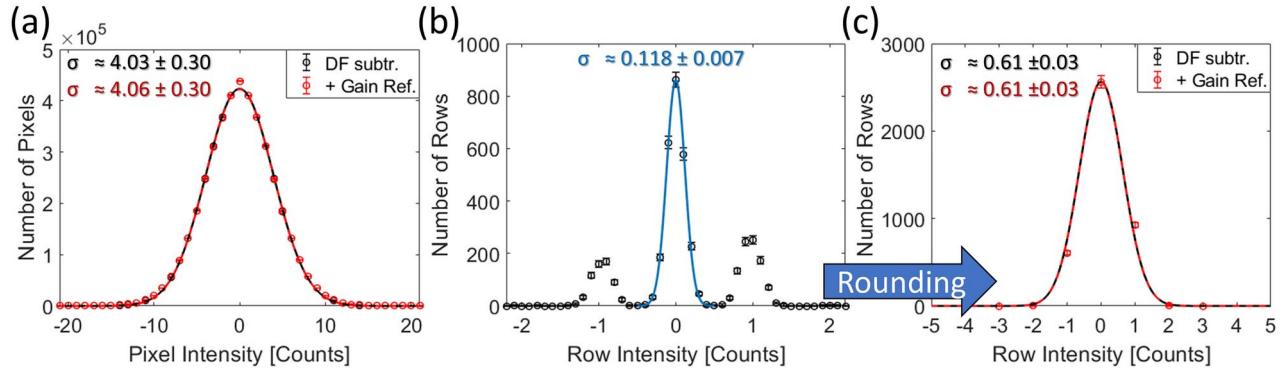

Fig. 7. Analysis of a dark frame subtracted image with zero exposure time $t_{acq} = 0$ s and with cosmic rays removed. (**a**) Distribution of the read-out noise σ_{read} of the dark frame subtracted image after subtraction of the rounded row artifacts, with a Gaussian fit (black) superimposed. The same image with the gain reference applied (red), exhibits a slightly broadened distribution with the standard deviation changing from $\sigma \approx 4.03$ to $\sigma \approx 4.06$ counts. The error bars for both graphs show the deviations expected by the Bernoulli distributed counts and the chance of calculating a wrong mean value for a row in the row noise. (**b**) Distribution of the row noise, with a Gaussian fit (blue) superimposing the central peak. The markers indicate values within an interval of 0.1 counts around their center. The standard deviation of the Gaussian peak $\sigma_{peak} = 0.118 \pm 0.007$ counts is within the 95% confidence interval of the standard deviation of the mean $\sigma_{mean} = 0.126 \pm 0.01$ counts of the individual rows. This means that the deviations from the integers can be fully attributed to the uncertainty of measuring the mean value of the rows under the given read-out noise σ_{read}. (**c**) Distribution of the rounded row noise $\sigma_{row,j}$ of the dark frame subtracted image (black) and the same image with the gain reference applied (red). Here, the markers represent an interval of 1 around their center. The distribution can be approximated by a Gaussian distribution with a standard deviation of $\sigma = 0.61 \pm 0.03$ counts for both cases. The application of the gain reference has basically no effect on the row noise.

noise σ_{read}(see Fig. 7a). Thus, it it useful to round the row artifacts to integer values (see Fig. 7c). By rounding the row mean values to integers, the error of measuring the wrong mean value can be squeezed to the order $\sigma_{mean} \approx 4 \cdot 10^{-5}$ counts, such that it is highly unlikely and statistically occurs only once every few images.

With these separate images, the noise distributions of both can be evaluated. In Fig. 7a, the overall count distribution of the read-out noise is shown to be approximated by a Gaussian. Since the image was taken with zero exposure time, it is to be expected that the thermal noise is negligible. By applying the gain reference, the noise distribution is slightly broadened (see red and black curve in Fig. 7a) according to theory (see Eq. 61). The row noise distribution in Fig. 7c, however, remains unchanged due to the rounding and the quite narrow distribution. It is also in good agreement to a Gaussian distribution. We would like to emphasize that, while being totally insignificant for regular images, the contribution of the row noise $\sigma_{row,j}$ to the overall detector noise becomes dominant for summations, e.g. for the total intensity of EEL spectra. We will show this later.

For the dark frame subtracted image ξ_{DS}, the count distribution is close to a Gaussian distribution. Applying the gain reference only leads to a slight broadening of the overall distribution.

To get a good approximation of the values for the read-out noise σ_{read} and thermal noise σ_{therm}, both must be separated. As thermal noise increases over time, as dark currents accumulate, we can utilize linear regression on a time series of dark frame subtracted images ξ_{DS}. Further, to verify a change in the noise introduced by the gain reference, we applied the gain reference to the same images. Following Eq. 65, we get to the regression equation:

$$\sigma^2_{total} = \left(\phi^{-2}_{ref,all} + \sigma^2_{ref,all}\right) \cdot \left(2\sigma^2_{read} + 2\sigma^2_{therm}\right) \quad , \text{with} \quad \sigma^2_{therm} \propto I_{dark} \cdot t \ , \tag{78}$$

where the gain reference introduces a multiplication by the mean value ϕ^{-2} and the variance σ^2_{ref} of the gain reference to both the read-out and thermal noises, according to Eq. 6. The mean value and the variance of the gain reference can be found in Fig. 5.

By comparing the results of both regressions in Fig. 8a,b, it can be seen, that applying the gain reference changes the read-out noise σ_{read}, represented as the offset, and the thermal noise σ_{therm}, represented as the slope of the regression. The change in value due to the application of the gain reference can be fully explained by the ϕ^{-1} and σ values from Fig. 5 and Eq. 78. Only the value for the read-out noises σ_{read} for Q1 deviates slightly from the theory. Nevertheless, Eq. 78 provides a good approximation. In Fig. 8c,d, the row noise is given as the mean value of the row artifacts across all images, where no time dependency is expected. Figure 8c,d might indicate some kind of different dependency for exposures below a second, which is important for EELS. Possibly due to some internal mode switching. However, the change in value due to the application of the gain reference is again according to theory (see Eq. 78).

Eventually, an important property of the detector noise is the correlation as expressed by the Pearson correlation coefficients (see "Section Noise correlation effects"). In case of a random signal, or white Gaussian noise, the coefficients are all zero except for the central element $\rho_{0,0} = 1$. For correlation, the coefficients $\rho_{m,n}$ are positive and for anti-correlation they are negative. In Fig. 9, the Pearson correlation coefficients of 30 gain corrected background images with $t_{acq} \approx 0.85$ s are averaged for all quadrants individually after the noise was separated into σ_{read} and σ_{therm}(compare Fig. 6c) as well as row noise $\sigma_{row,j}$(compare Eq. 6(d)).

The autocovariance function (see Eq. 28) of the dark frame subtracted image ξ_{DS} yields the Pearson coefficients multiplied by the variance σ^2_{total} of the image:

$$K\left(\xi_{DS}\right) = \sigma^2_{total} \cdot \rho(\xi_{DS}) \ , \tag{79}$$

where we obtain $\rho_{m,n}$ as the elements of $\rho(\xi_{DS})$. To further separate the read-out noise from the thermal noise (compare Eq. 78), we subtracted the values σ^2_{therm}(see Fig. 8) from the central element $\sigma^2_{total} \cdot \rho_{0,0}$, as we

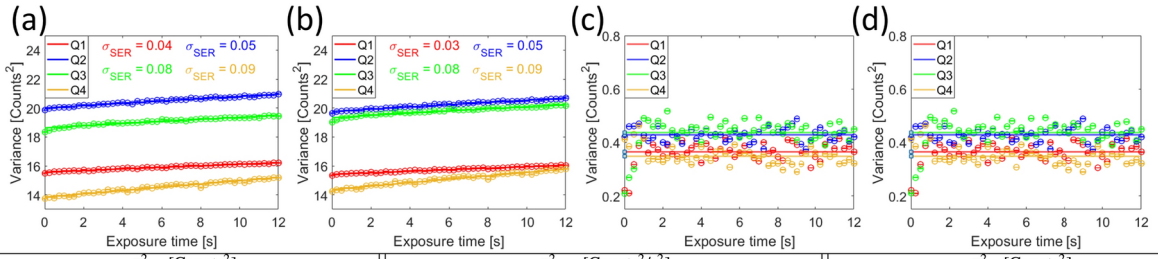

	σ^2_{read} [Counts^2]			σ^2_{therm} [Counts^2/s^2]			σ^2_{row} [Counts^2]		
	DF subtr.	Gain Ref.	Theory	DF subtr.	Gain Ref.	Theory	DF subtr.	Gain Ref.	Theory
Q1	7.786 ± 0.008	7.711 ± 0.008	7.694 ± 0.008	0.0268 ± 0.0011	0.0260 ± 0.0011	0.0265 ± 0.0011	0.180 ± 0.040	0.180 ± 0.040	0.180 ± 0.040
Q2	10.002 ± 0.012	9.882 ± 0.012	9.873 ± 0.012	0.0394 ± 0.0017	0.0384 ± 0.0017	0.0389 ± 0.0017	0.214 ± 0.022	0.214 ± 0.022	0.210 ± 0.021
Q3	9.314 ± 0.018	9.667 ± 0.019	9.651 ± 0.019	0.0363 ± 0.0025	0.0376 ± 0.0026	0.0376 ± 0.0026	0.220 ± 0.050	0.220 ± 0.050	0.230 ± 0.050
Q4	6.922 ± 0.020	7.183 ± 0.021	7.179 ± 0.021	0.0564 ± 0.0028	0.0590 ± 0.0030	0.0585 ± 0.0029	0.175 ± 0.029	0.175 ± 0.029	0.180 ± 0.030

Fig. 8. (**a**) Linear regression of the sample variance σ^2_{total} over exposure time of a series of dark frame subtracted background images, according to Eq. 78, without the gain reference applied. The graphs follow the same color scheme of Fig. 1. The read-out noise σ^2_{read} is given as the offset and the thermal noise σ^2_{therm} as the slope of all quadrants. The uncertainties of the results are derived from the standard error of regression σ_{SER} and a 95% confidence interval. The detector was cooled to a temperature $T_{Detector} \approx -20°$ C. (**b**) By applying the gain reference, the values change according to Eq. 61. (**c**) The row variance can be found as the mean value of the series and (**d**) does not change with the application of the gain reference due to rounding effects. Below the graphs, the table shows the noise sample variance of the read-out noise σ^2_{read}, thermal noise σ^2_{therm} and row noise $\sigma^2_{row,j}$ of the respective quadrants. These values are derived from the regression analyzes of the above graphs. For each noise, the table shows the values of the dark frame subtracted images (DF subtr.) and the same images with the gain reference (Gain Ref.) applied. We further calculated the theoretical values of the noises for the images treated with the gain reference (Theory), based on the values found in DF subtr. and the values from Fig. 5, according to Eq. 78. The values are in very good agreement, but we noted a small deviation in in the read-out noise of Q1, which is slightly outside of the measurement uncertainty.

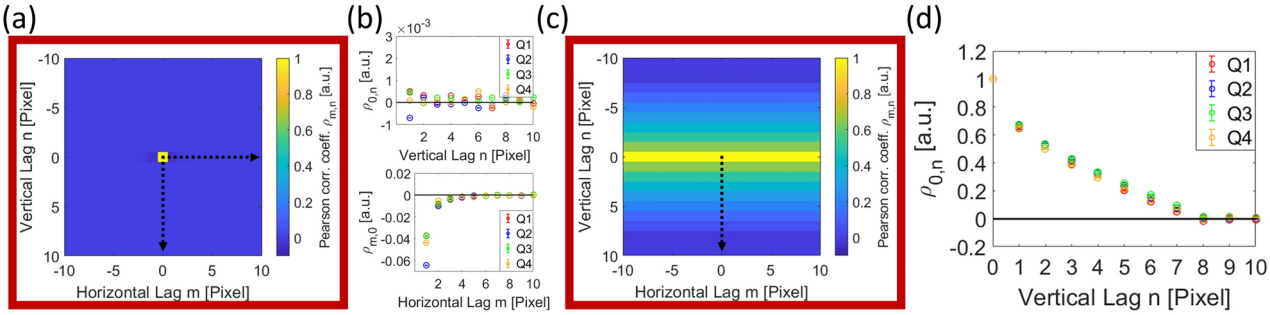

Fig. 9. (**a**) Pearson correlation coefficients $\rho_{m,n}$ of the read-out noise σ^2_{read} for the Q1 detector quadrant, indicated by the red box following the color scheme of Fig. 1. The images used for the autocovariance analyzes were cleared of the row noise (compare Fig. 6c) and averaged across 30 gain corrected background images with $t_{aqc} \approx 0.85$ s. The thermal noise σ^2_{therm}, which we expect to be uncorrelated, was subtracted from the central element $\sigma^2_{total} \cdot \rho_{0,0}$ before normalization. The black arrows indicate the position and direction in which (**b**) depicts the line profiles for all four quadrants across the respective coefficients. The values indicate a small anti-correlation in the horizontal direction, whereas the vertical profiles indicate close to no correlation effects. (**c**) Pearson correlation coefficients $\rho_{m,n}$ of the row noise $\sigma_{row,j}$(compare Fig. 6d) for the Q1 detector quadrant, averaged across 30 background images with the same acquisition time as before. Again, the red box indicates the quadrant Q1. The black arrow indicates the position and direction in which (**d**) the line profiles for all four quadrants are shown, just like before. The coefficients indicate a strong correlation in the row noise. This phenomenon is commonly known as 1/f-noise and is typical for CCD cameras.

expect the thermal noise to be uncorrelated and thus shaped as a Dirac delta peak δ. By normalizing with respect to the central element, we obtain the Pearson correlation coefficients of the read-out noise.

The correlation coefficients for the read-out noise σ_{read} in Fig. 9a,b indicate that there is a small anti-correlation in the horizontal row direction, whereas the noise in the vertical column direction seems to be rather uncorrelated. As the matrices derived from an autocorrelation process are necessarily Hermitian, as described in "Section Noise and convolution", the Pearson correlation coefficients $\rho_{1,n} = \rho_{1,-n}$ and $\rho_{m,1} = \rho_{-m,1}$, which is why we only show the positive coefficients here.

In Fig. 9c,d, the correlation coefficients of the row noise $\sigma_{row,j}$ show total correlation in the horizontal row direction, which is not surprising as all the pixels have the same value (compare Fig. 7c). In vertical direction, the coefficients reveal a strong correlation, which is typically described as 1/f-noise and is often observed in CCD cameras[66].

From the Pearson correlation coefficients in Fig. 9, we can calculate a factor β_{corr} by employing Eq. 22, to see how correlation changes the measured variances. However, the change induced by correlation to σ^2_{total} is two to three orders of magnitude lower than the uncertainty of the measurement, so it is negligible. With the values obtained from Fig. 9c, we calculate the change to $\sigma^2_{row,j}$ to be one order of magnitude below the uncertainty.

Binning of detector noises

In the following, we will show how a post-processing binning, like it is used to form EEL spectra, changes the variance of the noise. For this, we added up an increasing number of neighboring pixels to form new 'binned pixels', which are further analyzed. As the number of pixels is not divisible by e.g. three, we cropped the acquired images according to Fig. 1c. Since this operation changes the regarded part of the detector, we cropped the images in both directions and took the mean values of the variances.

Similar to Fig. 8, we used the regression on the same images to separate read-out noise σ_{read} and thermal noise σ_{therm} in a series of increasing binning values. In Fig. 10, we plot the resulting variances, where we binned H columns horizontally along the rows, shown in (a) and (d). We further binned V rows vertically along the columns, shown in Fig. 10b,e, and along a diagonal, where we binned columns and rows HV equally, as shown in Fig. 10d–f.

Under summation, the noise variance changes due to the covariances between the pixels, according to Fig. 25. We obtained the reconstructed noise variance from the Pearson correlation coefficients (see Fig. 9), shown as the colored lines for all quadrants in Fig. 10, to be within the uncertainty (shown as a colored shade) for the measured variances. The graphs indicate that the increase of both read-out and thermal variances grows nearly linear with the increasing number of added pixels. This is expected, as the correlation coefficients are small.

The same analysis can be conducted for the row noise $\sigma_{row,j}$ in Fig. 11. Since the mean value is identical for all pixels in a row, Fig. 11a reveals a quadratic increase of the noise variance under summation in this direction. In contrast to the read-out and thermal noises, we found a significant discrepancy between reconstruction and measured variances under binning for Q1 in Fig. 11b. Most likely, this occurs due to the high correlation of the noise and the considerably smaller sample size compared to the other noises. As the value only changes between rows, this reduces the sample size per image to a total of 1024 values per quadrant instead of 1024 times 1024 for the others. However, we think that the results of the reconstruction for the other three quadrants fit quite well.

In Fig. 11c, we obtain a cubic increase, when binning rows and columns equally. Again, we observe deviations due to the effects described in (b). One can easily see in comparison to Fig. 10 that this noise contribution

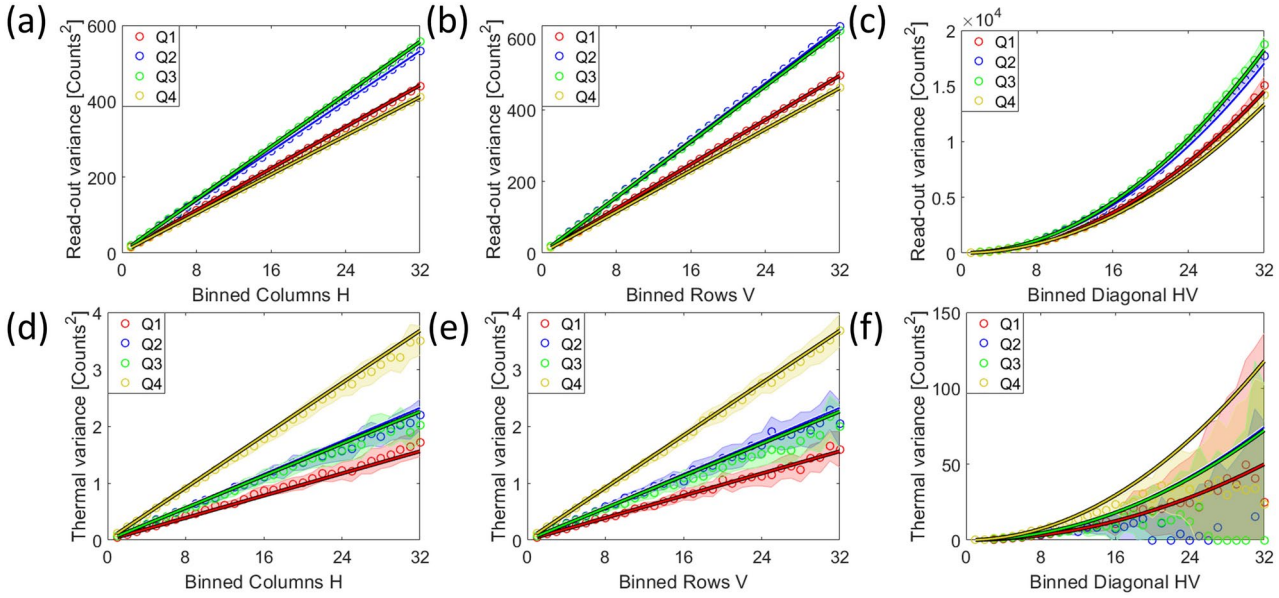

Fig. 10. Analyzes of the read-out noise σ^2_{read} and thermal noise variance σ^2_{therm} of gain normalized images under post-process binning of neighboring pixels. The lines represent the reconstruction using the Pearson correlation coefficients of Fig. 9 under binning. This is achieved following Eq. 26, which yields the variance of the binned image, as well as by utilizing Eqs. 27 and 22, which allow to calculate effect on the measured variance by the correlation of the binned image. The dots represent the results of the regression analyzes similar to Fig. 8. The colors indicate the respective detector quadrant and the colored shades depict the 95% confidence interval around the measured values. In (**a**), the read-out noise variances σ^2_{read} of a horizontal binning process are shown in dependence of the binning value H. In (**b**), the vertical binning in dependence of the binning value V is displayed and in (**c**), the diagonal binning is shown, where rows and columns HV were increased equally. In (**d**–**f**), the summations of the thermal noise σ^2_{therm} are shown using the same binning values as before. All reconstructions are in good agreement with the regression analyzes. However, the thermal noises seem to be underestimated by the regression analyzes that lead to the dots. As (**d**) and (**e**) show a linear increase of the thermal noise variance within tolerances, one would expect a quadratic increase for the binning in two directions. However, for higher diagonal binning values HV bigger than 10, the regression analyzes shows a discrepancy to this model.

becomes dominant for higher binning values. So far, we have shown that our model for the binning of detector noises in all directions is in good agreement with the theory shown in "Section Binning of the detector".

Having shown that the detector noises behave according to theory, it is yet to be shown, how signal and fixed-pattern noises behave under different operations and how they are affected by binning in order to confirm our noise models for binning (see Eq. 77).

Signal and fixed-pattern noise

To evaluate the signal and fixed-pattern noises, a very homogeneous signal is needed, which can be achieved in TEM-mode by spreading the beam disc at low magnification. All following signal measurements were performed at 200 kV accelerating voltage. To further reduce variations of the signals mean value, a new gain reference is acquired prior to the experiments. Afterwards, the measurements are carried out without changing the beam parameters. By employing this approach, we isolate the variations in the signal to be solely caused by Poisson and fixed-pattern noises. These noises are superimposed with the detector noises, which are thoroughly described in the previous section. We begin our investigation of the signal noises by analyzing the gain reference..

The fixed-pattern noise of the gain reference

For the gain reference, we acquired 30 homogeneous signal $\xi_{ref,SF}$ and dark frames $\xi_{ref,DF}$, both with the acquisition time of $t_{acq} = 0.84$ s. This results in a mean target intensity of $\hat{S}_{ref,c} \approx 7050$ counts for the measured signal. The dark frames $\xi_{ref,DF}$ were recorded before any signal hit the detector to avoid delayed fluorescence or phosphorescence of the scintillation layer. The dark frames were subtracted from the signal frames:

$$\xi_{ref,Sig} = \xi_{ref,SF} - \xi_{ref,DF} \ , \tag{80}$$

to obtain images that are solely consisting of the signal being altered by the distribution of quantum efficiencies superimposed by noise. For further analysis, we acquired an additional 30 pairs.

From the first 30 pairs, we determine a gain reference $\xi_{ref} = {}^{\xi_{ref,Sig}}/_{\hat{S}_{ref,c}}$ according to "Section The acquisition of a gain reference". The mean intensity of the electrons can be converted into counts $\hat{S}_{ref,c} = g \cdot \hat{S}_{ref}$,

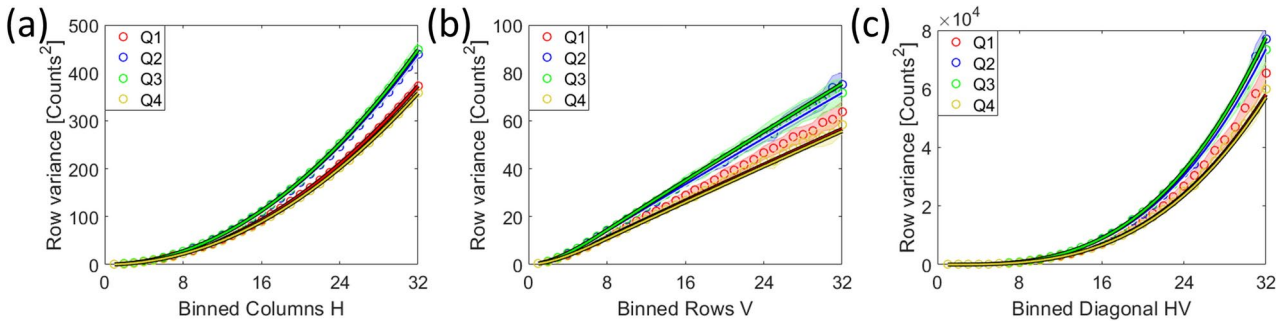

Fig. 11. Analyzes of the row variance $\sigma^2_{row,j}$ of gain normalized images under post-process binning of neighboring pixels. The lines represent the reconstruction using the Pearson correlation coefficients of Fig. 9 under binning. This is achieved following Eq. 26, which yields the variance of the binned image, as well as by utilizing Eqs. 27 and 22, which allow to calculate effect on the measured variance by the correlation of the binned image. The dots represent the results of the regression analyzes similar to Fig. 8. The colors indicate the respective detector quadrant and the colored shades depict the 95% confidence interval around the measured values. In (**a**), the row variance $\sigma_{row,j}$ of a horizontal binning process is shown in dependence of the binning value H. In (**b**), the vertical binning in dependence of the binning variable V and in (**c**), the diagonal binning is shown, where rows and columns were HV were increased equally. The Pearson reconstructions generally are in good agreement with the regression. However, the regression analysis of Q1 leading to the red dots, shows a slight deviation to higher values.

where g is the gain of the detector and $\hat{S}_{ref}$ is the original signal in electrons. As described in Eq. 57, the k_{ref} -value describes the uncertainty of the gain reference. Subtracting two gain references, acquired with the same mean signal, therefore allows to determine the k_{ref}-value in dependence of the target signal strength $\hat{S}_{ref,c}$ using the standard deviation (SD) of the difference image between both. By averaging an increasing number w of difference images with the same target intensity, this approach allows to check Eq. 57. We choose to increase the signal strength by adding up difference images of a fixed intensity rather than increasing the exposure time to avoid non-linearities, which could alter the relation between pixels, as described in "Section Gain non-linearities".

By increasing the number of summed frames w, we obtain the added pure-signal frames $\xi_{ref,Sig,w} = \sum_w \xi_{ref,Sig}$ and consequently a gain reference $\xi_{ref,w} = \xi_{ref,Sig,w} / \sum_w \hat{S}_{ref,c}$, according to "Section The acquisition of a gain reference". For a gain reference, the uncertainty k_{ref} is determined as:

$$k_{ref,w} = \frac{\mathrm{SD}\left\{\xi_{ref,w,1} - \xi_{ref,w,2}\right\}}{\sqrt{2 \cdot \left(1 + \sigma^2_{ref,all}\right)}} \,, \tag{81}$$

divided by $\sqrt{2}$, since the noise of both references is considered, and by the deviation of the quantum efficiencies $\sqrt{1 + \sigma^2_{ref,all}}$, which alters the noise according to Eqs. 57 and 6. As we do not use the inverse gain reference for our analysis (compare Eq. 78), we set the mean value $\phi = 1$. To get the best results, we increased the statistics by averaging the respective $k_{ref,w}$-values utilizing all other acquired images, too.

The uncertainty of measuring the true gain reference comprises a part that depends on the Poisson noise connected to smoothed gain $\beta \cdot g$, where g is the gain and β describes the smoothing of the noise variance by convolution and correlation, according to Eqs. 37 and 22. The other part of Eq. 57 depends on the detector noise σ_d. In Fig. 12a the standard deviation of the difference images k_{ref} is shown as a function of the summed up mean signal $\sum_w S_{ref,c}$ of the utilized gain references, displayed as black dots.

We obtain the detector noise as the standard deviation of the difference frames of the acquired backgrounds $\sigma^2_d = 8.77 \pm 0.01$ counts. One can compare this value with a combination of the values from our previous measurement in Fig. 8, added according to Eq. 52. This results in $\sigma_d = 8.74 \pm 0.06$ counts, which is in good agreement not only with the previous method, but also with the value determined by the fit of the k_{ref}-value. By knowing the detector noise, we can rearrange Eq. 57 and obtain:

$$\beta \cdot g = \hat{S}_{ref,c} \cdot \left(k^2_{ref,w} - 2 \cdot \frac{\sum_w \sigma^2_d}{\sum_w \hat{S}_{ref,c}} \right) \,, \tag{82}$$

the smoothed gain $\beta \cdot g \approx 1.5512 \pm 0.0002$ as the mean value across all summed up difference pairs. With both the smoothed gain and the detector noise, we can calculate the theoretical value of k_{ref} in dependence of the signal, according to Eq. 57. The resulting red curve is shown in Fig. 12a, where it is observed that the difference between the curve and the values obtained from Eq. 81 are insignificant. The difference between both are displayed in Fig. 12b as a residual plot. Considering the high precision of the experiment, we can confirm Eq. 57 as valid. By adding up 30 images for the gain reference shown in Fig. 5, we obtain a value for the uncertainty of $k_{ref} = 0.0027111 \pm 0.0000002$.

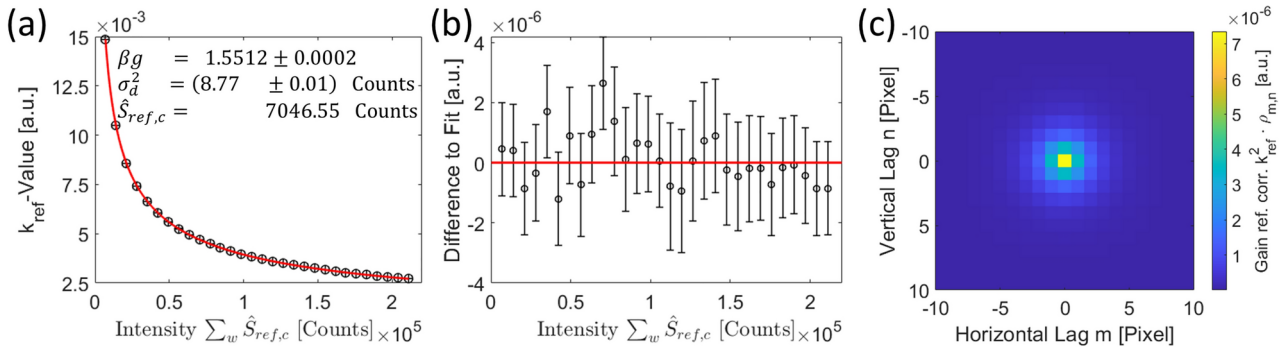

Fig. 12. (**a**) The k_{ref}-value as the standard deviation of the difference of two gain references according to Eq. 81 as a function of signal strength. The signal strength was increased by summing up w frames with a target intensity of $g \cdot \hat{S}_{ref,c} \approx 7050$ Counts. By fitting Eq. 57 to the data, the smoothed gain $\beta \cdot g$ of the detector can be found as a parameter knowing the variance of the detector noise σ_d^2. The resulting curve is shown in red. To demonstrate the validity of the model (**b**) shows the residual plot of the difference between fit and measured data, which indicates no significant deviation. The errorbars are mainly given as the uncertainty of the standard deviation of the difference images from the signal and background frames. In (**c**) the autocovariance function resulting from Eq. 83 of the gain reference as acquired from 30 signal and background frames is shown, where the central element gives k_{ref}^2. Comparing the k_{ref}-values from method (**a**) $k = 0.0027111 \pm 0.000002$ with method (**c**) $k = 0.0027101 \pm 0.0000002$, according to Eq. 83 shows marginal differences most likely occurring due to the restriction of Eq. 41. To get a correct comparison between both methods, we altered (**c**) by a smoothing with Eq. 22 due to the correlation.

As the detector correlates the signal between pixels, we also observe the pixel values of the gain reference to be correlated. Utilizing the autocovariance function from Eq. 28 allows to determine the Pearson correlation coefficients multiplied by the variance of the gain reference k^2 in Fig. 12c.

As variances are additive, we can simply add and subtract autocovariance functions from each other and try to rebuild Eq. 57 with them. By subtracting two dark frame subtracted (pure-)signal frames $\xi_{ref,Sig}$ from each other, we obtain the difference signal image $\xi_{ref,DS}$ to inherit twice the noise variance of the signal and four times the detector noise of the dark frame (see Eq. 80). Due to the subtraction, we obtain a mean value close to zero for all pixels, which is necessary for determining the autocovariance function. Since we aim to rebuild Eq. 57, the autocovariance function must be corrected for two times the detector noise of the dark frame, which can easily be found by the autocovariance function of a difference image of two dark frames $\xi_{ref,DB}$. So, by subtracting both autocovariance functions $K(\xi_{ref,DS}) - K(\xi_{ref,DB})$, we obtain the correct relation between signal and detector noises needed for Eq. 57. Similar to Eq. 81, we need to correct the noise for the quantum efficiency variation. To determine both, variance and Pearson coefficients of the gain reference, we repeat the process as described above, until all signal and dark frames used for the gain reference have been used for the respective autocorrelation functions and add them following:

$$k_{ref}^2 \cdot \rho\left(\xi_{ref}\right) = \frac{\sum_w \left(K^+(\xi_{ref,DS}) - K(\xi_{ref,DB})\right)}{\left(1+\sigma_{ref,all}^2\right) \cdot \sum_w \hat{S}_{ref,c}} \quad \text{, with} \quad \xi_{ref,DS} = \xi_{ref,Sig,1} - \xi_{ref,Sig,2} \quad \text{and} \quad \xi_{ref,DB} = \xi_{ref,DF,1} - \xi_{ref,DF,2} \ , \tag{83}$$

where K^+ denotes that all negative entries of the autocovariance function were set to zero, in order to correct for Eq. 41. Since the detector noise exhibits some anti-correlation effects leading to negative entries in the autocovariance function (as shown in Fig. 9), we decided not to correct these values of $K(\xi_{ref,DB})$. Summing up w pairs, contributing to the gain reference, and dividing by the summed total intensity reveals Fig. 12c and a $k_{ref} \approx 0.00271$.

The brighter-fatter effect

Expanding on the idea of Eq. 83, in a next step, we try to obtain the autocovariance function of the signal itself using Eq. 64. Again, all autocovariance functions must be of zero mean for all pixels for reliable results. We can rebuild Eq. 64, if we take the autocovariance function of a dark frame subtracted and gain normalized homogeneous signal frame with its mean value subtracted $K\left(\xi^* - \hat{S}_c\right)$. By doing so, we see that again we must subtract the noise variance contribution of twice the dark frame, which we obtain as the autocovariance function of the dark frame difference image $K(\xi_{ref,DB})$, as defined in Eq. 83. Further, we must subtract the noise of the gain reference altering the signal. We multiply the autocovariance function of the gain reference $K(\xi_{ref})$ by the mean signal $\hat{S}_c$. Eventually, we divide by $\left(1 + k_{ref}^2\right)$ to correct the signal from the alteration of the Poisson noise by the gain reference.

This procedure allows to calculate the smoothed gain and its Pearson coefficients as:

$$\beta_{conv} \cdot g \cdot \rho\left(\xi_{Sig}\right) = \frac{K\left(\xi_{Sig}\right)}{\hat{S}_c} \quad \text{, with} \quad K\left(\xi_{Sig}\right) = \frac{K^{+}\left(\xi^{*} - \hat{S}_c\right) - \hat{S}_c \cdot K^{+}\left(\xi_{ref}\right) - K\left(\xi_{ref,DB}\right)}{\left(1 + k_{ref}^{2}\right)} \,. \quad (84)$$

Again, K^{+} denotes that all negative entries of the autocovariance function were set to zero. The resulting autocovariance function yields the smoothed gain $\beta \cdot g$ as its central element, shown in Eq. 84(a). For the additionally acquired signal frames, which have the same intensity as the gain reference, we obtain a smoothed gain value $\beta \cdot g \approx 1.550$, slightly smaller than predicted by Eq. 83, which was $\beta \cdot g \approx 1.551$. This difference, however, can be explained by the restriction of Eq. 41.

Normalizing the autocovariance function in Fig. 13a with respect to the central element yields the Pearson coefficients. Successively increasing the exposure times of the signal frame allows for a comparison of the smoothing factors β throughout the intensity range. By following the idea of Eq. 37 that the smoothing is induced by the convolution with a detector PSF, one can easily imagine that a broader PSF leads to an increased smoothing. Adding up the Pearson coefficients, allows to determine the smoothing factor β_{conv}.

Following Astier et al.[63], we added up the Pearson coefficients of only the neighboring pixels, marked in red in Fig. 13a, to avoid noise in the higher coefficients. We obtain the relative change of the brighter-fatter smoothing factor β_{BF} in Fig. 13b, relative to the intensity of the gain reference, which we normalized to 1. This allows to describe the β_{BF} factor to model the smoothing with respect to a fixed reference point, making further analysis easier to understand. For very low intensities, we observe a sharp decrease of the smoothing factor indicating an increase of the detector PSF. A reason for this behavior could be an imperfect charge transport, where a small amount of a charge carriers belonging to a given pixel is read-out into its neighbor. This leads to an increased correlation between them[63]. Further, we observe the expected brighter-fatter-effect building up for higher intensities, as charge diffusion into neighboring pixels increases[63]. We found the Padé approximation[67], an extension of the Taylor series, of order [4/5] to fitting the signal strength dependency of β_{BF} quite well (see red curve in Fig. 13b).

The smoothing by the brighter-fatter effect is given by a squared Gaussian kernel, resembling the PSF. So, by using the values from Fig. 13b, we can reconstruct the brighter-fatter PSF by reversing Eq. 40 and utilizing Eq. 37, which yields the smoothing coefficient as a function of the Pearson coefficients. We can estimate the brighter-fatter PSF for e.g. a 30k counts high intensity spike signal, modeled by a Dirac delta. For this specific signal strength, we obtain a slight broadening resembled by the PSF in Fig. 13c, with a standard deviation of $\sigma_{BF} \approx 0.27$ pixel or equivalently a FWHM ≈ 0.64 pixel. Summing up the peak as in the standard procedure for EELS measurements, reveals Fig. 13d, where we show the change from to original Dirac delta peak signal to the broadened signal. We observe that for this specific signal, a total of 75 counts migrates to neighboring channels due to the brighter-fatter effect. A value that is totally negligible considering the Poisson noise connected to such a high signal and the width of a typical ZLP.

Correction of gain non-linearities

With all this, we can estimate the non-linearity function of the detector, following Eq. 64. The correction depends on the images before dark frame subtraction $\xi_{i,j}$ to include all offsets and is applied pixel-wise, because of large deviations in the gain distribution leading to a spectrum of different intensities within a single image. Assuming that the non-linearity function is similar for all pixels and the gain distribution is mainly altered by the fluorescence layer and the fiber optics, the goal is to determine the correction according to Eq. 67, which corrects the gain in both the image and the gain reference. As the gain is expected to change after the correction, we need to determine four fit parameters: x_1, x_2, x_3 and the smoothed gain $\beta \cdot g$.

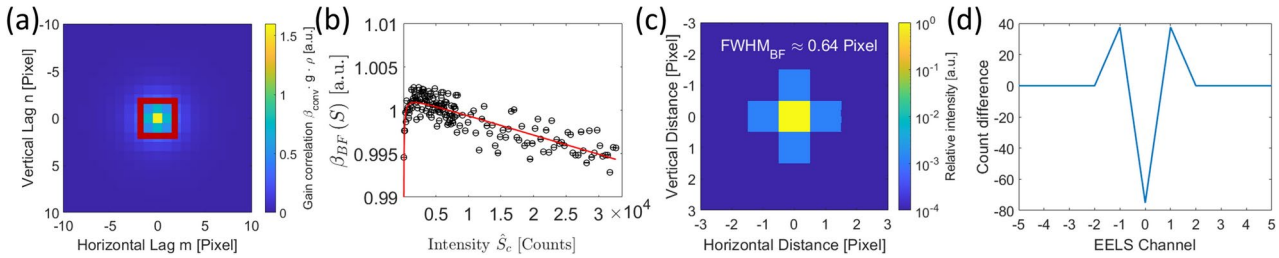

Fig. 13. (**a**) Autocovariance function of the signal according to Eq. 84. The central value, altered by Eq. 22 due to correlation, yields $\beta \cdot g = 1.55025 \pm 0.00002$. The red box marks the nearest neighbor coefficients that were used to calculate (**b**), which depicts the relative change in the smoothing factor β_{conv} when changing the intensity of the signal relative to the signal of the gain reference. The red curve depicts a Padé approximation of order [4/5][67]. It can be observed that the smoothing factor decreases sharply for very low and decreases rather linearly with increasing intensities. In (**c**) the PSF of the brighter-fatter effect is shown for a spike signal of 30k counts. The PSF was reconstructed by the smoothing value of $\beta_{BF} \approx 0.995$ counts obtained in (**b**), by reversing Eq. 40 and utilizing Eq. 37. In (**d**), we show the effect under vertical summation, as it is performed e.g. in EELS. It can be seen that the effect is negligible and well below the expected Poisson noise, as only 75 counts migrate to the neighboring channels as a result of the brighter-fatter effect.

In a series of images with homogeneous signal distribution and increasing exposure times, the total variance σ_{total} of the images can be obtained via the sample standard deviation. It is expected to follow Eq. 70, from which we can derive a formula for the total noise variance σ^2_{total} of the image, depending on the mean signal strength $\hat{S}_c$ in counts:

$$\sigma^2_{total} = \left(1 + k^2\right) \cdot \beta_{BF} \cdot \beta \cdot g \cdot \hat{S}_c + k^2 \cdot \hat{S}_c^2 + 2\sigma^2_{d,corr} \ . \tag{85}$$

where $k^2 = k^2_{ref} + k^2_{lin}$ is the uncertainty of the gain reference and the uncertainty of the linearization correction and $\beta = \beta_{conv} \cdot \beta_{corr}$ yields the smoothing factor of the measured gain $\beta \cdot g$. Further, it is important to take the brighter-fatter effect β_{BF} into account, since we regard a large range of signal strengths. The aim of the following minimization is to find a correction function $g_{lin}\left(\xi_{i,j}\right)$ following Eq. 67 that we apply to all contributing images of the gain reference $\xi^{corr}_{ref,i,j} = g_{lin}\left(\xi_{ref,i,j}\right) \cdot \xi_{ref,i,j}$ to correct it. By further applying it to the gain normalized image $\xi^{Corr}_{i,j} = g_{lin}\left(\xi_{i,j}\right) \cdot \xi^*_{i,j}$ that inherits the corrected gain reference, the linearization minimizes the difference of the functional:

$$\underset{x_1,x_2,x_3,\beta\cdot g}{\arg\min} \sum_{z}^{Z} \left(\sigma^{*\,2}_{total,z} - \left(1 + k^{*\,2}\right) \cdot \beta_{BF} \cdot \beta \cdot g^* \cdot \hat{S}^*_{c,z} - k^{*\,2} \cdot \hat{S}^{*\,2}_{c,z} - 2\sigma^{*\,2}_{d,corr}\right)^2 \ , \tag{86}$$

across the entire intensity range with Z different intensities, in our case 160 images. We marked all variables that are changed in this minimization process with an asterisk $*$. First, the mean signal strength of the image (in counts) $\hat{S}^*_c = \frac{1}{M,N} \cdot \sum_{i,j}^{M,N} g_{lin}\left(\xi_{i,j}\right) \cdot \xi^*_{i,j}$ changes with the linearization $\hat{S}_c = g \cdot \hat{S}_{el}$, as it encompasses the gain g that is to be linearized. Second, changing the gain automatically changes k_{ref}(see Eq. 57), as the gain is contained in the uncertainty. Third, the detector noise changes according to Eq. 69. Eventually, the sample variance of the linearization corrected image $\sigma^{*\,2}_{total} = \mathrm{VAR}\left\{g_{lin}\left(\xi_{i,j}\right) \cdot \xi^*_{i,j}\right\}$ changes due to the changed noise contributions.

To further avoid correcting all signals to zero, which indeed would be the minimum of the functional, we must restrict the correction function in Eq. 67. This is achieved by normalizing the correction function in Eq. 67 by the value of the correction function at the mean signal strength of the gain reference frames $g_{lin}\left(\xi_{ref}\right)$. Therefore, all signals are corrected with respect to the actual gain at that specific reference signal.

By iteratively choosing x_1, x_2, x_3 and $\beta \cdot g$ as fit parameters in Eq. 67, one eventually finds an optimal linearization correction for the gain, which minimizes Eq. 86 across the entire intensity range, as shown in Fig. 14a.

Using the autocovariance function on the corrected gain reference frames and on the additionally acquired signal frames of similar intensity, we obtain both the gain and k-value for the non-linearity corrected images $k \approx 0.002714$ and $g \approx 1.5544$, similar to Figs. 13a and 12c, which we can compare to the values of the regression fit in Fig. 14b. Here, we observe only small deviations. The residual plot Fig. 14c shows the differences between fit and data to be randomly distributed around the fit, showing that the applied correction really linearizes the acquired data across the entire intensity range.

However, to show that this correction actually corrects for the gain non-linearities of the system and not for some other effects, we conducted a second experiment some days apart. Again, we acquired a series of homogeneous signal frames with increasing exposure times. In contrast to the previous technique, where we utilized the noise properties of the signal in dependence on the mean value, we decided to use the mean value of the signal in dependence on the exposure time.

By employing this approach, we can completely ignore the brighter-fatter effect, as it does not alter the mean value of the signal but only the noise - carrier diffusion preserves the total amount of counts and thus the mean value. In this setup, we require the signal strength to be constant over time, such that we observe a linear relation between signal and exposure time. Deviations from the linear model can then be attributed to non-linearity effects. The problem with this technique is that the signal strength is not constant over time, but is affected by a decrease of the beam current over time.

To minimize this effect, we use a bracketed repeat-exposure (BRE) method to acquire a reference frame with a fixed exposure time of 1 s in between measurements, e.g. 0 s, 1 s, 1 s, 2 s, 1 s, 3 s, 1 s, 4 s and so on, and use the 1 s reference frames to correct for the changes in beam currents. To make deviations from a linear model easy to track, we used the region below 6600 counts to fit a sloped line to the respective data and subtract it. Thereby, we obtain the original relation as acquired (yellow) depicted in Fig. 14d, as corrected by the beam intensity decrease (orange) and additionally corrected by the non-linearity curve obtained in Fig. 14a (black). As can be seen, the correction curve linearizes the gain of this second measurement as well. We further fitted a sloped line (black) to the saturation corrected data. This slope is not significantly different from zero, which shows that the correction Fig. 14a indeed corrects for gain non-linearities and saturation effects.

We would like to note that the second experimental setup yields significantly larger deviations than the previous noise method, which we therefore consider as the better option. Again, we would like to point out that the non-linearity correction and the brighter-fatter effect are similar in magnitude. Thus, not having corrected for it in the noise-method would have lead to a significant overestimation of the non-linearity correction, which would draw visible effects in Fig. 14d. Everything fitting together so nicely is a good indication that the applied corrections are indeed valid.

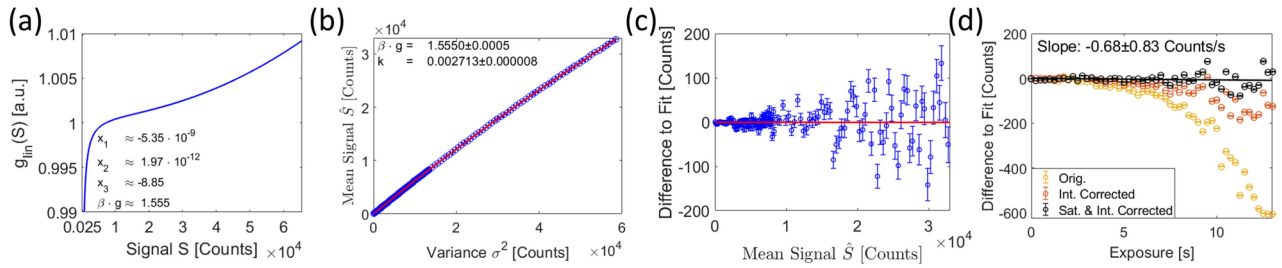

Fig. 14. (**a**) Non-linearity correction function from Eq. 67 as a result of the minimization of Eq. 86. The fit parameters are provided within the graph. (**b**) The mean value of the corrected signal in dependency of the variance of the corrected signal and (**c**) the residual plot of the difference to the fit. (**d**) To show that the gain non-linearity correction actually works as intended, a second measurement was conducted by using the bracketed repeat-exposure (BRE) method. In contrast to (**b**), we analyzed the mean value of the image (without dark frame subtraction) as a function of the exposure time. To pronounce deviations from a linear model that we aim to archive, we used the region below 6600 counts to fit a sloped line to the respective data and subtract it. The uncorrected original data (yellow) shows a drop in value with increasing exposure time relative to a linear increase. After correcting for deviations in the beam current (orange) by the BRE-method, the drop is significantly reduced but still observable. Applying both, the non-linearity correction from (**a**) and the beam current correction, leads to the desired linear behavior, where the difference to a linear fit shows randomly distributed deviations with increasing time. A linear fit across the entire range of the data, shown as the black line, shows no significant slope within tolerances.

Binning of signal and fixed-pattern noises

So far, we have shown that our model for the binning of detector noises is in good agreement with the theory shown in "Section Binning of the detector". As a final step in verifying our noise model, we need to show how the signal and fixed-pattern noises add up under binning. Adding these noises as a result of binning primarily affects the smoothing factor $\beta \to \beta_{H,V}$, with $\beta = \beta_{conv} \cdot \beta_{corr}$, and $\beta_{BF} \to \beta_{BF,H,V}$, with $\beta_{BF} = \beta_{BF,conv} \cdot \beta_{BF,corr}$, which both change the measured gain of the detector (see Eqs. 26 and 27). Since both β and β_{BF} act on the gain as a smoothing factor, we combine both into a new $\beta^* = \beta \cdot \beta_{BF}$. It follows that part of the convolution is removed in accordance to Eq. 37 as a consequence of binning. Therefore, the correlation of the data changes with Eq. 22.

To show the effects of detector correlation on the binning of pixels, we post-binned the data shown in the regression Fig. 14b with respect to the rows and the columns. Binning with values, which are not a divisor of 2048, leads to a remainder of pixels on one end of the detector. These pixels are discarded (see Fig. 1c). We take the average of the standard deviation of images binned both ways, front-to-end and end-to-front, in such cases. Smoothed gain $\beta^* \cdot g$ and the k-value, describing both uncertainty of the gain reference and the gain linearization $k^2 = k^2_{ref*} + k^2_{lin}$, are then parameters of the quadratic regression fit that can be plotted as a function of binning.

Higher exposure times, as were required for the non-linearity correction, were left out due to the increased number of cosmic rays (see Fig. 6). Replacing cosmic rays and their neighboring pixels (affected by the detector PSF) by the mean signal value of the image, causes the correlation of data to increase. Because of this, we decided to only use 1/5 of the total range of the detector, corresponding to an exposure time of around 2 s, where we expect less than 100 of such events. Further, we avoid larger uncertainties of the non-linearity correction, which might change the slope or curvature of the fit. Still, the regression analyzes contain 113 different intensities for a high precision measurement.

In Figs. 15a–d and 16a–c, we show the resulting gains and k-values of the regression fits as a function of the binning value in horizontal H, vertical V and diagonal direction HV, where we binned in both directions simultaneously. In red, we show the reconstruction solely based on adding the Pearson correlation coefficients (as described in Eq. 27) of the autocorrelation functions, shown in Figs. 12c and 13a. Additionally, the correlation effect β^*_{corr} was calculated using Eq. 22. We provide the differences between both methods in Figs. 15d–f and 16d–f in the lower rows.

The graphs in Fig. 15 demonstrate that the reconstruction is a good estimator to determine the gain under binning, as the difference between the reconstruction via Pearson coefficients does not differ significantly from the regressions. We can thus confirm the summation in Eq. 72. Especially, we would like to emphasize that in Fig. 15c, we observe a huge increase in the gain for higher diagonal binning, approaching the total intensity measured on the detector. Considering that a useful detector is expected to have a rather narrow PSF, this is a contradiction at first glance, which we will resolve in a moment. For Fig. 15a,b, the gain value seems to approach a constant value, which is expected.

Further, to show the necessity of regarding the β^*_{corr} coefficient (see Eq. 22), the same reconstructions without accounting for β^*_{corr} are shown as the black dashed line for (a-c) and can be seen to overestimate the gain, especially for the diagonal binning (c).

In Fig. 16, the development of the k-value is shown under binning (green curve). The signal is homogeneously distributed across the detector and thus we obtain the distribution factor $\alpha \approx 1$(see Eq. 74), making the

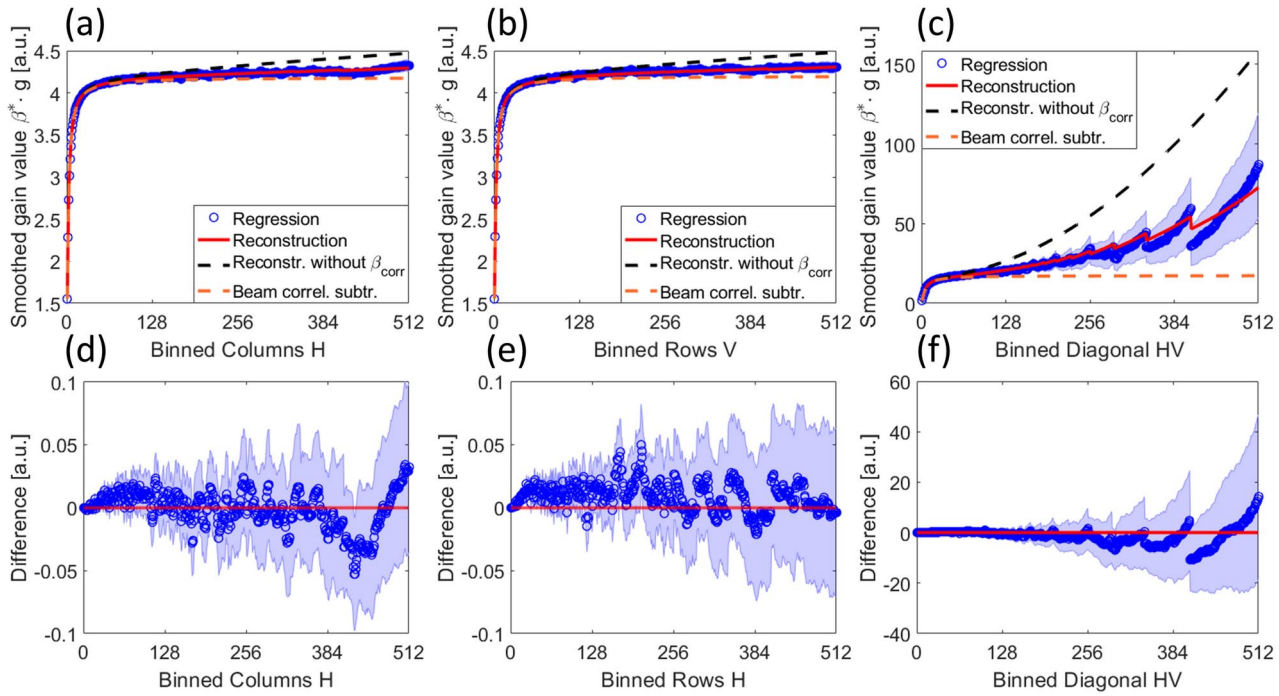

Fig. 15. (**a–c**) The smoothed gain $\beta \cdot g$, with $\beta = \beta_{corr} \cdot \beta_{conv}$ is depicted as a function of binned pixels, as described in Eq. 72. The blue dots represent the results based on a regression analyzes, similar to Fig. 14b, but with binned pixels. The red line displays the reconstruction, based on the Pearson correlation coefficients from Fig. 13a, following Eq. 26. Since binning changes the correlation within the data, we calculate the impact of it on the smoothing β_{corr} by Eqs. 27 and 22. The black dashed line represents the same reconstruction, but without regarding β_{corr}. The orange dashed line represents the reconstruction with the beam correlation corrected Pearson correlation coefficients. The results are shown for (**a**) horizontal binning with the binning value H (**b**) vertical binning with the binning value V and (**c**) diagonal binning along horizontal and vertical direction equally HV. It can be seen that both, beam correlation and β_{corr}, are necessary to find a good fit to the regression data. In the lower row (**d–f**), we provide the difference between both, the regression and the reconstruction methods. The shades depict the uncertainty within a 95% confidence interval, with again the red line representing the same reconstruction as in the upper row. It can be seen that the reconstructions via Pearson coefficients are in good agreement with the regressions.

addition as found in Eq. 73 easier. As described in "Section Gain non-linearities", we observe an offset of the k-values obtained from the regression, relative to the reconstruction of the autocovariance function (red curve). This offset represents the uncertainty of the gain linearization k_{lin}. Correcting the saturation and other non-linearities is limited to the precision of the measurement and the applicability of the model. Small deviations from the real gain non-linearities lead to a small increase in the noise, but as these deviations are not correlated between pixels, we obtain no observable change for higher binning. Theoretically, this offset should be a constant independent of the direction of binning. Here, we calculate k_{lin} based on a regression fit of the difference between the coefficients found by the mean-to-variance plot and the reconstruction by the Pearson coefficients. The latter must necessarily satisfy Eq. 41, as discussed previously, but mathematically it is unclear where the deviation in the Pearson coefficients manifests and thus the values might be more compromised in one direction than the other, which would explain the small deviations. Nevertheless, the deviation is so little that it accounts for only a few variance counts on the maximum intensity of the detector (without binning). Again, as k_{lin} acts on the gain linearity, it acts on the difference of the intensity of signals. Considering a maximum signal of ~ 65 k counts, we see that across the entire dynamic range of the detector, k_{lin} adds a maximum of 15 counts to the overall uncertainty of the measurement. This is well below the Poisson noise of that signal with 400 counts for the standard deviation. As images often consist of small gradients forming structures, one can easily see that k_{lin} is negligible for imaging.

We can thus confirm the summation Eqs. 73 and 76, as the results would otherwise deviate significantly. In total, we have shown that the binning derived in "Section Binning of the detector", based on the changes in the smoothing factor β^*, are according to theory.

We believe that the above results provide evidence that there is a good agreement between the shown reconstruction based on the autocovariance functions and the regression analyzes. It can therefore be assumed that the autocovariance function resembles the 'true' correlations within the data.

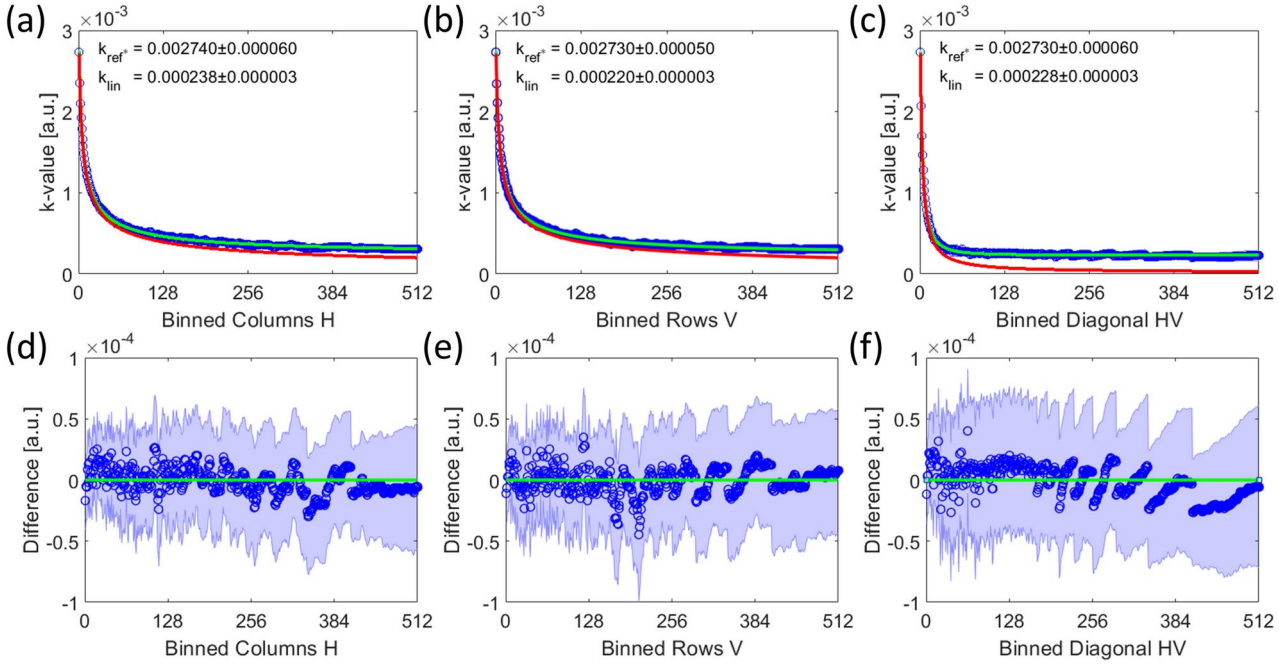

Fig. 16. (**a–c**) The k-value is displayed as a function of binned pixels, as shown in Eq. 73. Here, the distribution factor $\alpha = 1$, as the signal is homogeneously distributed across the detector. The blue dots represent the results based on a regression analyzes, similar to Fig. 14b, but with binned pixels. The red line displays the reconstruction based on the Pearson correlation coefficients from Fig. 12c, following Eqs. 26, 27 and 22. The uncertainty of the non-linearity correction k_{lin}^2 is independent of the binning (see Eq. 73). It is obtained by fitting an offset to the reconstructed uncertainty of the gain reference under binning $k_{H,V}^2 = k_{ref^*,H,V}^2 + k_{lin}^2$. Combining both uncertainties under a square root yields the green line. The results are shown for (**a**) horizontal binning with the binning value H (**b**) vertical binning with the binning value H and (**c**) diagonal binning along horizontal and vertical direction equally HV. In the lower row (**d–f**), we provide the difference between both methods. The shades depict the uncertainty within a 95% confidence interval. It can be seen that the reconstructions via Pearson coefficients plus the k_{lin} uncertainty are in good agreement with the regression analyzes.

Beam correlations and the reconstruction of the detector PSF

Having determined the Pearson correlation coefficients of the signal by normalizing Eq. 84, allows to reconstruct the PSF of the detector following Eq. 40. This is feasible here, because the gain of the fluorescence layer is sufficiently larger than 1. Furthermore, it is the first layer of the detector allowing the photons to spread out with the detector PSF, as described in "Section Noise and convolution". Typically, several hundreds to a few thousand photons are generated per incident beam electron. However, the reconstructed PSF from Fig. 17a shows a very low central peak and non-zero values in the periphery. Upon normalizing the distribution to determine the relative intensities of the PSF, we observe that only 18 out of 1000 counts are measured within the intended pixel. This is attributed to the large tails. Convolving any image with such a PSF renders it rather useless, as such a PSF diminishes any contrast. The very fact that we have contrast in the TEM is a good indication that the tails of this PSF cannot be connected to anything related to the detector itself.

Therefore, we need to take one step back and reexamine the distribution of the Pearson correlation coefficients, from which the PSF was derived. Interestingly, we observe large tails of the correlation distribution shown in (b), which means that despite the obvious small peak connected to the signal broadening as a result of diffusion, we have another low magnitude but far reaching correlation within the signal. So, the correlation must come from the electron beam itself as described in Eq. 43. Considering that effects leading to beam correlations are described and measured in[54,55], it is highly likely that the observed long tails in the distribution of Pearson coefficients can be attributed to such effects.

In order to determine the PSF of the detector Ω_d, the tails or offsets must be subtracted from the overall distribution of the Pearson correlation coefficients as Eq. 46 suggests. We found it suitable to approximate the beam correlation in the Pearson correlation coefficients as an offsetted 2D Gaussian $\mathscr{G}_{corr}$, which we fitted to the data shown in the inset of Fig. 17b. By omitting the region where the detector PSF dominates, we obtain the beam correlation shown as the red and the orange dashed lines in Fig. 17b. After subtracting this surface fit from the covariance function of the signal $K(\xi_{Sig})$, described in Eq. 84, we obtain the detector PSF shown in Fig. 17c by following Eq. 40 as:

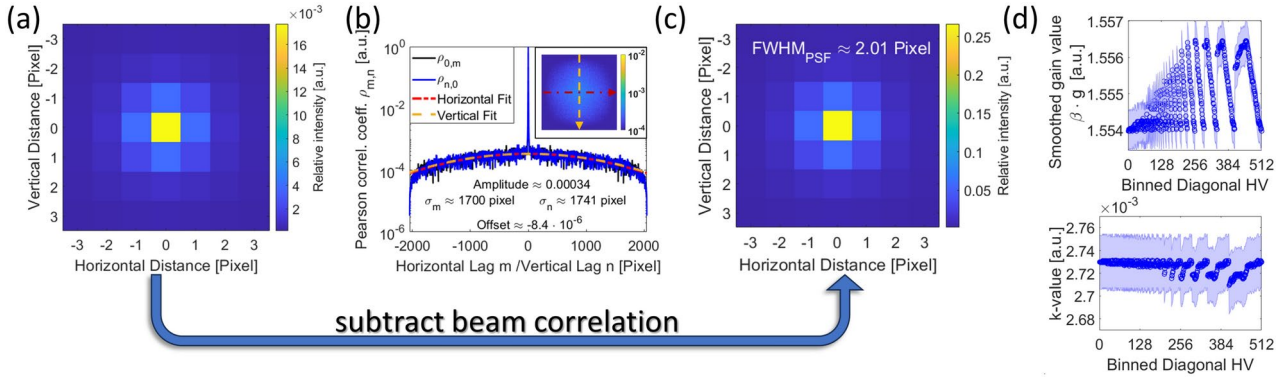

Fig. 17. (**a**) Shows the reconstructed PSF, following Eq. 40, from the Pearson correlation coefficients depicted in Fig. 13a. The distribution implie that only 18 out of 1000 photons are detected within the intended pixel, which is unlikely given the good contrasts measured with the detector. (**b**) Shows the Pearson correlation coefficients $\rho_{m,n}$ as line profiles with $m = 0$ for the horizontal profile and $n = 0$ for the vertical profile. The red and orange dotted lines represent the offsetted Gaussian surface fit, with which the beam correlation is determined. The fit parameters of the surface fit are provided within the graph along with an inset, showing all the Pearson coefficients of the signal on the detector logarithmically scaled for visibility. The red and yellow lines on the inset represent the direction the respective line profiles were taken. Subtracting the beam correlation before reconstructing the PSF leads to (**c**) the detector PSF. In comparison to (**a**) the probability of photons being measured in the intended pixel is significantly increased, making it more reasonable. (**d**) Shows the change in the measured smoothed gain (above) and k-value (below), when cropping the acquired frames according to the diagonal binning Fig. 15d but without the actual binning. It can be seen that the smoothed gain increases for 'binning values' that discard most of the detector, contrasting Fig. 15c. Further, it can be seen that independently of the gain, the k-value decreases for the same image section.

$$\Omega_d^* = \mathscr{F}^{-1}\left[\left(K\left(\xi_{Sig}\right) - \mathscr{G}_{corr}\right)^{1/2}\right] \ , \tag{87}$$

where Ω_d^* needs to be normalized with respect to the sum of all entries to obtain the relative probabilities of the detector PSF Ω_d. We observe that the PSF has lost the long tails, compared to Fig. 17a, and has a much more reasonable central element and a width of FWHM ≈ 2.01 pixel, which is in the typical range for such a scintillation-based CCD detector[68]. By following Eq. 44, we can further reconstruct the probability for correlated electrons p from the parameters from the fit Eq. 46 and determine $p \approx 1.7 \cdot 10^{-4}$. We can compare this value with the correlation found by Kodama et al.[54], which is in the order of $p_{Kodama} \approx 2 \cdot 10^{-3}$. Our electron beam exhibits correlation one order of magnitude lower, which is entirely reasonable given the different beam parameters and microscope. Thus, the correlation that we have measured falls well within the range that is already reported. The values for the width of the Ω_{TEM} distribution $\sigma_{TEM} \approx 1700$ pixel, however, are below our detector dimensions. For a homogeneous detector illumination, we would at least expect to see at least $\sigma_{TEM} \approx 4000$ pixel in width. This is a significant deviation, we cannot fully explain yet. At least Eq. 41 gives a reasonable explanation for this behavior of the autocovariance function.

For the development of the smoothed gain under binning, however, both beam and detector correlations have to be necessarily regarded. To illustrate this, we added an additional orange dashed line to Fig. 15, which shows the reconstruction according to Eqs. 27 and 22, similar to the red line, but omitting the beam correlation. Particularly in Fig. 15c, it is evident that the beam correlation is the dominant factor for the total intensity measured with the detector using higher diagonal binning. Here, the beam correlation leads to a steady increase of the smoothed gain, whereas the subtraction of these effects leads to a rather constant smoothed gain despite increasing the binning. For a detector with a small PSF, this constant behavior would be expected.

Far-reaching correlation has another notable effect on the smoothed gain $\beta^* \cdot g$, which is expected when only part of the detector is analyzed. This is specifically the case for high binning values, where we need to discard larger and larger parts of the detector like in Fig. 15c. To make the effect visible, we discarded parts of the detector like in Figs. 15c and 16c, and evaluated $\beta^* \cdot g$ in the non-discarded parts without binning. The results are shown in Fig. 17d, reveal the gain to steeply increase for 'binning' values that correspond to larger discarded parts of the detector. The reason for this behavior is that we cut out part of the correlation in the signal at the boundaries without changing the signal strength itself. From Eq. 22 follows that this must lead to a slight increase of the smoothed gain. This increase contrasts Fig. 15c at first glance, where we see the exactly opposite behavior, namely a steep decrease in the smoothed gain, where we discard large parts of the detector. Cutting away part of the correlation function drastically changes the smoothing factor to the downside, as under binning, these values now discarded would have been added up following Eq. 27. One can easily imagine that boundary effects dramatically increase for binned detectors. This explains the larger difference between the Pearson reconstruction and the regression values in Fig. 15c.

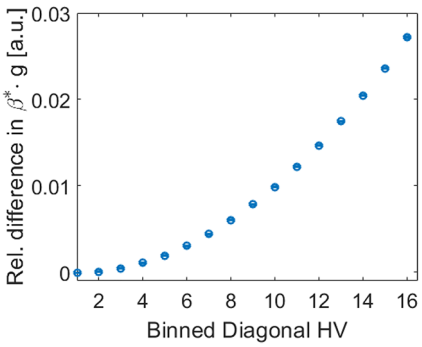

Fig. 18. Shows the relative difference, normalized to the initial smoothed gain without binning, between the red curve of Fig. 15c, representing the binning of both the beam correlation and the detector PSF, and the orange curve, representing only the detector PSF. The relative difference shows the impact of the beam correlation on the smoothing factor under binning. Considering that diagonal binning with a factor of 2 corresponds to halving the width of the beam disc, one can see that adjusting the beam disc has a slight but measurable impact on the smoothed gain $\beta^* \cdot g$. The relative difference super-linearly increases for higher binning values, which represent further contraction of the beam disc. While being rather negligible for small adjustments in the beam disc, this effect potentially plays a role for EELS measurements in STEM mode, where the beam appears as a small disc on the entrance aperture of the energy-filter.

For the k-values we consider the distribution of the quantum efficiencies, according to "Section The acquisition of a gain reference", to be more important than correlation or boundary effects, which is why we see an increase in k-value even though the gain in the upper graph drops for the same detector cutout.

Importantly, the beam correlation changes, when expanding or contracting the beam disc in TEM mode. The loss or gain of parts of the signal is equal to changing the beam current. With a constant correlation time, the beam correlation obviously changes. Further, by adjusting the beam, which is modeled by the deflection Ω^*_{TEM}, the smoothing factor $\beta_{TEM,conv}$(see Eq. 37) changes. So it is to be expected that the observed smoothed gain changes when (re-)optimizing the beam for different magnifications. This change is anticipated to be quite small. In Fig. 15c, we have shown the development of the gain with respect to binning horizontally and vertically, which with respect to the beam correlation to contracting the beam disc. Here, we must look in the difference between binning both detector PSF and beam correlation, as shown in the red curve, and the orange curve, which only gives the binning of the detector PSF. The difference should give a good approximation on how the beam correlation changes the smoothing factor β and is shown in Fig. 18. Thus, we must abandon the notion that there is just a single 'correct' gain to be measured, which is universally applicable for all experiments within a certain time frame, and instead accept that only a good enough approximation is possible.

Theoretical considerations on STEM-EELS measurements

Since the detector is also widely used for STEM-EELS measurements, we consider it important to also describe a noise model for EELS. Despite the change in operation mode, Eq. 48 remains valid for STEM with a few modifications, which we will explain in the following.

Due to a different beam path in comparison to TEM, we obtain the correlated beam from the point-source-like tip of the electron gun $S_{src,el}$ convolved with a different deflection kernel Ω^*_{STEM}, such that $S_{STEM,el} = \Omega^*_{STEM} \otimes S^*_{src,el}$ alters the beam correlation at the entrance aperture of the energy loss spectrometer that again cuts away part of the signal. Ω^*_{STEM} is again normalized to the height of one. By directing the electrons through magnetic lenses, the beam disperses into the energy distribution of the probe before being projected onto the detector. We can write the dispersed STEM probe as $B_{disp} = \Omega_{disp} \otimes \Omega^*_{STEM} \otimes S_{src,el}$, where the two convolutions Ω_{disp} and Ω^*_{STEM} affect the signal like in Eq. 42: the convolutions are written inside the Poisson distribution for the uncorrelated electrons $\mathscr{P}\left[\Omega_{disp} \otimes \Omega^*_{STEM} \otimes \hat{S}_{src,el}\right]$ and outside for the correlated electrons $\Omega_{disp} \otimes \Omega^*_{STEM} \otimes \mathscr{P}\left[\hat{S}_{src,el}\right]$. We obtain:

$$\begin{aligned} B_{disp} &= p_{STEM} \cdot \left(\Omega_{disp} \otimes \Omega^*_{STEM} \otimes \mathscr{P}\left[\hat{S}_{src,el}\right]\right) + (1 - p_{STEM}) \cdot \mathscr{P}\left[\Omega_{disp} \otimes \Omega^*_{STEM} \otimes \hat{S}_{src,el}\right] \\ &\approx \mathscr{P}\left[\Omega_{disp} \otimes \Omega^*_{STEM} \otimes \hat{S}_{src,el}\right] \end{aligned} . \tag{88}$$

Since the signal width is expected to be rather narrow, it is unclear but likely that this cutoff changes the probability for correlated electrons p_{STEM} significantly. Due to the reduced beam current flowing through the aperture, we cannot use the *p*-value from the analysis in Fig. 17b. In case that we can neglect the beam correlation, we can approximate $p_{STEM} \approx 0$. Otherwise we obtain the Pearson correlation coefficients as:

$$\begin{aligned}\rho_{disp,m,n} &= \left[\left(p_{STEM}\cdot\Omega^*_{disp}\otimes\Omega^*_{STEM}+(1-p_{STEM})\cdot\delta\right)\star\left(p_{STEM}\cdot\Omega^*_{disp}\otimes\Omega^*_{STEM}+(1-p_{STEM})\cdot\delta\right)\right]_{n,m}\\ &\approx \left[p^2_{STEM}\cdot\left(\Omega^*_{disp}\otimes\Omega^*_{STEM}\right)\otimes\left(\Omega^*_{disp}\otimes\Omega^*_{STEM}\right)+2\cdot p_{STEM}\cdot(1-p_{STEM})\cdot\Omega^*_{disp}\otimes\Omega^*_{STEM}+(1-p_{STEM})^2\cdot\delta\right]_{n,m},\end{aligned} \tag{89}$$

like in Eq. 43 on the basis of Eq. 40. Under the assumption that both the distribution on the entrance aperture Ω_{STEM} and the dispersion Ω_{disp} are symmetrical, one can replace the autocorrelation $\star$ by a convolution $\otimes$(see Eq. 30). This should be the case for Ω_{STEM}. However, a symmetrical Ω_{disp} requires the ZLP to be symmetrical. Since this is often not the case, especially not for measurements with all the scattering interactions, it would be favorable to retain the autocorrelation. Still, one can argue that the ZLP is rather symmetrical and thus writing a convolution instead of autocorrelation is possible. However, this is rather to be seen as an approximation. Again, Ω^*_{disp} and Ω^*_{dist} denote the normalized PSFs to the height of one of the respective distributions. Since the two convolutions are way smaller than Ω^*_{TEM} for a broad beam disc in TEM mode, we cannot approximate the first term as a constant.

Again, we observe the convolution with the detector PSF Ω_d to influence both the correlated and uncorrelated part of the signal equally, such that we obtain the 2D EELS signal in electrons as $S_{EELS,el}=\Omega_d\otimes B_{disp}$ with the Pearson correlation coefficients $\rho_{EELS}=\Omega^*_d\otimes\Omega^*_d\otimes\rho_{disp}$.

The three convolutions of the beam Ω^*_{STEM}, the dispersion Ω_{disp} and the detector PSF Ω_d can easily be measured in vacuum, as they describe the 2D representation of the ZLP of that measurement $\Omega^*_{ZLP}=\Omega_d\otimes\Omega_{disp}\otimes\Omega^*_{STEM}$. Thus, we obtain:

$$\begin{aligned}\rho_{EELS,m,n} &\approx \left[p^2_{STEM}\cdot(\Omega^*_{ZLP}\star\Omega^*_{ZLP})+2\cdot p_{STEM}\cdot(1-p_{STEM})\cdot(\Omega^*_d\otimes\Omega^*_{ZLP})+(1-p_{STEM})^2\cdot(\Omega^*_d\otimes\Omega^*_d)\right]_{n,m}\\ &\approx \left[\Omega^*_d\otimes\Omega^*_d\right]_{n,m},\end{aligned} \tag{90}$$

with Ω^*_{ZLP} denoting the normalized distribution to the height of one and, in case the beam correlation is negligible, we can again simplify the equation.

Under considerable beam correlation, it is rather impossible to directly reconstruct the smoothing factor β from the TEM mode for STEM-EELS. To obtain the smoothing factor β under such conditions, a direct measurement of the Pearson correlation coefficients of such an EELS signal would be necessary. This measurement should be possible by utilizing Eq. 28, but requires the expectation value of the signal to be subtracted from each point on the CCD camera. Since the signal is inhomogeneously distributed, a good estimate on the expectation value of the signal can be found as the mean value of several measurements, if the microscope remains very stable.

Fortunately, the PSF of the detector is identical for both operation modes and can be considered valid in TEM as well as in STEM mode. Provided, the impact of the beam correlation in STEM mode is rather small, the PSF might give an estimate for the Pearson correlation coefficients using Eqs. 37 and 22. In this case, we can indeed use measurements from TEM mode to obtain the smoothed gain in STEM mode, since the smoothing is only connected to the detector PSF, which we have already determined in Eq. 40. By correcting Eq. 84 for the beam correlation, as shown in the previous section, and reducing the signal strength $\hat{S}_c$ by the correlated electrons, we obtain the smoothed gain for STEM mode:

$$g\cdot\beta_{EELS}\cdot\rho\left(\xi_{Sig}\right)=\frac{K\left(\xi_{Sig}\right)-\mathscr{G}_{corr}}{(1-p)\cdot\hat{S}_c}\ . \tag{91}$$

As β is only determined by the detector PSF and the signal is fully confined on the detector, which is usually the case for EELS, Eq. 27 simplifies to the simple sum across all entries $\beta_{EELS}=\sum_{m,n}^{M,N}\rho_{EELS,m,n}$(see Eq. 90). We can thus add up all Pearson correlation coefficients of the corrected autocovariance function of the signal, as shown in Fig. 17b, and determine $\beta\approx 0.09$, from which we can calculate $g\approx 17.43$ counts/beam electron as the gain of our detector. Hart et al. reported a similar gain of 12.6 counts/beam electron[69] for an older model of our detector, the *US1000FTXP*, within a *Gatan GIF*.

Since the 2D EELS signal is summed up vertically along the columns with $V=260$ to form a spectrum on our detector, we need to consider the addition of the Pearson correlation coefficients Eq. 90 as shown in Eqs. 26 and 27. With it, we obtain $\beta_{EELS,1,260}=\beta_{EELS,conv,1,260}\cdot\beta_{EELS,corr,1,260}\approx 0.24$, following Eq. 37, for the smoothing by convolution and, following Eq. 22, for the smoothing by the correlation as values for our detector. We neglect the influence of the brighter-fatter effect, as it is contained in the measurement of a vacuum ZLP and alters it slightly with respect to the shape. As shown in Fig. 13d, it falls below the Poisson noise and is thus negligible for most measurements.

Implementing all this into Eq. 77, describing the post-binning of the detector, leads to the noise model:

$$\begin{aligned}\xi^{corr}_{EELS} &\approx g\cdot\beta_{EELS,1,V}\cdot\mathscr{P}\left[\frac{\sum_j^V\hat{S}_{EELS,c,i,j}}{g\cdot\beta_{EELS,1,V}}\right]+\mathscr{N}\left[0,\,\sigma^2_{EELS}\right] \quad \text{, with}\\ \sigma^2_{EELS} &= \alpha_{1,V}\cdot k^2_{ref^*,1,V}\cdot\left(\sum_j^V\hat{S}_{EELS,c,i,j}\right)^2+k^2_{ref^*,1,V}\cdot g\cdot\beta_{EELS,1,V}\cdot\sum_j^V\hat{S}_{EELS,c,i,j}+2\sum_j^V\sigma^2_{EELS,corr}\ ,\end{aligned} \tag{92}$$

where the EELS signal in counts is found as $S_{EELS,c}=g\cdot S_{EELS,el}$. Due to the vertical post-binning V to generate a spectrum from the 2D data for EELS, the distribution factor $\alpha_{1,V}$ can be derived from a 2D ZLP image, under the assumption that $\alpha_{1,V}$ is not (much) influenced by a specimen. Similar to Eq. 74, we obtain:

$$\alpha_{1,V} = \sum_{j}^{V} \left(\frac{\hat{S}_{EELS,el,i,j}}{\sum_{j}^{n} \hat{S}_{EELS,el,i,j}} \right)^2 . \tag{93}$$

As described previously, the uncertainty of the gain linearization k_{lin} can be neglected for normal measurements. So, we neglect it here and leave it with the uncertainty of the non-linearity corrected gain reference k_{ref^*}. Since the gain reference does not change between the operational modes of TEM and EELS, we can use the values from Fig. 16b for the amount of rows used for EELS and determine $k_{ref^*,1,260} \approx 2.8 \cdot 10^{-4}$.

For our detector, we observe that the EELS region is located in the middle of the four quadrants (see Fig. 1). Thus, we obtain the detector noise as the sum of the individual detector noises of Q1 and Q3 as well as Q2 and Q4, due to the positioning of the EELS region on the camera. As the noise depends on the respective quadrant and the EELS signal is spread across all of them, the respective value sets for the gain normalized and linearization corrected noises are given as $\sigma^2_{EELS,d} = \sum_{j}^{V} \sigma^2_{d,corr}$(see Eq. 52 with Eqs. 65 and 70). We consider this our EELS noise model.

As an EELS signal in vacuum consists of a large ZLP rather than a homogeneous signal, the only way verifying this model is by comparing vacuum EEL spectra measured multiple times, which is quite complex. Energy-drifts must be corrected, intensity changes of the beam must be normalized and energy jitters alter the shape of a ZLP. All of these noise features must be regarded and mathematically be described. Due to the complexity of verifying this model with an actual EELS measurement and considering the already lengthy paper until now, we leave it at that.

EELS is also just a signal on the detector, that in theory, should obey the above considerations. We have good evidence that the proposed noise model is valid for regular TEM measurements and thus we have little reason to believe that EELS fundamentally changes things on a theoretical level. A follow-up paper addressing the noises in EELS is provided in reference[70].

Conclusions

In this work, the mathematical derivation of a noise model for scintillation-based CCD detectors is presented and it is shown how corrective operations like gain normalization affect it. We have shown which different kinds of noises are to be expected by measuring gain normalized images. Contributions of both detector and signal noise are separated and analyzed in detail. As an example for the detector architecture, we considered a *Gatan GIF Quantum ER* image filter employing the widespread *US1000FX-XP 2* CCD detector.

By utilizing the autocovariance function in Eqs. 28 and 84, we could determine the Pearson correlation coefficients of a flat image in dependence of increasing signal strength in TEM mode, which allowed to examine the brighter-fatter effect of the detector. Based on our noise model in Eq. 48, we have shown how the gain non-linearity function can be obtained by utilizing a signal-to-variance fit to counteract gain non-linearities in the CCD camera. To further prove the applicability of this correction, we have validated it using a bracketed-repeat-exposure (BRE) technique on a different data set, corrected by this method. Such a non-linearity correction is necessary to calibrate the detector to the highest precision. It also allows to use a single gain reference for the entire dynamic range of the detector, whereas recent gain references are only valid for a limited intensity range around the target intensity they were acquired with. This is specifically important for EEL spectra that cover a high dynamic range, with the ZLP often being a thousand times more intense than the typical energy-loss features of a specimen.

With the Pearson correlation coefficients of several flat images, used to obtain the gain reference to correct images with, we found a Gaussian distributed spatial correlation in the electron beam as an offset to the coefficients related to the PSF. This offset must be subtracted before reconstructing the detector PSF.

Again, we would like to point out that getting the Pearson correlation coefficients from the signal and the gain reference in TEM mode is mathematically not expensive and comprises just a few Fourier transformations and simple subtractions and divisions. It should in theory be feasible to get them as a side-product of the acquisition of a suitable gain reference using a homogeneous signal. In this paper, we have shown both theoretically and experimentally how to acquire them. We could further use these coefficients to reconstruct the change in gain under binning of neighboring pixels following Eqs. 27, 37 and 22, which is a very good indication that these coefficients are valid. With a few more steps, one could calculate the detector PSF as an automated process.

Further, we have shown that the beam correlation must necessarily change when contracting or broadening the beam disc and with it, the smoothing factor β to the gain changes. Beam correlation contributes to the overall smoothed gain of a measurement and cannot be neglected for detector binning. This beam correlation has broader implications for STEM-EELS measurements.

Considering that beam correlation is not negligible in STEM-EELS, we concluded that it is rather impossible to reliably determine the smoothing factor β of a STEM measurement, e.g. for STEM-EELS, by only using a TEM measurement, without further knowledge on the change of the beam correlation probability p between TEM and STEM. This probability naturally changes due to different beam paths and apertures. Nevertheless, we could find a noise model for EELS measurements as a special case for the regular CCD measurement, where only the beam correlation probability p remains as an unknown. This probability would be necessary to obtain the Pearson correlation coefficients for EELS. Therefore, we described an experimental technique to determine the Pearson correlation coefficients for EELS.

However, the point spread function and the uncertainty of the gain reference remain valid for both modes. In case that the beam correlation is indeed negligible in STEM-EELS, due to reduced beam currents, correlation effects are only determined by the detector point spread function and can be genuinely reconstructed using measurements in TEM mode, as shown in "Section Theoretical considerations on STEM-EELS measurements".

All in all we found a consistent noise model, which allows to explain every change in the noise as a logical consequence of the previous image acquisition steps. We found mathematical descriptions and approximations of all these processes, which are mostly valid within the tolerance of our measurements and showed ways to utilize the noise to correct a CCD detector.

Noise and its statistics are powerful tools in the hands of operators, who know how to use them for their benefit. Even though it is often considered annoying to work with, we hope to have shown that sometimes it is worth to take a closer look at the noise.

Data availability

The data sets generated during this study are available from the corresponding author upon request. Additionally, the MATLAB scripts used to analyze the noises are provided in the supplementary materials section for open access and use.

Received: 28 March 2024; Accepted: 7 January 2025
Published online: 30 January 2025

References

1. Meyer, R. & Kirkland, A. The effects of electron and photon scattering on signal and noise transfer properties of scintillators in CCD cameras used for electron detection. *Ultramicroscopy* **75**, 23–33. https://doi.org/10.1016/S0304-3991(98)00051-5 (1998).
2. Ishikawa, R., Lupini, A. R., Findlay, S. D. & Pennycook, S. J. Quantitative annular dark field electron microscopy using single electron signals. *Microscopy Microanal.* **20**, 99–110. https://doi.org/10.1017/S1431927613013664 (2014).
3. Haruta, M. et al. Low count detection for EELS spectrum by reducing CCD read-out noise. *Microscopy Microanal.* **26**, 1202–1204. https://doi.org/10.1017/S1431927620017328 (2020).
4. Ikoma, H., Broxton, M., Kudo, T. & Wetzstein, G. A convex 3D deconvolution algorithm for low photon count fluorescence imaging. *Sci. Rep.* **8**, 11489. https://doi.org/10.1038/s41598-018-29768-x (2018).
5. Verbeeck, J. & Bertoni, G. Model-based quantification of EELS spectra: Treating the effect of correlated noise. *Ultramicroscopy* **108**, 74–83. https://doi.org/10.1016/j.ultramic.2007.03.004 (2008).
6. Egerton, R. F. *Electron Energy-Loss Spectroscopy in the Electron Microscope* (Springer, 2011).
7. Zuo, J. M. & Spence, J. C. H. *Advanced Transmission Electron Microscopy: Imaging and Diffraction in Nanoscience* (Springer, 2017).
8. Velazco, A., Béché, A., Jannis, D. & Verbeeck, J. Reducing electron beam damage through alternative stem scanning strategies, part I: Experimental findings. *Ultramicroscopy* **232**, 113398. https://doi.org/10.1016/j.ultramic.2021.113398 (2022).
9. Ilett, M. et al. Analysis of complex, beam-sensitive materials by transmission electron microscopy and associated techniques. *Philos. Trans. A Math. Phys. Eng. Sci.* **378**, 20190601. https://doi.org/10.1098/rsta.2019.0601 (2020).
10. Dang, Z., Luo, Y., Wang, X.-S., Imran, M. & Gao, P. Electron-beam-induced degradation of halide-perovskite-related semiconductor nanomaterials. *Chin. Opt. Lett.* **19**, 030002. https://doi.org/10.3788/COL202119.030002 (2021).
11. Buban, J. P., Ramasse, Q., Gipson, B., Browning, N. D. & Stahlberg, H. High-resolution low-dose scanning transmission electron microscopy. *J. Electron Microsc.* **59**, 103–112. https://doi.org/10.1093/jmicro/dfp052 (2010).
12. Ortega, E. & de Jonge, N. Analysis of the dose-limited spatial resolution in transmission electron microscopy. *Microscopy Microanal.* **26**, 1216–1217. https://doi.org/10.1017/S1431927620017365 (2020).
13. Zietlow, C. & Lindner, J. K. N. ADMM-TGV image restoration for scientific applications with unbiased parameter choice. *Numer. Algor.* **97**, 1481–1512. https://doi.org/10.1007/s11075-024-01759-2 (2024).
14. Iyudin, A. F. & Svertilov, S. I. Application of scintillation detectors in cosmic experiments. In *Engineering of Scintillation Materials and Radiation Technologies, vol. 227 of Springer Proceedings in Physics* (eds Korzhik, M. & Gektin, A.) 165–185 (Springer, 2019). https://doi.org/10.1007/978-3-030-21970-3_12.
15. Sahlholm, A., Svenonius, O. & Petersson, S. Scintillator technology for enhanced resolution and contrast in X-ray imaging. *Nuclear Instrum. Methods Phys. Res. Sect. A Accelerators Spectrometers Detect. Assoc. Equip.* **648**, S16–S19. https://doi.org/10.1016/j.nima.2011.01.113 (2011).
16. Xu, L.-J., Lin, X., He, Q., Worku, M. & Ma, B. Highly efficient eco-friendly X-ray scintillators based on an organic manganese halide. *Nat. Commun.* **11**, 4329. https://doi.org/10.1038/s41467-020-18119-y (2020).
17. Bugby, S. L., Jambi, L. K. & Lees, J. E. A comparison of CsI: Tl and GOS in a scintillator-CCD detector for nuclear medicine imaging. *J. Instrum.* **11**, P09009–P09009. https://doi.org/10.1088/1748-0221/11/09/P09009 (2016).
18. Yousefi, A., Jafari, H., Khorsandi, M. & Faezmehr, A. Assessment of a low-cost commercial CCD for use in X-ray imaging. *Appl. Radiat. Isotopes* **190**, 110476. https://doi.org/10.1016/j.apradiso.2022.110476 (2022).
19. Lacroix, F., Beaulieu, L., Archambault, L. & Beddar, A. S. Simulation of the precision limits of plastic scintillation detectors using optimal component selection. *Med. Phys.* **37**, 412–418. https://doi.org/10.1118/1.3276734 (2010).
20. Roncali, E., Mosleh-Shirazi, M. A. & Badano, A. Modelling the transport of optical photons in scintillation detectors for diagnostic and radiotherapy imaging. *Phys. Med. Biol.* **62**, R207–R235. https://doi.org/10.1088/1361-6560/aa8b31 (2017).
21. Beutel, J. et al. (eds) *Handbook of Medical Imaging* (SPIE Press, 2000).
22. Barrett, H. H. *Radiological Imaging: The Theory of Image Formation, Detection, and Processing* (Academic Press, 1981).
23. Barrett, H. H. & Myers, K. J. *Foundations of Image Science. Wiley Series in Pure and Applied Optics* (Wiley-Interscience, 2004).
24. Rabbani, M., Shaw, R. & van Metter, R. Detective quantum efficiency of imaging systems with amplifying and scattering mechanisms. *J. Opt. Soc. Am. A Opt. Image Sci.* **4**, 895–901. https://doi.org/10.1364/josaa.4.000895 (1987).
25. Cunningham, I. A., Westmore, M. S. & Fenster, A. A spatial-frequency dependent quantum accounting diagram and detective quantum efficiency model of signal and noise propagation in cascaded imaging systems. *Med. Phys.* **21**, 417–427. https://doi.org/10.1118/1.597401 (1994).
26. Gubbens, A. et al. The GIF Quantum, a next generation post-column imaging energy filter. *Ultramicroscopy* **110**, 962–970. https://doi.org/10.1016/j.ultramic.2010.01.009 (2010).
27. Tanguay, J., Yun, S., Kim, H. K. & Cunningham, I. A. Detective quantum efficiency of photon-counting X-ray detectors. *Med. Phys.* **42**, 491–509. https://doi.org/10.1118/1.4903503 (2015).
28. Stierstorfer, K., Hupfer, M. & Köster, N. Modeling the DQE(f) of photon-counting detectors: Impact of the pixel sensitivity profile. *Phys. Med. Biol.* **64**, 105008. https://doi.org/10.1088/1361-6560/ab1766 (2019).
29. Ross, S. M. *Introduction to Probability Models* 30th edn. (Academic Press, 2024).
30. Bretthorst, G. L. & Jaynes, E. T. (eds) *Probability Theory: The Logic of Science* 17th edn. (Cambridge University Press, 2017).
31. Klenke, A. *Probability Theory: A Comprehensive Course* 2nd edn. (Springer, 2013).
32. Lemons, D. S. *An Introduction to Stochastic Processes in Physics* (Johns Hopkins University Press, 2002).
33. Goodman, L. A. On the exact variance of products. *J. Am. Stat. Assoc.* **55**, 708. https://doi.org/10.2307/2281592 (1960).
34. Cui, G., Yu, X., Iommelli, S. & Kong, L. Exact distribution for the product of two correlated Gaussian random variables. *IEEE Signal Process. Lett.* **23**, 1662–1666. https://doi.org/10.1109/LSP.2016.2614539 (2016).

35. Díaz-Francés, E. & Rubio, F. J. On the existence of a normal approximation to the distribution of the ratio of two independent normal random variables. *Stat. Pap.* **54**, 309–323. https://doi.org/10.1007/s00362-012-0429-2 (2013).
36. Réfrégier, P. *Noise Theory and Application to Physics: From Fluctuations to Information. Advanced Texts in Physics* (Springer, 2004).
37. Skellam, J. G. The frequency distribution of the difference between two Poisson variates belonging to different populations. *J. R. Stat. Soc.* **109**, 296. https://doi.org/10.2307/2981372 (1946).
38. Kaas, R., Denuit, M., Dhaene, J. & Goovaerts, M. J. *Modern actuarial risk theory: Using R* 2nd edn. SpringerLink Bücher (Springer, 2008).
39. Bertalmío, M. (ed.) *Denoising of Photographic Images and Video: Fundamentals, Open Challenges and New Trends* SpringerLink Bücher (Springer International Publishing, 2018).
40. Rajdl, K., Lansky, P. & Kostal, L. Fano factor: A potentially useful information. *Front. Comput. Neurosci.* **14**, 569049. https://doi.org/10.3389/fncom.2020.569049 (2020).
41. Bousselham, A., Barrett, H. H., Bora, V. & Shah, K. Photoelectron anticorrelations and sub-Poisson statistics in scintillation detectors. *Nuclear Instrum. Methods Phys. Res. Sect. A Accelerators Spectrometers Detectors Assoc. Equip.* **620**, 359–362. https://doi.org/10.1016/j.nima.2010.03.152 (2010).
42. Bohm, G. & Zech, G. Statistics of weighted Poisson events and its applications. *Nuclear Instrum. Methods Phys. Res. Sect. A Accelerators Spectrometers Detectors Assoc. Equip.* **748**, 1–6. https://doi.org/10.1016/j.nima.2014.02.021 (2014).
43. Rudolf Schieder. Noise and correlation.
44. Pearson, K. & Galton Laboratory for National Eugenics. *Note on Regression and Inheritance in the Case of Two Parents*. Proceedings of the Royal Society (Royal Society, 1895).
45. Hogg, R. V., McKean, J. W. & Craig, A. T. *Introduction to Mathematical Statistics* 8th edn. (Pearson, London, 2018).
46. Wiener, N. Generalized harmonic analysis. *Acta Math.* **55**, 117–258. https://doi.org/10.1007/BF02546511 (1930).
47. Khintchine, A. Korrelationstheorie der stationren stochastischen Prozesse. *Math. Ann.* **109**, 604–615. https://doi.org/10.1007/BF01449156 (1934).
48. Lapidoth, A. *A Foundation in Digital Communication* (Cambridge University Press, 2017).
49. Gubner, J. A. *Probability and Random Processes for Electrical and Computer Engineers* (Cambridge University Press, 2006).
50. Yarlagadda, R. K. R. & Yarlagadda, R. K. R. *Analog and Digital Signals and Systems* Electrical engineering (Springer, 2010).
51. Gray, R. M. & Goodman, J. W. *Fourier Transforms: An Introduction for Engineers, vol. SECS 322 of The Kluwer International Series in Engineering and Computer Science* (Springer, 1995).
52. Guenther, B. D. *Modern Optics Simplified. Oxford Scholarship Online* 1st edn. (Oxford University Press, 2020)
53. Hassani, H. Sum of the sample autocorrelation function. *Random Oper. Stochastic Equ.*[SPACE]https://doi.org/10.1016/j.physa.2009.12.050 (2009).
54. Kodama, T., Osakabe, N. & Tonomura, A. Correlation in a coherent electron beam. *Phys. Rev. A*[SPACE]https://doi.org/10.1103/PhysRevA.83.063616 (2011).
55. Kodama, T. & Osakabe, N. Mechanism for correlation in a coherent electron beam. *Microscopy (Oxford, England)* **68**, 133–143. https://doi.org/10.1093/jmicro/dfy129 (2019).
56. van Nieuwenhove, V. et al. Dynamic intensity normalization using eigen flat fields in X-ray imaging. *Opt. Express* **23**, 27975–27989. https://doi.org/10.1364/OE.23.027975 (2015).
57. Seki, T., Ikuhara, Y. & Shibata, N. Theoretical framework of statistical noise in scanning transmission electron microscopy. *Ultramicroscopy* **193**, 118–125. https://doi.org/10.1016/j.ultramic.2018.06.014 (2018).
58. Liu, B., Li, Y., Wen, L., Zhang, X. & Guo, Q. Effects of hot pixels on pixel performance on backside illuminated complementary metal oxide semiconductor (CMOS) image sensors. *Sensors (Basel, Switzerland)*[SPACE]https://doi.org/10.3390/s23136159 (2023).
59. Carter, C. B. & Williams, D. B. *Transmission Electron Microscopy* (Springer International Publishing, 2016).
60. Snyder, D. L., Helstrom, C. W., Lanterman, A. D., White, R. L. & Faisal, M. Compensation for readout noise in CCD images. *J. Opt. Soc. Am. A* **12**, 272. https://doi.org/10.1364/JOSAA.12.000272 (1995).
61. Howell, S. B. *Handbook of CCD Astronomy* (Cambridge University Press, 2012).
62. Xia, G., Liu, Q., Zhou, H. & Yu, F. A non-linearity correction method of charge-coupled device array spectrometer. In *AOPC 2015: Optical Test, Measurement, and Equipment, SPIE Proceedings* (eds Han, S., Ellis, J. D., Guo, J. & Guo, Y.) 96770J (SPIE, 2015). https://doi.org/10.1117/12.2197725
63. Astier, P. et al. The shape of the photon transfer curve of CCD sensors. *Astron. Astrophys.* **629**, A36. https://doi.org/10.1051/0004-6361/201935508 (2019).
64. Downing, M., Baade, D., Sinclaire, P., Deiries, S. & Christen, F. CCD riddle: a) signal vs time: linear; b) signal vs variance: non-linear. In *High Energy, Optical, and Infrared Detectors for Astronomy II*, SPIE Proceedings (eds Dorn, D. A. & Holland, A. D.) 627609 (SPIE, 2006). https://doi.org/10.1117/12.671457.
65. Walter, C. W. The brighter-fatter and other sensor effects in CCD simulations for precision astronomy. *J. Instrum.* **10**, C05015–C05015. https://doi.org/10.1088/1748-0221/10/05/C05015 (2015).
66. Kuroda, T. *Essential Principles of Image Sensors* (CRC Press, 2015).
67. Padé, H. Sur la représentation approchée d'une fonction par des fractions rationnelles. *Annales scientifiques de l'École normale supérieure* **9**, 3–93. https://doi.org/10.24033/asens.378 (1892).
68. Plotkin-Swing, B. et al. Hybrid pixel direct detector for electron energy loss spectroscopy. *Ultramicroscopy* **217**, 113067. https://doi.org/10.1016/j.ultramic.2020.113067 (2020).
69. Hart, J. L. et al. Direct detection electron energy-loss spectroscopy: A method to push the limits of resolution and sensitivity. *Sci. Rep.* **7**, 8243. https://doi.org/10.1038/s41598-017-07709-4 (2017).
70. Zietlow, C. & Lindner, J. K. N. An applied noise model for low-loss EELS maps. *Ultramicroscopy* **270**, 114101. https://doi.org/10.1016/j.ultramic.2024.114101 (2025).

Acknowledgements

We acknowledge support for the publication costs by the Open Access Publication Fund of Paderborn University.

Author contributions

All authors contributed to the study conception and design. The manuscript was written by CZ. All authors read and approved the final manuscript.

Funding

Open Access funding enabled and organized by Projekt DEAL.

Declarations

Competing interests
The authors declare no competing interest.

Additional information
Supplementary Information The online version contains supplementary material available at https://doi.org/10.1038/s41598-025-85982-4.

Correspondence and requests for materials should be addressed to C.Z.

Reprints and permissions information is available at www.nature.com/reprints.

Publisher's note Springer Nature remains neutral with regard to jurisdictional claims in published maps and institutional affiliations.

An applied noise model for scintillation-based CCD detectors in transmission electron microscopy

Christian Zietlow[1,*] **and Jörg K. N. Lindner**[1]

[1]Nanopatterning-Nanoanalysis-Photonic Materials Group, Department of Physics, Paderborn University, Warburgerstr. 100, 33098 Paderborn
[*]christian.zietlow@upb.de

A Supplementary material

Our noise model contains a lot of (slightly) different variables. This supplementary information aims to support the readability of the paper by giving a short explanation of the respective variables.

Running indices and miscellaneous:

i,j	- index of the respective row, column.
m,n	- index of the respective horizontal, vertical lag.
M,N	- number of total pixels in horizontal, vertical direction.
H,V	- number of horizontally, vertically added pixels.
w	- added images.
p	- probability of correlated electrons in the electron beam.
p_{STEM}	- probability of correlated electrons in the electron beam for STEM-mode.
ρ_{TEM}	- Pearson correlation coefficient of the electron beam in TEM mode.
ρ	- Pearson correlation coefficient of the complete image formation.
ρ_{disp}	- Pearson correlation coefficient of the dispersed electron beam in STEM mode.
ρ_{EELS}	- Pearson correlation coefficient of a 2D EELS signal.
$K(\xi)$	- autocovariance function of the image ξ.
$K^{+}(\xi)$	- positivity constrained autocovariance function of the image ξ.
x_1, x_2, x_3	- fit parameters for the gain linearization correction.
Z	- used images for the non-linearity functional.
$\mathscr{G}_{corr}$	- offsetted Gaussian fit for the beam correlation in the Pearson correlation coefficients of the signal.

Gains and gain distributions:

g_{fl}	- gain of the fluorescence layer.
g_{opt}	- gain of the fiber optics layer.
g_{CCD}	- gain of the CCD detector.
g_c	- conversion gain from charge carriers in the CCD to counts.
g_d	- mean gain of the total detector including the gains g_{fl}, g_{opt} and g_{CCD}.
G_d	- gain of the detector including the variations from pixel to pixel.
$\mathscr{X}[g]$	- distribution of the quantum efficiencies from pixel to pixel.
g	- mean gain of the total detector g_d with the conversion gain g_c to convert charge carriers into counts.
$\mathscr{X}[\bar{g}]$	- normalized distribution of the quantum efficiencies from pixel to pixel around the mean gain g_d.
$\mathscr{X}_R$	- ration between the gain distribution at a given signal level and the signal level the gain reference was acquired with.
g_{lin}	- correction to linearize the non-linear gain throughout the whole dynamic range of the detector.
$\bar{g}_{lin}$	- mean value of the gain linearization of an image.

Noises, dark currents and uncertainties:

σ_{read}	- read out noise of the CCD.
σ_{therm}	- thermal noise of the CCD.
$\sigma_{row,j}$	- row noise of the CCD, where the offset value of a given row is constant over all pixels in that row.
μ_{row}	- offset value of a given row.
$\hat{\mu}_{read}$	- offset value of the detector due to row noise and the bias of the image to prevent negative counts.
μ_{therm}	- offset value of the detector due to dark currents.
$\Upsilon[\mu_{therm}]$	- distribution of dark currents.
I_{dark}	- dark current.
t_{acq}	- acquisition time.
σ_d	- detector noise, inheriting σ_{read}, σ_{therm} and $\sigma_{row,j}$.
k_{ref}	- uncertainty of the gain reference.
$k_{ref,w}$	- uncertainty of the gain reference with w summed up signal and background frames.
σ_{ref}	- standard deviation of the gain reference.
ϕ_{ref}	- mean value of the gain reference (all quadrant differ from 1).
σ_d^*	- detector noise varied by the standard deviation σ_{ref} of the gain reference and its respective mean value ϕ_{ref} of each detector quadrant.
σ_{QE}	- standard deviation of the quantum efficiencies of the detector.
k_{lin}	- uncertainty of the gain linearization correction.
k_{ref^*}	- uncertainty of the linearization corrected gain reference.
$\sigma_{d,corr}$	- detector noise varied by the the gain referenec and the gain linearization.
k	- combined uncertainty of the linearization corrected gain reference and the linearization correction.
$k_{ref^*,H,V}$	- uncertainty of the linearization corrected gain reference under binning H pixels horizontally and V pixels vertically.
$\alpha_{H,V}$	- distribution factor of the signal on the binned pixels.
σ_{total}	total noise standard deviation of a given image containing all noise contributions.

Signals of the electron beam:

$\hat{S}$	- expectation value of any of the following signals.
$\bar{S}$	- mean value of any of the following signals.
$S_{src,el}$	- stream of electrons from a point source or electron gun.
B_{el}	- total electron beam (consisting of uncorrelated and correlated electrons).
S_{el}	- total electron beam, broadened by the deflection of the electron-optical system.
S_d	- total electron beam converted into charge carriers by the CCD.
S_c	- total electron beam converted into counts.
$S_{\Omega,el}$	- total electron beam broadened by the detector point spread function.
S_{ref}	- total electron beam used for the acquisition of the gain reference.
$S_{ref,c}$	- total electron beam used for the acquisition of the gain reference, converted into counts.
$S_{ref,c,w}$	- total electron beam used for the acquisition of the gain reference, converted into counts and with w summed up signal and background frames.
B_{disp}	- dispersed total electron beam (consisting of uncorrelated and correlated electrons) in STEM mode.
$S_{EELS,el}$	- 2D EELS signal in electrons.
$S_{EELS,c}$	- 2D EELS signal converted into counts.

Signal broadening point spread functions (PSF) / convolution kernels:

Ω^*	- denotes the normalization of the respective PSF to the height of one.
Ω_{TEM}	- deflection acting on of all the beam electrons to form a beam disc in TEM mode, normalized to the height of one.
Ω_{fl}	- PSF of the fluorescence layer of the detector.
Ω_{opt}	- PSF of the fiber optics layer of the detector.
Ω_{CCD}	- PSF of the CCD of the detector.
Ω_d	- PSF of the complete detector, including Ω_{fl}, Ω_{opt} and Ω_{CCD}.
Ω_{STEM}	- deflection acting on of all the beam electrons to form a point like signal in STEM mode.
Ω_{disp}	- deflection acting on of all the beam electrons in the energy filter of the *Gatan GIF* to form a dispersed energy signal used for EELS measurements.
Ω_{ZLP}	- combines both the dispersion PSF Ω_{disp} and the detector PSF Ω_d to represent the PSF leading to a ZLP in vacuum.

Smoothing factors:

$\beta_{TEM,conv}$	- smoothing factor of the beam convolution with Ω_{TEM}.
$\beta_{TEM,corr}$	- smoothing factor of the beam correlation in TEM mode.
β_{TEM}	- smoothing factor including both beam smoothing factors for correlation and convolution in TEM mode.
$\beta_{fl,conv}$	- smoothing factor of the convolution of the fluorescence layer Ω_{fl}.
$\beta_{fl,corr}$	- smoothing factor of the correlation induced by the fluorescence layer.
β_{fl}	- smoothing factor including both fluorescence layer smoothing factors for correlation and convolution.
$\beta_{opt,conv}$	- smoothing factor of the convolution of the fiber optics layer Ω_{opt}.
$\beta_{opt,corr}$	- smoothing factor of the correlation induced by the fiber optics layer.
β_{opt}	- smoothing factor including both fiber optics layer smoothing factors for correlation and convolution.
$\beta_{CCD,conv}$	- smoothing factor of the convolution of the CCD Ω_{CCD}.
$\beta_{CCD,corr}$	- smoothing factor of the correlation induced by the CCD.
β_{CCD}	- smoothing factor including both CCD smoothing factors for correlation and convolution.
β_{conv}	- smoothing factor of all of the above convolutions.
β_{corr}	- smoothing factor of all of the above correlations.
β	- smoothing factor including both the smoothing factors for correlation and convolution of all of the above smoothing factors.
β_{BF}	- smoothing by the brighter-fatter effect.
$\beta_{H,V}$	- smoothing factor after binning H pixel horizontally and V pixel vertically.
$\beta_{BF,H,V}$	- brighter-fatter smoothing factor after binning H pixel horizontally and V pixel vertically.
β^*	- combines the smoothing factor β with the brighter-fatter smoothing β_{BF}.
β_{EELS}	- smoothing factor of a 2D EELS signal (similar to β_{TEM}).
$\beta_{EELS,1,V}$	- smoothing factor of an EEL spectrum after binning V pixels vertically.

Images:

ξ	- unprocessed image as acquired.
ξ_{dark}	- dark frame image.
ξ_{DS}	- dark frame subtracted image.
$\xi_{ref,SF}$	- unprocessed signal frame image of the gain reference.
$\xi_{ref,DF}$	- dark frame image of the gain reference.
$\xi_{ref,DS}$	- difference signal image of the gain reference.
$\xi_{ref,DB}$	- difference background image of the gain reference.
ξ_{ref}	- gain reference.
$\xi_{ref,w}$	- gain reference with w summed up signal and background frames.
ζ_{ref}	- actual representation of the noise on top of the gain reference.
ξ^*	- dark frame subtracted and gain normalized image.
ξ^{corr}	- dark frame subtracted, gain normalized and gain linearized image.
$\xi^{corr}_{Bin,H,V}$	- dark frame subtracted, gain normalized and gain linearized image, after binning H pixel horizontally and V pixels vertically.
ξ^{corr}_{ref}	- non-linearity corrected gain reference.
ξ^{corr}_{EELS}	- dark frame subtracted, gain normalized and gain linearized EEL spectrum.

Appendix B

An applied noise model for low-loss EELS maps

Ultramicroscopy 270 (2025) 114101

Contents lists available at ScienceDirect

Ultramicroscopy

journal homepage: www.elsevier.com/locate/ultramic

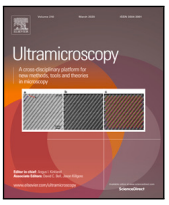

An applied noise model for low-loss EELS maps

Christian Zietlow *, Jörg K.N. Lindner

Nanopatterning-Nanoanalysis-Photonic Materials Group, Department of Physics, Paderborn University, Warburgerstr. 100, Paderborn, 33098, Germany

ARTICLE INFO

Keywords:
Noise model
EELS maps
EELS detector
ZLP alignment
Noise parameters
Point spread function EELS

ABSTRACT

Electron energy-loss spectroscopy (EELS) performed in a scanning transmission electron microscope (STEM) is susceptible to noise, just like every other measurement. EELS measurements are also affected by signal blurring, related to the energy distribution of the electron beam and the detector point spread function (PSF). Moreover, the signal blurring caused by the detector introduces correlation effects, which smooth the noise. A general understanding of the noise is essential for evaluating the quality of measurements or for designing more effective post-processing techniques such as deconvolution, which especially in the context of EELS is a common practice to enhance signals. Therefore, we offer theoretical insight into the noise smoothing by convolution and characterize the resulting noise correlations by Pearson coefficients. Additional effects play a role in EELS mapping, where multiple spectra are acquired sequentially at various specimen positions. These three-dimensional datasets are affected by energy drifts of the electron beam, causing spectra to shift relative to each other, and by beam current deviations, which alter their relative proportion. We investigate several energy alignment techniques to correct energy drifts on a sub-channel level and describe the intensity normalization necessary to correct for beam current deviations. Both procedures affect noises and uncertainties of the measurement to various degrees. In this paper, we mathematically derive an applied noise model for EELS measurements, which is straightforward to use. Therefore, we provide the necessary methods to determine the most important noise parameters of the EELS detector enabling users to adapt the model. In summary, we aim to provide a comprehensive understanding of the noises faced in EELS and offer the necessary tools to apply this knowledge in practice.

1. Introduction

Noise is an inherent component when carrying out a measurement. Large electron microscopes such as transmission-electron-microscopes (TEM) are no exception to this rule. Typically, these noises consist of two different noise statistics, the normal distributed Gaussian noise originating from the detector electronics [1,2] and the Poisson noise arising from the quantized signal itself [3,4]. In modern electron microscopy, a common type of detector is the scintillation-based CCD detector [5–8], converting the beam electrons into photons via a fluorescence layer before being measured by a CCD camera. This fluorescence layer typically generates several hundred photons per incident electron, thereby increasing the signal by a gain and modifying the Poisson distribution [9]. Another common detector type is the direct detector [5,7,10–12], which, lacking a scintillation layer, is directly exposed to the beam electrons. Image acquisition with both types of detectors results in a convolution of the signal with a detector point spread function (PSF), which broadens the signal and is primarily driven by diffusion processes [13,14]. The broadening inherently smooths the noise and introduces correlations in the measured signals that must be considered for a sufficient noise model [9].

Electron energy-loss spectroscopy (EELS) is a versatile technique with broad application in physics and materials science [15], in chemistry [16], and life sciences [17], as it enables the analysis of a specimen through the inelastic scattering processes of the beam electrons. These material specific interactions result in energy losses of the beam electrons, which are relevant for analyzing plasmonic behavior, material composition and bonding states.

Advanced techniques like EELS are often performed in scanning electron microscopy (STEM-)mode, where the electron beam is focused to a fine spot and scanned over a specimen. Magnetic fields in a spectrometer disperse the beam electrons according to their kinetic energy allowing to resolve energy losses at a given specimen position. The loss signal is recorded by a camera and summed to reveal a characteristic 1D spectrum.

* Corresponding author.
E-mail addresses: christian.zietlow@upb.de (C. Zietlow), lindner@physik.upb.de (J.K.N. Lindner).
URL: https://physik.uni-paderborn.de/en/lindner (J.K.N. Lindner).

https://doi.org/10.1016/j.ultramic.2024.114101
Received 16 August 2024; Received in revised form 29 November 2024; Accepted 29 December 2024
Available online 13 January 2025

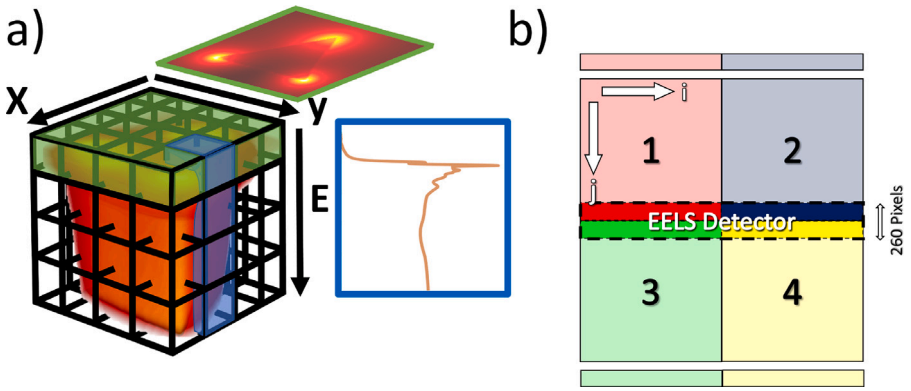

Fig. 1. **(a)** A low-loss EELS data cube simulated using the MNPBEM-toolbox [31] that is generated for a focused electron beam scanned in *x*-*y*-direction across a triangular gold nano-particle. The EEL signal is measured spectrum-by-spectrum by the CCD detector and then concatenated into a data cube. Note that the ZLP is not included in the data cube, as it is not calculated by the MNPBEM-toolbox. To clarify terminology, the green slice from the *3D-data-cube* is referred to as an *energy slice*, which represents an image of the specimen where all contributing beam electrons have experienced the same energy-losses. The blue extract is called a *spectrum* and comprises all dispersed beam electrons at a given point on the specimen. Therefore, the 3D data cube consists of tens to hundreds of thousands of individual data points, which are referred to as *voxels*. This distinction is important for differentiating the EELS measurement from the (detector-)*image* and *pixel*, respectively. **(b)** Schematic of the US1000FT-XP 2 detector, commonly used in Gatan GIF Quantum ER image filters [32]. Four distinct detector segments can be identified, labeled 1–4, of which only a narrow portion is used for EELS signal detection, as indicated by the colored boxes in the middle of the detector segments. The shaded areas are discarded. The inner region is 260 × 2048 pixels. All *rows* j of a *detector column* i get summed up to form *EEL channels*, therefore it is useful to refer to the *left side* (segment 1 and 3) and the *right* side (segment 2 and 4) of the detector. The detector segments are connected to their respective analogue-to-digital converters (ADC), indicated by the small boxes near the detector.

The most prominent feature in every EEL spectrum is the zero-loss peak (ZLP). The beam consists of electrons that have not undergone inelastic scattering [18]. These beam electrons retain their initial energy and thus their energy loss remains zero. In vacuum, this is the sole feature present. When measuring specimens, surface and bulk plasmons are typically found in the low-loss region, while the high-loss region provides information about material-specific core-loss features [18]. A comprehensive overview of EELS applications is given in [19].

EELS maps are an extension of the EELS technique enabling the consecutive measurement of several spectra on defined positions of a 1D or 2D array projected onto a specimen. Thereby, these measurements provide additional spacial information on the energy losses within the structures of interest. Consequently, EELS maps are multidimensional data sets, comprising one or two lateral dimensions and one energy dimension.

for analyzing plasmonic resonances [20–26] and determining the chemical composition of nano-structures [27–30].

Fig. 1(a) displays a simulated EELS map of a gold nano-triangle generated with the MNPBEM-toolbox [31]. EELS maps like these with two lateral dimensions are commonly referred to as 3D data cubes. As 3D data can be challenging to visualize, the data is often cut into *energy slices*, i.e. images with the same energy loss, or into the individual *spectra*, which represent the full acquired energy-loss spectrum at a specific position within the investigated area. To distinguish between terms related to the 3D data and images acquired on the detector, we will exclusively use the terms *image*, *pixel*, *row* and *column* for the images, whereas we will use the terms *energy slices*, *spectra* and *voxel* for the 3D data cube.

Understanding the noises associated with such measurements is crucial. Especially in quantitative EELS measurements, noise primarily determines the uncertainty associated with such a measurement. Moreover, the quality of EELS data can be enhanced by employing modern deconvolution techniques, such as 'alternating direction method of multipliers' (ADMM) algorithms [33], to sharpen spectra and reduce the noise to facilitate evaluation, or even enable data analysis in low-dose environments. Therefore, there are clear use-cases for an applied noise model.

In [34], we have developed mathematical descriptions and approximations to handle correlation effects related to the detector and demonstrated further how signals sum under the given noise condition. These findings can directly be applied to EELS measurements. The measurements in [34] were conducted in transmission electron microscopy (TEM-) mode, which provides homogeneous signals necessary to obtain highly precise results of the noise variances. In the present paper, we aim to demonstrate the applicability of our noise model to EELS measurements, too — despite the non-uniformity of signals in this mode.

The fundamental data acquisition processes and their mathematical descriptions are outlined in [34] and in the following, we will build upon this previous work to develop a well-suited noise model for EELS measurements. In the present paper, we will also extend our previous work to EELS maps, which in addition to the signal and detector noises, are affected by energy drifts and variations in beam intensity between consecutively acquired spectra. Therefore, two distinct layers of noise exist: one in the energy direction and another, the spacial noise, which arises from the sequential acquisition process and differs from the former.

However, EELS maps acquired in a vacuum enable us to analyze the noise of EELS measurements between spectra. We observe it as a fluctuation between spectra centered around a common mean value for each EEL channel. With a profound knowledge on the other noise contributions, this enables us to verify the noise model from [34] for EELS. To isolate the noise from external variations caused by an inhomogeneous specimen, it is crucial to take the measurement in vacuum. We utilized a cold field-emission gun (cFEG) in our experiments due to its narrow energy distribution of beam energies, although our setup lacks an additional energy filter in the microscope column. The measurements were performed at an accelerating voltage of 200 k eV.

Our work primarily focuses on a scintillation-based CCD detector, specifically the wide-spread US1000FT-XP 2 detector in a Gatan GIF Quantum ER image filter [32], enabling a maximum dispersion of 0.01 eV/channel. The scintillation-based CCD detector comprises three distinct layers: A fluorescence layer that converts incident electrons into photons, a second layer guiding these photons via fiber optics and a third layer, the CCD camera, which converts photons into counts.

Scintillation-based CCD detectors used for EELS share similar design principles. However, some detectors feature single or multiple read-out ports or employ a lens optics instead of fiber optics. These variations have a minor impact on the general noise model, primarily affecting the extend of noise contributions and convolutions. The principles of convolution and correlation also apply to direct electron detectors (DED). The mere differences between the two detectors, regarding convolution and correlation are the high gain and the extend of the point spread function.

Thus, the proposed noise model should also be valid for DEDs in general. However, several other factors distinguish between the two detector types, including the absence of read-out noise or dark currents in DEDs [5,35], which is due to their different acquisition mechanism. These changes must necessarily be taken into account, when adapting the noise model from CCD detectors to DEDs.

For the acquisition of EELS spectra, we discard most of the detector area, to minimize unnecessary detector noise, except for a narrow region of 260 × 2048 pixels in the middle of all four quadrants of the segmented detector (we show the utilized CCD schematically in Fig. 1(b)). Since all rows j in a given column i are summed to form so called EEL channels, it is more convenient to refer to the *left* and *right* side of the detector rather than to the individual quadrants. However, each quadrant has its signal read-out by a separate individual analogue-digital-converter (ADC). This segmentation enables very short read-out times.

As previously mentioned, EELS is utilized to measure both low and high energy-losses of electrons. To demonstrate our noise model, we need to perform repeated measurements of a constant signal in vacuum in order to compare them. In vacuum, the only signal measured is the ZLP. No higher losses are present. Therefore, we focus on low-loss spectra in this study. Although we focus on low-loss spectra, the principles discussed are largely transferable to high-energy or core-loss spectra and are applicable to element mapping.

Having introduced the terminology and principles of EELS and EELS maps, we will now discuss the fundamentals of the most prominent noise statistics, essential for the understanding of our noise model. We also explore how operations such as additions, multiplications and divisions alter the noise and provide a brief introduction into the Pearson correlation coefficients and their relationship with convolutions.

2. Fundamentals of different noise statistics

The noises in an EELS spectrum can be described with two key distributions, the Gaussian normal distribution $\mathcal{N}$ and the Poisson distribution $\mathcal{P}$ [36–38]:

$$\mathcal{N}\left[\mu\,,\,\sigma^2\right] = \frac{1}{\sqrt{2\pi\sigma^2}} \cdot \exp\left\{-\frac{(n-\mu)^2}{2\sigma^2}\right\} \qquad \text{and} \qquad \mathcal{P}\left[\hat{S}\right] = \frac{\hat{S}^{\,n}}{n!}\exp\left\{-\hat{S}\right\}\,, \tag{1}$$

where n denotes the number of counts in both cases. For the normal distribution, the mean value of a signal is denoted as μ and the variance of the noise as σ^2. For a Poisson distributed signal S, the expectation value $\hat{S}$ and the variance of the signal $\sigma_{\mathcal{P}}^2$ to be equal. This equality is a fundamental property of the Poisson distribution. Scaling both distributions with a (gain) factor g, which e.g. converts beam electrons into counts, results in [36,39]:

$$g \cdot \mathcal{N}\left[\mu\,,\,\sigma^2\right] = \mathcal{N}\left[g\cdot\mu\,,\,g^2\cdot\sigma^2\right] \qquad \text{and} \qquad g\cdot\mathcal{P}\left[\hat{S}^*\right] = g\cdot\mathcal{P}\left[\frac{\hat{S}}{g}\right] \quad \text{, with} \quad S = g\cdot S^*\,, \tag{2}$$

noting that the gain factor appears squared in the Gaussian noise. Because the Poisson distribution requires the noise variance to equal the expectation value of the signal, a Poisson distributed signal S^* scaled by a gain g, such that $S = g\cdot S^*$, must be rescaled to satisfy the Poisson distribution. The sum of a number W of either Gaussian or Poisson distributed random variables results in [37,38,40]:

$$\sum_{w=1}^{W}\mathcal{N}\left[\mu_w\,,\,\sigma_w^2\right] = \mathcal{N}\left[\sum_{w=1}^{W}\mu_w\,,\,\sum_{w=1}^{W}\sigma_w^2\right] \qquad \text{and} \qquad \sum_{w=1}^{W}\mathcal{P}\left[\hat{S}_w\right] = \mathcal{P}\left[\sum_{w=1}^{W}\hat{S}_w\right]\,. \tag{3}$$

The product of two independent Gaussian random variables, with expectation values μ_1 and μ_2 and variances σ_1^2 and σ_2^2, can be approximated as [41]:

$$\mathcal{N}\left[\mu_1,\sigma_1^2\right]\cdot\mathcal{N}\left[\mu_2,\sigma_2^2\right] \approx \mathcal{N}\left[\mu_1\cdot\mu_2,\left(\sigma_1^2+\mu_1^2\right)\cdot\left(\sigma_2^2+\mu_2^2\right)-\mu_1^2\mu_2^2\right], \tag{4}$$

The inverse of a Gaussian distributed variable can be approximated by a normal distribution, if the denominator is closely distributed around its mean value [42]:

$$\mathcal{N}\left[\mu,\sigma^2\right]^{-1} \approx \mathcal{N}\left[\mu^{-1},\frac{\sigma^2}{\mu^4}\right]\,. \tag{5}$$

We found that when the ratio of $\frac{\sigma^2}{\mu^2} < 0.05$ the inversion is sufficiently precise for our noise model.

For a sufficiently high signal $\hat{S}$, the Poisson distribution can be approximated by a Gaussian [38]:

$$\lim_{\hat{S}\to\infty}\mathcal{P}\left[\hat{S}\right] = \mathcal{N}\left[\hat{S}\,,\,\hat{S}\right]\,. \tag{6}$$

The Pearson correlation coefficients ρ_m [43] quantify the normalized covariance between two pixels x_i and x_{i+m}, which defines the correlation:

$$\rho_m = \frac{\mathrm{cov}\left[x_i\,,\,x_{i+m}\right]}{\sigma_{x_i}\cdot\sigma_{x_{i+m}}}\,, \tag{7}$$

where the index m denotes the distance between the two EEL channels. Note that the distance between channels is bidirectional, so there are also negatively numbered Pearson correlation coefficients, i.e. from $m\in[-(M-1),\dots,M-1]$, where M denotes the total number of EEL channels. Since the Pearson correlation coefficients can be obtained by the autocovariance function, m is often referred to as the lag of the noise.

Furthermore, we have demonstrated that a scattering process associated with a sufficient gain and a point spread function Ω results in a smoothing of the Poisson noise. For a Poisson distributed signal S^* scaled by a gain g, such that $S = g\cdot S^*$, we find [34]:

$$g\cdot\Omega\otimes\mathcal{P}\left[\hat{S}^*\right] = \beta_{conv}\cdot\beta_{corr}\cdot g\cdot\mathcal{P}\left[\frac{\Omega\otimes\hat{S}}{\beta_{conv}\cdot\beta_{corr}\cdot g}\right] \qquad \text{for} \quad g\gg 1 \quad \text{, with} \tag{8}$$

$$\beta_{conv} = \left(\sum_{m=-(M-1)}^{M-1}\rho_m\right)^{-1} \tag{9}$$

$$\text{and} \qquad \beta_{corr} = \frac{M}{M-1}\cdot\left(1-\frac{1}{M^2}\sum_{m=-(M-1)}^{M-1}(M-|m|)\cdot\rho_m\right) \tag{10}$$

$$\text{as well as} \quad \rho_m = \left[\Omega^* \otimes \Omega^*\right]_m \quad , \tag{11}$$

for the 1D signal. The formulas for 2D images can be found in [34]. Here, β_{conv} describes the smoothing of the noise due to convolution, β_{corr} describes the smoothing of the noise due to correlation effects, ρ_m denotes the Pearson correlation coefficients for the lag m, as discussed earlier, and Ω^* is the convolution kernel, such as a ZLP, normalized to the height of one. It is worth noting that β_{corr} only affects the noise within a single measurement, not in between consecutive measurements. For the above model, it is required that multiple photons per incident beam electron are produced in the scintillation layer, allowing them to spread out. A scattering event without such a gain would result in a blurring of the signal, but would not affect the noise [44].

In [34] we presented a method for recovering the Pearson correlation coefficients of the signal under homogeneous illumination in TEM mode. We applied the Wiener–Khinchin theorem [45,46], which states that the autocovariance function of a random process and the power spectral density (PSD) form a Fourier-transform pair. Using the Pearson correlation coefficients obtained by this method, one can reconstruct the point spread function of the detector. However, it was demonstrated in [3] that the modulation transfer function (MTF), which is closely related to the PSF, obtained by analyzing the noises should only be considered an approximation of the true PSF of the system. Since we are more interested in the correlation effects, which are precisely measured by the autocovariance function, rather than determining the true PSF of the system, we consider this approximation sufficient for a practical noise model.

3. The noise model

Below, we will briefly explain our noise model for acquiring a single EELS spectrum. A detailed derivation of a noise model for scintillation-based CCD detectors is presented in [34]. Note that the output from the microscope in counts does not necessarily represent the number of incident electrons. Therefore, we will denote a signal either S_{el} for electrons or S_c for counts. In the following, we will discuss a detector that has undergone gain linearization.

We begin with the number of beam electrons $S_{src,el}$ emitted by the point-source like electron gun. The beam electrons are deflected by the electron optics of the microscope, resulting in the distribution Ω^*_{STEM} at the entrance aperture of the energy-loss spectrometer. As before, the asterisk indicates normalization with respect to the height of the convolution kernel, since we are interested in the distribution at the entrance and not in the initial beam current leaving the electron gun. The beam is then dispersed into its energy distribution Ω_{disp} by the spectrometer magnets. Finally, the beam is broadened by the detector point spread function Ω_D.

For independent beam electrons, which appears to be the case in our experiments, the Poisson statistics is not affected by the deflection. From a mathematical perspective, this is equivalent to the convolution occurring inside the Poisson term. Kodama et al. [47,48] have demonstrated that beam correlations are possible; therefore, we have also examined a case that includes beam correlations for the sake of completeness and provided the general formula for the Pearson correlation coefficients for such a case in [34]. Since correlations seem to be negligible for our experiments, we continue with the case of uncorrelated beam electrons.

In contrast to the previous convolution, the spreading caused by the detector PSF does indeed alter the Poisson statistics. The distribution of the electron beam B for EELS on the CCD is therefore given by:

$$B = \Omega_D \otimes \mathcal{P}\left[\Omega_{disp} \otimes \Omega^*_{STEM} \otimes \hat{S}_{src,el}\right] \quad , \tag{12}$$

As the electrons in the beam propagate through a specimen, they lose some of their energy due to inelastic scattering, which contributes to the deflection $\Omega_{disp} = \Omega_E \otimes \Omega_{Sig}$, where Ω_E describes the energy distribution of the electron beam emitted by the electron gun and Ω_{Sig} is the desired information about the beam interactions with the specimen. Therefore, the signals of interest appears to be heavily convolved with other distributions. Fortunately, the various convolutions can be directly measured together as the 2D ZLP in vacuum $\Omega_{Vac} = \Omega_D \otimes \Omega_E \otimes \Omega^*_{STEM}$.

Using Eq. (11), we obtain the Pearson correlation coefficients of the 2D signal on the detector as [34]:

$$\rho_{m,n} \approx \left[\Omega^*_D \otimes \Omega^*_D\right]_{m,n} \quad . \tag{13}$$

Therefore, the Pearson correlation coefficients of independent beam electrons only depend on the detector PSF. In [34], we have demonstrated how to measure this detector PSF from the signal noises in TEM mode and have analyzed it in detail.

Furthermore, the signal is stored in the pixels and read-out from the detector, which introduces thermal and read-out noise. A detailed description of the detector noises of scintillation-based CCD detectors can also be found in [34]. The detector noises are modified by applying a gain reference, which corrects for quantum deviations in the detector, and a non-linearity correction, which linearizes the gain across the entire dynamic range of the detector. Both processes are mathematically described and evaluated in [34]. Methods for measuring uncertainties related to the gain reference and for determining the gain non-linearity function of the detector are also proposed there.

The signal is ultimately summed by software to create a spectrum from the 2D data. By summing the 2D representation of the dispersed electron beam distribution along the rows j, we obtain the convolved EELS signal measured in the corresponding EEL channel i on the detector as:

$$S_{c,i} = \sum_j^N B_{i,j} = \left[\Omega_{ZLP} \otimes g \cdot S_{el}\right]_i \quad \text{with} \quad \Omega_{ZLP,i} = \sum_j^N \Omega_{Vac,i,j} \quad \text{and} \quad S_{el,i} = \sum_j^N \left[\Omega_{Sig} \otimes S_{src,el}\right]_{i,j} \quad , \tag{14}$$

The index c denotes the signal in counts instead of el for electrons, where $S_c = g \cdot S_{el}$. The gain of the detector g converts electrons into counts, which is how the microscope displays the results. For brevity, we write $S_c = \Omega_{ZLP} \otimes S_c$ for the entire signal instead of the convolution, where Ω_{ZLP} denotes the vacuum ZLP summed to a spectrum. For convenience, we also define the point spread function for EELS as $\Omega_{PSF} = \sum_j^N \Omega_D$.

Upon summing the signal, part of the correlation due to the detector PSF is eliminated. As described in [34], the new Pearson correlation coefficients can be obtained as:

$$\rho_m = \frac{\sum_{n=-(N-1)}^{N-1} \rho_{m,n}}{\sum_{n=-(N-1)}^{N-1} \rho_{0,n}} \quad , \tag{15}$$

if the signal is fully contained within the EELS region in the vertical direction, which usually is the case for EELS.

According to the summation rules from Eq. (3), the formation process for a single EELS measurement ξ in the EEL channel i can be expressed as:

$$\xi_i \approx \underbrace{g \cdot \beta_{conv} \cdot \beta_{corr} \cdot \mathcal{P}\left[\frac{\hat{S}_{c,i}}{g \cdot \beta_{conv} \cdot \beta_{corr}}\right]}_{1)} + \mathcal{N}\left[0, \Theta_i^2\right] \quad \text{, with} \tag{16}$$

$$\Theta_i^2 \approx \underbrace{\alpha \cdot k_{ref}^2 \cdot \hat{S}_{c,i}^2}_{2)} + \underbrace{k_{ref}^2 \cdot g \cdot \beta_{conv} \cdot \beta_{corr} \cdot \hat{S}_{c,i}}_{3)} + \underbrace{2\sigma_{D,i}^2}_{4)} \quad .$$

We separate the noise into a Poisson distributed part 1) for the signal noise and Gaussian normal distributed parts 2–4) for the noises inherent of the detector. In 1), we identify two distinct smoothing factors for the noise: β_{conv} is the smoothing factor connected to the convolution according to Eq. (9), and β_{corr} is the smoothing factor due to correlation, according to Eq. (10). Both of these factors depend on the Pearson correlation coefficients described in Eq. (15). We also determine the expectation value of the EELS signal $\hat{S}_{c,i} = \left[\Omega_{ZLP} \otimes \Omega_{Sig} \otimes g \cdot \hat{S}_{src,el}\right]_i$.

Images are often corrected with a gain reference to account for deviations in the quantum efficiencies in the fluorescence layer and the CCD detector itself. Due to uncertainties in the measurement of the gain reference k_{ref}, applying it to an EELS measurement introduces a fixed-pattern noise, which is described in term 2).

In brief, the gain reference is acquired in TEM mode with homogeneous illumination and a target intensity $\hat{S}_{ref}$. A set of W images is acquired and summed, and then W background images are subtracted. The resulting image is them normalized by the target intensity $\sum_w^W \hat{S}_{ref}$. For EELS, we also need to sum the pixels within the EELS region, which results in both the Poisson and Gaussian noises (and their correlations) increasing. By summing, the target intensity $\hat{S}_{ref}$ increases as well. The uncertainty of this gain reference for EELS is described in [34] as:

$$k_{ref}^2 = \frac{g^2 \cdot \beta_{conv} \cdot \beta_{corr} \cdot \sum_j^N \sum_w^W \hat{S}_{ref} + 2 \cdot \sum_j^N \sum_w^W \sigma_{D,i,j}^2}{\left(\sum_j^N \sum_w^W \hat{S}_{ref}\right)^2} \, , \tag{17}$$

where $\sigma_{D,i,j}$ gives the detector noise of the 2D image. Therefore, the uncertainty of the gain reference can be reduced in two ways: either by increasing the number of counts per image or by increasing the number of acquired frames W. Initially, it appears that increasing the number of counts per frame is preferable, since this does not increase read-out noises. However, as discussed in [34], non-linearities of the gain that arise at higher count numbers may make this option less desirable, so it is often preferable to combine multiple frames with reasonable low intensity.

In [34], we described methods for determining k_{ref} in detail and experimentally demonstrated its changes due to pixel summations, as performed for EELS.

The pixel-wise summation of the gain reference requires the introduction of a factor α, which describes the signal distribution on the 2D detector along the columns before summation to form a spectrum. The factor is given by [34]:

$$\alpha \approx \sum_j^N \left(\frac{\xi_{Vac,c,i,j}}{\sum_j^n \xi_{Vac,c,i,j}}\right)^2 \, , \tag{18}$$

where ξ_{Vac} is the measurement of the 2D EELS signal in vacuum before summation. The distribution factor α is valid under the assumption that the signal distribution along the column forming a given EEL channel is very similar to the distribution of the signal in every other EEL channel, except for a scaling factor related to the amplitude of the channels. For a homogeneously distributed signal, the distribution factor is $\alpha = 1$. However, it decreases for non-uniform signals e.g. a Gaussian distributed signal along the column, or when some pixels within the column are not exposed to a signal. Part 3) of Eq. (16) describes the variation of the Poisson noise of the signal due to the application of the gain reference, while part 4) describes the detector noises σ_D as varied by the gain reference. A detailed description of the detector noises is also presented in [34]. The factor of 2 applied to the detector noise reflects the background subtraction, which doubles the detector noise, as described in Eq. (3).

3.1. EELS maps

So far, we have discussed the noise properties of single EELS measurements, which we now try to extend to EELS maps and find that the noise changes depending on weather we consider the noise within a spectrum or the noise between spectra. Considering arrays of multiple EEL spectra, we have the energy dimension, or *spectrum*, which is acquired in a single measurement, and one or two lateral dimensions consisting of independent measurements of the *energy slice* (see Fig. 1(a)).

Acquiring multiple EEL spectra in a row or in an array as in EELS profiles or in EELS mapping also allows for changes in beam intensity between spectra, since the beam current is expected to fluctuate slightly around a mean value within short time intervals, due to the influence of electron stimulated desorption of adsorbents from the tip of the electron gun [49]. Furthermore, the beam intensity is Poisson distributed and decreases over time, so no two spectra have exactly the same intensity. Additionally, energy drifts may modify not only the width of the ZLP but also the energy alignment between different spectra. However, these changes do not affect the spectrum itself, but rather alter the distributions between the spectra in the lateral dimensions. Therefore, having multiple energy spectra in a single data cube allows for a greater variety of effects of to occur, beyond just correlation effects. This emphasizes the necessity of two distinct noise models — one for the energy direction of the individual spectra and one for the lateral directions between spectra.

The commonly used way to eliminate intensity deviations is by normalization of the total counts of the spectrum, and there are multiple methods to realign the spectra. Both normalization and realignment introduce new uncertainties that must be considered.

Since users are often more interested in loss probabilities than absolute counts, normalization serves two purposes simultaneously. Dividing the individual spectra by their respective summed intensity leads to:

$$\xi_{x,y,i} = \xi_{x,y,M} \cdot \frac{\xi_{x,y,i}}{\xi_{x,y,M}} \quad \text{, with} \quad \xi_{x,y,M} = \sum_i^M \xi_{x,y,i} \, . \tag{19}$$

The first part describes the variations in the measured beam intensity and the second part describes the normalized spectra (or energy loss probabilities under certain conditions, which will be evaluated later). In this context, the EEL spectrum at the position (x, y) in the array is summed

over the EEL channel index i to M channels in total. To allow for intensity variation between spectra, the signal $\hat{S}_{c,x,y,i} = \mathcal{I}_{x,y} \cdot \hat{s}_{x,y,i}$ is defined as the energy loss probability $\hat{s}_{x,y,i}$, which represents the beam distribution between EEL channels i, multiplied by the intensity map $\mathcal{I}_{x,y}$. The intensity map captures the total intensity measured by the detector at position (x, y) on the EELS map. It is given as:

$$\mathcal{I}_{x,y} = g \cdot S_{src,el,x,y} \cdot T_{x,y} \ , \tag{20}$$

with the beam current $S_{src,el,x,y}$ at the corresponding position (x, y), multiplied by the transmission probability of the specimen $T_{x,y}$ and the gain g to convert the signal from electrons to counts.

Additionally, the acquisition of the background frame differs slightly between EELS maps and single EELS measurements, as shown in Eq. (16). In the Gatan software '*Digital Micrograph*', a 'high quality' background is averaged over a heuristic of $A = \sqrt{X \cdot Y}$ dark frames, for a 2D spectrum array with a side-length of X and Y spectra. This background is then subtracted from every spectrum in the array. The noise changes depending on the direction, whether in the lateral directions of an energy slice or in energy direction of the spectrum. We begin by considering the energy direction, which we denote with the underlined index $\underline{i}$. The noise from Eq. (16) can be rewritten to:

$$\begin{aligned} \xi_{x,y,\underline{i}} &\approx g \cdot \beta_{conv} \cdot \beta_{corr} \cdot \mathcal{P}\left[\frac{\mathcal{I}_{x,y} \cdot \hat{s}_{x,y,i}}{g \cdot \beta_{conv} \cdot \beta_{corr}}\right] + \mathcal{N}\left[0, \Theta^2_{x,y,\underline{i}}\right] \quad \text{, with} \\ \Theta^2_{x,y,\underline{i}} &= \alpha \cdot k^2_{ref} \cdot \left(\mathcal{I}_{x,y} \cdot \hat{s}_{x,y,i}\right)^2 + k^2_{ref} \cdot g \cdot \beta_{conv} \cdot \beta_{corr} \cdot \left(\mathcal{I}_{x,y} \cdot \hat{s}_{x,y,i}\right) + \left(1 + \frac{1}{A}\right) \cdot \sigma^2_{D,i} \quad , \end{aligned} \tag{21}$$

for the spectrum in energy direction, we find the factor $\left(1 + \frac{1}{A}\right)$ for the detector noises, rather than the factor of 2 found in Eq. (16).

For the lateral directions, which we will again denote with the underlined indices, here $\underline{x, y}$, we find:

$$\begin{aligned} \xi_{\underline{x,y},i} &\approx g \cdot \beta_{conv} \cdot \mathcal{P}\left[\frac{\mathcal{I}_{x,y} \cdot \hat{s}_{x,y,i}}{g \cdot \beta_{conv}}\right] + \mathcal{N}\left[0, \Theta^2_{\underline{x,y},i}\right] \quad \text{, with} \\ \Theta^2_{\underline{x,y},i} &\approx \alpha \cdot \varphi \cdot k^2_{ref} \cdot \left(\mathcal{I}_{x,y} \cdot \hat{s}_{x,y,i}\right)^2 + k^2_{ref} \cdot g \cdot \beta_{conv} \cdot \left(\mathcal{I}_{x,y} \cdot \hat{s}_{x,y,i}\right) + \left(1 + \frac{\varphi}{A}\right) \cdot \sigma^2_{D,i} \ . \end{aligned} \tag{22}$$

When considering the noise between spectra, the smoothing factor β_{corr} vanishes as we are interested in the noise between spectra rather than within a given spectrum. This is in contrast to the noise in the energy direction, where we need the correlation factor β_{corr}.

Furthermore, for the detector noise, it is essential that the same background is subtracted from all spectra equally, so it does not affect the noise in between them in the array, causing the factor $\left(1 + \frac{1}{A}\right)$ to disappear. Because an energy alignment of the spectra alters the positions at which each EEL channel is measured on the detector column for every spectrum, we introduce a shifting factor φ, to account for the shift in detector columns. The same applies for the fixed-pattern noise on the signal. As the name suggests, fixed-pattern noises introduce the same deviations to all spectra equally, so that they do not affect the relation between them. If an energy drift occurs between the spectra, an EEL channel will get recorded by a different pixel column. Therefore, the energy shift of the signal reintroduces some of the fixed-pattern noise that would not occur without it. However, the variation of the Poisson noise caused by the gain reference is not affected by drifts and thus φ does not apply in this case. The shifting coefficient φ can be calculated as the mean drift over all spectra:

$$\varphi \approx \frac{1}{XY\,(XY-1)} \sum_{x,y}^{X,Y} \sum_{x',y'}^{X,Y} \sum_{i}^{M} \left|\delta_{x,y,i} - \delta_{x',y',i}\right| \quad \text{, with } (x', y') > (x, y) \ , \tag{23}$$

where δ denotes a Dirac delta distribution at the peak position of the ZLP in every spectrum of the array. By summing the differences of the delta functions, such that each spectrum is subtracted from every other spectrum in the array once, we obtain a shifting factor of $\varphi = 0$ if no drift occurs at all, and $\varphi = 1$ if the mean drift of the spectra is equal or greater than one channel. If some spectra are recorded as already perfectly aligned while others are not, the shifting factor will give a value between $\varphi \in [0, \ldots, 1]$, indicating the percentage of channel shift per spectrum.

Thus far, we have discussed two distinct noise models that describe slightly different noise volatility in their respective directions, which arises from the acquisition of the EELS data cube as a series of individual measurements concatenated. To determine the uncertainty of measuring a certain intensity in an individual voxel of an EELS map, we must compare the individual noise contributions between both directions term-by-term and consider the maximum contribution in each case. This yields the overall uncertainty of an individual voxel in the reference frame of the EELS map measurement, given by:

$$\begin{aligned} \xi_{x,y,i} &\approx g \cdot \beta_{conv} \cdot \mathcal{P}\left[\frac{\mathcal{I}_{x,y} \cdot \hat{s}_{x,y,i}}{g \cdot \beta_{conv}}\right] + \mathcal{N}\left[0, \Theta^2_{x,y,i}\right] \quad \text{, with} \\ \Theta^2_{x,y,i} &\approx \alpha \cdot \varphi \cdot k^2_{ref} \cdot \left(\mathcal{I}_{x,y} \cdot \hat{s}_{x,y,i}\right)^2 + k^2_{ref} \cdot g \cdot \beta_{conv} \cdot \left(\mathcal{I}_{x,y} \cdot \hat{s}_{x,y,i}\right) + \left(1 + \frac{1}{A}\right) \cdot \sigma^2_{D,i} \ . \end{aligned} \tag{24}$$

To demonstrate that the uncertainty is independent of the direction, we omit the underlining of indices. Both noise models, which consider volatility, and the overall uncertainty are equally important and have their respective use case. The first two equations (see Eqs. (21) and (22)) are used to characterize the uncertainty when comparing e.g. two energy-loss peaks within a spectrum or in between spectra of an EELS cube, or when using a 'total variation' approach for denoising or deconvolution (see Refs. [2,33] as examples). The overall uncertainty in Eq. (24) is important for e.g. comparing plasmons that appear as a 3D structure or for designing a Bayesian likelihood functional for denoising or deconvolution (again see Refs. [2,33] as examples).

Since the directional noise models comprise the overall uncertainty, we will continue working with these models in the following sections instead of the overall uncertainty. Ultimately, we will again combine them to obtain the overall uncertainty, thereby reestablishing the trio.

3.1.1. Uncertainty of alignment

As time passes between the acquisition of multiple spectra in an array, the spectra can drift significantly in the energy direction with respect to each other. To compensate for the energy drift, a common technique is to realign the spectra by fitting e.g. a Gaussian function to the ZLP and using its center as a reference point for realigning all spectra. However, fitting is affected by uncertainties which leads to deviations σ_{fit} in the alignment. The influence of the alignment on the noise in lateral directions is closely related to the slope in the energy direction of the spectra, given by $\frac{d}{di}\hat{S}_{c,x,y,i}$. The faster the intensities change, the stronger the deviations are; conversely, there is no change for plain signals. The

drift also affects the width and shape of the ZLP, as the signal drifts during the exposure time. For a drift below one channel, the influence can be approximately described by the intensity change and a factor σ_{drift}, which describes the drift deviations during the exposure time t_{acq}. By combining both uncertainties, we obtain the uncertainty of misalignment, given by $\sigma^2_{MA} = \sigma^2_{fit} + \sigma^2_{drift}$. Based on this, we can derive the noise term that accounts for the implications of the energy shift in EELS maps:

$$\sigma^2_{Shift} = \sigma^2_{MA} \cdot \left(\mathcal{I}_{x,y} \cdot \frac{d}{di}\, \hat{s}_{x,y,i} \right)^2 , \tag{25}$$

which increases the noise of the lateral directions, but does not affect the noise in the energy direction.

Current state-of-the-art alignments methods recommend sub-channel alignments using cross-correlation [50,51]. Since the EEL channels intensities are discrete, this type of alignment requires interpolation to estimate the intensities between channels. For simplicity, we use linear interpolation in this work. Interpolating EEL channels $\xi_{i-\Delta}$ with an interpolation shift of Δ leads to:

$$\begin{aligned} \xi_{i+|\Delta|} &= (1-|\Delta|)\cdot\xi_i + |\Delta|\cdot\xi_{i+1} \\ &= \left[\xi \otimes \Omega_{Inter,\Delta}\right]_i \qquad \text{, with} \quad \Omega_{Inter,\Delta} = \begin{pmatrix} 1-|\Delta| & |\Delta| & 0 & \dots & 0 \end{pmatrix}. \end{aligned} \tag{26}$$

We suggest $|\Delta| \leq 0.5$ channel, as otherwise it is more beneficial to shift the entire signal by one channel and then interpolate in the opposite direction. Since the drift is expected to be continuous throughout the measurement, we assume a continuous distribution of the interpolation shift Δ, which is later confirmed by experiment. For a perfect alignment fit, the misalignment of the spectra has an expectation value of at least $|\Delta|$, resulting in an uncertainty of $\sigma_{MA} \geq \int_{-0.5}^{0.5} d\Delta\, |\Delta| = \frac{1}{4}$ channels for non-interpolated EELS data cubes.

Linear interpolation can be viewed as a convolution of the spectrum with an 'interpolation kernel' that smooths the noises without broadening the spectrum. For the largely uncorrelated detector noise, we can easily find the expectation value for the smoothing factor β_D by integrating over all Δ. This yields $\beta_D \approx \int_{-0.5}^{0.5} d\Delta\, (1-|\Delta|)^2 + |\Delta|^2 = \frac{2}{3}$, since the noise of both channels is added squared (see Eq. (3)). This value can be used to estimate an 'effective interpolation shift' of $\bar{\Delta} \approx 0.211$ channels, which can then be used to calculate the effective interpolation kernel $\bar{\Omega}_{Inter,\bar{\Delta}}$. However, it is essential to note that the additional smoothing of the noises differs significantly between detector and signal noise. In case of linear interpolation, we find that the Pearson correlation coefficients of the signal from Eq. (13) change to:

$$\rho_{Inter,\Delta,m,n} \approx \left[\Omega^*_{Inter,\Delta} \star \Omega^*_{Inter,\Delta} \otimes \Omega^*_D \otimes \Omega^*_D \right]_{m,n} , \tag{27}$$

where $\star$ denotes the auto-correlation of the interpolation kernel $\Omega^*_{Inter,\Delta}$, defined in Eq. (26), Ω^*_D is the detector PSF, and the asterisk indicates normalization to a height of one for all kernels.

This additional convolution necessarily alters the coefficients β_{conv} and β_{corr} of the Poisson signal noise, as described by Eqs. (9) and (10). By inserting $\bar{\Omega}_{Inter,\bar{\Delta}}$ into Eq. (27), we can determine the change in the Pearson coefficients of the signal. In general, the overall impact of the smoothing on the signal noise is significantly reduced compared to the detector noise, since the signal is already smoothed by the detector PSF. The wider the detector PSF, the lesser the impact of interpolation on noise smoothing. It can be concluded that correlated noises are affected differently by interpolation than uncorrelated noises. Since the fixed-pattern noise is uncorrelated, we find a similar impact on it as on the Gaussian detector noise, with $\beta_{FP} = \frac{2}{3}$. Due to this smoothing of both detector and fixed-pattern noise, we expect some minor correlations to emerge within these noises, leading to further smoothing similar to β_{corr} within the spectra in energy direction. We can neglect this influence since $\beta_{corr,\bar{\Delta}} \approx 0.9997$ (as per Eq. (10)) for both the detector and fixed-pattern noise.

However, linear interpolation is subject to uncertainties. Usually, these are negligible, as they are small compared to the impact of misalignment. A brief discussion on the uncertainty of interpolation is found in Appendix A.1. For simplicity, we assume that these deviations follow a Gaussian distribution, which completes our noise model for the lateral directions:

$$\begin{aligned} \xi_{\bar{A},\underline{x,y,i}} &\approx \underbrace{g\cdot\beta_{conv}\cdot\mathcal{P}\left[\frac{\mathcal{I}_{x,y}\cdot\hat{s}_{x,y,i}}{g\cdot\beta_{conv}}\right] + \mathcal{N}\left[0,\, \Theta^2_{A,\underline{x,y,i}}\right]}_{=\xi_{A,\underline{x,y,i}}} + \mathcal{N}\left[0,\, \sigma^2_A\right] && \text{, with} \\ \Theta^2_{A,\underline{x,y,i}} &\approx \alpha\cdot\varphi\cdot\beta_{FP}\cdot k^2_{ref}\cdot\left(\mathcal{I}_{x,y}\cdot\hat{s}_{x,y,i}\right)^2 + k^2_{ref}\cdot g\cdot\beta_{conv}\cdot\mathcal{I}_{x,y}\cdot\hat{s}_{x,y,i} + \left(1+\frac{\varphi}{A}\right)\cdot\beta_D\cdot\sigma^2_{D,i} && \text{and} \\ \sigma^2_A &\approx \sigma^2_{MA}\cdot\left(\mathcal{I}_{x,y}\cdot\frac{d}{di}\,\hat{s}_{x,y,i}\right)^2 && , \end{aligned} \tag{28}$$

where σ^2_A denotes the total uncertainty of alignment. Here, $\xi_{A,\underline{x,y,i}}$ denotes the noise in the lateral directions, excluding the uncertainty of alignment but including smoothing effects of interpolation. This expression $\xi_{A,\underline{x,y,i}}$ will be relevant later. Additionally, we must slightly modify the noise model in the energy direction to account for the interpolation:

$$\begin{aligned} \xi_{A,x,y,\underline{i}} &\approx g\cdot\beta_{conv}\cdot\beta_{corr}\cdot\mathcal{P}\left[\frac{\mathcal{I}_{x,y}\cdot\hat{s}_{x,y,i}}{g\cdot\beta_{conv}\cdot\beta_{corr}}\right] + \mathcal{N}\left[0,\, \Theta^2_{A,x,y,\underline{i}}\right] && \text{, with} \\ \Theta^2_{A,x,y,\underline{i}} &\approx \alpha\cdot\beta_{FP}\cdot k^2_{ref}\cdot\left(\mathcal{I}_{x,y}\cdot\hat{s}_{x,y,i}\right)^2 + k^2_{ref}\cdot g\cdot\beta_{conv}\cdot\beta_{corr}\cdot\left(\mathcal{I}_{x,y}\cdot\hat{s}_{x,y,i}\right) + \left(1+\frac{1}{A}\right)\cdot\beta_D\cdot\sigma^2_{D,i} && . \end{aligned} \tag{29}$$

Once again, we obtain the updated β_{conv} (see Eq. (9)) and β_{corr} (see Eq. (10)), both calculated according to Eq. (27), as well as the smoothing of the detector noise β_D. We do not consider the uncertainty of alignment σ_{shift} or the uncertainty of interpolation σ_{Inter} at this point, as neither affects the volatility of the noise in energy direction.

3.1.2. Summed intensities

To normalize EELS maps, we require a suitable noise model for the summed intensities, which will enable us to obtain the first part of the separation in Eq. (19), approximating the intensity map $\mathcal{I}_{x,y}$. Once again, we must consider differences in the noise model between the energy and lateral directions.

First, we begin by summing the noise model for the lateral directions, as given in Eq. (28), where the underlining $\underline{x,y}$ is used to indicate the considered direction again. With regards to the addition of Gaussian and Poisson noises (see Eq. (3)), we sum the intensities with respect to the EEL channel i, resulting in:

$$\xi_{A,\underline{x,y},M} = \sum_i^M \xi_{A,\underline{x,y},i} \approx \underbrace{g \cdot \mathcal{P}\left[\frac{\mathcal{I}_{x,y}\sum_i^M \hat{s}_{x,y,i}}{g}\right]}_{1)} + \mathcal{N}\left[0,\, \Theta^2_{A,\underline{x,y},M}\right] \quad \text{, with} \quad \Theta^2_{A,\underline{x,y},M} = \sum_i^M \Theta^2_{A,\underline{x,y},i} \quad \text{and} \tag{30}$$

$$\Theta^2_{A,\underline{x,y},M} = \underbrace{\alpha_M \cdot \varphi_M \cdot k^2_{ref,M} \cdot \left(\mathcal{I}_{x,y} \cdot \sum_i^M \hat{s}_{x,y,i}\right)^2}_{2)} + \underbrace{k^2_{ref,M} \cdot g \cdot \left(\mathcal{I}_{x,y} \cdot \sum_i^M \hat{s}_{x,y,i}\right)}_{3)} + \underbrace{\sigma^2_{D,M}}_{4)} \quad .$$

where in term 1) and 3) the smoothing factor β_{conv}, while in 2) the smoothing factor β_{FP} and in 4) the smoothing factor β_D vanish. All these factors vanish because of the summation in energy direction, which effectively removes the correlation. In the terms 2) and 3) we observe a change from $k_{ref} \rightarrow k_{ref,M}$, resulting from the summation of M channels, as demonstrated in [34]. A more detailed discussion on the exact summation can be found in Section 4.

In term 2), we examine the summation of the fixed-pattern noises, for which we need a new distribution factor α_M. This factor can be approximated using an average of the normalized EELS signal over the array:

$$\alpha_M \approx \alpha \cdot \frac{1}{X \cdot Y} \sum_{x,y}^{X,Y} \sum_i^M \left(\frac{\xi_{A,x,y,i}}{\xi_{x,y,M}}\right)^2 \tag{31}$$

under the general assumption that k_{ref} is relatively homogeneously distributed, which is expected for a homogeneously distributed signal in TEM mode used for acquiring a gain reference. Additionally, we assume that α remains constant between EEL channels, similar to the assumptions made in Eq. (18).

Additionally, we must introduce a new shifting factor, as $\varphi \rightarrow \varphi_M$, which is similar to the one presented in Eq. (23). Unlike the shifting factor φ in Eq. (23), which uses the Dirac delta to measure the drift, φ_M utilizes the mean difference between all normalized spectra, prior to alignment. Therefore, we refer to φ_M as the 'overlap factor'. As the fixed-pattern noise, which accounts for the uncertainty of the gain reference, is fixed to the EEL channels, it only varies the signal by the difference of the signal between measurements. Consequently, we find that the fixed-pattern noise depends on the overlap of the spectra. The overlap factor can be calculated as:

$$\varphi_M \approx \frac{1}{XY\,(XY-1)} \sum_{x,y}^{X,Y} \sum_{x',y'}^{X,Y} \sum_i^M \left| \frac{\xi_{x,y,i}}{\xi_{x,y,M}} - \frac{\xi_{x',y',i}}{\xi_{x',y',M}} \right| \quad \text{, with } (x',y') > (x,y) \text{ ,} \tag{32}$$

summing up pairs in such a way that each unaligned spectrum $\xi_{x,y}$ is subtracted from every other spectrum $\xi_{x',y'}$ in the array exactly once. In this case, $\varphi_M \approx 0$ when all spectra overlap completely and $\varphi_M \approx 1$ when all spectra do not overlap at all. Normalization is crucial to cancel out differences in the intensity as good as possible.

As the same background is subtracted from all spectra equally in term 4), the factor $\left(1 + \frac{\varphi}{A}\right)$ associated with the detector noise $\sigma^2_{D,i}$ disappears. Furthermore, alignments do not affect this result, since intensities are summed over all EEL channels. Consequently, the factor disappears in the summed intensities, in comparison to Eq. (28). We observe that the detector noise changes from $\sigma^2_D \rightarrow \sigma^2_{D,M}$, due to the summation of M channels, as shown in Eq. (3). However, due to correlations within the detector noise, as demonstrated in [34], the summed detector noise is significantly larger than the sum of the individual detector noises of the EEL channels, indicating that $\sigma^2_{D,M} \gg \sum_i^M \sigma^2_{D,i}$. This will be demonstrated later in the evaluation of the noises.

Ultimately, we must consider the impact of the alignments, but it is clear that they do not play a significant role in this case, as the drift noise disappears when all spectra are summed, provided that no regions of high intensity are excluded or truncated by the detector. Generally, this holds true as long as the ZLP is not positioned near the detector edge, which would otherwise lead to boundary effects.

Additionally, interpolation has no impact on the total sum of the noises, since it preserves the total count (see Eq. (26)), which is subject to the noise.

Following a similar approach, we derive a summed noise model from Eq. (29), denoted by the underlined index $\underline{M}$ for the energy direction:

$$\xi_{A,x,y,\underline{M}} = \sum_i^M \xi_{A,x,y,\underline{i}} \approx g \cdot \mathcal{P}\left[\frac{\mathcal{I}_{x,y}\sum_i^M \hat{s}_{x,y,i}}{g}\right] + \mathcal{N}\left[0,\, \Theta^2_{A,x,y,\underline{M}}\right] \quad \text{, with} \quad \Theta^2_{A,x,y,\underline{M}} = \sum_i^M \Theta^2_{A,x,y,\underline{i}} \quad \text{and} \tag{33}$$

$$\Theta^2_{A,x,y,\underline{M}} = \alpha_M \cdot k^2_{ref,M} \cdot \left(\mathcal{I}_{x,y} \cdot \sum_i^M \hat{s}_{x,y,i}\right)^2 + k^2_{ref,M} \cdot g \cdot \left(\mathcal{I}_{x,y} \cdot \sum_i^M \hat{s}_{x,y,i}\right) + \left(1 + \frac{1}{A}\right) \cdot \sigma^2_{D,M} \quad ,$$

where the difference between the noise model in lateral directions to the above model lies in the absence of the overlap factor φ_M and the presence of the factor of $\left(1 + \frac{1}{A}\right)$ in the detector noises, where the shifting factor φ is absent. In this reference frame, the background subtracted dark frame contributes to the noise of the total intensities regardless of any realignments.

Having such a noise model for the summed intensities is important e.g. for deriving an uncertainty for thickness mapping, where the intensity within the ZLP is compared to the overall intensity of the spectrum.

At a glance, having two different noise models for the same quantity, namely the summed intensities, may seem redundant. However, this apparent luxury is resolved upon closer inspection. It is worth noting that we have now derived two equally valid noise models, which differ in their approach to incorporate fixed-pattern noises and background subtraction into the uncertainty of the measurement. In fact, one could argue that the differences between values at different positions on the total intensity map $\xi_{\underline{x,y},M}$ can be seen as the overall uncertainty. Alternatively, one could consider the summed intensities $\xi_{x,y,\underline{M}}$ individually and determine the uncertainty based on the expected deviation at that position between multiple consecutively acquired total intensity maps. In this case, the uncertainty associated with background subtraction must be taken into account. Both perspectives are represented in their corresponding noise models. Later in this work, we will combine these models to develop a noise model for the individual voxel that is applicable to all directions. However, at this stage, we will proceed with both noise models.

3.1.3. Intensity normalization and loss probabilities

Having established a noise model for the summed intensities $\xi_{A,\underline{x,y},M}$ in Eq. (30) and $\xi_{A,x,y,\underline{M}}$ in Eq. (33), which provide the first factor of the separation Eq. (19) from different perspectives on the noise, we now require a noise model for the normalized EEL spectra, which constitute the second factor in Eq. (19), in order to complete the separation. As previously demonstrated, the noise in lateral directions must be viewed separately from the noise in energy direction. Therefore, in a next step, we utilize the summed intensities $\xi_{A,\underline{x,y},M}$ from Eq. (30) and $\xi_{A,x,y,\underline{M}}$ from Eq. (33) as estimates of the true intensity map $\mathcal{I}_{x,y}$ to normalize the individual spectra.

We begin again by examining the noise in the lateral directions. By applying the summation rule in Eq. (3), we can decompose Eq. (28) into a part $\xi_{A,\underline{x,y},i}$ and a Gaussian distributed part that accounts for the uncertainty of alignment:

$$\xi^{*}_{A,\underline{x,y},i} = \frac{\xi_{\tilde{A},\underline{x,y},i}}{\xi_{A,\underline{x,y},M}} = \frac{\xi_{A,\underline{x,y},i}}{\xi_{A,\underline{x,y},M}} + \frac{\mathcal{N}\left[0\,,\,\sigma_A^2\right]}{\xi_{A,\underline{x,y},M}}\,. \tag{34}$$

However, upon normalizing the EELS map, we observe that the energy slice of interest $\xi_{A,\underline{x,y},i}$ from Eq. (28) is contained within the summed intensities $\xi_{A,\underline{x,y},M}$ from Eq. (30):

$$\xi_{A,\underline{x,y},M} = \xi_{A,\underline{x,y},R} + \xi_{A,\underline{x,y},i} \quad \text{, with} \quad \xi_{A,\underline{x,y},R} = \sum_{h\neq i}^{M} \xi_{A,\underline{x,y},h} \quad , \tag{35}$$

with $\xi_{A,\underline{x,y},R}$ describing the intensity in all other remaining EEL channels. Since $\xi_{A,\underline{x,y},R}$ is very similar to $\xi_{A,\underline{x,y},M}$ in Eq. (30), we provide the corresponding formula in Appendix A.2. With this reduction by the regarded channel i, the uncertainty of the gain reference changes $k^2_{ref,M} \to k^2_{ref,R}$, as well as the summed detector noise of all remaining EEL channels $\sigma^2_{D,M} \to \sigma^2_{D,R}$, the distribution factor of the remaining EEL channels $\alpha_M \to \alpha_R$ and the overlap factor of the remaining EEL channels $\varphi_M \to \varphi_R$ for the fixed-pattern noise. Since α_R and φ_R are very similar to Eq. (31) and Eq. (32), both are given in Appendix A.2.

To solve the first term on the right-hand side of Eq. (34), we can rewrite the denominator into Eq. (35). By taking a measurement, the EEL channels take distinct values $\mathcal{I}_{x,y}\cdot\zeta_{A,\underline{x,y},i} \in \xi_{A,\underline{x,y},i}$ from the distribution, collapsing it to the actual representation of loss probabilities $\zeta_{A,\underline{x,y},i}$ multiplied by the intensity map $\mathcal{I}_{x,y}$. Thus, we find the loss probabilities $\zeta_{A,\underline{x,y},i} \in \mathcal{N}\left[\mu_i\,,\,k^2_{A,\underline{x,y},i}\right]$ and $\zeta_{A,\underline{x,y},R} \in \mathcal{N}\left[\mu_R\,,\,k^2_{A,\underline{x,y},R}\right]$. As the corresponding uncertainties $k_{A,\underline{x,y},i}$ and $k_{A,\underline{x,y},R}$ are lengthy, both are derived in Appendix A.2. The corresponding mean values, however, are given as:

$$\mu_i = \frac{\hat{s}_{x,y,i}}{\sum_i^M \hat{s}_{x,y,i}} \approx \hat{s}_{x,y,i} \quad \text{and} \quad \mu_R = \frac{\sum_{h\neq i}^M \hat{s}_{x,y,h}}{\sum_i^M \hat{s}_{x,y,i}} \approx \sum_{h\neq i}^{M} \hat{s}_{x,y,h}\,. \tag{36}$$

From these mean values, a first criterion for the normalization of EELS maps is identified as the aforementioned normalization based on the total transmitted intensity, which is only useful if the acquired loss probability $\sum_i^M \hat{s}_{x,y,i} \approx 1$, which means that it is large enough to cover a high percentage of the transmitted intensity of the intensity map $\mathcal{I}_{x,y}$. Alternatively, the loss probability $\sum_i^M \hat{s}_{x,y,i} = \text{const.}$ should remain constant over all energy spectra (x, y), thereby preserving the relation between them. Typically, one of these conditions is satisfied when the ZLP does not drift outside the CCD array and the plasmonic peaks are not truncated. This is due to the fact that both combined account for the majority of the overall intensity of the signal.

As a consequence, normalized low-loss EELS measurements, which often do not fully capture the bulk plasmonic peaks, artificially overestimate the loss probability of materials with high plasmonic resonance, typically metals, relative to those of lower resonance, such as semiconductors, organic materials or polymers. This has significant implications for the evaluation of such material systems!

We use the equality of $\zeta_{A,\underline{x,y},i}$ in both nominator and denominator to obtain:

$$\frac{\xi_{A,\underline{x,y},i}}{\xi_{A,\underline{x,y},M}} = \frac{\mathcal{I}_{x,y}\cdot\zeta_{A,\underline{x,y},i}}{\mathcal{I}_{x,y}\cdot\left(\zeta_{A,\underline{x,y},R} + \zeta_{A,\underline{x,y},i}\right)} = \frac{1}{\frac{\zeta_{A,\underline{x,y},R}}{\zeta_{A,\underline{x,y},i}} + 1}\,. \tag{37}$$

From this point, it can be inferred that when normalizing energy slices of EELS data cubes by the summed intensities, additional information regarding the total intensity from all other slices, excluding the one of interest, is required. The greater the contribution of a single energy slice to the total intensity of the spectra, the more uncertain it gets to normalize that particular slice by the total intensity. Therefore, we identify the second criterion for intensity normalization: The signal of the EEL spectra should ideally be distributed over a broader portion of the spectrum. Typically, this condition is met when the ZLP is not confined to a single EEL channel, but rather is broadened over several dozen channels or alternatively this is true for all channels, except for the channels containing a narrow ZLP. The resulting noise model for intensity normalized EELS maps in the lateral directions can be expressed as:

$$\xi^{*}_{A,\underline{x,y},i} = \underbrace{\frac{g\cdot\beta_{conv}\cdot\mu_R^2}{I}\cdot\mathcal{P}\left[\frac{I\cdot\hat{s}_{x,y,i}}{g\cdot\beta_{conv}\cdot\mu_R^2}\right]}_{1)} + \underbrace{\mathcal{N}\left[0\,,\,\frac{\mu_i^2\cdot g\cdot I\cdot\sum_{h\neq i}^M\hat{s}_{x,y,h}}{I^2}\right]}_{5)} + \mathcal{N}\left[0\,,\,\frac{\mu_R^2\cdot\Theta^{*2}_{A,\underline{x,y},i} + \mu_i^2\cdot\Theta^{*2}_{A,\underline{x,y},R} + \sigma^2_{A^*}}{I^2}\right] \quad , \tag{38}$$

$$\Theta^{*2}_{A,\underline{x,y},i} \approx \underbrace{\alpha\cdot\varphi\cdot\beta_{FP}\cdot k^2_{ref}\cdot\left(I\cdot\hat{s}_{x,y,i}\right)^2}_{2)} + \underbrace{\left(k^2_{ref} + \frac{\left(1+k^2_{ref}\right)\cdot\sigma^2_{Int}}{4I^2}\right)\cdot g\cdot\beta_{conv}\cdot\left(I\cdot\hat{s}_{x,y,i}\right)}_{3)} + \underbrace{\left(1+\frac{\sigma^2_{Int}}{I^2}\right)\cdot\left(1+\frac{\varphi}{A}\right)\cdot\beta_D\cdot\sigma^2_{D,i}}_{4)} \quad ,$$

$$\Theta^{*2}_{A,\underline{x,y},R} \approx \underbrace{\alpha_R\cdot\varphi_R\cdot k^2_{ref,R}\cdot\left(I\cdot\sum_{h\neq i}^{M}\hat{s}_{x,y,h}\right)^2}_{6)} + \underbrace{\left(k^2_{ref,R} + \frac{\left(1+k^2_{ref,M}\right)\cdot\sigma^2_{Int}}{4I^2}\right)\cdot g\cdot\left(I\cdot\sum_{h\neq i}^{M}\hat{s}_{x,y,h}\right)}_{7)} + \underbrace{\left(1+\frac{\sigma^2_{Int}}{I^2}\right)\cdot\sigma^2_{D,R}}_{8)} \quad ,$$

$$\sigma^2_{A^*} = \left(1 + k^2_{A,\underline{x,y},M}\right) \cdot \sigma^2_{MA} \cdot \left(I \cdot \frac{d}{d\underline{i}}\, \hat{s}_{x,y,\underline{i}}\right)^2 \quad ,$$

where μ_R as well as μ_i are defined in Eq. (36), the distribution factor α is given in Eq. (18), the shifting factor φ is presented in Eq. (23), and φ_R and α_R are found in Appendix A.2 Eq. (53), where the subscript R denotes the reduction in channels (see Eq. (35)). Additionally, β_{conv} and β_{corr} are smoothing factors while k_{ref} and $k_{ref,R}$ describe the uncertainty of the gain reference and the reduced summed gain reference, respectively. The gain is denoted as g, the mean intensity of the intensity map $\mathcal{I}_{x,y}$ is given as I, and σ^2_{Int} denotes the variance of the intensity map, as described in Appendix A.2. The detector noise and reduced summed detector noise are represented by σ_D and $\sigma_{D,R}$. Additionally σ_{MA} characterizes the misalignment of the individual spectra with respect to each other. The derivation of the above noise model is quite extensive and would compromise the readability of the paper. Therefore, we present it only in Appendix A.3.

Within the noise model, we identify four terms associated with the spectrum and an additional four terms related to the summed intensity used for the intensity normalization of the spectra. Both μ_R and μ_i serve as weighting factors for the noise terms related to the spectrum and the normalization. Beginning with the noise terms associated with the spectrum itself, we identify: 1) The first term that describes the Poisson distributed signal noise. 2) The second term that describes the fixed-pattern noise induced by applying the gain reference. 3) A third term that describes alterations of the Poisson noise by the application of the gain reference and by applying the intensity normalization. A last term 4) that describes the read-out noise of the detector.

Four terms are also associated with the intensity normalization, consisting of: 5) A term that resembles the Poisson signal noise of all other channels R, which we cannot be transformed back into the Poisson distribution using Eq. (6) due to its zero mean value. 6) Another term that describes the fixed-pattern noise induced by the gain reference to all other channels R. 7) A term that describes alterations of the Poisson noise in all other channels R by applying the gain reference and by applying the intensity normalization. A last term 8) that describes the read-out noise of the detector in all other channels R. Upon comparison with the terms 1–4), a clear repetition becomes apparent.

Eventually, we identify a term representing the uncertainty of misalignment and another term that describes a multiplication (see Eq. (4)) between the noises of the spectrum and the noises of the normalization, which is subsequently deemed insignificant and therefore neglected in this context.

It is crucial to note that the validity of this noise model is limited to sufficiently high beam intensities, as it relies on several approximations that require this condition to be met (a strong ZLP usually suffices this condition). Consequently, we establish a third criterion for normalization: the uncertainty of the normalization must be sufficiently small $k_{A,\underline{x,y},M} < 0.05$ (see Eq. (5), Appendix A.2 and Appendix A.3) to enable an accurate estimate of the noise.

Regarding the noise model in energy direction, we obtain:

$$\xi^*_{A,x,y,\underline{i}} = \frac{\xi_{A,x,y,\underline{i}}}{\xi_{A,x,y,\underline{M}}} \quad . \tag{39}$$

Notably, the above equation can be viewed from two distinct perspectives — one focusing on the noise volatility of the measurement and the other focusing on the uncertainty of the measurement. These two perspectives represent fundamentally different entities:

It is readily apparent that the summed intensities act as a scalar with respect to the individual spectra, and dividing a spectrum by a scalar does not change the noise volatility within the spectrum, except for a scaling of the variance. Normalizing by the summed intensities does not introduce additional noise terms in energy direction, unlike the lateral noise model presented in Eq. (38). In the lateral directions, such a normalization significantly alters the variance, beyond the obvious scaling effect. In contrast, the change in variance for the energy direction remains solely a scaling effect. Thus one could conclude at Eq. (39). It is worth noting that such a variance model plays a crucial role for the 'total variation' approach employed in denoising or deconvolution.

From the perspective of the uncertainty associated with measuring such spectra, a completely different picture emerges. In this context, the precision of the normalization plays a crucial role and must be taken into account. Consequently, we obtain a similar model to Eq. (38). Using the same line of reasoning as before, we must replace $\xi_{A,x,y,\underline{i}}$ from Eq. (29) and $\xi_{A,x,y,\underline{M}}$ from Eq. (33) by their actual representations, which yields a noise model similar to Eq. (37):

$$\xi^*_{A,x,y,\underline{i}} = \frac{\xi_{A,x,y,\underline{i}}}{\xi_{A,x,y,\underline{M}}} = \frac{\mathcal{I}_{x,y} \cdot \zeta_{A,x,y,\underline{i}}}{\mathcal{I}_{x,y} \cdot \left(\zeta_{A,x,y,\underline{R}} + \zeta_{A,x,y,\underline{i}}\right)} = \frac{1}{\frac{\zeta_{A,x,y,\underline{R}}}{\zeta_{A,x,y,\underline{i}}} + 1} \quad . \tag{40}$$

We subsequently obtain the overall uncertainty for normalized EELS spectra in the energy direction as:

$$\xi^*_{A,x,y,\underline{i}} = \frac{g \cdot \beta_{conv} \cdot \beta_{corr} \cdot \mu^2_R}{I} \cdot \mathcal{P}\left[\frac{I \cdot \hat{s}_{x,y,i}}{g \cdot \beta_{conv} \cdot \beta_{corr} \cdot \mu^2_R}\right] + \mathcal{N}\left[0, \frac{\mu^2_i \cdot g \cdot I \cdot \sum_{h\neq i}^{M} \hat{s}_{x,y,h}}{I^2}\right] + \mathcal{N}\left[0, \frac{\mu^2_R \cdot \Theta^{*2}_{A,x,y,\underline{i}} + \mu^2_i \cdot \Theta^{*2}_{A,x,y,\underline{R}}}{I^2}\right] \quad , \tag{41}$$

$$\Theta^{*2}_{A,x,y,\underline{i}} \approx \alpha \cdot \beta_{FP} \cdot k^2_{ref} \cdot \left(I \cdot \hat{s}_{x,y,i}\right)^2 + \left(k^2_{ref} + \frac{\left(1+k^2_{ref}\right) \cdot \sigma^2_{Int}}{4I^2}\right) \cdot g \cdot \beta_{conv} \cdot \beta_{corr} \cdot \left(I \cdot \hat{s}_{x,y,i}\right) + \left(1 + \frac{\sigma^2_{Int}}{I^2}\right) \cdot \left(1 + \frac{1}{A}\right) \cdot \beta_D \cdot \sigma^2_{D,i} \quad ,$$

$$\Theta^{*2}_{A,x,y,\underline{R}} \approx \alpha_R \cdot k^2_{ref,R} \cdot \left(I \cdot \sum_{h\neq i}^{M} \hat{s}_{x,y,h}\right)^2 + \left(k^2_{ref,R} + \frac{\left(1 + k^2_{ref,M}\right) \cdot \sigma^2_{Int}}{4I^2}\right) \cdot g \cdot \left(I \cdot \sum_{h\neq i}^{M} \hat{s}_{x,y,h}\right) + \left(1 + \frac{\sigma^2_{Int}}{I^2}\right) \cdot \left(1 + \frac{1}{A}\right) \cdot \sigma^2_{D,R} \quad .$$

Unlike the volatility model, the uncertainty model presented above is relevant for calculating the total uncertainty of a normalized voxel, similar to Eq. (24). However at this stage, we find that a combined noise model is too complex to be readily applicable. Therefore, we will examine the impact of the different noise terms on the total noise and omit certain terms in advance.

Consequently, we must consider two very distinct noise models in energy direction, depending on the purpose, whereas the noise model in the lateral directions simultaneously characterizes both volatility and uncertainty.

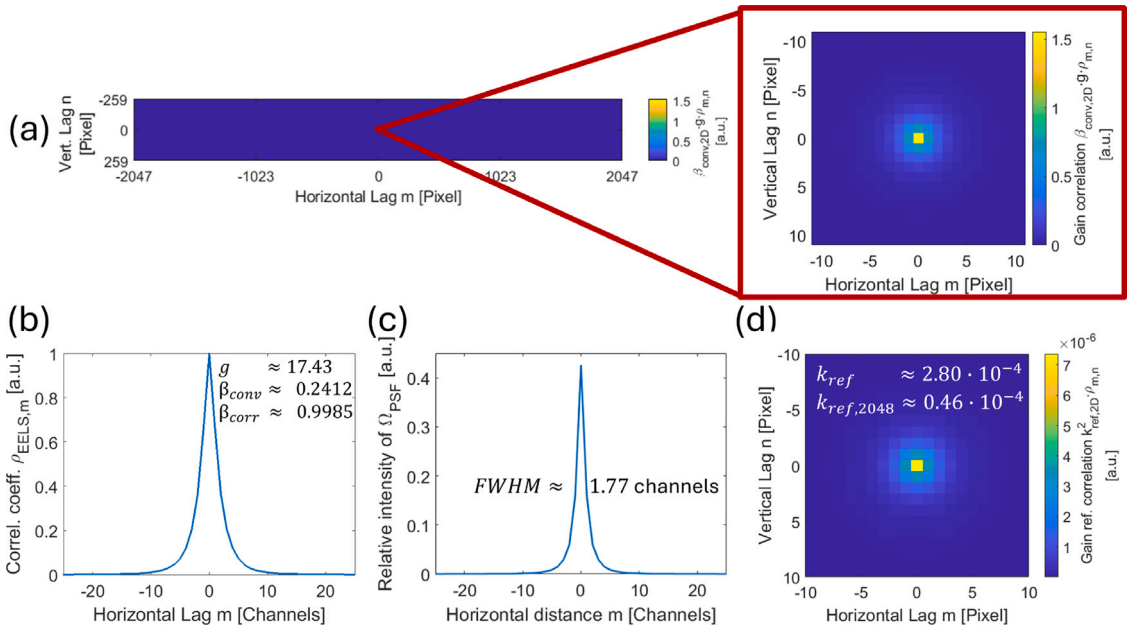

Fig. 2. **(a)** Displays the average autocovariance function from Eq. (42) of a homogeneous signal recorded in TEM mode divided by the target intensity of $\hat{S}_{ref} \approx 7000$ counts, as described in [34]. We cropped the full autocovariance function of the regular 2D image to the EELS region and found that only the very central elements contribute to the function, as shown in the cutout on the right side. The autocovariance function yields the variance of the Poisson noise σ_p^2 multiplied by the Pearson correlation coefficients $\rho_{m,n}$ of the 2D image (see Eq. (42)). Dividing the Poisson noise variance $\sigma_p^2 = \beta_{conv,2D} \cdot g \cdot \hat{S}_{ref}$ by the target intensity $\hat{S}_{ref}$ yields the smoothed gain as the central element $\beta_{conv,2D} \cdot g \cdot \rho_{0,0} \approx 1.55$ of the 2D signal, since $\rho_{0,0} = 1$ by definition. Upon vertically summing the autocovariance function shown in (a), according to Eq. (15), we find $\beta_{conv} \cdot g \cdot \rho_0 \approx 4.2$ as an estimate of the smoothed gain for EELS measurements, again with $\rho_0 = 1$. By normalizing the resulting distribution to the height of one, the Pearson correlation coefficients are revealed, as shown in **(b)**. Using these coefficients, we can calculate β_{conv} and β_{corr} according to Eq. (9) and Eq. (10). Having calculated both β_{conv} and the smoothed gain estimate $\beta_{conv} \cdot g$ for EELS, we can readily determine the total gain of the detector g. **(c)** Displays the detector PSF for EELS Ω_{PSF}, calculated using Eq. (43). **(d)** Shows the uncertainty of the gain reference $k_{ref,2D}^2 \cdot \rho_{m,n}$ for regular 2D images, multiplied by its Pearson correlation coefficients. Vertical summation according to Eq. (15) and Eq. (17) yields the uncertainty of the gain reference for EEL spectra k_{ref}^2 and subsequent horizontal summation provides the uncertainty of the gain reference for the entire spectrum $k_{ref,M=2048}^2$. Taking the square root of both values yields the results presented in (d).

4. Estimation of the noise parameters

To apply the noise model, it is essential to determine the contributing factors and coefficients. This section aims to demonstrate how to determine these parameters, thereby tailoring the noise model to the detector.

In our previous work [34], we demonstrated how to determine the Pearson correlation coefficients $\rho(\xi_{ref})$ for a signal under homogeneous illumination conditions in TEM mode, similar to those used for the gain reference ξ_{ref}. By applying the Wiener–Khitchine theorem [45,46] and analyzing the autocovariance function $K(\xi_{ref})$ for such a frame, we gained insight into the correlations within the signal:

$$K(\xi_{ref}) = \sigma_p^2 \cdot \rho(\xi_{ref}) \ , \tag{42}$$

with the variance of the Poisson noise σ_p^2. The Pearson correlation coefficients of the signal comprise the individual elements $\rho_{m,n}$, with horizontal lag $m \in [-(M-1), \dots, M-1]$ and vertical lag $n \in [-(N-1), \dots, N-1]$. Consequently, the size of $\rho(\xi_{ref})$ is nearly twice that of the initial frame, which has $M \times N$ pixels in each direction. Therefore, we must crop the frame to match the size of the EELS region, as illustrated in Fig. 2(a). For instance, an EELS region of 260×2048 pixels yields 519×4095 Pearson correlation coefficients. The autocovariance function Eq. (42) provides the Pearson correlation coefficients scaled by the variance of the Poisson noise of the 2D image $\sigma_p^2 \cdot \rho_{m,n}$. The Poisson noise variance is then given by the product of the smoothed gain of 2D images $\beta_{conv,2D} \cdot g$ and the target intensity $\hat{S}_{ref}$, resulting in $\sigma_p^2 = \beta_{conv,2D} \cdot g \cdot \hat{S}_{ref}$. By dividing the Poisson noise variance by the target intensity, which was approximately $\hat{S}_{ref} \approx 7000$ counts, we obtain the smoothed gain of the 2D image at the central element of the gain correlation map, as illustrated in Fig. 2(a). This follows from the fact that $\rho_{0,0} = 1$ by definition. Consequently, the smoothed gain can be expressed as $\beta_{conv,2D} \cdot g = \frac{\sigma_p^2}{\hat{S}_{ref}} \approx 1.55$, which applies to regular 2D images acquired with our detector.

s a result of the smoothing caused by the detector PSF, the Pearson correlation coefficients are distributed densely around the center. We therefore display the central region as an extract in Fig. 2(a) marked by the red box. All other correlation coefficients, located in the periphery, are zero.

Since the signal is expected to be entirely contained within the detector region used for EELS, we can directly sum all correlation coefficients from Fig. 2(a) (according to Eq. (15)) to obtain the smoothing factors $\beta_{conv} \approx 0.2412$ (according to Eq. (9)) and $\beta_{corr} \approx 0.9985$ (according to Eq. (9)) for EELS measurements [34]. with the smoothed gain $\beta_{conv} \cdot g$ and β_{conv} known, we can readily calculate the initial gain of our US1000FT-X2 camera to be $g \approx 17.43$ counts/beam electron, which is comparable to the gain of 12.6 counts/beam electron reported for a US1000FTXP detector in a Gatan GIF [5].

By summing the Pearson coefficients from Fig. 2(a) vertically, according to Eq. (15), we obtain Fig. 2(b), which displays the correlation coefficients for EELS measurements.

Furthermore, using the distribution of the Pearson correlation coefficients in Fig. 2(b), we can compute the detector point spread function Ω_{PSF} for EELS measurements, which differs from the detector PSF for regular 2D images Ω_D. This is achieved by taking the square root of the normalized

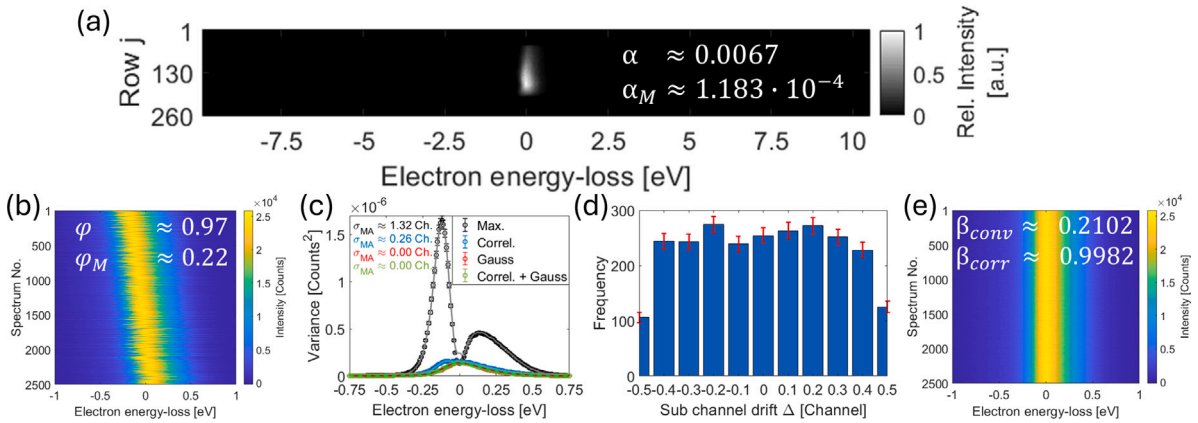

Fig. 3. **(a)** Displays the relative intensity of a ZLP measured on the detector in 2D, with an acquisition time of $t_{acq.} = 10^{-3}$ s. According to Eq. (18) and Eq. (31), we determine the distribution factors α and α_M. **(b)** By acquiring a 50 × 50 2D EELS map, again with $t_{acq.} = 10^{-3}$ s, and rearranging them to a sequential order along the vertical direction, we observe that the zero-loss peaks, shown in yellow, exhibit drift over the course of the experiment. The entire acquisition process of the 50 × 50 EELS map took approximately 5 min. Using this image, we can calculate the shifting and overlap factors φ and φ_M according to Eq. (23) and Eq. (32). Furthermore, we can utilize this arrangement to evaluate strategies for ZLP alignment. The variance in vertical direction serves as a reliable indicator, as it approaches a minimum for optimal alignment. To minimize deviations in the beam current, the spectra were normalized. We employed the noise model from Eq. (38) using the standard deviation of the misalignment σ_{MA} as a fitting parameter. The results for various alignment techniques are presented in **(c)**, where we plot the noise model as a line with slightly different shade than the experimental data represented by dots. It can be seen that aligning with respect to the maximum position (Max.) of the peak, shown as the black dots, is the least precise technique, yielding $\sigma_{MA} \approx 1.32$ channels. Here, it is best seen that the uncertainty of alignment closely follows the first derivative of the mean signal I. The cross-correlation method, which is the standard procedure used in '*Gatan Digital Micrograph*', yields improved results, with $\sigma_{MA} \approx 0.26$ channels. The fit reveals a result close to the expected standard deviation σ_{MA} of a quarter channel, as derived in Section 3.1.1. Therefore, the theory is in good agreement with the data. By applying a Gaussian fit to the tip of the ZLP or to the cross-correlation function yields a precise estimate of the sub-channel drift, enabling to interpolate between channels and to correct the drift. Both procedures lead to the best results, with $\sigma_{MA} \approx 0$ channels. **(d)** The sub-channel drifts obtained using these methods are presented as a histogram with a bar width of 0.1 channel. The results suggest a homogeneous distribution, consistent with the uncertainties of the Bernoulli distribution. Both channels at ±0.5 eV exhibit only half the frequency of appearance compared to the others, since channels are effectively cut in half due to the threshold for shifting the spectrum by a whole channel. **(e)** Shows the alignment after interpolation. However, interpolating the spectra causes slight changes in β_{conv} and β_{corr} compared to Fig. 2, due to the additional convolution described in Eq. (27).

Pearson correlation coefficients for EELS in Fourier space (see Eq. (11)):

$$\Omega_{PSF} = \mathcal{F}^{-1}\left[\mathcal{F}\left[\left(\frac{\rho_m}{\sum_m \rho_m}\right)\right]^{1/2}\right] . \tag{43}$$

The resulting detector PSF is displayed in Fig. 2(c) and is comparable with the line spread function (LSF) obtained on other detectors employing the knife-edge method [52,53] or integrated single spot illumination [54].

In Fig. 2(d) we present the distribution of the Pearson correlation coefficients for the gain reference, multiplied by its variance. Dividing by the target intensity S_{ref}, according to Eq. (17), yields $k_{ref}^2 \cdot \rho_{m,n}$. For a detailed explanation and analysis, we refer to [34]. The interpretation of this result is analogous to that of the extract of the gain correlation of the signal noise in Fig. 2(a). Likewise, we display an extract centered around the central element, which reveals $k_{ref}^2 \cdot \rho_{0,0} \approx 7.37 \cdot 10^{-6}$, given that $\rho_{0,0} = 1$ by definition. By taking the square root, we obtain the uncertainty of the gain reference $k_{2D,ref} \approx 2.72 \cdot 10^{-3}$ for regular 2D images. To determine the uncertainty of the gain reference for EELS measurements and the total count of an EELS measurement, we require the vertical sum and the total sum of all coefficients, respectively. The procedure is analogous to that of the gain correlation in Fig. 2(a). However, summing the gain reference also involves summing the target intensity with which it was acquired (see Eq. (17)). Since the gain reference for 2D images is already normalized by the total target intensity, we simply divide by the square of the number of added pixels, which is 260^2 for EELS spectra and $(260 \cdot 2048)^2$ for summed EELS spectra, as required for the normalization of the total count to account for beam current fluctuations. By taking the square root of the uncertainty variances k_{ref}^2 and $k_{ref,M=2048}^2$, we obtain the new uncertainties $k_{ref} \approx 2.8 \cdot 10^{-4}$ for EELS measurements and $k_{ref,M=2048} \approx 0.46 \cdot 10^{-4}$ for the summed intensities.

For the subsequent EELS measurements, we used the highest dispersion available to us, which is 0.01 eV/channel. All measurements were performed at a magnification of x 400k and for a good energy resolution, we employed a cold FEG in our microscope.

In Fig. 3(a) we depict a 2D representation of the ZLP on the EELS region of the detector, allowing to calculate the distribution factors $\alpha \approx 0.0067$ from Eq. (18) and $\alpha_M \approx 1.183 \cdot 10^{-4}$ from Eq. (31). These two factors affect the impact of the fixed-pattern noise cause by the uncertainty of the gain reference (see Eq. (16) and Eq. (30)). The coefficient α_R from Appendix A.2 Eq. (53) can be determined by omitting the respective column i.

To validate the EELS noise model, we must demonstrate that the noise behaves as expected. However, the signal in EELS is far from being homogeneously distributed, as required for the standard deviation analysis, instead forming a large peak — the ZLP. Consequently, noise analysis is only possible to conduct between sequentially acquired spectra with the same expectation value $\hat{S}$, which are energy aligned. We therefore acquired an EELS map in vacuum, which corresponds to a time series of the vacuum ZLP, allowing for channel-wise evaluation.

In Fig. 3(b) we present such a measurement of a 50 × 50 EELS map in vacuum with an acquisition time of $t_{acq.} = 10^{-3}$ s and an overall measurement time of approx. 5 min. We rearranged all acquired spectra, such that they are sequentially displayed as a series of spectra. It is evident that the high intensity ZLP (shown in yellow) drifts throughout the measurement, necessitating alignment to conduct noise measurements, which require a homogeneous expectation value of the signal $\hat{S}$ within a given energy loss channel.

Shifting the spectra also shifts the fixed-pattern noise, requiring the calculation of shifting factors $\varphi \approx 0.97$ following Eq. (23) and $\varphi_M \approx 0.22$ following Eq. (32), to account for the shift in the fixed-pattern noises.

A perfect energy alignment minimizes the standard deviation among all spectra within a given EEL channel. Consequently, we can utilize the variance to compare various alignment strategies and identify the most suitable one, as illustrated in Fig. 3(c). We evaluated alignment methods

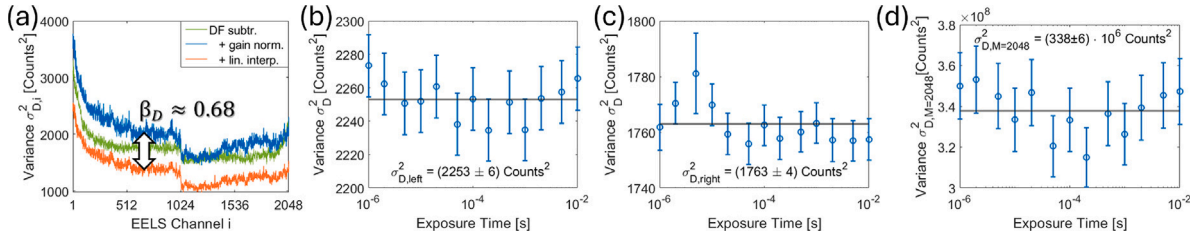

Fig. 4. By acquiring a 50 × 50 EELS maps without signal and rearranging it similar to Fig. 3(a), the variance of every channel can easily be determined by applying the standard deviation vertically. The resulting variances $\sigma^2_{D,i}$ are presented in **(a)** as the green curve, without gain reference applied, where only a dark frame background subtraction was performed for each spectrum (DF subtr.), and the blue curve, with gain reference applied in addition. It can be observed that the variance varies significantly from channel to channel, and that applying a of a gain reference substantially alters the noise distribution. Upon interpolating the spectra with a continuous sub-channel drift Δ, we obtain the orange curve, which exhibits a significant reduction in variances. The smoothing factor obtained between the blue and orange curve agrees well with the theoretical value of $\beta_D = 2/3$ (see Section 3.1.1). In **(b)** and **(c)**, we display the mean variance over all channels without interpolation (and thus colored blue) as a function of exposure time, for the left side and for the right side of the segmented detector, respectively. We find no time dependency in either case, which enables to neglect noise contributions from dark currents. This allows to determine a mean value $\sigma^2_{D,i}$ for each side of the detector, which is represented by the black line in the graphs. In **(d)** we show the variance of the sum of the entire spectrum $\sigma_{D,M=2048}$ for 2048 channels, again with no visible time dependency within the considered time intervals and without interpolation. Again, the mean value is represented by the black line.

based on the position of the maximum intensity (Max.), the alignment with the cross-correlation function (Correl.) as well as an alignment by fitting a Gaussian function to the tip (10–15 channels) of the ZLP (Gauss) and fitting a Gaussian to the cross-correlation function (Correl. + Gauss). The latter two allow for sub-channel alignments, but require some kind of interpolation between channels. To keep things simple, we used linear interpolation leading to a smoothing of the other noises as described in Section 3.1.1 and an additional uncertainty of interpolation.

To further reduce the variance, we normalized the spectra with respect to the total sum of counts, thereby accounting for changes in beam intensity. According to Eq. (38), we calculated the expected noise and fitted the alignment noise term σ_{A^*} (see Eq. (38) term 8) to the data. As will be show later, the influence of the intensity variation σ^2_{Int}/I^2 can be neglected for normalized spectra in vacuum. The results (black data points, gray fit curve) clearly indicate that aligning with respect to the maximum position is the least favorable technique, resulting in a misalignment of $\sigma_{MA} \approx 1.32$ channels. Furthermore, it is evident that the model for alignment uncertainty, as proposed in Eq. (25), indeed exhibits a dependence on the first derivative of the signal. This is evident from the two maxima adjacent to the position of the ZLP tip, which are well fitted by the gray curve, based on the first derivative of the signal, according to Eq. (38) term 8).

The standard procedure in '*Gatan Digital Micrograph*' involves alignment via cross-correlation [32], which indeed yields better results than the maximum intensity technique (dark blue data points, light blue fit curve). However, we still observe a residual misalignment of $\sigma_{MA} \approx 0.26$ channels. Assuming a continuous distribution of the sub-channel drift, the result is in good agreement to the expected mean value of $\sigma_{MA} = 0.25$ channels, which we derived in Section 3.1.1. Small deviations from this value are expected, as the sub-channel drift Δ is Bernoulli distributed within small intervals, reflecting the common uncertainty in histograms. Such a histogram will be shown below.

We found that both techniques, fitting a Gaussian either to the tip of the ZLP (dark red data points, light red fit curve) or to the cross-correlation function (dark green data points, light green fit curve) are best suited for alignment, as both enable sub-channel adjustments and reduce the uncertainty of alignment below the measurable $\sigma_{MA} \approx 0$ channels. For actual measurements of EEL spectra on specimens we found that fitting the cross-correlation function is better suited for alignments, owing to its greater symmetry compared to the ZLP of a specimen.

The histogram in Fig. 3(d), displays the frequency of occurrence of the sub-channel drift Δ ranging from −0.5 to 0.5 channels, in intervals of 0.1 channels in width. The red error bars represent the uncertainty, characterized by the Bernoulli distribution, within a 95% percent confidence interval. Obviously, all sub-channel intervals are nearly equally likely, suggesting a continuous distribution. As the intervals around both ±0.5 channels are cut in half, due to threshold for shifting the entire spectrum by a whole channel, the frequency of occurrence is also reduced by half.

The interpolation that corrects this sub-channel drift can be described by an additional convolution, as depicted in Eq. (27), resulting in an increased correlation among the other noises. Consequently, we observe additional smoothing, corresponding to changes in $\beta_{conv} \approx 0.2412 \rightarrow 0.2102$ and $\beta_{corr} \approx 0.9985 \rightarrow 0.9982$, due to interpolation. Following interpolation, the spectra become sub-channel aligned, as shown in Fig. 3(e). This enables the evaluation of the noise model, since the expectation value $\hat{S}_i$ of the signal remains constant within a given EEL channel i.

The last parameters required for evaluating the noise model are the read-out noises from the CCD detector, which are displayed in Fig. 4(a–d). Analogous to Fig. 3, we rearranged a 50 × 50 EELS map, acquired with the electron beam blanked, and determined the variance of a given channel as the deviation between spectra.

Fig. 4(a) displays the variance of the detector noise for an EELS map, resolved across all channels. We present three curves, each with an acquisition time of $t_{acq.} = 10^{-3}$ s, which differ by the corrections applied to the spectrum. The green curve represents the detector noise without a gain reference applied, which has only undergone dark frame subtraction. The blue curve displays the variances with a gain reference additionally applied; and we will discuss the orange line later. All curves demonstrate that the detector noise significantly varies from channel to channel, particularly between the left and the right side of the detector, as evidenced by the abrupt decrease in variance after 1024 channels, which marks the transition between detector segments. Additionally, the green curve reveals a significant increase in variance towards the edges of the detector.

As demonstrated in [34], the detector noise is significantly affected by the application of a gain reference. Consequently, the gain reference employed to correct for differences in the quantum efficiencies of the detector pixels modulates the detector noise, resulting in the observed change in distribution between the green and blue curve of the detector noise.

Additionally, it is also interesting weather the detector noise depends on the acquisition time, as dark currents accumulate and increase the noise. To explore this, we acquired a time series of the mean value of the noise variance across all channels, separately for the left and the right side of the segmented detector. This approach allows us to account for different behavior of the read-out electronics of the detector segments. As EELS measurement are typically gain normalized, we conducted consecutive measurements on the gain normalized data. We observe that the detector noise remains relatively stable within typical acquisition times, which are well below a second for both the left side in Fig. 4(b) and for the right side in (c) of the segmented detector, indicating that time dependencies, such as dark currents are negligible. Given that the camera is

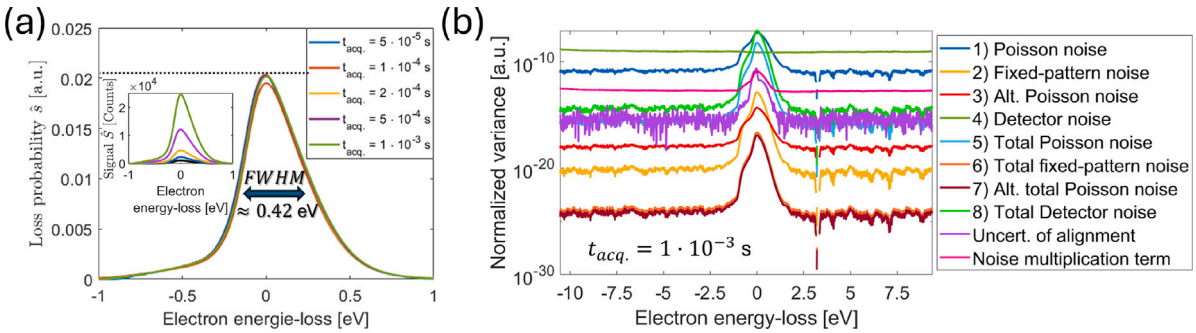

Fig. 5. **(a)** The inset displays the mean values of the rearranged 50 × 50 2D EELS map in vacuum, similar to Fig. 3(b), as a function of the electron energy-loss for increasing acquisition times. To minimize variances, the spectra were sub-channel aligned using a Gaussian fit to the cross-correlation function. In the main figure, the spectra were normalized with respect to the summed counts. Notably, all spectra exhibit a similar shape, with a common FWHM ≈ 0.42 eV and a zero loss probability of $\hat{s}_{0\,eV} \approx 0.02$, as indicated by the black dotted line. **(b)** We calculated the noise contribution of the individual terms from Eq. (38) based on the parameters determined in the previous figures, for the most intense spectrum in (a), represented by the green curve at an acquisition time of $t_{acq.} = 1 \cdot 10^{-3}$ s. The results indicate that only the signal noise terms 1) and 4) and the detector noise terms 4) and 8) contribute significantly to the noise. All other noise contributions are several orders of magnitude smaller and can therefore be neglected.

cooled to $T \approx -20°$ C, this is not unexpected. On average, across all channels (left and right), we obtain a detector noise of $\sigma_{D,i} \approx 45$ counts. For a more detailed examination of the time dependency, we refer to [34].

Eventually, we must determine the detector noise for the summed intensities required for normalizing the EEL spectra. Summing EEL spectra results in the addition of the detector noise variance of all channels, as described in Eq. (3). The noise variance, however, increases super-linearly. As we have demonstrated in [34], the pixels within a row of the detector are offsetted by a common mean value, which varies from row to row. This row noise arises from fluctuations in the bias voltage used to suppress negative counts [34]. For example, consider a detector with a single row of 1024 pixels, where the signal is offset by only one count. Consequently, the sum of the entire row is offset by a value of 1024 counts. Since the mean value of the row varies between measurements with a standard deviation of σ_{row}, this results in a noise variance of $\left(1024 \cdot \sigma_{row}\right)^2$. Consequently, summing the row noise results in a quadratic increase of the variance. For our detector, this results in a summed detector noise of $\sigma_{D,M=2048} \approx 18\,400$ counts, which is far larger than the simple sum of $\sqrt{1024 \cdot 2253 + 1024 \cdot 1763}$ counts ≈ 2028 counts that would be expected without row noise. As observed earlier for the respective sides of the detector, the noise remains constant within the uncertainties for short acquisition times.

Notably, when the number of pixels contributing to an EEL channel is doubled, for instance from 260 to 520 pixels, the detector noise variance $\sigma^2_{D,i}$ also doubles. As demonstrated in [34], the detector noise is independent in column direction, resulting in a linear increase in noise variance when adding pixels within a column.

To demonstrate the effects of linear interpolation, we artificially interpolated each spectrum from the 50 × 50 EELS map of the detector noise measurement, using the respective sub-channel drifts evaluated for the 50 × 50 EELS map in Fig. 3. The result is the orange curve in Fig. 4(a), which represents the channel variance of the gain normalized and interpolated spectra. Both blue (gain normalized) and orange (gain normalized and interpolated) noise distributions differ by a constant smoothing factor of $\beta_D \approx 0.68$. This result is in close agreement with the expectation value of $\beta_D = 2/3$, predicted in Section 3.1.1. The slight deviation of the theoretical value from the value shown in Fig. 3(a) is within the uncertainty of the Bernoulli distribution of the sub-channel drifts in Fig. 3(d).

To demonstrate the overall validity of our noise model in Eq. (38), we acquired five 50 × 50 EELS maps in vacuum with increasing acquisition times. We consistently employed a dispersion of 0.01 eV/channel, enabling us to cover a total range of 20.48 eV, out of which only a fraction (∼ 2 eV) is occupied by the signal of the ZLP. The signal measured in these channels spans a range of 0 to 25k counts (or approximately 1430 beam electrons). This number of counts significantly exceeds the typical range, in which plasmonic low-loss features are observed with our microscope.

We again aligned all spectra using the fitted cross-correlation method to achieve sub-channel precision, thereby minimizing the variance within each EEL channel. The corresponding mean values per channel are displayed in the inset of Fig. 5(a). After the normalizing to the total sum of counts, we observe small deviations between spectra Fig. 5(a), as well as an overall FWHM ≈ 0.42 eV and a maximum zero-loss probability of $\hat{s}_{0\,eV} \approx 0.02$, denoted by the black dotted line. In Fig. 5(b), we display the contributions of the individual noise components. Notably, the Poisson distributed signal noise from Eq. (38) term 1), represented by the dark blue line, dominates for higher intensities, whereas the Gaussian detector read-out noise from Eq. (38) term 4) contributes a relatively constant offset to the variance, as shown by the dark green line. Additionally, both the Poisson noise of the summed intensities from Eq. (38) term 5), represented by the light blue line, and the Gaussian detector noise of the summed intensities Eq. (38) term 8), shown in light green, exhibit a dependence on the squared signal and dominate at the highest intensities. These two contributions can be regarded as the primary contributions to the uncertainty of the normalization. All other contributions appear to be several orders of magnitude smaller than the variance of the detector noise and thus can be neglected: The fixed-pattern noises, represented in orange from Eq. (38) term 2) and in yellow for Eq. (38) term 6); the alteration of the Poisson noise due to the gain reference from Eq. (38) term 3) in red and from Eq. (38) term 7) in dark red; the alignment noise from Eq. (38) in purple; and the noise multiplication term between spectrum and normalization noise (comparable to Eq. (4)), which we previously proposed to neglect in Eq. (38), shown in pink.

Thus far, we have overlooked the contribution of a specimen to the beam variation $\frac{\sigma^2_{Int}}{I^2}$. Therefore, a closer examination is necessary. In Eq. (20), we defined the intensity map $I_{x,y} = g \cdot S_{src,el,x,y} \cdot T_{x,y}$ as the product of the gain g with, the beam current of the electron source $\hat{S}_{src,el,x,y}$, and the transmittance $T_{x,y}$, both at the spectrum position (x, y). In vacuum, where all the measurements were performed, $T_{x,y} = 1$ is uniformly equal at all positions. For measurements on specimen, we observe:

$$\mathcal{I}_{x,y} \approx g \cdot S_{src,el} \cdot \mathcal{N}\left[1, \frac{\sigma^2_{src}}{S^2}\right] \cdot T \cdot \mathcal{N}\left[1, \frac{\sigma^2_T}{T^2}\right] \approx I \cdot \mathcal{N}\left[1, \overbrace{\frac{T^2 \cdot \sigma^2_{src} + S^2 \cdot \sigma^2_T + \sigma^2_{src} \cdot \sigma^2_T}{I^2}}^{\sigma^2_{Int}}\right]. \tag{44}$$

The transmittance is clearly not normal distributed, but rather follows the shape, thickness and composition of a specimen. However, for simplicity, we approximate it with a Gaussian distribution. Based on the multiplication of Gaussian distributions (see Eq. (4)), we derive Eq. (44), which involves the mean beam current $S_{src,el}$ in electrons, the mean transmittance T, and consequently, the mean intensity $I = g \cdot S_{src,el} \cdot T$ of the EELS map.

Since we anticipate that the deviation due to the transmittance $T_{x,y,}$ will be significantly larger for typical specimen than the deviation of the electron beam $S_{src,el,x,y}$, the intensity deviations cannot be readily negligible in our noise model and must be taken into account, despite their relative insignificance in vacuum.

Determining $\frac{\sigma^2_{Int}}{I^2} \approx \frac{\mathrm{VAR}\left[\xi_{x,y,M}\right]}{I^2}$ is straight forward for a specimen, with the variance of the intensity map $\mathrm{VAR}\left[\xi_{\underline{x,y},M}\right]$. In this case, the majority of the variance arises from the variation of the beam due to the specimen. Consequently, we can simplify our noise model in Eq. (38) for normalized spectra in lateral directions, assuming sub-channel energy alignment and a suitable gain reference with a sufficiently low uncertainty k_{ref}. We obtain the simplification for an applied noise model in lateral directions by replacing $\mu_i = \hat{s}_{x,y,i}$ with the original expression (see Eq. (36)):

$$\xi^*_{A,\underline{x,y},i} \approx \frac{g \cdot \beta_{conv} \cdot \mu_R^2}{I} \cdot \mathcal{P}\left[\frac{I \cdot \hat{s}_{x,y,i}}{g \cdot \beta_{conv} \cdot \mu_R^2}\right] + \mathcal{N}\left[0, \Theta_{N,\underline{x,y},i}\right] \quad , \tag{45}$$

$$\text{with} \quad \Theta_{N,\underline{x,y},i} \approx \frac{\sigma^2_{Int}}{4I^2} \cdot \frac{g \cdot \beta_{conv} \cdot \mu_R^2}{I} \cdot \hat{s}_{x,y,i} + k^2_{N,\underline{x,y},i} \cdot \hat{s}^2_{x,y,i} + \frac{\left(1 + \frac{\sigma^2_{Int}}{I^2}\right) \cdot \mu_R^2 \cdot \left(1 + \frac{\varphi}{A}\right) \cdot \beta_D \cdot \sigma^2_{D,i}}{I^2} \quad ,$$

$$\text{and} \quad k^2_{N,\underline{x,y},i} \approx \frac{\left(1 + \frac{\sigma^2_{Int}}{4I^2}\right) \cdot g \cdot I \cdot \sum_{h \neq i}^{M} \hat{s}_{x,y,h} + \left(1 + \frac{\sigma^2_{Int}}{I^2}\right) \cdot \sigma^2_{D,R}}{I^2} \quad ,$$

which includes the overall uncertainty of the normalization $k^2_{Norm,i}$. Similarly, we obtain a simplification for the unnormalized EELS maps in lateral directions:

$$\xi_{\underline{x,y},i} \approx g \cdot \beta_{conv} \cdot \mathcal{P}\left[\frac{I \cdot \hat{s}_{x,y,i}}{g \cdot \beta_{conv}}\right] + \mathcal{N}\left[0, \frac{\sigma^2_{src}}{4S^2} \cdot \left(I \cdot \hat{s}_{x,y,i}\right)^2 + \left(1 + \frac{\varphi}{A}\right) \cdot \beta_D \cdot \sigma^2_{D,i}\right] \quad , \tag{46}$$

with the beam source variation $\frac{\sigma^2_{src}}{S^2}$, which solely accounts for the deviation of $S_{src,el,x,y}$, as opposed to the beam intensity variation $\frac{\sigma^2_{Int}}{I^2}$, which also encompasses the variations in transmittance $T_{x,y}$ of the specimen. However, when evaluating the noise variance in vacuum we find $\frac{\sigma^2_{Int}}{I^2} = \frac{\sigma^2_{src}}{I^2}$. For measurements performed on specimen $\frac{\sigma^2_{src}}{I^2}$ is not readily determined, as it depends on the current state of the microscope. Therefore, it may be advantageous to normalize the data, allowing all parameters to be determined, which in term enables the establishment of a well-defined noise model. Accordingly, we recommend the use of Eq. (45) instead of Eq. (46).

Based on our results in Fig. 5(b), we can also simplify the noise model in energy direction by omitting insignificant noise terms:

$$\xi^*_{A,x,y,\underline{i}} \approx \frac{g \cdot \beta_{conv} \cdot \beta_{corr} \cdot \mu_R^2}{I} \cdot \mathcal{P}\left[\frac{I \cdot \hat{s}_{x,y,i}}{g \cdot \beta_{conv} \cdot \beta_{corr} \cdot \mu_R^2}\right] + \mathcal{N}\left[0, \Theta_{N,x,y,\underline{i}}\right] \quad , \tag{47}$$

$$\text{with} \quad \Theta_{N,x,y,\underline{i}} \approx \frac{\sigma^2_{Int}}{4I^2} \cdot \frac{g \cdot \beta_{conv} \cdot \beta_{corr} \cdot \mu_R^2}{I} \cdot \hat{s}_{x,y,i} + k^2_{N,x,y,\underline{i}} \cdot \hat{s}^2_{x,y,i} + \frac{\left(1 + \frac{\sigma^2_{Int}}{I^2}\right) \cdot \mu_R^2 \cdot \left(1 + \frac{1}{A}\right) \cdot \beta_D \cdot \sigma^2_{D,i}}{\left(I \cdot \sum_i^M \hat{s}_{x,y,i}\right)^2} \quad ,$$

$$\text{and} \quad k^2_{N,x,y,\underline{i}} \approx \frac{\left(1 + \frac{\sigma^2_{Int}}{4I^2}\right) \cdot g \cdot I \cdot \sum_{h \neq i}^{M} \hat{s}_{x,y,h} + \left(1 + \frac{\sigma^2_{Int}}{I^2}\right) \cdot \left(1 + \frac{1}{A}\right) \cdot \sigma^2_{D,R}}{I^2} \quad .$$

In Fig. 6, we evaluate the performance of both the normalized and the unnormalized noise models for the lateral directions. The upper row Fig. 6(a-c) demonstrates the applicability of Eq. (46) for the unnormalized EELS maps, while the lower row Fig. 6(d–f) demonstrates the applicability of Eq. (45) for the normalized EELS maps. In Fig. 6(a) we used the first three spectra from Fig. 5(a), which correspond to the shortest acquisition times of $t_{acq.} = 5 \cdot 10^{-5}$ s to $2 \cdot 10^{-4}$ s. Rather than measuring the mean value per channel, we analyzed the variance to facilitate a comparison with our noise model across several acquisition times. The red lines represent the noise model without accounting for beam variations; in contrast, the green lines represent the model with beam variations, we fitted to the experimental data, revealing a decrease in σ_{Int}/I for an increase in acquisition time. This outcome is not unsuspected, as increased acquisition time leads to a regression towards the mean of the beam currents, which is an anticipated result. In Fig. 6(b) for $t_{acq.} = 1 \cdot 10^{-4}$ s and (c) $t_{acq.} = 2 \cdot 10^{-4}$ s, we organized the variances by their mean channel value to generate mean–variance plots, allowing for a straightforward assessment of the linearity of the data. To distinguish between left and right side of the ZLP, we employed distinct color shades. We display the expected noise variance from Eq. (46), with the parameters shown in the previous figures, in black for the left and in red for the right side of the ZLP, assuming negligible beam variances as $\frac{\sigma^2_{Int}}{I^2} = 0$. It is readily apparent that the model deviates from a linear behavior at higher intensities, indicating beam deviations cannot be neglected. However, in the lower count regime, a linear behavior is observed, which agrees well with the estimated smoothing of the Poisson noise for interpolated spectra (see Fig. 3(e)) and the corresponding offset due to the smoothed detector noise (see Fig. 4(a)). In dark/bright green we display the expected noise variance from Eq. (46); in contrast to the black/red line, we fitted the beam variance $\frac{\sigma^2_{Int}}{I^2}$ to the experimental data, which shows a good agreement. However, fitting the beam variation is a poor predictor of the validity of the noise model, as the fit could also account for unknown noise contributions – a reliable noise model must be self-consistent. We therefore present the last two spectra from Fig. 5(a), which have the longest acquisition times of $t_{acq.} = 5 \cdot 10^{-4}$ s and $1 \cdot 10^{-3}$ s, normalized with respect to their summed intensity, as shown in Fig. 6(f). In the lower row Fig. 6(d–f), we display the variances predicted by the noise model in Eq. (45). In contrast to the upper row, we observe lower normalized variances for longer acquisition times, which is a result of the normalization applied in (d). For (e) $t_{acq.} = 5 \cdot 10^{-4}$ s and (f) $t_{acq.} = 1 \cdot 10^{-3}$ s, we again organized the channels by their respective mean values

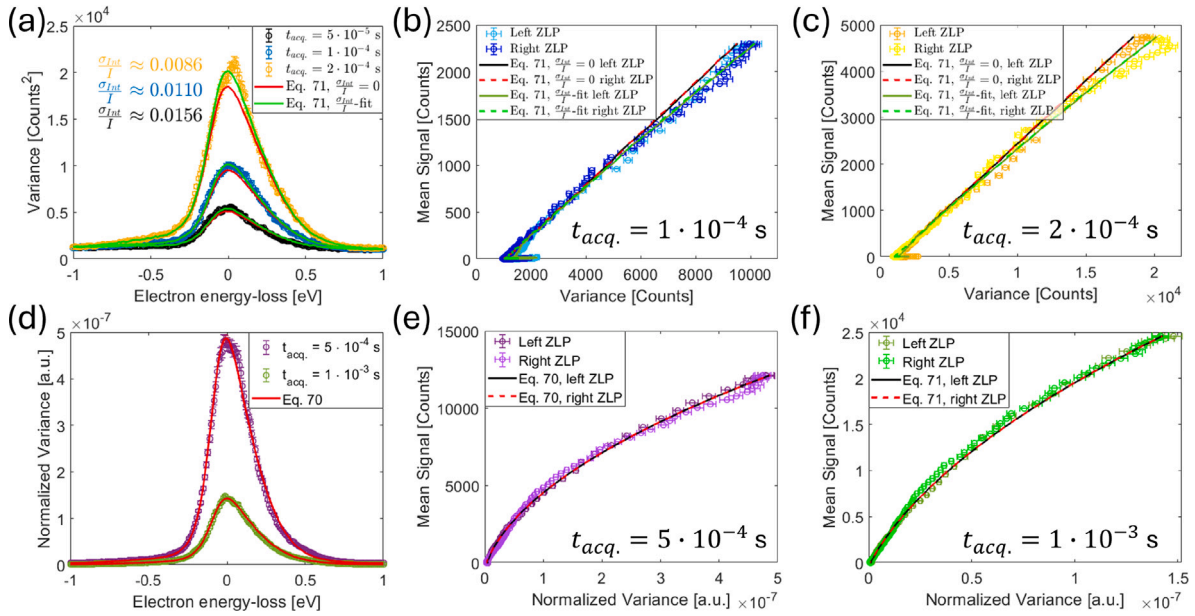

Fig. 6. **(a)** The graphs display the experimental data for the noise variance per EEL channel with increasing acquisition time ranging from $t_{acq.} = 5 \cdot 10^{-5}$ s to $2 \cdot 10^{-4}$ s, similar to the inset in Fig. 5(a), which shows the mean value per channel. The red lines represent our noise model for the unnormalized EELS maps (see Eq. (46)), were we neglected the influence of the beam variance. The green line represents the noise model with the beam variance fitted to the data, revealing a significant change in the results with acquisition time. To demonstrate the applicability of the noise model, we sorted the channels by their respective mean values, shown in **(b)** for $t_{acq.} = 1 \cdot 10^{-4}$ s and **(c)** for $t_{acq.} = 2 \cdot 10^{-4}$ s. Also, we maintained the color scheme from (a), but differentiated between the mean values on the left and on the right side of the ZLP, which are represented by differently shaded data points. In both (b) and (c), we display the estimates from the noise model, represented by black lines (for left side of the ZLP) and red lines (right side) without beam variation, and by darker green lines (left side) and lighter green lines (right side) with the beam variation values obtained in (a). Both (b) and (c) suggest that the beam variance cannot be easily neglected, as there is a significant discrepancy between the unfitted noise model and the experimental data, while the fitted noise model exhibits a good fit. Since the beam variation changes between measurements, we normalized each spectrum with respect to the sum of the total intensity and then determined the channel variance, as shown in **(d)** for $t_{acq.} = 5 \cdot 10^{-4}$ s and $1 \cdot 10^{-3}$ s. In contrast to (a), we observe that the normalized variance to decreases with increasing acquisition time. Here, we display our noise model for normalized EELS maps (see Eq. (45)) as red lines. In **(e)** and **(f)** we again sorted the normalized variances by the respective mean values, similar to (b) and (c). We observe a good fit of our intensity normalized noise model to the normalized data.

to generate the mean–variance plots. Upon normalizing the spectra by their total intensity, without further fitting, we observe good agreement between the prediction of the noise model and the experimental data in both cases, indicating that the noise model is indeed valid. In Fig. 6(d–f), we present the normalized noise model only for the longer acquisition times, due to the normalization requirement $k_{A,x,y,M} < 0.05$, as explained in Section 3.1.3. Furthermore, we observe small discrepancies between data points on the left and right side of the ZLP with similar mean values, which are likely caused by beam instabilities.

With this framework, we are unable to demonstrate the validity of the noise model in energy direction from Eq. (47), as the signal is inhomogeneous and forms the ZLP, rendering it impossible to quantify the noise precisely enough using standard deviation or variance. However, our experimental results in [34] have demonstrated that the underlying theory of Eq. (47) is highly accurate. Given that the noise model in lateral directions accurately fits the data and the expected noise in energy direction is similar, there is little reason to question the validity in energy direction, even without explicit demonstration.

As a final step, we must determine a global uncertainty for measuring a voxel (x, y, i) within a normalized EELS data cube, which involves combining the uncertainties of both noise models in the respective directions from Eq. (47) and from Eq. (45), following a similar approach to that used in Eq. (24).

In fact, the noise models in energy direction from Eq. (47) and the lateral noise model from Eq. (45) exhibit strong similarities. However, the Poisson noise contribution of the lateral directions is slightly larger than that in energy direction, due to the absence of additional smoothing from β_{corr}. Regarding the detector noise contributions, we observe that the noise in energy direction is slightly larger, since $\varphi \leq 1$ and $\left(1 + \frac{1}{A}\right) > 1$. Consequently, the noise model for measuring an individual voxel within an EELS data cube can be expressed as:

$$\xi^*_{A,x,y,i} \approx \frac{g \cdot \beta_{conv} \cdot \mu_R^2}{I} \cdot \mathcal{P}\left[\frac{I \cdot \hat{s}_{x,y,i}}{g \cdot \beta_{conv} \cdot \mu_R^2}\right] + \mathcal{N}\left[0,\, \Theta_{N,x,y,i}\right] \quad , \tag{48}$$

$$\text{with} \quad \Theta_{N,x,y,i} \approx \frac{\sigma_{Int}^2}{4I^2} \cdot \frac{g \cdot \beta_{conv} \cdot \mu_R^2}{I} \cdot \hat{s}_{x,y,i} + k^2_{N,x,y,i} \cdot \hat{s}^2_{x,y,i} + \frac{\left(1 + \frac{\sigma_{Int}^2}{I^2}\right) \cdot \mu_R^2 \cdot \left(1 + \frac{1}{A}\right) \cdot \beta_D \cdot \sigma^2_{D,i}}{I^2} \quad ,$$

$$\text{and} \quad k^2_{N,x,y,i} \approx \frac{\left(1 + \frac{\sigma_{Int}^2}{4I^2}\right) \cdot g \cdot I \cdot \sum_{h \neq i}^{M} \hat{s}_{x,y,h} + \left(1 + \frac{\sigma_{Int}^2}{I^2}\right) \cdot \left(1 + \frac{1}{A}\right) \cdot \sigma^2_{D,R}}{I^2} \quad ,$$

where $\hat{s}_{x,y,i}$ denotes the expected loss probability for a given EEL channel i at position (x, y) on the EELS map. Here, g is the gain of the detector, β_{conv} describes the smoothing of the Poisson noise by convolution with the detector PSF, and I denotes the mean intensity of the intensity map $\mathcal{I}_{x,y}$. Additionally, μ_R (see Eq. (36)) originates from the fact that the original noise of a given EEL channel is also incorporated in the intensity

normalization (see Appendices A.2 and A.3), which is defined as the sum over all EEL channels $\sum_i^M \hat{s}_{x,y,i}$. We also have the variance of the intensity map σ^2_{Int}, the detector noise variance $\sigma_{D,i}$, the number of averaged background frames A to be subtracted from the signal, and the smoothing of the detector noise by interpolation $\beta_D \approx 0.66$, as derived and discussed in Section 3.1.1. Finally, we have the uncertainty of the intensity normalization $k_{N,x,y,i}$, which includes the summed detector noises $\sigma_{D,R}$, representing the sum of detector noises of all EEL channels except the one in question.

5. Conclusions

In this paper, we have investigated the noises present in EELS and EELS maps recorded with a camera mounted on a scanning transmission electron microscope. The noise model to be described therein has been shown to be valid for scintillation-based CCD detectors and is expected to be applicable to direct electron detectors (DED) as well. For single EEL spectra (see Eq. (16)), the first noise contribution is the Gaussian distributed detector noise, whose variance doubles due the to background subtractions required to eliminate detector offsets. The variance of the detector noise varies from channel to channel due to differences in the detector electronics. Upon applying a gain normalization to account for quantum efficiency deviations on the detector, the channel variances also change.

The second major contribution is the Poisson distributed signal noise, which is dependent on the signal strength. Due to the conversion of incident beam electrons into counts, which are received as output from the microscope, the Poisson distribution is modified by a gain factor. The signal is also broadened by the detector point spread function, resulting in correlation effects in the noise between neighboring EEL channels. These correlation effects lead to a smoothing of the signal noise.

Based on the autocovariance function of homogeneously illuminated TEM images, we can describe the correlation in regular 2D images using the Pearson correlation coefficients, as previously explained in [34]. The present paper extends these descriptions and demonstrates how correlations change when calculating 1D spectra from 2D images, as is typically performed in EELS. We demonstrate that this operation significantly reduces the noise correlation and provide a theoretical description of the change. Furthermore, we present a method for estimating the total gain of the detector based on the correlation coefficients and the general property of the Poisson noise, which has equal expectation values of the signal and variance. This enables the application of our noise model to detectors without electron-to-count calibration.

Additional contributions to the noise, in the form of fixed-pattern noise induced by the uncertainty of the gain reference, are mathematically characterized (see Eq. (17)) and experimentally verified to be negligible. Owing to the inhomogeneity of the EELS signal, it is not possible to directly determine the signal noise within a single EEL spectrum by using standard deviation and variance. However, with a relatively stable ZLP, it is possible to measure signal noises between consecutively measured spectra, assuming a constant expectation value of the signal within each respective EEL channel. This assumption enables us to evaluate signal noises in the first place, provided that the energy drift between consecutive spectra is minimized.

To measure the signal noise, we had to further extended the EELS noise model to accommodate the requirements of EELS mapping (see Eq. (22)). However, both energy misalignment of the ZLP and deviations in the beam current are big contributors to the overall noise between spectra and must be taken into account. We conclude that, due to these deviations, a separate noise model is necessary to describe the deviations between spectra that differs from the EELS noise model in energy direction.

We have experimentally tested several methods of energy realignment and found that the uncertainty of alignment is dependent on the first derivative of the signal in energy direction (see Eq. (29)). The standard method employed by '*Gatan Digital Micrograph*', namely the cross-correlation method, results in an uncertainty with an expected standard deviation of approximately 0.25 channels, which we have derived theoretically and confirmed experimentally. This is due to the fact that sub-channel drifts cannot be corrected by this method alone. By fitting a Gaussian to the cross-correlation function used for the energy alignment, we can estimate the sub-channel drift and determine it to be continuous. The residual sub-channel drift can be corrected by interpolating the respective spectra. We demonstrate that this alignment operation minimizes the noise between spectra to the extend that no uncertainty misalignment can be measured, which strongly suggests the success of the method.

Interpolation, however, affects all other noise components. Since interpolation can be considered as an additional convolution applied to the noises, as shown in Eq. (26), it smooths signal and detector noises to varying degree. This is because the detector noise is largely uncorrelated, whereas the signal noise is already affected by a convolution with the detector point spread function. Consequently, interpolation results in a more pronounced smoothing of detector noise compared to signal noise.

To mitigate the effect of beam current fluctuations, we normalized all spectra within an EELS map by the sum of all counts within the respective spectrum. We discussed three criteria for the success of such a normalization: First, for normalization to be effective, it is essential that the spectrum encompasses a high percentage of the overall loss probabilities, or that the loss probabilities remain constant across the entire EELS map, thereby preserving the proportions between spectra. From this, we concluded that in low-loss spectra, which do not fully encompass the bulk plasmons of all materials within the specimen, an artificial overestimation of materials with a high plasmonic resonance is expected. This results in an overestimation of e.g. surface plasmonic peaks of metals in comparison to those of semiconductor or organic substrates. The second criterion is that, to normalize a specific EEL channel, sufficient intensity is required in all other EEL channels. The third criterion is that the uncertainty of the total intensity (see Appendix A.2 Eq. (62)) must be sufficiently small (standard deviation below 5%) for the mathematical model to yield precise results.

When using intensity normalized EELS maps, an additional noise term is introduced, which depends on the uncertainty of the total intensity of the spectra. This uncertainty is primarily determined by the detector noises and the Poisson noise of the total signal. Furthermore, we find that deviations in the total intensity of a spectrum, naturally induced by specimen, must be taken into account and contribute to an increase of the overall noise of all respective noise terms.

We omit additional contributions for sub-pixel aligned spectra such as uncertainties in linear interpolation and the uncertainty of alignment, as they are all below the detector read-out noise. By omitting these minor contributions, we can combine the noise models in energy direction with those in lateral directions, thereby deriving an uncertainty model for an individual voxel within the normalized EELS data cube (see Eq. (48)).

For DEDs, some modifications to the noise contributions are necessary to account for differences in the acquisition process. However, the applicability of the proposed noise model to DEDs appears straightforward, but its validity remains to be experimentally verified. We hope that this noise model will find widespread application in estimating uncertainties in EELS and enable better deconvolution results with well-suited deconvolution algorithms. To this end, we provide methods for determining all necessary factors for the most important noise contributions, which can be used as input parameters for the noise model. This enables the measurement of noise parameters on any EELS detector, making this noise model widely applicable to everyone.

An example of applying this noise model in conjunction with the '*alternating direction method of multipliers*' (ADMM) deconvolution algorithm will be presented in a forthcoming article [55].

CRediT authorship contribution statement

Christian Zietlow: Writing – original draft, Visualization, Validation, Software, Methodology, Investigation, Formal analysis, Data curation. **Jörg K.N. Lindner:** Writing – review & editing, Supervision, Resources, Project administration, Conceptualization.

Declaration of competing interest

The authors declare that they have no known competing financial interests or personal relationships that could have appeared to influence the work reported in this paper.

Appendix

A.1. Uncertainty of interpolation

Linear interpolation itself has limitations in terms of precision when reconstructing the signal. Typically, the error bounds for a polynomial interpolation of degree n are given as [56]:

$$E_n\left(\hat{S}_{c,x,y,i}\right) = \frac{f^{n+1}\left(\hat{S}_{c,x,y,i}\right)}{(n+1)!} \cdot \left(\hat{S}_{c,x,y,i+1} - \hat{S}_{c,x,y,i}\right)^{n+1} \longrightarrow E_1\left(\hat{S}_{c,x,y,i}\right) = \mathcal{I}_{x,y} \cdot \frac{d^2}{di^2}\frac{\hat{s}_{x,y,i}}{2} \cdot \Delta^2 \,, \tag{49}$$

which leads to the expected uncertainty for linear interpolation with $n = 1$, as shown on the right-hand side of the above equation. By considering a continuous distribution of the interpolation shift Δ and by integrating $\int_{-0.5}^{0.5} d\Delta\, |\Delta|^2 = \frac{1}{12}$ one finds the expectation value for the interpolation error as $E_1\left(\hat{S}_{c,x,y,i}\right) \approx \mathcal{I}_{x,y} \cdot \frac{d^2}{di^2}\frac{\hat{s}_{x,y,i}}{2} \cdot \frac{1}{12}$. Therefore, the uncertainty of the interpolation can be expressed as:

$$\sigma^2_{Inter} = \left(\frac{1}{24} \cdot \mathcal{I}_{x,y} \cdot \frac{d^2}{di^2}\hat{s}_{x,y,i}\right)^2 \,. \tag{50}$$

Since the uncertainty of interpolation is given as the second derivative of the signal, it is significantly smaller than the uncertainty of the alignment depending on the first derivative of the signal. However, the uncertainty of interpolation provides a lower bound on a general realignment error.

A.2. The intensity map

For the derivation of the noise model for the intensity map, we need a formula for the square root of a Gaussian distribution in addition to the formulas described in Section 2. The square root of a Gaussian distribution can be found by applying the well-known rules of uncertainty propagation [57], which employ a Taylor expansion to derive:

$$\sqrt{\mathcal{N}\left[\mu\,,\,\sigma^2\right]} \approx \mathcal{N}\left[\sqrt{\mu}\,,\,\frac{\sigma^2}{4\mu}\right] \,. \tag{51}$$

We provide an alternative derivation in the appendix Appendix A.4, which demonstrates that the distribution remains Gaussian for sufficiently large μ compared to the variance σ^2.

We start with the noise model in lateral directions and find it similar to Eq. (30) as:

$$\xi_{A,\underline{x,y},R} \approx g \cdot \mathcal{P}\left[\frac{\mathcal{I}_{x,y}\sum_{h\neq i}^{M}\hat{s}_{x,y,h}}{g}\right] + \mathcal{N}\left[0\,,\,\Theta^2_{A,\underline{x,y},R}\right] \quad \text{, with} \quad \Theta^2_{A,\underline{x,y},R} = \sum_{h\neq i}^{M}\Theta^2_{A,\underline{x,y},h} \quad \text{and} \tag{52}$$

$$\Theta^2_{A,\underline{x,y},R} = \alpha_R \cdot \varphi_R \cdot k^2_{ref,R} \cdot \left(\mathcal{I}_{x,y} \cdot \sum_{h\neq i}^{M}\hat{s}_{x,y,h}\right)^2 + k^2_{ref,R} \cdot g \cdot \left(\mathcal{I}_{x,y} \cdot \sum_{h\neq i}^{M}\hat{s}_{x,y,h}\right) + \sigma^2_{D,R} \,.$$

with the modified uncertainty of the gain reference $k^2_{ref,M} \to k^2_{ref,R}$, the summed detector noise of all remaining EEL channels $\sigma^2_{D,M} \to \sigma^2_{D,R}$, with $\sigma^2_{D,R} \approx \sigma^2_{D,M} - \sigma^2_{D,i}$, the distribution factor of the remaining EEL channels α_R (similar to Eq. (31)) and the overlap factor of the remaining EEL channels φ_R for the fixed-pattern noise (similar to Eq. (32)):

$$\alpha_R \approx \alpha \cdot \frac{1}{X \cdot Y}\sum_{x,y}^{X,Y}\sum_{h\neq i}^{M}\left(\frac{\xi_{x,y,h}}{\xi_{x,y,R}}\right)^2 \quad \text{and} \quad \varphi_R \approx \frac{1}{XY\,(XY-1)}\sum_{x,y}^{X,Y}\sum_{x',y'}^{X,Y}\sum_{h\neq i}^{M}\left|\frac{\xi_{x,y,h}}{\xi_{Int,x,y}} - \frac{\xi_{x',y',h}}{\xi_{Int,x',y'}}\right| \text{, with } (x',y') > (x,y) \quad . \tag{53}$$

By approximating the Poisson distributed component by a Gaussian normal distribution for high counts (see Eq. (6)) and factoring out (see Eq. (2)) the total counts $\mathcal{I}_{x,y}\cdot\sum_i^M \hat{s}_{x,y,i}$, we find the overall probability to obtain a representation of the summed intensities by measurement $\xi_{A,\underline{x,y},M} \to \zeta_{A,\underline{x,y},M}$ resembling the intensity map $\mathcal{I}_{x,y}$ as:

$$Pr\left[\zeta_{A,\underline{x,y},M} = \mathcal{I}_{x,y} \cdot \left(\zeta_{A,\underline{x,y},R} + \zeta_{A,\underline{x,y},i}\right)\right] \approx \left(\mathcal{I}_{x,y} \cdot \sum_{i}^{M}\hat{s}_{x,y,i}\right) \cdot \left(\mathcal{N}\left[\mu_R\,,\,k^2_{Int,R}\right] + \mathcal{N}\left[\mu_i\,,\,k^2_{Int,i}\right]\right) \quad \text{, with} \tag{54}$$

$$\mu_R = \frac{\sum_{h\neq i}^{M}\hat{s}_{x,y,h}}{\sum_i^M \hat{s}_{x,y,i}} \quad \text{and} \quad k^2_{Int,R} = \frac{g\cdot\mathcal{I}_{x,y}\cdot\sum_{h\neq i}^{M}\hat{s}_{x,y,i} + \Theta^2_{A,\underline{x,y},R}}{\left(\mathcal{I}_{x,y}\cdot\sum_i^M \hat{s}_{x,y,h}\right)^2} \quad , \tag{55}$$

$$\mu_i = \frac{\hat{s}_{x,y,i}}{\sum_i^M \hat{s}_{x,y,i}} \quad \text{and} \quad k^2_{Int,i} = \frac{g\cdot\beta_{conv}\cdot\mathcal{I}_{x,y}\cdot\hat{s}_{x,y,i} + \Theta^2_{A,\underline{x,y},i}}{\left(\mathcal{I}_{x,y}\cdot\sum_i^M \hat{s}_{x,y,i}\right)^2} \quad . \tag{56}$$

By measuring EEL spectra and their respective sums, we collapse the probability distributions for the lateral directions into an actual representation, denoted as $\zeta_{A,\underline{x,y},i}$, in which the noises are fixed. This is of significant importance for Section 3.1.3. We obtain the realized values from the Gaussian

normal distributions, characterized by the mean values μ_R and μ_i as well as the uncertainties associated with the intensity normalization $k^2_{Int,R}$ and $k^2_{Int,I}$, multiplied by the sum of the loss probabilities $\sum_i^M \hat{s}_{x,y,i}$.

The EELS map $\mathcal{I}_{x,y}$ can exhibit variations between positions due to fluctuations in the beam current or differences in specimen transmittance. We can roughly approximate the intensity map using a Gaussian, such that $\mathcal{I}_{x,y} \approx I \cdot \mathcal{N}\left[1, \frac{\sigma^2_{Int}}{I^2}\right]$, which varies with a standard deviation σ_{Int} around a mean value I. We can further use Eq. (3) to decompose the normal distribution Eq. (54) into parts depending on $\mathcal{I}_{x,y}$ in the denominator, parts depending on $\mathcal{I}^2_{x,y}$ and parts that are independent on the intensity. By inversely applying the multiplication with a scalar (see Eq. (2)), the square root of a Gaussian distributed random variable Eq. (51) and the multiplication of Gaussian distributed random variables Eq. (4), the uncertainties of the intensity normalization including the beam current variations are obtained. We denote these as $k^2_{A,\underline{x,y},R}$ and $k^2_{A,\underline{x,y},i}$ for the uncertainties of the respective beam intensity parts and the combined uncertainty $k^2_{A,\underline{x,y},M}$. Assuming $\sum_i^M \hat{s}_{x,y,i} \approx 1$, these uncertainties can be expressed as:

$$k^2_{A,\underline{x,y},M} \approx \frac{\left(1+\frac{\sigma^2_{Int}}{4\cdot I^2}\right)\cdot\left(1+k^2_{ref,M}\right)\cdot g}{I} + \frac{\left(1+\frac{\sigma^2_{Int}}{I^2}\right)\cdot\sigma^2_{D,M}}{I^2} + \alpha_M\cdot\varphi_M\cdot k^2_{ref,M}\,, \tag{57}$$

$$k^2_{A,\underline{x,y},R} \approx \frac{\left(1+\frac{\sigma^2_{Int}}{4\cdot I^2}\right)\cdot\left(1+k^2_{ref,R}\right)\cdot g}{I}\cdot\sum_{h\neq i}^{M}\hat{s}_{x,y,h} + \frac{\left(1+\frac{\sigma^2_{Int}}{I^2}\right)\cdot\sigma^2_{D,R}}{I^2} + \alpha_R\cdot\varphi_R\cdot k^2_{ref,R}\cdot\left(\sum_{h\neq i}^{M}\hat{s}_{x,y,h}\right)^2\,, \tag{58}$$

$$k^2_{A,\underline{x,y},i} \approx \frac{\left(1+\frac{\sigma^2_{Int}}{4\cdot I^2}\right)\cdot\left(1+k^2_{ref}\right)\cdot\beta_{conv}\cdot g}{I}\cdot\hat{s}_{x,y,i} + \frac{\left(1+\frac{\sigma^2_{Int}}{I^2}\right)\cdot\left(1+\frac{\varphi}{A}\right)\cdot\beta_D\cdot\sigma^2_{D,i}}{I^2} + \alpha\cdot\varphi\cdot\beta_{FP}\cdot k^2_{ref}\cdot\hat{s}^2_{x,y,i}\,. \tag{59}$$

If $\sum_i^M \hat{s}_{x,y,i} \approx \text{const.}$, then the constant can be incorporated as an additional factor into the mean intensity I, effectively reducing it. By applying the inverse of the Gaussian distribution in Eq. (5), we can express the actual representation of the intensity map denoted as $\zeta_{A,\underline{x,y},M}$ from Eq. (54) as:

$$\zeta_{A,\underline{x,y},M} = \mathcal{I}_{x,y}\cdot\left(\zeta_{A,\underline{x,y},R}+\zeta_{A,\underline{x,y},i}\right),\ \text{with}\quad \zeta_{A,\underline{x,y},R} \in \mathcal{N}\left[\mu_R\,,\,k^2_{A,\underline{x,y},R}\right] \in [0\,,\,\infty)\,, \tag{60}$$

$$\text{and}\quad \zeta_{A,\underline{x,y},i} \in \mathcal{N}\left[\mu_i\,,\,k^2_{A,\underline{x,y},i}\right] \in [0\,,\,\infty)\,, \tag{61}$$

$$\text{and thus}\quad \zeta_{A,\underline{x,y},M} \in \mathcal{I}_{x,y}\cdot\mathcal{N}\left[1\,,\,k^2_{A,\underline{x,y},M}\right] \in [0\,,\,\infty)\,. \tag{62}$$

Accordingly, we adjust the factors μ_R and μ_i to account for $\sum_i^M \hat{s}_{x,y,i} \approx 1$:

$$\mu_R = \sum_{h\neq i}^{M}\hat{s}_{x,y,h} \quad\text{and}\quad \mu_i = \hat{s}_{x,y,i}\,. \tag{63}$$

Following the same line of argumentation, we obtain the uncertainties of the intensity map in energy direction as:

$$k^2_{A,x,y,\underline{M}} \approx \frac{\left(1+\frac{\sigma^2_{Int}}{4\cdot I^2}\right)\cdot\left(1+k^2_{ref,M}\right)\cdot g}{I} + \frac{\left(1+\frac{\sigma^2_{Int}}{I^2}\right)\cdot\left(1+\frac{1}{A}\right)\cdot\sigma^2_{D,M}}{I^2} + \alpha_M\cdot k^2_{ref,M}\,, \tag{64}$$

$$k^2_{A,x,y,\underline{R}} \approx \frac{\left(1+\frac{\sigma^2_{Int}}{4\cdot I^2}\right)\cdot\left(1+k^2_{ref,R}\right)\cdot g}{I}\cdot\sum_{h\neq i}^{M}\hat{s}_{x,y,h} + \frac{\left(1+\frac{\sigma^2_{Int}}{I^2}\right)\cdot\left(1+\frac{1}{A}\right)\cdot\sigma^2_{D,R}}{I^2} + \alpha_R\cdot k^2_{ref,R}\cdot\left(\sum_{h\neq i}^{M}\hat{s}_{x,y,h}\right)^2\,, \tag{65}$$

$$k^2_{A,x,y,\underline{i}} \approx \frac{\left(1+\frac{\sigma^2_{Int}}{4\cdot I^2}\right)\cdot\left(1+k^2_{ref}\right)\cdot\beta_{conv}\cdot\beta_{corr}\cdot g}{I}\cdot\hat{s}_{x,y,i} + \frac{\left(1+\frac{\sigma^2_{Int}}{I^2}\right)\cdot\left(1+\frac{\varphi}{A}\right)\cdot\beta_D\cdot\sigma^2_{D,i}}{I^2} + \alpha\cdot\beta_{FP}\cdot k^2_{ref}\cdot\hat{s}^2_{x,y,i}\,, \tag{66}$$

from which we derive the probabilities of obtaining an actual representation of the intensity map $\zeta_{A,x,y,\underline{M}}$:

$$\zeta_{A,x,y,\underline{M}} = \mathcal{I}_{x,y}\cdot\left(\zeta_{A,x,y,\underline{R}}+\zeta_{A,x,y,\underline{i}}\right),\ \text{with}\quad \zeta_{A,x,y,\underline{R}} \in \mathcal{N}\left[\mu_R\,,\,k^2_{A,x,y,\underline{R}}\right] \in [0\,,\,\infty)\,, \tag{67}$$

$$\text{and}\quad \zeta_{A,x,y,\underline{i}} \in \mathcal{N}\left[\mu_i\,,\,k^2_{A,x,y,\underline{i}}\right] \in [0\,,\,\infty)\,, \tag{68}$$

$$\text{and thus}\quad \zeta_{A,x,y,\underline{M}} \in \mathcal{I}_{x,y}\cdot\mathcal{N}\left[1\,,\,k^2_{A,x,y,\underline{M}}\right] \in [0\,,\,\infty)\,. \tag{69}$$

In general, it can be stated that the higher the signal intensity measured by the detector, the lower the uncertainty of the intensity map will be.

A.3. Derivation of the normalized noise

We can rewrite the denominator of Eq. (37) as:

$$\frac{\left(\sum_i^M \hat{s}_{x,y,i}\right)\cdot\mathcal{N}\left[\mu_R\,,\,k^2_{A,\underline{x,y},R}\right]}{\left(\sum_i^M \hat{s}_{x,y,i}\right)\cdot\mathcal{N}\left[\mu_i\,,\,k^2_{A,\underline{x,y},i}\right]} + 1 \approx \mathcal{N}\left[\frac{\mu_R}{\mu_i}+1\,,\,\mu^2_R\cdot k^2_{A,\underline{x,y},i} + \mu^2_i\cdot k^2_{A,\underline{x,y},R} + k^2_{A,\underline{x,y},R}\cdot k^2_{A,\underline{x,y},i}\right]\,, \tag{70}$$

by utilizing the inverse of a Gaussian random variable (see Eq. (5)) and the property of multiplication of Gaussian random variables (see Eq. (4)). Since the above expression is found in the denominator, we apply the inverse of a Gaussian (see Eq. (5)) and find with $\mu_R + \mu_i = 1$ that:

$$\begin{aligned}\frac{\xi_{A,\underline{x,y},i}}{\xi_{A,\underline{x,y},M}} &\approx \mathcal{N}\left[\mu_i\,,\,\mu_R^2\cdot k^2_{A,\underline{x,y},i} \;+\; \mu_i^2\cdot k^2_{A,\underline{x,y},R} \;+\; k^2_{A,\underline{x,y},R}\cdot k^2_{A,\underline{x,y},i}\right]\\ &\approx \mathcal{N}\left[\mu_i\,,\,\mu_R^2\cdot k^2_{A,\underline{x,y},i}\right] + \mathcal{N}\left[0\,,\,\mu_i^2\cdot k^2_{A,\underline{x,y},R}\right] \quad ,\end{aligned} \tag{71}$$

which we can split into separate normal distributions according to the summation rule in Eq. (3) and neglect the term $\mathcal{N}\left[0\,,\,k^2_{A,\underline{x,y},R}\cdot k^2_{A,\underline{x,y},i}\right]$ due to its insignificance, as shown in the main manuscript. This term is referred to as the noise multiplication term there. By rewriting $\mathcal{N}\left[\mu_i\,,\,\mu_R^2\cdot k^2_{A,\underline{x,y},i}\right]$ in a form similar to Eq. (29), we obtain:

$$\mathcal{N}\left[\mu_i\,,\,\mu_R^2\cdot k^2_{A,\underline{x,y},i}\right] = \underbrace{\frac{g\cdot\beta_{conv}\cdot\mu_R^2}{I}\cdot\mathcal{P}\left[\frac{I\cdot\hat{s}_{x,y,i}}{g\cdot\beta_{conv}\cdot\mu_R^2}\right]}_{1)} + \mathcal{N}\left[0\,,\,\frac{\mu_R^2\cdot\Theta^{*2}_{A,\underline{x,y},i}}{I^2}\right] \quad \text{, with} \tag{72}$$

$$\Theta^{*2}_{A,\underline{x,y},i} \approx \underbrace{\alpha\cdot\varphi\cdot\beta_{FP}\cdot k^2_{ref}\cdot\left(I\cdot\hat{s}_{x,y,i}\right)^2}_{2)} + \underbrace{\left(k^2_{ref} + \frac{\left(1+k^2_{ref}\right)\cdot\sigma^2_{Int}}{4I^2}\right)\cdot g\cdot\beta_{conv}\cdot\left(I\cdot\hat{s}_{x,y,i}\right)}_{3)} + \underbrace{\left(1+\frac{\sigma^2_{Int}}{I^2}\right)\cdot\left(1+\frac{\varphi}{A}\right)\cdot\beta_D\cdot\sigma^2_{D,i}}_{4)} \quad .$$

We can identify four terms: 1) The first term, which we can re-transform into the initial Poisson distributed part by utilizing Eq. (6). 2) The second term, which describes the fixed-pattern noise of the gain reference. 3) A third term, which describes alterations of the Poisson noise due to the gain reference and intensity normalization and 4) a last term, which describes the read-out noise of the detector.

By further rewriting $\mathcal{N}\left[0\,,\,\mu_i^2\cdot k^2_{A,\underline{x,y},R}\right]$ in a form similar to Eq. (52), we obtain:

$$\mathcal{N}\left[0\,,\,\mu_i^2\cdot k^2_{A,\underline{x,y},R}\right] = \underbrace{\mathcal{N}\left[0\,,\,\frac{\mu_i^2\cdot g\cdot I\cdot\sum_{h\neq i}^{M}\hat{s}_{x,y,h}}{I^2}\right]}_{5)} + \mathcal{N}\left[0\,,\,\frac{\mu_i^2\cdot\Theta^{*2}_{A,\underline{x,y},R}}{I^2}\right] \quad \text{, with} \tag{73}$$

$$\Theta^{*2}_{A,\underline{x,y},R} = \underbrace{\alpha_R\cdot\varphi_R\cdot k^2_{ref,R}\cdot\left(I\cdot\sum_{h\neq i}^{M}\hat{s}_{x,y,h}\right)^2}_{6)} + \underbrace{\left(k^2_{ref,R} + \frac{\left(1+k^2_{ref,M}\right)\cdot\sigma^2_{Int}}{4I^2}\right)\cdot g\cdot\left(I\cdot\sum_{h\neq i}^{M}\hat{s}_{x,y,h}\right)}_{7)} + \underbrace{\left(1+\frac{\sigma^2_{Int}}{I^2}\right)\cdot\sigma^2_{D,R}}_{8)} \quad ,$$

Additionally, obtain four more terms: 5) A term that incorporates the Poisson signal noise of all other channels R, which cannot be transformed back into the Poisson distribution due to its mean value of zero. 6) Another term, which describes the fixed-pattern noise of the gain reference for all other channels R. 7) A term, which describes alterations of the Poisson noise of all other channels R due to the gain reference and the intensity normalization and 8) a last term, which describes the read-out noise of the detector for all other channels R. Comparing these terms with the terms 1–4), a repetition is apparent.

Eventually, we need to find a solution for the normalized uncertainty of alignment in order to complete Eq. (34). By replacing $\xi_{A,\underline{x,y},M}$ with the representation $\zeta_{A,\underline{x,y},M}$ (see Eq. (62)) and utilizing the inverse of a Gaussian (see Eq. (5)) as well as the multiplication property of Gaussian distributions (see Eq. (4)), we can rewrite:

$$\frac{\mathcal{N}\left[0\,,\,\sigma_A^2\right]}{\xi_{A,\underline{x,y},M}} = \frac{\mathcal{N}\left[0\,,\,\sigma_A^2\right]}{\mathcal{I}_{x,y}\cdot\mathcal{N}\left[1\,,\,k^2_{A,\underline{x,y},M}\right]} = \mathcal{N}\left[0\,,\,\frac{\sigma^{*2}_A}{I^2}\right] \quad \text{, with} \tag{74}$$

$$\sigma^2_{A^*} = \left(1+k^2_{A,\underline{x,y},M}\right)\cdot\left[\sigma^2_{MA}\cdot\left(I\cdot\frac{d}{di}\,\hat{s}_{x,y,i}\right)^2 + \left(\frac{1}{24}\cdot I\cdot\frac{d^2}{di^2}\,\hat{s}_{x,y,i}\right)^2\right] \quad . \tag{75}$$

Combining all the terms leads to a noise model for the lateral directions for intensity normalized EELS maps:

$$\xi^*_{A,\underline{x,y},i} = \frac{g\cdot\beta_{conv}\cdot\mu_R^2}{I}\cdot\mathcal{P}\left[\frac{I\cdot\hat{s}_{x,y,i}}{g\cdot\beta_{conv}\cdot\mu_R^2}\right] + \mathcal{N}\left[0\,,\,\frac{\mu_i^2\cdot g\cdot I\cdot\sum_{h\neq i}^{M}\hat{s}_{x,y,h}}{I^2}\right] + \mathcal{N}\left[0\,,\,\frac{\mu_R^2\cdot\Theta^{*2}_{A,\underline{x,y},i} + \mu_i^2\cdot\Theta^{*2}_{A,\underline{x,y},R} + \sigma^2_{A^*}}{I^2}\right], \tag{76}$$

where we obtain $\Theta^{*2}_{A,\underline{x,y},i}$ in Eq. (72), $\Theta^{*2}_{A,\underline{x,y},R}$ in Eq. (73), $\sigma^2_{A^*}$ in Eq. (75), with μ_R and μ_i given by:

$$\mu_R = \sum_{h\neq i}^{M}\hat{s}_{x,y,h} \quad \text{and} \quad \mu_i = \hat{s}_{x,y,i} \quad . \tag{77}$$

A.4. Square root of the Gaussian distribution

To find the square root of a Gaussian random variable, we utilize the χ^2-distribution [58–60] and its well-known square root, the χ-distribution [61,62].

$$\chi^2_\nu = \frac{x^{\nu/2-1}\exp\{-x/2\}}{2^{\nu/2}\Gamma\left[\frac{\nu}{2}\right]} \approx \mathcal{N}[\nu\,,\,2\nu] \quad \text{and} \quad \chi_\nu = \frac{x^{\nu-1}\exp\left\{-x^2/2\right\}}{2^{\nu/2-1}\Gamma\left[\frac{\nu}{2}\right]} \approx \mathcal{N}\left[\sqrt{\nu-1/2}\,,\,1/2\right] \quad \text{both for} \quad x \geq 0\,, \tag{78}$$

in the large-ν approximation, where Γ [x] represents the Gamma function of x and ν gives the degrees of freedom. So, by utilizing the approximation and rewriting the Gaussian:

$$\mathcal{N}\left[\mu\,,\,\sigma^2\right] = \frac{\sigma^2}{2\mu}\cdot\mathcal{N}\left[2\mu^2/\sigma^2\,,\,4\mu^2/\sigma^2\right] \approx \frac{\sigma^2}{2\mu}\chi^2_\nu \quad \text{with} \quad \nu = 2\mu^2/\sigma^2\,, \tag{79}$$

the square root of the Gaussian can easily be found as:

$$\sqrt{\mathcal{N}\left[\mu\,,\,\sigma^2\right]} \approx \mathcal{N}\left[\sqrt{\mu}\,,\,\frac{\sigma^2}{4\mu}\right]\,, \tag{80}$$

where we neglect the $-1/2$ term in the mean value of the resulting Gaussian for large μ to simplify the equation.

Data availability

Data will be made available on request.

References

[1] Mitsutaka Haruta, Yoshifumi Fujiyoshi, Takashi Nemoto, Akimitsu Ishizuka, Kazuo Ishizuka, Hiroki Kurata, Low count detection for EELS spectrum by reducing CCD read-out noise, Microsc. Microanal. Off. J. Microscopy Soc. Am. Microbeam Anal. Soc., Microsc. Soc. Can. 26 (S2) (2020) 1202–1204.
[2] Hayato Ikoma, Michael Broxton, Takamasa Kudo, Gordon Wetzstein, A convex 3D deconvolution algorithm for low photon count fluorescence imaging, Sci. Rep. 8 (1) (2018) 11489.
[3] Rüdiger R. Meyer, Angus Kirkland, The effects of electron and photon scattering on signal and noise transfer properties of scintillators in CCD cameras used for electron detection, Ultramicroscopy 75 (1) (1998) 23–33.
[4] Ryo Ishikawa, Andrew R. Lupini, Scott D. Findlay, Stephen J. Pennycook, Quantitative annular dark field electron microscopy using single electron signals, Microsc. Microanal. Off. J. Microscopy Soc. Am., Microbeam Anal. Soc., Microsc. Soc. Can. 20 (1) (2014) 99–110.
[5] James L. Hart, Andrew C. Lang, Asher C. Leff, Paolo Longo, Colin Trevor, Ray D. Twesten, Mitra L. Taheri, Direct detection electron energy-loss spectroscopy: A method to push the limits of resolution and sensitivity, Sci. Rep. 7 (1) (2017) 8243.
[6] Wilco Zuidema, Pieter Kruit, Transmission imaging on a scintillator in a scanning electron microscope, Ultramicroscopy 218 (2020) 113055.
[7] Barnaby D.A. Levin, Direct detectors and their applications in electron microscopy for materials science, J. Phys. Mater. 4 (4) (2021) 042005.
[8] Yves Auad, Michael Walls, Jean-Denis Blazit, Odile Stéphan, Luiz H.G. Tizei, Mathieu Kociak, Francisco de La Peña, Marcel Tencé, Event-based hyperspectral EELS: towards nanosecond temporal resolution, Ultramicroscopy 239 (2022) 113539.
[9] J. Verbeeck, G. Bertoni, Model-based quantification of EELS spectra: treating the effect of correlated noise, Ultramicroscopy 108 (2) (2008) 74–83.
[10] Alan Maigné, Matthias Wolf, Low-dose electron energy-loss spectroscopy using electron counting direct detectors, Microsc. (Oxford, England) 67 (suppl_1) (2018) i86–i97.
[11] Benjamin Plotkin-Swing, George J. Corbin, Sacha de Carlo, Niklas Dellby, Christoph Hoermann, Matthew V. Hoffman, Tracy C. Lovejoy, Chris E. Meyer, Andreas Mittelberger, Radosav Pantelic, Luca Piazza, Ondrej L. Krivanek, Hybrid pixel direct detector for electron energy loss spectroscopy, Ultramicroscopy 217 (2020) 113067.
[12] Adham Basha, George Levi, Lothar Houben, Tamir Amrani, Ilan Goldfarb, Amit Kohn, Evaluating direct detection detectors for short-range order characterization of amorphous materials by electron scattering, Ultramicroscopy 249 (2023) 113737.
[13] Pierre Astier, Pierre Antilogus, Claire Juramy, Rémy Le Breton, Laurent Le Guillou, Eduardo Sepulveda, The shape of the photon transfer curve of CCD sensors, Astron. Astrophys. 629 (2019) A36.
[14] D. Grois, I. Shcherback, T. Danov, O. Yadid-Pecht, Theoretical approach to CMOS APS PSF and MTF modeling - evaluation, IEEE Sens. J. 6 (1) (2006) 118–124.
[15] Christopher Hobbs, Clive Downing, Sonia Jaskaniec, Valeria Nicolosi, TEM and EELS characterization of Ni–Fe layered double hydroxide decompositions caused by electron beam irradiation, Npj 2D Mater. Appl. 5 (1) (2021).
[16] Xingxu Yan, Chaitanya A. Gadre, Toshihiro Aoki, Xiaoqing Pan, Probing molecular vibrations by monochromated electron microscopy, Trends Chem. 4 (1) (2022) 76–90.
[17] Richard D. Leapman, Application of EELS and EFTEM to the life sciences enabled by the contributions of Ondrej Krivanek, Ultramicroscopy 180 (2017) 180–187.
[18] R.F. Egerton, Electron Energy-Loss Spectroscopy in the Electron Microscope, Springer US, Boston, MA, 2011.
[19] R.F. Egerton, Electron energy-loss spectroscopy in the TEM, Rep. Progr. Phys. 72 (1) (2009) 016502.
[20] Bernhard Schaffer, Werner Grogger, Gerald Kothleitner, Ferdinand Hofer, Comparison of EFTEM and STEM EELS plasmon imaging of gold nanoparticles in a monochromated TEM, Ultramicroscopy 110 (8) (2010) 1087–1093.
[21] Emilie Ringe, Christopher J. DeSantis, Sean M. Collins, Martial Duchamp, Rafal E. Dunin-Borkowski, Sara E. Skrabalak, Paul A. Midgley, Resonances of nanoparticles with poor plasmonic metal tips, Sci. Rep. 5 (2015) 17431.
[22] Sø ren Raza, Majid Esfandyarpour, Ai Leen Koh, N. Asger Mortensen, Mark L. Brongersma, Sergey I. Bozhevolnyi, Electron energy-loss spectroscopy of branched gap plasmon resonators, Nature Commun. 7 (2016) 13790.
[23] Anton Hörl, Georg Haberfehlner, Andreas Trügler, Franz-Philipp Schmidt, Ulrich Hohenester, Gerald Kothleitner, Tomographic imaging of the photonic environment of plasmonic nanoparticles, Nature Commun. 8 (1) (2017) 37.
[24] Yueying Wu, Guoliang Li, Jon P. Camden, Probing nanoparticle plasmons with electron energy loss spectroscopy, Chem. Rev. 118 (6) (2018) 2994–3031.
[25] Yujia Yang, Richard G. Hobbs, Phillip D. Keathley, Karl K. Berggren, Electron energy loss of ultraviolet plasmonic modes in aluminum nanodisks, Opt. Express 28 (19) (2020) 27405–27414.
[26] Akira Yasuhara, Masateru Shibata, Wakaba Yamamoto, Izzah Machfuudzoh, Sotatsu Yanagimoto, Takumi Sannomiya, Momentum-resolved EELS and CL study on 1D-plasmonic crystal prepared by FIB method, Microsc. (Oxford, England) (2024).
[27] L.J. Allen, A.J. D'Alfonso, S.D. Findlay, J.M. LeBeau, N.R. Lugg, S. Stemmer, Elemental mapping in scanning transmission electron microscopy, J. Phys. Conf. Ser. 241 (2010) 012061.
[28] Daniel J. Kelly, Mingwei Zhou, Nick Clark, Matthew J. Hamer, Edward A. Lewis, Alexander M. Rakowski, Sarah J. Haigh, Roman V. Gorbachev, Nanometer resolution elemental mapping in graphene-based TEM liquid cells, Nano Lett. 18 (2) (2018) 1168–1174.
[29] Yi Wang, Michael R.S. Huang, Ute Salzberger, Kersten Hahn, Wilfried Sigle, Peter A. van Aken, Towards atomically resolved EELS elemental and fine structure mapping via multi-frame and energy-offset correction spectroscopy, Ultramicroscopy 184 (Pt B) (2018) 98–105.
[30] Jonathan Schwartz, Zichao Wendy Di, Yi Jiang, Alyssa J. Fielitz, Don-Hyung Ha, Sanjaya D. Perera, Ismail El Baggari, Richard D. Robinson, Jeffrey A. Fessler, Colin Ophus, Steve Rozeveld, Robert Hovden, Imaging atomic-scale chemistry from fused multi-modal electron microscopy, Npj Comput. Mater. 8 (1) (2022).
[31] Ulrich Hohenester, Andreas Trügler, MNPBEM – A matlab toolbox for the simulation of plasmonic nanoparticles, Comput. Phys. Comm. 183 (2) (2012) 370–381.

[32] Alexander Gubbens, Melanie Barfels, Colin Trevor, Ray Twesten, Paul Mooney, Paul Thomas, Nanda Menon, Bernd Kraus, Chengye Mao, Brian McGinn, The GIF Quantum, a next generation post-column imaging energy filter, Ultramicroscopy 110 (8) (2010) 962–970.
[33] Christian Zietlow, Jörg K.N. Lindner, ADMM-TGV image restoration for scientific applications with unbiased parameter choice, Numer. Algorithms 97 (2024) 1481–1512.
[34] Christian Zietlow, Jörg K.N. Lindner, An applied noise model for scintillation-based CCD detectors in transmission electron microscopy, Sci. Rep. accepted (2025).
[35] Georg Haberfehlner, Sebastian F. Hoefler, Thomas Rath, Gregor Trimmel, Gerald Kothleitner, Ferdinand Hofer, Benefits of direct electron detection and PCA for EELS investigation of organic photovoltaics materials, Micron (Oxford, Engl. : 1993) 140 (2021) 102981.
[36] Sheldon M. Ross, Introduction to Probability Models, tirteenth ed., Academic Press, San Diego, CA and London, 2024.
[37] Don S. Lemons, An Introduction to Stochastic Processes in Physics, Johns Hopkins University Press, Baltimore, Md. and London, 2002.
[38] Philippe Réfrégier, Noise Theory and Application to Physics: From Fluctuations to Information, in: Advanced Texts in Physics, Springer, New York, NY, 2004.
[39] Kamil Rajdl, Petr Lansky, Lubomir Kostal, Fano factor: A potentially useful information, Front. Comput. Neurosci. 14 (2020) 569049.
[40] Achim Klenke, Probability theory: A comprehensive course, second ed., Springer, London, 2013.
[41] Leo A. Goodman, On the exact variance of products, J. Amer. Statist. Assoc. 55 (292) (1960) 708.
[42] Eloísa Díaz-Francés, Francisco J. Rubio, On the existence of a normal approximation to the distribution of the ratio of two independent normal random variables, Statist. Papers 54 (2) (2013) 309–323.
[43] K. Pearson, Galton Laboratory for National Eugenics, Note on Regression and Inheritance in the Case of Two Parents, in: Proceedings of the Royal Society, Royal Society, 1895.
[44] M. Rabbani, R. Shaw, R. van Metter, Detective quantum efficiency of imaging systems with amplifying and scattering mechanisms, J. Opt. Soc. Am. A, Opt. Image Sci. 4 (5) (1987) 895–901.
[45] Norbert Wiener, Generalized harmonic analysis, Acta Math. 55 (1930) 117–258.
[46] A. Khintchine, Korrelationstheorie der stationren stochastischen Prozesse, Math. Ann. 109 (1) (1934) 604–615.
[47] Tetsuji Kodama, Nobuyuki Osakabe, Akira Tonomura, Correlation in a coherent electron beam, Phys. Rev. A 83 (6) (2011).
[48] Tetsuji Kodama, Nobuyuki Osakabe, Mechanism for correlation in a coherent electron beam, Microsc. (Oxford, England) 68 (2) (2019) 133–143.
[49] Stan Konings, Maarten Bischoff, A cold field emission gun optimized for Cryo-EM applications, Microsc. Microanal. 26 (S2) (2020) 566–567.
[50] Sebastian Schneider, Darius Pohl, Andrew Stevens, Nigel D. Browning, Kornelius Nielsch, Bernd Rellinghaus, Digital super-resolution in EELS, Microsc. Microanal. 23 (S1) (2017) 146–147.
[51] Jordan A. Hachtel, Andrew R. Lupini, Juan Carlos Idrobo, Exploring the capabilities of monochromated electron energy loss spectroscopy in the infrared regime, Sci. Rep. 8 (1) (2018) 5637.
[52] Rdiger R. Meyer, Angus I. Kirkland, Characterisation of the signal and noise transfer of CCD cameras for electron detection, Microsc. Res. Tech. 49 (3) (2000) 269–280.
[53] Chong Fan, Guanda Li, Chao Tao, Slant edge method for point spread function estimation, Appl. Opt. 54 (13) (2015) 4097.
[54] Axel Lubk, Falk Röder, Tore Niermann, Christophe Gatel, Sebastien Joulie, Florent Houdellier, César Magén, Martin J. Hÿtch, A new linear transfer theory and characterization method for image detectors. Part II: experiment, Ultramicroscopy 115 (2012) 78–87.
[55] Christian Zietlow, Jörg K.N. Lindner, An unbiased ADMM-TGV algorithm for the deconvolution of STEM-EELS maps, 2024, (submitted).
[56] Richard L. Burden, John Douglas Faires, Annette M. Burden, Numerical Analysis, tenth ed., Cengage Learning, Boston, MA, 2016.
[57] Philip R. Bevington, D. Keith Robinson, Data Reduction and Error Analysis for the Physical Sciences, third ed., [Nachdr.], McGraw-Hill, Boston, Mass., 2003.
[58] Kevin Allan Sales, Stirling's formula via the chi-square distribution, Revista ElectrÓNica de Comun. Y Trabajos de ASEPUMA 19 (2) (2018) 107–110.
[59] Sami Mekki, Jean-Luc Danger, Benoit Miscopein, Joseph J. Boutros, Chi-squared distribution approximation for probabilistic energy equalizer implementation in impulse-radio UWB receiver, in: 2008 11th IEEE Singapore International Conference on Communication Systems, IEEE, 2008, pp. 1539–1544.
[60] Michael J. Panik, Advanced Statistics from an Elementary Point of View, Elsevier Academic Press, Amsterdam and Heidelberg, 2005.
[61] D.D. Dyer, Estimation of the scale parameter of the chi distribution based on sample quantiles, Technometrics 15 (3) (1973) 489–496.
[62] Harald Cramér, Mathematical Methods of Statistics (PMS-9), in: Princeton Mathematical Series, vol. 9, Princeton University Press, Princeton, NJ, 1946.

Appendix C

ADMM-TGV image restoration for scientific applications with unbiased parameter choice

Numerical Algorithms (2024) 97:1481–1512
https://doi.org/10.1007/s11075-024-01759-2

ORIGINAL PAPER

ADMM-TGV image restoration for scientific applications with unbiased parameter choice

Christian Zietlow[1] · **Jörg K. N. Lindner**[1]

Received: 1 August 2023 / Accepted: 10 January 2024 / Published online: 10 February 2024

Abstract

Image restoration via alternating direction method of multipliers (ADMM) has gained large interest within the last decade. Solving standard problems of Gaussian and Poisson noise, the set of "Total Variation" (TV)-based regularizers proved to be efficient and versatile. In the last few years, the "Total Generalized Variation" (TGV) approach combined TV regularizers of different orders adaptively to better suit local regions in the image. This improved the technique significantly. The approach solved the staircase problem inherent of the first-order TV while keeping the beneficial edge preservation. The iterative minimization for the augmented Lagrangian of TGV problems requires four important parameters: two penalty parameters ρ and η and two regularization parameters λ_0 and λ_1. The choice of penalty parameters decides on the convergence speed, and the regularization parameters decide on the impact of the respective regularizer and are determined by the noise level in the image. For scientific applications of such algorithms, an automated and thus objective method to determine these parameters is essential to receive unbiased results independent of the user. Obviously, both sets of parameters are to be well chosen to achieve optimal results, too. In this paper, a method is proposed to adaptively choose optimal ρ and η values for the iteration to converge faster, based on the primal and dual residuals arising from the optimality conditions of the augmented Lagrangian. Further, we show how to choose λ_0 and λ_1 based on the inherent noise in the image.

Keywords ADMM · Residual balancing · Total generalized variation · TGV · Gaussian noise · Poisson noise

Mathematics Subject Classification (2010) 65B99

✉ Christian Zietlow
christian.zietlow@upb.de

Jörg K. N. Lindner
lindner@physik.upb.de

[1] Department of Physics, Paderborn University, Warburger Str. 100, Paderborn 33098, Germany

1 Introduction

Every measurement contains noise, which most of the time is undesirable, as it disguises the signal and thus the information to be extracted from it [1]. Often, iterative denoising [2–6] is needed to recover part of the information hidden by the noise. For recovering as much of information as possible, the algorithm has to address the right noise statistics, obtain a suitable prior, and, of course, converge to a certain solution. One category of algorithms for denoising relies on the principles of solving the "augmented Lagrangian," which is adaptable to a large variety of problems concerning image optimization. One of these algorithms is the "alternating direction method of multipliers" (ADMM) algorithm, which was first described by Glowinski and Marroco [7] and Gabay and Mercier [8]. It has proven to be a good tool to solve these kinds of ill-posed inverse problems successfully and thus has gained huge interest within the last decade, during which huge efforts were made to optimize specialized priors or regularizers for all types of structure occurring in images [9–15]. Many of these algorithms interpret the principle of "total variation" (TV) by Rudin et al. [16] in slightly different ways. The newest approach called "total generalized variation" (TGV) from Bredis et al. [17] utilizes an adaptive mixture of different higher orders of TV and applies them on suiting local regions on the image, solving the staircase problem of first order TV, with the benefit of preserving sharp edges, that would otherwise be lost in higher-order TV approaches [18].

As will be shown in this work, successful denoising and deconvolution in the context of total variation break down to the choice of two sets of parameters: the penalty parameters ρ and η, which have a great influence on the convergence speed [19–22], and the regularization parameters λ_0 and λ_1, that depend on the amount of noise and determine the quality of the outcome [23, 24]. To use these ADMM-based algorithms to evaluate experimental data in a scientific context, the choice of these parameters must necessarily be objective to avoid altering the results by the user. Today, this hurdle restricts natural scientist to switch to better-suited algorithms. Instead, it pushes them to use algorithms, such as the "Richardson-Lucy-Algorithm" (RLA), Fourier-ratio deconvolution, or Wiener filtering [25–31], that cannot compete with modern algorithms, such as the ADMM, in terms of adaptability and versatility.

By balancing primal and dual residuals, arising from optimality conditions for the ADMM, the penalty parameters can be found adaptively in a stable scheme for image denoising or deconvolution, speeding up convergence and making the algorithm independent on the initial choice of these parameters. Further, we will show how regularization parameters λ_0 and λ_1 need to be chosen in order to improve the image quality significantly, based on the standard deviation of the noise. With our work, the ADMM-based TGV algorithm can be designed such that it operates purely on a mathematical foundation and on noise parameters that can be determined experimentally by analyzing the used detector itself. Thus, our algorithm enables experimental scientist to use ADMM-based denoising and deconvolution techniques, adapt them to their respective experiments, and improve their data evaluation significantly.

By testing sets of these four parameters ρ and η and λ_0 and λ_1 for noisy images, we can further show that regions of optimal results can be found for different noise types and different priors, allowing to compare results of the standard ADMM-TGV

algorithm with the ones of the residual balanced. In this way, we can show that the automated choice does not only objectify the parameters, but also increases the convergence speed for most initial values. In the following subsections, the noise and the fundamentals of the respective algorithms are explained in detail.

1.1 Gaussian noise fundamentals

Whenever images are captured, the acquisition process adds noise. Gaussian noise is inflicted in terms of, e.g., camera read-out noise and can be described as an additive process. The image formation process equates the following [16]:

$$\boldsymbol{\xi} = \boldsymbol{\Omega}\mathbf{x} + \mathcal{N}\left(\mu, \sigma^2\right) , \tag{1}$$

with the measured image $\boldsymbol{\xi}$, a point-spread-function (PSF) $\boldsymbol{\Omega}$ convolved with the noise-free image $\mathbf{x}$ and Gaussian noise $\mathcal{N}$ with the mean value μ and the variance σ^2. To clarify notations, in the following, we will use bold letters to indicate vectors or matrices. Scalars and indices remain in normal font.
The mean value can be leveled by subtracting a background image. For removing noise with the variance σ^2 from the data, denoising is required. In terms of Bayes' theorem [32], the likelihood $L_{\mathcal{N}}$ of having a good estimate of the "true" convolved image $\boldsymbol{\Omega}\mathbf{x}$ can be expressed as the conditional probability P knowing $\boldsymbol{\xi}$ [33]:

$$\begin{aligned} L_{\mathcal{N}}(\boldsymbol{\Omega}\mathbf{x}) &= P(\boldsymbol{\xi} \mid \boldsymbol{\Omega}\mathbf{x}) \\ &= \prod_{m,n}^{M,N} \frac{1}{\sqrt{2\pi\sigma^2}} \exp\left\{ -\frac{\left([\boldsymbol{\Omega}\mathbf{x}]_{m,n} - \boldsymbol{\xi}_{m,n}\right)^2}{2\sigma^2} \right\}, \end{aligned} \tag{2}$$

with the individual pixels m, n of an $M \times N$ image. This equation can be reformulated into the negative log-likelihood functional [33]:

$$\begin{aligned} F_{\mathcal{N}}(\boldsymbol{\Omega}\mathbf{x}) \propto -\ln\left\{L_{\mathcal{N}}(\boldsymbol{\Omega}\mathbf{x})\right\} &\propto \sum_{m,n}^{M,N} \frac{\left([\boldsymbol{\Omega}\mathbf{x}]_{m,n} - \boldsymbol{\xi}_{m,n}\right)^2}{2\sigma^2} \\ &= \frac{1}{2\sigma^2} \parallel \boldsymbol{\Omega}\mathbf{x} - \boldsymbol{\xi} \parallel_F^2 \quad , \end{aligned} \tag{3}$$

with the Frobenius norm $\| \cdot \|_F$ as an extension of the Euclidean norm for matrices.

1.2 Poisson noise fundamentals

Due to the quantized nature of photons or electrons used for imaging, the Poisson noise occurs as count fluctuations. It thus differs from the Gaussian noise in the overall image statistics, as it is deeply embedded in the signal [34]:

$$\boldsymbol{\xi} = \mathcal{P}(\boldsymbol{\Omega}\mathbf{x}) \ , \tag{4}$$

with the Poisson noise $\mathcal{P}$. Similar to flipping a coin, a probability of counting a certain number of incidents can be assigned to every pixel. Utilizing Bayes' theorem again to have the true convolved image $\mathbf{\Omega x}$, the likelihood can be expressed as follows [34]:

$$\begin{aligned} L_{\mathcal{P}}(\mathbf{\Omega x}) &= P\left(\boldsymbol{\xi} \mid \mathbf{\Omega x}\right) \\ &= \prod_{n,m}^{N,M} \frac{[\mathbf{\Omega x}]_{n,m}^{\xi_{n,m}} \exp\left\{-[\mathbf{\Omega x}]_{n,m}\right\}}{\xi_{n,m}!}, \end{aligned} \tag{5}$$

with the negative log-likelihood functional [34]:

$$G_{\mathcal{P}}\left(\mathbf{\Omega x}\right) \propto -\ln\left\{L_{\mathcal{P}}(\mathbf{\Omega x})\right\} \tag{6}$$

$$= \sum_{n,m}^{N,M} -\ln\left\{[\mathbf{\Omega x}\}_{n,m}\right\}\left(\xi_{n,m}\right) + [\mathbf{\Omega x}]_{n,m}. \tag{7}$$

In the formulation of $G_{\mathcal{P}}$, the factorial in the denominator can be left out, as it vanishes in the derivation and thus plays no further role in the minimization.

1.3 General scaled ADMM

The general scaled ADMM algorithm solves problems in the form of [22]:

$$\begin{aligned} \underset{\mathbf{x},\mathbf{z}}{\arg\min} \quad & f(\mathbf{x}) + g(\mathbf{z}) \\ \text{subject to} \quad & \mathbf{Ax} + \mathbf{Bz} = \mathbf{c}, \end{aligned} \tag{8}$$

with two convex functions f and g applied to the variables $\mathbf{x}$ and $\mathbf{z}$. $\mathbf{A}$ and $\mathbf{B}$ then are operators applied to the variables, and $\mathbf{c}$ is a constant.
As an example in imaging, f and g can be functions that correspond to a given noise statistic or allow to distinguish between a "true" image without blur and noise and the noise itself. The variable $\mathbf{x}$ in this case corresponds to the "true" image and $\mathbf{z}$ to the noise to be separated. Both variables are connected via one or several conditions, including the operators $\mathbf{A}$ and $\mathbf{B}$ that for example could act as a convolution with a blur kernel or difference operators. The application of ADMM for image treatments is shown in Sect. 2.

Staying with more general expressions, the overall problem can be formulated into the scaled augmented Lagrangian to be minimized, which is given by the following [22]:

$$\mathcal{L}_{\rho}(\mathbf{x}, \mathbf{z}, \mathbf{u}) = f(\mathbf{x}) + g(\mathbf{z}) + \frac{\rho}{2}\|\mathbf{Ax} + \mathbf{Bz} - \mathbf{c} + \mathbf{u}\|_2^2 - \frac{\rho}{2}\|\mathbf{u}\|_2^2, \tag{9}$$

with the Euclidean norm $\|\cdot\|_2$, the scaled dual variable (or Lagrange multiplier) $\mathbf{u} = \frac{1}{\rho}\mathbf{y}$ associated with the constraint $\mathbf{Ax} + \mathbf{Bz} = \mathbf{c}$, and $\mathbf{y}$ being the unscaled dual

variable. The iterative minimization process then can be decomposed and carried out in a three-step pattern [22]:

$$\mathbf{x}^{k+1} = \arg\min_{\mathbf{x}} \left\{ f(\mathbf{x}) + \frac{\rho}{2} \| \mathbf{A}\mathbf{x} + \mathbf{B}\mathbf{z}^k - \mathbf{c} + \mathbf{u}^k \|_2^2 \right\} , \tag{10}$$

$$\mathbf{z}^{k+1} = \arg\min_{\mathbf{z}} \left\{ g(\mathbf{z}) + \frac{\rho}{2} \| \mathbf{A}\mathbf{x}^{k+1} + \mathbf{B}\mathbf{z} - \mathbf{c} + \mathbf{u}^k \|_2^2 \right\}, \tag{11}$$

$$\mathbf{u}^{k+1} = \mathbf{u}^k + \mathbf{A}\mathbf{x}^{k+1} + \mathbf{B}\mathbf{z}^{k+1} - \mathbf{c} , \tag{12}$$

minimizing with respect to $\mathbf{x}$ first, $\mathbf{z}$ second and then updating the dual variable $\mathbf{u}$. In this context, $\rho > 0$ appears as a penalty parameter. Its careful choice is crucial for the convergence speed, as a good choice might result in an accurate solution within a few tens of iterations, while a bad choice might delay convergence to a couple of thousand iterations or even lead to divergence. Obviously, it is desirable to minimize time cost, so somehow, an optimal ρ choice has to be found.

1.4 Optimality conditions and residual balancing

Three feasibility conditions have to be fulfilled for the ADMM to optimally converge. These arise from the Karush-Kuhn-Tucker conditions [35], which utilize first-order derivatives to find a saddle point in the Lagrangian. Deriving $\mathcal{L}_\rho(\mathbf{x}, \mathbf{z}, \mathbf{u})$ with respect to the unscaled Lagrange parameter $\mathbf{y}$ yields the primal feasibility condition [9, 22]:

$$0 = \mathbf{A}\mathbf{x}^\star + \mathbf{B}\mathbf{z}^\star - \mathbf{c} , \tag{13}$$

with the star marking the optimum choice of the respective variable. As the Lagrangian is minimized by the updates $\mathbf{x}^{k+1}$ and $\mathbf{z}^{k+1}$, the difference from zero of the above equation gives the primal residual [9, 22]:

$$\mathbf{R}^{k+1} = \mathbf{A}\mathbf{x}^{k+1} + \mathbf{B}\mathbf{z}^{k+1} - \mathbf{c} . \tag{14}$$

Second, both the $\mathbf{x}$- and $\mathbf{z}$-updates must satisfy the dual feasibility conditions with respect to the unscaled dual variable $\mathbf{y} = \rho\mathbf{u}$, yielding the following [9, 22]:

$$0 \in \partial_{\mathbf{x}} f(\mathbf{x}^\star) + \rho \mathbf{A}^T \mathbf{u}^\star, \tag{15}$$

$$0 \in \partial_{\mathbf{z}} g(\mathbf{z}^\star) + \rho \mathbf{B}^T \mathbf{u}^\star, \tag{16}$$

with $\mathbf{A}^T, \mathbf{B}^T$ denoting the adjoint operator of $\mathbf{A}$ and $\mathbf{B}$. The subdifferential operator ∂ can be replaced by a gradient and the $\in$ by an equal sign, in the case of g and f being differentiable [22]. Further, assuming ρ^k to be variable between iterations, where τ^k optimizes ρ^{k+1}:

$$\rho^{k+1} = \tau^k \cdot \rho^k , \tag{17}$$

$$\mathbf{u}^{k+1} = \frac{\mathbf{y}^k}{\rho^{k+1}} = \frac{\mathbf{u}^k + \mathbf{R}^{k+1}}{\tau^k}. \tag{18}$$

Then, the scaled dual variable has to be rescaled inversely [22], to adjust for the right $\mathbf{y}^{k+1}$. To make it easier to follow the general idea, we switch the order of both dual feasibility conditions for a moment. The approach for the residual balancing is hidden in (15), eventually. However, (16) is needed for completeness:
As the $\mathbf{z}$-update happens after the $\mathbf{x}$-update, $\mathbf{x}^{k+1} \leftarrow \mathbf{x}^k$ is already updated. Per definition, the $\mathbf{z}$-update $\mathcal{L}_\rho(\mathbf{x}^{k+1}, \mathbf{z}, \mathbf{u}^k)$ is minimized by $\mathbf{z}^{k+1}$, and deriving with respect to $\mathbf{z}$ and substituting it into the equation (16) yield the following [22]:

$$\begin{aligned} 0 \in\ & \partial_{\mathbf{z}} \mathcal{L}_\rho(\mathbf{x}^{k+1}, \mathbf{z}^{k+1}, \mathbf{u}^k) \\ =\ & \partial_{\mathbf{z}} g(\mathbf{z}^{k+1}) + \rho^k \mathbf{B}^T \mathbf{u}^k + \rho^k \mathbf{B}^T \left(\mathbf{A}\mathbf{x}^{k+1} + \mathbf{B}\mathbf{z}^{k+1} - \mathbf{c} \right) \\ =\ & \partial_{\mathbf{z}} g(\mathbf{z}^{k+1}) + \rho^{k+1} \mathbf{B}^T \mathbf{u}^{k+1}, \end{aligned} \tag{19}$$

showing that optimality is always assured by $\mathbf{z}^{k+1}$ and $\mathbf{u}^{k+1}$, even when ρ is changing. Thus, it is left to show how the $\mathbf{x}$-update satisfies (15). Since the $\mathbf{x}$-update comes before the $\mathbf{z}$-update, $\mathbf{z}^k$ has not been updated yet. As per definition, the $\mathbf{x}$-update $\mathcal{L}_\rho(\mathbf{x}, \mathbf{z}^k, \mathbf{u}^k)$ is minimized by $\mathbf{x}^{k+1}$, and deriving with respect to $\mathbf{x}$ and substituting it into the equation (15) yield the following [22]:

$$\begin{aligned} 0 \quad \in\quad & \partial_{\mathbf{x}} \mathcal{L}_\rho(\mathbf{x}^{k+1}, \mathbf{z}, \mathbf{u}^k) \\ =\quad & \partial_{\mathbf{x}} f(\mathbf{x}^{k+1}) + \rho^k \mathbf{A}^T \mathbf{u}^k + \rho^k \mathbf{A}^T \left(\mathbf{A}\mathbf{x}^{k+1} + \mathbf{B}\mathbf{z}^k - \mathbf{c} \right) \\ =\quad & \partial_{\mathbf{x}} f(\mathbf{x}^{k+1}) + \rho^{k+1} \mathbf{A}^T \mathbf{u}^{k+1} + \rho^k \mathbf{A}^T \mathbf{B} \left(\mathbf{z}^k - \mathbf{z}^{k+1} \right) \\ \Leftrightarrow\ & \rho^k \mathbf{A}^T \mathbf{B} \left(\mathbf{z}^{k+1} - \mathbf{z}^k \right) \in \partial_{\mathbf{x}} f(\mathbf{x}^{k+1}) + \rho^{k+1} \mathbf{A}^T \mathbf{u}^{k+1}. \end{aligned} \tag{20}$$

In order to assure optimality, the first term, which can be seen as the dual residual [9, 22]

$$\mathbf{S}^{k+1} = \rho^k \mathbf{A}^T \mathbf{B} \left(\mathbf{z}^{k+1} - \mathbf{z}^k \right), \tag{21}$$

has to vanish. Further, Wohlberg suggested the usage of relative residuals [36] making them invariant to problem scaling. In contrast to his approach, we propose to alter the normalization of the relative primal residual $\mathbf{R}_{rel}^{k+1}$ slightly, such that $\mathbf{c}$ is grouped with the $\mathbf{B}\mathbf{z}^{k+1}$ norm, making the norm more resilient against high constants $\mathbf{c}$:

$$\mathbf{S}_{rel}^{k+1} = \frac{\rho^k \mathbf{A}^T \mathbf{B} \left(\mathbf{z}^{k+1} - \mathbf{z}^k \right)}{\max \left\{ \| \partial_{\mathbf{x}} f(\mathbf{x}^{k+1}) \|_2,\ \| \rho^k \mathbf{A}^T \left(\mathbf{u}^k + \mathbf{R}^{k+1} \right) \|_2 \right\}}, \tag{22}$$

$$\mathbf{R}_{rel}^{k+1} = \frac{\mathbf{A}\mathbf{x}^{k+1} + \mathbf{B}\mathbf{z}^{k+1} - \mathbf{c}}{\max \left\{ \| \mathbf{A}\mathbf{x}^{k+1} \|_2,\ \| \mathbf{B}\mathbf{z}^{k+1} - \mathbf{c} \|_2 \right\}}. \tag{23}$$

He et al. [37] define the distance from convergence for ADMM based on these residuals as $D^{k+1} = \| \mathbf{R}^{k+1} \|_2^2 + \| \mathbf{S}^{k+1} \|_2^2$ allowing to increase the performance of the algorithm. Equations (10) and (11) suggest a decreasing norm of the primal residual for an increasing ρ, but (21) suggests an increase of dual residual norm simultaneously—for decreasing ρ vice versa. So, somehow, balancing ρ, such that

both residuals approach zero, seems to be a reasonable heuristic for minimizing the overall distance [36]. As both norms for the relative residuals converge, a similar relative distance measure $D_{rel}^{k+1} = \| \mathbf{R}_{rel}^{k+1} \|_2^2 + \| \mathbf{S}_{rel}^{k+1} \|_2^2$ must also vanish, showing that the normalization of the residuals is also a valid strategy.
For the purpose of utilizing both residuals, Boyd proposes an update scheme for ρ, which keeps both residuals in the same magnitude, called "residual balancing" [22]:

$$\rho^{k+1} = \begin{cases} \rho^k \cdot \tau & \text{if } \| \mathbf{R}^{k+1} \|_2 > \mu \| \mathbf{S}^{k+1} \|_2 \\ \rho^k / \tau & \text{if } \| \mathbf{S}^{k+1} \|_2 > \mu \| \mathbf{R}^{k+1} \|_2 \\ \rho^k & \text{otherwise} \end{cases}, \tag{24}$$

with a balancing parameter $\mu = 10$ and $\tau = 2$. This approach was found successful by various authors [38–41]. In the proof by He et al. [37], convergence for this adaptive scheme comes down to bounds on the sequence ρ^k [37]:

$$\inf_k \left\{ \rho^k \right\} > 0 \quad \text{and} \quad \sup_k \left\{ \rho^k \right\} < +\infty, \tag{25}$$

$$\text{with} \quad \sum_{k=0}^{\infty} \tau_k - 1 < +\infty \quad . \tag{26}$$

The latter is a slight variation of the original proof, as He et al. define their factor (here $\hat{\tau}$) slightly different than the authors do $\tau = (\hat{\tau} + 1)$. The main consequence of this proof is that $\tau \to 1$ must converge eventually. Since the definition $\tau > 1$ is necessary for τ to be useful, it increases the sum (26) every iteration indefinitely until it converges to 1. In Boyd's approach, the infinite sum is mainly prevented by a high value of μ, hoping that at some point, $\mathbf{R}$ and $\mathbf{S}$ diverge so slowly from one another, that this threshold basically stops any further updates from happening. A low value of μ in contrast would be desirable, as it would adjust ρ much faster. However, a low μ leads to balancing ρ^k regularly, making it oscillate around an optimal ρ and never attaining it. This necessarily violates (26) for any value $\tau \neq 1$, which, despite converging, would be pointless. This scheme is thus compelled to updating ρ quite slowly, as it takes time for $\mathbf{R}$ and $\mathbf{S}$ to diverge from one another.

Both residuals can be utilized in a more direct way, as Wohlberg showed by using relative residuals, extending the scheme to choosing $\tau = \tau^k$ at each iteration and utilizing a ratio of the relative residuals υ^{k+1} to make the ρ update much faster [36]:

$$\tau^{k+1} = \begin{cases} \upsilon^{k+1} & \text{if } \tau_{max} \geq \upsilon^{k+1} \geq 1 \\ \left(\upsilon^{k+1}\right)^{-1} & \text{if } \tau_{max}^{-1} \leq \upsilon^{k+1} < 1 \quad \text{with} \\ \tau_{max} & \text{otherwise} \end{cases} \tag{27}$$

$$\upsilon^{k+1} = \sqrt{\| \mathbf{R}_{rel}^{k+1} \|_2 / \| \mathbf{S}_{rel}^{k+1} \|_2}.$$

Since τ_{max} provides a bound on τ, convergence still holds for the extension, as the sequence ρ^k would be bounded away from zero and infinity [36]. But again, τ must eventually settle to 1 or updates must unnecessarily be delayed by a high value of μ.

However, the general idea of delaying the updates is not wrong, but the method of thresholding the residuals by a factor μ proves to be unpredictable. Since the initial choice of ρ determines the development of both primal and dual residual, respectively, it depends on that very choice whether the first balancing of ρ appears sooner or later during the iterations. But since the progress in the early iterations is much larger than in the later ones, it is important to place ρ on the right track, as early as possible.

Here, we propose a similar method with neither the strict requirement $\tau \to 1$ nor the unpredictability. By choosing $\mu = 1$, the above extended scheme (24) with (27) can be simplified to the following:

$$\tau^{k+1} = \begin{cases} \upsilon^{k+1} & \text{if} \quad 0 < \upsilon^{k+1} < \infty \\ \min\left\{\rho^{-1},\ \tau_{ext}\right\} & \text{elseif } \rho < 1 \\ \max\left\{\rho^{-1},\ \tau_{ext}^{-1}\right\} & \text{elseif } \rho > 1 \\ 1 & \text{otherwise} \end{cases}. \tag{28}$$

$$\rho^{k+1} = \begin{cases} \rho^k \cdot \tau^{k+1} & \text{if} \quad \rho_{max}^{-1} \le \rho^k \cdot \tau^{k+1} \le \rho_{max} \\ \rho_{max}^{-1}/\rho^k & \text{if} \quad \rho_{max}^{-1} < \rho^k \cdot \tau^{k+1} \\ \rho_{max}/\rho^k & \text{if} \quad \rho^k \cdot \tau^{k+1} > \rho_{max} \end{cases} \tag{29}$$

We propose to balance ρ by the above equations, but to increase the length of the update interval exponentially. This could be done by, e.g., updating ten times per magnitude of iterations, such that the updates are exponentially spaced:

$$\tau^{k+1} = \begin{cases} \tau^{k+1} & \text{if } k \in \text{Val} \\ 1 & \text{otherwise} \end{cases}, \tag{30}$$

where Val is a series of exponentially growing values. Thus, the update occurs regularly in the early iterations, where it is necessary to find a good ρ, and fades out at a later stage, when convergence is more important. With the exponential increase of the update interval, the interval length eventually approaches infinity, which is equal to the standard ADMM, assuring convergence. Since $\tau^k = 1$ for every step without balancing, the mean value of all τ^k between two balancing events approaches one, which satisfies (26).

In the above equations, ρ is bounded away from zero and infinity by forbidding a direct scaling with these and by limiting the number of update steps. However, υ^{k+1} being either zero or infinity indicates an over-extension of the balancing parameter ρ. A useful strategy is to relief an overextended ρ by pushing the parameter back towards 1 by introducing a factor $\tau_{ext} > 1$, with which ρ is either increased or decreased monotonically until $\upsilon^{k+1} \in (0, \infty)$ again is within boundaries and is well defined. For both, increasing or decreasing ρ monotonically He et al. proved convergence [37]. Further, the authors suggest to set a limit ρ_{max} to assure the numerical stability of the algorithm.

2 ADMM with total generalized variation

In order to distinguish "true" image $\mathbf{x}$ and noise, some additional information about the image needs to be taken into consideration. The total variation approach relies on the assumption that images are smooth to a certain degree and noise is highly volatile. Consequently, derivatives can be utilized to find the noise, as the derivative of the noise is expected a lot higher than the derivative of the smooth and slowly changing image. However, if the image has a gradient itself, this assumption in inconvenient as part of the image slope is forced to be piece-wise constant in the reconstruction, leading to staircase artifacts [18]. Here, a higher-order derivative can help to smoothen the gradient of the image, instead of the image itself, leading to a better approximation of the image, but at the cost of preserving sharp edges.
Total generalized variation of second order as a method for image smoothing was first described by Bredis et al. [17] aiming to combine both orders of derivatives in a beneficial way, such that regions of the image are denoised in the most optimal manner with the help of self-adapting filter masks.
In terms of an isotropic TGV penalizer, an ADMM algorithm can be formulated following Shirai and Okuda [42]:

$$\|\mathbf{x}\|_{TGV}^{\lambda_0,\lambda_1} := \min_{\mathbf{Dx}=\mathbf{s}+\mathbf{t}} \left(\lambda_0 \|\mathbf{s}\|_F + \lambda_1 \|\mathbf{Gt}\|_F\right) . \tag{31}$$

The auxiliary matrices $\mathbf{s}$ and $\mathbf{t}$ are linked to the flat and sloped region of the image, where $\mathbf{t}$ contains the latter. The matrices $\mathbf{D}$ and $\mathbf{G}$ contain derivatives in all possible directions. For images, they are given as follows [42]:

$$\mathbf{D} = \begin{pmatrix} \mathbf{D}_h \\ \mathbf{D}_v \end{pmatrix} \quad , \quad \mathbf{G}^T = \begin{pmatrix} \mathbf{D}_h & \mathbf{D}_v & \mathbb{0} \\ \mathbb{0} & \mathbf{D}_h & \mathbf{D}_v \end{pmatrix} , \tag{32}$$

where the individual entries $\mathbf{D}_h$ and $\mathbf{D}_v$ are forward difference operators for the horizontal and vertical direction. Both and the matrix of zeros $\mathbb{0}$ follow a "block circulant with circulant blocks" (BCCB) structure [42]. So for an image with $N \times M$ pixels, all entries $\mathbf{D}_{h,v}$ and the matrix of zeros $\mathbb{0}$ have the same size and dimension as said image $\{\mathbf{D}_h, \mathbf{D}_v, \mathbb{0}\} \in \mathbb{R}^{N\times M}$. According to (31), the minimization separates the image in flat and sloped regions, which later serve as filter masks for first- and second-order smoothing. Thus, $\mathbf{t}$ contains the first-order derivatives of the sloped regions of the image, at which a further derivation $\mathbf{G}$ is applied. These sloped regions get subtracted from $\mathbf{Dx}$ leaving over the first-order filter mask $\mathbf{s}$, which then only contains the flat regions of the image.

2.1 Gaussian noise ADMM with TGV

Depending on the noise type, the structure of the ADMM must be adapted. For the Gaussian-type noise, following (3), it can be formulated as follows [42]:

$$\underset{\mathbf{x},\mathbf{z}_1,\mathbf{z}_2}{\arg\min} \quad 1/(2\sigma^2)\, \|\mathbf{\Omega x} - \boldsymbol{\xi}\|_F^2 + \lambda_0 \|\mathbf{z}_1\|_F + \lambda_1 \|\mathbf{z}_2\|_F$$

$$\text{subject to} \qquad \mathbf{z}_1 = \mathbf{D}\mathbf{x} - \mathbf{t},\, \mathbf{z}_2 = \mathbf{G}\mathbf{t} \qquad , \tag{33}$$

with the acquired image $\boldsymbol{\xi}$, a point-spread-function $\boldsymbol{\Omega}$, and the regularization parameters λ_0 and λ_1. The augmented Lagrangian to be solved is given as follows [42]:

$$\begin{aligned} \mathcal{L}_{\rho,\eta}\left(\mathbf{x}, \mathbf{t}, \mathbf{z}_1, \mathbf{z}_2, \mathbf{u}_1, \mathbf{u}_2\right) = {}& {}^1/(2\sigma^2)\|\boldsymbol{\Omega}\mathbf{x} - \boldsymbol{\xi}\|_F^2 \\ & + \lambda_0 \|\mathbf{z}_1\|_F + {}^\rho/_2 \|\mathbf{D}\mathbf{x} - \mathbf{t} - \mathbf{z}_1 + \mathbf{u}_1\|_F^2 - {}^\rho/_2 \|\mathbf{u}_1\|_F^2 \\ & + \lambda_1 \|\mathbf{z}_2\|_F + {}^\eta/_2 \|\mathbf{G}\mathbf{t} - \mathbf{z}_2 + \mathbf{u}_2\|_F^2 \qquad - {}^\eta/_2 \|\mathbf{u}_2\|_F^2. \end{aligned} \tag{34}$$

with the penalty parameters ρ and η. Note that for pure denoising problems, the "deconvolution kernel" $\boldsymbol{\Omega}$ simplifies to a matrix of ones $\boldsymbol{\Omega} = \mathbb{1}$. Further, it is important to mention that often in literature, σ^2 is found to be absorbed into $\hat{\rho} = \rho\sigma^2$ and $\hat{\eta} = \eta\sigma^2$ and thus excluded from the equation. But to show the dependency of the optimal $\lambda \propto {}^1/_\sigma$, it is more convenient to stay with the definition chosen here.
Starting with $\mathbf{x}^0 = \mathbb{0}$, $\mathbf{t}_i^0 = \mathbb{0}$, $\mathbf{z}_{1,i}^0 = \mathbb{0}$, $\mathbf{z}_{2,j}^0 = \mathbb{0}$, $\mathbf{u}_{1,i}^0 = \mathbb{0}$ and $\mathbf{u}_{2,j}^0 = \mathbb{0}$, with i and j denoting the respective directions of the derivatives and $\mathbb{0}$ being matrices of zeros, the iteration steps are given as follows [42]:

$$\begin{aligned} \left\{\mathbf{x}^{k+1}, \mathbf{t}^{k+1}\right\} &= \underset{\mathbf{x},\mathbf{t}}{\arg\min}\, \mathcal{L}_{\rho,\eta}\left(\mathbf{x}, \mathbf{t}, \mathbf{z}_1^k, \mathbf{z}_2^k, \mathbf{u}_1^k, \mathbf{u}_2^k\right) \quad , \\ \mathbf{z}_{1,i}^{k+1} &= \underset{\mathbf{z}_{1,i}}{\arg\min}\, \mathcal{L}_{\rho}\left(\mathbf{x}^{k+1}, \mathbf{t}_i^{k+1}, \mathbf{z}_{1,i}, \mathbf{u}_{1,i}^k\right) , \\ \mathbf{z}_{2,j}^{k+1} &= \underset{\mathbf{z}_{2,j}}{\arg\min}\, \mathcal{L}_{\eta}\left(\mathbf{x}^{k+1}, \mathbf{t}^{k+1}, \mathbf{z}_{2,j}, \mathbf{u}_{2,j}^k\right) , \\ \mathbf{u}_{1,i}^{k+1} &= \mathbf{u}_{1,i}^k + \left(\left[\mathbf{D}\mathbf{x}^{k+1}\right]_i - \mathbf{t}_i^{k+1} - \mathbf{z}_{1,i}^{k+1}\right) \quad , \\ \mathbf{u}_{2,j}^{k+1} &= \mathbf{u}_{2,j}^k + \left(\left[\mathbf{G}\mathbf{t}^{k+1}\right]_j - \mathbf{z}_{2,j}^{k+1}\right) \qquad . \end{aligned} \tag{35}$$

For images $i \in \{h, v\}$ and $j \in \{h, d, v\}$, with d denoting the diagonal direction connected to both horizontal and vertical derivatives. Further, $\mathbf{t}$, $\mathbf{z}_{1,2}$, and $\mathbf{u}_{1,2}$ are given as follows [42]:

$$\begin{aligned} \mathbf{t} &= \begin{pmatrix} \mathbf{t}_h \\ \mathbf{t}_v \end{pmatrix} \quad , \\ \mathbf{z_1} &= \begin{pmatrix} \mathbf{z}_{1,h} \\ \mathbf{z}_{1,v} \end{pmatrix} \quad , \quad \mathbf{u_1} = \begin{pmatrix} \mathbf{u}_{1,h} \\ \mathbf{u}_{1,v} \end{pmatrix} \quad , \\ \mathbf{z_2} &= \begin{pmatrix} \mathbf{z}_{2,h} \\ \mathbf{z}_{2,d} \\ \mathbf{z}_{2,v} \end{pmatrix} \quad , \quad \mathbf{u_2} = \begin{pmatrix} \mathbf{u}_{2,h} \\ \mathbf{u}_{2,d} \\ \mathbf{u}_{2,v} \end{pmatrix} \quad , \end{aligned} \tag{36}$$

with, according to the BCCB structure, all entries having the size of the image. The solution for the $\mathbf{x}$- and $\mathbf{t}$- update is shown in detail by Shirai and Okuda [42]. Note, however, that both $\mathbf{x}$- and $\mathbf{t}$-updates minimize the same Lagrangian, but with respect

to different variables. The minimization of $\mathbf{z}_{1,i}$ and $\mathbf{z}_{2,j}$ can be done via the "block soft threshold operator" $\mathcal{S}_\gamma$ [42], which is given as follows [42]:

$$\mathcal{S}_\gamma\,(\mathbf{v}) = \max\left\{\left(1 - \frac{\gamma}{\|\,\mathbf{v}\,\|_2}\right)\mathbf{v}_i\,,\;0\right\}\,, \tag{37}$$

such that:

$$\mathbf{z}_{1,i}^{k+1} = \mathcal{S}_{\lambda_0/\rho}\left(\mathbf{D}\mathbf{x}^{k+1} - \mathbf{t}^{k+1} + \mathbf{u}_1^k\right), \tag{38}$$

$$\mathbf{z}_{2,j}^{k+1} = \mathcal{S}_{\lambda_1/\eta}\left(\mathbf{G}\mathbf{t}^{k+1} + \mathbf{u}_2^k\right) \qquad , \tag{39}$$

with i and j denoting the respective direction of the derivative, which in 2D is $i \in \{h, v\}$ for (38) and $j \in \{h, d, v\}$ for (39). This operator is applied pixel-wise to the image.

2.2 Poisson noise ADMM with TGV

Incorporating the log-likelihood functional (7) directly into ADMM leads to problems of finding a straightforward solution for the $\mathbf{x}$- and $\mathbf{t}$-update. Thus, it is usually used as a penalizer functional $g(\mathbf{z})$, as these problems do not occur then. For data corrupted with Poisson noise, the minimization states as follows:

$$\begin{aligned} &\underset{\mathbf{x},\mathbf{z}_0,\mathbf{z}_1,\mathbf{z}_2}{\arg\min} \quad G_{\mathcal{P}}(\mathbf{z}_0) + \lambda_0\|\mathbf{z}_1\|_F + \lambda_1\|\mathbf{z}_2\|_F \\ &\text{subject to} \;\; \mathbf{z}_0 = \boldsymbol{\Omega}\mathbf{x},\, \mathbf{z}_1 = \mathbf{D}\mathbf{x} - \mathbf{t},\, \mathbf{z}_2 = \mathbf{G}\mathbf{t} \end{aligned} \tag{40}$$

with the corresponding augmented Lagrangian:

$$\begin{aligned} \mathcal{L}_{\varphi,\rho,\eta}\,(\mathbf{x},\mathbf{t},\mathbf{z}_0,\mathbf{z}_1,\mathbf{z}_2,\mathbf{u}_0,\mathbf{u}_1,\mathbf{u}_2) = \;& G_{\mathcal{P}}(\mathbf{z}_0) + \varphi/2\|\boldsymbol{\Omega}\mathbf{x} - \mathbf{z}_0 + \mathbf{u}_0\|_F^2 \quad - \varphi/2\,\|\,\mathbf{u}_0\,\|_F^2 \\ &+\lambda_0\|\mathbf{z}_1\|_F + \rho/2\|\mathbf{D}\mathbf{x} - \mathbf{t} - \mathbf{z}_1 + \mathbf{u}_1\|_F^2 - \rho/2\,\|\,\mathbf{u}_1\,\|_F^2 \\ &+\lambda_1\|\mathbf{z}_2\|_F + \eta/2\|\mathbf{G}\mathbf{t} - \mathbf{z}_2 + \mathbf{u}_2\|_F^2 \quad - \eta/2\,\|\,\mathbf{u}_2\,\|_F^2. \end{aligned} \tag{41}$$

As initial values for the algorithm, the following are chosen: $\mathbf{x}^0 = \mathbb{0}$, $\mathbf{t}_i^0 = \mathbb{0}$, $\mathbf{z}_0^0 = \boldsymbol{\xi}$, $\mathbf{z}_{1,i}^0 = \mathbb{0}$, $\mathbf{z}_{2,j}^0 = \mathbb{0}$, $\mathbf{u}_0^0 = \mathbb{0}$, $\mathbf{u}_{1,i}^0 = \mathbb{0}$ and $\mathbf{u}_{2,j}^0 = \mathbb{0}$. With this, the iteration steps then are given as:

$$\begin{aligned} \left\{\mathbf{x}^{k+1},\mathbf{t}^{k+1}\right\} &= \underset{\mathbf{x},\mathbf{t}}{\arg\min}\;\mathcal{L}_{\varphi,\rho,\eta}\left(\mathbf{x},\mathbf{t},\mathbf{z}_0^k,\mathbf{z}_1^k,\mathbf{z}_2^k,\mathbf{u}_0^k,\mathbf{u}_1^k,\mathbf{u}_2^k\right), \\ \mathbf{z}_0^{k+1} &= \underset{\mathbf{z}_0}{\arg\min}\;\mathcal{L}_{\varphi}\left(\mathbf{x}^{k+1},\mathbf{t}^{k+1},\mathbf{z}_0,\mathbf{u}_0^k\right) \qquad , \\ \mathbf{z}_{1,i}^{k+1} &= \underset{\mathbf{z}_{1,i}}{\arg\min}\;\mathcal{L}_{\rho}\left(\mathbf{x}^{k+1},\mathbf{t}^{k+1},\mathbf{z}_1,\mathbf{u}_1^k\right) \qquad , \\ \mathbf{z}_{2,j}^{k+1} &= \underset{\mathbf{z}_{2,j}}{\arg\min}\;\mathcal{L}_{\eta}\left(\mathbf{x}^{k+1},\mathbf{t}^{k+1},\mathbf{z}_2,\mathbf{u}_2^k\right) \qquad , \\ \mathbf{u}_0^{k+1} &= \mathbf{u}_0^k \;\; + \left(\boldsymbol{\Omega}\mathbf{x}^{k+1} - \mathbf{z}_0^{k+1}\right) \qquad , \end{aligned} \tag{42}$$

$$\begin{aligned}\mathbf{u}_{1,i}^{k+1} &= \mathbf{u}_{1,i}^{k} + \left(\left[\mathbf{D}\mathbf{x}^{k+1}\right]_i - \mathbf{t}_i^{k+1} - \mathbf{z}_{1,i}^{k+1}\right) \quad , \\ \mathbf{u}_{2,j}^{k+1} &= \mathbf{u}_{2,j}^{k} + \left(\left[\mathbf{G}\mathbf{t}^{k+1}\right]_j - \mathbf{z}_{2,j}^{k+1}\right) \quad ,\end{aligned}$$

The resulting Lagrangian can be solved in the same manner as the Gaussian noise ADMM as shown by Shirai and Okuda [42]. However, despite the slight changes in the $\mathbf{x}$- and $\mathbf{t}$-update, the only difference in the iteration pattern is the additional $\mathbf{z}_0$ and $\mathbf{u}_0$-update step, together with the introduction of a new penalty parameter φ. The minimization with respect to $\mathbf{z}_0$ is given by the Poisson noise operator, which equates to the following [34]:

$$\mathbf{z}_0^{k+1} = \underset{\mathcal{P}_\varphi}{\text{prox}}\left(\mathbf{\Omega}\mathbf{x}^{k+1} + \mathbf{u}_0^k\right) , \tag{43}$$

with the operator being defined as follows [34]:

$$\underset{\mathcal{P}_\varphi}{\text{prox}}\,(\mathbf{v}) = -\frac{1-\varphi\mathbf{v}}{2\varphi} + \sqrt{\left(\frac{1-\varphi\mathbf{v}}{2\varphi}\right)^2 + \frac{\boldsymbol{\xi}}{\varphi}}. \tag{44}$$

Again, this operator is applied pixel-wise. All other $\mathbf{z}$-updates are carried out as in the Gaussian ADMM.

3 ADMM-TGV with residual balancing

When utilizing the residual balancing for ADMM-TGV algorithms, as described in Sect. 1.4, ρ, η, and φ are to be balanced here. So, the overall structure can be divided into two parts for the Gaussian algorithm—one for the ρ-balancing and one for the η-balancing. Further, a third part for the Poisson algorithm is needed—the φ-balancing.

3.1 Primal feasibility conditions of ADMM-TGV

Since ρ, η, and φ are scalars, acting on all pixels equally, we need to find global residuals, depending on all pixels. Following the pattern of Sect. 1.4 by deriving the augmented Lagrangian for Gaussian (see (34)) or Poisson noise (41) with respect to the unscaled dual variables $\mathbf{y}_{1,i} = \rho\mathbf{u}_{1,i}$ and $\mathbf{y}_{2,j} = \rho\mathbf{u}_{2,j}$ (and additionally $\mathbf{y}_0 = \rho\mathbf{u}_0$ for Poisson) for all respective directions leads to the primal feasibility conditions with their respective relative residuals:

$$R_{rel,\rho}^{k+1} = \frac{\|\mathbf{R}_\rho^{k+1}\|_F}{N\left(\mathbf{R}_\rho^{k+1}\right)} = \frac{\|\mathbf{D}\mathbf{x}^{k+1} - \mathbf{t}^{k+1} - \mathbf{z}_1^{k+1}\|_F}{\max\left\{\|\mathbf{D}\mathbf{x}^{k+1} - \mathbf{t}^{k+1}\|_F,\ \|\mathbf{z}_1^{k+1}\|_F\right\}} , \tag{45}$$

$$R_{rel,\eta}^{k+1} = \frac{\|\mathbf{R}_\eta^{k+1}\|_F}{N\left(\mathbf{R}_\eta^{k+1}\right)} = \frac{\|\mathbf{G}\mathbf{t}^{k+1} - \mathbf{z}_2^{k+1}\|_F}{\max\left\{\|\mathbf{G}\mathbf{t}^{k+1}\|_F,\ \|\mathbf{z}_2^{k+1}\|_F\right\}} , \tag{46}$$

with the standard primal residual $\|\mathbf{R}_\rho^{k+1}\|_F$ in the numerator and the normalization for the scaled residual $N\left(\mathbf{R}_\rho^{k+1}\right)$ in the denominator. Here, $\mathbf{D}\mathbf{x}^{k+1} - \mathbf{t}^{k+1} = \mathbf{s}^{k+1}$ form

a single norm in the normalization (45) instead of appearing as separated norms like (23) suggests, because both are coupled via (31).
For the Poisson TGV, a primal residual for the new penalty parameter φ can be found as follows:

$$R_{rel,\varphi}^{k+1} = \frac{\|\mathbf{R}_{\varphi}^{k+1}\|_F}{N\left(\mathbf{R}_{\varphi}^{k+1}\right)} = \frac{\|\boldsymbol{\Omega}\mathbf{x}^{k+1} - \mathbf{z}_0^{k+1}\|_F}{\max\left\{\|\boldsymbol{\Omega}\mathbf{x}^{k+1}\|_F^2\ ,\ \|\mathbf{z}_0^{k+1}\|_F^2\right\}}\ . \tag{47}$$

3.2 Dual feasibility conditions of ADMM-TGV

Since the updates happen jointly in (35) and (42), $\mathbf{x}^k$ and all $\mathbf{t}_i^k$ are not updated yet, regardless which variable we consider. To find the whole set of dual residuals, the augmented Lagrangian has to be derived with respect to $\mathbf{x}$ and to all $\mathbf{t}_i$. This leads to the equations:

$$\mathbf{x}^{k+1} = \arg\min_{\mathbf{x}} \mathcal{L}_{\rho,\eta}\left(\mathbf{x}, \mathbf{t}^k, \mathbf{z}_1^k, \mathbf{z}_2^k, \mathbf{u}_1^k, \mathbf{u}_2^k\right) \quad , \tag{48}$$

$$\mathbf{t}_i^{k+1} = \arg\min_{\mathbf{t}_i} \mathcal{L}_{\rho,\eta}\left(\mathbf{x}^k, \mathbf{t}_i, \mathbf{t}_l^k, \mathbf{z}_1^k, \mathbf{z}_2^k, \mathbf{u}_1^k, \mathbf{u}_2^k\right), \tag{49}$$

with $\mathbf{t}_l$ denoting all other vector elements of $\mathbf{t}$ excluding the i-th element (for images $l \in \{h, v \,|\, l \neq i\}$) as both $\mathbf{x}$ and $\mathbf{t}_i$ rely on the former iterates of the respective other variables.
Deriving the augmented Lagrangian with respect to $\mathbf{x}$ leads to the first dual feasibility condition:

$$\begin{aligned} 0 &= \partial_x f(\mathbf{x}) + \rho^k \mathbf{D}^T\left(\mathbf{D}\mathbf{x}^{k+1} - \mathbf{t}^k - \mathbf{z}_1^k + \mathbf{u}_1^k\right) \\ &= \partial_{\mathbf{x}} f(\mathbf{x}) + \rho^k \mathbf{D}^T\left(\mathbf{u}_1^{k+1} + \mathbf{t}^{k+1} + \mathbf{z}_1^{k+1} - \mathbf{t}^k - \mathbf{z}_1^k\right) \\ \Leftrightarrow -\rho^k \mathbf{D}^T&\left(\mathbf{t}^{k+1} + \mathbf{z}_1^{k+1} - \mathbf{t}^k - \mathbf{z}_1^k\right) = {}^1\!/\!_{\sigma^2}\, \boldsymbol{\Omega}^T\left(\boldsymbol{\Omega}\mathbf{x} - \boldsymbol{\xi}\right) + \rho^{k+1}\mathbf{D}^T\mathbf{u}_1^{k+1}, \end{aligned} \tag{50}$$

which can be seen as the dual residual, with $f(\mathbf{x}) = {}^1\!/\!_{2\sigma^2}\|\boldsymbol{\Omega}\mathbf{x} - \boldsymbol{\xi}\|_F^2$ (see (34)) for the Gaussian algorithm. The corresponding relative dual residual is given as follows:

$$S_{rel,\rho,x}^{k+1} = \frac{\|\mathbf{S}_{\rho,x}^{k+1}\|_F}{N\left(\mathbf{S}_{\rho,x}^{k+1}\right)} = \frac{\| -\rho^k\left[\mathbf{D}^T\left(\mathbf{t}^{k+1} - \mathbf{t}^k + \mathbf{z}_1^{k+1} - \mathbf{z}_1^k\right)\right]\|_F}{\max\left\{\|{}^1\!/\!_{\sigma^2}\,\boldsymbol{\Omega}^T\left(\boldsymbol{\Omega}\mathbf{x} - \boldsymbol{\xi}\right)\|_F\ ,\ \|\rho^k\mathbf{D}^T\left(\mathbf{u}_1^k + \mathbf{R}_1^{k+1}\right)\|_F\right\}}\ , \tag{51}$$

with the standard dual residual $\|\mathbf{S}_{\rho,x}^{k+1}\|$ in the numerator and the normalization for the scaled residual $N\left(\mathbf{S}_{\rho,x}^{k+1}\right)$ in the denominator.

For the Poisson algorithm, however, the dual feasibility condition equates to the following:

$$-\varphi^k \mathbf{\Omega}^T\left(\mathbf{z}_0^{k+1}-\mathbf{z}_0^k\right)-\rho^k \mathbf{D}^T\left(\mathbf{t}^{k+1}+\mathbf{z}_1^{k+1}-\mathbf{t}^k-\mathbf{z}_1^k\right)=\varphi^{k+1}\mathbf{\Omega}^T\mathbf{u}_0^{k+1}+\rho^{k+1}\mathbf{D}^T\mathbf{u}_1^{k+1}, \tag{52}$$

with $f(\mathbf{x})=\mathbb{0}$ (see (41)). Since all residuals must vanish eventually, we can rearrange the dual residual into a residual for the balancing of ρ and for φ:

$$S_{rel,\rho,x}^{k+1}=\frac{\|\mathbf{S}_{\rho,x}^{k+1}\|_F}{N\left(\mathbf{S}_{\rho,x}^{k+1}\right)}=\frac{\|\mathbf{S}_{\rho,x}^{k+1}\|_F}{\max\left\{\|\mathbf{N}^*\left(\mathbf{S}_{\rho,x}^{k+1}\right)\|_F,\ \|\mathbf{N}^*\left(\mathbf{S}_{\varphi,x}^{k+1}\right)-\mathbf{S}_{\varphi,x}^{k+1}\|_F\right\}}, \tag{53}$$

$$S_{rel,\varphi,x}^{k+1}=\frac{\|\mathbf{S}_{\varphi,x}^{k+1}\|_F}{N\left(\mathbf{S}_{\varphi,x}^{k+1}\right)}=\frac{\|\mathbf{S}_{\varphi,x}^{k+1}\|_F}{\max\left\{\|\mathbf{N}^*\left(\mathbf{S}_{\varphi,x}^{k+1}\right)\|_F,\ \|\mathbf{N}^*\left(\mathbf{S}_{\rho,x}^{k+1}\right)-\mathbf{S}_{\rho,x}^{k+1}\|_F\right\}}, \tag{54}$$

with:

$$\begin{aligned}
\mathbf{S}_{\rho,x}^{k+1} &= -\rho^k\left[\mathbf{D}^T\left(\mathbf{t}^{k+1}-\mathbf{t}^k+\mathbf{z}_1^{k+1}-\mathbf{z}_1^k\right)\right] &,\\
\mathbf{N}^*\left(\mathbf{S}_{\rho,x}^{k+1}\right) &= \rho^k\mathbf{D}^T\left(\mathbf{u}_1^k+\mathbf{R}_1^{k+1}\right) &,\\
\mathbf{S}_{\varphi,x}^{k+1} &= -\varphi^k\mathbf{\Omega}^T\left(\mathbf{z}_0^{k+1}-\mathbf{z}_0^k\right) &,\\
\mathbf{N}^*\left(\mathbf{S}_{\varphi,x}^{k+1}\right) &= \varphi^k\mathbf{\Omega}^T\left(\mathbf{u}_0^k+\mathbf{R}_0^{k+1}\right) &.
\end{aligned}$$

For both Poisson and Gaussian, (51) and (53) show that a change between iterations in $\mathbf{z}_{1,i}$ can be induced by a change in $\mathbf{t}$, but then does not change the residual for the $\mathbf{x}$-update.

Deriving the augmented Lagrangian ((34) or (41)) with respect to the dual variables $\mathbf{t}_i$ with n-dimensions leads to the following:

$$\begin{aligned}
0=&-\rho^k\left(\mathbf{D}_i\mathbf{x}^k-\mathbf{t}_i^{k+1}-\mathbf{z}_{1,i}^k+\mathbf{u}_{1,i}^k\right)\\
&+\eta^k\begin{pmatrix}\left[\mathbf{G}^T\right]_i\\ \left[\mathbf{G}^T\right]_l\end{pmatrix}\left[\begin{pmatrix}\left[\mathbf{G}^T\right]_i^T & \left[\mathbf{G}^T\right]_l^T\end{pmatrix}\begin{pmatrix}\mathbf{t}_i^{k+1}\\ \mathbf{t}_l^k\end{pmatrix}\right]+\eta^k\mathbf{D}_i\left(\mathbf{u}_{2,i}^k-\mathbf{z}_{2,i}^k\right)\\
&+\eta^k\sum_l\mathbf{D}_l\left(\mathbf{u}_{2,il}^k-\mathbf{z}_{2,il}^k\right),
\end{aligned} \tag{55}$$

with i being the direction of the derivative (or vector row) and (il) denoting all the diagonal vector elements for i, here for images $(il)\in\{hv,vh\}=\{d\}$. Solving for the relative dual residuals connected to both ρ and η leads to the following:

$$S_{rel,\rho,t_i}^{k+1}=\frac{\|\mathbf{S}_{\rho,t_i}^{k+1}\|_F}{N\left(\mathbf{S}_{\rho,t_i}^{k+1}\right)}=\frac{\|\mathbf{S}_{\rho,t_i}^{k+1}\|_F}{\max\left\{\|\mathbf{N}^*\left(\mathbf{S}_{\rho,t_i}^{k+1}\right)\|_F,\ \|\mathbf{N}^*\left(\mathbf{S}_{\eta,t_i}^{k+1}\right)-\mathbf{S}_{\eta,t_i}^{k+1}\|_F\right\}}, \tag{56}$$

$$S_{rel,\eta,t_i}^{k+1} = \frac{\|\mathbf{S}_{\eta,t_i}^{k+1}\|_F}{N\left(\mathbf{S}_{\eta,t_i}^{k+1}\right)} = \frac{\|\mathbf{S}_{\eta,t_i}^{k+1}\|_F}{\max\left\{\|\mathbf{N}^*\left(\mathbf{S}_{\eta,t_i}^{k+1}\right)\|_F,\ \|\mathbf{N}^*\left(\mathbf{S}_{\rho,t_i}^{k+1}\right) - \mathbf{S}_{\rho,t_i}^{k+1}\|_F\right\}}, \quad (57)$$

with:

$$\begin{aligned}
\mathbf{S}_{\rho,t_i}^{k+1} &= \rho^k\left[\mathbf{D}_i\left(\mathbf{x}^k - \mathbf{x}^{k+1}\right) + \mathbf{z}_{1,i}^{k+1} - \mathbf{z}_{1,i}^k\right] &&,\\
\mathbf{N}^*\left(\mathbf{S}_{\rho,t_i}^{k+1}\right) &= \rho^k\left[\mathbf{u}_{1,i}^k + \mathbf{R}_{1,i}^{k+1}\right] &&,\\
\mathbf{S}_{\eta,t_i}^{k+1} &= -\eta^k\left[\mathbf{D}_i\left(\mathbf{z}_{2,i}^{k+1} - \mathbf{z}_{2,i}^k\right) + \sum_l \mathbf{D}_l\left(\mathbf{D}_i^T\left(\mathbf{t}_l^k - \mathbf{t}_l^{k+1}\right) + \mathbf{z}_{2,il}^{k+1} - \mathbf{z}_{2,il}^k\right)\right],\\
\mathbf{N}^*\left(\mathbf{S}_{\eta,t_i}^{k+1}\right) &= \eta^k\left[\mathbf{D}_i\left(\mathbf{u}_{2,i}^k + \mathbf{R}_{2,i}^{k+1}\right) + \sum_l \mathbf{D}_l\left(\mathbf{u}_{2,il}^k + \mathbf{R}_{2,il}^{k+1}\right)\right] &&.
\end{aligned}$$

These equations show that a change in $\mathbf{z}_{1,i}$ in between iterations might be induced by a change in $\mathbf{x}$, which then also does not appear in the residual for the $\mathbf{t}_i$ filter mask update. The same holds for a change in the diagonal $\mathbf{z}_{il}$ elements, which can occur due to a change in the other $\mathbf{t}_l$ filter masks.

Since $\mathbf{x}$ and $\mathbf{t}_i$ can be represented as a vector $\begin{pmatrix}\mathbf{x}\\ \mathbf{t}\end{pmatrix}$, the same holds for the dual residuals. Thus, applying the Frobenius norm to form a global relative residual for the ρ, η, and φ balancing seems logical:

$$S_{rel,\rho}^{k+1} = \sqrt{\frac{\|\mathbf{S}_{\rho,x}^{k+1}\|_F^2 + \sum_i \|\mathbf{S}_{\rho,t_i}^{k+1}\|_F^2}{N\left(\mathbf{S}_{\rho,x}^{k+1}\right)^2 + \sum_i N\left(\mathbf{S}_{\rho,t_i}^{k+1}\right)^2}}, \quad (58)$$

$$S_{rel,\eta}^{k+1} = \sqrt{\frac{\sum_i \|\mathbf{S}_{\eta,t_i}^{k+1}\|_F^2}{\sum_i N\left(\mathbf{S}_{\eta,t_i}^{k+1}\right)^2}} \quad , \quad (59)$$

$$S_{rel,\varphi}^{k+1} = \frac{\|\mathbf{S}_{\varphi,x}^{k+1}\|_F}{N\left(\mathbf{S}_{\varphi,x}^{k+1}\right)} \quad . \quad (60)$$

The dual residuals arising from the derivation with respect to $\mathbf{t}$ stay identical to the Poisson ADMM-TGV.

These primal and dual residuals are used for balancing ρ and η in the following according to (28). The residual balanced algorithms are hereafter called ADMM-RBTGV for Gauss or Poisson noise.

3.3 ADMM for Gaussian and Poisson noise with RBTGV

Implementing the residual balanced algorithm for Gaussian noise gives the following algorithm, with starting conditions $\mathbf{x}^0 = \mathbb{0}$, $\mathbf{t}_i^0 = \mathbb{0}$, $\mathbf{z}_{1,i}^0 = \mathbb{0}$, $\mathbf{z}_{2,j}^0 = \mathbb{0}$, $\mathbf{u}_{1,i}^0 = \mathbb{0}$,

$\mathbf{u}_{2,j}^0 = \mathbb{0}$ and finally $\rho^0 = 1$, $\eta^0 = 1$, leading to the following:

$$
\begin{aligned}
\left\{\mathbf{x}^{k+1}, \mathbf{t}^{k+1}\right\} &= \underset{\mathbf{x},\mathbf{t}}{\arg\min}\ \mathcal{L}_{\rho^k,\eta^k}\left(\mathbf{x}, \mathbf{t}, \mathbf{z}_1^k, \mathbf{z}_2^k, \mathbf{u}_1^k, \mathbf{u}_2^k\right) \quad , \quad \text{(after [42])} \\
\mathbf{z}_{1,i}^{k+1} &= \underset{\mathbf{z}_{1,i}}{\arg\min}\ \mathcal{L}_{\rho^k}\left(\mathbf{x}^{k+1}, \mathbf{t}_i^{k+1}, \mathbf{z}_{1,i}, \mathbf{u}_{1,i}^k\right) , \quad \text{(after (38))} \\
\mathbf{z}_{2,j}^{k+1} &= \underset{\mathbf{z}_{2,j}}{\arg\min}\ \mathcal{L}_{\eta^k}\left(\mathbf{x}^{k+1}, \mathbf{t}^{k+1}, \mathbf{z}_{2,j}, \mathbf{u}_{2,j}^k\right) , \quad \text{(after (39))} \\
&\text{if} \quad k \in \text{Val} \\
&\qquad \tau_\rho^{k+1} \leftarrow \tau_\rho^k, \quad \tau_\eta^{k+1} \leftarrow \tau_\eta^k \quad , \quad \text{(after (28))} \\
&\qquad \rho^{k+1} \leftarrow \rho^k, \quad \eta^{k+1} \leftarrow \eta^k \quad , \quad \text{(after (29))} \\
&\text{else} \\
&\qquad \tau_\rho^{k+1} = 1, \quad \tau_\eta^{k+1} = 1 \quad , \\
&\text{end} \\
\mathbf{u}_{1,i}^{k+1} &= \frac{\mathbf{u}_{1,i}^k + \left(\left[\mathbf{D}\mathbf{x}^{k+1}\right]_i - \mathbf{t}_i^{k+1} - \mathbf{z}_{1,i}^{k+1}\right)}{\tau_\rho^{k+1}} \quad , \\
\mathbf{u}_{2,j}^{k+1} &= \frac{\mathbf{u}_{2,j}^k + \left(\left[\mathbf{G}\mathbf{t}^{k+1}\right]_j - \mathbf{z}_{2,j}^{k+1}\right)}{\tau_\eta^{k+1}} \quad ,
\end{aligned}
\tag{61}
$$

with *Val* being a series of exponentially growing values, such that the residual balancing occurs less and less often. The initial values are the same as in the algorithm for the standard Gaussian ADMM with TGV (35).

The residual balanced algorithm for Poisson noise, with the starting conditions of the Gaussian algorithm plus $\mathbf{z}_{1,i}^0 = \boldsymbol{\xi}$ and $\mathbf{u}_0^0 = \mathbb{0}$, is given as follows:

$$
\begin{aligned}
\left\{\mathbf{x}^{k+1}, \mathbf{t}^{k+1}\right\} &= \underset{\mathbf{x},\mathbf{t}}{\arg\min}\ \mathcal{L}_{\varphi^k,\rho^k,\eta^k}\left(\mathbf{x}, \mathbf{t}, \mathbf{z}_0^k, \mathbf{z}_1^k, \mathbf{z}_2^k, \mathbf{u}_0^k, \mathbf{u}_1^k, \mathbf{u}_2^k\right), \quad \text{(after [42])} \\
\mathbf{z}_0^{k+1} &= \underset{\mathbf{z}_0}{\arg\min}\ \mathcal{L}_{\varphi^k}\left(\mathbf{x}^{k+1}, \mathbf{t}^{k+1}, \mathbf{z}_0, \mathbf{u}_0^k\right) \quad , \quad \text{(after (47))} \\
\mathbf{z}_{1,i}^{k+1} &= \underset{\mathbf{z}_{1,i}}{\arg\min}\ \mathcal{L}_{\rho^k}\left(\mathbf{x}^{k+1}, \mathbf{t}^{k+1}, \mathbf{z}_1, \mathbf{u}_1^k\right) \quad , \quad \text{(after (38))} \\
\mathbf{z}_{2,j}^{k+1} &= \underset{\mathbf{z}_{2,j}}{\arg\min}\ \mathcal{L}_{\eta^k}\left(\mathbf{x}^{k+1}, \mathbf{t}^{k+1}, \mathbf{z}_2, \mathbf{u}_2^k\right) \quad , \quad \text{(after (39))} \\
&\text{if} \quad k \in \text{Val} \\
&\qquad \tau_\rho^{k+1} \leftarrow \tau_\rho^k, \quad \tau_\eta^{k+1} \leftarrow \tau_\eta^k, \quad \tau_\varphi^{k+1} \leftarrow \tau_\varphi^k \quad , \quad \text{(after (28))} \\
&\qquad \rho^{k+1} \leftarrow \rho^k, \quad \eta^{k+1} \leftarrow \eta^k, \quad \varphi^{k+1} \leftarrow \varphi^k \quad , \quad \text{(after (29))} \\
&\text{else} \\
&\qquad \tau_\rho^{k+1} = 1, \quad \tau_\eta^{k+1} = 1, \quad \tau_\varphi^{k+1} = 1 \quad , \\
&\text{end} \\
\mathbf{u}_0^{k+1} &= \frac{\mathbf{u}_0^k + \left(\boldsymbol{\Omega}\mathbf{x}^{k+1} - \mathbf{z}_0^{k+1}\right)}{\tau_\varphi^{k+1}} \quad ,
\end{aligned}
\tag{62}
$$

$$\mathbf{u}_{1,i}^{k+1} = \frac{\mathbf{u}_{1,i}^{k} + \left(\left[\mathbf{D}\mathbf{x}^{k+1} \right]_i - \mathbf{t}_i^{k+1} - \mathbf{z}_{1,i}^{k+1} \right)}{\tau_\rho^{k+1}} \quad ,$$

$$\mathbf{u}_{2,j}^{k+1} = \frac{\mathbf{u}_{2,j}^{k} + \left(\left[\mathbf{G}\mathbf{t}^{k+1} \right]_j - \mathbf{z}_{2,j}^{k+1} \right)}{\tau_\eta^{k+1}} \quad .$$

4 Evaluation of the algorithms

In this section, the algorithms are tested on images for denoising and deconvolution problems to demonstrate the success of residual balancing and to show its impact on the convergence of the respective algorithm.
An image is superimposed with noise, such that it is easy to compare the restoration with the original image and show which parameter sets work best. For TGV, four parameters have to be well chosen to achieve optimality, ρ and η, λ_0 and λ_1; for Poisson, this list extends by an additional penalty parameter φ.
For evaluating the algorithm, a quality measure is defined. For the quality of the restoration, the mean squared error (MSE) after iteration k

$$\mathrm{MSE}^k = \frac{1}{M \cdot N} \sum_{m,n}^{M,N} \left(\mathbf{x}_{i,j}^k - \boldsymbol{\xi}_{i,j}^{Orig.} \right)^2 \quad , \tag{63}$$

is a commonly used criterion, with the original image $\boldsymbol{\xi}^{Orig.}$ known and the current iterate image $\mathbf{x}^k$. In order to make optimal regions for the parameter choices visible, initially, $\rho = \eta (= \varphi$ for Poisson) and $\lambda_0 = \lambda_1$ are chosen over orders of magnitude from $10^{-5} \leq \rho \leq 10^5$ and ${}^{10^{-5}}/_{\omega\sigma} \leq \lambda_0 \leq {}^{10^5}/_{\omega\sigma}$, where σ is the standard deviation of the inherent noise in the image and ω is an attenuation coefficient depending on the deconvolution kernel.
Looking at the total generalized variation ADMM approach for Gaussian noise (33) and setting $a \cdot \lambda = \lambda_0$, $b \cdot \lambda = \lambda_1$, with $\boldsymbol{\Omega} = \mathbb{1}$,

$$\begin{aligned} \underset{\mathbf{x},\mathbf{z}_1,\mathbf{z}_2}{\arg\min} \quad & {}^1/_{2\sigma^2} \left\| \mathbf{x} - \boldsymbol{\xi} \right\|_F^2 + \lambda \left(a \cdot \left\| \mathbf{z}_1 \right\|_F + b \cdot \left\| \mathbf{z}_2 \right\|_F \right) \\ \text{subject to} \quad & \mathbf{z}_1 = \mathbf{D}\mathbf{x} - \mathbf{t}, \mathbf{z}_2 = \mathbf{G}\mathbf{t} \end{aligned} \quad , \tag{64}$$

the following can be seen: If the true, noise-free image $\mathbf{x}^*$ could be found, the first term of the minimization would equal:

$$\frac{1}{2\sigma^2} \left\| \mathbf{x}^* - \boldsymbol{\xi} \right\|_F^2 = \sum_{n,m}^{N,M} \frac{1}{2} \quad \Longleftrightarrow \quad \left\| \mathbf{x}^* - \boldsymbol{\xi} \right\|_F^2 = \sum_{n,m}^{N,M} \sigma^2 \, , \tag{65}$$

by definition of the standard deviation σ, as σ characterizes the mean noise level of all

contributing pixels. In a perfect setting with perfect noise detection, the TGV prior would be that exact difference:

$$\lambda \cdot (a \cdot \|\mathbf{z}_1\|_F + b \cdot \|\mathbf{z}_2\|_F) = \lambda \cdot \|\mathbf{x}^* - \boldsymbol{\xi}\|_F = \left(\sum_{n,m}^{N,M} \lambda^2 \cdot \sigma^2 \right)^{1/2} . \tag{66}$$

Since we have perfect noise estimation in this example, the noise level would be irrelevant for the noise detection and for the image. Putting (65) and (66) into the minimization (64) shows that the minimum only depends on the total amount of pixels, if $\lambda = 1/\sigma$ is chosen as an optimal regularization parameter:

$$\underset{\mathbf{x},\mathbf{z}_1,\mathbf{z}_2}{\arg\min} \quad \sum_{n,m}^{N,M} \frac{1}{2} + \left(\sum_{n,m}^{N,M} \lambda^2 \cdot \sigma^2 \right)^{1/2} . \tag{67}$$

But as the image can only be separated into piece-wise flat or sloped regions either connected to $\|\mathbf{z}_1\|_F$ or $\|\mathbf{z}_2\|_F$, a and b must add to 1 to comprise the whole image. However, as noise cannot be predicted perfectly, the optimal λ deviates according to the quality and applicability of the prior. In case of a bad prior, distortions are induced and may at some point outweigh the benefits to the restoration process. Conversely, this would reduce the optimal regularization parameter compared to what would be the case with a good prior. However, as most images comprise piece-wise flat or sloped regions, it is reasonable to assume that TGV is close to approaching the optimal regularization parameter of $\lambda = 1/\sigma$. If the standard deviation of the noise σ is sufficiently known, optimality mainly depends on the choice of a and b weighting $\|\mathbf{z}_1\|_F$ and $\|\mathbf{z}_2\|_F$, respectively.

The same argumentation also holds for Poisson noise, as it approaches Gaussian noise for the increasing number of counts. However, for deconvolution, the $\mathbf{z}_1$ and $\mathbf{z}_2$ are applied to the deconvolved estimate of the image $\mathbf{x}$ and not to the convolved estimate $\boldsymbol{\Omega}\mathbf{x}$ (see (35) and (42)). The noise is thus attenuated by a factor ω which depends on the convolution kernel the image is convolved with. The wider the kernel $\boldsymbol{\Omega}$ for deconvolution, the more of the noise gets drawn into a single pixel. By normalizing the kernel to its maximum peak, we can find the contributions of the other pixel noises to the attenuated noise. Since adding noises corresponds to adding their variances, this leads to the following:

$$\omega^2 = \sum_{i,j}^{N,M} \frac{\boldsymbol{\Omega}_{i,j}}{\max\left\{ \boldsymbol{\Omega}_{i,j} \right\}} . \tag{68}$$

So, the overall scaling needs to be $1/\omega\sigma$. For denoising, the attenuation is $\omega^2 = 1$, since Ω corresponds to a delta peak function.

To make regions visible where the overall quality improves the MSE of a given iteration, k can divided by the initial MSE^0:

$$\mathrm{NormMSE}^k = \frac{\mathrm{MSE}^k}{\mathrm{MSE}^0} , \tag{69}$$

showing how much the image improves relatively.

4.1 Denoising of images with Gaussian noise

The first original image can be found in Fig. 1a. In Fig. 1b, Gaussian noise of $\sigma = 50$ was added to the image to achieve a signal-to-noise ratio of SNR ≈ 20. To visualize the effect of residual balancing, a suboptimal choice of the penalty parameters ρ and η was done, while the regularization parameters λ_0 and λ_1 were kept close to the optimum. In Fig. 1 c and d, the denoised images for the ADMM-TGV and ADMM-RBTGV algorithms after 1000 iterations are compared.

The difference between both denoised images Fig. 1 c and d is rather easy to spot, as c looks blurry compared to d. The suboptimal choice of ρ and η diminishes the progress of the denoising. However, as residual balancing equalizes the denoising result over all penalty parameters, making the result independent of the initial choice, the progress of the algorithm is further advanced, and thus, the quality of the reconstruction is significantly improved.

To show that penalty parameters ρ and η for residual balancing can in fact be arbitrarily chosen, Fig. 2 displays the course of thousand iterations for a wide range of regularization parameters. The NormMSE (see (69)) is displayed such that it shows parameter sets improving the image quality in blue and the rest in yellow. This depiction allows to quickly get an insight into the relevant range of the parameters, that an operator would preferably choose from.

It can be seen that the original ADMM-TGV algorithm in the upper row of Fig. 2 strongly depends on the initial choice of ρ and η as the blue-colored optimal region slowly shifts to higher ρ and η in the course of iterations. With a higher number of iterations, the NormMSE-map of the original ADMM-TGV forms an inverted L-shaped optimal region that grows in ρ-direction with increasing the number of iterations. Thus, the optimality map can be divided into three regions: the first region at low values of λ bordered by the first red line, in which the algorithm does not improve the image quality significantly, because the noise is estimated too low, leading to under-smoothing; the second, inside the red boundaries, where the algorithm converges to a better-than-before solution around the optimum; and a third region in which the algorithm decreases image quality due to over-smoothing, eventually. In the left outer regions at some point in the iterations, an optimum is reached for some ρ at a given

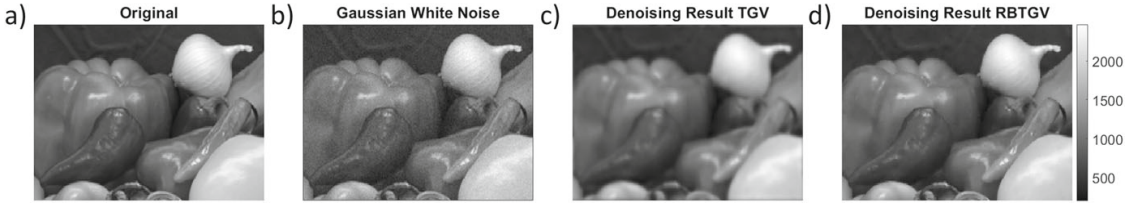

Fig. 1 **a** Test image "onion" from MATLAB. The pixel intensities were multiplied by a factor of 10. **b** Image with additional Gaussian white noise with a standard deviation of $\sigma = 50$ and the attenuation $\omega = 1$. **c** The result of the original ADMM-TGV (see (35)) and **d** the result of our ADMM-RBTGV algorithm (see (61)), after 1000 iterations and with unfavorable starting values for the penalty parameters $\rho = \eta = 1$ and optimal regularization parameters $\lambda_0 = \lambda_1 \approx {}^{0.63}/_{\omega\sigma}$ as values, respectively

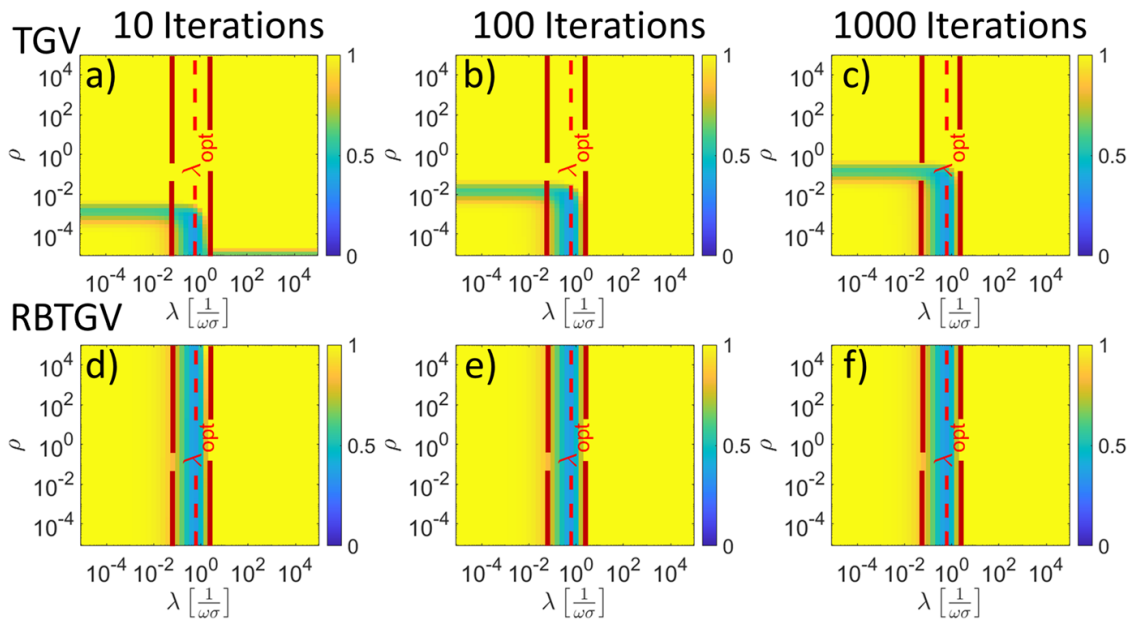

Fig. 2 NormMSE maps generated from applying both ADMM-TGV and ADMM-RBTGV algorithms on Fig. 1, with the individual pixels showing the denoising results under Gaussian noise of the respective $(\rho = \eta \,|\, \lambda_0 = \lambda_1)$- pair. In the upper row, the results of the original ADMM-TGV are shown after **a** 10, **b** 100, and **c** 1000 iterations. In the lower row (**d**–**f**), the results of the residual balanced ADMM-RBTGV approach are displayed at the same iteration stages. The two red lines in every map indicate the region, in which the algorithm eventually improves the image quality compared to the initial noisy image, and the dashed line indicates the $\lambda_0 = \lambda_1$- value in units of $1/\omega\sigma$ at which results are optimal ($\lambda_{opt} \approx 0.63/\omega\sigma$)

iterate, but lost due to convergence to another result. It is, however, not predictable for a given image, when this incident occurs and thus recommended to stay in the second, optimal region. For every ρ in this optimal region, the TGV algorithm converges eventually to the same result for a given λ, but might need many iterations due to a poor choice of ρ.

In order to investigate convergence for all initial choices of $\rho = \eta$, the residual balancing is applied in the second row of Fig. 2. Here, the results at a given $\lambda_0 = \lambda_1$ column are constant for all starting values $\rho = \eta$ as early as after ten iterations, indicating that the residual balanced approach does not depend heavily on the initial choice of ρ and η.

To elaborate further, if a faster convergence of the algorithm compared to the original, the drop rate of the R and S residuals connected to ρ and η are evaluated in Figs. 3 a and b, respectively.

The developments of the R and S residuals are shown for the optimal choice of $\lambda_0 = \lambda_1 \approx 0.63\, 1/\omega\sigma$ and an unfavorable $\rho = \eta = 1$ value as found in Fig. 2. By comparing the residuals for the ADMM-TGV algorithm in Fig. 3a and the ADMM-RBTGV algorithm in b, it can be seen that the regular rebalancing of the R and S pairs leads to an increased drop rate of all residuals. Combining all residuals to a distance measure $D^{k+1} = \| \mathbf{R}_\rho^{k+1} \|_F^2 + \| \mathbf{S}_\rho^{k+1} \|_F^2 + \| \mathbf{R}_\eta^{k+1} \|_F^2 + \| \mathbf{S}_\eta^{k+1} \|_F^2$ following the scheme of He et al. [37] leads to a clearer picture. In Fig. 3c, the distance D of the residual balanced ADMM-RBTGV (RB) can be seen to drop faster than the distance for the original ADMM-TGV. These trends stand out even more, when analyzing relative residuals (rel.) in Fig. 3 a and b as defined in (45) and (46) as well as in (58) and

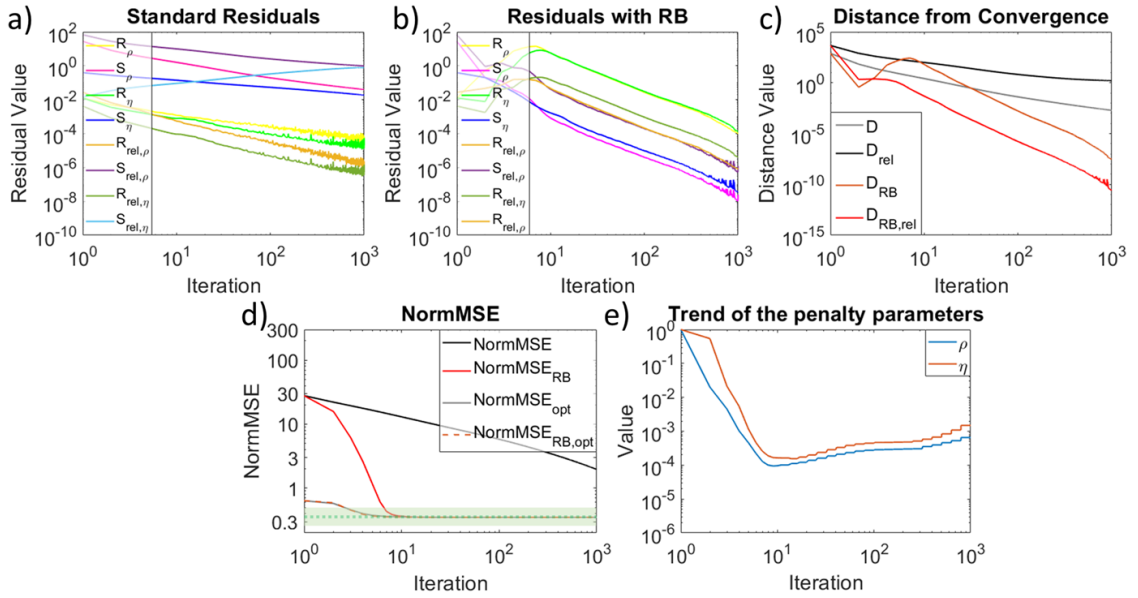

Fig. 3 **a** Trend of the R and S residuals connected to both ρ and η belonging to the standard ADMM-TGV algorithm for Gaussian noise (Fig. 2d) and the relative residuals $\mathrm{R_{rel}}$ and $\mathrm{S_{rel}}$ described in Sect. 3.1 and Sect. 3.2. Unfavorable starting values of $\rho = \eta = 1$ and optimal values for $\lambda_0 = \lambda_1 = \lambda_{opt} \approx 0.63\,1/\omega\sigma$ were chosen to compare with **b** the residuals of the residual balanced ADMM-RBTGV denoted as RB. The optimal values for $\lambda_0 = \lambda_1$ were found as the column with minimal NormMSE values in Fig. 2d. It can be seen that for the residual balancing, the respective R and S residuals for ρ and η are bound to each other and drop faster than for the original algorithm. **c** Combining all four residuals to a distance measure D confirms increased drop rates for the residual balancing. **d** The NormMSE shows that the RBTGV algorithm (red) converges faster than the original algorithm (black), as it approaches the optimum zone (green) of the converged result (green dotted line) from early on. The NormMSE values for an optimal choice (denoted as opt) of $\rho = \eta \approx 6.3 \cdot 10^{-5}$, however, are faster for both algorithms with the residual balancing (orange dotted line) being equally fast as the original algorithm (gray). **e** Development of ρ and η in the course of the iterations

(60). Here, the relative $S_{rel,\eta}$ residual increases for the original algorithm whereas it decreases in the residual balanced.

The residual balancing thus results in a faster convergence, as can be seen in Fig. 3d, where the NormMSE value of the residual balanced ADMM-RBTGV settles close to a value of 0.3 after around ten iterations, whereas the non-balanced ADMM-TGV requires several thousand. To set this into perspective, the NormMSE value for the optimal choice of $\rho = \eta = 6.3 \cdot 10^{-5}$, as found as the column with minimum values in Fig. 2, settles after four iterations, with no difference between residual balancing and the original algorithm. Thus, ADMM-RBTGV is beneficial when the optimal ρ and η values are unknown, which in general is true without excessive testing of both values.

In Fig. 3e, the trends of ρ and η for the residual balanced algorithm are shown, which indicate that the initial (unfavorable) choice was indeed set too high, as the residual balancing corrects these values significantly to lower values.

4.2 Deconvolution of images with Poisson noise

To further demonstrate the versatile applicability to other types of data reconstruction, in a next example, residual balancing is applied to an image affected by blur and pure

Poisson noise. The original image can be found in Fig. 4a. After convolution with a Gaussian kernel (FWHM = 1 Pixel), Poisson noise ($\sigma_{mean} \approx 31.7$) is added in Fig. 4b. Further, in Fig. 4 c and d, the deconvolved image for the ADMM-TGV and ADMM-RBTGV algorithms after 1000 iterations, respectively, is displayed.

At a glance, the image reconstructed by the ADMM-RBTGV looks sharper compared to the ADMM-TGV-treated image, and further analysis can confirm this: Similar to the Gaussian noise results, regions of optimality for $\rho = \eta = \varphi$ and $\lambda_0 = \lambda_1$ can be found via the NormMSE maps as shown in Fig. 5. Again, the convergence of the original algorithm (Fig. 5 a–c) lags behind the ADMM-RBTGV (Fig. 5 d–f) convergence for most $\rho = \eta = \varphi$ values. Our algorithm shows nearly the same result for all ρ of a given λ after approximately ten iterations (Fig. 5e), indicating that the residual balancing is applicable here, too. But the convergence is slightly slower than in the Gaussian example, as an additional penalizer for the Poisson noise must be balanced in.

Figure 6a indicates that the residual for ρ, η, and φ are bound to each other and drop faster in the residual balanced case (Fig. 6b) altogether for an unfavorable choice of $\rho = \eta = \varphi = 1$. Despite all three R_{rel}-residuals being significantly lower from the start for the ADMM-TGV, the S_{rel}-residuals do not decrease at all. As all residuals must vanish, convergence is slowed down significantly for the original algorithm. In Fig. 6 a and b, we only display the relative residuals, as they give a better impression on the development of the algorithm. For completeness, in Fig. 6c, again, both original and relative distances from convergence are shown. Here, the distance $D^{k+1} = \| \mathbf{R}_\rho^{k+1} \|_F^2 + \| \mathbf{S}_\rho^{k+1} \|_F^2 + \| \mathbf{R}_\eta^{k+1} \|_F^2 + \| \mathbf{S}_\eta^{k+1} \|_F^2 + \| \mathbf{R}_\varphi^{k+1} \|_F^2 + \| \mathbf{S}_\varphi^{k+1} \|_F^2$ is extended by the residuals of φ. It can be seen that the distance from convergence vanishes faster with residual balancing overall. The same behavior is shown in Fig. 6d for the NormMSE. Interestingly, both the distance from convergence D and the NormMSE increase significantly within the first five iterations of the ADMM-RBTGV, as the R_{rel}-residuals rise. As the log-likelihood functional for Poisson noise (3), which is tied to the original image, is influenced by the residual balancing, the difference between the new iteration of $\mathbf{x}^k$ and the original image is significantly increased. But the increase is only transient as with increasing iterations, the average τ converges to 1 due to increased intervals between balancing steps. After approximately 16 iterations, convergence is close for the ADMM-RBTGV (indicated as the green dotted line within the green optimum zone in Fig. 6d), while the original ADMM-TGV has not

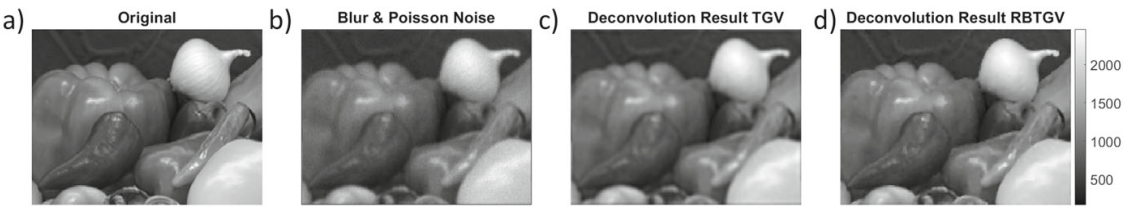

Fig. 4 **a** Gray scaled test image "onion" from Matlab. The pixel intensities were multiplied by a factor of 10. **b** Image with pure Poisson noise ($\sigma_{mean} \approx 31.7$) added after convolution with a 2D Gaussian kernel (FWHM = 1 Pixel). **c** The result of the ADMM-TGV and **d** the ADMM-RBTGV algorithm after 1000 iterations, with unfavorable penalty parameters $\rho = \eta = \varphi = 1$ and optimal regularization parameters $\lambda_0 = \lambda_1 \approx 0.4/\omega\sigma$ as starting values, respectively. According to (68), the attenuation ω amounts to $\omega \approx 2.5$

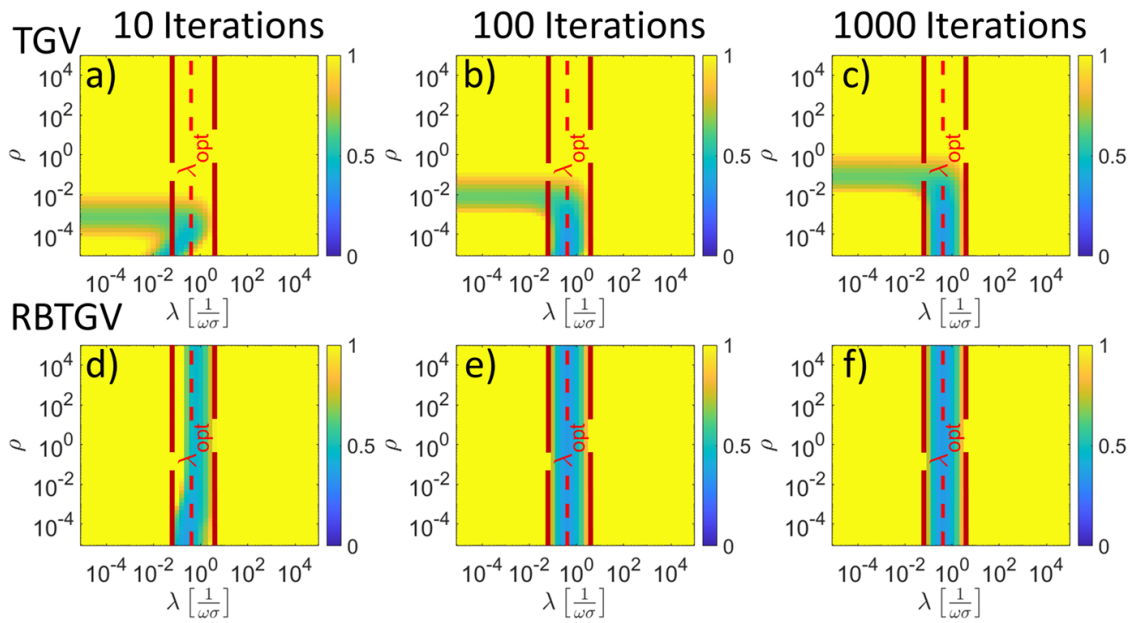

Fig. 5 NormMSE maps, with the individual pixels showing the deconvolution results under Poisson noise with a Gaussian kernel (FWHM = 1 Pixel) of the respective ($\rho = \eta = \varphi \,|\, \lambda_0 = \lambda_1$)- pairs. In the upper row, the results of the original ADMM-TGV are shown after **a** 10, **b** 100, and **c** 1000 iterations. In the lower row **d**–**f**, the results of the residual balanced ADMM-RBTGV are displayed at the same iteration stages. The two red lines in every map indicate the region, in which the algorithm eventually improves the image quality compared to the initial noisy image, and the dashed line indicates the $\lambda_0 = \lambda_1$- value in units of $1/\omega\sigma$, with the standard deviation $\sigma = 31.7$ of the noise and the attenuation $\omega \approx 2.5$, at which results are optimal ($\lambda_{opt} \approx {}^{0.4}/_{\omega\sigma}$)

made significant progress. Even for the choice of a close to optimal (denoted as opt) $\rho = \eta = \varphi = 6.3 \cdot 10^{-3}$, the original ADMM-TGV (gray) is slower than the residual balanced ADMM-RBTGV (orange), since all three penalty parameters are identically chosen and thus suboptimal. Finding the optimal penalty parameters often is time-consuming, whereas residual balancing is fully automated and allows to quickly adapt all penalty parameters to optimal values. Figure 6e shows the development of ρ, η, and φ due to the residual balancing, indicating that the initial values were chosen too high.

4.3 Optimality for λ_0 and λ_1

Having established the residual balancing for Gaussian and Poisson problems, ρ, η, and φ are no longer necessary to be chosen by the user, but instead are automatically set by the algorithm. The parameter choice thus reduces to λ_0 and λ_1 to achieve optimality. Therefore, the NormMSE maps for Gaussian denoising and Poisson deconvolution are displayed in Fig. 7 a and c for pairs of λ_1 and λ_0, with the starting values fixed to $\rho = 1$, $\eta = 1$ and $\varphi = 1$ for the Poisson case.

Both maps exhibit two branches of optimality forming an L-shape. The first is connected to the value for λ_0, which controls the impact of the derivatives $\mathbf{D}$ acting on the flat parts of the image, and the second is connected to the λ_1 value controlling the derivatives $\mathbf{G}$ acting like a second-order derivative applied to the sloped regions of the image. Depending on the features of the image, both parameters have to be chosen

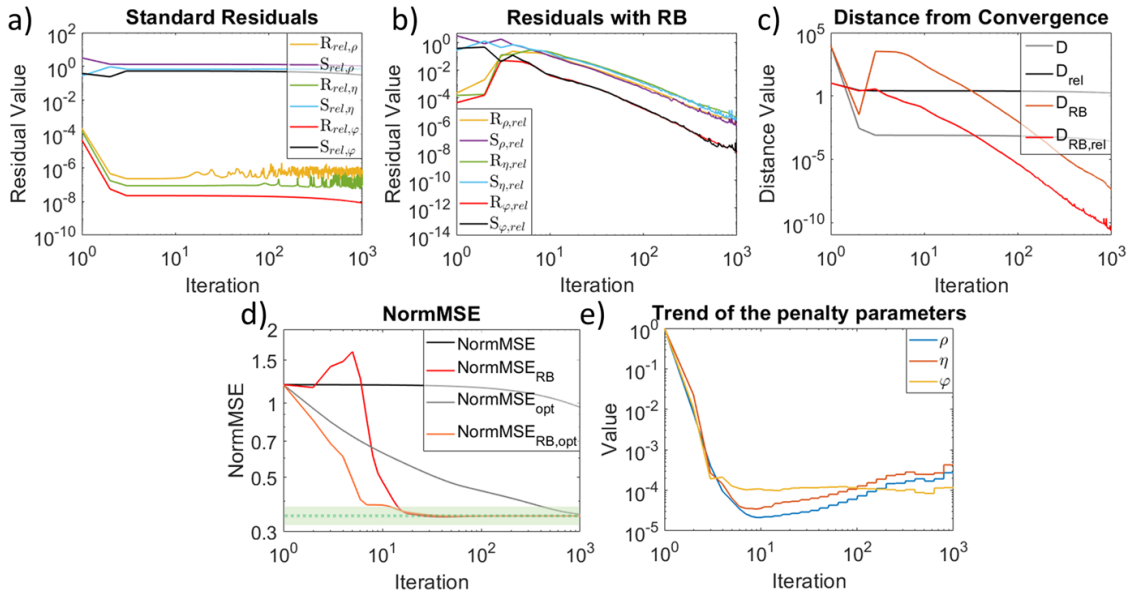

Fig. 6 **a** Trend of the relative R_{rel} and S_{rel} residuals (described in Sect. 3.1 and Sect. 3.2) connected to ρ, η, and φ belonging to the standard ADMM-TGV algorithm for deconvolution under Poisson noise (Fig. 5d). Unfavorable starting values of $\rho = \eta = \varphi = 1$ and optimal values for $\lambda_0 = \lambda_1 = \lambda_{opt} \approx {}^{0.4}/_{\omega\sigma}$ were chosen to compare with **b** the residuals of the residual balanced ADMM-RBTGV denoted as RB. The optimal values for $\lambda_0 = \lambda_1$ were found as the column with minimal NormMSE values in Fig. 5d. It can be seen that for the residual balancing, the respective relative R_{rel} and S_{rel} residuals for ρ, η, and φ stay bound together and drop faster, whereas the relative residuals of the original algorithm stagnate. Initially, this leads to a rise in all three R_{rel}- residuals. **c** Combining all six residuals to a distance measure D confirms the impression of a faster drop rate for the residual balancing. However, D_{RB} and $D_{RB,rel}$ show a transient increase in iteration three, where the increase in D_{RB} is more pronounced. **d** The NormMSE shows that the residual balancing (red) leads to a faster convergence than the original algorithm (black), as it approaches the optimal zone (green) of the converged result (green dotted line) from iteration 16 on. The NormMSE values for the "optimal" choice of $\rho = \eta = \varphi = 1 \cdot 10^{(-3)}$ converges a lot slower in the original algorithm (gray) than for residual balancing (orange). Like the initial rise of the distance measure D suggests, the NormMSE initially increases before seeing a fast convergence. **e** The development of ρ, η, and φ in the course of the iteration

carefully and therefore typically require experience.

Since the chosen image comprises of flat and sloped features, optimality is influenced by the choice of both, the λ_0 and λ_1-parameter. As long as λ_0 is above a certain threshold of ${}^{2}/_{\omega\sigma}$, the result dominantly depends on the λ_1- parameter. The same is true as long as λ_1 is above ${}^{2}/_{\omega\sigma}$, vice versa. Raising either λ_0 or λ_1 to unreasonably high numbers leads to large distances to the image. To reduce the distance, the filter masks adapt and minimize the parts of the image it is applied to. Thus, only the other derivative takes part in the minimization.

The optima of both branches differ significantly from 1 in Fig. 7 a and c, which is an indication that neither first- nor second-order TV alone is optimal. But λ_1 being slightly closer to 1 than λ_0 in a and by much in c shows that it is better suited and comes with lower cost. While in a, both branches are equal, the difference between both in c is large which shows as the much darker color of the λ_1 branch.

As the biggest advantage of TGV is the mixture between both orders of total variation, it appears that when both types of structure, piece-wise flat and sloped, are combined in one image, the optimal λ_0, λ_1 pair is found in the overlap region of both branches.

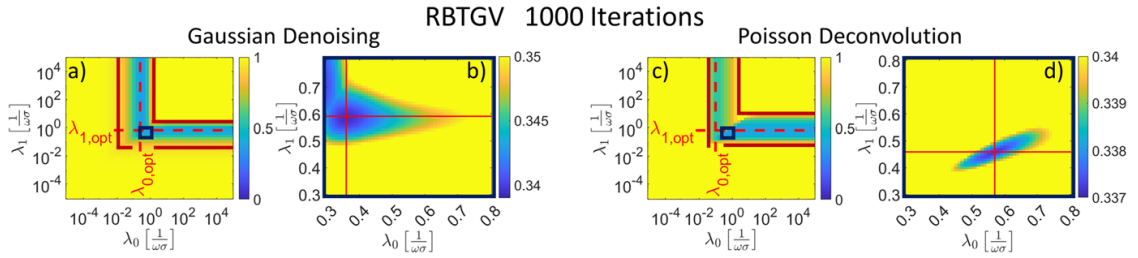

Fig. 7 NormMSE as a function of λ_0 and λ_1 after applying 1000 iterations of RBTGV for Gaussian denoising **a** of Fig. 1b, with the zoomed extract marked with a blue box in **b**. The same for Poisson deconvolution **c** of Fig. 4b, with the zoomed extract marked with a blue box in **d**. The red lines in **a** and **c** indicate the region, in which the algorithm eventually improves the image quality compared to the initial noisy image. For both, **a** Gaussian denoising with the noise standard deviation $\sigma = 50$ and the attenuation of $\omega = 1$ as well as **c** Poisson deconvolution with $\sigma \approx 31.7$ and the attenuation of $\omega \approx 2.5$, two branches occur forming an L-shape at which results are better than before. The first branch is connected to the λ_0 balancing parameter for the first order total variation, and the second branch is connected to λ_1; the dotted red line indicates the position of the optimal $\lambda_{0,opt}$ and $\lambda_{1,opt}$ value connected to either branch. For **a** Gaussian denoising, these values are $(\lambda_{0,opt} \,|\, \lambda_{1,opt}) \approx (0.25 \,|\, 0.63)\ ^1/_{\omega\sigma}$ and for **c** Poisson deconvolution $(\lambda_{0,opt} \,|\, \lambda_{1,opt}) \approx (0.1 \,|\, 0.63)\ ^1/_{\omega\sigma}$. **b** and **d** show the overlap region of the branches for Gaussian denoising and Poisson deconvolution, respectively. Here, the red cross indicates the optimal point, at which the overall minimum is found. For **b** Gaussian denoising, the optimal value is found at $(\lambda_0 \,|\, \lambda_1)_{opt} \approx (0.36 \,|\, 0.59)\ ^1/_{\omega\sigma}$. For **d** Poisson deconvolution, the optimal value is found at $(\lambda_0 \,|\, \lambda_1)_{opt} \approx (0.57 \,|\, 0.46)\ ^1/_{\omega\sigma}$

Since this overlap is only possible with the TGV approach, it shows the advantage over using only simple first- or second-order TV approaches.
Figures 7 b and d display the respective overlap regions, where the optimum values can be found, as indicated by the red cross.
It appears that for both denoising and deconvolution, the optimum values for λ_0 and λ_1 add up to one, approximately. This indicates both are dependent on $^1/_{\omega\sigma}$ introduced in (67) and (68). The clear difference between both sets for Gaussia denoising $(\lambda_0 \,|\, \lambda_1)_{opt} \approx (0.36 \,|\, 0.59)\ ^1/_{\omega\sigma}$ in b and for Poisson deconvolution $(\lambda_0 \,|\, \lambda_1)_{opt} \approx (0.57 \,|\, 0.46)\ ^1/_{\omega\sigma}$ in d is an indication that the balancing between $\|\mathbf{z}_1\|_F$ and $\|\mathbf{z}_2\|_F$ does not solely depend on the original image, as it is identical for both restorations, but rather on the significant features, which can be distinguished from the noise. This produces a dilemma in scientific applications that cannot be resolved, as features are not only unknown, but also the main subject of the debate, to which the restoration should add to. For an unbiased choice, we propose to weight both λ_0 and λ_1 equally with $^1/_{2\omega\sigma}$, since this choice will always increase the outcome quality significantly, while preserving an unbiased and thus scientific approach to the data.

4.4 Comparison of residual balancing strategies

To further show the benefit of using our approach, it is tested against the former approaches of Boyd [22] and Wohlberg [36] (see (24) and (27)) in Fig. 8 for both denoising with Gaussian noise (a–f) and deconvolution with Poisson (g–l) noise under different parameters μ and τ. Boyd suggested values of $\mu = 10$ and $\tau = 2$ for his algorithms (see (24)) as used in Fig. 8a for Gaussian and g for Poisson noise. Further, we tested the same values for Wohlberg d and j again for both types of noise. Both approaches show unstable and inconsistent results. As residual balancing is only

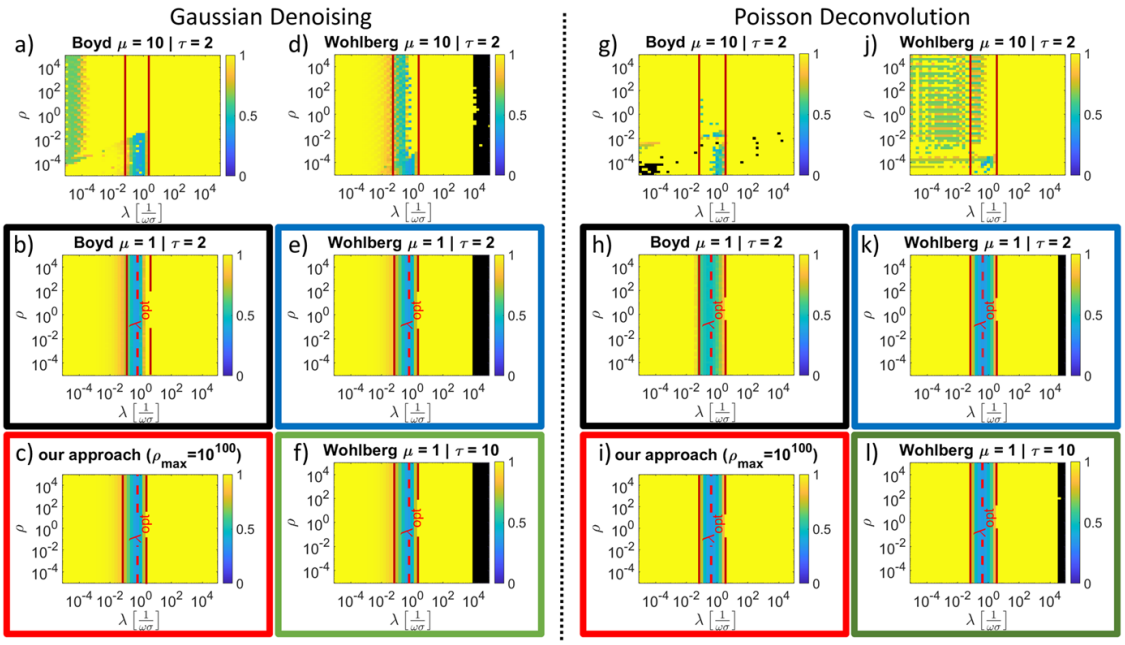

Fig. 8 NormMSE maps with the individual pixels showing the denoising results under Gaussian noise **a**–**f** with standard deviation $\sigma = 50$ (same problem as Fig. 2). The approaches of Boyd [22] **a** and **b** and Wohlberg [36] **d**–**f** are tested with different μ and τ parameters (see Sect. 1.4) against **c** ours after 1000 iterations, respectively. It can be seen that only $\mu = 1$ produces the same result for all given $\rho = \eta$ for every $\lambda_0 = \lambda_1$. The black regions in the Wohlberg approach show the algorithm diverging to infinity and thus failing for the respective pairs. The colored boxes mark all results that are further analyzed in Fig. 9a, since they at least converge for optimal choices of λ. Images **g**–**l** show the deconvolution results under Poisson noise with standard deviation $\sigma \approx 31.7$ and a 2D Gaussian Kernel with FWHM =1 pixel (same problem as Fig. 5) under the same conditions as for the Gaussian noise aforementioned

applied when R and S residuals differ by one order of magnitude, it leads to the respective algorithms balancing the penalty parameters at different iterations depending on their initial value, which leads to different results at a given iteration. However, for this problem, we found $\mu = 1$ as proposed by Wohlberg [36] in Fig. 8 b and h as well as e and k more convincing. Since the residual balancing is now applied every iteration, differences between the initial penalty parameters are reduced more effectively. In a test for several μ, stability increased both for Boyds and Wohlbergs algorithms as $\mu \to 1$.

Increasing τ leads to a faster adaption of all penalty parameters as the residuals can be balanced in larger steps. However, as Boyd's algorithm does not further adapt the step size in the course of iterations, the optimal ρ and η can only be reached within a factor of τ, which is why we stayed with the proposed value of $\tau = 2$ by Boyd. Wohlberg's algorithm, in contrast, allows to approach the optimal ρ, η and φ since τ is variable between 0 and its maximum value τ_{max}.

However, choosing τ too high leads to divergences for Wohlberg's algorithm, marked as black areas in d–f and j–l. For both Gaussian denoising and Poisson deconvolution, this happens if the λ- values are estimated too high leading to over-smoothing.

Compared to Wohlberg's algorithm, ours showed stability in both cases (Fig. 8 c and i). The main difference between Wohlbergs and our proposed algorithm here is the upper limit on ρ, η, and φ instead of the limit on τ_{max}, that prevents our algorithm

from divergence, and the increasing number of iterations between two consecutive balancing steps, which enforces convergence instead.
As Fig. 8 does not show the speed or progress of the respective algorithms, all converging strategies marked with colored boxes are tested against each other in Fig. 9 at an unfavorable $\rho = \eta = \varphi = 1$ and λ_{opt} pair (similar to Fig. 3d and Fig. 6d). The graphs indicate that the approach of Boyd for Gaussian denoising (Fig. 9a) and Poisson deconvolution (Fig. 9b) is the slowest, since the optimal penalty parameters can never be reached due to the limitation of τ, which is overcome by Wohlberg's approach with $\tau_{max} = 2$. For the first six iterations, both Boyd and Wohlberg's approach show the same NormMSE values, indicating that afterwards, the variable τ is beneficial. Further increasing τ_{max} leads to a faster convergence, as the maximum balancing step is increased. Our approach is superior to the others in terms of convergence speed, since we do not limit the step size at all, but only set an upper limit to ρ, η, and φ.

5 Application examples

In Fig. 10, we give two examples of applications in physics. Figure 10a shows gold nanoparticles on a silicon oxide substrate as acquired with a scanning transmission electron microscope (STEM) in annular dark field mode (ADF) with inherent blur by the point-spread-function of the electron beam and some minor defocus. Deconvolving with a more specialized and adaptable mixed Poisson-Gaussian noise model (MPG) [43] with our ADMM-RBTGV (b) improves the overall quality of the reconstruction compared to the original as can especially be seen in the zoomed extract of c, where the crystalline structures appear much clearer.
The second example in Fig. 10d demonstrates the application of the ADMM-RBTGV algorithm to 1D data (spectra), here an electron-energy loss spectrum (EELS) recorded in a STEM. EEL spectra suffer from both the finite energy width of the impinging

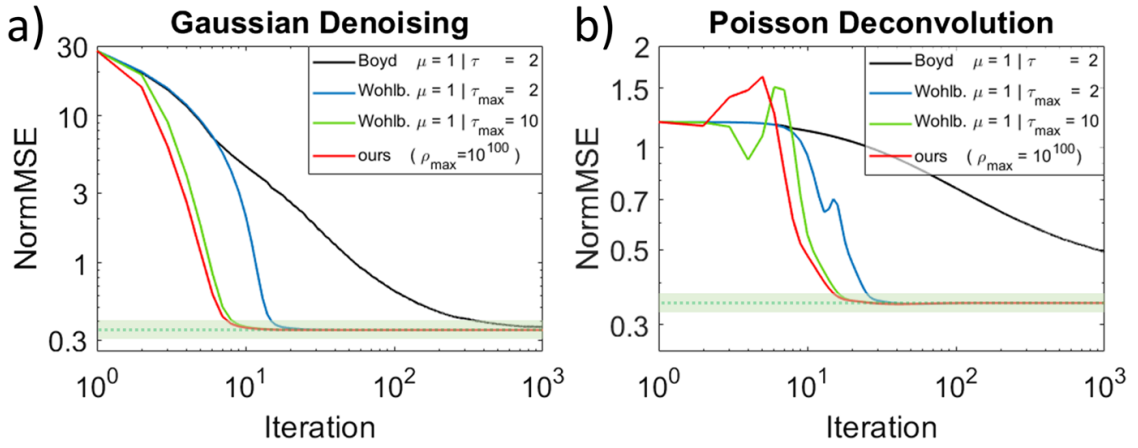

Fig. 9 The graphs display the progress of the NormMSE within 1000 iterations. To show differences in the speed of convergence from the respective stable ADMM-RBTGV algorithms for **a** Gaussian and **b** Poisson noise (see Fig. 8) marked with the same line color as the boxes before. It can be seen that Boyd's (black) approach [22] is the slowest of all for both problems. It is observed that an increase of the τ_{max} translates into a faster convergence for Wohlberg's approach [36] (blue and green). The fastest convergence is achieved with our algorithm (red) by only limiting ρ and η instead of τ

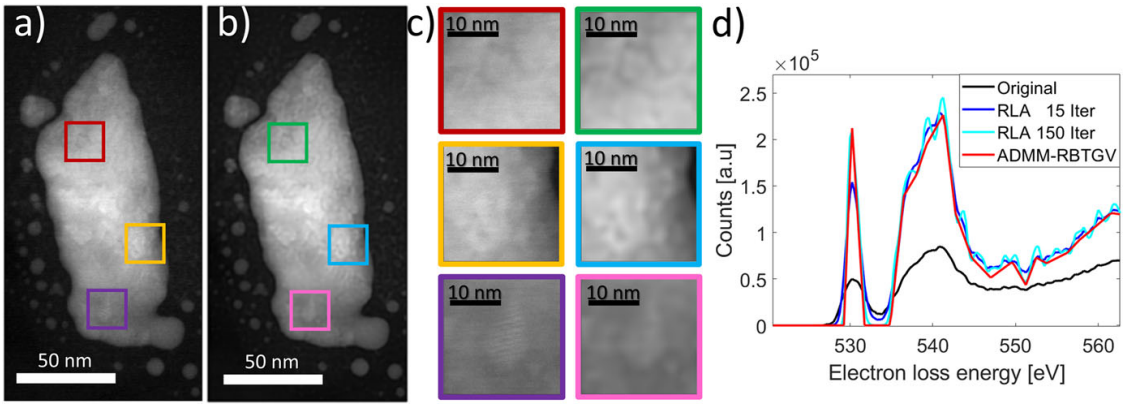

Fig. 10 **a** Noisy image of a metallic nanoparticle acquired in a transmission electron microscope. **b** The deconvolved image with the ADMM-RBTGV after 1500 iterations. **c** Comparison of zoomed extracts of both, original and deconvolved images at the positions marked with the respective colors. **d** Electron energy loss signal from the oxygen K-edge of a Hematite (Fe_2O_3) nanoparticle with only the background subtracted (black), deconvolved with the zero-loss-peak by the commonly used RLA after 15 iterations (blue), 150 iterations (cyan) iterations (red), and the ADMM-RBTGV after 1500 iterations, with a mixed Poisson-Gauss noise model [43]. It can be seen that our approach produces a much smoother outcome, due to the better-adjusted noise model. Additionally, our result leaves much less room for interpretations of additional peaks, that occur around 540 eV in both RLA results

electron beam, leading to a convolution of characteristic spectral features, and noise, owing to the limited electron dose used in a measurement. The black spectrum was recorded from a catalytic metal oxide nanoparticle near the oxygen K-edge, where a background was subtracted using a common power-law mode. The blue and cyan curves show the spectrum after applying the commonly used Richardson-Lucy algorithm (RLA) 15 and 150 times, respectively. Deconvolving the image with the RLA sharpens the edges, but due to a misfit in the noise model by completely ignoring Gaussian read-out noise and not regarding the change in statistics by the subtraction of the background, the RLA diverges with increasing iterations. This is why the RLA is often limited to 15 iterations in EELS applications [44]. Oscillations occurring after 150 iterations of RLA near the spectral maximum at 542 eV might be easily misinterpreted as characteristic features. At energy losses above 550 eV, RLA-treated spectra show additional oscillations with the same amplitude as the peaks around 542 eV are produced by the RLA. These artifacts are commonly known as ringing artifacts [45–47]. In comparison, the spectrum obtained by applying the ADMM-RBTGV (1500 times) nicely corresponds to the spectra expected for metal oxide particles [48–51]. Thus, by utilizing MPG with our ADMM-RBTGV, the overall quality of the reconstruction improves significantly compared to the other as the signal appears much smoother and less noisy. All in all, the examples show that ADMM-RBTGV can reliably improve image and signal quality, unbiased by the choice of input parameters by the user.

6 Conclusions

In this paper, a novel residual balancing approach for ADMM image denoising and deconvolution with total generalized variation is described. It is applied to standard images as well as scientific 2D and 1D data superimposed with both Gaussian- and

Poisson-type noises. The usefulness, objectivity, and fast convergence of the algorithm are demonstrated. By automatically choosing penalty parameters ρ, η, and φ for the Poisson case and equalizing their initial choice after a few iterations, residual balancing makes the algorithm user-friendly and unbiased. Moreover, it increases the convergence speed for almost all initial choices of the penalty parameters significantly. If the optimum is already known, residual balancing is indeed slower than the original algorithm, but does not delay convergence by much. However, as the optimum is hard to guess, residual balancing provides an easy and successful way of choosing ρ and η in the case of the Gaussian noise ADMM and an additional φ for the Poisson case. It is shown that the original algorithm and the residual balanced one converge to the same result for different initial choices of the penalty parameters over several orders of magnitude for the same values for the regularization parameters λ_0 and λ_1. Further, we could show that our approach of residual balancing is superior to others, as it provides the fastest convergence and is stable at all tested pairs.

As the applicability is clearly shown, this work allows to adapt the principles of residual balancing to other penalizers for image restoration in general and for different dimensionality of the data.

By reducing the set of four parameters (or five in the Poisson case) to be chosen by the user to two, optimal regions can be found by only testing $(\lambda_0 \mid \lambda_1)$-pairs. This makes visualization easier and reduces computational time for finding the optimal set.

It is shown that the regularization parameters λ_0 connected to the first derivative and λ_1 connected to the second derivative depend on the inverse standard deviation of the noise $1/\omega\sigma$, that gets attenuated by a factor of ω in the case of a deconvolution. This factor depends on the deconvolution kernel, as it drags more noise into a single pixel. Selecting either λ_0 or λ_1 too high while keeping the other close to the optimum leads to the filter masks adapting and minimizing the influence of the respective first or second matrix of derivatives $\mathbf{D}$ or $\mathbf{G}$. The conclusion drawn from this is that TGV can either converge to results of the standard first-order TV or the second-order TV. However, as most images consist of both flat and sloped parts, optimality is found in the overlap of both λ_0 and λ_1 regions. Here, we could show that both regularization parameters λ_0 and λ_1 must add up to a total value of $1/\omega\sigma$ to achieve optimality. The ratio between both depends on the significant features in the image, which can be distinguished from the noise. Thus, for the same image under different noise conditions, the optimality of these parameters is not identical, but changes significantly.

Finally, with our work, the algorithm can be set up such that it operates on objective criteria and not on the arbitrary choice of user inputs: The penalty parameters are chosen automatically on a mathematical foundation, and the regularization parameters λ_0 and λ_1 can be chosen equal to $1/2\omega\sigma$, such that they only depend on the noise standard deviation σ. Since the features in an image are not known in a scientific context, the true optimality of the ratio of both parameters cannot be achieved without introducing a certain bias. But fixing the ratio of both regularization parameters still improves images significantly, since both parameters continue to be located within the optimality region. This allows for an unbiased approach on the restoration of experimental data as there is no room for altering the results. With sufficient knowledge of the noise in an experiment, which can be found by carefully investigating the detector, our work enables the use of the ADMM-based image restoration algorithms for scientific tasks.

Acknowledgements The authors thank the associated editor and anonymous reviewers for the helpful comments and suggestions.

Author contribution All authors contributed to the study conception and design. The manuscript was written by CZ. All authors read and approved the final manuscript.

Funding Open Access funding enabled and organized by Projekt DEAL.

Availability of data and materials Not applicable

Code availability Not applicable

Declarations

Ethics approval Not applicable

Consent for publication All authors give their consent for publication.

Conflict of interest The authors declare no competing interests.

References

1. Sur, F., Grédiac, M.: Measuring the noise of digital imaging sensors by stacking raw images affected by vibrations and illumination flickering. SIAM J. Imaging Sci. **3**(1), 611–643 (2015)
2. Wen, Y.W., Ng, M.K., Ching, W.K.: Iterative algorithms based on decoupling of deblurring and denoising for image restoration. SIAM J. Sci. Comput. **30**(5), 2655–2674 (2008)
3. Cohen, R., Elad, M., Milanfar, P.: Regularization by denoising via fixed-point projection (RED-PRO). SIAM J. Imaging Sci. **14**(3), 1374–1406 (2021)
4. Vogel, C.R., Oman, M.E.: Iterative methods for total variation denoising. SIAM J. Sci. Comput. **17**(1), 227–238 (1996)
5. Chan, S.H., Wang, X., Elgendy, O.A.: Plug-and-play ADMM for image restoration: fixed-point convergence and applications. IEEE Trans. Comput. Imaging **3**(1), 84–98 (2017)
6. Bredies, K., Sun, H.: Preconditioned Douglas-Rachford splitting methods for convex-concave saddle-point problems. SIAM J. Numer. Anal. **53**(1), 421–444 (2015)
7. Glowinski, R., Marroco, A.: Sur l'approximation, par éléments finis d'ordre un, et la résolution, par pénalisation-dualité d'une classe de problèmes de Dirichlet non linéaires. ESAIM Math. Model. Numer. Anal. **9**(R2), 41–76 (1975)
8. Gabay, D., Mercier, B.: A dual algorithm for the solution of nonlinear variational problems via finite element approximation. Comput. Math. Appl. **2**(1), 17–40 (1976)
9. Goldstein, T., O'Donoghue, B., Setzer, S., Baraniuk, R.: Fast alternating direction optimization methods. SIAM J. Imaging Sci. **7**(3), 1588–1623 (2014)
10. Figueiredo, M.: On the use of ADMM for imaging inverse problems: the pros and cons of matrix inversions. In: Topics in Applied Analysis and Optimisation, pp. 159–181. Springer International Publishing, ISBN: 978-3-030-33115-3 (2019)

11. Cheon, W., Min, B.J., Seo, Y.S., Lee, H.: Non-blind deconvolution with an alternating direction method of multipliers (ADMM) after noise reduction in nondestructive testing. JINST **14**, P11032 (2019)
12. Wang, X., Chan,S.H.: Parameter-free plug-and-play ADMM for image restoration. IEEE Proc. IEEE Int Conf Acoust Speech Signal Process (ICASSP), pp. 1323-1327 (2017)
13. Xie, W.S., Yang, Y.F., Zhou, B.: An ADMM algorithm for second-order TV-based MR image reconstruction. Numer Algor. **67**, 827–843 (2014)
14. Fang, Z., Liming, T., Liang, W., Liu, H.: A nonconvex TV_q-ℓ_1 regularization model and the ADMM based algorithm. Sci. Rep. **12**, 7942 (2022)
15. Eksioglu, E.M., Tanc, A.K.: Denoising AMP for MRI reconstruction: BM3D-AMP-MRI. SIAM J. Imaging Sci. **11**(3), 2090–2109 (2018)
16. Rudin, L.I., Osher, S., Fatemi, E.: Nonlinear total variation based noise removal algorithms. Physica D **60**(1–4), 259–268 (1992)
17. Bredies, K., Kunisch, K., Pock, T.: Total generalized variation. SIAM J. Imaging Sci. **3**(3), 492–526 (2010)
18. Knoll, F., Bredis, K., Pock, T., Stollberger, R.: Second order total generalized variation (TGV) for MRI. Magn. Reson. Med. **65**(2), 480–491 (2011)
19. Ghadimi, E., Teixeira, A., Shames, I., Johansson, M.: Optimal parameter selection for the alternating direction method of multipliers (ADMM): quadratic problems. IEEE Trans. Automat. Contr. **60**(3), 644–658 (2015)
20. Chorfi, A., Koko, J.: Alternating direction method of multiplier for the unilateral contact problem with an automatic penalty parameter selection. Appl. Math. Model. **78**, 706–723 (2020)
21. Lin, Y., Wohlberg, B., Vesselinov, V.: ADMM penalty parameter selection with Krylov subspace recycling technique for sparse coding. In: IEEE International Conference on Image Processing (ICIP), pp. 1945–1949 (2017)
22. Boyd, S., Parikh, N., Chu, E., Peleato, B., Eckstein, J.: Distributed optimization and statistical learning via the alternating direction method of multipliers. Found. Trends Mach. Learn. **3**(1) (2010)
23. Sanders, T.: Parameter selection for HOTV regularization. Appl. Numer. Math. **125**, 1–9 (2018)
24. Wen, Y.W., Chan, R.H.: Parameter selection for total-variation-based image restoration using discrepancy principle. IEEE Trans. Image Process **21**(4), 1770–1781 (2012)
25. Das, P.P., Guzzinati, G., Coll, C., Gomez Perez, A., Nicolopoulos, S., Estrade, S., Peiro, F., Verbeeck, J., Zompra, A.A., Galanis, A.S.: Reliable characterization of organic & pharmaceutical compounds with high resolution monochromated eel spectroscopy. Polymers **12**, 1434 (2020)
26. Brokkelkamp, A., ter Hoeve, J., Postmes, I., van Heijst, S.E., Maduro, L., Davydov, A.V., Krylyuk, S., Rojo, J., Conesa-Boj, S.: Spatially resolved band gap and dielectric function in two-dimensional materials from electron energy loss spectroscopy. J. Phys. Chem. A. **126**(7), 1255–1262 (2022)
27. Eljarrat, A., López-Conesa, L., Estradé, S., Peiró, F.: Electron energy loss spectroscopy on semiconductor heterostructures for optoelectronics and photonics applications. J. Microsc **262**, 142–150 (2016)
28. Lajaunie, L., Ramasubramaniam, A., Panchakarla, L.S., Arenal, R.: Optoelectronic properties of calcium cobalt oxide misfit nanotubes. Appl. Phys. Lett. **16**;113(3), 031102 (2018)
29. Song, Y., Li, H., Zhai, G., He, Y., Bian, S., Zhou, W.: Comparison of multichannel signal deconvolution algorithms in airborne LiDAR bathymetry based on wavelet transform. Sci. Rep. **11**, 16988 (2021)
30. Perez, V., Chang, B.J., Stelzer, E.: Optimal 2D-SIM reconstruction by two filtering steps with Richardson-Lucy deconvolution. Sci. Rep. **6**, 37149 (2016)
31. Ishizuka, A., et al.: Improving the depth resolution of STEM-ADF sectioning by 3D deconvolution. Microscopy **70**(2), 241–249 (2021)
32. Bayes, T.: LII. An essay towards solving a problem in the doctrine of chances. By the late Rev. Mr.Bayes, F. R. S. communicated by Mr. Price, in a letter to John Canton, A. M. F. R. S. In: Philosophical Transactions of the Royal Society of London, Vol. 53, pp. 370–418 (1763)
33. Held, L., Sabanés Bové, D.: Applied statistical inference: likelihood and Bayes. Springer, Berlin Heidelberg (2014)
34. Ikoma, H., Broxton, M., Kudo, T., Wetzstein, G.: A convex 3D deconvolution algorithm for low photon count fluorescence imaging supplementary material. Sci. Rep. **8**, 11489 (2018)
35. Kuhn, H.W., Tucker, A.W.: Nonlinear programming. Proc. Second Berkeley Symp. Math. Statist. Prob. (Univ. of Calif. Press), 481–492 (1951)
36. Wohlberg, B.: ADMM penalty parameter selection by residual balancing. arXiv:1704.06209v1
37. He, B.S., Yang, H., Wang, S.L.: Alternating direction method with self-adaptive penalty parameters for monotone variational inequalities. J. Optim. Theory Appl. **106**(2), 337–356 (2000)

38. Liu, Z., Hansson, A., Vandenberghe, L.: Nuclear norm system identification with missing inputs and outputs. Syst. Control. Lett. **62**(8), 605–612 (2013)
39. Iordache, M.D., Bioucas-Dias, J.M., Plaza, A.: Collaborative sparse regression for hyperspectral unmixing. IEEE Trans. Geosci. Remote Sens. **52**(1), 341–354 (2014)
40. Wohlberg, B.: Efficient convolutional sparse coding. In: IEEE International Conference on Acoustics, Speech and Signal Processing (ICASSP), pp. 7173–7177 (2014)
41. Weller, D.S., Pnueli, A., Radzyner, O., Divon, G., Eldar, Y.C., Fessler, J.A.: Phase retrieval of sparse signals using optimization transfer and ADMM. In: IEEE International Conference on Image Processing (ICIP), pp. 1342–1346 (2014)
42. Shirai, K., Okuda, M.: FFT based solution for multivariable L_2 equations using KKT system via FFT and efficient pixel-wise inverse calculation. In: IEEE International Conference on Acoustics, Speech and Signal Processing (ICASSP), pp. 2629–2633 (2014)
43. Ding, Q., Long, Y., Zhang, X., Fessler, J.A.: Statistical image reconstruction using mixed Poisson-Gaussian noise model for X-ray CT. arXiv:1801.09533
44. Egerton, R.F., Wang, F., Malac, M., Moreno, M.S., Hofer, F.: Fourier-ratio deconvolution and its Bayesian equivalent. Micron **39**(6), 642–647 (2008)
45. Cui, G., Feng, H., Xu, Z., Li, Q., Chen, Y.: A modified Richardson-Lucy algorithm for single image with adaptive reference maps. Opt. Laser Technol. **58**, 100–109 (2014)
46. Zeng, G.L.: Gibbs artifact reduction by nonnegativity constraint. J. Nucl. Med. Technol. **39**(3), 213–9 (2011)
47. Wang, W., Wang, W., Yin, J.: A bilateral filtering based ringing elimination approach for motion-blurred restoration image. Curr. Opt. Photonics **4**(3), 200–209 (2020)
48. Wang, C., Yiqian Wang, Y., Liu, X., Yang, H., Sun, J., Yuan, L., Zhou, G., Rosei, F.: Structure versus properties in α-Fe_2O_3 nanowires and nanoblades. Nanotechnology **27**(3), 035702 (2015)
49. Cortés-Llanos, B., Serrano, A., Muñoz-Noval, A., Urones-Garrote, E., del Campo, A., Marco, J.F., Ayuso-Sacido, A., Pérez, L.: Thermal route for the synthesis of maghemite/hematite core/shell nanowires. J. Phys. Chem. C **121**(41), 23158–23165
50. Guo, Q., Luo, H., Zhang, J., Ruan, Q., Prakash Periasamy, A., Fang, Y., Xie, Z., Li, X., Wang, X., Tang, J., Briscoe, J., Titirici, M., Jorge, A.B.: The role of carbon dots - derived underlayer in hematite photoanodes. Nanoscale **12**(39), 20220–20229 (2020)
51. Ullrich, A., Rahman, M.M., Longo, P., Horn, S.: Synthesis and high-resolution structural and chemical analysis of iron-manganese-oxide core-shell nanocubes. Sci. Rep. **9**, 19264 (2019)

Numerical Algorithms
https://doi.org/10.1007/s11075-025-02105-w

CORRECTION

Correction to: ADMM-TGV image restoration for scientific applications with unbiased parameter choice

Christian Zietlow[1] · **Jörg K. N. Lindner**[1]

Unfortunately, we found inconsistencies in the use of indices denoting the dimensions of the images at five places in the finally published version of this paper. These inconsistencies, however, do not affect the correctness of the mathematics of this paper.

1) The first instance is on p.1484 in (5) and (7), where the indices m, n and M, N are swapped and must read m, n and M, N instead. Accordingly, the correct equations are:

$$\begin{aligned} L_{\mathcal{P}}\left(\boldsymbol{\Omega}\mathbf{x}\right) &= P\left(\boldsymbol{\xi} \mid \boldsymbol{\Omega}\mathbf{x}\right) \\ &= \prod_{m,n}^{M,N} \frac{[\boldsymbol{\Omega}\mathbf{x}]_{m,n}^{\xi_{m,n}} \exp\{-[\boldsymbol{\Omega}\mathbf{x}]_{m,n}\}}{\xi_{m,n}!} , \end{aligned} \tag{5}$$

$$G_{\mathcal{P}}\left(\boldsymbol{\Omega}\mathbf{x}\right) \propto -\ln\left\{L_{\mathcal{P}}\left(\boldsymbol{\Omega}\mathbf{x}\right)\right\} \tag{6}$$

$$= \sum_{m,n}^{M,N} -\ln\left\{[\boldsymbol{\Omega}\mathbf{x}]_{m,n}\right\}\left(\xi_{m,n}\right) + [\boldsymbol{\Omega}\mathbf{x}]_{m,n} \ . \tag{7}$$

This is to match the definition of the dimension of the images as provided in (2) of the manuscript.

2) Furthermore, we have spotted the same swapping of indices on page 1489, where we refer to an "image with $N \times M$ pixels", while an "image with $M \times N$ pixels" would be correct in view of (2) of the manuscript. Consequently, the continuation of said passage: "all entries $\mathbf{D}_{h,v}$ and the matrix of zeros $\mathbb{0}$ have the same size and dimension as said image $\{\mathbf{D}_h, \mathbf{D}_v, \mathbb{0}\} \in \mathbb{R}^{M\times N}$", would be correct.

3) Another inconsistency is found on p. 1497 in (63), where the summation indices m, n do not match the indices of the variables to be summed i, j. The correct equation should instead be:

The original article can be found online at https://doi.org/10.1007/s11075-024-01759-2.

✉ Christian Zietlow
christian.zietlow@upb.de

Jörg K. N. Lindner
lindner@physik.upb.de

[1] Department of Physics, Paderborn University, Warburger Str. 100, Paderborn 33098, Germany

Published online: 23 June 2025

$$\mathrm{MSE}^k = \frac{1}{M \cdot N} \sum_{m,n}^{M,N} \left(\mathbf{x}_{m,n}^k - \boldsymbol{\xi}_{m,n}^{Orig.} \right)^2 , \tag{63}$$

4) Again, N, M should be swapped to M, N and n, m should be swapped to m, n on p. 1497 and p. 1498 in (65), (66), and (67):

$$\frac{1}{2\sigma^2} \|\mathbf{x}^* - \boldsymbol{\xi}\|_F^2 = \sum_{m,n}^{M,N} \frac{1}{2} \quad \Longleftrightarrow \quad \|\mathbf{x}^* - \boldsymbol{\xi}\|_F^2 = \sum_{m,n}^{M,N} \sigma^2 , \tag{65}$$

$$\lambda \cdot (a \cdot \|\mathbf{z}_1\|_F + b \cdot \|\mathbf{z}_2\|_F) = \lambda \cdot \|\mathbf{x}^* - \boldsymbol{\xi}\|_F = \left(\sum_{m,n}^{M,N} \lambda^2 \cdot \sigma^2 \right)^{1/2} . \tag{66}$$

$$\underset{\mathbf{x},\mathbf{z}_1,\mathbf{z}_2}{\operatorname{argmin}} \quad \sum_{m,n}^{M,N} \frac{1}{2} + \left(\sum_{m,n}^{M,N} \lambda^2 \cdot \sigma^2 \right)^{1/2} . \tag{67}$$

5) Finally, on p. 1498 in (68) the indices should be m, n instead of i, j and M, N instead of N, M for a consistent notation. Therefore, (68) should read:

$$\omega^2 = \sum_{m,n}^{M,N} \frac{\boldsymbol{\Omega}_{m,n}}{\max\left\{\boldsymbol{\Omega}_{m,n}\right\}} . \tag{68}$$

In this context ω should be called "amplification coefficient", because $\omega \geq 1$. It was called "attenuation" coefficient due to a different definition in a previous version of the manuscript. Accordingly, the words "attenuation" or "attenuated" appear ten times in the paper (once on p. 1497, three times on 1498, once in the caption of Fig. 1 on p. 1499, once in the caption of Fig. 4 on p. 1502, once in the caption of Fig. 5 on p. 1503, twice in the caption of Fig. 7 on p. 1505, and once on p. 1509) and should be replaced by "amplification" and "amplified".

MATLAB scripts of the algorithms are now provided in MathWorks. The link is: https://www.mathworks.com/matlabcentral/fileexchange/159873-automated-admm-tgv-denoising-deconvolution-for-images.

Appendix D

An unbiased ADMM-TGV algorithm for the deconvolution of STEM-EELS maps

Ultramicroscopy 275 (2025) 114159

Contents lists available at ScienceDirect

Ultramicroscopy

journal homepage: www.elsevier.com/locate/ultramic

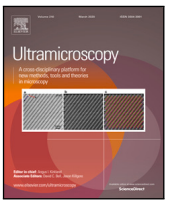

An unbiased ADMM-TGV algorithm for the deconvolution of STEM-EELS maps

Christian Zietlow *, Jörg K.N. Lindner

Nanopatterning-Nanoanalysis-Photonic Materials Group, Department of Physics, Paderborn University, Warburgerstr. 100, Paderborn, 33098, Germany

ARTICLE INFO

Keywords:
EELS map
Deconvolution
ADMM
Total generalized variation (TGV)
Plasmonics

ABSTRACT

Electron-energy-loss-spectroscopy (EELS) spectra in the scanning transmission electron microscope (STEM) are affected by various types of noise. Additionally, they are convolved with the detector point spread function and the energy distribution of the electron source. Often, iterative deconvolution is employed to sharpen peaks and improve the data. However, since the Richardson–Lucy algorithm (RLA) has become the standard deconvolution algorithm in EELS, little progress has been made in terms of technique. In this paper, the authors aim to provide an update to STEM-EELS deconvolution and demonstrate how to significantly improve results compared to those achievable with the RLA. The major limitation of the RLA is that it does not guarantee convergence. Furthermore, the RLA is restricted to pure Poisson noise and lacks adaptability due to limitations in its general structure, particularly when compared to more modern algorithms. A new and versatile approach is the Alternating Direction Method of Multipliers (ADMM), which is based on Lagrangian methods and enables to overcome these restrictions. The generality of ADMM allows us to develop a deconvolution algorithm tailored to EELS maps and incorporate a recent noise model. We extend the standard Bayesian maximum likelihood of the RLA to a maximum a-posteriori approach in ADMM, which enables us to leverage the principles of total general variation (TGV) to enforce convergence. Furthermore, we define the algorithm such that it operates unbiased of the user. To demonstrate the superiority of the ADMM, it is tested against the RLA using simulated data. Eventually, our algorithm is successfully applied to experimental data as well.

1. Introduction

Every measurement is subject to noise. The most prominent noise types in electron energy-loss spectroscopy (EELS) are certainly Poisson noise, which arises from the quantized nature of the signal [1,2], and Gaussian read-out noise originating from the detector electronics [3,4]. However, as noted by Verbeeck and Bertoni [5], the Poisson statistics is significantly altered by the different layers in the scintillator detector, which introduce gains and correlations into the data. We will describe the most important noise parameters in EELS and utilize a noise model that we have theoretically derived and experimentally validated in [6,7].

Noise is only one aspect of the problem when performing EELS measurements. Since every energy-loss is measured with a given energy distribution of the electron gun. Therefore, the signals of interest are convolved and appear blurred. Additionally, the detector point spread function contributes to the blurring and also correlates the noise. These correlation effects necessarily alter the noise statistics and must be taken into account for optimal deconvolution results. However, the energy distribution of the electron gun, combined with the smaller detector convolutions, can easily be measured in vacuum. Since beam electrons do not undergo inelastic scattering in vacuum, the energy-loss remains zero. The resulting peak is therefore referred to as the zero-loss-peak (ZLP). This peak also occurs when a specimen is inserted into the beam path, since the probability of the electrons not losing any energy is quite high.

Deconvolution is a process that enables to address both noise and blur. Several algorithms are used for the deconvolution of EEL spectra, including Fourier deconvolution [8,9], Wiener deconvolution [8,10,11], maximum entropy [8,12], or the widely used Richardson–Lucy algorithm (RLA) [13,14].

In EELS, the iterative Richardson–Lucy-algorithm has become a popular choice [8,9,15,16], largely replacing other algorithms. By utilizing a ZLP as the deconvolution kernel and assuming pure Poisson noise, it has been claimed that energy-loss peaks can be distinguished that were

* Corresponding author.
E-mail addresses: christian.zietlow@upb.de (C. Zietlow), lindner@physik.upb.de (J.K.N. Lindner).
URL: https://physik.uni-paderborn.de/en/lindner (J.K.N. Lindner).

https://doi.org/10.1016/j.ultramic.2025.114159
Received 10 September 2024; Received in revised form 28 April 2025; Accepted 3 May 2025
Available online 16 May 2025

previously hidden in the ZLP [17]. Particularly in the low-loss regime, where optical transitions and plasmonics are situated, this procedure has become a standard method for differentiating between the ZLP and signal, as well as for sharpening these peaks.

However, all these algorithms mentioned above suffer from limited adaptability and impose strict requirements on the inherent noise of the data. In particular, the RLA is only valid for pure Poisson noise, as it is directly derived from the log-likelihood functional of pure Poisson statistics. The RLA ignores the Gaussian distributed detector read-out noises and other noise contributions. Therefore, the image statistics used by the RLA is inherently incomplete, which poses a significant problem for deconvolution. Particularly, when subtracting backgrounds such as the ZLP in the low-loss region or a power-law background in the high-loss region, the noise statistics assumed by the RLA and the actual noise statistics bear little resemblance. The direct consequence of this mismatch between mathematical foundation of the algorithm and the actual noise is a divergent algorithm. Recent research of the RLA fundamentals even indicates that the algorithm is doomed to diverge even for the true Poisson noise statistics, it was inherently build upon [18], therefore leaving it without proper use-cases where it would converge to a fixed result.

Divergence, however, is the most undesirable outcome for such an algorithm, as it leads to the amplification of noise peaks and unstable solutions, which have been widely reported in literature [19–22] and are also observed in EELS [23]. The ancient Latin principle of deductive reasoning: 'Ex falso quodlibet – from falsehood, [anything] follows' is particularly relevant here as it casts doubt on the validity of results obtained from a divergent algorithm.

In an attempt to mitigate the damage to the result, it has been suggested that the number of iterations of the RLA be limited to 15 [15], 20 [16] or some other arbitrary number [8,9,11,17,24,25]. Indeed, limiting the number of iterations prevents the results from diverging; however, the limit should be set to a relatively low number of iterations, as suggested by Egerton [15]. It is evident that premature termination limits the ability of the RLA to reach its full potential.

In this paper, we propose to use the alternating direction method of multipliers (ADMM) as a deconvolution algorithm for EELS. ADMM has been reported to be highly successful in the field of medical imaging [26–28], in biology [4,29,30] and has also been applied in electron microscopy [31,32]. However, to the best of our knowledge, it has not been used for EELS data processing yet. Therefore, this paper will provide the reader with all necessary information to set up the ADMM deconvolution algorithm for EELS data. Owing to its mathematical structure, ADMM is guaranteed to converge within a reasonable number of iterations [33] and, unlike the RLA, does not require early termination. This enables the algorithm to be utilized to its full potential and also makes it relatively independent of the exact number of iterations, especially when convergence is nearly achieved. We will demonstrate how to utilize self-adjusting parameters and noise estimates, which can be measured directly on the detector, to fine-tune the convergence properties of the algorithm and optimize the results. Since all parameters are selected based on objective criteria and mathematical properties, the results remain unbiased by the user.

ADMM enables to incorporate a-priori information into the deconvolution process extending the maximum likelihood (ML) approach to a maximum a-priori (MAP) approach. Such a-priori information encompasses general properties of the data that are known in advance, such as the non-negativity of EELS signals, since there cannot be a negative number of incident beam electrons, and the relative smoothness of the data compared to the noise, which is highly volatile and rough. This principle is known as total variation (TV) and was first introduced by Rudin, Osher and Fatemi [34]. Clearly noise is highly volatile and simulations can easily demonstrate that the assumption of smoothness is valid for plasmonic features and other signals of interest, thereby validating the use of TV approaches for EELS. In the subsequent sections, we will provide a more detailed explanation of this concept.

Total generalized variation (TGV), introduced by Bredies et al. [26,35], is a more advanced extension of the TV principle, which also leverages the roughness of the noise to distinguish it from the signal. However, TGV employs self-adjusting filter masks to better adapt to the data. A detailed explanation of TGV will be provided in Section 4.5.

These filter masks are especially beneficial for EELS map measurements, which are a lateral extension to the regular EEL spectrum. In EELS map measurements, several spectra of a structure of interest are acquired in a raster pattern and allow to visualize, e.g. the lateral distribution of plasmons.

Through the implementation of TGV, ADMM enables the coupling of deconvolution results between the spectra, thereby allowing us to apply the deconvolution to the entire dataset, rather than just individual decoupled spectra, as is the case with the RLA. With a larger number of data points available to the algorithm, in the vicinity of a data point to be restored, the success of deconvolution is significantly improved.

For the application of TGV, it is advantageous to provide data that are as smooth as possible. However, the EELS features are overlaid with variations in the measured beam intensity, which are induced not only by changes in beam current but also by variations in specimen thickness and material composition, resulting in differences in the transmittance of the direct beam. All these factors contribute to an increase in data roughness. Normalizing all spectra to their respective total count allows to remove this additional roughness, but comes at the expense of significantly altering the noise statistics.

Here, the generality of ADMM comes in handy and enables us to rescale the image during the iterations. This allows preserving a much simpler noise statistics compared to the normalized noise statistics that would otherwise be necessary while maintaining the benefits of reduced data roughness.

The advantages of ADMM yield superior results compared to the RLA, as will be demonstrated on a simulated dataset using the MNPBEM-toolbox [36]. This simulated dataset will be treated with various types of noise, as encountered in EELS measurements, by imitating the image formation process. Subsequently, this dataset will be deconvolved with the proposed ADMM algorithm as well as with the RLA. This approach allows to objectively evaluate the results against the original dataset by means of the mean square error (MSE) and therefore enables a direct comparison between ADMM and RLA algorithms. The success of the described ADMM deconvolution method will also be demonstrated on a real measurement of a truncated pyramidal gold nanostructure. Finally, we will present an experimental comparison of the plasmonic behavior of a bottle-shaped gold and a bottle-shaped gold-platinum Janus particle, highlighting the advantages of the proposed ADMM algorithm. The presented study on the Janus particle would be impossible to conduct by only employing recent RLA techniques, while in contrast, the proposed ADMM deconvolution algorithm reveals important plasmonic features, which were formerly hidden within the noise.

2. A noise model for EELS

It is well established that EELS measurements are affected by two distinct types of noise, the Gaussian distribution $\mathcal{N}$, which describes the read-out noises of the detector [6,7,37–39] and the Poisson distribution $\mathcal{P}$ [5–7,38,39], which describes the inherent noise of the signal itself.

Owing to the quantized nature of the beam electrons used for the measurement of EELS, it is either possible to detect an electron within a given time interval or not detecting it. These fluctuations are inherent in the nature of electrons. Both distributions can be described as [40–42]:

$$\mathcal{N}\left[\mu\,,\,\sigma^2\right] = \frac{1}{\sqrt{2\pi\sigma^2}} \cdot \exp\left\{-\frac{(n-\mu)^2}{2\sigma^2}\right\} \qquad \text{and} \qquad \mathcal{P}\left[\hat{S}\right] = \frac{\hat{S}^{\,n}}{n!}\exp\left\{-\hat{S}\right\}\ . \tag{1}$$

We can determine the probability of measuring n counts for both distributions. For the Gaussian distribution, the probabilities are distributed around a mean value μ with the variance σ^2. For the Poisson distribution, the probability of measuring n counts primarily depends on the signal S; both, the mean and variance of the Poisson distribution are equal to the expectation value of the signal $\hat{S}$. This is a fundamental property of the Poisson distribution. However, for a scintillation-based CCD detector, we expect a gain in the conversion of incident beam electrons S_{el} to photons and subsequently into counts S, which are output to the user. Scaling the Gaussian and the Poisson distribution by a gain g yields [6]:

$$g \cdot \mathcal{N}\left[\mu\,,\,\sigma\right] = \mathcal{N}\left[g\cdot\mu\,,\,g^2\cdot\sigma\right] \quad \text{and} \quad g\cdot\mathcal{P}\left[\hat{S}_{el}\right] = g\cdot\mathcal{P}\left[\frac{\hat{S}}{g}\right] \quad \text{, with} \quad S = g\cdot S_{el}\ . \tag{2}$$

Therefore, multiplying a noisy signal with a factor results in multiplying the variance by the squared factor, while the mean value is only changed linearly. This is why the gain factor cannot be simply incorporated into the notation of the Poisson noise, as this operation changes the relation between mean signal and noise level.

While the sum of W Gaussian or Poisson distributed random variables is given by [41–43]:

$$\sum_{w=1}^{W}\mathcal{N}\left[\mu_w\,,\,\sigma_w^2\right] = \mathcal{N}\left[\sum_{w=1}^{W}\mu_w\,,\,\sum_{w=1}^{W}\sigma_w^2\right] \quad , \quad \sum_{w=1}^{W}\mathcal{P}\left[\hat{S}_w\right] = \mathcal{P}\left[\sum_{w=1}^{W}\hat{S}_w\right]\ , \tag{3}$$

such that the sum of the respective mean values and variances of both distributions comprises the resulting distribution.

Measuring a signal on an imperfect detector causes the signal to be blurred by a point spread function Ω_D, and also introduces correlation effects between the noises of neighboring EEL channels. These correlations can be characterized by Pearson correlation coefficients ρ_m, which are given as [44]:

$$\rho_m = \frac{\mathrm{cov}\left[x_i\,,\,x_{i+m}\right]}{\sigma_i\cdot\sigma_{i+m}}\ , \tag{4}$$

where m represents the distance between two EEL channels. The Pearson correlation coefficients are defined as the covariance between two channels x_i and x_{i+m} on a detector, normalized to the standard deviations of both channels, such that $\rho_m \in [-1,\dots,1]$. For $\rho_m = -1$ we observe total anti-correlation, for $\rho_m = 0$ the channels are uncorrelated, and for $\rho_m = 1$, there is total correlation between both channels. Since $m \in [-(M-1),\dots,M-1]$, where M represents the number of EEL channels, there are nearly twice as many Pearson correlation coefficients as EEL channels. Consequently, for $M = 2048$ EEL channels found on our detector, we obtain 4095 Pearson correlation coefficients ρ_m.

Due to convolution with the detector PSF, positive correlation is expected in the EELS data and results in a smoothing of the signal noise [5]. In [6], we mathematically described this smoothing for regular 2D images and subsequently extended it in [7] to accommodate the needs of EELS. We derived that a convolution $\otimes$ of the signal with the detector PSF Ω_D acts on the Poisson distribution, such that [7]:

$$g\cdot\Omega_D\otimes\mathcal{P}\left[\hat{S}_{el}\right] = g\cdot\beta_{conv}\cdot\beta_{corr}\cdot\mathcal{P}\left[\frac{\Omega_D\otimes\hat{S}}{g\cdot\beta_{conv}\cdot\beta_{corr}}\right] \qquad \text{for} \quad g\gg 1 \quad \text{, with} \tag{5}$$

$$\beta_{conv} = \left(\sum_{m=-(M-1)}^{M-1}\rho_m\right)^{-1} \tag{6}$$

$$\text{and} \qquad \beta_{corr} = \frac{M}{M-1}\cdot\left(1-\frac{1}{M^2}\sum_{m=-(M-1)}^{M-1}(M-|m|)\cdot\rho_m\right) \tag{7}$$

$$\text{as well as} \quad \rho_m = \left[\Omega_D^*\otimes\Omega_D^*\right]_m \quad , \tag{8}$$

where ρ_m represents the Pearson correlation coefficients and Ω_D^* is the detector point spread function in EELS, normalized to the height of one. Consequently, two distinct smoothing coefficients are observed in EELS. Firstly, β_{conv} describes a smoothing resulting from the convolution of the noise with the detector PSF, and secondly, β_{corr} describes an additional smoothing of the noise due to the correlation induced by this operation. The latter smoothing coefficient β_{corr} describes the influence of the correlation on the measured sample variance. For correlated noise, it is apparent that the measured variance is reduced compared to uncorrelated noise, since the noise counts of neighboring channels tend to deviate in the same direction. However, larger sample sizes, i.e. many EEL channels, typically mitigate this effect because the correlation length is often short, making the noise of distant channels independent of the channel in question. Therefore, the measured variance approaches that of uncorrelated noise in such cases. However, correlation is restricted to the measured spectrum and therefore changes the measured noise only within this spectrum, without affecting the noise between spectra. So, β_{corr} is rather an effect occurring when measuring the sample variance of correlated data. In contrast, β_{conv} accounts for the effect that convolution broadens the noise of a given channel to the neighboring channels mixing them. This results in the noise of neighboring channels canceling each other out to a certain degree, leading to a smoothing of the noise that is observed. This effect affects the noise variance both within and between measurements and is independent of the sample size. Both effects, which lead to β_{corr} and β_{conv}, are caused by convolution and occur simultaneously due to their close relationship.

However, it is essential to note that the above formulas Eq. (5) to Eq. (7) are only valid for processes where multiple photons are generated as a result of a scattering event in the scintillation layer, leading to $g \gg 1$. Particles are discrete entities; therefore, several of them must be created in order to spread laterally and smooth out the noise. A single particle would merely be dislocated, resulting in a blur of the signal, but the noise would remain unaffected by the convolution [45]. For scintillation-based CCD detectors in TEM, however, this condition is readily met, as hundreds to thousands of photons are generated by a single incident electron.

In [6], we demonstrated a method for precisely measuring the Pearson correlation coefficients for the entire detector using the autocovariance function on homogeneously illuminated images in TEM mode. Furthermore, we demonstrated how to reconstruct the 2D detector PSF from

the Pearson coefficients obtained by this method. Homogeneous illumination conditions, which are required for the acquisition of the Pearson correlation coefficients, are commonly encountered during the acquisition process of a gain reference, a standard procedure for image corrections in transmission electron microscopy. In [7], we detailed the calculation the Pearson correlation coefficients for EELS measurements, based on those measured for 2D images, and described the reconstruction of the 1D detector PSF for EELS.

In EELS, the signal arises from inelastic scattering processes of the beam electrons with a specimen, resulting in a loss of kinetic energy. The electrons are directed to the entrance aperture of the EEL spectrometer by the magnetic lenses of the microscope. Within the spectrometer, the beam is further dispersed by magnets according to the kinetic energy of the electrons and eventually reaches the detector with a certain distribution. This distribution encompasses the desired information about the interactions with a specimen, represented as the signal S, as well as the energy distribution Ω_E of the emitter. Furthermore, due to the small diameter of the aperture in the spectrometer, the signal exhibits a minimal diameter on the detector, which we characterize using Ω_{STEM}, as it is dependent on the optics of the system in STEM mode. However, these convolutions Ω_{STEM} and Ω_E do not affect the noise properties of the Poisson distribution, but only describe the distribution of the signal on the detector. We consider all above convolutions Ω to be normalized, such that the probabilities sum to one $\sum_{m=-(M-1)}^{M-1} \Omega_m = 1$, facilitating a straightforward mathematical description. In conjunction with a conversion gain g, which converts incident beam electrons into counts as the output from the microscope, we obtain [6,7]:

$$\begin{aligned} \Omega_D \otimes g \cdot \mathcal{P}\left[\frac{\Omega_{STEM} \otimes \Omega_E \otimes \hat{S}}{g}\right] &= g \cdot \beta_{conv} \cdot \beta_{corr} \cdot \mathcal{P}\left[\frac{\Omega_{STEM} \otimes \Omega_E \otimes \Omega_D \otimes \hat{S}}{g \cdot \beta_{conv} \cdot \beta_{corr}}\right] \\ &= g \cdot \beta_{conv} \cdot \beta_{corr} \cdot \mathcal{P}\left[\frac{\Omega \otimes \hat{S}}{g \cdot \beta_{conv} \cdot \beta_{corr}}\right] \quad \text{, with} \quad \Omega = \Omega_{STEM} \otimes \Omega_E \otimes \Omega_D \,. \end{aligned} \tag{9}$$

Measuring an EELS signal in vacuum yields the vacuum ZLP Ω, which comprises the distributions at the entrance aperture of the spectrometer Ω_{STEM}, the energy distribution of the electron gun Ω_E, and the detector PSF Ω_D. The vacuum ZLP determines the energy resolution of the microscope. As no energy-losses are expected in the absence of a specimen, the signal S is represented by a Dirac delta function that is broadened by the ZLP characteristics.

Acquiring any signal using a CCD or a CMOS camera introduces read-out noise and dark currents into the measurement, thereby altering the signal. To eliminate dark currents, background subtractions are performed as a standard procedure. These subtractions, however, while canceling out dark currents, double the variance of the read-out noise and introduce additional noise arising from the Poisson distribution of the dark currents. We denote the cumulative noise from the detector electronics as $\sigma_{D,i}$, for each channel i, respectively. This is due to the significant variation of the noise from channel to channel [7]. As the resulting dark frame subtracted spectrum consist of two independent measurements, we find $2 \cdot \sigma_{D,i}^2$ to be the variance of an additional noise term in EELS. In [6], we presented a detailed analysis of the detector noises, including how they are affected by the application of a gain reference and gain non-linearity corrections. The formation process of an EELS measurement ξ can be described as [7]:

$$\xi_i \approx g \cdot \beta_{conv} \cdot \beta_{corr} \cdot \mathcal{P}\left[\frac{\left[\Omega \otimes \hat{S}\right]_i}{g \cdot \beta_{conv} \cdot \beta_{corr}}\right] + \mathcal{N}\left[0,\, 2 \cdot \sigma_{D,i}^2\right] \,, \tag{10}$$

where the conversion gain g relates the incident electrons to the number of counts presented as output, and $\left[\Omega \otimes \hat{S}\right]_i$ represents the convolved signal within the ith EEL channel. The signal noise is reduced due to convolution with the 1D detector PSF for EELS, yielding two smoothing factors β_{conv} and β_{corr}. We therefore obtain the desired signal S in counts, convolved with the vacuum ZLP Ω, and an additional Gaussian noise term associated with twice the detector noise, due to the background subtraction.

In [7], we demonstrated how to determine the gain g for EELS using the autocovariance function and the resulting Pearson correlation coefficients. This enables the use of the noise model even with detectors lacking electron-to-counts calibration.

2.1. Noise model for EELS maps

In this section, we extend the noise model for single EEL spectra from Eq. (10) to EELS maps. EELS maps comprise multiple sequentially acquired spectra, concatenated in the lateral dimension, thereby forming 3D data cubes. To facilitate better data visualization, these cubes are often sectioned into *energy slices*, comprising the same EEL channel i from all corresponding EEL spectra, thereby revealing only the lateral distribution (x, y) of a specific energy loss; or into a *spectrum*, which solely displays the energy-loss distribution across all EEL channels for a particular position on a specimen. *Voxels* represent the smallest unit (x, y, i) of information within the 3D data cube, serving as the fundamental building blocks of the dataset. As demonstrated in [6], EELS maps necessitate two separate noise models: one for the energy dimension, denoted by the underlined index $\underline{i}$, and another in the lateral dimensions, denoted by the underlined indices $\underline{x, y}$. This concept will be elaborated upon in the subsequent sections.

In the Gatan software '*Digital Micrograph*', a slightly different background subtraction approach is employed compared to single EEL spectra. Specifically, a '**H**igh **Q**uality'-background is generated by averaging across $A = \sqrt{X \cdot Y}$ dark frames, where the EELS map has a side-length of X and Y spectra. This HQ background is then subtracted uniformly from all spectra. Since the background is averaged over A spectra, the corresponding noise in this frame is firstly added up according to Eq. (3), resulting in $\sum_A \sigma_{D,i}^2 = A \cdot \sigma_{D,i}^2$, and then divided by a factor of A^2, according to Eq. (2), resulting in $\frac{1}{A} \cdot \sigma_{D,i}^2$. Consequently, by removing the averaged backround frame instead of a simple background frame without averaging, the factor changes from 2 to $\left(1 + \frac{1}{A}\right)$ for the variance of the detector noise in energy direction. However, the noise volatility in the lateral dimensions remains unaffected by this correction, since the HQ-background is subtracted uniformly from all EEL spectra within the EELS map. Each energy slice is therefore effectively subtracted by the same corresponding scalar value within this reference frame.

As an example, consider three consecutive energy slices of a STEM-EELS data cube, which get background subtracted. Since the background is acquired as a spectrum, the noise is in energy direction. Concatenating copies of said spectrum laterally results in the first energy slice being subtracted by an exemplary value of 3, the second gets subtracted for instance by 7 and the third by -2. It is apparent that, since all values in a given energy slice get subtracted by the same value, the volatility inside the energy slice cannot increase by subtracting this background, but since the 'noisy' values 2,7,-3 are being subtracted from consecutive slices, the variance between them increases.

Therefore, subtracting a HQ-background does not contribute to the noise volatility in the lateral dimensions, and the factor $\left(1 + \frac{1}{A}\right)$ reduces to 1. This serves as a first example of why two distinct noise models are necessary for the respective directions.

In general, the noise volatility is different between the different directions of data, i.e. between the lateral dimensions and the spectral (or energy) dimension. This is a consequence of the data cube being recorded spectrum by spectrum – one at a time as a whole – and then being merged laterally. One can easily imagine that for example the convolution with a detector point spread function only affects the spectrum per se and cannot act between spectra. This results in the necessity for a bifurcated noise model, split between lateral and energy directions.

In EELS maps, energy drifts may occur between spectra due to their sequential acquisition. To correct these drifts, the spectra must be realigned with respect to the ZLP or any other significant feature that is shared among all spectra at the same energy position. In [7], we demonstrated the effectiveness of a sub-channel alignment using the cross-correlation function, to which we fitted a Gaussian distribution. However, this realignment reintroduces some noise due to background subtraction in the lateral dimension, resulting in a factor of $\left(1+\frac{\varphi}{A}\right)$, similar to the energy direction, but with a shifting factor φ. This factor can be estimated as the mean drift across all spectra [7]:

$$\varphi \approx \frac{1}{XY\,(XY-1)} \sum_{x,y}^{X,Y} \sum_{x',y'}^{X,Y} \sum_{i}^{M} \left| \delta_{x,y,i} - \delta_{x',y',i} \right| \quad , \text{with } (x',y') > (x,y) \ , \tag{11}$$

with a Dirac delta distribution δ, positioned at the peak of a significant feature that is common to every spectrum in the array at the same energy, such as a ZLP. This approach enables to quantify the difference in shift by summing the differences between the delta functions. We subtract the Delta peaks in a manner that ensures each spectrum is subtracted once from every other spectrum in the array. In the absence of an energy shift, this results in a shifting factor of $\varphi = 0$. Conversely, if the mean drift between neighboring channels is equal to or exceeds one EEL channel, we obtain $\varphi = 1$. Therefore, the shifting factor is found to be within the range between $\varphi \in [0, \dots, 1]$, indicating the percentage of channel shift per spectrum.

Sub-channel alignments require some form of interpolation. As demonstrated in [6], linear interpolation of the spectra between channels renders the uncertainty of alignment negligible. However, interpolation is not a standard procedure in '*Gatan Digital Micrograph*' [46]. For non-interpolated spectra, we found a dependence of the uncertainty on the first derivative of the signal. Furthermore, we mathematically derived the overall uncertainty of alignment $\sigma_{MA} \geq 0.25$ channels, and experimentally verified it, assuming a continuous distribution of the energy shift. The uncertainty can be described as [7]:

$$\sigma_A^2 = \sigma_{MA}^2 \cdot \left(\frac{d}{di} S_{x,y,i} \right)^2 \ , \tag{12}$$

which we assume to be Gaussian distributed for simplicity. For the present paper, we utilize interpolated spectra to achieve optimal results, and therefore neglect this term.

Interpolation results in an additional convolution with Ω_I, which smooths the noises and consequently leads to a slight modification in β_{conv} and β_{corr}, due to the altered Pearson correlation coefficients. The Pearson correlation coefficients for the interpolated signal ρ and the detector noises ρ_D are given as:

$$\rho_m = \left[\Omega_D \otimes \Omega_D \otimes \Omega_I \star \Omega_I \right]_m \quad \text{and} \quad \begin{aligned} \rho_{D,m} &= \left[\Omega_I \star \Omega_I \right]_m && \text{, with} \\ \Omega_I &= \left[(1-|\Delta|) \ , \ |\Delta| \ , \ \dots \ , \ 0 \right] && , \end{aligned} \tag{13}$$

where $\star$ represents cross-correlation, Δ represents the sub-channel drift, and $[\,\cdot\,]_m$ represents the mth element of the distribution. Consequently, according to Eq. (6), we obtain an additional smoothing factor for the detector noises, denoted as β_D. We have observed that the sub-channel drift is uniformly distributed in the acquisition of a typical EELS map and derived in [7] that $\beta_D = \frac{2}{3}$ as the mathematical consequence, which we could validate experimentally. According to Eq. (6), this smoothing corresponds to an average effective sub-channel shift of $\Delta \approx 0.211$ channels. Subsequently, we neglect the smoothing effect of the correlation β_{corr} induced by interpolation due to its minor impact. However, although interpolation affects the noise, it does not alter the width of the ZLP nor any of its component. The ZLP width is still given as $\Omega = \Omega_{STEM} \otimes \Omega_E \otimes \Omega_D$.

It is worth reiterating that the smoothing effect of correlation β_{corr} is only applicable within a given spectrum and not between spectra. Additionally, the background is subtracted uniformly from all spectra, resulting in two distinct noise models for the lateral directions and the energy direction [7]. To specify direction being referred to when describing the noise volatility, we denote them by underlining the corresponding indices $\underline{x,y}$ or the index $\underline{i}$:

$$\xi_{x,y,\underline{i}} \approx g \cdot \beta_{conv} \cdot \beta_{corr} \cdot \mathcal{P} \left[\frac{\left[\Omega \otimes \hat{S}_{x,y} \right]_i}{g \cdot \beta_{conv} \cdot \beta_{corr}} \right] + \mathcal{N} \left[0, \left(1 + \frac{1}{A} \right) \cdot \beta_D \cdot \sigma_{D,i}^2 \right] \ , \tag{14}$$

$$\xi_{\underline{x,y},i} \approx g \cdot \beta_{conv} \cdot \mathcal{P} \left[\frac{\left[\Omega \otimes \hat{S}_{x,y} \right]_i}{g \cdot \beta_{conv}} \right] + \mathcal{N} \left[0, \left(1 + \frac{\varphi}{A} \right) \cdot \beta_D \cdot \sigma_{D,i}^2 \right] \ , \tag{15}$$

where $\left[\Omega \otimes \hat{S}_{x,y} \right]_i$ represents the ith EEL channel of the convolved signal, located at position (x, y) on the EELS map.

Thus far, we have developed two distinct noise models for standard EELS measurements, one for the energy and one for the lateral directions, as presented in Eqs. (14) and (15), respectively. The lateral model describes the noise volatility between spectra, whereas the energy direction model describes it within a given spectrum.

Such volatile noise is at the foundation of the total variation approach that distinguishes noise and signal by volatility, i.e. by employing derivatives, as will be explained in the corresponding section Section 4.5. Data fidelity is a different concept and is equally important, but does not necessarily need all the aspects of volatility. Imagine having measured a signal, a spectrum for example. This spectrum is, as a whole, offset by a value subject to noise. That means, the first measurement is offset by 1, the second by −5 and a third by 0. While the noise volatility inside the spectrum is, by any means, unaffected by this varying offset, the result is subject to uncertainty that would be characterized by employing error calculus or propagation of uncertainty. Such an approach of uncertainty is necessary to define the data fidelity employed by the log-likelihood constraint, which in greater detail will be explored in the corresponding section Section 4.3.

Therefore, we must determine the maximum contributions, term by term, between both models to establish the total uncertainty associated with measuring a voxel within the data cube:

$$\xi_{x,y,i} \approx g \cdot \beta_{conv} \cdot \mathcal{P} \left[\frac{\left[\Omega \otimes \hat{S}_{x,y} \right]_i}{g \cdot \beta_{conv}} \right] + \mathcal{N} \left[0, \left(1 + \frac{1}{A} \right) \cdot \beta_D \cdot \sigma_{D,i}^2 \right] \ , \tag{16}$$

as per definition $\beta_{corr} \leq 1$ and $\varphi \leq 1$. The above noise model represents the uncertainty of an EEL spectrum within the array as a combination of both noise models, where we omit the underlined indices since this noise model provides the total uncertainty in all directions. This noise model will be crucial in defining the Bayesian likelihood approach for deconvolution, as it enables the voxel-wise comparison of deconvolution results with the original measurement. Based on the probability distribution of the noise components, the likelihood approach establishes a distance measure that penalizes deconvolution estimates that deviate significantly from the original data. This concept will be further elaborated upon in Section 4.3.

However, the sequential acquisition of spectra within the EELS map allows for beam current fluctuations between measurements. To account for these changes in, we rewrite the EELS signal as $\hat{S}_{x,y} = \mathcal{I}_{x,y} \cdot \hat{s}_{x,y}$, where the intensity map $\mathcal{I}_{x,y} = \hat{S}_{src,x,y} \cdot T_{x,y}$, comprises the beam current $\hat{S}_{src,x,y}$ incident on the specimen, and the transmittance of the specimen $T_{x,y}$ at the corresponding position (x, y) in the EELS map. Furthermore, we denote the loss probabilities using the lowercase letter $\hat{s}_{x,y}$.

The intensity map can be estimated by summing the spectra along the energy direction. Normalizing the spectra using such a map allows to eliminate both beam intensity fluctuations in $S_{src,x,y}$ and variations in the transmittance $T_{x,y}$ of the specimen from the equation. Frequently, the loss probabilities are more relevant than the overall counts. This normalization approach effectively addresses both issues simultaneously. However, summing all EEL channels M also results in the summation of all noise components, making the total summed intensity $\sum_i^M \xi_{\underline{x,y,i}}$ only an estimate of the intensity map $\mathcal{I}_{x,y}$, which is subject to uncertainties. For a sufficiently large signal, the estimate is precise enough to be usable. We obtain [7]:

$$\mathcal{I}_{x,y} \approx \sum_i^M \xi_{\underline{x,y,i}} \approx \left(\mathcal{I}_{x,y} \cdot \sum_i^M \left[\Omega \otimes \hat{s}_{x,y}\right]_i \right) \cdot \mathcal{N}\left[1\,,\, k^2_{\underline{N,x,y,M}}\right] \quad \text{, with} \tag{17}$$

$$k^2_{N,\underline{x,y,M}} \approx \frac{\left(1 + \frac{\sigma^2_{Int}}{4I^2}\right) \cdot g \cdot I \cdot \sum_i^M \left[\Omega \otimes \hat{s}_{x,y}\right]_i + \left(1 + \frac{\sigma^2_{Int}}{I^2}\right) \cdot \sigma^2_{D,M}}{\left(I \cdot \sum_i^M \left[\Omega \otimes \hat{s}_{x,y}\right]_i\right)^2} \quad .$$

where $k_{N,\underline{x,y,M}}$ represents the uncertainty in measuring the intensity map $\mathcal{I}_{x,y}$, which is necessary for a normalization of the measurement in a next step. Further, $\sigma^2_{D,M}$ represents the sum of detector noises across all channels M. We obtain the mean value as $I = \frac{1}{X \cdot Y} \sum_{x,y}^{X,Y} \mathcal{I}_{x,y}$ and the variance of the intensity map as $\sigma^2_{Int} = \frac{1}{X \cdot Y} \sum_{x,y}^{X,Y} \left(\mathcal{I}_{x,y} - I\right)^2$. However, the variance of the summed detector noises, denoted as $\sigma^2_{D,M}$, is significantly higher for CCD detectors than the expected sum of variances in Eq. (3) suggests. This discrepancy arises from an offset in the individual detector rows, which vary from row to row, as was demonstrated in [6,7].

The normalization approach, based on summed intensities, is effective under three conditions [7]: Firstly, either $\sum_i^M \hat{s}_{x,y,i} \approx 1$ is required to encompass a significant portion of the loss probabilities throughout the specimen, or $\sum_i^M \hat{s}_{x,y,i} \approx \text{const.}$ must hold, ensuring independence from the specimen position (x, y) and thus maintaining the relative proportion between all spectra. In the case of low-loss EEL spectra, which often truncate large bulk plasmonic peaks, this approach inevitably results in an artificial overestimation of the loss probabilities for materials exhibiting high plasmonic resonance. This phenomenon typically occurs in material systems comprising a metal particle on a semiconductor or organic material substrate.

Secondly, the condition $k_{N,\underline{x,y,M}} < 0.05$ is necessary, as the mathematical approximations for the noise model rely on this assumption. Thirdly, to ensure sufficient normalization of an EEL channel, it is necessary that all other channels contribute a significant portion of the overall loss probabilities. This is due to the fact that, when normalizing a given EEL channel by the sum of all channels, the channel itself is included in the sum, resulting in a slight modification of the noise models.

Considering these factors, we derive a noise model for the noise volatility in the lateral dimensions of normalized EEL channels [7]:

$$\xi_{N,\underline{x,y,i}} \approx \underbrace{\frac{g \cdot \beta_{conv} \cdot \mu_R^2}{I} \cdot \mathcal{P}\left[\frac{I \cdot \left[\Omega \otimes \hat{s}_{x,y}\right]_i}{g \cdot \beta_{conv} \cdot \mu_R^2}\right]}_{(1)} + \mathcal{N}\left[0\,,\, \Theta^2_{N,\underline{x,y,i}}\right] \quad , \tag{18}$$

$$\text{with } \Theta^2_{N,\underline{x,y,i}} \approx \underbrace{\frac{\sigma^2_{Int}}{4I^2} \cdot \frac{g \cdot \beta_{conv} \cdot \mu_R^2}{I} \cdot \left[\Omega \otimes \hat{s}_{x,y}\right]_i}_{(2)} + \underbrace{k^2_{N,\underline{x,y,i}} \cdot \left[\Omega \otimes \hat{s}_{x,y}\right]_i^2}_{(3)} + \underbrace{\frac{\left(1 + \frac{\sigma^2_{Int}}{I^2}\right) \cdot \mu_R^2 \cdot \left(1 + \frac{\varphi}{A}\right) \cdot \beta_D \cdot \sigma^2_{D,i}}{I^2}}_{(4)} \quad ,$$

$$\text{and } k^2_{N,\underline{x,y,i}} \approx \frac{\left(1 + \frac{\sigma^2_{Int}}{4I^2}\right) \cdot g \cdot I \cdot \sum_{h \neq i}^M \left[\Omega \otimes \hat{s}_{x,y}\right]_h + \left(1 + \frac{\sigma^2_{Int}}{I^2}\right) \cdot \sigma^2_{D,R}}{I^2} \quad \text{as well as} \quad \mu_R = \sum_{h \neq i}^M \left[\Omega \otimes \hat{s}_{x,y}\right]_h \quad ,$$

where μ_R represents a factor that arises from the inclusion of the respective EEL channel within the total sum. Accordingly, $\sigma^2_{D,R} = \sigma^2_{D,M} - \sigma^2_{D,i}$ corresponds mostly to $\sigma^2_{D,M}$. In Eq. (18) the following terms are present: (1) The Poisson distributed signal noise, smoothed by the convolution with the detector PSF and interpolation. (2) The variation of the smoothed Poisson noise by the distribution of the intensity map, which contains beam current fluctuations and variations of the specimen transmittivity. (3) The uncertainty associated with intensity normalization. Additionally, one finds (4) the smoothed detector noise resulting from interpolation. All terms are normalized by the mean intensity I of the intensity map, which appears in the denominator.

Both, the comprehensive derivation of the formulas and the experimental validation of this noise model are presented in [7]. Additionally, [6,7] demonstrate how to experimentally measure all the relevant parameters, enabling the noise model to be tailored to each EELS detector.

The volatility model in energy direction for normalized EEL channels is relatively straightforward [7]:

$$\xi_{N,x,y,\underline{i}} = \frac{\xi_{x,y,\underline{i}}}{\sum_i^M \xi_{x,y,\underline{i}}} \quad , \tag{19}$$

since all EEL channels i of a given spectrum are divided by the same summed intensity value. Therefore, intensity normalization does not alter the noise volatility in energy direction. Instead, the noise is scaled by the denominator, which serves as a scalar for each position (x, y) in the EELS map.

In the next section, a ZLP will be subtracted from the spectra. Hence, the subtraction of the ZLP must be incorporated into the noise model. Since there are multiple ways of creating such a ZLP for subtraction, no definite noise model can be provided. However, some thoughts on this subtraction shall be shared in this regard.

For a ZLP that is provided by fitting some formula to the ZLP, no additional noise volatility is expected, since the fit is smooth. However, there is an uncertainty in fitting that must be regarded between spectra, which depends on the fitting model itself.

In an alternative case where the ZLP is measured, preferably in vacuum, and averaged across several measurements, as was done for the measurements in this paper, the above noise models for volatility and uncertainty also do apply to the ZLP to be subtracted. They must be incorporated in the same way as the background subtraction: by multiplying the ZLP noise variance, as calculated by the respective noise models, by one over the number of averaged spectra.

An easy way to subtract such a vacuum ZLP from a measurement is by fitting it to all spectra separately. In this case, a scaling factor is introduced for each spectrum, similar to Eq. (2), which appears squared in the noise. Due to the similarities between the ZLP and a Gaussian, an uncertainty of the fit can be approximated by the same uncertainty as a Gaussian fit would inherit. When averaging several dozen ZLP's with a number of counts similar to that of the measurement spectra of interest, the noise can often be neglected.

Having established the deconvolution kernel in Eq. (9), as well as a noise model of the original measurement in Eq. (16) (for the likelihood approach in Section 4.3) and a model for the noise volatility in all directions of the intensity normalized loss probabilities in Eq. (18) and Eq. (19) (for a total variation approach in Section 4.5), we now introduce the necessary data preparations. These preparations are crucial before defining a deconvolution algorithm that aims to recover the desired information, as we will elaborate upon subsequently.

3. Data preparation

To obtain good results with the deconvolution, it is essential to correct the detector. A standard procedure is the application of a gain reference. In [6], we calculated the uncertainties associated with this procedure and described the fixed-pattern noises it introduces. Additionally, we demonstrated in [7] how to calculate the uncertainty underlying the summations performed for EELS, and showed that this uncertainty is negligible for sufficiently large counts in the gain reference. However, we found it advisable for our detector to acquire multiple gain reference frames with a target intensity not exceeding 10% of the total dynamic range of the detector, in order to avoid gain non-linearities. We also demonstrated in [6] how to correct these non-linearities after acquiring a gain reference. In this paper, we apply both gain reference and non-linearity corrections to the data for the measurements performed.

Additionally, cosmic rays can alter the signal, manifesting as spike events. It is essential to remove these artifacts prior to deconvolution, as they follow a long-term statistics that is fundamentally different from the general image statistics. A straightforward method applicable for EELS maps involves comparing a voxel within its respective energy slice and checking the standard deviation of the surrounding voxels. If the respective voxel falls outside a 10σ threshold, it is typically a cosmic ray. The voxel can be replaced by using the main value of the surrounding voxels. This approach is the standard method employed in *Gatan Digital Micrograph* for EELS data cubes [46].

Eventually, the spectra must be aligned. We investigated several methods in [7] and found the cross-correlation method to be the most effective. This method is also the standard procedure used by *Gatan Digital Micrograph* [46]. By incorporating an additional fitting of the peak of the cross-correlation function, we achieved sub-channel alignment of the spectra, resulting in even better outcomes. We applied this method to align the EELS spectra used in this paper prior to deconvolution.

Additional steps must be taken prior to deconvolution, including the subtraction of the ZLP, determination of the deconvolution kernel, and padding of the spectra. These steps are described in detail below.

3.1. Subtraction of the ZLP

When deconvolving EEL spectra, regardless of whether RLA or ADMM algorithms are used, the results sometimes suffer from ringing artifacts, a well-reported issue in EELS [15,24,47,48]. These artifacts are typically associated with an imprecise noise model or noise within the deconvolution kernel [22] and are particularly pronounced at sharp edges within the deconvolved data. The ZLP can often be considered as such a sharp edge. As the ZLP dominates the entire spectrum, these ringing artifacts can severely distort low-loss plasmonic features or even surpass them in intensity. In [49], we demonstrated how such artifacts in the high-loss region, arising from an incorrect noise model in the RLA, can be easily misinterpreted as actual features in an EEL spectrum. As an example for the alteration of the deconvolution results by not subtracting the ZLP prior to deconvolution, we present in Fig. 1(a) a simulated EEL spectrum of a gold nanoparticle with a dispersion of 0.01 eV per channel, calculated using the MNPBEM toolbox [36]. To this simulation data, we added a Dirac delta peak at the zero-loss position. We consider this spectrum (green) to be the ground truth for evaluating the deconvolution results. This ground truth spectrum was convolved with a Gaussian shaped ZLP with a FWHM = 1 eV and superimposed with true Poisson noise (black). It is evident that the ZLP overlaps the plasmonic peak. In red, we present the deconvolution result obtained with the RLA after 15 iterations, without subtracting the ZLP prior to deconvolution. In blue, we present the results obtained with the same parameters, but with the ZLP removed prior to deconvolution. By comparing both results to the ground truth, it is evident that the ZLP subtraction is necessary. Only the RLA with the ZLP removed yields the correct position of the plasmonic peak, whereas the peak of the RLA without prior ZLP removal appears to be shifted. This shift is caused by the ringing artifacts, which superimpose on the result and displace the peak position as the artifacts grow in intensity with increasing number of iterations.

Note that the RLA algorithm relies on the assumption that the measured intensity and the noise variance are equal, which is a characteristic of true Poisson noise. For low-loss EEL spectra, this necessary step of ZLP subtraction immediately introduces a significant mismatch in the Poisson noise at the region of interest for surface plasmons. This miss-match, in turn, gives rise to ringing artifacts in the RLA results, which is why the iteration is often terminated prematurely. Therefore, even for EEL spectra with matching noise statistics, the application of the RLA is inherently flawed by design. The ZLP removal dilemma is one of the primary reasons why we deem the RLA unsuitable for deconvolving low-loss EEL spectra.

The ringing behavior near large peaks is not unique to the RLA, but also occurs with ADMM. To mitigate these ringing artifacts in our algorithm, we must subtract the ZLP from each spectrum prior to deconvolution. In ADMM, however, this does not pose a problem, as the signal used for the image statistics can differ from the signal being deconvolved. This enables the restoration of correct signal statistics during deconvolution, even for background subtracted datasets.

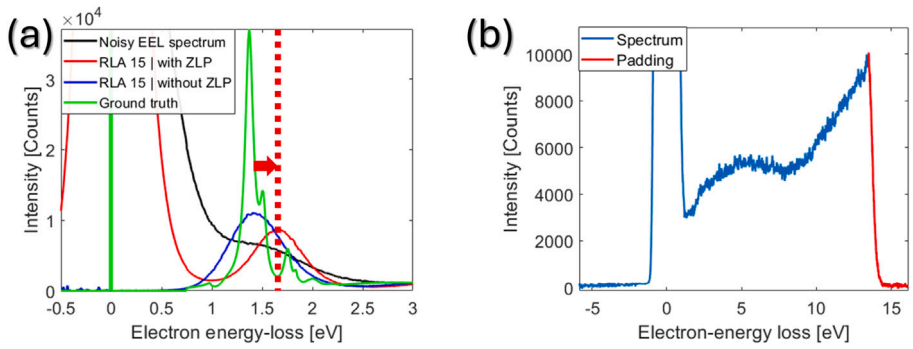

Fig. 1. **(a)** Simulated EEL spectrum (green) calculated using the MNPBEM toolbox [36], serving as the ground truth. This spectrum was convolved with a Gaussian shaped ZLP (FWHM = 1 eV), causing the ZLP to overlap with the plasmonic peak, and true Poisson noise was superimposed (black). This spectrum was deconvolved using the RLA with 15 iterations, without removing the ZLP prior to deconvolution (red). As can be seen, that the peak position of the deconvolution result, marked with the dotted red line, is shifted relative to the ground truth. In contrast, removing the ZLP prior to applying the RLA with 15 iterations yields the correct peak position in the deconvolution results (blue), which demonstrates the necessity of removing the ZLP. **(b)** Illustrates the padding (red) of an EEL spectrum as an extension of the regular spectrum (blue), creating circular boundary conditions for deconvolution. The padding comprises the right side of the ZLP measured in vacuum and is fitted to the end of the spectrum. Similar noise, as found in the spectrum, is added to blend in the padding seamlessly.

The ZLP, as measured in vacuum, is mathematically described by Eq. (9). We measure the ZLP with the same acquisition time before and after acquiring the EELS map, using a hole in the specimen. By acquiring a 15 x 15 EELS map in vacuum, aligning the spectra sub-channel with respect to their energy drift and averaging the ZLPs across all spectra, we obtain a good estimate, which can be fitted in height to each spectrum in the EELS map of interest. Since we have acquired two vacuum ZLPs, we can fit a linear combination of both to account for any deviations in the ZLP that may occur during the measurement.

Subtracting ZLPs measured in vacuum adds noise to the EELS map, which must be taken into account for optimal deconvolution results according to the thoughts provided in Section 2.1. However, it is often sufficient to neglect these noises.

3.2. Deconvolution kernel

The same spectrum used for ZLP subtraction can also be used for deconvolution. When deconvolving with an average ZLP measured in vacuum, as described in the previous section, it is advisable to set the low-count regime of that ZLP to zero to prevent ringing artifacts.

There is a method reported, which utilizes the spectra from ‘background’ regions on the specimen, additionally enabling the deconvolution of substrate characteristics, such as bulk plasmons from thicker regions, from low-loss spectra [9,15]. This deconvolution method is also commonly applied to core-loss spectra in a slightly different form, where the low-loss spectrum is used as the deconvolution kernel to mitigate the convolution effects of the plasmonic peaks. However, this approach requires ‘padding’ of the spectra to be deconvolved; otherwise, deconvolution will lead to ringing artifacts. Through padding, which is explained in the next section, these artifacts can be minimized.

3.3. Padding

Deconvolution frequently employs the fast Fourier transform (FFT). For a spectrum with M EEL channels, a deconvolution kernel with an equal amount of channels is used. However, this approach assumes circular boundary conditions of the dataset, implying that the spectrum is periodic and repeats after M channels. Without additional measures, this can readily lead to mutual influence between the boundaries in the deconvolution result [21,50]. This is clearly undesirable.

The discrete convolution two distributions f and g, both with a finite number of EEL channels M, represents the true convolution in the microscope:

$$[f \otimes g]_m = \sum_{m^*=-M}^{M} f_{m-m^*}\, g_{m^*} \ . \tag{20}$$

To perform (de-)convolution in a mathematically correct sense, we must pad the EEL spectrum with an array of $\frac{M}{2}$ additional channels to each side of the original spectrum, creating circular boundaries without interference between them. Fortunately, the vacuum ZLP comprises only a few dozen EEL channels at high dispersion levels, while the other channels exhibit no measurable signal. Therefore, we can limit the overall padding to the number of non-zero channels in the ZLP.

In an ideal case, both ends of the spectrum already exhibit zero intensity, indicating that in the original (unconvolved) spectrum, the first and last features are separated by at least the number of non-zero elements of the ZLP, circularly.

The presence of intensity in the first or the last channel of an EEL spectrum complicates the padding. This is often the case in EELS, as the number of EEL channels is finite and therefore truncates peaks at the end of the detector array. In this case, we need to find a padding solution that allows the signal to approach zero intensity without disrupting the continuity of the convolved signal with respect to the ZLP shape. Failing to meet this requirement necessarily leads to boundary artifacts, which propagate into the deconvolved result with the width equal to half the number of non-zero elements in the deconvolution kernel. To minimize artifacts, we found that padding the boundary with the right side of the ZLP measured in vacuum is a useful and straightforward method. By fitting the height to the end of the EEL signal, one can create a padding that maintains the ZLP shape as the signal approaches zero. We also recommend adding the same types of noises present in the regular data to padded region to make the padding blend in. An example of such padding is shown in Fig. 1(b) as a red extension to the spectrum.

However, the deconvolved boundary region should not be trusted with respect to the validity of the deconvolution result, as padding cannot recover the lost information outside of the boundary, which in turn affects the deconvolution result at the boundary region.

To accelerate the FFT, it may be beneficial to pad a few additional channels, so that the number of channels (including the padded channels) has a high number of prime factors in its prime factorization [51].

4. Deconvolution with ADMM

The fundamental concept of deconvolution is to invert the effect of convolution. To facilitate the readability of the algorithm, we will denote variables containing one or multiple matrices having the size of the EELS map data in bold letters subsequetly. In Fourier space, convolution is equivalent to the multiplication of a signal $\hat{\mathbf{S}}$ by a kernel $\mathbf{\Omega}$. Therefore, it is evident that deconvolution can be achieved through simple division in Fourier space [9], hence the term Fourier ratio deconvolution. In the absence of noise, the process would be straightforward. However, noise is unavoidable, and deconvolving a noisy signal results in an amplification of the noise to the point where the signal becomes unusable. The Richardson–Lucy algorithm (RLA) [13,14] involves estimating the unconvolved signal, convolving it with the deconvolution kernel, and comparing the results to the measurement data using Bayesian methods and the Poisson statistics, thereby obtaining an improved estimate in the next iteration step. The mathematical formulation of Fourier ratio deconvolution and the RLA are as follows:

$$\hat{\mathbf{S}} = \mathcal{F}^{-1}\left[\frac{\mathcal{F}[\boldsymbol{\xi}]}{\mathcal{F}[\mathbf{\Omega}]}\right] \quad \text{and} \quad \hat{\mathbf{S}}^{k+1}_{\mathrm{RLA}} = \hat{\mathbf{S}}^{k}_{\mathrm{RLA}} \cdot \left(\frac{\boldsymbol{\xi}}{\mathbf{\Omega} \otimes \hat{\mathbf{S}}^{k}_{\mathrm{RLA}}} \otimes \mathbf{\Omega}^{T}\right), \tag{21}$$

where $\mathbf{\Omega}^T$ is the adjoint operator of $\mathbf{\Omega}$ and $\boldsymbol{\xi}$ represents the noisy signal measured, which is convolved with a kernel $\mathbf{\Omega}$, while $\hat{\mathbf{S}}$ denotes the underlying signal of interest. Therefore, the underlying principle of RLA is to minimize the distance between convolved estimate and measured noisy data. As we have reasoned in the previous sections, RLA is not suitable for the deconvolution of EEL spectra. However, minimization can nevertheless be a powerful tool to obtaining a good estimate of the signal $\hat{\mathbf{S}}_{RLA}$.

Having established both a suitable noise model and the necessary data preparation, the final step is to define a useful minimization to improve the data through deconvolution. The objective of this section is to apply the mathematical concepts and experimentally determined parameters discussed previously. In the following sections, we will develop an ADMM algorithm that converges to a reliable estimate of the underlying electron energy-loss probabilities of the signal $\hat{\mathbf{s}}_{\mathrm{ADMM}}$.

4.1. ADMM in general

To achieve convergence, a more general approach to deconvolution is required, one that can be tailored to the specific needs of the data. In this context, Lagrangian minimization provides offers a highly versatile alternative, as it is neither restricted to specific noise statistics nor data treatment. One approach to solving such a Lagrangian is the alternating direction method of multipliers (ADMM), which can solve minimization problems of the form [33]:

$$\begin{aligned} &\underset{\mathbf{x},\mathbf{z}}{\arg\min} && f(\mathbf{x}) + g(\mathbf{z}) \\ &\text{subject to} && \mathbf{A}\mathbf{x} + \mathbf{B}\mathbf{z} + \mathbf{c} = 0\,. \end{aligned} \tag{22}$$

In the context of deconvolution, f and g are convex functions that define desired properties of the result, such as suitable noise statistics, ensuring that the deconvolution outcome remains close to the measured data. Other desirable properties include the smoothness of the deconvolution result and its strict non-negativity, as all signals in an EELS map are inherently non-negative. The functions f and g are applied to distinct variables $\mathbf{x}$ and $\mathbf{z}$. Further, $\mathbf{A}$ and $\mathbf{B}$ define operators that are applied to $\mathbf{x}$ and $\mathbf{z}$. Following this example $\mathbf{x}$ contains the estimate of the noise-free signal of the EELS map, which is blurred by a convolution kernel $\mathbf{A}$. In deconvolution, $\mathbf{B}$ is often chosen to be a negative matrix of ones $-\mathbb{1}$, such that we obtain $\mathbf{A}\mathbf{x} - \mathbf{z} + \mathbf{c} = 0$. This equation can be rearranged, such that e.g. $\mathbf{z} = \mathbf{A}\mathbf{x} + \mathbf{c}$ stores the blurred dataset $\mathbf{A}\mathbf{x}$ and a background $\mathbf{c}$ that is added. Therefore, $\mathbf{z}$ serves as an auxiliary variable that depends on $\mathbf{x}$.

It is evident that a functional $g(\mathbf{z})$, incorporating the noise statistics in this example, would preserve the correct signal statistics, even if the deconvolution result $\mathbf{x}$ is background subtracted. In this example, a suitable deconvolution minimization for Poisson noise can be obtained with $f(\mathbf{x}) = 0$, since f is not required in this case. In the following sections, we will derive a functional $g(\mathbf{z})$ specifically tailored to EELS.

Generally, imaging problems of this type can be formulated as Lagrangian functions to be minimized, yielding a good deconvolution result. One obtains [33]:

$$\mathcal{L}_{\gamma}(\mathbf{x}, \mathbf{z}, \mathbf{u}) = f(\mathbf{x}) + g(\mathbf{z}) + \frac{\gamma}{2}\|\mathbf{A}\mathbf{x} + \mathbf{B}\mathbf{z} + \mathbf{c} + \mathbf{u}\|_2^2 - \frac{\gamma}{2}\|\mathbf{u}\|_2^2\,. \tag{23}$$

Here, $\|\cdot\|_2$ depicts the Euclidean norm, where $\mathbf{u}$ is called the scaled dual variable associated with the constraint $\mathbf{A}\mathbf{x} + \mathbf{B}\mathbf{z} + \mathbf{c} = 0$, and γ is a penalty parameter that primarily controls the convergence rate of the algorithm. The last term $\|\mathbf{u}\|_2$ is commonly referred to as the augmentation, which resembles a repetition of the preceding term, enhancing the convergence properties of the algorithm [33]. Therefore, Eq. (23) is commonly known as the '*augmented Lagrangian*'. The iterative minimization process is performed in a three-step pattern [33]:

$$\mathbf{x}^{k+1} = \underset{\mathbf{x}}{\arg\min}\left\{ f(\mathbf{x}) + \frac{\gamma}{2}\,\|\,\mathbf{A}\mathbf{x} + \mathbf{B}\mathbf{z}^{k} + \mathbf{c} + \mathbf{u}^{k}\,\|_2^2 \right\}\,, \tag{24}$$

$$\mathbf{z}^{k+1} = \underset{\mathbf{z}}{\arg\min}\left\{ g(\mathbf{z}) + \frac{\gamma}{2}\,\|\,\mathbf{A}\mathbf{x}^{k+1} + \mathbf{B}\mathbf{z} + \mathbf{c} + \mathbf{u}^{k}\,\|_2^2 \right\}\,, \tag{25}$$

$$\mathbf{u}^{k+1} = \mathbf{u}^{k} + \mathbf{A}\mathbf{x}^{k+1} + \mathbf{B}\mathbf{z}^{k+1} + \mathbf{c}\,, \tag{26}$$

minimizing the Lagrangian with respect to $\mathbf{x}$ first, followed by a minimization with respect to $\mathbf{z}$ and finally updating the dual variable $\mathbf{u}$.

Additional information about ADMM can be found in [33,52], which provide a comprehensive overview. Details on the specific application of ADMM to deconvolution can be found in [4,49,53,54].

4.2. Residual balancing

In [49], we proposed a method for automatically selecting the parameter γ, called '*residual balancing*' (RB). We consider this additional selection step crucial, not only because it accelerates the algorithm and simplifies its operation, but also because it determines the parameter based on mathematical properties of the algorithm, thereby eliminating the need for manual user input. This automated selection ensures the algorithm's objectivity and unbiasedness.

Residual balancing is based on the Karush-Kuhn–Tucker conditions [55], which enable the derivation of optimality conditions by evaluating the saddle point of the Lagrangian $\mathcal{L}_\gamma(\mathbf{x},\mathbf{z},\mathbf{u})$. Two residuals can be defined: the primal residual $\mathbf{R}$ and the dual residual $\mathbf{S}$ [33]. The concept of residual balancing involves maintaining relative residuals of similar magnitude, as both residuals approach zero, which is the prerequisite for the algorithm to converge. Using a suitable normalization, the relative residuals can be obtained as [49,56]:

$$\mathbf{R}_{rel}^{k+1} = \frac{\mathbf{A}\mathbf{x}^{k+1} + \mathbf{B}\mathbf{z}^{k+1} + \mathbf{c}}{\max\left\{\|\mathbf{A}\mathbf{x}^{k+1}\|_2\,,\ \|\mathbf{B}\mathbf{z}^{k+1} + \mathbf{c}\|_2\right\}} \quad \text{and} \quad \mathbf{S}_{rel}^{k+1} = \frac{\gamma^k \mathbf{A}^T\mathbf{B}\left(\mathbf{z}^{k+1} - \mathbf{z}^k\right)}{\max\left\{\|\partial_{\mathbf{x}} f(\mathbf{x}^{k+1})\|_2\,,\ \|\gamma^k \mathbf{A}^T\left(\mathbf{u}^k + \mathbf{A}\mathbf{x}^{k+1} + \mathbf{B}\mathbf{z}^{k+1} + \mathbf{c}\right)\|_2\right\}}\,, \tag{27}$$

which are easier to compare in terms of magnitude, wherein the numerator of the above equations provides the unnormalized residuals $\mathbf{R}^{k+1}$ and $\mathbf{S}^{k+1}$. Again, $\mathbf{A}^T$ denotes the adjoint operator of $\mathbf{A}$. Using both relative residuals, a multiplication factor τ^{k+1} can be determined as:

$$\tau^{k+1} = \begin{cases} \upsilon^{k+1} & \text{if} \quad 0 < \upsilon^{k+1} < \infty \\ \min\left\{\gamma^{-1}\,,\ \tau_{ext}\right\} & \text{elseif } \gamma < 1 \\ \max\left\{\gamma^{-1}\,,\ \tau_{ext}^{-1}\right\} & \text{elseif } \gamma > 1 \\ 1 & \text{otherwise} \end{cases}, \quad \text{with} \quad \upsilon^{k+1} = \sqrt{\|\mathbf{R}_{rel}^{k+1}\|_2 / \|\mathbf{S}_{rel}^{k+1}\|_2}\,, \tag{28}$$

to adjust the penalty parameter γ^k such that it is optimal for the next iteration:

$$\gamma^{k+1} = \begin{cases} \gamma^k \cdot \tau^{k+1} & \text{if} \quad \gamma_{max}^{-1} \le \gamma^k \cdot \tau^{k+1} \le \gamma_{max} \\ \gamma_{max}^{-1}/\gamma^k & \text{if} \quad \gamma_{max}^{-1} < \gamma^k \cdot \tau^{k+1} \\ \gamma_{max}/\gamma^k & \text{if} \quad \gamma^k \cdot \tau^{k+1} > \gamma_{max} \end{cases}. \tag{29}$$

with an upper limit $\gamma_{max} = 10^{100}$ of the penalty parameter, which is necessary for maintaining numerical stability in all cases [49]. If either $\|\mathbf{R}_{rel}^{k+1}\|_2$ or $\|\mathbf{S}_{rel}^{k+1}\|_2$ become zero or infinity during the iterations, it indicates that the penalty parameter γ^k has been over-extended. A useful strategy for relieving the parameter is to push it back towards 1, using a value of $\tau_{ext} > 1$ [49]. In our experience $\tau_{ext} = 10$ has proven effective. Additionally, it is crucial to gradually reduce the frequency of the residual balancing, such that [49]:

$$\tau^{k+1} = \begin{cases} \tau^{k+1} & \text{if } \ k \in \text{Val} \\ 1 & \text{otherwise} \end{cases}, \tag{30}$$

where Val is a sequence of exponentially increasing values that dictate when residual balancing should occur. Consequently, the balancing occurs e.g. only ten times per order of magnitude of iteration, resulting in an exponential increase in interval length throughout the progression of the algorithm. Eventually, the dual variable $\mathbf{u}^{k+1}$ must be scaled inversely with respect to τ^{k+1}. Combining all of the above, we obtain the ADMM-RB:

$$\mathbf{x}^{k+1} = \arg\min_{\mathbf{x}} \left\{ f(\mathbf{x}) + \frac{\gamma^k}{2} \| \mathbf{A}\mathbf{x} + \mathbf{B}\mathbf{z}^k + \mathbf{c} + \mathbf{u}^k \|_2^2 \right\}, \tag{31}$$

$$\mathbf{z}^{k+1} = \arg\min_{\mathbf{z}} \left\{ g(\mathbf{z}) + \frac{\gamma^k}{2} \| \mathbf{A}\mathbf{x}^{k+1} + \mathbf{B}\mathbf{z} + \mathbf{c} + \mathbf{u}^k \|_2^2 \right\}, \tag{32}$$

if $k \in \text{Val}$

$$\tau^{k+1} \leftarrow \tau^k, \quad \text{(acc. to Eq. (28))} \tag{33}$$

$$\gamma^{k+1} \leftarrow \gamma^k, \quad \text{(acc. to Eq. (29))} \tag{34}$$

else

$$\tau^{k+1} = 1, \tag{35}$$

$$\gamma^{k+1} = \gamma^k, \tag{36}$$

end

$$\mathbf{u}^{k+1} = \frac{\mathbf{u}^k + \mathbf{A}\mathbf{x}^{k+1} + \mathbf{B}\mathbf{z}^{k+1} + \mathbf{c}}{\tau^{k+1}}. \tag{37}$$

For further details on residual balancing, we refer to [49].

4.3. Log-likelihood of the noise model

Having discussed ADMM as well as the residual balancing in general, we must now tailor the algorithm to accommodate the noise model expected for EELS maps. To incorporate the noise model into an ADMM framework, we require a convex function that, when minimized, penalizes discrepancies between a reconstructed blurred signal relying upon the deconvolution result and the original measurement data itself. This penalization ensures that the deconvolution result remains tied to the measured data, thereby providing a reliable estimate of the original underlying signal.

In ADMM, this is achieved by utilizing the variable $\mathbf{x}$ that is set up to approaching the loss probabilities $\hat{\mathbf{s}}$ during the iterations and eventually resembling them without all the noise $\mathbf{x}^K \approx \hat{\mathbf{s}}$, when convergence of the ADMM algorithm is achieved after K iterations. However, the desired loss probabilities $\hat{\mathbf{s}}$ are not directly accessible by the real measurement $\boldsymbol{\xi}$. In the real measurement $\boldsymbol{\xi}$, the loss probabilities $\hat{\mathbf{s}}$ are convolved with a convolution kernel, i.e. the vacuum ZLP, altered by beam current deviations and superimposed by offsets, such as tails of the ZLP. Obviously, these measured signals are of course also subject to noise. To facilitate a statistical comparison with the measurement $\boldsymbol{\xi}$, we must define an auxiliary

variable $\mathbf{z}_A$ resembling the measurement $\boldsymbol{\xi} \approx \mathbf{z}_A$, but without the noise. Since we want to eventually recover the loss probabilities by optimization, the auxiliary variable $\mathbf{z}_A$ must depend on the deconvolution estimate $\mathbf{x}$ approaching the loss probabilities. The estimate $\mathbf{x}$ must therefore be altered in $\mathbf{z}_A$ in the same manner as $\hat{\mathbf{s}}$ is altered in $\boldsymbol{\xi}$ to make both entities comparable in the first place.

Since the desired result of deconvolution $\mathbf{x}^K$ shall resemble the deconvolved, normalized, and ZLP subtracted loss probabilities, we invert these operations to obtain a reconstructed signal $\mathbf{z}_A = \mathbf{N} \cdot \boldsymbol{\Omega}\mathbf{x} + \mathbf{c}$. Here, $\mathbf{N} = \sum_i^M \boldsymbol{\xi}_{x,y,i}$ represents the normalization factor, calculated as the total sum of the spectra $\boldsymbol{\xi}$, $\mathbf{c}$ represents the ZLP to be subtracted, $\boldsymbol{\Omega}$ is the deconvolution kernel. Therefore $\boldsymbol{\Omega}\mathbf{x}$ is the blurred loss probability estimate of a current iteration.

Accordingly, the basic scheme of the algorithm is to find a new estimate $\mathbf{x}$, update the auxiliary variable $\mathbf{z}_A$, according to the above formula, and compare the reconstructed signal $\mathbf{z}_A$ to the noisy measurement $\boldsymbol{\xi}$ by statistical means. Based on this scheme, the algorithm is intended to iteratively find the most likely deconvolution result $\mathbf{x}^K$ by continuously approaching the true loss probabilities $\hat{\mathbf{s}}$.

The right tool for such a statistical comparison is the Bayesian likelihood [57]. This likelihood describes the probabilities $P\left(\mathbf{z}_A \mid \boldsymbol{\xi}\right)$ of observing a reconstructed noise-free signal $\mathbf{z}_A$, given that a noise affected EELS map $\boldsymbol{\xi}$ has been measured.

According to Bayes, the conditional probability in terms of $\mathbf{z}_A$ and $\boldsymbol{\xi}$ can be expressed as:

$$P\left(\mathbf{z}_A \mid \boldsymbol{\xi}\right) = \frac{P\left(\boldsymbol{\xi} \mid \mathbf{z}_A\right) \cdot P\left(\mathbf{z}_A\right)}{P\left(\boldsymbol{\xi}\right)} \,, \tag{38}$$

with the probability $P\left(\mathbf{z}_A \mid \boldsymbol{\xi}\right)$ that the reconstructed signal $\mathbf{z}_A$ is observed, given that $\boldsymbol{\xi}$ has been measured, the prior probability $P\left(\mathbf{z}_A\right)$ of the reconstructed signal $\mathbf{z}_A$, $P\left(\boldsymbol{\xi}\right)$ is the probability of obtaining measurement $\boldsymbol{\xi}$ and $P\left(\boldsymbol{\xi} \mid \mathbf{z}_A\right)$ is the probability of measuring $\boldsymbol{\xi}$ given that the reconstructed signal $\mathbf{z}_A$ is present.

The left-hand side of the equation defines a distance metric between $\mathbf{z}_A$ and the measurement $\boldsymbol{\xi}$, where larger distances correspond to lower probabilities. The optimal estimate the reconstructed signal $\mathbf{z}_A$ is obtained by maximizing the right-hand side of the equation. One method for finding the maximum is the 'maximum likelihood approach' (ML) [58]:

$$\mathrm{ML}(\mathbf{z}_A) = \arg\max\left[P\left(\boldsymbol{\xi} \mid \mathbf{z}_A\right)\right] \,. \tag{39}$$

Note that this approach disregards the probabilities $P\left(\boldsymbol{\xi}\right)$ and $P\left(\mathbf{z}_A\right)$. However, the probability $P\left(\boldsymbol{\xi}\right)$ is trivial, since we have already obtained a measured EELS map $\boldsymbol{\xi}$. Consequently, this term does not affect the maximization process. $P\left(\mathbf{z}_A\right)$ is called the '*a-priori*' knowledge and will be crucial in the next section, where we introduce the '*non-negativity constraint*' and the 'total generalized variation' approach. Therefore, it will be addressed later.

For now, we will focus on the maximum likelihood approach. To calculate probabilities, a noise model for the measurement is required that characterizes the uncertainty.

Since the original (and therefore unnormalized) measurement $\boldsymbol{\xi}$ is compared to $\mathbf{z}_A$, no normalizations are to be incorporated into the noise model. Therefore, the simple noise model previously proposed in Eq. (16) is applicable.

The noise probability distribution encountered in EELS is a mixture of Poisson distributed signal noise and Gaussian distributed detector noise. However, a closed-form solution of the likelihood of such a mixed noise model is unattainable due to the presence of infinite sums. As demonstrated in [59], a precise approximation of this mixed distribution is complex but feasible, albeit at a high computational cost. Consequently, the computations with the true distribution are quite slow, and the benefits are limited compared to approximations such as the shifted-Poisson model (SP) [4] or the mixed-Poisson-Gauss (MPG) model [60].

A significant advantage is only anticipated in the low-count regime, where the detector noise standard deviation $\sigma_D < 10$ counts. The difference between the Gaussian and Poisson probability distribution for 40+ counts is on the order of 0.1% (as can be easily calculate using Eq. (1)). Given that we measure $\sigma_D \approx 45$ counts on our detector, it is clear that the true distribution is not worth the additional computational cost — approximating the distribution will suffice, with minimal error.

In the following, we will employ the MPG model, as it provides a better fit to the probability distribution of the low intensity regime, given the high Gaussian noise level [60]. In contrast, the difference between the SP and the MPG is expected to be negligible for the high-intensity regime.

In the MPG approximation, we assume that the entire noise follows a Gaussian distribution, with a variable variance that depends on the signal and includes the detector noise as an offset. Therefore, we can derive a total variance from Eq. (16):

$$\begin{aligned} \sigma^2_{x,y,i} &= g \cdot \beta_{conv} \cdot \left[\boldsymbol{\Omega} \otimes \hat{\mathbf{S}}_{x,y}\right]_i + \left(1 + \frac{1}{A}\right) \cdot \beta_D \cdot \sigma^2_{D,i} \\ &\approx g \cdot \beta_{conv} \cdot \underbrace{\boldsymbol{\xi}_{x,y,i}}_{\approx \mathbf{z}_{A,x,y,i}} + \left(1 + \frac{1}{A}\right) \cdot \beta_D \cdot \sigma^2_{D,i} \,, \end{aligned} \tag{40}$$

on the position (x, y, i) of the signal. Since we do not have direct access to the signal, we can approximate it with the noisy measurement $\boldsymbol{\xi}_{x,y,i}$, which we, in turn, can replace by the auxiliary variable $\mathbf{z}_A$ resembling it without the noise. The variance $\sigma^2_{x,y,i}$ based on $\mathbf{z}_A$ can be directly incorporated into the Gaussian probability density function for the MPG approach to compare $\mathbf{z}_A$ to the measurement $\boldsymbol{\xi}$.

In the case of correlated Gaussian noise, however, the probability density function is given by a multivariate Gaussian distribution and as a consequence the probability $P\left(\boldsymbol{\xi} \mid \mathbf{z}_A\right)$ must be expressed as:

$$P\left(\boldsymbol{\xi} \mid \mathbf{z}_A\right) = \prod_{x,y}^{X,Y} P\left(\boldsymbol{\xi}_{x,y} \mid \mathbf{z}_{A,x,y}\right) = \prod_{x,y}^{X,Y} \frac{1}{\sqrt{(2\pi)^M \cdot \det\left(\boldsymbol{\Phi}\right)}} \cdot \exp\left\{-\frac{1}{2}\left(\mathbf{z}_{A,x,y} - \boldsymbol{\xi}_{x,y}\right)^T \boldsymbol{\Phi}^{-1}\left(\mathbf{z}_{A,x,y} - \boldsymbol{\xi}_{x,y}\right)\right\} \quad \text{, with:} \tag{41}$$

$$\mathbf{z}_{A,x,y} = \begin{pmatrix} \mathbf{z}_{A,x,y,1} & \cdots & \mathbf{z}_{A,x,y,M} \end{pmatrix}^T \quad , \quad \boldsymbol{\xi}_{x,y} = \begin{pmatrix} \boldsymbol{\xi}_{x,y,1} & \cdots & \boldsymbol{\xi}_{x,y,M} \end{pmatrix}^T \quad \text{, and}$$

$$\boldsymbol{\Phi} = \begin{pmatrix} \rho^*_0 \sigma_{x,y,1}\sigma_{x,y,1} & \rho^*_1 \sigma_{x,y,1}\sigma_{x,y,2} & \rho^*_2 \sigma_{x,y,1}\sigma_{x,y,3} & \cdots & \rho^*_{M-1}\sigma_{x,y,1}\sigma_{x,y,M} \\ \rho^*_{-1}\sigma_{x,y,2}\sigma_{x,y,1} & \rho^*_0 \sigma_{x,y,2}\sigma_{x,y,2} & \rho^*_1 \sigma_{x,y,2}\sigma_{x,y,3} & \cdots & \rho^*_{M-2}\sigma_{x,y,2}\sigma_{x,y,M} \\ \rho^*_{-2}\sigma_{x,y,3}\sigma_{x,y,1} & \rho^*_{-1}\sigma_{x,y,3}\sigma_{x,y,2} & \rho^*_0 \sigma_{x,y,3}\sigma_{x,y,3} & \cdots & \rho^*_{M-3}\sigma_{x,y,3}\sigma_{x,y,M} \\ \vdots & \vdots & \vdots & \ddots & \vdots \\ \rho^*_{-(M-1)}\sigma_{x,y,M}\sigma_{x,y,1} & \rho^*_{-(M-2)}\sigma_{x,y,M}\sigma_{x,y,2} & \rho^*_{-(M-3)}\sigma_{x,y,M}\sigma_{x,y,3} & \cdots & \rho^*_0 \sigma_{x,y,M}\sigma_{x,y,M} \end{pmatrix} \,,$$

where $\mathbf{z}_{A,x,y}$ and $\boldsymbol{\xi}_{x,y}$ are vectors that contain all the entries of the respective matrices in energy direction at the position (x, y) on the EELS map, with T denoting the transpose. $\boldsymbol{\Phi}$ represents the covariance matrix, which comprises the Pearson correlation coefficients ρ^*_m, where the index m indicates the distance between the considered EEL channels. $\sigma_{x,y,i}$ and $\sigma_{x,y,i+m}$ represent the noise standard deviations of the EEL channels i and $i+m$, respectively. Based on the total noise present in the EEL channels following Eq. (40), one can separate $\sigma^2_{x,y,i}$ into a noise contribution $\sigma^2_{S,x,y,i} \approx g \cdot \beta_{conv} \cdot \mathbf{z}_{A,x,y,i}$ depending on the signal strength and a noise contribution depending on the detector noise $\sigma^2_{D,x,y,i} \approx \beta_D \cdot \left(1 + \frac{1}{A}\right) \cdot \sigma^2_{D,i}$. This is possible, because Gaussian noise is additive. Since signal and detector noise are independent of each other, we can regard the signal and detector noises independently. With respect to Eq. (41), this is equal to separating the one Gaussian into two separate Gaussians with variances $\sigma^2_{S,x,y,i}$ and $\sigma^2_{D,x,y,i}$, according to Eq. (3). Therefore, we can express the respective elements of the covariance matrix of the signal noise $\boldsymbol{\Phi}_S$ and of the detector noise $\boldsymbol{\Phi}_D$ independently as:

$$\rho^*_{S,m}\sigma_{S,x,y,i}\sigma_{S,x,y,i+m} = \rho_m \cdot g \cdot \beta_{conv} \cdot \sqrt{\mathbf{z}_{A,x,y,i} \cdot \mathbf{z}_{A,x,y,i+m}} \quad \text{and} \quad \rho^*_{D,m}\sigma_{D,x,y,i}\sigma_{D,x,y,i+m} = \rho_{D,m} \cdot \beta_D \cdot \left(1 + \frac{1}{A}\right) \cdot \sigma_{D,i} \cdot \sigma_{D,i+m} \,. \tag{42}$$

By again combining both Gaussians, the entries of the overall covariance matrix $\boldsymbol{\Phi}$ of Eq. (41) can be expressed as:

$$\rho^*_m\sigma_{x,y,i}\sigma_{x,y,i+m} = \rho_m \cdot g \cdot \beta_{conv} \cdot \sqrt{\mathbf{z}_{A,x,y,i} \cdot \mathbf{z}_{A,x,y,i+m}} + \rho_{D,m} \cdot \beta_D \cdot \left(1 + \frac{1}{A}\right) \cdot \sigma_{D,i} \cdot \sigma_{D,i+m} \,, \tag{43}$$

where ρ_m represent the Pearson correlation coefficients of the EEL signal, and $\rho_{D,m}$ represents the Pearson correlation coefficients of the detector noise resulting from interpolation. Because the spectra at positions $\boldsymbol{\xi}_{x,y}$ are acquired sequentially, no correlations are expected between them. Therefore, the overall probability can be expressed as the product of the individual spectra probabilities.

One can see that, by assuming independence of EEL channels for a given distance between them, the covariance matrix $\boldsymbol{\Phi}$ takes the form of a sparse banded matrix, where all non-zero entries are confined to a diagonal band, while all other entries are zero. Additionally, $\boldsymbol{\Phi}$ is symmetric, since $\rho^*_m\sigma_{x,y,i}\sigma_{x,y,i+m} = \rho^*_{-m}\sigma_{x,y,i+m}\sigma_{x,y,i}$, owing to the symmetry of the Pearson coefficients.

Maximizing the overall probability is equivalent to minimizing its negative logarithm:

$$-\ln\left[P\left(\boldsymbol{\xi} \mid \mathbf{z}_A\right)\right] = \sum_{x,y,}^{X,Y} \frac{1}{2}\ln\left[\det\left(\boldsymbol{\Phi}\right)\right] + \frac{1}{2}\left(\mathbf{z}_{A,x,y} - \boldsymbol{\xi}_{x,y}\right)^T \boldsymbol{\Phi}^{-1}\left(\mathbf{z}_{A,x,y} - \boldsymbol{\xi}_{x,y}\right) + \frac{M}{2}\ln\left[2\pi\right] \,. \tag{44}$$

The sparsity of $\boldsymbol{\Phi}$ and its general structure can be leveraged to simplify the matrices within the likelihood $P\left(\boldsymbol{\xi} \mid \mathbf{z}_A\right)$. However, it is clear that minimizing the above probability with respect to $\mathbf{z}_A$ remains extremely challenging and computationally expensive, as no analytic solution exists. Therefore, we must simplify the above equation. A common approach is to neglect the correlations and assume independence between data points. This approach, however, is insufficient, since neglecting correlations without further action readily overestimates the data fidelity. Therefore, we propose the decomposition of the likelihood as if no correlations were present, but also to remove the smoothing factors β_{conv} and β_D resulting from the correlations as well. The idea behind this is pretty simple: The ZLP $\boldsymbol{\Omega}$ is significantly larger than the detector PSF $\boldsymbol{\Omega}_D$ causing the correlations. As a consequence, the size of any meaningful feature is large compared to the correlation length. Therefore, we can assume similar signal strength across the entire correlation length of a given EEL channel, hence $\mathbf{z}_{A,x,y,i} \approx \mathbf{z}_{A,x,y,i+m}$ and $\sigma_{D,i} \approx \sigma_{D,i+m}$. Since convolution 'mixes' the uncertainty of the signal of several neighboring channels into a single channel and the uncertainty of neighboring channels is very similar to each respective other channel due to their similar signal strength, it follows that the convolution, with e.g. a comparably small detector PSF $\boldsymbol{\Omega}_D$ or an interpolation kernel $\boldsymbol{\Omega}_{Inter}$, do not change much the uncertainty. It is as if the convolution never happened. Therefore, we can regard the uncertainty of the given EEL channel as if correlation was not there – and consequently, we must neglect the smoothing factors for the data fidelity term to create the conditions of the initial uncertainties before convolution. Note that this is completely opposed to the observed noise variance appearing drastically smoothed, which is why we introduced the smoothing factors in the first place. This will be important later in the manuscript.

As a result of the above thoughts, we can decompose Eq. (41) into:

$$P\left(\boldsymbol{\xi} \mid \mathbf{z}_A\right) \approx \prod_{x,y,i}^{X,Y,M} P\left(\boldsymbol{\xi}_{x,y,i} \mid \mathbf{z}_{A,x,y,i}\right) \quad \text{, with} \tag{45}$$

$$P\left(\boldsymbol{\xi}_{x,y,i} \mid \mathbf{z}_{A,x,y,i}\right) \approx \frac{1}{\sqrt{2\pi \cdot \left(g \cdot \mathbf{z}_{A,x,y,i} + \left(1 + \frac{1}{A}\right) \cdot \sigma^2_{D,i}\right)}} \cdot \exp\left\{-\frac{\left(\mathbf{z}_{A,x,y,i} - \boldsymbol{\xi}_{x,y,i}\right)^2}{2 \cdot \left(g \cdot \mathbf{z}_{A,x,y,i} + \left(1 + \frac{1}{A}\right) \cdot \sigma^2_{D,i}\right)}\right\} . \tag{46}$$

Maximizing the probability of the entire spectrum is equivalent to minimizing the following functional:

$$\begin{aligned} \mathcal{G}_{\mathrm{MPG}}\left(\mathbf{z}_A\right) &= -\ln\left[P\left(\boldsymbol{\xi} \mid \mathbf{z}_A\right)\right] \\ &= \sum_{x,y,i}^{X,Y,M} \frac{\left(\mathbf{z}_{A,x,y,i} - \boldsymbol{\xi}_{x,y,i}\right)^2}{2 \cdot \left(g \cdot \mathbf{z}_{A,x,y,i} + \left(1 + \frac{1}{A}\right) \cdot \sigma^2_{D,i}\right)} + \frac{1}{2}\ln\left[\left(g \cdot \mathbf{z}_{A,x,y,i} + \left(1 + \frac{1}{A}\right) \cdot \sigma^2_{D,i}\right)\right] \,, \end{aligned} \tag{47}$$

where we omit the additional term $\frac{1}{2}\ln\left[\pi\right]$ since it does not affect the minimization process, being merely an offset. This functional is referred to as the '*negative log-likelihood*' functional of the MPG model. We can rewrite it as:

$$\mathcal{G}_{\mathrm{MPG}}\left(\mathbf{z}_A\right) = \min_{\mathbf{z}_A} \frac{1}{2}\left\| \frac{\mathbf{z}_A - \boldsymbol{\xi}}{\left(g \cdot \mathbf{z}_A + \sigma^2\right)^{1/2}} \right\|^2_F + \frac{1}{2}\left\langle \ln\left[g \cdot \mathbf{z}_A + \sigma^2\right] \,,\, \mathbb{1} \right\rangle_F \quad \text{, with} \quad \sigma^2 = \left(1 + \frac{1}{A}\right) \cdot \sigma^2_{D,i} \,. \tag{48}$$

by utilizing the Frobenius norm $\|\cdot\|_F$ as an extension of the Euclidean norm for matrices and the Frobenius inner product $\langle\cdot,\cdot\rangle_F$ to simplify the notation, where $\mathbb{1}$ represents a matrix of ones with the same dimension as the EELS data cube.

However, there is a minor issue with this approach: the expression $\mathbf{z}_A = \mathbf{N} \cdot \boldsymbol{\Omega}\mathbf{x} - \mathbf{c}$ significantly increases the complexity of the overall algorithm. From a complexity standpoint, it is advantageous to define $\mathbf{z}_0 = \boldsymbol{\Omega}\mathbf{x}$ and perform the rescaling with the total intensity $\mathbf{N}$, as well as the re-addition of the background $\mathbf{c}$, within the functional itself. This simplification helps maintain a clear and efficient overall ADMM algorithm. Since the uncertainty of all voxels is approximately independent of each other voxel, as explained above, it is sufficient to minimize the functional for each voxel

individually. For this reason, minimizing for each voxel individually is equivalent to minimizing the sum over all voxels and therefore allows to further simplify the algorithm. With the changes applied, we now define the new signal-restoring MPG functional (RMPG) as:

$$\mathcal{G}_{\mathrm{RMPG}}\left(\mathbf{z}_0\right)=\min_{\mathbf{z}_0}\begin{cases}\frac{1}{2}\left\|\frac{(\mathbf{N}\cdot\mathbf{z}_0+\mathbf{c})-\boldsymbol{\xi}}{\left(g\cdot(\mathbf{N}\cdot\mathbf{z}_0+\mathbf{c})+\sigma^2\right)^{1/2}}\right\|_2^2+\frac{1}{2}\ln\left[g\cdot\left(\mathbf{N}\cdot\mathbf{z}_0+\mathbf{c}\right)+\sigma^2\right] & \text{for all } \mathbf{z}_{0,x,y,i}>0\in\Psi\\ 0 & \text{otherwise}\end{cases}, \tag{49}$$

for every voxel (x, y, i) within the original dataset Ψ (without padding) and set all values of $\mathbf{z}_0 \leq 0$ to zero, as signals are always meant to be positive. We assign no penalty to the padded region, as it is an artificial construct that should adapt maintain the continuity of the deconvolved signal.

4.4. Non-negativity constraint

With the aid of additional information about the dataset, referred to as '*prior [knowledge]*', the minimization can be defined in such a way that it yields a more accurate result, provided that our understanding of the data is correct. We can formulate a maximum '*a-posteriori*' (MAP) approach:

$$\mathrm{MAP}(\mathbf{z}_0)=\arg\max\left[P\left(\boldsymbol{\xi}\mid\mathbf{z}_0\right)\ P\left(\mathbf{z}_0\right)\right], \tag{50}$$

by extending the negative log likelihood to:

$$\begin{aligned}-\ln\left[P\left(\boldsymbol{\xi}\mid\mathbf{z}_0\right)\ P\left(\mathbf{z}_0\right)\right] &= \mathcal{G}_{\mathrm{RMPG}}\left(\mathbf{z}_0\right)-\ln\left[P\left(\mathbf{z}_0\right)\right] && \text{, with} \quad P\left(\mathbf{z}_0\right)=\exp\left\{-g_1\left(\mathbf{z}_1\right)-\ldots-g_n\left(\mathbf{z}_n\right)\right\}\\ &= \mathcal{G}_{\mathrm{RMPG}}\left(\mathbf{z}_0\right)+g_1\left(\mathbf{z}_1\right)+\ldots+g_n\left(\mathbf{z}_n\right) && ,\end{aligned} \tag{51}$$

where $\mathbf{z}_{1\ldots n}$ represent criteria related to $\mathbf{x}$, which are penalized, and $g_{1\ldots n}$ are convex functions that determine the impact of the penalty. It is evident that the ML-approach can be easily extended by incorporating additional knowledge terms.

Since the deconvolution results represent the loss probabilities $\hat{\mathbf{s}}$ of the data cube, we know that these probabilities are always positive. With this knowledge, we can penalize negativity within the voxels. This prior knowledge therefore helps ensure the meaningfulness of the result. We define a non-negativity constraint $G_+\left(\mathbf{z}_+\right)=I_{\mathbb{R}_+}\left(\mathbf{z}_+\right)$, with the indicator function $I_{\mathbb{R}_+}$, which is defined as [4,61]:

$$I_{\mathbb{R}_+}\left(\mathbf{z}_+\right)=\begin{cases}0 & \mathbf{z}_+\in\mathbb{R}_+\\ \infty & \mathbf{z}_+\notin\mathbb{R}_+\end{cases}, \tag{52}$$

where we set $\mathbf{z}_+ = \mathbf{x}$, as we require the outcome of the deconvolution to be non-negative. The idea is therefore again to update $\mathbf{x}$, then to update $\mathbf{z}_+$, and to include this new information additionally to the statistical comparison from the last section into the new $\mathbf{x}$ of the next iteration.

4.5. Total generalized variation (TGV)

Another prior relies upon the assumption that the loss probabilities exhibit smooth transitions with respect to both the lateral and the energy dimension, at least to a certain extend, whereas in contrast noise is highly volatile.

This distinction between noise-free signals and noise can be leveraged and forms the basis of the '*total variation*' approach, which was first introduced by Rudin, Osher and Fatemi [34]. They explain how derivatives can be used to identify noise: The derivative of the noise is expected to be significantly higher than that of the smooth, slowly changing signal. However, for signals that inherently possess a gradient, this assumption in insufficient. A portion of the slope is attributed to noise, resulting in staircase artifacts [26]. Employing higher-order derivatives can help mitigate this issue by smoothing the gradient of the signal instead of the signal itself, although this comes at the expense of losing sharp edges.

Total generalized variation (TGV) effectively combines first- and second-order derivatives. Bredies et al. [35] first introduced TGV, which employs self-adapting filter masks that adjust to different signal regions, thereby optimally utilizing first- and second-order derivatives.

Following Shirai and Okuda [62], an isotropic TGV penalizer can be formulated within the ADMM framework as:

$$\|\mathbf{x}\|_{TGV}^{\lambda_1,\lambda_2}:=\min_{\mathbf{z}_1=\mathbf{s}=\mathbf{D}\mathbf{x}-\mathbf{t},\,\mathbf{z}_2=\mathbf{G}\mathbf{t}}\left(\lambda_1\|\mathbf{z}_1\|_2+\lambda_2\|\mathbf{z}_2\|_2\right). \tag{53}$$

According to TGV theory, $\mathbf{s}$ and $\mathbf{t}$ represent filter masks associated with the flat and sloped regions of the signal. The above minimization enforces the separation of the data, since the derivatives $\mathbf{D}$ of the data $\mathbf{x}$ contained in $\mathbf{z}_1$ become minimal when only flat regions are treated therein. This is because the derivative of data with a gradient is non-zero. As a consequence $\mathbf{t}$ must adapt to the derivative of the sloped regions in order to subtract them in $\mathbf{z}_1 = \mathbf{s} = \mathbf{D}\mathbf{x} - \mathbf{t}$ to minimize $\|\mathbf{z}_1\|_2$. Therefore, $\|\mathbf{z}_2\|_2$ aims at minimizing the derivatives $\mathbf{G}$ of the slope of the data $\mathbf{t}$, corresponding to second-order derivatives of the data. Consequently, by minimizing the above functional, we continue to distinguish $\mathbf{x}$ into flat regions in the filter mask $\mathbf{s}$ and sloped regions in the filter mask $\mathbf{t}$ in order to denoise them.

The idea of the algorithm is therefore to update the gradient $\mathbf{D}\mathbf{x}$ employed in $\mathbf{z}_1$ on the basis of the deconvolution result $\mathbf{x}$, and to subtract the sloped filter mask $\mathbf{t}$ providing the gradient of the sloped regions. Both terms constitute the filter mask $\mathbf{s}$, which is therefore only providing the gradient of the flat regions of the data. Then the second-order gradients in $\mathbf{z}_2$ are updated based on the filter mask $\mathbf{t}$, which describes the gradient of the sloped regions of the data. In addition to the statistical comparison and the non-negativity from the last two sections, all this TGV information is also included in the updated estimate of $\mathbf{x}$ and the updated filter mask $\mathbf{t}$ of the next iteration. Since all the derivatives employed in $\mathbf{z}_1$ and $\mathbf{z}_2$ are sensitive to noise, minimizing both norms, $\|\mathbf{z}_1\|_2$ and $\|\mathbf{z}_2\|_2$, suppresses the noise in the next iteration of $\mathbf{x}$ and $\mathbf{t}$ and, consequently, leads to a better adaption of $\mathbf{s}$ and $\mathbf{t}$ to the significant features of the data in a positive feedback loop.

Following the TGV notation, the operators $\mathbf{D}$ and $\mathbf{G}$ contain the derivatives in all possible directions. We have not found these operators being defined for 3D data in literature yet, however, by closely following Shirai and Okuda [62], it is readily apparent that the scheme can be easily expanded into 3D space. Showing this for $\mathbf{D}$ is quite trivial by simply expanding it by one dimension. For $\mathbf{G}$, the operator must be expanded by the new derivative and their mixed derivatives with the other two dimensions. It is to remark that both $\mathbf{D}^T\mathbf{D}$ and $\mathbf{G}^T\mathbf{G}$, following the above notation,

remain identical for 2D and 3D data if one derivative is set to zero. As a consequence, $\mathbf{D}$ and $\mathbf{G}$ do contain their 2D representation as a special case. For 3D EELS maps, $\mathbf{D}$ and $\mathbf{G}$ can be expressed as:

$$\mathbf{D} = \begin{pmatrix} \mathbf{D}_h \\ \mathbf{D}_v \\ \mathbf{D}_s \end{pmatrix} \quad , \quad \mathbf{G}^T = \begin{pmatrix} \mathbf{D}_h & \mathbf{D}_v & \mathbb{0} & \mathbf{D}_s & \mathbb{0} & \mathbb{0} \\ \mathbb{0} & \mathbf{D}_h & \mathbf{D}_v & \mathbb{0} & \mathbf{D}_s & \mathbb{0} \\ \mathbb{0} & \mathbb{0} & \mathbb{0} & \mathbf{D}_h & \mathbf{D}_v & \mathbf{D}_s \end{pmatrix} , \tag{54}$$

where $\mathbf{D}_h$ represents the horizontal finite difference operator, $\mathbf{D}_v$ represents the vertical finite difference operator, and $\mathbf{D}_s$ represents the finite difference operator in energy direction, with the energy slices stacked. For a data cube with $X \times Y \times (M+P)$ data points, where P denotes the number of additional padding channels, each finite difference operator is represented by a matrix having the same size as the data cube, i.e. $\{\mathbf{D}_h, \mathbf{D}_v, \mathbf{D}_s, \mathbb{0}\} \in \mathbb{R}^{X\times Y\times(M+P)}$, with the matrix of zeros $\mathbb{0}$. Examples of the operators $\mathbf{D}_h$ and $\mathbf{D}_v$ in 2D space are provided in the supplementary materials, since 3D representations are hard to provide on a paper sheet. From these examples, the reader may unambiguously derive the 3D representations of $\mathbf{D}_h$, $\mathbf{D}_v$, and $\mathbf{D}_v$ in 3D space.

Furthermore, $\mathbf{t}$, $\mathbf{z}_1$ as well as $\mathbf{z}_2$ and the corresponding dual variables $\mathbf{u}_1$ as well as $\mathbf{u}_2$ are defined as follows [62]:

$$\mathbf{t} = \begin{pmatrix} \mathbf{t}_h \\ \mathbf{t}_v \\ \mathbf{t}_s \end{pmatrix} \quad , \quad \mathbf{z}_1 = \begin{pmatrix} \mathbf{z}_{1,h} \\ \mathbf{z}_{1,v} \\ \mathbf{z}_{1,s} \end{pmatrix} , \quad \mathbf{u}_1 = \begin{pmatrix} \mathbf{u}_{1,h} \\ \mathbf{u}_{1,v} \\ \mathbf{u}_{1,s} \end{pmatrix} , \quad \mathbf{z}_2 = \begin{pmatrix} \mathbf{z}_{2,h} \\ \mathbf{z}_{2,hv} \\ \mathbf{z}_{2,v} \\ \mathbf{z}_{2,hs} \\ \mathbf{z}_{2,vs} \\ \mathbf{z}_{2,s} \end{pmatrix}, \quad \mathbf{u}_2 = \begin{pmatrix} \mathbf{u}_{2,h} \\ \mathbf{u}_{2,hv} \\ \mathbf{u}_{2,v} \\ \mathbf{u}_{2,hs} \\ \mathbf{u}_{2,vs} \\ \mathbf{u}_{2,s} \end{pmatrix} , \tag{55}$$

with hv, hs, vs denoting the diagonal directions connected to their respective directions. Each entry, once more, has the size of the data cube.

The last two parameters to be defined are λ_1 and λ_2, which are regularization parameters that determine the impact of the respective part of the penalizer. In [49], we have shown that the optimal choice of both λ-parameters for deconvolution is anti-proportional to the mean noise volatility of the data σ_{mean}. Therefore, only the volatility aspect of the noise is of importance here, which is in contrast to the derivation of the log-likelihood prior derived in Section 4.3, where the uncertainty aspect was of interest.

In the context of an unbiased parameter choice, both λ_1 and λ_2 are set equal. To account for the increase in noise due to deconvolution, we introduced an amplification coefficient ω that modifies the impact of the regularizer, which depends on the deconvolution kernel $\mathbf{\Omega}$. We have found [6]:

$$\lambda_1 = \lambda_2 = \frac{1}{2 \cdot \omega \cdot \sigma_{mean}} \quad \text{, with} \quad \omega^2 = \sum_{x,y,i}^{X,Y,(M+P)} \mathbf{\Omega}^*_{x,y,i} \, , \tag{56}$$

where $\mathbf{\Omega}^*_{x,y,i}$ represents the values of the deconvolution kernel, which specifically comprises the ZLP in our case. The asterisk $*$ indicates normalization to the height of one. Note that since deconvolution in EELS only acts in energy direction, the deconvolution kernel only incorporates the ZLP oriented in energy direction once (e.g. in $x = 1$, $y = 1$), whereas all other entries are set zero, such that the kernel $\mathbf{\Omega}$ has the same dimension as the EELS data cube. In this context, the independent noise variance of multiple channels is added – one could say that deconvolution can be thought of as consolidating the noise from several channels into a single channel, thereby amplifying it [49]. This necessitates correction by amplifying the noise.

Since the TGV prior is applied to the deconvolution estimate $\mathbf{x}$, which is normalized, we need to apply the normalized noise models from Eqs. (18) and (19) to derive σ_{mean}.

However, ω was defined for uncorrelated noise and must be modified to account for the correlations. Since the deconvolution kernel, i.e. the ZLP measured in vacuum $\mathbf{\Omega}$, is much broader than the convolutions leading to noise correlation, the smoothing factors β are eliminated. The same applies to the convolution kernel of the detector PSF $\mathbf{\Omega}_D$ or the interpolation kernel to accommodate sub-channel drifts for the ZLP-alignment $\mathbf{\Omega}_{Inter}$, as explained in Eq. (13). The above implies that part of the amplification coefficient must be the inverse of β_{conv} from Eq. (6) (and additionally β_{corr} from Eq. (7) in energy direction).

Based on this, we can decompose the deconvolution into two consecutive deconvolutions. One part removes the detector PSF $\mathbf{\Omega}_D$ as well as the interpolation kernel $\mathbf{\Omega}_{Inter}$, which are responsible for the correlation effects. Another part further describes the amplification factor applied to the uncorrelated noise after removing the detector PSF and the interpolation kernel. Therefore, we need to decompose the full deconvolution kernel into:

$$\mathbf{\Omega} = \mathbf{\Omega}_D \otimes \mathbf{\Omega}_{Inter} \otimes \underbrace{\mathcal{F}^{-1}\left[\frac{\mathcal{F}[\mathbf{\Omega}]}{\mathcal{F}\left[\mathbf{\Omega}_D \otimes \mathbf{\Omega}_{Inter}\right]}\right]}_{=\mathbf{\Omega}_{R,S}} \quad \Longrightarrow \quad \omega^2_{Sig} = \underbrace{\left(\sum_{m=-(M-1)}^{M-1} \rho_m\right)}_{=\frac{1}{\beta_{conv}(\cdot\beta_{corr})}} \cdot \underbrace{\left(\sum_{x,y,i}^{X,Y,(M+P)} \mathbf{\Omega}_{R,S,x,y,i}\right)}_{=\omega^2_S} , \tag{57}$$

where $\mathbf{\Omega}_{R,S}$ describes the reduced deconvolution kernel of the signal, $\mathbf{\Omega}_{Inter} = \mathbf{\Omega}_I \star \mathbf{\Omega}_I$ represents the auto-correlation of the interpolation kernel, ω_{Sig} describes the overall amplification factor applied to the signal noise, and ω_S describes the leftover amplification coefficient applied to the signal noise. The first term of ω^2_{Sig} eliminates the smoothing caused by convolution β_{corr} and, in energy direction, also the smoothing caused by correlation β_{corr}, as indicated by the brackets. The second term, denoted as ω^2_S, provides additional amplification due to the deconvolution kernel being larger than the correlation kernel. Similarly, we obtain the amplification coefficient applied to the detector noise as:

$$\mathbf{\Omega} = \mathbf{\Omega}_{Inter} \otimes \underbrace{\mathcal{F}^{-1}\left[\frac{\mathcal{F}[\mathbf{\Omega}]}{\mathcal{F}\left[\mathbf{\Omega}_{Inter}\right]}\right]}_{=\mathbf{\Omega}_{R,D}} \quad \Longrightarrow \quad \omega^2_{Det} = \underbrace{\left(\sum_{m=-(M-1)}^{M-1} \rho_{D,m}\right)}_{=\frac{1}{\beta_D}} \cdot \underbrace{\left(\sum_{x,y,i}^{X,Y,(M+P)} \mathbf{\Omega}_{R,D,x,y,i}\right)}_{=\omega^2_D} , \tag{58}$$

where $\mathbf{\Omega}_{R,D}$ describes the reduced deconvolution kernel of the detector noise, ω_{Det} describes the overall amplification factor applied to the detector noise and ω_D describes the leftover amplification coefficient applied to the detector noise. Using both amplification coefficients, we can determine the mean noise level σ of the deconvolved data set, as required by Eq. (56).

Given that we have two noise models for normalized EELS maps, one in the lateral directions (Eq. (18) and one in the energy direction (Eq. (19)), it is useful to slightly modify the TGV prior:

$$\|\mathbf{x}\|_{DTGV}^{\lambda_1,\lambda_2} := \min_{\mathbf{z}_1=\mathbf{s}=\mathbf{Dx}-\mathbf{t},\,\mathbf{z}_2=\mathbf{Gt}} \left(\|\lambda_2^2\mathbf{z}_1\|_2 + \|\lambda_1^2\mathbf{z}_2\|_2\right) \quad \text{, with:} \quad \lambda_1^2 = \begin{pmatrix}\lambda_{1,h}^2\\ \lambda_{1,v}^2\\ \lambda_{1,s}^2\end{pmatrix} \quad \text{and} \quad \lambda_2^2 = \begin{pmatrix}\lambda_{2,h}^2\\ \lambda_{2,h}\lambda_{1,v}\\ \lambda_{2,v}^2\\ \lambda_{2,h}\lambda_{1,s}\\ \lambda_{2,v}\lambda_{1,s}\\ \lambda_{2,s}^2\end{pmatrix} . \tag{59}$$

When λ_h, λ_v and λ_s are equal, the prior in Eq. (59) is equivalent to Eq. (53). Here, the multiplications $\lambda_1^2\mathbf{z}_1$ and $\lambda_2^2\mathbf{z}_2$ can be understood in terms of a Hadamard product, where the respective elements are multiplied element-wise. However, by differentiating between these parameters, we can specify the noise in different directions, leading to the concept of '*directionally distinguished TGV*' (DTGV). Unlike the log-likelihood functional defined in Section 4.3, which required a global noise model to specify the uncertainty of individual voxels, the TGV prior treats noise based on its volatility. Since volatility varies across different directions, we must account for those changes to achieve optimal results. Furthermore, we found that multiplying the normalized data cube by the mean value of the intensity map $I = \frac{1}{X\cdot Y}\sum_{x,y}^{X,Y} \mathcal{I}_{x,y}$ is beneficial for the results obtained, since the minimization enforcing non-negativity will work more efficiently with this variant of the algorithm.

Based on the above considerations and utilizing Eq. (19), we derive the noises for the energy direction. From Eq. (19), which finds its basis in Eq. (14), we can define a total noise level as:

$$\boldsymbol{\sigma}_{x,y,\underline{i}}^2 \approx \underbrace{g\cdot\beta_{conv}\cdot\beta_{corr}\cdot\frac{I^2}{\left(\sum_i^M \xi_{x,y,i}\right)^2}\cdot\xi_{x,y,i}}_{\boldsymbol{\sigma}_{Sig,x,y,\underline{i}}^2} + \underbrace{\frac{I^2}{\left(\sum_i^M \xi_{x,y,i}\right)^2}\cdot\left(1+\frac{1}{A}\right)\cdot\beta_D\cdot\sigma_{D,i}^2}_{\boldsymbol{\sigma}_{Det,x,y,\underline{i}}^2} , \tag{60}$$

where we again replaced the signal $\left[\boldsymbol{\Omega}\otimes\hat{\mathbf{S}}_{x,y}\right]_i$ by the measured signal $\xi_{x,y,i}$. Along with the amplification factors, we can derive:

$$\omega^2\cdot\boldsymbol{\sigma}_{x,y,\underline{i}}^2 = \omega_{Sig}^2\cdot\boldsymbol{\sigma}_{Sig,x,y,\underline{i}}^2 + \omega_{Det}^2\cdot\boldsymbol{\sigma}_{Det,x,y,\underline{i}}^2 , \tag{61}$$

where we observe that all the smoothing factors β_{conv}, β_{corr} and β_D are eliminated, and all noises are multiplied by their respective leftover amplification coefficients, as described in Eqs. (57) and (58).

Similarly and according to Eq. (18), we can derive the total noise level in the lateral direction as:

$$\boldsymbol{\sigma}_{\underline{x,y},i}^2 \approx \underbrace{\left(1+\frac{\sigma_{Int}^2}{4I^2}\right)\cdot g\cdot\beta_{conv}\cdot\mu_R^2\cdot I\cdot\left(\frac{\xi_{x,y,i}}{\sum_i^M\xi_{x,y,i}}\right)}_{\boldsymbol{\sigma}_{Sig,\underline{x,y},i}^2} + \underbrace{k_{N,\underline{x,y},i}^2\cdot I^2\cdot\left(\frac{\xi_{x,y,i}}{\sum_i^M\xi_{x,y,i}}\right)^2}_{\boldsymbol{\sigma}_{Norm,\underline{x,y},i}^2} + \underbrace{\left(1+\frac{\sigma_{Int}^2}{I^2}\right)\cdot\mu_R^2\cdot\left(1+\frac{\varphi}{A}\right)\cdot\beta_D\cdot\sigma_{D,i}^2}_{\boldsymbol{\sigma}_{Det,\underline{x,y},i}^2} , \tag{62}$$

where we replaced the convolved loss probabilities $\left[\boldsymbol{\Omega}\otimes\hat{\mathbf{s}}_{x,y}\right]_i$ by the normalized signal $\frac{\xi_{x,y,i}}{\sum_i^M\xi_{x,y,i}}$. Along with the noise amplification coefficients, we can derive:

$$\omega^2\cdot\boldsymbol{\sigma}_{\underline{x,y},i}^2 = \omega_{Sig}^2\cdot\boldsymbol{\sigma}_{Sig,\underline{x,y},i}^2 + \boldsymbol{\sigma}_{Norm,\underline{x,y},i}^2 + \omega_{Det}^2\cdot\boldsymbol{\sigma}_{Det,\underline{x,y},i}^2 . \tag{63}$$

Once again, the smoothing factors β_{conv} and β_D are eliminated through deconvolution. Because the uncertainty of normalization is multiplicative and orthogonal to the direction in which deconvolution operates, no amplification coefficient is applicable to $\boldsymbol{\sigma}_{Norm,\underline{x,y},i}^2$.

Eventually, we determine the optimal regularization parameters as the mean value of the noise multiplied with the amplification coefficient in the respective direction, averaged across all voxels (padding included):

$$\lambda_{1,h,v}^2 = \lambda_{2,h,v}^2 = \frac{1}{4\cdot\frac{1}{X\cdot Y\cdot(M+P)}\sum_{x,y,i}^{X,Y,M+P}\left(\omega^2\cdot\boldsymbol{\sigma}_{\underline{x,y},i}^2\right)} \quad \text{and} \quad \lambda_{1,s}^2 = \lambda_{2,s}^2 = \frac{1}{4\cdot\frac{1}{X\cdot Y\cdot(M+P)}\sum_{x,y,i}^{X,Y,M+P}\left(\omega^2\cdot\boldsymbol{\sigma}_{x,y,\underline{i}}^2\right)} , \tag{64}$$

where P denotes the number of padded channels.

With the regularization parameters established, we have now defined the DTGV approach.

Having read the last sections concerning a-priori information, it is apparent that all these concepts must by weighted in to come to useful results. Here, we have come full circle, because this weighting is provided by the principles of residual balancing approach, described in Section 4.2. In the following section, we will therefore integrate the various components and formulate a deconvolution algorithm for normalized EELS maps.

4.6. Deconvolution algorithm for EELS maps

As demonstrated in [49], we have established a method for setting up a Poisson deconvolution algorithm that operates based on mathematically determined parameters, thereby eliminating user bias and ensuring convergence. The underlying concept of the present algorithm is to deconvolve the loss probabilities associated with a measured EELS map, rather than the direct measurement itself. This approach offers the advantage that the loss probabilities are smoother than the original image, since transmittances and beam current fluctuations are mitigated through normalization to the total intensity of the respective spectra. Consequently, the normalized data is smoother in the first place, enabling the DTGV prior to smooth the data more efficiently due to reduced data roughness. Additionally, since loss probabilities cannot be negative, we impose a non-negativity prior on the deconvolved data. To facilitate comparison between the deconvolution result $\mathbf{x}$ with the original data, we must rescale $\mathbf{x}$ by the normalization factor $\mathbf{N}$, reconvolve it with the deconvolution kernel $\boldsymbol{\Omega}$, i.e. the ZLP in vacuum, and then reintroduce the previously subtracted background $\mathbf{c}$. This process is incorporated into the negative log-likelihood operator of the MPG noise model. The algorithm can be formulated as follows:

$$\underset{\mathbf{x},\mathbf{z}_0,\mathbf{z}_+,\mathbf{z}_1,\mathbf{z}_2}{\arg\min} \quad \mathcal{G}_{\mathrm{RMPG}}\left(\mathbf{z}_0\right) + \mathcal{G}_+\left(\mathbf{z}_+\right) + \|\lambda_1^2\mathbf{z}_1\|_2 + \|\lambda_2^2\mathbf{z}_2\|_2$$

$$\text{subject to} \quad \mathbf{z}_0 = \mathbf{\Omega x}\ ,\ \mathbf{z}_+ = \mathbf{x}\ ,\ \mathbf{z}_1 = \mathbf{Dx} - \mathbf{t}\ ,\ \mathbf{z}_2 = \mathbf{Gt} \quad , \tag{65}$$

utilizing the deconvolution kernel $\mathbf{\Omega}$ and regularization parameters λ_1 and λ_2, as calculated in Eq. (64). The augmented Lagrangian that needs to be solved for each voxel individually is defined as [62]:

$$\begin{aligned}\mathcal{L}_{\gamma_0,\gamma_+,\gamma,\eta}\left(\mathbf{x},\mathbf{t},\mathbf{z}_0,\mathbf{z}_+,\mathbf{z}_1,\mathbf{z}_2,\mathbf{u}_0,\mathbf{u}_+,\mathbf{u}_1,\mathbf{u}_2\right) = \quad & \mathcal{G}_{\mathrm{RMPG}}\left(\mathbf{z}_0\right) + \gamma_0/2\,\|\mathbf{\Omega x} - \mathbf{z}_0 + \mathbf{u}_0\|_2^2 \quad - \gamma_0/2\,\|\mathbf{u}_0\|_2^2 \\ & + \mathcal{G}_+\left(\mathbf{z}_+\right) + \gamma_+/2\|\mathbf{x} - \mathbf{z}_+ + \mathbf{u}_+\|_2^2 \quad - \gamma_+/2\,\|\mathbf{u}_+\|_2^2 \\ & + \|\lambda_1^2\mathbf{z}_1\|_2 + \gamma/2\,\|\mathbf{Dx} - \mathbf{t} - \mathbf{z}_1 + \mathbf{u}_1\|_2^2 \quad - \gamma/2\,\|\mathbf{u}_1\|_2^2 \\ & + \|\lambda_2^2\mathbf{z}_2\|_2 + \eta/2\|\mathbf{Gt} - \mathbf{z}_2 + \mathbf{u}_2\|_2^2 \quad - \eta/2\,\|\mathbf{u}_2\|_2^2\ .\end{aligned} \tag{66}$$

where γ_0, γ_+, γ and η denote the penalty parameters. This Lagrangian function can be minimized iteratively using the three-step pattern of the ADMM described in Section 4.1, which involves a sequence of updates ($\mathbf{x}$-update, $\mathbf{z}$-update and $\mathbf{u}$-update), each comprising multiple sub-updates. In extension, the residual balancing approach outlined in Section 4.1, is employed.

We initialize the iteration at $k = 0$ with $\mathbf{x}^0 = \mathbb{0}$, $\mathbf{t}_i^0 = \mathbb{0}$, $\mathbf{z}_0^0 = \max\left(\frac{\boldsymbol{\xi}-\mathbf{c}}{\mathbf{N}}, \mathbb{0}\right)$, $\mathbf{z}_+^0 = \max\left(\frac{\boldsymbol{\xi}-\mathbf{c}}{\mathbf{N}}, \mathbb{0}\right)$, $\mathbf{z}_{1,i}^0 = \mathbb{0}$, $\mathbf{z}_{2,j}^0 = \mathbb{0}$, $\mathbf{u}_0^0 = \mathbb{0}$, $\mathbf{u}_{1,i}^0 = \mathbb{0}$ and $\mathbf{u}_{2,j}^0 = \mathbb{0}$, where $\mathbb{0}$ represents matrices of zeros. Additionally, we define $\mathbf{N} = \frac{\mathcal{I}_{x,y}}{I}$, where $\mathcal{I}_{x,y} = \sum_i^M \boldsymbol{\xi}_i$ represents the intensity map and $I = \frac{1}{X \cdot Y}\sum_{x,y}^{X,Y} \mathcal{I}_{x,y}$ denotes the mean value of the intensity map. Here, $\mathbf{c}$ represents the background subtracted from the data, such as a fitted vacuum ZLP. Since $\mathbf{N}$ takes the form of a 2D map for 3D EELS maps, it needs to be applied to each energy slice individually, e.g. by repeating and concatenating $\mathbf{N}$ such that it matches the energy dimension. The iteration steps are presented below:

$$\left\{\mathbf{x}^{k+1}, \mathbf{t}^{k+1}\right\} = \underset{\mathbf{x},\mathbf{t}}{\arg\min}\ \mathcal{L}_{\gamma_0^k,\gamma_+^k,\gamma^k,\eta^k}\left(\mathbf{x},\mathbf{t},\mathbf{z}_0^k,\mathbf{z}_+^k,\mathbf{z}_1^k,\mathbf{z}_2^k,\mathbf{u}_0^k,\mathbf{u}_+^k,\mathbf{u}_1^k,\mathbf{u}_2^k\right) \quad , \tag{67}$$

$$\mathbf{z}_0^{k+1} = \underset{\mathbf{z}_0}{\arg\min}\ \mathcal{L}_{\gamma_0^k}\left(\mathbf{x}^{k+1}, \mathbf{z}_0, \mathbf{u}_0^k\right) \quad , \tag{68}$$

$$\mathbf{z}_+^{k+1} = \underset{\mathbf{z}_+}{\arg\min}\ \mathcal{L}_{\gamma_+^k}\left(\mathbf{x}^{k+1}, \mathbf{z}_+, \mathbf{u}_+^k\right) \quad , \tag{69}$$

$$\mathbf{z}_{1,i}^{k+1} = \underset{\mathbf{z}_{1,i}}{\arg\min}\ \mathcal{L}_{\gamma^k}\left(\mathbf{x}^{k+1}, \mathbf{t}^{k+1}, \mathbf{z}_1, \mathbf{u}_1^k\right) \quad , \tag{70}$$

$$\mathbf{z}_{2,j}^{k+1} = \underset{\mathbf{z}_{2,j}}{\arg\min}\ \mathcal{L}_{\eta^k}\left(\mathbf{x}^{k+1}, \mathbf{t}^{k+1}, \mathbf{z}_2, \mathbf{u}_2^k\right) \quad , \tag{71}$$

if $k \in \mathrm{Val}$

$$\tau_{\gamma_0}^{k+1} \leftarrow \tau_{\gamma_0}^k, \quad \tau_{\gamma_+}^{k+1} \leftarrow \tau_{\gamma_+}^k, \quad \tau_{\gamma}^{k+1} \leftarrow \tau_{\gamma}^k, \quad \tau_{\eta}^{k+1} \leftarrow \tau_{\eta}^k \quad , \tag{72}$$

$$\gamma_0^{k+1} \leftarrow \gamma_0^k, \quad \gamma_+^{k+1} \leftarrow \gamma_+^k\ , \quad \gamma^{k+1} \leftarrow \gamma^k\ , \quad \eta^{k+1} \leftarrow \eta^k \quad , \tag{73}$$

else

$$\tau_{\gamma_0}^{k+1} = 1, \quad \tau_{\gamma_+}^{k+1} = 1, \quad \tau_{\gamma}^{k+1} = 1, \quad \tau_{\eta}^{k+1} = 1 \quad , \tag{74}$$

$$\gamma_0^{k+1} = \gamma_0^k, \quad \gamma_+^{k+1} = \gamma_+^k\ , \quad \gamma^{k+1} = \gamma^k\ , \quad \eta^{k+1} = \eta^k \quad , \tag{75}$$

end

$$\mathbf{u}_0^{k+1} = \frac{\mathbf{u}_0^k + \left(\mathbf{\Omega x}^{k+1} - \mathbf{z}_0^{k+1}\right)}{\tau_{\gamma_0}^{k+1}} \quad , \tag{76}$$

$$\mathbf{u}_+^{k+1} = \frac{\mathbf{u}_+^k + \left(\mathbf{x}^{k+1} - \mathbf{z}_+^{k+1}\right)}{\tau_{\gamma_+}^{k+1}} \quad , \tag{77}$$

$$\mathbf{u}_{1,i}^{k+1} = \frac{\mathbf{u}_{1,i}^k + \left(\left[\mathbf{Dx}^{k+1}\right]_i - \mathbf{t}_i^{k+1} - \mathbf{z}_{1,i}^{k+1}\right)}{\tau_{\gamma}^{k+1}} \quad , \tag{78}$$

$$\mathbf{u}_{2,j}^{k+1} = \frac{\mathbf{u}_{2,j}^k + \left(\left[\mathbf{Gt}^{k+1}\right]_j - \mathbf{z}_{2,j}^{k+1}\right)}{\tau_{\eta}^{k+1}} \quad , \tag{79}$$

where Val represents a sequence of exponentially increasing values that determine when residual balancing is performed. To obtain the desired loss probabilities, we must divide the deconvolution result $\mathbf{x}^K$ after K iterations of the above algorithm by the mean intensity I of the intensity map, yielding:

$$\hat{\mathbf{s}}_{\mathrm{ADMM}}^K = \mathbf{x}^K / I\ . \tag{80}$$

In the above equations, several Lagrangian functions with a reduced set of indices and arguments are found, such as the Lagrangian function $\mathcal{L}_{\gamma_0^k}\left(\mathbf{x}^{k+1}, \mathbf{z}_0, \mathbf{u}_0^k\right)$ in Eq. (68). These Lagrangian functions refer to the original Lagrangian function $\mathcal{L}_{\gamma_0,\gamma_+,\gamma,\eta}\left(\mathbf{x},\mathbf{t},\mathbf{z}_0,\mathbf{z}_+,\mathbf{z}_1,\mathbf{z}_2,\mathbf{u}_0,\mathbf{u}_+,\mathbf{u}_1,\mathbf{u}_2\right)$ as defined in Eq. (66) after k iterations. Since this Lagrangian is minimized with respect to a different variable, e.g. $\mathcal{L}_{\gamma_0^k}\left(\mathbf{x}^{k+1}, \mathbf{z}_0, \mathbf{u}_0^k\right)$ is minimized with respect to $\mathbf{z}_0$, most of the terms in Eq. (66) vanish to zero. In this example, this relates to all the lines in Eq. (66) except the first one. Therefore, lines 2–4 could have been left out in the first place for the minimization. Accordingly, it is useful to define a reduced Lagrangian function $\mathcal{L}_{\gamma_0^k}\left(\mathbf{x}^{k+1}, \mathbf{z}_0, \mathbf{u}_0^k\right)$ for a concise notation focusing on the relevant terms. This reduction is often encountered in the ADMM literature.

In the subsequent sections, we will demonstrate how to tackle the minimization problems presented in Eq. (67) to Eq. (71) and define the required relative residuals for residual balancing.

4.6.1. The $\{\mathbf{x}, \mathbf{t}\}$-update

Minimizing the augmented Lagrangian in Eq. (67) with respect to $\mathbf{x}$ and $\mathbf{t}$ yields a Karush-Kuhn–Tucker (KKT) system, as demonstrated in [62]:

$$\begin{pmatrix} \gamma_0^k \boldsymbol{\Omega}^T \boldsymbol{\Omega} + \gamma_+^k \mathbb{1} + \gamma^k \mathbf{D}^T \mathbf{D} & -\gamma^k \mathbf{D}^T \\ -\gamma^k \mathbf{D} & \gamma^k \mathbf{1}_n + \eta^k \mathbf{G}^T \mathbf{G} \end{pmatrix} \begin{pmatrix} \mathbf{x}^k \\ \mathbf{t}^k \end{pmatrix} = \begin{pmatrix} \gamma_0^k \boldsymbol{\Omega}^T \left(\mathbf{z}_0^k - \mathbf{u}_0^k\right) + \gamma_+^k \left(\mathbf{z}_+^k - \mathbf{u}_+^k\right) + \gamma^k \mathbf{D}^T \left(\mathbf{z}_1^k - \mathbf{u}_1^k\right) \\ -\gamma^k \left(\mathbf{z}_1^k - \mathbf{u}_1^k\right) + \eta^k \mathbf{G}^T \mathbf{G} \left(\mathbf{z}_2^k - \mathbf{u}_2^k\right) \end{pmatrix}, \tag{81}$$

where $\mathbf{1}_n$ represents the identity matrix corresponding to the dimensionality n of the data. We also note a minor correction to the work of Shirai and Okuda [62], where the transposes in the first column of the first matrix are adjusted. For a three-dimensional data cube, such as those found in EELS maps, the matrices can be expressed as:

$$\mathbf{G}^T \mathbf{G} = \begin{pmatrix} \mathbf{D}^T \mathbf{D} & \mathbf{D}_v \mathbf{D}_h^T & \mathbf{D}_s \mathbf{D}_h^T \\ \mathbf{D}_h \mathbf{D}_v^T & \mathbf{D}^T \mathbf{D} & \mathbf{D}_s \mathbf{D}_v^T \\ \mathbf{D}_h \mathbf{D}_d^T & \mathbf{D}_s \mathbf{D}_v^T & \mathbf{D}^T \mathbf{D} \end{pmatrix} \quad \text{with} \quad \mathbf{D}^T \mathbf{D} = \mathbf{D}_h^T \mathbf{D}_h + \mathbf{D}_v^T \mathbf{D}_v + \mathbf{D}_s^T \mathbf{D}_s \quad \text{and} \quad \mathbf{1_3} = \begin{pmatrix} \mathbb{1} & \mathbb{0} & \mathbb{0} \\ \mathbb{0} & \mathbb{1} & \mathbb{0} \\ \mathbb{0} & \mathbb{0} & \mathbb{1} \end{pmatrix}. \tag{82}$$

As before, $\mathbb{0}$ and $\mathbb{1}$ represent matrices of zeros and ones, respectively, with dimensions matching those of the data cube. The equation system in Eq. (81) can be expressed in the form $\mathbf{P}\mathbf{r} = \mathbf{q}$, as demonstrated in [62]:

$$\mathbf{P} = \begin{pmatrix} \gamma_0^k \boldsymbol{\Omega}^T \boldsymbol{\Omega} + \gamma_+^k \mathbb{1} + \gamma^k \mathbf{D}^T \mathbf{D} & -\gamma^k \mathbf{D}_h^T & -\gamma^k \mathbf{D}_v^T & -\gamma^k \mathbf{D}_s^T \\ -\gamma^k \mathbf{D}_h & \gamma^k \mathbb{1} + \eta^k \mathbf{D}^T \mathbf{D} & \eta^k \mathbf{D}_v \mathbf{D}_h^T & \eta^k \mathbf{D}_s \mathbf{D}_h^T \\ -\gamma^k \mathbf{D}_v & \eta^k \mathbf{D}_h \mathbf{D}_v^T & \gamma^k \mathbb{1} + \eta^k \mathbf{D}^T \mathbf{D} & \eta^k \mathbf{D}_s \mathbf{D}_v^T \\ -\gamma^k \mathbf{D}_s & \eta^k \mathbf{D}_h \mathbf{D}_s^T & \eta^k \mathbf{D}_v \mathbf{D}_s^T & \gamma^k \mathbb{1} + \eta^k \mathbf{D}^T \mathbf{D} \end{pmatrix}, \quad \mathbf{r} = \begin{pmatrix} \mathbf{x}^k \\ \mathbf{t}_h^k \\ \mathbf{t}_v^k \\ \mathbf{t}_s^k \end{pmatrix}, \tag{83}$$

$$\mathbf{q} = \begin{pmatrix} \gamma_0^k \boldsymbol{\Omega}^T \left(\mathbf{z}_0^k - \mathbf{u}_0^k\right) & +\gamma_+^k \left(\mathbf{z}_+^k - \mathbf{u}_+^k\right) & +\gamma^k \mathbf{D}_h^T \left(\mathbf{z}_{1,h}^k - \mathbf{u}_{1,h}^k\right) & +\gamma^k \mathbf{D}_v^T \left(\mathbf{z}_{1,v}^k - \mathbf{u}_{1,v}^k\right) & +\gamma^k \mathbf{D}_s^T \left(\mathbf{z}_{1,s}^k - \mathbf{u}_{1,s}^k\right) \\ & -\gamma^k \left(\mathbf{z}_{1,h}^k - \mathbf{u}_{1,h}^k\right) & +\eta^k \mathbf{D}_h \left(\mathbf{z}_{2,h}^k - \mathbf{u}_{2,h}^k\right) & +\eta^k \mathbf{D}_v \left(\mathbf{z}_{2,hv}^k - \mathbf{u}_{2,hv}^k\right) & +\eta^k \mathbf{D}_s \left(\mathbf{z}_{2,hs}^k - \mathbf{u}_{2,hs}^k\right) \\ & -\gamma^k \left(\mathbf{z}_{1,v}^k - \mathbf{u}_{1,v}^k\right) & +\eta^k \mathbf{D}_h \left(\mathbf{z}_{2,hv}^k - \mathbf{u}_{2,hv}^k\right) & +\eta^k \mathbf{D}_v \left(\mathbf{z}_{2,v}^k - \mathbf{u}_{2,v}^k\right) & +\eta^k \mathbf{D}_s \left(\mathbf{z}_{2,vs}^k - \mathbf{u}_{2,vs}^k\right) \\ & -\gamma^k \left(\mathbf{z}_{1,s}^k - \mathbf{u}_{1,s}^k\right) & +\eta^k \mathbf{D}_h \left(\mathbf{z}_{2,hs}^k - \mathbf{u}_{2,hs}^k\right) & +\eta^k \mathbf{D}_v \left(\mathbf{z}_{2,vs}^k - \mathbf{u}_{2,vs}^k\right) & +\eta^k \mathbf{D}_s \left(\mathbf{z}_{2,s}^k - \mathbf{u}_{2,s}^k\right) \end{pmatrix}. \tag{83}$$

The equation for $\mathbf{x}$ and $\mathbf{t}$ can be solved by applying the Fourier transformation to the individual block elements, yielding $\mathcal{F}\left\{\mathbf{P}_{i,j}\right\} = \tilde{\mathbf{P}}_{i,j}$, $\mathcal{F}\left\{\mathbf{r}_i\right\} = \tilde{\mathbf{r}}_i$ and $\mathcal{F}\left\{\mathbf{q}_i\right\} = \tilde{\mathbf{q}}_i$, as described in [62]:

$$\begin{aligned} & \tilde{\mathbf{P}}\tilde{\mathbf{r}} = \tilde{\mathbf{q}} \\ \Leftrightarrow & \begin{pmatrix} \tilde{\mathbf{P}}_{1,1} & \tilde{\mathbf{P}}_{1,2} & \tilde{\mathbf{P}}_{1,3} & \tilde{\mathbf{P}}_{1,4} \\ \tilde{\mathbf{P}}_{2,1} & \tilde{\mathbf{P}}_{2,2} & \tilde{\mathbf{P}}_{2,3} & \tilde{\mathbf{P}}_{2,4} \\ \tilde{\mathbf{P}}_{3,1} & \tilde{\mathbf{P}}_{3,2} & \tilde{\mathbf{P}}_{3,3} & \tilde{\mathbf{P}}_{3,4} \\ \tilde{\mathbf{P}}_{4,1} & \tilde{\mathbf{P}}_{4,2} & \tilde{\mathbf{P}}_{4,3} & \tilde{\mathbf{P}}_{4,4} \end{pmatrix} \begin{pmatrix} \tilde{\mathbf{r}}_1 \\ \tilde{\mathbf{r}}_2 \\ \tilde{\mathbf{r}}_3 \\ \tilde{\mathbf{r}}_4 \end{pmatrix} = \begin{pmatrix} \tilde{\mathbf{q}}_1 \\ \tilde{\mathbf{q}}_2 \\ \tilde{\mathbf{q}}_3 \\ \tilde{\mathbf{q}}_4 \end{pmatrix}. \end{aligned} \tag{84}$$

We can employ the adjugate method to compute the inverse matrix $\tilde{\mathbf{P}}^{-1} = \mathrm{adj}\left\{\tilde{\mathbf{P}}\right\} \det^{-1}\left\{\tilde{\mathbf{P}}\right\}$, and subsequently obtain $\tilde{\mathbf{r}} = \tilde{\mathbf{P}}^{-1}\tilde{\mathbf{q}}$. Finally, we can apply the inverse Fourier transformation to obtain $\mathbf{r} = \mathcal{F}^{-1}\{\tilde{\mathbf{r}}\}$. The adjugate can be computed by transposing the cofactor matrix $\mathbf{C}$, which is comprised of the minor determinants. Consequently, the adjugate can be expressed as $\mathrm{adj}\left\{\tilde{\mathbf{P}}\right\} = \tilde{\mathbf{C}}^T$. The determinant $\det\left\{\tilde{\mathbf{P}}\right\}$ can be computed using the Laplace expansion method. Due to the large size of the resulting matrices, the detailed calculation steps for the exact $\{\mathbf{x}, \mathbf{t}\}$-update are provided in the supplementary materials.

4.6.2. The $\mathbf{z}_0$-update

Next, we minimize the Lagrangian in Eq. (68) with respect to $\mathbf{z}_0$, where the functional $\mathcal{G}_{\mathrm{RMPG}}$ is defined in Eq. (49). Although the Lagrangian is differentiable, it lacks an analytical solution. Therefore, we employ Newton's method to solve the functional, using Iter iterations [60]:

$$\begin{aligned} & \mathbf{z}_{0,0}^k = \max\left\{\mathbf{z}_{0,0}^k, 0\right\} \\ & \text{for} \quad I = 1 \text{ to Iter} \\ & \quad \mathbf{z}_{0,I}^k = \begin{cases} \mathbf{z}_{0,I-1}^k - \dfrac{\frac{\partial}{\partial \mathbf{z}_0} \mathcal{L}_{\gamma_0^k}\left(\mathbf{x}^{k+1}, \mathbf{z}_0, \mathbf{u}_0^k\right)}{\frac{\partial^2}{\partial \mathbf{z}_0^2} \mathcal{L}_{\gamma_0^k}\left(\mathbf{x}^{k+1}, \mathbf{z}_0, \mathbf{u}_0^k\right)} & \text{for all } \mathbf{z}_{0,I-1,x,y,i}^k \in \Psi \\ \mathbf{v}_0 & \text{otherwise} \end{cases}, \text{ with } \mathbf{v}_0 = \boldsymbol{\Omega}\mathbf{x}^{k+1} + \mathbf{u}_0^k \quad . \\ & \quad \mathbf{z}_{0,I}^k = \max\left\{\mathbf{z}_{0,I}^k, 0\right\} \\ & \text{end} \\ & \mathbf{z}_0^{k+1} = \mathbf{z}_{0,\mathrm{Iter}}^k \end{aligned} \tag{85}$$

As will be demonstrated in the evaluation Section 5, a single Newton iteration Iter is sufficient for the algorithm to converge to a satisfactory result.

We apply this minimization to each voxel (x, y, i) within the original dataset Ψ. In contrast, the padded regions do not require adherence to the noise statistics, as they are artificially introduced – these regions are updated without penalty as $\mathcal{G}_{RMPG} = 0$, rendering the derivation of augmented Lagrangian in Eq. (68) straightforward for these cases. Since $\mathbf{z}_0$ comprises of the EELS map signal including some background, it must be non-negative. Therefore, we impose the constraint $\mathbf{z}_0 \geq 0$.

The first and second derivatives of the augmented Lagrangian in Eq. (68), required for the Newton iteration, are given as:

$$\frac{\partial}{\partial \mathbf{z}_0} \mathcal{L}_{\gamma_0^k}\left(\mathbf{x}^{k+1}, \mathbf{z}_0, \mathbf{u}_0^k\right) = \frac{\mathbf{N} \cdot (\boldsymbol{\mathcal{O}} - \boldsymbol{\xi})}{\left(g \cdot \boldsymbol{\mathcal{O}} + \sigma^2\right)} - \frac{g \cdot \mathbf{N} \cdot (\boldsymbol{\mathcal{O}} - \boldsymbol{\xi})^2}{2 \cdot \left(g \cdot \boldsymbol{\mathcal{O}} + \sigma^2\right)^2} + \frac{g \cdot \mathbf{N}}{2 \cdot \left(g \cdot \boldsymbol{\mathcal{O}} + \sigma^2\right)} - \gamma_0 \left(\mathbf{v}_0 - \mathbf{z}_{0,i-1}^k\right), \tag{86}$$

$$\frac{\partial^2}{\partial \mathbf{z}_0^2}\mathcal{L}_{\gamma_0^k}\left(\mathbf{x}^{k+1},\mathbf{z}_0,\mathbf{u}_0^k\right)=\frac{g^2\cdot\mathbf{N}^2\cdot(\boldsymbol{\mathcal{O}}-\boldsymbol{\xi})^2}{\left(g\cdot\boldsymbol{\mathcal{O}}+\sigma^2\right)^3}-\frac{2\cdot g\cdot\mathbf{N}^2\cdot(\boldsymbol{\mathcal{O}}-\boldsymbol{\xi})}{\left(g\cdot\boldsymbol{\mathcal{O}}+\sigma^2\right)^2}+\frac{\mathbf{N}^2}{\left(g\cdot\boldsymbol{\mathcal{O}}+\sigma^2\right)}-\frac{g^2\cdot\mathbf{N}^2}{2\cdot\left(g\cdot\boldsymbol{\mathcal{O}}+\sigma^2\right)^2}+\gamma_0\mathbb{1}\ , \tag{87}$$

where the restored signal is given by $\boldsymbol{\mathcal{O}}=\mathbf{N}\cdot\mathbf{z}_{0,I-1}^k+\mathbf{c}$, and the variance is calculated as $\sigma^2=\left(1+\frac{1}{A}\right)\cdot\sigma_{D,i}^2$, as per Eq. (48). The above formulas are to be understood as element-wise operations, voxel-per-voxel, where the matrices $\boldsymbol{\mathcal{O}}$, $\mathbf{N}$ (after being repeated as explained in Section 4.6), $\mathbf{c}$, $\mathbf{z}_0$, $\mathbf{v}_0$ and matrix of ones $\mathbb{1}$ all have the same dimension as the EELS map.

4.6.3. The $\mathbf{z}_+$-update

By definition, the minimization of the Lagrangian in Eq. (69) with respect to $\mathbf{z}_+$ can be expressed using the proximal operator [61]. Applying this to Eq. (69), we obtain:

$$\mathbf{z}_+^{k+1}=\underset{I_{\mathbb{R}_+}}{\text{prox}}(\mathbf{v}_+)=\begin{cases}\mathbf{v}_+ & \text{if } \mathbf{v}_+\geq 0\\ 0 & \text{otherwise}\end{cases}\ \text{, with}\quad \mathbf{v}_+=\mathbf{x}^{k+1}+\mathbf{u}_+^k\ , \tag{88}$$

where the above operation is again performed element wise, voxel-per-voxel. Additional details on the solution of the $\mathbf{z}_+$-update are provided in the supplementary materials.

4.6.4. The $\mathbf{z}_1$- and $\mathbf{z}_2$-updates

We can minimize $\mathbf{z}_{1,i}$ and $\mathbf{z}_{2,j}$, which perform the actual smoothing, using the '*block soft threshold*' operator [62]. In this context, i,j represent the respective directions of the derivatives. Specifically, for three-dimensional EELS maps, we have $i\in\{h,v,s\}$ and $j\in\{h,v,s,hv,hs,vs\}$. Since we anticipate slightly different noise volatility in energy and lateral directions, as demonstrated in Eq. (59), we modify the block soft threshold operator by incorporating λ into the norm. This approach yields the '*weighted block soft threshold*' operator $\mathcal{S}_{\lambda,\gamma}$:

$$\mathbf{z}_i^{k+1}=\mathcal{S}_{\lambda,\gamma}(\mathbf{v})=\max\left\{\left(1-\frac{\lambda_i^2/\gamma}{\|\lambda^2\mathbf{v}\|_2}\right)\mathbf{v}_i\ ,\ 0\right\}\ . \tag{89}$$

The derivation of the weighted block soft threshold operator is provided in the supplementary materials. Using the weighted block soft threshold operator, we can calculate the $\mathbf{z}_1$- and $\mathbf{z}_2$- updates as:

$$\mathbf{z}_{1,i}^{k+1}=\mathcal{S}_{\lambda_1,\gamma^k}\left[\left(\mathbf{D}\mathbf{x}^{k+1}-\mathbf{t}^{k+1}+\mathbf{u}_1^k\right)\right]\ , \tag{90}$$

$$\mathbf{z}_{2,j}^{k+1}=\mathcal{S}_{\lambda_2,\eta^k}\left[\left(\mathbf{G}\mathbf{t}^{k+1}+\mathbf{u}_2^k\right)\right]\qquad . \tag{91}$$

Again, the operations are performed voxel-per-voxel.

4.6.5. The γ_0-, γ_+-, γ- and η-updates

To perform residual balancing on the penalty parameters γ_0, γ_+, γ and η, we must define the relative primal residuals $\mathbf{R}_{rel}^{k+1}$ and dual residuals $\mathbf{S}_{rel}^{k+1}$ for each penalty parameter, as described in Eq. (27). In our previous work [49], we derived the residuals for a Poisson deconvolution ADMM with TGV. These residuals can be extended to the algorithm presented here. The relative primal residuals are obtained as:

$$R_{rel,\gamma_0}^{k+1}=\frac{\|\mathbf{R}_{\gamma_0}^{k+1}\|_F}{N\left(\mathbf{R}_{\gamma_0}^{k+1}\right)}=\frac{\|\boldsymbol{\Omega}\mathbf{x}^{k+1}-\mathbf{z}_0^{k+1}\|_F}{\max\left\{\|\boldsymbol{\Omega}\mathbf{x}^{k+1}\|_F^2\ ,\ \|\mathbf{z}_0^{k+1}\|_F^2\right\}}\quad,\quad R_{rel,\gamma_+}^{k+1}=\frac{\|\mathbf{R}_{\gamma_+}^{k+1}\|_F}{N\left(\mathbf{R}_{\gamma_+}^{k+1}\right)}=\frac{\|\mathbf{x}^{k+1}-\mathbf{z}_+^{k+1}\|_F}{\max\left\{\|\mathbf{x}^{k+1}\|_F^2\ ,\ \|\mathbf{z}_+^{k+1}\|_F^2\right\}}\ , \tag{92}$$

$$R_{rel,\gamma}^{k+1}=\frac{\|\mathbf{R}_{\gamma}^{k+1}\|_F}{N\left(\mathbf{R}_{\gamma}^{k+1}\right)}=\frac{\|\mathbf{D}\mathbf{x}^{k+1}-\mathbf{t}^{k+1}-\mathbf{z}_1^{k+1}\|_F}{\max\left\{\|\mathbf{D}\mathbf{x}^{k+1}-\mathbf{t}^{k+1}\|_F\ ,\ \|\mathbf{z}_1^{k+1}\|_F\right\}}\quad,\quad R_{rel,\eta}^{k+1}=\frac{\|\mathbf{R}_{\eta}^{k+1}\|_F}{N\left(\mathbf{R}_{\eta}^{k+1}\right)}=\frac{\|\mathbf{G}\mathbf{t}^{k+1}-\mathbf{z}_2^{k+1}\|_F}{\max\left\{\|\mathbf{G}\mathbf{t}^{k+1}\|_F\ ,\ \|\mathbf{z}_2^{k+1}\|_F\right\}}\ , \tag{93}$$

where $\|\cdot\|_F$ again denotes the Frobenius norm as an extension to the Euclidean norm for matrices. The Frobenius norm is employed here as scalar values are needed for balancing. To compute the relative residuals $N(\cdot)$ is required, which represents the norm of the residuals. Unlike the primal residuals, the dual residuals comprise two sets, one associated with the $\mathbf{x}$-update and the other with the $\mathbf{t}$-update. These two sets must be combined to obtain the total relative residuals, which are then used in the residual balancing approach.

The first set of relative dual residuals, associated with the $\mathbf{x}$-update, is given by:

$$S_{rel,\gamma_0,x}^{k+1}=\frac{\|\mathbf{S}_{\gamma_0,x}^{k+1}\|_F}{N\left(\mathbf{S}_{\gamma_0,x}^{k+1}\right)}=\frac{\|\mathbf{S}_{\gamma_0,x}^{k+1}\|_F}{\max\left\{\|\mathbf{N}^*\left(\mathbf{S}_{\gamma_0,x}^{k+1}\right)\|_F\ ,\ \|\mathbf{N}^*\left(\mathbf{S}_{\gamma,x}^{k+1}\right)+\mathbf{N}^*\left(\mathbf{S}_{\gamma_+,x}^{k+1}\right)-\mathbf{S}_{\gamma,x}^{k+1}-\mathbf{S}_{\gamma_+,x}^{k+1}\|_F\right\}}\ , \tag{94}$$

$$S_{rel,\gamma_+,x}^{k+1}=\frac{\|\mathbf{S}_{\gamma_+,x}^{k+1}\|_F}{N\left(\mathbf{S}_{\gamma_+,x}^{k+1}\right)}=\frac{\|\mathbf{S}_{\gamma_+,x}^{k+1}\|_F}{\max\left\{\|\mathbf{N}^*\left(\mathbf{S}_{\gamma_+,x}^{k+1}\right)\|_F\ ,\ \|\mathbf{N}^*\left(\mathbf{S}_{\gamma,x}^{k+1}\right)+\mathbf{N}^*\left(\mathbf{S}_{\gamma_0,x}^{k+1}\right)-\mathbf{S}_{\gamma,x}^{k+1}-\mathbf{S}_{\gamma_0,x}^{k+1}\|_F\right\}}\ , \tag{95}$$

$$S_{rel,\gamma,x}^{k+1}=\frac{\|\mathbf{S}_{\gamma,x}^{k+1}\|_F}{N\left(\mathbf{S}_{\gamma,x}^{k+1}\right)}=\frac{\|\mathbf{S}_{\gamma,x}^{k+1}\|_F}{\max\left\{\|\mathbf{N}^*\left(\mathbf{S}_{\gamma,x}^{k+1}\right)\|_F\ ,\ \|\mathbf{N}^*\left(\mathbf{S}_{\gamma_0,x}^{k+1}\right)+\mathbf{N}^*\left(\mathbf{S}_{\gamma_+,x}^{k+1}\right)-\mathbf{S}_{\gamma_0,x}^{k+1}-\mathbf{S}_{\gamma_+,x}^{k+1}\|_F\right\}}\ . \tag{96}$$

with:

$$\mathbf{S}_{\gamma_0,x}^{k+1}=-\gamma_0^k\boldsymbol{\Omega}^T\left(\mathbf{z}_0^{k+1}-\mathbf{z}_0^k\right)\quad,\quad\mathbf{N}^*\left(\mathbf{S}_{\gamma_0,x}^{k+1}\right)=\gamma_0^k\boldsymbol{\Omega}^T\left(\mathbf{u}_0^k+\mathbf{R}_{\gamma_0}^{k+1}\right)\ , \tag{97}$$

$$\mathbf{S}_{\gamma_+,x}^{k+1}=-\gamma_+^k\quad\left(\mathbf{z}_+^{k+1}-\mathbf{z}_+^k\right)\quad,\quad\mathbf{N}^*\left(\mathbf{S}_{\gamma_+,x}^{k+1}\right)=\gamma_+^k\quad\left(\mathbf{u}_+^k+\mathbf{R}_{\gamma_+}^{k+1}\right)\ , \tag{98}$$

$$\mathbf{S}_{\gamma,x}^{k+1}=-\gamma^k\left[\mathbf{D}^T\left(\mathbf{t}^{k+1}-\mathbf{t}^k+\mathbf{z}_1^{k+1}-\mathbf{z}_1^k\right)\right]\quad,\quad\mathbf{N}^*\left(\mathbf{S}_{\gamma,x}^{k+1}\right)=\gamma^k\mathbf{D}^T\left(\mathbf{u}_1^k+\mathbf{R}_{\gamma}^{k+1}\right)\ , \tag{99}$$

and the second set of relative dual residuals, associated with the $\mathbf{t}$-update, where we have the $\mathbf{t}_i$-sub-updates for all three dimensions of the data cube. The corresponding residuals are given as:

$$S^{k+1}_{rel,\gamma,t_i} = \frac{\|\mathbf{S}^{k+1}_{\gamma,t_i}\|_F}{N\left(\mathbf{S}^{k+1}_{\gamma,t_i}\right)} = \frac{\|\mathbf{S}^{k+1}_{\gamma,t_i}\|_F}{\max\left\{\|\mathbf{N}^*\left(\mathbf{S}^{k+1}_{\gamma,t_i}\right)\|_F\,,\ \|\mathbf{N}^*\left(\mathbf{S}^{k+1}_{\eta,t_i}\right)-\mathbf{S}^{k+1}_{\eta,t_i}\|_F\right\}}\,, \tag{100}$$

$$S^{k+1}_{rel,\eta,t_i} = \frac{\|\mathbf{S}^{k+1}_{\eta,t_i}\|_F}{N\left(\mathbf{S}^{k+1}_{\eta,t_i}\right)} = \frac{\|\mathbf{S}^{k+1}_{\eta,t_i}\|_F}{\max\left\{\|\mathbf{N}^*\left(\mathbf{S}^{k+1}_{\eta,t_i}\right)\|_F\,,\ \|\mathbf{N}^*\left(\mathbf{S}^{k+1}_{\gamma,t_i}\right)-\mathbf{S}^{k+1}_{\gamma,t_i}\|_F\right\}}\,, \tag{101}$$

with:

$$\mathbf{S}^{k+1}_{\gamma,t_i} = \gamma^k\left[\mathbf{D}_i\left(\mathbf{x}^k-\mathbf{x}^{k+1}\right)+\mathbf{z}^{k+1}_{1,i}-\mathbf{z}^k_{1,i}\right]\,, \tag{102}$$

$$\mathbf{N}^*\left(\mathbf{S}^{k+1}_{\gamma,t_i}\right) = \gamma^k\left[\mathbf{u}^k_{1,i}+\left[\mathbf{D}\mathbf{x}^{k+1}\right]_i-\mathbf{t}^{k+1}_i-\mathbf{z}^{k+1}_{1,i}\right]\,, \tag{103}$$

$$\mathbf{S}^{k+1}_{\eta,t_i} = -\eta^k\left[\mathbf{D}_i\left(\mathbf{z}^{k+1}_{2,i}-\mathbf{z}^k_{2,i}\right)+\sum_l \mathbf{D}_l\left(\mathbf{D}_i^T\left(\mathbf{t}^k_l-\mathbf{t}^{k+1}_l\right)+\mathbf{z}^{k+1}_{2,il}-\mathbf{z}^k_{2,il}\right)\right]\,, \tag{104}$$

$$\mathbf{N}^*\left(\mathbf{S}^{k+1}_{\eta,t_i}\right) = \eta^k\left[\mathbf{D}_i\left(\mathbf{u}^k_{2,i}+\left[\mathbf{G}\mathbf{t}^{k+1}\right]_i-\mathbf{z}^{k+1}_{2,i}\right)+\sum_l \mathbf{D}_l\left(\mathbf{u}^k_{2,il}+\left[\mathbf{G}\mathbf{t}^{k+1}\right]_{il}-\mathbf{z}^{k+1}_{2,il}\right)\right]\,. \tag{105}$$

where the indices $i \in \{h,v,s\}$ represent the three dimensions of the derivative $\mathbf{D}$ for EELS maps, while $(il) \in \{hv,hs,vs\}$ specifically denote the diagonal entries associated with each direction i. For instance, if i represents the horizontal direction h, then $l \in \{v,s\}$, resulting in $(hl) \in \{hv,hs\}$.

By combining the $\mathbf{x}$- and $\mathbf{t}$-residuals, we obtain the total relative dual residuals:

$$S^{k+1}_{rel,\gamma_0} = \frac{\|\mathbf{S}^{k+1}_{\gamma_0,x}\|_F}{N\left(\mathbf{S}^{k+1}_{\gamma_0,x}\right)}\,,\quad S^{k+1}_{rel,\gamma_+} = \frac{\|\mathbf{S}^{k+1}_{\gamma_+,x}\|_F}{N\left(\mathbf{S}^{k+1}_{\gamma_+,x}\right)}\,, \tag{106}$$

$$S^{k+1}_{rel,\gamma} = \sqrt{\frac{\|\mathbf{S}^{k+1}_{\gamma,x}\|_F^2+\sum_i\|\mathbf{S}^{k+1}_{\gamma,t_i}\|_F^2}{N\left(\mathbf{S}^{k+1}_{\gamma,x}\right)^2+\sum_i N\left(\mathbf{S}^{k+1}_{\gamma,t_i}\right)^2}}\,,\quad S^{k+1}_{rel,\eta} = \sqrt{\frac{\sum_i\|\mathbf{S}^{k+1}_{\eta,t_i}\|_F^2}{\sum_i N\left(\mathbf{S}^{k+1}_{\eta,t_i}\right)^2}}\,, \tag{107}$$

With all relative residuals R_{rel} and S_{rel} calculated, we can now update the penalty parameters using Eqs. (28) and (29).

However, implementing the algorithm may be challenging for users without prior experience in ADMM. To facilitate implementation, we provide a MATLAB script of our ADMM algorithm in the supplementary materials.

5. Comparison of the ADMM-TGV with the RLA on a simulated nanoparticle

To evaluate the algorithm, we require a signal that closely resembles a real EELS map measurement, including all of its characteristic features, since in a real-world measurement, the ground truth would be unknown. Hence, it essential to simulate such an EELS map to employ an objective comparison between a deconvolution result and the ground truth. Therefore, we simulated an EELS map of a truncated gold nano-pyramid, 25 nm in height, on a SiO_2 substrate (depicted in Fig. 2(a) top view and in Fig. 2(b) side view), as an exemplary data set. A particle of similar shape and size, as shown in the STEM annular dark field (ADF) image in Fig. 2(e), is subsequently evaluated in a real measurement. Consequently, the simulated data can be used for comparison with a real EELS map later in this paper. The gold nanoparticle in Fig. 2(a) was simulated using a ray-tracing algorithm for a *nanosphere-lithography* (NSL) [63,64] process, as described in [65]. This process involves using a self-organized monolayer of hexagonally close-packed spheres as a shadow mask for depositing a regular array of nanoparticles. We modified the algorithm to incorporate a different mask closing mechanism, which is described later, allowing to fine-tune the aperture size between three neighboring nanospheres, as depicted in Fig. 2(c) side view and in Fig. 2(d) top view. As shown in Fig. 2(d), the evaporation of material through the nanomask, orthogonal to the substrate, results in nanoparticles with a triangular base. The deposited material not only forms particles but also accumulates on top of the nanomask, causing it to clog. To account for mask-clogging during the evaporation process, the simulation iteratively considers the deposition of material on top of the nanospheres. The mask-clogging material is represented by the red layer on top of the green spheres, which is visible in the side view Fig. 2(c). The green spheres represent the initial state of the nanosphere mask prior to the evaporation process.

We used the particle depicted in Fig. 2(a) and (b) to simulate an EELS map with a dispersion of 0.01 eV/channel and a range of 0.75 – 5 eV, employing the MNPBEM toolbox [36]. Due to the difficulty in visualizing 3D data cubes as a whole, we selected three dominant plasmonic resonances at 0.99 eV (black frame), 1.91 eV (cyan frame), and 2.49 eV (magenta frame). We display these as 0.01 eV thick slices in Fig. 3(a-c) to illustrate the spatial distribution of the plasmonic mode. The green line indicates the boundaries of the nano-particle for orientation purposes. Additionally, we present the respective spectra in Fig. 3(d) measured at the tip of the triangular projection of the nano-pyramid, where the first plasmonic resonance reaches its maximum, at the middle of the particle, where the third mode is maximal, and at the bottom, where the second mode is maximal. The locations where the spectra were obtained are indicated in Fig. 3(a-c) by small boxes matching the corresponding color. The corresponding spectra in Fig. 3(d,h,l,p) display the average of all spectra within these boxes. All spectra maintain the same color scheme and display an energy region of interest (ROI) from 0.75 – 3 eV, which corresponds to the location of the relevant surface plasmons. We regard the data in Fig. 3(a-d) as the ground truth for our analysis.

To simulate data as measured by our detector, we scale the data to a typical intensity range for plasmonic resonances and convolve it with a Gaussian shaped probe characteristic, featuring a full width at half maximum (FWHM) of FWHM = 0.5 eV. Additionally, we superimpose the data with beam intensity, signal and detector noises, as described by the noise model in Eq. (10), using the parameters evaluated in [7] ($\frac{\sigma_{Int}}{I} = 0.008$, $g \approx 17.43$ counts/beam electron and $\sigma_D \approx 45$ counts, from which a background that was averaged across $A = 100$ frames was subtracted). This result in an average SNR ≈ 10 for the ROI from 0.75 – 3 eV across the data. We also utilize the detector PSF $\mathbf{\Omega}_D$ (FWHM ≈ 1.77 EEL channels corresponding to approximately 0.018 eV, which results in $\beta_{corr} \approx 0.24$), which we have measured on our detector [7], to introduce noise correlations in the Poisson

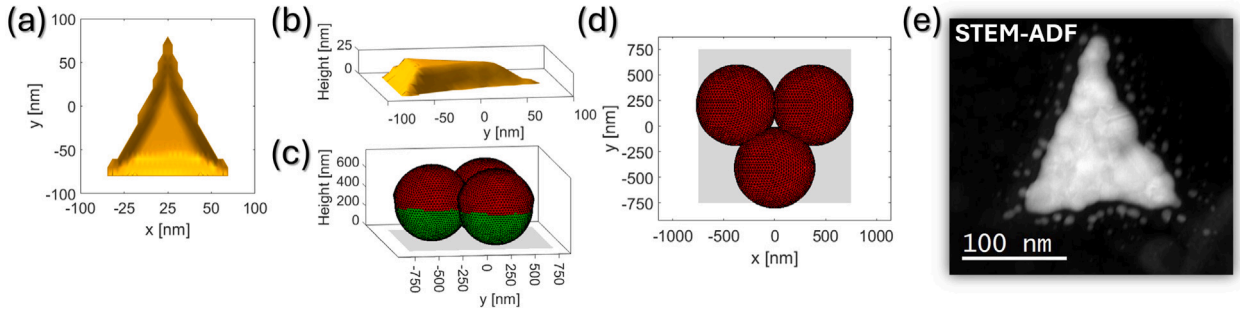

Fig. 2. Simulated **(a)** top view and **(b)** side view of a truncated gold nano-pyramid, 25 nm in height on top of a SiO_2 substrate. The particle was simulated using a ray-trace algorithm (similar [65]) to model a nanosphere lithography (NSL) process. A nanosphere mask, depicted in side view **(c)** and top view **(d)**, was created for the simulation, featuring nanospheres with a diameter of 750 nm. As evident in (d), the nanosphere mask blocks the beam paths of evaporated materials, except for the aperture formed between three adjacent spheres. Consequently, a truncated nano-pyramid is formed during the lithography process. Additionally, material is deposited onto the mask, clogging the aperture. This is accounted for in the simulation by iteratively adding material to both the substrate (creating the particle) and the nanomask (to model clogging). The initial spheres (green), visible in (c), become coated with clogging material (red), causing the aperture to gradually close as more material is deposited. Consequently, the particle in (a) and (b) tapers towards the top, forming a pyramidal height profile. A particle of this type is subsequently used to simulate EELS maps, as shown in Fig. 3. **(e)** STEM annular dark field (STEM-ADF) image of a real truncated nano-pyramid, analogous to the simulated particle in (a) and (b). This real particle is used to demonstrate the applicability of the ADMM-TGV algorithm to real EELS maps.

noise. In Fig. 3(e-h) we display the blurred and noisy data for the three dominant resonance modes, along with their respective spectra at the same positions as above.

As proposed in Section 3.1, we subtracted the ZLP before deconvolution for evaluation purposes. We display the results obtained using the commonly employed RLA (as described in Eq. (21)) with 15 iterations in Fig. 3(i-l), and the results obtained using the proposed ADMM-TGV algorithm (as described in the previous section) with 1500 iterations in Fig. 3(m-p). According to Eq. (80), the ADMM algorithm is defined to reveal loss-probabilities as an output. Since the RLA does not reveal loss-probabilities but outputs counts, we need to undo the division of the ADMM result by the mean value of the original beam intensity I as of Eq. (80) to enable a direct comparison between the two results.

A visual inspection reveals that the ADMM-TGV results (m-o) exhibit lower noise levels compared to the RLA results. Moreover, the ADMM-TGV algorithm Fig. 3(p) significantly enhances the peak sharpness compared to the RLA Fig. 3(l), demonstrating the effectiveness of the ADMM-based deconvolution process.

Nevertheless, the overall effectiveness of deconvolution is constrained by the width of the convolution kernel and the overall noise level of the data. The Nyquist-Shannon sampling theorem [66,67] states that a feature can only be fully resolved if the sampling rate is at least twice the highest contributing frequency. In the frequency domain, convolution with a broad kernel functions as a low-pass filter, attenuating the higher frequencies in the data. The kernel width significantly influences the attenuation of the higher frequencies, with broader kernels resulting in greater attenuation. Noise, on the other hand, introduces a background in frequency domain that is either flat (for white, independent Gaussian noise) or sloped (for colored, correlated noise). If a frequency is obscured by this noise background, it cannot contribute to the reconstruction of the original data, leading to a loss of features as predicted by the Nyquist-Shannon sampling theorem and observed in Fig. 3(d) compared to Fig. 3(l) or (p). Therefore, it is essential to optimize the microscope and beam parameters prior to measuring EELS maps, minimizing the convolution kernel to the greatest extend possible. The quality of the deconvolution algorithm solely determines the number of frequencies that can be restored under the given conditions. Consequently, the overall success of deconvolution is inherently limited by the point at which the signal frequencies become mathematically indistinguishable from the noise background. Given the finite set of a-priori information available to aid in reconstructing these frequencies, this limit imposes a significant constrain on scientifically sound algorithms – a constrain that artificial intelligence (AI) based algorithms must also necessarily respect.

Although deconvolution is subject to this limitation, it remains a valuable tool for enhancing EEL spectra and EELS maps. However, the comparison in Fig. 3 is largely qualitative in nature. To establish an objective criterion and demonstrate the effectiveness of deconvolution, we introduce a distance measure defined as the '*mean squared error*' (MSE) between the deconvolution result $\hat{\mathbf{s}}^k_{\mathrm{ADMM}}$ at the kth iteration (see Eq. (80)) and the normalized ground truth $\hat{\mathbf{s}}_{Sim}$ from the simulation representing the true loss-probabilities:

$$\mathrm{MSE}^k = \frac{1}{X \cdot Y \cdot \theta} \| \hat{\mathbf{s}}_{\mathrm{Sim},\Theta} - \hat{\mathbf{s}}^k_{\mathrm{ADMM},\Theta} \|_F^2 \quad , \tag{108}$$

$$\mathrm{NormMSE}^k = \frac{\mathrm{MSE}^k}{\mathrm{MSE}^0} \quad , \tag{109}$$

where Θ denotes the energy ROI, which we have defined as the range of EEL channels from 0.75 – 3 eV, as this region primarily contains the plasmonic peaks, and $\| \cdot \|_F$ again denotes the Frobenius norm as an extension of the Euclidean norm for matrices. Additionally, we define θ as the number of channels contributing to the ROI. For the RLA results, these calculations are performed equivalently, but since the RLA produces an estimate of the signal $\hat{\mathbf{S}}_{\mathrm{RLA}}$, instead of loss probabilities $\hat{\mathbf{s}}_{\mathrm{RLA},x,y,i} = \frac{\hat{\mathbf{S}}_{\mathrm{RLA},x,y,i}}{\sum_i^M \hat{\mathbf{S}}_{\mathrm{RLA},x,y,i}}$, the results are normalized. To illustrate the convergence properties of both the RLA and the ADMM-TGV algorithm, we compute the MSE^k at each iteration k. For comparative purposes, it is helpful to normalize the MSE^k with respect to the initial MSE^0, obtained before running the algorithms. This normalization enables a clear visualization of the extend to which deconvolution enhances the noisy and blurry data.

A review of [9,11,15,17,23,68] might lead one to conclude that the FWHM of the deconvolved ZLP could be a valid criterion for evaluating the success of deconvolution. However, while this idea looks promising at first, it really is not. As we have discussed previously, the ability to restore features is linked to the Nyquist-Shannon theorem, which states that a signal can only be restored if it is sampled at twice the highest contributing frequency. One could argue that a sharp ZLP with a low FWHM is an indication of an algorithm's ability to restore these high frequencies better, but unfortunately, this is often not the case. A prominent example is provided by the RLA itself, which amplifies the higher frequencies, leading to a

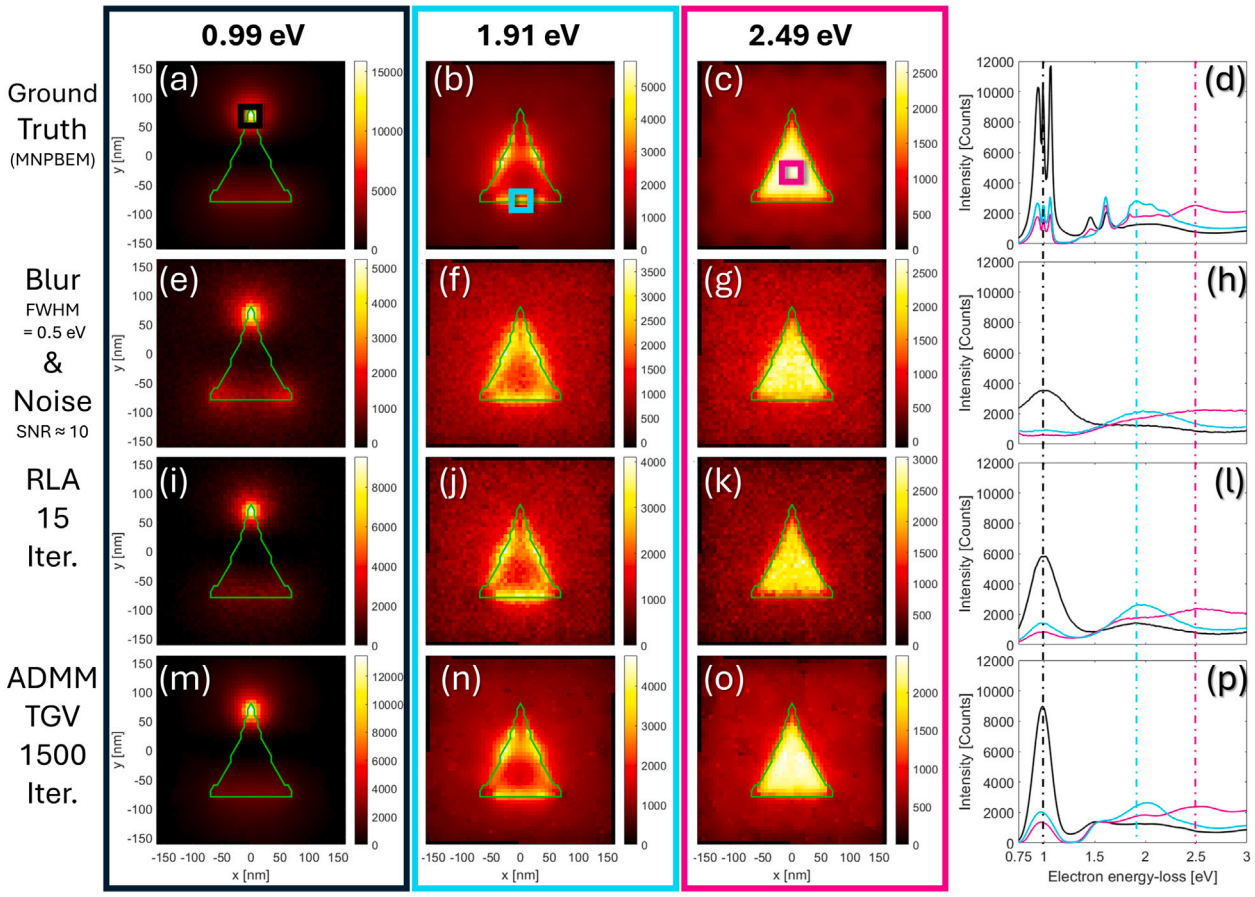

Fig. 3. **(a-c)** EELS map slices with a dispersion of 0.01 eV/channel were simulated using the MNPBEM toolbox [36] for the particle depicted in Fig. 2, at three distinct energy losses. The entire data cube was scaled to ensure that the plasmonic peaks are of the same order of magnitude as those measure by our detector. The modes at 0.99 eV, 1.91 eV, and 2.49 eV emerge as the dominant plasmonic modes of this particle, exhibiting the highest intensities. Each plasmon is linked o a specific location on the particle, as indicated the by colored boxes in (a-c), while the green line indicates the boundary of the nanoparticle. The average spectra of the boxed regions are displayed in **(d)**, with the positions of 0.99 eV, 1.91 eV, and 2.49 eV marked by dash-dotted lines in their respective colors. The second row **(e-h)** presents the data in the same manner as above, but with the addition of a convolution using a Gaussian energy distribution of FWHM = 0.5 eV and a beam current deviation of $\frac{\sigma_{I_{el}}}{I} = 0.008$ between spectra, as per [7]. Poisson noise, with a gain of $g = 17.41$ counts/beam electron (as reported in [7]) is superimposed on the signal, which is then convolved with the detector PSF (FWHM ≈ 0.02 eV which corresponds to approximately 2 EEL channels, as described in [7]), to introduce correlations within the noise, with $\beta_{corr} \approx 0.24$. Finally, read-out noise ($\sigma_D \approx 45$ counts) is added – all according to the noise model outlined in Eq. (10), except that the background used for subtraction was averaged across $A = 100$ frames. This result in an average SNR ≈ 10 for the ROI from 0.75 – 3 eV across the data. The spectra were also not shifted nor realigned. Since no sub-channel realignment is therefore necessary, no interpolation can induce further correlations into the signal nor into the detector noise. The third row **(i-l)** presents the deconvolution results obtained using the RLA after 15 iterations, while the fourth row **(m-p)** displays the deconvolution results obtained using the proposed ADMM-TGV algorithm after 1500 iterations. In a direct comparison of the ground truth (a-c) with the deconvolution results obtained using the RLA in (i-k) and the ADMM-TGV in (m-p) reveals that both algorithms improve the data quality. However, it is also apparent that the estimates obtained using our proposed algorithm are less noisy than those obtained using the RLA and appear to be more closely aligned with the ground truth (a-c). A comparison of the spectra in (d) with the results obtained using the RLA in (l) and the ADMM-TGV in (p) reveals that the features in the latter are significantly sharper than those reconstructed using the RLA. However, neither algorithm is able to fully recover the fine features of the ground truth in (d), owing to the broad convolution kernel and a substantial noise level.

sharpening of the ZLP; however, it also increases the noise to the point where it dominates the spectrum, yet the ZLP still appears sharp. An algorithm must not simply amplify the higher frequencies but also distinguish these frequencies from the noise background correctly for deconvolution to be successful. Thus, the FWHM is not the right measure for success. Further, the spectra also consist of a multitude of different frequencies, which all need to be restored for an optimal deconvolution result. The individual contribution of these factors to the sharpness of the ZLP is relatively limited. To illustrate this point, consider the Fourier transform of a narrow Gaussian peak, which is predominantly comprised of lower frequency components with respect to their amplitude. In contrast, the higher frequency components have a relatively minor impact. Consequently, comparing ZLPs obtained from different algorithms does not necessarily provide a reliable indication of the algorithms' ability to restore the higher frequency components. Therefore, we use the MSE, which is a significantly better criterion for comparison.

In Fig. 4(a), we display the NormMSE^k as a function of the iteration number, up to 1500 iterations, for both the RLA (dashed lines) and the ADMM-TGV (solid lines) algorithms, with an energy resolution of FWHM = 0.5 eV (blue curves). Additionally, we present results for energy resolutions of FWHM = 0.3 eV (orange curves) and FWHM = 0.1 eV (green curves) to illustrate the effect of the convolution kernel width on the deconvolution result, while maintaining constant noise levels. The detector PSF $\mathbf{\Omega}_D$ is kept constant across all three scenarios, allowing us to isolate the effect of changing energy resolution. It is evident that the RLA diverges after 10–100 iterations. However, without extensive testing, determining the exact iteration yielding the best deconvolution result is impossible to the best of our knowledge. As the ZLP narrows, this optimal iteration appears to occur earlier. However, excessive iteration of the RLA eventually leads to divergence and produces results that are worse than the initial estimate, as evident from the NormMSE exceeding 1. Due to the risk of missing the optimal iteration, which is significant given the unknown optimal iteration number, the RLA is frequently terminated prematurely, as discussed in the introduction Section 1.

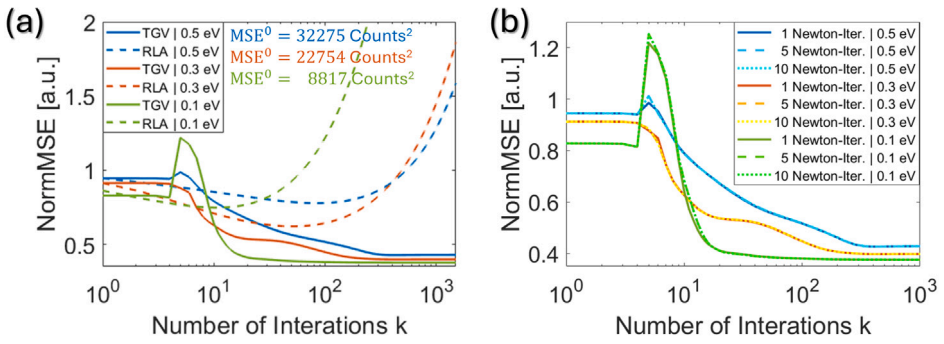

Fig. 4. **(a)** NormMSE, as defined in Eq. (109), serves as a distance measure between the deconvolution result $\hat{\mathbf{s}}^k_{\mathrm{ADMM}}$ at iteration k and the simulated ground truth $\hat{\mathbf{s}}_{Sim}$. The same applies to the distance between ground truth $\hat{\mathbf{s}}_{Sim}$ and $\hat{\mathbf{s}}^k_{\mathrm{RLA}}$. A value NormMSE > 1 indicates a worse-than-before result, while NormMSE < 1 indicates a better-than-before result. To help contextualizing the results with respect to data quality, we provide the MSE^0 of the initial data. The results obtained using the RLA are represented by dashed lines, while the results obtained using the ADMM-TGV are represented by solid lines. To illustrate the effect of the ZLP width, we computed the results for three different energy resolutions: FWHM = 0.5 eV (blue), FWHM = 0.3 eV (orange) and FWHM = 0.1 eV (green), all with a constant detector PSF $\mathbf{\Omega}_D$ (FWHM ≈ 0.02 eV). It is evident that the RLA diverges after few iterations, whereas the proposed ADMM-TGV algorithm converges to stable result. Given that the NormMSE of the converged ADMM-TGV is significantly lower than that of the RLA terminated at the optimal iteration, it is clear that the ADMM-TGV algorithm outperforms the RLA. **(b)** Dependence of the results in (a) on the number of Newton iterations used for the $\mathbf{z}_0$-update (see Section 4.6.2). We retained the color coding used in (a) to represent the width of the energy distribution, with the results for 1 Newton iteration displayed as solid lines, 5 iterations as dashed lines, and 10 iterations as dotted lines, where the color shade lightens with increasing Newton iterations. It is evident that the results are virtually identical for all three cases, leading us to recommend using only 1 Newton iteration for the $\mathbf{z}_0$-update.

In contrast, the proposed ADMM-TGV algorithm converges after a certain number of iterations, with the convergence point dependent on the width of the ZLP convolving the data. Notably, the timing of iteration termination is inconsequential, as the results remain consistent after convergence is attained. This advantage should not be underestimated. The results can be deemed valid and final after a specified number of iterations, at which point the changes between iterations become negligible. Consequently, convergence plays a crucial role for the development of an unbiased deconvolution algorithm. We recommend 500 iterations for our algorithm to guarantee convergence. This number has been found to be sufficient in numerous experiments conducted under various beam conditions.

The peak observed in the green and blue curves in Fig. 4(a) and (b) after the third iteration is a consequence of the residual balancing establishing a suitable value for all penalty parameters γ_0, γ_+, γ and η, respectively, as discussed in Section 4.2. For further explanations, we refer the reader to [49], where this phenomenon is described in detail.

Under typical beam conditions for our detector, we find that the ADMM-TGV reduces the MSE by approximately 60% relative to the original data, whereas the RLA achieves a maximum reduction of 40%, albeit with the risk of missing the optimal iteration. In practice, terminating the RLA after 15 iterations results in an overall performance that is only half that of our proposed ADMM-TGV algorithm. Therefore, although the RLA is computationally faster than ADMM-TGV, the latter demonstrates superior accuracy. The speed of the algorithm in comparison to the RLA will be evaluated later in Section 8.

In [15], it is suggested to apply the RLA multiple times instead of only once to further improve the results. However, the ability to restore information is linked to the algorithm's ability to recover the frequencies of the EEL spectra. Since no new information enters into the second application of the RLA (e.g. in the form of new a-priori information), one cannot expect to gain new true features within the results. Moreover, the noise statistics are fundamentally obscured by the previous application of the RLA, which means that reapplying it results in a mismatch between the noise anticipated by the RLA model and the data it is intended to improve. Therefore, although the results may appear smoother after the second application, this comes at the cost of losing even more features.

Fig. 4(b) illustrates the dependence of the ADMM-TGV algorithm on the number of Newton iterations used for the $\mathbf{z}_0$-update (see Section 4.6.2). We present the results for all three deconvolutions, corresponding to different kernel widths, as shown in Fig. 4(a), where FWHM = 0.5 eV is displayed as the blue curves, FWHM = 0.3 eV as the orange curves and FWHM = 0.1 eV as the green curve, with varying numbers of Newton iterations as Iter = 1 (solid line, darkest color shade), Iter = 5 (dashed line, medium color shade) and Iter = 10 (dotted line, lightest color shade), maintaining the color scheme from Fig. 4(a). It is evident that the choice of the number of Newton iterations has negligible impact on the convergence and does not significantly affect the number of iterations required to achieve convergence. Therefore, we recommend using only one Newton iteration, as this is clearly the most computationally efficient approach.

6. Deconvolution of an experimental plasmonic EELS map

Having demonstrated the success of ADMM-TGV on simulated data, we must now validate its applicability to real measurements. The measurements presented in the following were acquired using a *JEOL JEM-ARM200F* with a *Gatan imaging filter system (GIF) Quantum ER* having a *US1000FT-XP 2* detector attached. The convergence semi-angle and collection semi-angle were 70 mrad and 20.833 mrad, respectively, for all EELS measurements. We prepared gold nano-pyramids on a SiO_2 substrate, one of which is depicted in Fig. 2(e). This particle was prepared using *electron beam physical vapor deposition* (EBPVD) [69] within a nanosphere-lithography (NSL) setup [70]. In this process, polystyrene nanospheres with a diameter of 750 nm were applied to the substrate using the doctor blade technique [71,72]. The spheres were then coated with a layer of SiO_2, and the triangular mask openings were partially closed by applying Stöber's method [73,74], resulting in a radial growth on top of the SiO_2 coating. Finally, 25 nm of gold was deposited on top of a 3 nm thick adhesion layer of titanium through the mask. This process yields nanoparticles on the substrate with a triangularly shaped base. The nanospheres are then removed in a toluene bath, leaving only the truncated nano-pyramids on the specimen, which is further prepared for TEM analysis.

Analogous to Fig. 3, we conducted an EELS map measurement with a dispersion of 0.01 eV/channel and present three 0.01 eV thick energy slices of the data cube at the corresponding energy-loss positions of 0.99 eV, 1.91 eV and 2.49 eV (Fig. 5(a-c)). Additionally, we provide three

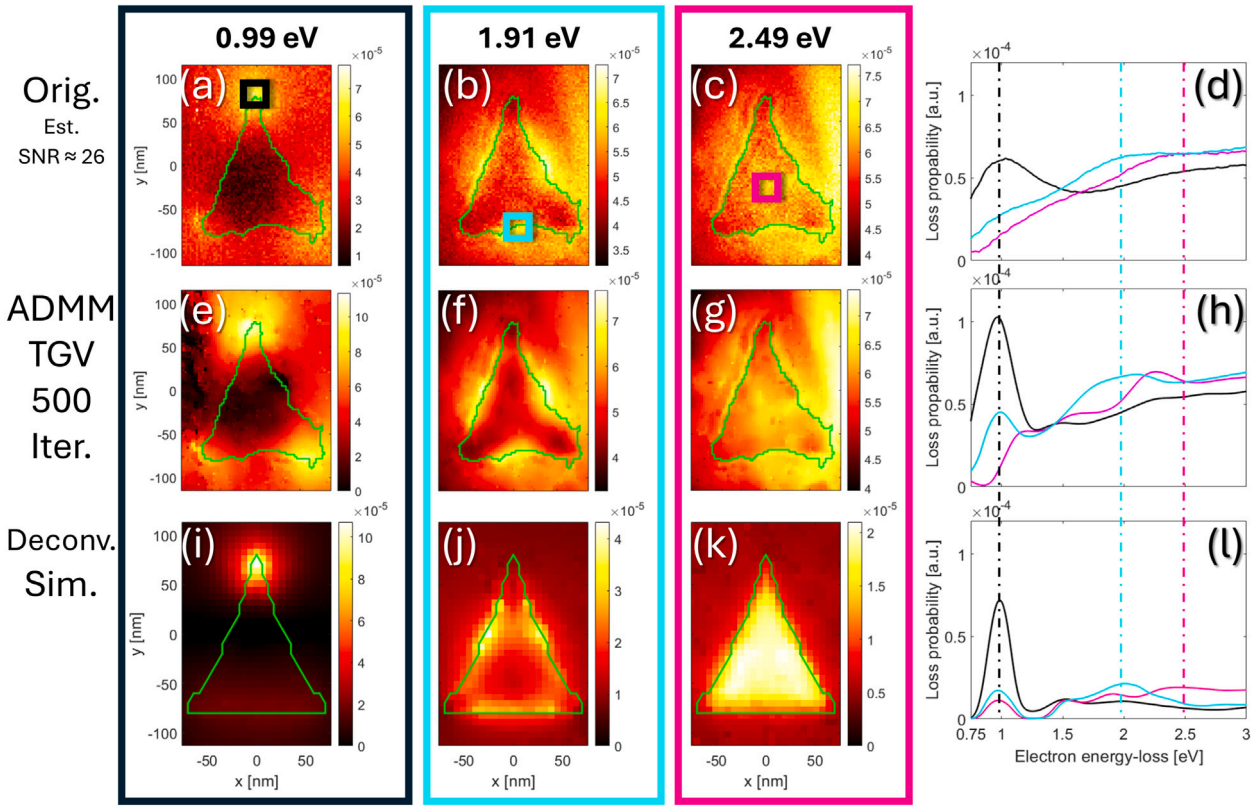

Fig. 5. **(a-c)** Visualization of the normalized EELS map, measured for the truncated nano-pyramid depicted in Fig. 2(e) without deconvolution applied. We estimate the signal-to-noise ratio of the ROI shown from 0.75 – 3 eV based on our noise model Eq. (16) to be SNR ≈ 26. Analogous to Fig. 3, we present three energy slices with a dispersion of 0.01 eV, displaying the spatial distributions of plasmonic modes at 0.99 eV (black frame), 1.91 eV (cyan frame) and 2.49 eV (magenta frame). These three modes were found to be dominant in the simulation data displayed in Fig. 3 and are used again to facilitate comparison between the two datasets. Each plasmon is liked to a specific location on the particle, as indicated by colored boxes in (a-c), while the green line indicates the boundary of the nanoparticle. The average spectra of the boxed regions are displayed in **(d)**, with the positions of 0.99 eV, 1.91 eV, and 2.49 eV marked by dash-dotted lines in their respective colors. The second row **(e-h)** presents the data in the same manner as above, but deconvolved using the proposed ADMM-TGV algorithm after 500 iterations. The third row **(i-l)** displays the deconvolved simulation data from Fig. 3(m-p), rescaled to match the loss probabilities of the measurement above. This dataset was chosen because deconvolution is unable to restore the fine features within the spectrum. For comparison purposes, it is therefore more suitable to use the deconvolved simulation data. Generally, it is observed that deconvolution significantly improves the results (a-d) compared to the simulated data (i-l). This is particularly evident in the reduced noise of (e-g) compared to (a-c). Additionally, the features in (h) appear sharper compared to those in (d). In general, the deconvolution results (e-h) show good agreement with the simulated data (i-l), particularly for the edge mode at 1.91 eV, which exhibits a high degree of similarity between the two datasets. Deviations occurring between (h) and (l) may be attributed to differences between the simulated particle and the measured particle, which can be observed in Fig. 2(a) and (e), especially with respect to the internal grain structure, which is not represented in the simulation. The tip mode at 0.99 eV exhibits a positional match between (h) and (l). In the deconvolved experimental data (e), the lateral distribution of the plasmon appears more pronounced than in (i), particularly at the bottom of the structure. However, the breathing mode at 2.49 eV remains significantly underpronounced in (g) compared to (k). Upon comparing the magenta spectra in (h) and (l), it is evident that the peak of the real measurement is shifted to slightly lower energies relative to the simulated data. For the sake of completeness, the corresponding energy slice is provided in the supplementary materials.

spectra in (d), corresponding to the tip (black), middle position (magenta), and bottom (cyan) of the projection of the truncated nano-pyramid indicated, as indicated by the colored boxes in (a-c). The colored dash-dotted lines within the spectra indicate the respective energies at which the energy slices (a-c) were acquired. We present the original normalized data, as acquired from the microscope, in Fig. 5(a-d), the ADMM-TGV deconvolved data after 500 iterations in Fig. 5(e-h) and the rescaled dataset from the ADMM-TGV deconvolved simulation data Fig. 3(m-p) for comparison in Fig. 5(i-l). Given that deconvolution is expected to result in a loss of small features, it is more insightful to compare the deconvolved real data with the deconvolved simulation data.

Generally, we observe a good agreement between the deconvolved experimental data and the simulation. The tip mode at 0.99 eV exhibits good agreement in (e) and (i), and the peak positions in the black spectra (h) and (l) match well. However, the bottom part is more pronounced in the real data than in the simulated data. The exact shape of the real particle differs slightly from that of the simulated particle, owing to agglomerations of gold atoms at positions with low height and grain structure inside the material. Additionally, the titanium layer was omitted in the simulation. Consequently, small deviations in the plasmonic characteristics are anticipated and indeed observed. The edge mode at 1.91 eV exhibits a particularly good fit, both in the energy slices in (f) and (j) and in the cyan spectra (h) and (l). The breathing mode at 2.49 eV is underpronounced in (g) compared to (k). Notably, upon comparing the magenta spectra in (h) and (l), it is evident that the peak of the measurement appears shifted to lower energies. The lateral distribution of the plasmon at 2.26 eV, which illustrates the corresponding breathing mode, is provided in the supplementary materials.

From a broader perspective, it is evident that deconvolution using the proposed ADMM-TGV algorithm significantly enhances the data, particularly in terms of feature width in all spectra (d) and (h), as well as the overall smoothness of the data (e-g) compared to (a-c). Given the similarity between the deconvolved data and the expected simulation data, we consider the deconvolution results to be valid.

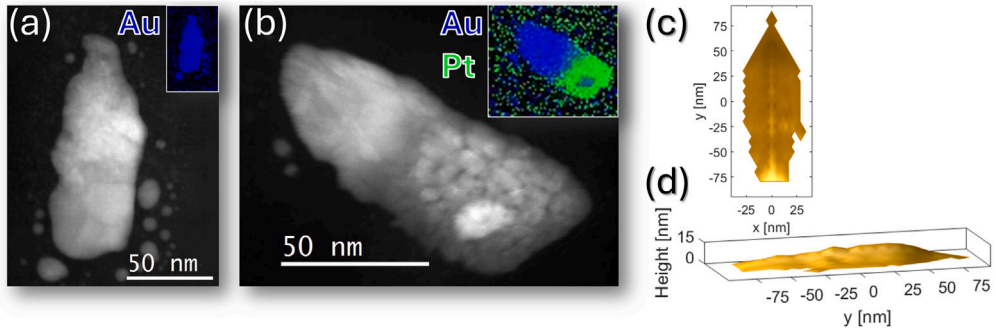

Fig. 6. **(a)** STEM-ADF image of a gold, bottle-shaped nanostructure. An EDS map, located in the top right corner as an inset, reveals that the particle is composed of gold (blue). **(b)** STEM-ADF image of a gold-platinum, bottle-shaped Janus nanostructure. An EDS image, located in the top right corner as an inset, reveals that the particle comprises a gold top (blue) and a platinum bottom (green). Additionally, we simulated the bottle particles using our ray-tracing algorithm [65]. The simulated particle is depicted in **(c)** in top view and in **(d)** in side view.

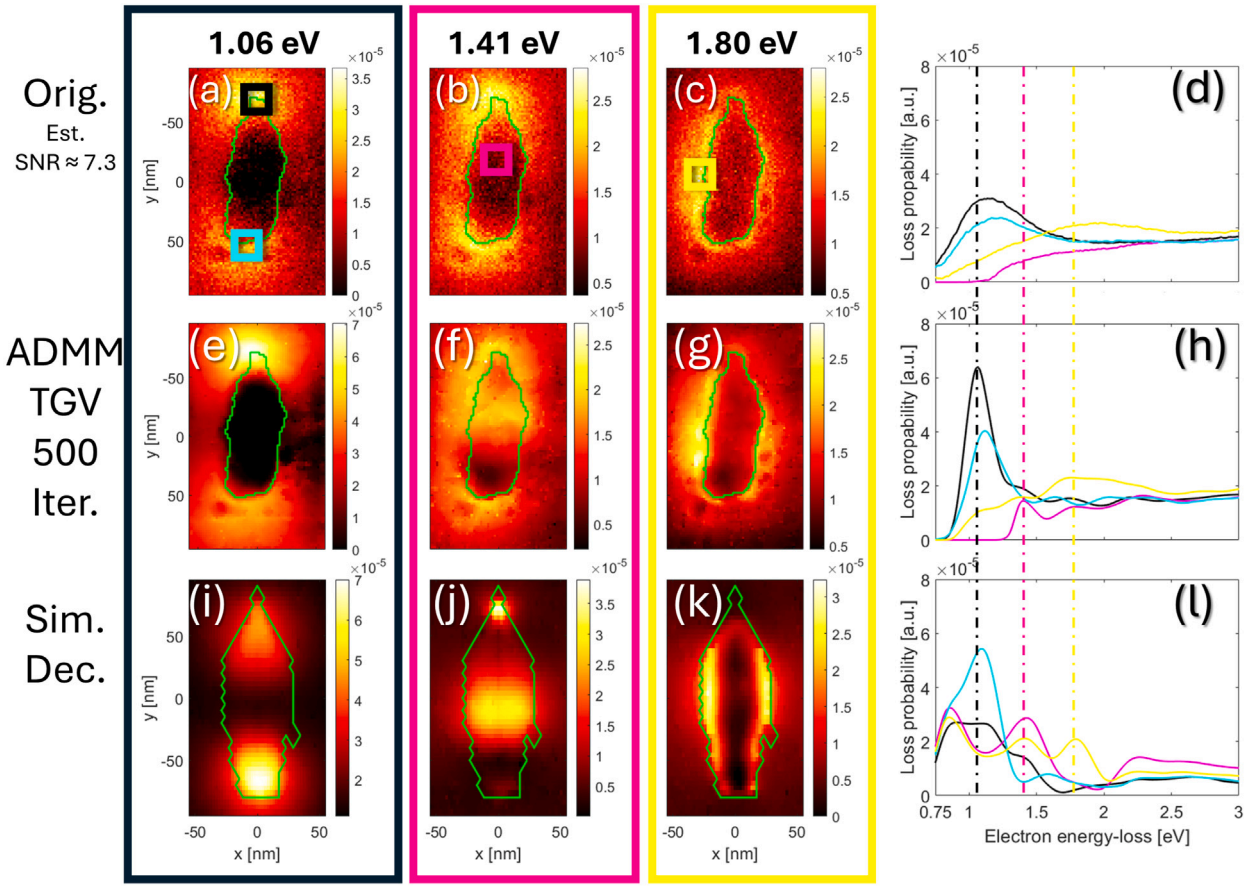

Fig. 7. **(a-c)** Visualization of the normalized EELS map measured for the gold nano-bottle depicted in Fig. 6(a), presented as original data prior to deconvolution. The estimated signal-to-noise ratio of the ROI is SNR ≈ 7.3. We present three slices that display the spatial distributions of the plasmonic modes at 1.06 eV (black frame), 1.41 eV (magenta frame), and 1.80 eV (yellow frame). Each plasmon is linked to a distinct position on the particle, indicated by colored boxes in (a-c), while the green line indicates the boundary of the nano-bottle. The average spectra of the boxed regions are displayed in **(d)**, with the positions of 1.06 eV, 1.41 eV, and 1.80 eV marked with dash-dotted lines in their respective color. The second row **(e-h)** displays the data in the same manner as above, but deconvolved using the proposed ADMM-TGV algorithm after 500 iterations. It is evident that the second mode at 1.41 eV becomes visible only after deconvolution. This is confirmed by the results in the third row **(i-l)**, which present the deconvolved simulation data obtained using the MNPBEM toolbox [36]. Here, it is clear that the mode at 1.41 eV is predicted by theory and becomes visible only through our deconvolution algorithm. Generally, we observe a very good agreement between the deconvolution results and the simulation data.

7. Comparison of two bottle-shaped (Janus) particles

In the following section, we compare two bottle-shaped particles, each approximately 15 nm in height, one composed of pure gold and the other a Janus particle with a gold top and a platinum bottom. Both particles are depicted in Fig. 6(a) and (b). To determine the elemental composition, we conducted *energy dispersive X-ray spectroscopy* (EDS) on both particles, with the results displayed as insets in the top right corners of (a) and (b).

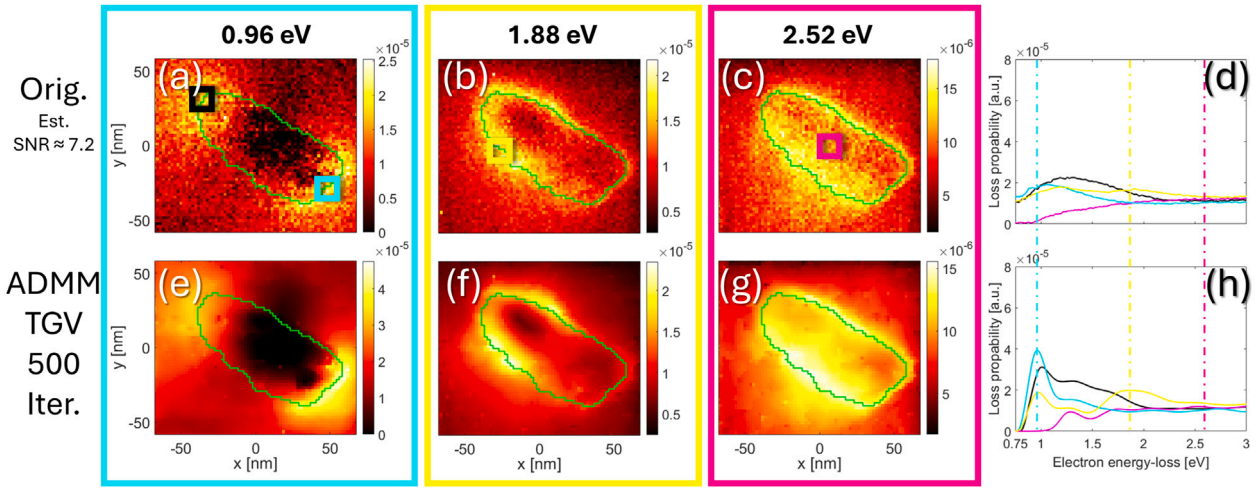

Fig. 8. **(a-c)** Displays the visualization of the normalized EELS map measured for the gold-platinum Janus particle depicted in Fig. 6(b), prior to deconvolution. The estimated signal-to-noise ratio of the ROI is SNR ≈ 7.2. We present three slices that display the spatial distributions of the plasmonic modes at **(a)** 0.96 eV (cyan frame), **(b)** 1.88 eV (yellow frame), and **(c)** 2.52 eV (magenta frame). Each plasmon is linked to a distinct position on the particle, indicated by a colored box in (a-c), while the green line indicates the boundary of the nano-bottle. The average spectra of the boxed regions are displayed in **(d)**, with the positions of 0.96 eV, 1.88 eV, and 2.52 eV marked by dash-dotted lines in the respective colors. The second row **(e-h)** presents the data in the same manner as above, but deconvolved using the proposed ADMM-TGV algorithm after 500 iterations.

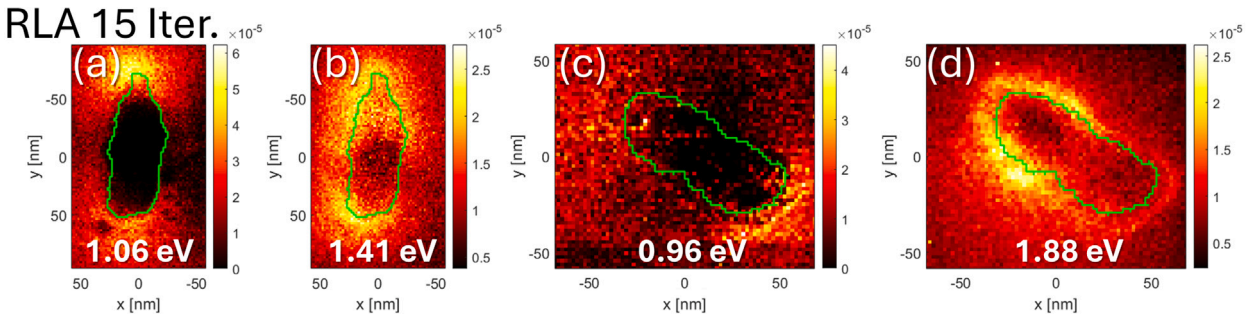

Fig. 9. Intensity normalized results of the RLA deconvolution after 15 iterations for both bottle structures depicted in Fig. 6(a) and (b). The first two images display the energy slices at **(a)** 1.06 eV (compare Fig. 7(e)) and **(b)** 1.44 eV (compare Fig. 7(f)) for the pure gold structure. The energy slices of the gold-platin Janus particle are displayed in next two images at **(c)** 0.96 eV (compare Fig. 8(e)) and at **(d)** 1.88 eV (compare Fig. 8(f)).

The bottle-shape was created using *double-angle resolved NSL* [65], a technique that enables the 'drawing' of particles by tilting the sample relative to the material flux during EBPVD. As a result, the projection of the aperture moves across the sample, depositing material along its path, which is determined by the tilting and azimuthal angles. Both samples were fabricated on a 1 nm thick chromium adhesion layer. Using our ray-tracing algorithm [65], we simulated a bottle particle, which is depicted in Fig. 6(c) and (d) in top and side views. We measured the EELS map again with a dispersion of 0.01 eV/channel and performed simulations using the MNPBEM toolbox [36] for the particle in Fig. 6(c), in order to verify the deconvolution results. To ensure comparability, we also blurred and deconvolved the simulation data.

Fig. 7 presents EELS data for the gold bottle shown in Fig. 6(a). We present the original normalized EELS data in the first row (Fig. 7(a-d)) and the deconvolved data in the second row (Fig. 7(e-h)). The third row (Fig. 7(i-l)) displays the simulation results. Three energy slices were selected at 1.06 eV, 1.41 eV, and 1.80 eV, and the corresponding spectra are presented in (d) with the positions marked in (a-c) using the respective colors. Similarly, the energy positions of slices are indicated by dash-dotted lines in (d).

Upon comparing the original data (a-c) with the deconvolved data (e-h), it becomes apparent that without deconvolution, the intermediate mode at 1.41 eV, featuring three maxima, would have remained undetected. This mode is also present in the simulation data (Fig. 7(i)). All three modes observed through deconvolution exhibit good agreement with the simulation data.

Fig. 8 displays EELS data for the gold-platinum Janus bottle depicted in Fig. 6(b). Analogous to Fig. 7, the original normalized EELS data are presented in the first row (Fig. 8(a-d)), and the deconvolved data are presented in the second row (Fig. 8(e-h)).

Unfortunately, the MNPBEM toolbox [36] is incapable of performing corresponding simulations, as it yields negative loss probabilities in the overlap region of the simulated gold and platinum layers of the Janus particle. Consequently, we omit these simulations and do not include them in this paper. Fig. 8(a-c) presents three energy slices at 0.96 eV, 1.88 eV, and 2.52 eV, with the corresponding spectra of the boxed regions displayed in (d).

Upon comparing the energy slices of the Janus particle (Fig. 8(e-g)) with the corresponding data for the pure gold particle (Fig. 7(e-g)), it becomes apparent that, despite a small energy shift, the first tip mode is nearly identical for both structures.

However, the three-maxima mode of the pure gold particle (Fig. 7(f)) at 1.41 eV, is notably absent in the Janus particle. The mode is expected to be located at the interface between the two materials. We hypothesize that scattering of the plasmons at the interface is the primary reason for the mode's absence. Notably, we observe an edge mode for both particles at approximately 1.80 – 1.90 eV. This mode completely extends across

Table 1
Computation times of the deconvolution results of Figs. 5, 7 and 8 employing the ADMM-TGV algorithm with 500 iterations compared to employing the RLA with 1 iterations. The deconvolutions were calculated using a i9-10900X CPU and a Quadro RTX 4000 GPU for both single and double precision values in MATLAB. For the ADMM-TGV, 500 iterations were used as proposed in Section 5, for the RLA 15 iterations were used, as proposed by [15]. The size of the data is indicated as $X \times Y \times (M + P)$ voxels, where X and Y refer to the lateral dimension of the EELS maps, and $M + P$ refer to the energy direction, padding (see Section 3.3) included.

		Fig. 5 $100 \times 100 \times 2204$ voxels		Fig. 7 $100 \times 60 \times 2182$ voxels		Fig. 8 $60 \times 70 \times 2164$ voxels	
		ADMM-TGV 500 Iter.	RLA 15 Iter.	ADMM-TGV 500 Iter.	RLA 15 Iter.	ADMM-TGV 500 Iter.	RLA 15. Iter
CPU	single	4211 s	17 s	2559 s	8 s	1694 s	6 s
	double	5432 s	20 s	3351 s	10 s	2265 s	8 s
GPU	single	2444 s	2 s	1476 s	1 s	905 s	1 s
	double	5043 s	7 s	2561 s	4 s	1548	2 s

both sides of the gold nano-bottle (Fig. 7(f)), whereas for the Janus particle, we find the edge mode to be confined to the gold part at a higher energy (2.52 eV). However, at higher energies, we observe the side-mode of the Janus bottle extending to the platinum part.

It becomes readily apparent that without considering the deconvolution results from our ADMM-TGV deconvolution algorithm in the second rows of Figs. 7 and 8, this analysis would not have been feasible at our energy resolution (ZLP with FWHM $\approx 0.4 - 0.45$ eV), as the different modes were not clearly resolvable.

To demonstrate that these results are not attainable using standard RLA deconvolution, we deconvolved both nano-bottle datasets with the RLA, employing 15 iterations and normalized them with respect to the total intensity of the individual spectra. The results are presented in Fig. 9(a-c). Despite the disparity in the noise levels between the results, it is readily apparent that the modes of the gold bottle at 1.41 eV (compare Fig. 9(b) and Fig. 7(f)) and the mode of the gold-platinum Janus bottle at 0.96 eV (compare Fig. 9(c) and Fig. 8(e)) are not resolvable using the RLA, but rather only with the proposed ADMM-TGV algorithm. This example effectively illustrates the advantages of utilizing our algorithm over the RLA.

In light of the success of this method, we believe it is essential to share our novel algorithm for EELS deconvolution. It may be anticipated that ADMM-TGV will also enable to resolve finer features in future EELS data recorded at much improved energy resolution.

8. Speed comparison of the ADMM-TGV with the RLA

To get an impression on how long the novel ADMM-TGV deconvolution algorithm takes to iterate compared to the commonly employed RLA, the computation times that were used to calculate Fig. 5, Figs. 7 and 8 with the ADMM-TGV algorithm and the computation times for the RLA results, respectively, are provided Table 1. The computations were performed on a i9-10900X CPU and a Quadro RTX 4000 GPU for both algorithms. While we employ 500 iterations for the ADMM-TGV algorithm, as we have proposed in this paper, we employ only 15 iterations for the RLA algorithm, as proposed by [15] to avoid divergence.

It is rather obvious, given the complexity of the proposed ADMM-TGV algorithm that it takes much more time to compute (in the order of 1 h) with respect to the rather simple RLA algorithm from Eq. (21) (in the order of seconds). However, the success of the ADMM-TGV algorithm relative to the RLA, as demonstrated in the previous sections, may outweigh the time increase in deconvolution time.

The above cited figures provide applied examples from measuring plasmonic nanostructures. To resolve them sufficiently, EELS maps with a side-length of 50–100 spectra are necessary. Acquiring larger maps in EELS often comes with significant disadvantages such as increased energy drifts, beam instabilities, and contamination during beam exposure of the specimen due to the increase in acquisition time and are therefore difficult to perform. The reader might also wonder, why the length of the spectra varies from the usually encountered 2048 channels. This is because ZLP-realignment shifts the spectra with respect to each other, resulting in a protrusion at the edges. These must be cut off. The additional channels are then a result of the padding-procedure described in Section 3.3. Hence, these examples provide a good impression on how long deconvolution with our algorithm may take. Given that both GPU and CPU components are already more than 5 years on the market, more recent configurations may provide a significant boost in computation time.

We recommend using a GPU for the calculations due to their known benefits for matrix-heavy computations. Since the Quadro RTX 4000 GPU only comes with 4 GB of VRAM, the computations could not fully be performed on the GPU but required frequent transfer of data from CPU to GPU, vise versa, which takes a considerable about of time for each transfer. These transfers are clearly viewed as a bottleneck of our employed setup. Therefore, we expect much faster computations, if a GPU with more VRAM is utilized for the computations. Nevertheless, we consider computation times of up to one hour as absolutely tolerable, especially given the huge increase in data quality.

Eventually, we could not find any visible difference between using single precision values over using double precision values for the calculation in MATLAB. Since the computations with the latter are much slower, we recommend the readers of this paper the usage of single precision values.

9. Conclusions

In this work, we propose a novel algorithm for the deconvolution of intensity normalized EELS maps. The algorithm is based on a Lagrangian function and is solved using the alternating direction method of multipliers (ADMM). One of the key advantages of this approach is that it is more versatile and adaptable than the Richardson–Lucy algorithm (RLA), which is commonly used for the deconvolution of EELS data.

Since ADMM represents a novel approach to EELS deconvolution, the fundamental principles of the algorithm are outlined in this paper. The algorithm typically requires user-defined parameters, which influence its convergence properties. To eliminate dependence on initial parameter selection, we exploit the mathematical properties of the algorithm, enabling automatic parameter choice. This is achieved through residual balancing, which was derived and demonstrated in [49].

By leveraging the versatility of the Lagrangian function, we implemented a mixed Gaussian-Poisson distribution for the Bayesian log-likelihood data fidelity term. This likelihood is based on a noise model that accounts for the original data as captured by the microscope. The accuracy of this noise model has been validated in [6,7], where it is shown how to determine the relevant noise parameters for the EELS detector. These noise

parameters are then used to fine-tune the proposed algorithm for our specific detector. Additionally, we discuss how correlations affect the data fidelity functional, binding the deconvolution result to the measured data.

Using prior knowledge, we extend the classical likelihood approach to a maximum a-posteriori (MAP) framework. To prevent the algorithm from producing negative results for the deconvolved EEL probabilities, we introduce a non-negativity prior. Since loss probabilities in EELS are inherently non-negative, this constraint is particularly useful. Additionally, we incorporate the total generalized variation (TGV) approach as a smoothness prior, which helps reduce noise in the deconvolution results. Plasmons exhibit smooth and continuous behavior to some extend, while noise is typically rough and highly volatile. This distinction allows us to effectively discriminate between noise and signal. The TGV method employs adaptive filter masks, based on derivatives, to optimally denoise both flat and sloped regions of the data.

The TGV approach also requires manually set parameters. However, we have demonstrated how to select these parameters based on the noise characteristics of the detector, ensuring that the parameter choice remains objective.

Deconvolution generally requires some data preparation to achieve optimal results, such as the padding to address circular boundaries or the subtraction of the zero-loss peak (ZLP) to avoid ringing artifacts. These preprocessing steps are explained in detail in this work.

To demonstrate the advantages of the proposed algorithm compared to the RLA, we tested both on simulated EELS data generated using the MNPBEM toolbox [36]. The key advantage of using simulation data is that the ground truth is known. The simulation data were then convolved with a detector point spread function and a Gaussian energy distribution of the electron beam. To make the data as realistic as possible, noise was superimposed according to our noise model and the noise parameters of our detector. As a result, the simulated noisy dataset closely resembles EELS data as measured on a real detector, but in contrast to real EELS data, the ground truth is known. The noisy datasets were then deconvolved using both ADMM-TGV and RLA methods.

Using the mean squared error (MSE) between the ground truth and the deconvolution results, we demonstrate that the proposed ADMM-TGV algorithm outperforms the RLA by 60% in terms of its proximity to the original data. Most notably, we show that the proposed algorithm converges, whereas the RLA tends to diverge after an unspecified number of iterations – which is why the RLA is often terminated after 15 iterations.

However, the deconvolution results of both methods reveal fewer features than the original ground truth. We attribute this discrepancy to the attenuation of high frequencies in Fourier space caused by convolution, as well as the presence of a noise background that obscures these frequencies, making them unrecoverable. According to the Nyquist-Shannon theorem, this leads to the observed loss of small features. Consequently, we conclude that the effectiveness of deconvolution is fundamentally limited. This underscores the importance of optimizing beam parameters and alignments to minimize the ZLP for the best EELS results.

Note that the limitations imposed by the Nyquist-Shannon theorem do also apply to algorithms employing artificial intelligence (AI) or machine learning (ML), at least if these algorithms shall suffice basic scientific standards. This means that results must be deduced from the measured data itself and not be subject to algorithms interpreting features into the data that are below significance. Since the proposed algorithm employs a deterministic and purely mathematical approach, it may therefore also serve to cross-check results of such AI or ML algorithms in order to train them to fulfill these standards.

To underscore the success of our approach, we have demonstrated the applicability of the proposed ADMM-TGV algorithm to real data by comparing it with corresponding simulations. Given the strong agreement between the deconvolution results and the simulated data, this comparison supports the validity of the deconvolution results. This shows that our algorithm is not only effective with artificially created simulation data but also significantly improves real measurements.

To further highlight the advantage of the proposed algorithm, we present an example where the ADMM-TGV method enables to distinguish additional plasmonic modes, which were previously obscured in the original data and could not be recovered using the RLA. These plasmonic modes were further validated by simulations, confirming their existence.

In summary, we have mathematically derived an algorithm for the deconvolution of EELS maps and demonstrated its advantages over the commonly used Richardson–Lucy algorithm. The proposed algorithm significantly enhances real data at the cost of a much increased computation time relative to the RLA. The computation time to achieve convergence of the ADMM-TGV deconvolution algorithm proposed in this paper is in the order of 1 h for regular EELS map measurements using regular desktop computers.

Importantly, recognizing that the implementation may be complex for users without prior experience with ADMM, we provide the ADMM-TGV algorithm as a MATLAB script in the supplementary materials, making it accessible for all users.

CRediT authorship contribution statement

Christian Zietlow: Writing – original draft, Visualization, Methodology, Investigation, Formal analysis, Data curation, Conceptualization. **Jörg K.N. Lindner:** Writing – review & editing, Validation, Supervision, Resources, Project administration, Conceptualization.

Declaration of competing interest

The authors declare that they have no known competing financial interests or personal relationships that could have appeared to influence the work reported in this paper.

Appendix A. Supplementary data

Additional information about the algorithm and the evaluation is found in the supplementary materials.
Supplementary material related to this article can be found online at https://doi.org/10.1016/j.ultramic.2025.114159.

Data availability

The deconvolution algorithm is attached to the supplementary materials and is also provided as a MATLAB script. Experimental and simulation data is availlable upon request.

References

[1] Rüdiger R. Meyer, Angus Kirkland, The effects of electron and photon scattering on signal and noise transfer properties of scintillators in CCD cameras used for electron detection, Ultramicroscopy 75 (1) (1998) 23–33.
[2] Ryo Ishikawa, Andrew R. Lupini, Scott D. Findlay, Stephen J. Pennycook, Quantitative annular dark field electron microscopy using single electron signals, Microsc. Microanal. : Off. J. Microsc. Soc. Am. Microbeam Anal. Soc. Microsc. Soc. Can. 20 (1) (2014) 99–110.
[3] Mitsutaka Haruta, Yoshifumi Fujiyoshi, Takashi Nemoto, Akimitsu Ishizuka, Kazuo Ishizuka, Hiroki Kurata, Low count detection for EELS spectrum by reducing CCD read-out noise, Microsc. Microanal. : Off. J. Microsc. Soc. Am. Microbeam Anal. Soc. Microsc. Soc. Can. 26 (S2) (2020) 1202–1204.
[4] Hayato Ikoma, Michael Broxton, Takamasa Kudo, Gordon Wetzstein, A convex 3D deconvolution algorithm for low photon count fluorescence imaging, Sci. Rep. 8 (1) (2018) 11489.
[5] J. Verbeeck, G. Bertoni, Model-based quantification of EELS spectra: treating the effect of correlated noise, Ultramicroscopy 108 (2) (2008) 74–83.
[6] Christian Zietlow, Jörg K.N. Lindner, An applied noise model for scintillation-based CCD detectors in transmission electron microscopy, Sci. Rep. 15 (1) (2025) 3815.
[7] Christian Zietlow, Jörg K.N. Lindner, An applied noise model for low-loss EELS maps, Ultramicroscopy 270 (2025) 114101.
[8] J. Verbeeck, G. Bertoni, Deconvolution of core electron energy loss spectra, Ultramicroscopy 109 (11) (2009) 1343–1352.
[9] Feng Wang, Ray Egerton, Marek Malac, Fourier-ratio deconvolution techniques for electron energy-loss spectroscopy (EELS), Ultramicroscopy 109 (10) (2009) 1245–1249.
[10] Norbert Wiener, Generalized harmonic analysis, Acta Math. 55 (1930) 117–258.
[11] Kazuo Ishizuka, Koji Kimoto, Yoshio Bando, Improving energy resolution of EELS spectra by deconvolution using maximum-entropy and Richardson–Lucy algorithms, Microsc. Microanal. 9 (S02) (2003) 832–833.
[12] M.H.F. Overwijk, D. Reefman, Maximum-entropy deconvolution applied to electron energy-loss spectroscopy, Micron (Oxf. Engl. : 1993) 31 (4) (2000) 325–331.
[13] William Hadley Richardson, Bayesian-based iterative method of image restoration*, J. Opt. Soc. Am. 62 (1) (1972) 55.
[14] L.B. Lucy, An iterative technique for the rectification of observed distributions, Astron. J. 79 (1974) 745.
[15] R.F. Egerton, F. Wang, M. Malac, M.S. Moreno, F. Hofer, Fourier-ratio deconvolution and its Bayesian equivalent, Micron (Oxf. Engl. : 1993) 39 (6) (2008) 642–647.
[16] S. Lazar, G.A. Botton, H.W. Zandbergen, Enhancement of resolution in core-loss and low-loss spectroscopy in a monochromated microscope, Ultramicroscopy 106 (11–12) (2006) 1091–1103.
[17] Edson P. Bellido, David Rossouw, Gianluigi A. Botton, Toward 10 meV electron energy-loss spectroscopy resolution for plasmonics, Microsc. Microanal. 20 (3) (2014) 767–778.
[18] Yiming Liu, Spozmai Panezai, Yutong Wang, Sjoerd Stallinga, Noise amplification and ill-convergence of Richardson–Lucy deconvolution, Nat. Commun. 16 (1) (2025) 911.
[19] Nicolas Dey, Laure Blanc-Feraud, Christophe Zimmer, Pascal Roux, Zvi Kam, Jean-Christophe Olivo-Marin, Josiane Zerubia, Richardson–Lucy algorithm with total variation regularization for 3D confocal microscope deconvolution, Microsc. Res. Tech. 69 (4) (2006) 260–266.
[20] S. Heinz, I. Jung, C. Stegmann, Systematic studies of the Richardson–Lucy deconvolution algorithm applied to VHE gamma data, Astropart. Phys. 36 (1) (2012) 146–150.
[21] Mariana S.C. Almeida, Mario Figueiredo, Deconvolving images with unknown boundaries using the alternating direction method of multipliers, IEEE Trans. Image Process. : A Publ. the IEEE Signal Process. Soc. 22 (8) (2013) 3074–3086.
[22] Ali Mosleh, J.M. Pierre Langlois, Paul Green, Image deconvolution ringing artifact detection and removal via PSF frequency analysis, in: David Fleet, Tomas Pajdla, Bernt Schiele, Tinne Tuytelaars (Eds.), Computer Vision – ECCV 2014, in: Lecture Notes in Computer Science, Vol. 8692, Springer International Publishing, Cham, 2014, pp. 247–262.
[23] R.F. Egerton, H. Qian, M. Malac, Improving the energy resolution of X-ray and electron energy-loss spectra, Micron (Oxf. Engl. : 1993) 37 (4) (2006) 310–315.
[24] Veerendra C. Angadi, Thomas Walther, Influence of background subtraction and deconvolution on calculation of EELS core–loss intensities, in: European Microscopy Congress 2016: Proceedings, Wiley, 2016, pp. 891–892.
[25] Nicolas Brodusch, Karim Zaghib, Raynald Gauvin, Improvement of the energy resolution of energy dispersive spectrometers (EDS) using Richardson–Lucy deconvolution, Ultramicroscopy 209 (2020) 112886.
[26] Florian Knoll, Kristian Bredies, Thomas Pock, Rudolf Stollberger, Second order total generalized variation (TGV) for MRI, Magn. Reson. Med. 65 (2) (2011) 480–491.
[27] Itthi Chatnuntawech, Adrian Martin, Berkin Bilgic, Kawin Setsompop, Elfar Adalsteinsson, Emanuele Schiavi, Vectorial total generalized variation for accelerated multi-channel multi-contrast MRI, Magn. Reson. Imaging 34 (8) (2016) 1161–1170.
[28] Bo Zhou, Yu-Fei Yang, A coupling model and ADMM algorithm based on TGV and shearlet regularization term for MRI reconstruction, Comput. Appl. Math. 40 (3) (2021).
[29] Yi Zhang, Yuling Wang, Mingrui Wang, Yuduo Guo, Xinyang Li, Yifan Chen, Zhi Lu, Jiamin Wu, Xiangyang Ji, Qionghai Dai, Multi-focus light-field microscopy for high-speed large-volume imaging, PhotoniX 3 (1) (2022).
[30] Yueshu Xu, Yile Sun, Hanmeng Wu, Wen Cao, Ling Bai, Siwei Tao, Zonghan Tian, Yudong Cui, Xiang Hao, Cuifang Kuang, Xu Liu, Regularized deconvolution for structured illumination microscopy via accelerated linearized ADMM, Opt. Laser Technol. 169 (2024) 110119.
[31] Toby Sanders, Anne Gelb, Rodrigo B. Platte, Ilke Arslan, Kai Landskron, Recovering fine details from under-resolved electron tomography data using higher order total variation $\ell 1$ regularization, Ultramicroscopy 174 (2017) 97–105.
[32] Daniel Nicholls, Jack Wells, Andrew Stevens, Yalin Zheng, Jony Castagna, Nigel D. Browning, Sub-sampled imaging for STEM: Maximising image speed, resolution and precision through reconstruction parameter refinement, Ultramicroscopy 233 (2022) 113451.
[33] Stephen Boyd, Distributed optimization and statistical learning via the alternating direction method of multipliers, Found. Trends®Mach. Learn. 3 (1) (2010) 1–122.
[34] Leonid I. Rudin, Stanley Osher, Emad Fatemi, Nonlinear total variation based noise removal algorithms, Phys. D: Nonlinear Phenom. 60 (1–4) (1992) 259–268.
[35] Kristian Bredies, Karl Kunisch, Thomas Pock, Total generalized variation, SIAM J. Imaging Sci. 3 (3) (2010) 492–526.
[36] Ulrich Hohenester, Andreas Trügler, MNPBEM – a Matlab toolbox for the simulation of plasmonic nanoparticles, Comput. Phys. Comm. 183 (2) (2012) 370–381.
[37] Lingli Kong, Zhengran Ji, Huolin L. Xin, Electron energy loss spectroscopy database synthesis and automation of core-loss edge recognition by deep-learning neural networks, Sci. Rep. 12 (1) (2022) 22183.
[38] Etienne Monier, Thomas Oberlin, Nathalie Brun, Marcel Tence, Marta de Frutos, Nicolas Dobigeon, Reconstruction of partially sampled multiband images—application to STEM-EELS imaging, IEEE Trans. Comput. Imaging 4 (4) (2018) 585–598.
[39] Sirong Lu, Kristy J. Kormondy, Alexander A. Demkov, David J. Smith, An EELS signal-from-background separation algorithm for spectral line-scan/image quantification, Ultramicroscopy 195 (2018) 25–31.
[40] Sheldon M. Ross, Introduction To Probability Models, thirteenth ed., Academic Press, San Diego, CA and London, 2024.
[41] Don S. Lemons, An Introduction To Stochastic Processes in Physics, Johns Hopkins University Press, Baltimore, Md. and London, 2002.
[42] Philippe Réfrégier, Noise Theory and Application To Physics: From Fluctuations To Information, Advanced Texts in Physics, Springer, New York, NY, 2004.
[43] Achim Klenke, Probability Theory: A Comprehensive Course, second ed., Springer, London, 2013.
[44] K. Pearson, Galton Laboratory for National Eugenics, Note on regression and inheritance in the case of two parents, in: Proceedings of the Royal Society, Royal Society, 1895.
[45] M. Rabbani, R. Shaw, R. van Metter, Detective quantum efficiency of imaging systems with amplifying and scattering mechanisms, J. Opt. Soc. Am. A, Opt. Image Sci. 4 (5) (1987) 895–901.
[46] GMS 3 Documentation: Spectrum Imaging Base, Gatan Inc., 2016, Number Rev 3.3.2.2403.
[47] Isabelle Jouanny, Valérie Demange, Jaafar Ghanbaja, Elisabeth Bauer-Grosse, Structural characterization of Fe–C coatings prepared by reactive triode-magnetron sputtering, J. Mater. Res. 25 (9) (2010) 1859–1869.
[48] Megan E. Holtz, Yingchao Yu, Jie Gao, Héctor D. Abruña, David A. Muller, In situ electron energy-loss spectroscopy in liquids, Microsc. Microanal. 19 (4) (2013) 1027–1035.
[49] Christian Zietlow, Jörg K.N. Lindner, ADMM-TGV image restoration for scientific applications with unbiased parameter choice, Numer. Algorithms 97 (4) (2024) 1481–1512.
[50] M. Bertero, P. Boccacci, A simple method for the reduction of boundary effects in the Richardson–Lucy approach to image deconvolution, Astron. Astrophys. 437 (1) (2005) 369–374.
[51] Nikhilesh Bhagat, Daniel Valencia, Amirhossein Alimohammad, Fred Harris, High–throughput and compact FFT architectures using the Good–Thomas and Winograd algorithms, IET Commun. 12 (8) (2018) 1011–1018.
[52] Mário A.T. Figueiredo, On the use of ADMM for imaging inverse problems: the pros and cons of matrix inversions, in: Michael Hintermüller, José Francisco Rodrigues (Eds.), Topics in Applied Analysis and Optimisation, in: CIM Series in Mathematical Sciences, Springer International Publishing, Cham, 2019, pp. 159–181.

[53] Stanley H. Chan, Xiran Wang, Omar A. Elgendy, Plug-and-play ADMM for image restoration: Fixed-point convergence and applications, IEEE Trans. Comput. Imaging 3 (1) (2017) 84–98.
[54] Wei-Si Xie, Yu-Fei Yang, Bo Zhou, An ADMM algorithm for second-order TV-based MR image reconstruction, Numer. Algorithms 67 (4) (2014) 827–843.
[55] Harold W. Kuhn, Albert W. Tucker, Nonlinear programming, in: Giorgio Giorgi, Tinne Hoff Kjeldsen (Eds.), Traces and Emergence of Nonlinear Programming, Springer Basel, Basel, 2014, pp. 247–258.
[56] Brendt Wohlberg, ADMM penalty parameter selection by residual balancing.
[57] Thomas Bayes, LII. an essay towards solving a problem in the doctrine of chances. by the late Rev. Mr. Bayes, F.R.S. communicated by Mr. Price, in a letter to John Canton, A.M.F.R.S., Philos. Trans. R. Soc. Lond. 53 (1763) 370–418.
[58] Karen Egiazarian, Patrizio Campisi, Blind Image Deconvolution: Theory and Applications, CRC Press, Boca Raton, 2007.
[59] Manu Ghulyani, Muthuvel Arigovindan, Fast roughness minimizing image restoration under mixed Poisson-Gaussian noise, IEEE Trans. Image Process. : A Publ. the IEEE Signal Process. Soc. 30 (2021) 134–149.
[60] Qiaoqiao Ding, Yong Long, Xiaoqun Zhang, Jeffrey A. Fessler, Statistical image reconstruction using mixed Poisson-Gaussian noise model for X-ray CT.
[61] Neal Parikh, Proximal algorithms, Found. Trends® Optim. 1 (3) (2014) 127–239.
[62] Keiichiro Shirai, Masahiro Okuda, FFT based solution for multivariable L2 equations using KKT system via FFT and efficient pixel-wise inverse calculation, in: 2014 IEEE International Conference on Acoustics, Speech and Signal Processing, ICASSP, IEEE, 2014, pp. 2629–2633.
[63] Christy L. Haynes, Richard P. van Duyne, Nanosphere lithography: A versatile nanofabrication tool for studies of size-dependent nanoparticle optics, J. Phys. Chem. B 105 (24) (2001) 5599–5611.
[64] Pierre Colson, Catherine Henrist, Rudi Cloots, Nanosphere lithography: A powerful method for the controlled manufacturing of nanomaterials, J. Nanomater. 2013 (1) (2013).
[65] Christoph Brodehl, Siegmund Greulich-Weber, Jörg K.N. Lindner, An algorithm for tailoring of nanoparticles by double angle resolved nanosphere lithography, in: MRS Proceedings, 2015, p. 1748.
[66] C.E. Shannon, Communication in the presence of noise, Proc. the IRE 37 (1) (1949) 10–21.
[67] H. Nyquist, Certain topics in telegraph transmission theory, Trans. Am. Inst. Electr. Eng. 47 (2) (1928) 617–644.
[68] A. Gloter, A. Douiri, M. Tencé, C. Colliex, Improving energy resolution of EELS spectra: an alternative to the monochromator solution, Ultramicroscopy 96 (3–4) (2003) 385–400.
[69] Tahir Iqbal Awan, Almas Bashir, Aqsa Tehseen, Chemistry of Nanomaterials: Fundamentals and Applications, Elsevier, Amsterdam and Kidlington, Oxford and Cambridge, MA, 2020.
[70] Christoph Brodehl, Siegmund Greulich-Weber, Jörg K.N. Lindner, Fabrication of tailored nanoantennas on large areas for plasmonic devices, Mater. Today: Proc. 4 (2017) S44–S51.
[71] Hongta Yang, Peng Jiang, Large-scale colloidal self-assembly by doctor blade coating, Langmuir : ACS J. Surfaces Colloids 26 (16) (2010) 13173–13182.
[72] Thomas Riedl, Jörg K.N. Lindner, Automated SEM image analysis of the sphere diameter, sphere-sphere separation, and opening size distributions of nanosphere lithography masks, Microsc. Microanal. 28 (1) (2022) 185–195.
[73] Werner Stöber, Arthur Fink, Ernst Bohn, Controlled growth of monodisperse silica spheres in the micron size range, J. Colloid Interface Sci. 26 (1) (1968) 62–69.
[74] Dirk L.J. Vossen, Joan J. Penninkhof, Alfons van Blaaderen, Chemical modification of colloidal masks for nanolithography, Langmuir : ACS J. Surfaces Colloids 24 (11) (2008) 5967–5969.

Supplementary materials – An unbiased ADMM-TGV algorithm for the deconvolution of STEM-EELS maps

Christian Zietlow[a], Jörg K. N. Lindner[a]

[a]*Nanopatterning-Nanoanalysis-Photonic Materials Group, Department of Physics, Paderborn University, Warburgerstr. 100, Paderborn, 33098, Germany*

A. On the derivatives $\mathbf{D}_{h,v,s}$ and the kernel $\mathbf{\Omega}$

The finite difference operators can be applied to the data via convolution. The corresponding matrices are given as $\mathbf{D}_h$, $\mathbf{D}_v$ and $\mathbf{D}_s$. Since 3D matrices are complicated to provide on a paper sheet, we will provide the 2D matrices corresponding to $\mathbf{D}_h$ and $\mathbf{D}_v$, from which the reader can easily deduce the corresponding 3D matrices by expanding zeros into the third dimension:

$$\mathbf{D}_h = \begin{pmatrix} 1 & -1 & 0 & \dots & 0 \\ 0 & 0 & 0 & \dots & 0 \\ 0 & 0 & 0 & \dots & 0 \\ \vdots & \vdots & \vdots & \ddots & \vdots \\ 0 & 0 & 0 & \dots & 0 \end{pmatrix} \quad , \quad \mathbf{D}_v = \begin{pmatrix} 1 & 0 & 0 & \dots & 0 \\ -1 & 0 & 0 & \dots & 0 \\ 0 & 0 & 0 & \dots & 0 \\ \vdots & \vdots & \vdots & \ddots & \vdots \\ 0 & 0 & 0 & \dots & 0 \end{pmatrix} \quad . \tag{1}$$

For a data cube with $X \times Y \times (M + P)$ data points, each derivative is represented by a matrix of the size of the data cube, i.e. $\left\{\mathbf{D}_h, \mathbf{D}_v, \mathbf{D}_s, \mathbb{0}\right\} \in \mathbb{R}^{X \times Y \times (M+P)}$.
While the above examples correspond to the forward difference operators $\mathbf{D}_h$, $\mathbf{D}_v$ and $\mathbf{D}_s$, the corresponding adjoint operators $\mathbf{D}_h^T$, $\mathbf{D}_v^T$ and $\mathbf{D}_s^T$ provide the backward difference operators with the same dimension:

$$\mathbf{D}_h^T = \begin{pmatrix} 1 & 0 & 0 & \dots & -1 \\ 0 & 0 & 0 & \dots & 0 \\ 0 & 0 & 0 & \dots & 0 \\ \vdots & \vdots & \vdots & \ddots & \vdots \\ 0 & 0 & 0 & \dots & 0 \end{pmatrix} \quad , \quad \mathbf{D}_v^T = \begin{pmatrix} 1 & 0 & 0 & \dots & 0 \\ 0 & 0 & 0 & \dots & 0 \\ 0 & 0 & 0 & \dots & 0 \\ \vdots & \vdots & \vdots & \ddots & \vdots \\ -1 & 0 & 0 & \dots & 0 \end{pmatrix} \quad , \tag{2}$$

and can easily be calculated from the forward operators by using the complex conjugate in Fourier space and then re-transforming, i.e.:

$$\mathbf{D}_h^T = \mathcal{F}^{-1}\left[\mathrm{conj}\left(\mathcal{F}\left[\mathbf{D}_h\right]\right)\right] \quad . \tag{3}$$

Accordingly, the adjoint convolution kernel $\mathbf{\Omega}^T$ is also defined as the complex conjugate of the convolution kernel $\mathbf{\Omega}$ in Fourier space. Therefore, the adjoint operators can be seen as mirrored variants of the original operators.

Further information about the implementation can be appreciated from the MATLAB algorithm appended to this document.

*Corresponding author
christian.zietlow@upb.de (C. Zietlow); lindner@physik.upb.de (J.K.N. Lindner)
https://physik.uni-paderborn.de/en/lindner (J.K.N. Lindner)
ORCID(s): 0000-0001-9696-619X (C. Zietlow); 0000-0003-2367-9610 (J.K.N. Lindner)

B. On the $\{\mathbf{x}, \mathbf{t}\}$-update

To solve the $\{\mathbf{x}, \mathbf{t}\}$-update, we require the inverse $\tilde{\mathbf{P}}$ from Eq. 83 and Eq. 84 of the main paper. The adjugate method enables us to invert the matrix:

$$\tilde{\mathbf{P}}^{-1} = \mathrm{adj}\{\tilde{\mathbf{P}}\}\,\det{}^{-1}\{\tilde{\mathbf{P}}\}\ . \tag{4}$$

The adjugate of $\tilde{\mathbf{P}}$ can be determined by transposing the cofactor matrix $\mathrm{adj}\,\{\tilde{\mathbf{P}}\} = \tilde{\mathbf{C}}^{\mathrm{T}}$, which is given by the matrix of the minor determinants $\tilde{\mathbf{P}}_{\mathrm{i,j}}$:

$$\tilde{\mathbf{C}} = \begin{pmatrix} \det\{\tilde{\mathbf{P}}_{1,1}\} & -\det\{\tilde{\mathbf{P}}_{1,2}\} & \det\{\tilde{\mathbf{P}}_{1,3}\} & -\det\{\tilde{\mathbf{P}}_{1,4}\} \\ -\det\{\tilde{\mathbf{P}}_{2,1}\} & \det\{\tilde{\mathbf{P}}_{2,2}\} & -\det\{\tilde{\mathbf{P}}_{2,3}\} & \det\{\tilde{\mathbf{P}}_{2,4}\} \\ \det\{\tilde{\mathbf{P}}_{3,1}\} & -\det\{\tilde{\mathbf{P}}_{3,2}\} & \det\{\tilde{\mathbf{P}}_{3,3}\} & -\det\{\tilde{\mathbf{P}}_{3,4}\} \\ -\det\{\tilde{\mathbf{P}}_{4,1}\} & \det\{\tilde{\mathbf{P}}_{4,2}\} & -\det\{\tilde{\mathbf{P}}_{4,3}\} & \det\{\tilde{\mathbf{P}}_{4,4}\} \end{pmatrix}, \tag{5}$$

where the transpose is obtained by swapping the indices, such that:

$$\tilde{\mathbf{C}}^{T} = \begin{pmatrix} \det\{\tilde{\mathbf{P}}_{1,1}\} & -\det\{\tilde{\mathbf{P}}_{2,1}\} & \det\{\tilde{\mathbf{P}}_{3,1}\} & -\det\{\tilde{\mathbf{P}}_{4,1}\} \\ -\det\{\tilde{\mathbf{P}}_{1,2}\} & \det\{\tilde{\mathbf{P}}_{2,2}\} & -\det\{\tilde{\mathbf{P}}_{3,2}\} & \det\{\tilde{\mathbf{P}}_{4,2}\} \\ \det\{\tilde{\mathbf{P}}_{1,3}\} & -\det\{\tilde{\mathbf{P}}_{2,3}\} & \det\{\tilde{\mathbf{P}}_{3,3}\} & -\det\{\tilde{\mathbf{P}}_{4,3}\} \\ -\det\{\tilde{\mathbf{P}}_{1,4}\} & \det\{\tilde{\mathbf{P}}_{2,4}\} & -\det\{\tilde{\mathbf{P}}_{3,4}\} & \det\{\tilde{\mathbf{P}}_{4,4}\} \end{pmatrix}. \tag{6}$$

For a $\tilde{\mathbf{P}}_{4\times4}$ matrix representing the DTGV in three dimensions, this yields 16 determinants of 3×3 minors, which are defined as:

$$\det\{\tilde{\mathbf{P}}_{1,1}\} = \begin{vmatrix} \tilde{p}_{2,2} & \tilde{p}_{2,3} & \tilde{p}_{2,4} \\ \tilde{p}_{3,2} & \tilde{p}_{3,3} & \tilde{p}_{3,4} \\ \tilde{p}_{4,2} & \tilde{p}_{4,3} & \tilde{p}_{4,4} \end{vmatrix} = \begin{matrix} +\tilde{p}_{2,2}\,\tilde{p}_{3,3}\,\tilde{p}_{4,4} \\ +\tilde{p}_{2,3}\,\tilde{p}_{3,4}\,\tilde{p}_{4,2} \\ +\tilde{p}_{2,4}\,\tilde{p}_{3,2}\,\tilde{p}_{4,3} \\ -\tilde{p}_{4,2}\,\tilde{p}_{3,3}\,\tilde{p}_{2,4} \\ -\tilde{p}_{4,3}\,\tilde{p}_{3,4}\,\tilde{p}_{2,2} \\ -\tilde{p}_{4,4}\,\tilde{p}_{3,2}\,\tilde{p}_{2,3} \end{matrix}, \quad \det\{\tilde{\mathbf{P}}_{2,1}\} = \begin{vmatrix} \tilde{p}_{1,2} & \tilde{p}_{1,3} & \tilde{p}_{1,4} \\ \tilde{p}_{3,2} & \tilde{p}_{3,3} & \tilde{p}_{3,4} \\ \tilde{p}_{4,2} & \tilde{p}_{3,4} & \tilde{p}_{4,4} \end{vmatrix} = \begin{matrix} +\tilde{p}_{1,2}\,\tilde{p}_{3,3}\,\tilde{p}_{4,4} \\ +\tilde{p}_{1,3}\,\tilde{p}_{3,4}\,\tilde{p}_{4,2} \\ +\tilde{p}_{1,4}\,\tilde{p}_{3,2}\,\tilde{p}_{4,3} \\ -\tilde{p}_{4,2}\,\tilde{p}_{3,3}\,\tilde{p}_{1,4} \\ -\tilde{p}_{4,3}\,\tilde{p}_{3,4}\,\tilde{p}_{1,2} \\ -\tilde{p}_{4,4}\,\tilde{p}_{3,2}\,\tilde{p}_{1,3} \end{matrix},$$

$$\det\{\tilde{\mathbf{P}}_{1,2}\} = \begin{vmatrix} \tilde{p}_{2,1} & \tilde{p}_{2,3} & \tilde{p}_{2,4} \\ \tilde{p}_{3,1} & \tilde{p}_{3,3} & \tilde{p}_{3,4} \\ \tilde{p}_{4,1} & \tilde{p}_{4,3} & \tilde{p}_{4,4} \end{vmatrix} = \begin{matrix} +\tilde{p}_{2,1}\,\tilde{p}_{3,3}\,\tilde{p}_{4,4} \\ +\tilde{p}_{2,3}\,\tilde{p}_{3,4}\,\tilde{p}_{4,1} \\ +\tilde{p}_{2,4}\,\tilde{p}_{3,1}\,\tilde{p}_{4,3} \\ -\tilde{p}_{4,1}\,\tilde{p}_{3,3}\,\tilde{p}_{2,4} \\ -\tilde{p}_{4,3}\,\tilde{p}_{3,4}\,\tilde{p}_{2,1} \\ -\tilde{p}_{4,4}\,\tilde{p}_{3,1}\,\tilde{p}_{2,3} \end{matrix}, \quad \det\{\tilde{\mathbf{P}}_{2,2}\} = \begin{vmatrix} \tilde{p}_{1,1} & \tilde{p}_{1,3} & \tilde{p}_{1,4} \\ \tilde{p}_{3,1} & \tilde{p}_{3,3} & \tilde{p}_{3,4} \\ \tilde{p}_{4,1} & \tilde{p}_{4,3} & \tilde{p}_{4,4} \end{vmatrix} = \begin{matrix} +\tilde{p}_{1,1}\,\tilde{p}_{3,3}\,\tilde{p}_{4,4} \\ +\tilde{p}_{1,3}\,\tilde{p}_{3,4}\,\tilde{p}_{4,1} \\ +\tilde{p}_{1,4}\,\tilde{p}_{3,1}\,\tilde{p}_{4,3} \\ -\tilde{p}_{4,1}\,\tilde{p}_{3,3}\,\tilde{p}_{1,4} \\ -\tilde{p}_{4,3}\,\tilde{p}_{3,4}\,\tilde{p}_{1,1} \\ -\tilde{p}_{4,4}\,\tilde{p}_{3,1}\,\tilde{p}_{1,3} \end{matrix},$$

$$\det\{\tilde{\mathbf{P}}_{1,3}\} = \begin{vmatrix} \tilde{p}_{2,1} & \tilde{p}_{2,2} & \tilde{p}_{2,4} \\ \tilde{p}_{3,1} & \tilde{p}_{3,2} & \tilde{p}_{3,4} \\ \tilde{p}_{4,1} & \tilde{p}_{4,2} & \tilde{p}_{4,4} \end{vmatrix} = \begin{matrix} +\tilde{p}_{2,1}\,\tilde{p}_{3,2}\,\tilde{p}_{4,4} \\ +\tilde{p}_{2,2}\,\tilde{p}_{3,4}\,\tilde{p}_{4,1} \\ +\tilde{p}_{2,4}\,\tilde{p}_{3,1}\,\tilde{p}_{4,2} \\ -\tilde{p}_{4,1}\,\tilde{p}_{3,2}\,\tilde{p}_{2,4} \\ -\tilde{p}_{4,2}\,\tilde{p}_{3,4}\,\tilde{p}_{2,1} \\ -\tilde{p}_{4,4}\,\tilde{p}_{3,1}\,\tilde{p}_{2,2} \end{matrix}, \quad \det\{\tilde{\mathbf{P}}_{2,3}\} = \begin{vmatrix} \tilde{p}_{1,1} & \tilde{p}_{1,2} & \tilde{p}_{1,4} \\ \tilde{p}_{3,1} & \tilde{p}_{3,2} & \tilde{p}_{3,4} \\ \tilde{p}_{4,1} & \tilde{p}_{4,2} & \tilde{p}_{4,4} \end{vmatrix} = \begin{matrix} +\tilde{p}_{1,1}\,\tilde{p}_{3,2}\,\tilde{p}_{4,4} \\ +\tilde{p}_{1,2}\,\tilde{p}_{3,4}\,\tilde{p}_{4,1} \\ +\tilde{p}_{1,4}\,\tilde{p}_{3,1}\,\tilde{p}_{4,2} \\ -\tilde{p}_{4,1}\,\tilde{p}_{3,2}\,\tilde{p}_{1,4} \\ -\tilde{p}_{4,2}\,\tilde{p}_{3,4}\,\tilde{p}_{1,1} \\ -\tilde{p}_{4,4}\,\tilde{p}_{3,1}\,\tilde{p}_{1,2} \end{matrix},$$

$$\det\{\tilde{\mathbf{P}}_{1,4}\} = \begin{vmatrix} \tilde{p}_{2,1} & \tilde{p}_{2,2} & \tilde{p}_{2,3} \\ \tilde{p}_{3,1} & \tilde{p}_{3,2} & \tilde{p}_{3,3} \\ \tilde{p}_{4,1} & \tilde{p}_{4,2} & \tilde{p}_{4,3} \end{vmatrix} = \begin{matrix} +\tilde{p}_{2,1}\,\tilde{p}_{3,2}\,\tilde{p}_{4,3} \\ +\tilde{p}_{2,2}\,\tilde{p}_{3,3}\,\tilde{p}_{4,1} \\ +\tilde{p}_{2,3}\,\tilde{p}_{3,1}\,\tilde{p}_{4,2} \\ -\tilde{p}_{4,1}\,\tilde{p}_{3,2}\,\tilde{p}_{2,3} \\ -\tilde{p}_{4,2}\,\tilde{p}_{3,3}\,\tilde{p}_{2,1} \\ -\tilde{p}_{4,3}\,\tilde{p}_{3,1}\,\tilde{p}_{2,2} \end{matrix}, \quad \det\{\tilde{\mathbf{P}}_{2,4}\} = \begin{vmatrix} \tilde{p}_{1,1} & \tilde{p}_{1,2} & \tilde{p}_{1,3} \\ \tilde{p}_{3,1} & \tilde{p}_{3,2} & \tilde{p}_{3,3} \\ \tilde{p}_{4,1} & \tilde{p}_{4,2} & \tilde{p}_{4,3} \end{vmatrix} = \begin{matrix} +\tilde{p}_{1,1}\,\tilde{p}_{3,2}\,\tilde{p}_{4,3} \\ +\tilde{p}_{1,2}\,\tilde{p}_{3,3}\,\tilde{p}_{4,1} \\ +\tilde{p}_{1,3}\,\tilde{p}_{3,1}\,\tilde{p}_{4,2} \\ -\tilde{p}_{4,1}\,\tilde{p}_{3,2}\,\tilde{p}_{1,3} \\ -\tilde{p}_{4,2}\,\tilde{p}_{3,3}\,\tilde{p}_{1,1} \\ -\tilde{p}_{4,3}\,\tilde{p}_{3,1}\,\tilde{p}_{1,2} \end{matrix}, \tag{7}$$

$$\det\{\tilde{\mathbf{P}}_{3,1}\} = \begin{vmatrix} \tilde{p}_{1,2} & \tilde{p}_{1,3} & \tilde{p}_{1,4} \\ \tilde{p}_{2,2} & \tilde{p}_{2,3} & \tilde{p}_{2,4} \\ \tilde{p}_{4,2} & \tilde{p}_{4,3} & \tilde{p}_{4,4} \end{vmatrix} = \begin{matrix} +\tilde{p}_{1,2}\,\tilde{p}_{2,3}\,\tilde{p}_{4,4} \\ +\tilde{p}_{1,3}\,\tilde{p}_{2,4}\,\tilde{p}_{4,2} \\ +\tilde{p}_{1,4}\,\tilde{p}_{2,2}\,\tilde{p}_{4,3} \\ -\tilde{p}_{4,2}\,\tilde{p}_{2,3}\,\tilde{p}_{1,4} \\ -\tilde{p}_{4,3}\,\tilde{p}_{2,4}\,\tilde{p}_{1,2} \\ -\tilde{p}_{4,4}\,\tilde{p}_{2,2}\,\tilde{p}_{1,3} \end{matrix}, \quad \det\{\tilde{\mathbf{P}}_{4,1}\} = \begin{vmatrix} \tilde{p}_{1,2} & \tilde{p}_{1,3} & \tilde{p}_{1,4} \\ \tilde{p}_{2,2} & \tilde{p}_{2,3} & \tilde{p}_{2,4} \\ \tilde{p}_{3,3} & \tilde{p}_{3,3} & \tilde{p}_{3,4} \end{vmatrix} = \begin{matrix} +\tilde{p}_{1,2}\,\tilde{p}_{2,3}\,\tilde{p}_{3,4} \\ +\tilde{p}_{1,3}\,\tilde{p}_{2,4}\,\tilde{p}_{3,2} \\ +\tilde{p}_{1,4}\,\tilde{p}_{2,2}\,\tilde{p}_{3,3} \\ -\tilde{p}_{3,2}\,\tilde{p}_{2,3}\,\tilde{p}_{1,4} \\ -\tilde{p}_{3,3}\,\tilde{p}_{2,4}\,\tilde{p}_{1,2} \\ -\tilde{p}_{3,4}\,\tilde{p}_{2,2}\,\tilde{p}_{1,3} \end{matrix},$$

$$\det\left\{\tilde{\mathbf{P}}_{3,2}\right\} = \begin{vmatrix} \tilde{p}_{1,1} & \tilde{p}_{1,3} & \tilde{p}_{1,4} \\ \tilde{p}_{2,1} & \tilde{p}_{2,3} & \tilde{p}_{2,4} \\ \tilde{p}_{4,1} & \tilde{p}_{4,3} & \tilde{p}_{4,4} \end{vmatrix} = \begin{matrix} +\tilde{p}_{1,1}\,\tilde{p}_{2,3}\,\tilde{p}_{4,4} \\ +\tilde{p}_{1,3}\,\tilde{p}_{2,4}\,\tilde{p}_{4,1} \\ +\tilde{p}_{1,4}\,\tilde{p}_{2,1}\,\tilde{p}_{4,3} \\ -\tilde{p}_{4,1}\,\tilde{p}_{2,3}\,\tilde{p}_{1,4} \\ -\tilde{p}_{4,3}\,\tilde{p}_{2,4}\,\tilde{p}_{1,1} \\ -\tilde{p}_{4,4}\,\tilde{p}_{2,1}\,\tilde{p}_{1,3} \end{matrix} \quad , \quad \det\left\{\tilde{\mathbf{P}}_{4,2}\right\} = \begin{vmatrix} \tilde{p}_{1,1} & \tilde{p}_{1,3} & \tilde{p}_{1,4} \\ \tilde{p}_{2,1} & \tilde{p}_{2,3} & \tilde{p}_{2,4} \\ \tilde{p}_{3,1} & \tilde{p}_{3,3} & \tilde{p}_{3,4} \end{vmatrix} = \begin{matrix} +\tilde{p}_{1,1}\,\tilde{p}_{2,3}\,\tilde{p}_{3,4} \\ +\tilde{p}_{1,3}\,\tilde{p}_{2,4}\,\tilde{p}_{3,1} \\ +\tilde{p}_{1,4}\,\tilde{p}_{2,1}\,\tilde{p}_{3,3} \\ -\tilde{p}_{3,1}\,\tilde{p}_{2,3}\,\tilde{p}_{1,4} \\ -\tilde{p}_{3,3}\,\tilde{p}_{2,4}\,\tilde{p}_{1,1} \\ -\tilde{p}_{3,4}\,\tilde{p}_{2,1}\,\tilde{p}_{1,3} \end{matrix},$$

$$\det\left\{\tilde{\mathbf{P}}_{3,3}\right\} = \begin{vmatrix} \tilde{p}_{1,1} & \tilde{p}_{1,3} & \tilde{p}_{1,4} \\ \tilde{p}_{2,1} & \tilde{p}_{2,3} & \tilde{p}_{2,4} \\ \tilde{p}_{4,1} & \tilde{p}_{4,3} & \tilde{p}_{4,4} \end{vmatrix} = \begin{matrix} +\tilde{p}_{1,1}\,\tilde{p}_{2,2}\,\tilde{p}_{4,4} \\ +\tilde{p}_{1,2}\,\tilde{p}_{2,4}\,\tilde{p}_{4,1} \\ +\tilde{p}_{1,4}\,\tilde{p}_{2,1}\,\tilde{p}_{4,2} \\ -\tilde{p}_{4,1}\,\tilde{p}_{2,2}\,\tilde{p}_{1,4} \\ -\tilde{p}_{4,2}\,\tilde{p}_{2,4}\,\tilde{p}_{1,1} \\ -\tilde{p}_{4,4}\,\tilde{p}_{2,1}\,\tilde{p}_{1,2} \end{matrix} \quad , \quad \det\left\{\tilde{\mathbf{P}}_{4,3}\right\} = \begin{vmatrix} \tilde{p}_{1,1} & \tilde{p}_{1,2} & \tilde{p}_{1,4} \\ \tilde{p}_{2,1} & \tilde{p}_{2,2} & \tilde{p}_{2,4} \\ \tilde{p}_{3,1} & \tilde{p}_{3,2} & \tilde{p}_{3,4} \end{vmatrix} = \begin{matrix} +\tilde{p}_{1,1}\,\tilde{p}_{2,2}\,\tilde{p}_{3,4} \\ +\tilde{p}_{1,2}\,\tilde{p}_{2,4}\,\tilde{p}_{3,1} \\ +\tilde{p}_{1,4}\,\tilde{p}_{2,1}\,\tilde{p}_{3,2} \\ -\tilde{p}_{3,1}\,\tilde{p}_{2,2}\,\tilde{p}_{1,4} \\ -\tilde{p}_{3,2}\,\tilde{p}_{2,4}\,\tilde{p}_{1,1} \\ -\tilde{p}_{3,4}\,\tilde{p}_{2,1}\,\tilde{p}_{1,2} \end{matrix},$$

$$\det\left\{\tilde{\mathbf{P}}_{3,4}\right\} = \begin{vmatrix} \tilde{p}_{1,1} & \tilde{p}_{1,2} & \tilde{p}_{1,3} \\ \tilde{p}_{2,1} & \tilde{p}_{2,2} & \tilde{p}_{2,3} \\ \tilde{p}_{4,1} & \tilde{p}_{4,2} & \tilde{p}_{4,3} \end{vmatrix} = \begin{matrix} +\tilde{p}_{1,1}\,\tilde{p}_{2,2}\,\tilde{p}_{4,3} \\ +\tilde{p}_{1,2}\,\tilde{p}_{2,3}\,\tilde{p}_{4,1} \\ +\tilde{p}_{1,3}\,\tilde{p}_{2,1}\,\tilde{p}_{4,2} \\ -\tilde{p}_{4,1}\,\tilde{p}_{2,2}\,\tilde{p}_{1,3} \\ -\tilde{p}_{4,2}\,\tilde{p}_{2,3}\,\tilde{p}_{1,1} \\ -\tilde{p}_{4,3}\,\tilde{p}_{2,1}\,\tilde{p}_{1,2} \end{matrix} \quad , \quad \det\left\{\tilde{\mathbf{P}}_{4,4}\right\} = \begin{vmatrix} \tilde{p}_{1,1} & \tilde{p}_{1,2} & \tilde{p}_{1,3} \\ \tilde{p}_{2,1} & \tilde{p}_{2,2} & \tilde{p}_{2,3} \\ \tilde{p}_{3,1} & \tilde{p}_{3,2} & \tilde{p}_{3,3} \end{vmatrix} = \begin{matrix} +\tilde{p}_{1,1}\,\tilde{p}_{2,2}\,\tilde{p}_{3,3} \\ +\tilde{p}_{1,2}\,\tilde{p}_{2,3}\,\tilde{p}_{3,1} \\ +\tilde{p}_{1,3}\,\tilde{p}_{2,1}\,\tilde{p}_{3,2} \\ -\tilde{p}_{3,1}\,\tilde{p}_{2,2}\,\tilde{p}_{1,3} \\ -\tilde{p}_{3,2}\,\tilde{p}_{2,3}\,\tilde{p}_{1,1} \\ -\tilde{p}_{3,3}\,\tilde{p}_{2,1}\,\tilde{p}_{1,2} \end{matrix}.$$

The determinant can be calculated using the Laplace expansion method:

$$\det\left\{\tilde{\mathbf{P}}\right\} = \tilde{p}_{1,1} \cdot \det\left\{\tilde{\mathbf{P}}_{1,1}\right\} - \tilde{p}_{2,1} \cdot \det\left\{\tilde{\mathbf{P}}_{2,1}\right\} + \tilde{p}_{3,1} \cdot \det\left\{\tilde{\mathbf{P}}_{3,1}\right\} - \tilde{p}_{4,1} \cdot \det\left\{\tilde{\mathbf{P}}_{4,1}\right\} \ . \tag{8}$$

Having obtained both $\mathrm{adj}\left\{\tilde{\mathbf{P}}\right\}$ and $\det\left\{\tilde{\mathbf{P}}\right\}$, we can now determine:

$$\tilde{\mathbf{P}}^{-1} = \frac{1}{\det\left\{\tilde{\mathbf{P}}\right\}} \cdot \begin{pmatrix} \det\left\{\tilde{\mathbf{P}}_{1,1}\right\} & -\det\left\{\tilde{\mathbf{P}}_{2,1}\right\} & \det\left\{\tilde{\mathbf{P}}_{3,1}\right\} & -\det\left\{\tilde{\mathbf{P}}_{4,1}\right\} \\ -\det\left\{\tilde{\mathbf{P}}_{1,2}\right\} & \det\left\{\tilde{\mathbf{P}}_{2,2}\right\} & -\det\left\{\tilde{\mathbf{P}}_{3,2}\right\} & \det\left\{\tilde{\mathbf{P}}_{4,2}\right\} \\ \det\left\{\tilde{\mathbf{P}}_{1,3}\right\} & -\det\left\{\tilde{\mathbf{P}}_{2,3}\right\} & \det\left\{\tilde{\mathbf{P}}_{3,3}\right\} & -\det\left\{\tilde{\mathbf{P}}_{4,3}\right\} \\ -\det\left\{\tilde{\mathbf{P}}_{1,4}\right\} & \det\left\{\tilde{\mathbf{P}}_{2,4}\right\} & -\det\left\{\tilde{\mathbf{P}}_{3,4}\right\} & \det\left\{\tilde{\mathbf{P}}_{4,4}\right\} \end{pmatrix}. \tag{9}$$

Finally, to proceed with the $\{\mathbf{x}, \mathbf{t}\}$-update, we must define $\tilde{\mathbf{q}}$, which is given as:

$$\tilde{\mathbf{q}} = \begin{pmatrix} \tilde{\mathbf{q}}_1 \\ \tilde{\mathbf{q}}_2 \\ \tilde{\mathbf{q}}_3 \\ \tilde{\mathbf{q}}_4 \end{pmatrix} = \begin{pmatrix} \gamma_0^k \mathcal{F}\left\{\boldsymbol{\Omega}^T \mathbf{v}_0\right\} + \gamma_+^k \mathcal{F}\left\{\ \mathbf{v}_+^k\ \right\} & +\gamma^k \mathcal{F}\left\{\mathbf{D}_h^T \mathbf{v}_{1,h}^k\right\} & +\gamma^k \mathcal{F}\left\{\mathbf{D}_v^T \mathbf{v}_{1,v}^k\right\} & +\gamma^k \mathcal{F}\left\{\mathbf{D}_s^T \mathbf{v}_{1,s}^k\right\} \\ -\gamma^k \mathcal{F}\left\{\mathbf{v}_{1,h}^k\right\} & +\eta^k \mathcal{F}\left\{\mathbf{D}_h \mathbf{v}_{2,h}^k\right\} & +\eta^k \mathcal{F}\left\{\mathbf{D}_v \mathbf{v}_{2,hv}^k\right\} & +\eta^k \mathcal{F}\left\{\mathbf{D}_s \mathbf{v}_{1,hs}^k\right\} \\ -\gamma^k \mathcal{F}\left\{\mathbf{v}_{1,v}^k\right\} & +\eta^k \mathcal{F}\left\{\mathbf{D}_h \mathbf{v}_{2,hv}^k\right\} & +\eta^k \mathcal{F}\left\{\mathbf{D}_v \mathbf{v}_{2,v}^k\right\} & +\eta^k \mathcal{F}\left\{\mathbf{D}_s \mathbf{v}_{1,vs}^k\right\} \\ -\gamma^k \mathcal{F}\left\{\mathbf{v}_{1,s}^k\right\} & +\eta^k \mathcal{F}\left\{\mathbf{D}_h \mathbf{v}_{2,hs}^k\right\} & +\eta^k \mathcal{F}\left\{\mathbf{D}_v \mathbf{v}_{2,vs}^k\right\} & +\eta^k \mathcal{F}\left\{\ \mathbf{D}_s \mathbf{v}_{1,s}^k\right\} \end{pmatrix}, \tag{10}$$

where we define $\mathbf{v}_*^k = \mathbf{z}_*^k - \mathbf{u}_*^k$ for all indices $*$ above. With this definition, we can solve for $\tilde{\mathbf{r}} = \tilde{\mathbf{P}}^{-1}\tilde{\mathbf{q}}$ in Fourier space and subsequently obtain the solution via inverse Fourier transformation $\mathbf{r} = \mathcal{F}^{-1}\{\tilde{\mathbf{r}}\}$, yielding:

$$\begin{pmatrix} \mathbf{x}^{k+1} \\ \mathbf{t}_\mathbf{h}^{k+1} \\ \mathbf{t}_\mathbf{v}^{k+1} \\ \mathbf{t}_\mathbf{s}^{k+1} \end{pmatrix} = \begin{pmatrix} \mathcal{F}^{-1}\left\{\tilde{\mathbf{P}}_{1,1}^{-1}\tilde{\mathbf{q}}_1 + \tilde{\mathbf{P}}_{1,2}^{-1}\tilde{\mathbf{q}}_2 + \tilde{\mathbf{P}}_{1,3}^{-1}\tilde{\mathbf{q}}_3 + \tilde{\mathbf{P}}_{1,4}^{-1}\tilde{\mathbf{q}}_4\right\} \\ \mathcal{F}^{-1}\left\{\tilde{\mathbf{P}}_{2,1}^{-1}\tilde{\mathbf{q}}_1 + \tilde{\mathbf{P}}_{2,2}^{-1}\tilde{\mathbf{q}}_2 + \tilde{\mathbf{P}}_{2,3}^{-1}\tilde{\mathbf{q}}_3 + \tilde{\mathbf{P}}_{2,4}^{-1}\tilde{\mathbf{q}}_4\right\} \\ \mathcal{F}^{-1}\left\{\tilde{\mathbf{P}}_{3,1}^{-1}\tilde{\mathbf{q}}_1 + \tilde{\mathbf{P}}_{3,2}^{-1}\tilde{\mathbf{q}}_2 + \tilde{\mathbf{P}}_{3,3}^{-1}\tilde{\mathbf{q}}_3 + \tilde{\mathbf{P}}_{3,4}^{-1}\tilde{\mathbf{q}}_4\right\} \\ \mathcal{F}^{-1}\left\{\tilde{\mathbf{P}}_{4,1}^{-1}\tilde{\mathbf{q}}_1 + \tilde{\mathbf{P}}_{4,2}^{-1}\tilde{\mathbf{q}}_2 + \tilde{\mathbf{P}}_{4,3}^{-1}\tilde{\mathbf{q}}_3 + \tilde{\mathbf{P}}_{4,4}^{-1}\tilde{\mathbf{q}}_4\right\} \end{pmatrix} \ . \tag{11}$$

We have solved the $\{\mathbf{x}, \mathbf{t}\}$-update.

C. On the $\mathbf{z}_+$-update

In its general form, the proximal operator is defined as [1]:

$$\underset{g,\lambda}{\text{prox}}(\mathbf{v}) = \arg\min_{\mathbf{z}} \quad g(\mathbf{z}) + \frac{1}{2\lambda} \| \mathbf{v} - \mathbf{z} \|_2^2 \,, \tag{12}$$

provided that g is a closed convex function and does not evaluate to infinity everywhere. Notably, this proximal operator yields finite results, even when $g(\mathbf{z})$ evaluates to infinity at certain points. Applying this to Eq. 69 of the main paper, we obtain:

$$\mathbf{z}_+^{k+1} = \underset{\mathcal{I}_{\mathbb{R}_+},\gamma_+}{\text{prox}}(\mathbf{v}_+) = \arg\min_{\mathbf{z}_+} \quad \mathcal{I}_{\mathbb{R}_+}(\mathbf{z}_+) + \frac{\gamma_+}{2} \| \mathbf{z}_+ - \mathbf{v}_+ \|_2^2 \quad \text{, with} \quad \mathbf{v}_+ = \mathbf{x}^{k+1} + \mathbf{u}_+^k \quad , \tag{13}$$

from which two distinct cases can be derived:

Case $\mathbf{v}_+ \geq 0$:

In this scenario, since $\mathcal{I}_{\mathbb{R}_+}(\mathbf{z}_+) = 0$, Eq. 13 reduces to:

$$\mathbf{z}_+^{k+1} = \arg\min_{\mathbf{z}_+} \quad \| \mathbf{z}_+ - \mathbf{v}_+ \|_2^2 \quad \Longrightarrow \quad \mathbf{z}^{k+1} = \mathbf{v}_+ \,. \tag{14}$$

Notably, the factor $\frac{\gamma_+}{2}$ has no effect in thi scenario, and we obtain the $\mathbf{z}_+$-update for the first case.

Case $\mathbf{v}_+ < 0$:

In this scenario, $\mathcal{I}_{\mathbb{R}_+}(\mathbf{z}_+) = \infty$, which is far from minimal. Instead, we select a $\mathbf{z}_+$ that is closest to a negative $\mathbf{v}_+$ while still satisfying the condition $\mathcal{I}_{\mathbb{R}_+}(\mathbf{z}_+) = 0$. This yields:

$$\mathbf{z}_+^{k+1} = \arg\min_{\mathbf{z}_+} \| \mathbf{z}_+ - \mathbf{v}_+ \|_2^2 \text{ , with } \mathbf{v}_+ < 0 \quad \Longrightarrow \quad \mathbf{z}^{k+1} = 0 \,. \tag{15}$$

We have defined the $\mathbf{z}_+$-update.

D. On the *weighted block soft threshold* operator

Consider a Lagrangian that incorporates a total variation norm, e.g. a Lagrangian similar to that of the $\mathbf{z}_1$-update:

$$\mathcal{L}_\gamma\left(\mathbf{x}^{k+1}, \mathbf{t}^{k+1}, \mathbf{z}, \mathbf{u}^k\right) = \|\lambda^2 \mathbf{z}\|_2 + \gamma/2 \|\mathbf{D}\mathbf{x}^{k+1} - \mathbf{t}^{k+1} - \mathbf{z} + \mathbf{u}^k\|_2^2 \,, \tag{16}$$

where each of the matrices $\mathbf{D}$, $\mathbf{t}$, $\mathbf{z}$, and $\mathbf{u}$ is comprised of three sub-matrices $\mathbf{D}_i$, $\mathbf{t}_i$, $\mathbf{z}_i$, and $\mathbf{u}_i$, representing all three possible directions in a 3D data cube. We disregard all other variables, as they do not affect the minimization of $\mathbf{z}$.
To perform the $\mathbf{z}$-update, the Lagrangian must be minimized with respect to each $\mathbf{z}_i$. By setting the derivative of the Lagrangian equal to zero, we obtain the optimal value of $\mathbf{z}_i^{k+1}$ that minimizes the following equation:

$$\partial_{\mathbf{z}_i} \|\lambda^2 \mathbf{z}\|_2 - \gamma\left(\mathbf{D}_i \mathbf{x}^{k+1} - \mathbf{t}^{k+1} - \mathbf{z}_i^{k+1} + \mathbf{u}_i^k\right) = 0 \iff \mathbf{z}_i^{k+1} = \left(\mathbf{D}_i \mathbf{x}^{k+1} - \mathbf{t}^{k+1} + \mathbf{u}_i^k\right) - (1/\gamma)\, \partial_{\mathbf{z}_i} \|\lambda^2 \mathbf{z}\|_2 \,, \tag{17}$$

with the sub-differential [1]:

$$\partial_{\mathbf{v}_i} \|\mathbf{v}\|_2 = \partial_{\mathbf{v}_i} \sqrt{\sum_n \mathbf{v}_n^2} = \begin{cases} \frac{\mathbf{v}_i}{\|\mathbf{v}\|_2} & \text{if} \quad \|\mathbf{v}\|_2 \neq 0 \\ \omega_i \,:\, \|\omega\|_2 \leq 1 & \text{if} \quad \|\mathbf{v}\|_2 = 0 \end{cases} . \tag{18}$$

The general minimization equation $\mathbf{D}\mathbf{x} - \mathbf{t} - \mathbf{z} + \mathbf{u} = 0$ indicates that the vectors $\mathbf{D}\mathbf{x} - \mathbf{t}$ and $\mathbf{z}$ point in the same direction and have a similar length, differing only by the vector $\mathbf{u}$. Therefore, the ratio can be expressed as $\frac{\mathbf{z}_i^{k+1}}{\|\mathbf{z}^{k+1}\|_2} = \frac{\mathbf{D}_i \mathbf{x}^{k+1} - \mathbf{t}_i^{k+1} + \mathbf{u}_i^k}{\|(\mathbf{D}\mathbf{x}^{k+1} - \mathbf{t}^{k+1} + \mathbf{u}^k)\|_2}$. Scaling by a scalar λ_i preserves the direction. It follows that the sub-differential of the Euclidean norm of $\|\lambda^2 \mathbf{z}\|_2$ can be expressed as:

$$\partial_{\mathbf{z}_i} \|\lambda^2 \mathbf{z}\|_2 = \partial_{\mathbf{z}_i} \sqrt{\sum_n \lambda_n^2 \mathbf{z}_n^2} = \begin{cases} \frac{\lambda_i^2 \left(\mathbf{D}_i \mathbf{x}^{k+1} - \mathbf{t}_i^{k+1} + \mathbf{u}_i^k\right)}{\|\lambda^2 (\mathbf{D}\mathbf{x}^{k+1} - \mathbf{t}^{k+1} + \mathbf{u}^k)\|_2} & \text{if} \quad \|\lambda^2 \left(\mathbf{D}\mathbf{x}^{k+1} - \mathbf{t}^{k+1} + \mathbf{u}^k\right)\|_2 \neq 0 \\ \omega_i \,:\, \|\omega\|_2 \leq 1 & \text{if} \quad \|\lambda^2 \left(\mathbf{D}\mathbf{x}^{k+1} - \mathbf{t}^{k+1} + \mathbf{u}^k\right)\|_2 = 0 \end{cases} , \tag{19}$$

with the minimization splitting up into two cases:

Case $\|\lambda^2 \left(\mathbf{D}\mathbf{x}^{k+1} - \mathbf{t}^{k+1} + \mathbf{u}^k\right)\|_2 \neq 0$:

For the first case, the minimization problem is formulated as:

$$\mathbf{z}_i^{k+1} = \left(\mathbf{D}_i \mathbf{x}^{k+1} - \mathbf{t}_i^{k+1} + \mathbf{u}_i^k\right) - \lambda_i^2/\gamma \, \frac{\left(\mathbf{D}_i \mathbf{x}^{k+1} - \mathbf{t}_i^{k+1} + \mathbf{u}_i^k\right)}{\|\lambda^2 \left(\mathbf{D}\mathbf{x}^{k+1} - \mathbf{t}^{k+1} + \mathbf{u}^k\right)\|_2} \,. \tag{20}$$

Case $\|\lambda^2 \left(\mathbf{D}\mathbf{x}^{k+1} - \mathbf{t}^{k+1} + \mathbf{u}^k\right)\|_2 = 0$:

In the second case, the equation takes the form:

$$0 \in \left(\mathbf{D}_i \mathbf{x}^{k+1} - \mathbf{t}_i^{k+1} + \mathbf{u}_i^k\right) - (1/\gamma) \left\{\omega_i \,:\, \|\omega\|_2 \leq 1\right\} \,. \tag{21}$$

Rearranging yields:

$$\begin{aligned} & \gamma \left(\mathbf{D}_i \mathbf{x}^{k+1} - \mathbf{t}_i^{k+1} + \mathbf{u}_i^k\right) \in \quad \left\{\omega_i \,:\, \|\omega\|_2 \leq 1\right\} \\ \iff \quad & \lambda_i^2 \gamma \left(\mathbf{D}_i \mathbf{x}^{k+1} - \mathbf{t}_i^{k+1} + \mathbf{u}_i^k\right) \in \lambda_i^2 \left\{\omega_i \,:\, \|\omega\|_2 \leq 1\right\} \,, \end{aligned} \tag{22}$$

from which can be concluded:

$$\|\gamma \lambda^2 \left(\mathbf{D}\mathbf{x}^{k+1} - \mathbf{t}^{k+1} + \mathbf{u}^k\right)\|_2 \leq \lambda_i^2 \quad \iff \quad \|\lambda^2 \left(\mathbf{D}\mathbf{x}^{k+1} - \mathbf{t}^{k+1} + \mathbf{u}^k\right)\|_2 \leq \lambda_i^2/\gamma \,. \tag{23}$$

Consequently, if $\|\lambda^2 \left(\mathbf{D}\mathbf{x}^{k+1} - \mathbf{t}^{k+1} + \mathbf{u}^k\right)\|_2 \leq \lambda_i^2/\gamma$, then the $\mathbf{z}_i$-update reduces to zero: $\mathbf{z}_i^{k+1} = 0$.

By combining both cases, we obtain the so-called *'weighted block soft threshold'* operator [1]:

$$\begin{aligned}\mathbf{z}_i^{k+1} &= \mathcal{S}_{\lambda,\gamma}\left[\mathbf{D}_i\mathbf{x}^{k+1} - \mathbf{t}_i^{k+1} + \mathbf{u}_i\right] \\ &= \max\left\{\left(1 - \frac{\lambda_i^2/\gamma}{\| \lambda^2(\mathbf{D}\mathbf{x}^{k+1} - \mathbf{t}^{k+1} + \mathbf{u}^k)\|_2}\right)\cdot\left(\mathbf{D}_i\mathbf{x}^{k+1} - \mathbf{t}_i^{k+1} + \mathbf{u}_i^k\right),\, 0\right\}. \end{aligned} \tag{24}$$

In the case where $\lambda_i = \lambda$, which is commonly encountered in literature, the regular block soft threshold operator emerges as a special case.
We have also defined the $\mathbf{z}_{1,i}$-updates and the $\mathbf{z}_{2,j}$-updates, as both sets exhibit a similar structural form.

For readers interested in further details, an alternative and more elegant approach to demonstrating the properties of this $\mathbf{z}$-minimization is available through its Fenchel conjugate. Specifically, the indicator function combined with the support function of the unit ball of ℓ_2, as well as Moreau's decomposition [1]. However, at least in the opinion of an experimental physicist, this way is less intuitive, which is why we provide the above derivation.

E. Plasmonic map of a truncated gold nano-pyramid at 2.26 eV

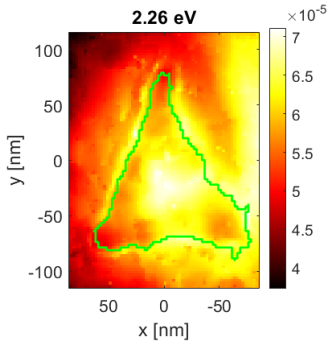

Fig. 1: Deconvolution result obtained using the ADMM-TGV algorithm for the plasmonic map of the truncated gold nano-pyramid from Fig. 5 at an electron energy-loss of 2.26 eV.

F. MATLAB-Script of the Algorithm

The software for the evaluation of noise parameters can be found at `https://de.mathworks.com/matlabcentral/fileexchange/180009-noise-evaluation-in-transmission-electron-microscopy-tem`.

A software to read '.dm4' files from Gatan Digital Micrograph can be found at `https://www.mathworks.com/matlabcentral/fileexchange/45933-gatan-digital-micrograph-file-reader`.

On the following pages, the MATLAB script of the ADMM-TGV deconvolution algorithm for STEM-EELS maps can be found appended to this PDF. Updates of the algorithm are provided in `https://www.mathworks.com/matlabcentral/fileexchange/181166-admm-tgv-deconvolution-algorithm-for-stem-eels-maps`.

If you use the algorithm or parts of it, please quote our paper.

References

[1] Neal Parikh. Proximal algorithms. *Foundations and Trends® in Optimization*, 1(3):127–239, 2014.

```
function DecResult = ADMM_TGV_EELS_maps(EELSData,Kernel,SubtrBack,DetectorPSF,Gain,ReadVAR,Phi,TotalVAR,BackVAR,isInterp,Iter,ZLPPos,set_ZLP_zero)

%% Please cite the paper:
% Christian Zietlow and Jörg K. N. Lindner
% An unbiased ADMM-TGV algorithm for the deconvolution of STEM-EELS maps
% Ultramicroscopy 275 (2025), Article 114159
% https://doi.org/10.1016/j.ultramic.2025.114159

% Please note, however, that the authors disclaim any liability for damages or consequences arising from the use of the provided scripts.
% Users are responsible for ensuring the proper functioning and application of the code.

% A software to read '.dm4' files from Gatan Digital Micrograph can be found at https://www.mathworks.com/matlabcentral/fileexchange/45933-gatan-digital-micrograph-file-reader .
% The software for the evaluation of noise parameters can be found at https://de.mathworks.com/matlabcentral/fileexchange/180009-noise-evaluation-in-transmission-electron-microscopy-tem .

% Updates of the below deconvolution algorithm are provided at https://www.mathworks.com/matlabcentral/fileexchange/181166-admm-tgv-deconvolution-algorithm-for-stem-eels-maps .

%% ----------------------------------------_Definition of input paramter_----------------------------------------
% In the following, EnergyDim characterizes a speficic number of EELS channels, that must be equal for the dimension size of all input
% data that it is mentioned in. For 'Kernel' and 'DetectorPSF', deviations from EnergyDim are automatically corrected for in the script.

% EELSData contains the EELS data cube without padding._____________________________________Requires size of (YDim,XDim,EnergyDim) as single/double
% Kernel contains e.g. a ZLP measured in vacuum used for the deconvolution._____________________Requires size of (1,EnergyDim)         as single/double
% SubtrBack contains the signal background that is subtracted from the EELS data cube, e.g. a ZLP._____Requires size of (YDim,XDim,EnergyDim) as single/double
% DetectorPSF contains the detector point-spread function, with the maximum in the middle of the array._Requires size of (1,EnergyDim)         as single/double
% Gain is the total gain (not the smoothed gain) of the detector in counts / beam electron._____________Requires scalar  (Gain)                as single/double
% ReadVAR contains all detector noises measured for the individual EELS channels._____________________Requires scalar  (ReadVAR)             as single/double
% Phi contains the shifting factor that indicates the energy drift in [0,1]._____________________Requires scalar  (Phi)                 as single/double
% TotalVAR contains all detector noises measured for all EELS channels combined._____________________Requires scalar  (TotalVAR)             as single/double
% BackVAR contains all noises for the background subtracted from the EELS data cube._____________________Requires size of (YDim,XDim,EnergyDim) as single/double
% isInterp set (1) if EELS data was energy aligned using interpolation, else set (0)._____________Requires logical (1) or (0)            as logical
% Iter gives the number of ADMM-TGV iterations._____________________________________________Requires scalar  (Iterations)          as single/double
% ZLPPos gives the index (not loss energy!) where the ZLP starts and ends (StartIndex,EndIndex)._______Requires size of (1,2)                 as single/double

% set_ZLP_zero deletes the ZLP region during deconvolution_____________________________________Requires logical (1) or (0))          as logical
% This might be helpful for the algorithm to succeed if large residuals
% remain after subtraction. These residuals do not necessarily obey the
% regular noise statistics due to missmatches if the subtraction differs much from the data ZLPs.
% If applicable, these residuals might ruin the deconvolution and must be removed.

%% ----------------------------------------_Check input paramters_----------------------------------------

% Check number of input parameters
if nargin<13
    warndlg('Input parameters missing for ADMM_TGV_EELS_maps script!')
    return
elseif nargin>13
    warndlg('To many input parameters for ADMM_TGV_EELS_maps script!')
    return
end

% Check size EELSData vs SubtrBack
if ~all(size(EELSData)==size(SubtrBack))
    warndlg('EELSData and SubtrBack must have the same dimensions for ADMM_TGV_EELS_maps script!')
    return
end
% Check size BackVAR vs SubtrBack
if ~all(size(BackVAR)==size(SubtrBack))
    warndlg('BackVAR and SubtrBack must have the same dimensions for ADMM_TGV_EELS_maps script!')
    return
end

% Check size Kernel
if size(size(Kernel),2)> 2 || size(size(Kernel),2)<2
   warndlg('Kernel has the wrong number of dimension for ADMM_TGV_EELS_maps script!')
   return
elseif size(Kernel,1)>1 && size(Kernel,2)>=1
    warndlg('Kernel has the wrong dimension for ADMM_TGV_EELS_maps script!')
    return
end

% Check DetectorPSF
if size(size(DetectorPSF),2)> 2 || size(size(DetectorPSF),2)<2
   warndlg('DetectorPSF has the wrong number of dimension for ADMM_TGV_EELS_maps script!')
   return
elseif size(DetectorPSF,1)>1 && size(DetectorPSF,2)>=1
    warndlg('DetectorPSF has the wrong dimension for ADMM_TGV_EELS_maps script!')
    return
end
[~,Ind] = max(ifftshift(DetectorPSF));
if Ind~=1
    warndlg('DetectorPSF maximum is not in the middle of the array!')
    DetectorPSF = fftshift(DetectorPSF);
    [~,Ind]     = max(ifftshift(DetectorPSF));
    if Ind~=1
        return
    end
end

%% ----------------------------------------_Create Padding_----------------------------------------
% Padding is necessary to create circular boundaries for the deconvolution.
% Not creating this circular boundary creates artifacts that alter the
% deconvolution results.

OrigLength = size(EELSData,3);
Padding    = EELSPadding(EELSData,ZLPPos,DetectorPSF,Gain,ReadVAR,Phi,isInterp);
EELSData   = cat(3,EELSData,Padding);
```

```
% Adjust the Kernel size accordingly
Diff       = size(EELSData,3)-size(Kernel,2);

[~,MaxInd] = max(Kernel,[],2);
Kernel     = circshift(Kernel,-MaxInd+1,2);
Kernel     = fftshift(Kernel);
if Diff>0
   pad1   = zeros([1,ceil( Diff/2)]);
   pad2   = zeros([1,floor(Diff/2)]);
   Kernel = [pad1,Kernel,pad2];
elseif Diff<0
   Ind1   = - floor(Diff/2);
   Ind2   = -  ceil(Diff/2);
   Kernel = Kernel(1,Ind1:end-Ind2);
end
Kernel = ifftshift(Kernel);

% Adjust the background variance size accordingly
Diff       = size(EELSData,3)-size(SubtrBack,3);
if Diff>0
   pad       = zeros([size(SubtrBack,1),size(SubtrBack,2),Diff]);
   BackVAR   = cat(3,BackVAR  ,pad);
elseif Diff<0
   BackVAR   = BackVAR(:,:,1:end-Diff);
end

% Adjust the subtracted background size accordingly
SubtrBack = BackPadding(SubtrBack,EELSData,DetectorPSF,ZLPPos);

% Adjust the detector PSF size accordingly
Diff       = size(EELSData,3)-size(DetectorPSF,2);
if Diff>0
   pad1        = zeros([1,ceil( Diff/2)]);
   pad2        = zeros([1,floor(Diff/2)]);
   DetectorPSF = [pad1,DetectorPSF,pad2];
elseif Diff<0
   Ind1        = - floor(Diff/2);
   Ind2        = -  ceil(Diff/2);
   DetectorPSF = DetectorPSF(1,Ind1:end-Ind2);
end

%% ----------------------------------------_Parameter choice for the TGV prior_----------------------------------------


% Start script
WB                      = waitbar(0,'Define Parameters');
ReadStd                 = sqrt(ReadVAR);
EELSData(EELSData+ReadStd<0) = randn.*ReadStd;                  % replace negative values that differ too much from the noise statistics.

EELSSignal              = max(EELSData,0);                      % for the mean noise level, we need a signal that is positive.
                                                                % This does not alter the data to be deconvolved.

EELSSig = EELSSignal;
if set_ZLP_zero
  SubtrBack( :,:,ZLPPos(1):ZLPPos(2)) = EELSSignal(:,:,ZLPPos(1):ZLPPos(2)); % sets the region of the ZLP to 0 if selected.
                                                                % This might be helpful if data ZLP and subtracted ZLP differ much.
  EELSSignal(:,:,ZLPPos(1):ZLPPos(2)) = 0;
  BackVAR(   :,:,ZLPPos(1):ZLPPos(2)) = 0;
end

% Calculate amplification factors of the signal noise: omega_s
DetectorPSF = DetectorPSF./sum(DetectorPSF,2);
Kernel      = Kernel    ./sum(Kernel,2);

SizeDiff    = (size(DetectorPSF,2) - size(Kernel,2)+1)/2;
DetectorPSF = DetectorPSF(1,ceil(SizeDiff):end-floor(SizeDiff));

omega_s     = ifft(fft(Kernel,[],2)./fft(DetectorPSF,[],2),[],2);
omega_s     = omega_s./max(omega_s,[],2);
omega_s     = sum(omega_s,2);
clearvars DetectorPSF

%   Calculate amplification factors of the detector noise: omega_d
% & Calculate derivative of the signal: Deriv

if isInterp
   PearsInterp          = zeros([1,size(EELSSignal,3)]);
   PearsInterp(1,1:2)   = [2/3,1/6];
   PearsInterp(1,end)   = 1/6;
   PSFInter             = ifft(sqrt(abs(fft(PearsInterp,[],2))),[],2);
   PSFInter(PSFInter<0) = 0;
   PSFInter             = PSFInter./sum(PSFInter,'all');

   omega_d              = ifft(fft(Kernel,[],2)./fft(PSFInter,[],2),[],2);
   omega_d              = omega_d./max(omega_d,[],2);
   omega_d              = sum(omega_d,2);
   clearvars PearsInterp PSFInter

   Deriv                = zeros(size(EELSSignal));
   Sigma_Interp         = 0;
else
   omega_d              = 1;

   Deriv                = reshape(EELSSignal,[size(EELSSignal,1)*size(EELSSignal,2),size(EELSSignal,3)]);
   Deriv                = mean(Deriv,1);
```

```
    Deriv               = (Deriv - circshift(Deriv,-1,2)).^2;
    Deriv               = reshape(Deriv,[1,1,size(Deriv,3)]);
    Deriv               = repmat(Deriv,[size(EELSSignal,1),size(EELSSignal,2),1]);
    Sigma_Interp        = 1/4;
end
clearvars isInterp

% Calculate Noise Sums
Sum            = sum(EELSSig(:,:,1:OrigLength),3);
Mean           = mean(Sum,'all');
Norm           = Sum./Mean;
IntDev         = std(Sum,0,'all')./Mean;
A              = round(sqrt(size(EELSSignal,1)*size(EELSSignal,2)));

% Noise Estimate in Energy Direction and Lambda_Z paramters
ReadVAR        = repmat(ReadVAR,size(EELSSignal));
SignalNoise    = omega_s.*Gain.*EELSSignal   ./Sum.^2;
DetecNoise     = omega_d.*(1 + 1./A).*ReadVAR./Sum.^2;
BackSubtrNoise = omega_s.*BackVAR            ./Sum.^2;

NoiseEst_Z     = Mean.*sqrt(mean(SignalNoise + DetecNoise + BackSubtrNoise,'all'));

lambda_1z      = 1./(2.*NoiseEst_Z);
lambda_2z      = 1./(2.*NoiseEst_Z);

% Noise Estimate in Lateral Direction and Lambda_XY paramters
sig            = EELSSignal;
sig(:,:,OrigLength+1:end)=0;
mu_R           = (Sum - sig)./Sum;
Read_R         = TotalVAR - ReadVAR;
Read_R(:,:,OrigLength+1:end)=0;

k_square       = (1 + IntDev.^2./4) .* Gain .* mu_R.*Mean + (1 + IntDev.^2).*Read_R;
k_square       = k_square./Mean.^2;

SignalNoise    = omega_s.*(1 + IntDev.^2./4).* Gain.*mu_R.^2 .* EELSSignal./Sum./Mean ;
NormNoise      = k_square .*(EELSSignal./Sum).^2;
DetecNoise     = omega_d.*(1 + IntDev.^2).*(1 + Phi./A).*mu_R.^2 .*ReadVAR./Mean.^2 ;
BackSubtrNoise = omega_s.*IntDev.^2.*BackVAR./Sum./Mean;
Deriv          = Sigma_Interp.^2 .* Deriv./Mean.^2;

NoiseEst_XY    = Mean.*sqrt(mean(SignalNoise + NormNoise + DetecNoise + BackSubtrNoise + Deriv, 'all'));
lambda_1xy     = 1./(2.*NoiseEst_XY);
lambda_2xy     = 1./(2.*NoiseEst_XY);

% Parameter for Deconvolution Algorithm
ReadVAR        = (1+1./A).*ReadStd.^2;
clearvars -except EELSData Kernel SubtrBack Gain ReadVAR OrigLength Iter lambda_1z lambda_2z lambda_1xy lambda_2xy WB Norm Mean


%% ---------------------------------------_Initialize deconvolution algorithm_---------------------------------------


waitbar(0.5,WB,'Initialize Deconvolution');

% Initialize Residual Balancing Limits
lim            = 10;
Lim            = 100;

% Initialize Penalty Parameters
gamma          = 1;
gamma_0        = 1;
gamma_p        = 1;
eta            = 1;

% Initialize lambda_2xyz
lambda_2xyz    = sqrt(lambda_2xy.*lambda_2z);

% Initialize z-Variables
SizeImg        = size(EELSData);

z0             = max((EELSData- SubtrBack)./Norm,0);
zp             = max((EELSData- SubtrBack)./Norm,0);
z1x            = zeros(SizeImg);
z1y            = zeros(SizeImg);
z1z            = zeros(SizeImg);
z2x            = zeros(SizeImg);
z2y            = zeros(SizeImg);
z2z            = zeros(SizeImg);
z2xy           = zeros(SizeImg);
z2xz           = zeros(SizeImg);
z2yz           = zeros(SizeImg);

% Initialize u-Variables
u0             = zeros(SizeImg);
up             = zeros(SizeImg);
u1x            = zeros(SizeImg);
u1y            = zeros(SizeImg);
u1z            = zeros(SizeImg);
u2x            = zeros(SizeImg);
u2y            = zeros(SizeImg);
u2z            = zeros(SizeImg);
u2xy           = zeros(SizeImg);
u2xz           = zeros(SizeImg);
u2yz           = zeros(SizeImg);
```

```
% Initialize x/t-Variables
x             = zeros(SizeImg);
T1            = zeros(SizeImg);
T2            = zeros(SizeImg);
T3            = zeros(SizeImg);

% Initialize Kernel
kernel        = Kernel;
Kernel        = zeros(SizeImg);
Kernel(1,1,:) = kernel;
A             = fftn(Kernel,SizeImg);
clearvars Kernel kernel

At            = conj(A);
AtA           = At.*A;

% Initialize Total Generalalized Variation
dx            = [1,-1,0] ;
dy            = [1,-1,0]';
dz(:,:,1)     =  1;
dz(:,:,2)     = -1;
dx            = fftn(dx,SizeImg);
dy            = fftn(dy,SizeImg);
dz            = fftn(dz,SizeImg);
dtx           = conj(dx);
dty           = conj(dy);
dtz           = conj(dz);

DtD           = dtx.*dx + dty.*dy + dtz.*dz;

% Initialize denominator for x/t- update
A11 = gamma_0.*AtA + gamma_p + gamma.*DtD ; A12 =        - gamma     .*dtx ; A13 =         - gamma     .*dty ; A14 =        - gamma     .*dtz ;
A21 =                        - gamma.*dx  ; A22 =  gamma + eta  .*DtD     ; A23 =           eta  .*dy .*dtx ; A24 =          eta  .*dz .*dtx ;
A31 =                        - gamma.*dy  ; A32 =          eta  .*dx .*dty ; A33 =  gamma + eta  .*DtD     ; A34 =          eta  .*dz .*dty ;
A41 =                        - gamma.*dz  ; A42 =          eta  .*dx .*dtz ; A43 =           eta  .*dy .*dtz ; A44 =  gamma + eta  .*DtD     ;

C11 =   ( (A22.*A33.*A44) + (A23.*A34.*A42) + (A24.*A32.*A43) - (A42.*A33.*A24)- (A43.*A34.*A22) - (A44.*A32.*A23) );
C12 =  -( (A21.*A33.*A44) + (A23.*A34.*A41) + (A24.*A31.*A43) - (A41.*A33.*A24)- (A43.*A34.*A21) - (A44.*A31.*A23) );
C13 =   ( (A21.*A32.*A44) + (A22.*A34.*A41) + (A24.*A31.*A42) - (A41.*A32.*A24)- (A42.*A34.*A21) - (A44.*A31.*A22) );
C14 =  -( (A21.*A32.*A43) + (A22.*A33.*A41) + (A23.*A31.*A42) - (A41.*A32.*A23)- (A42.*A33.*A21) - (A43.*A31.*A22) );

C21 =  -( (A12.*A33.*A44) + (A13.*A34.*A42) + (A14.*A32.*A43) - (A42.*A33.*A14)- (A43.*A34.*A12) - (A44.*A32.*A13) );
C22 =   ( (A11.*A33.*A44) + (A13.*A34.*A41) + (A14.*A31.*A43) - (A41.*A33.*A14)- (A43.*A34.*A11) - (A44.*A31.*A13) );
C23 =  -( (A11.*A32.*A44) + (A12.*A34.*A41) + (A14.*A31.*A42) - (A41.*A32.*A14)- (A42.*A34.*A11) - (A44.*A31.*A12) );
C24 =   ( (A11.*A32.*A43) + (A12.*A33.*A41) + (A13.*A31.*A42) - (A41.*A32.*A13)- (A42.*A33.*A11) - (A43.*A31.*A12) );

C31 =   ( (A12.*A23.*A44) + (A13.*A24.*A42) + (A14.*A22.*A43) - (A42.*A23.*A14)- (A43.*A24.*A12) - (A44.*A22.*A13) );
C32 =  -( (A11.*A23.*A44) + (A13.*A24.*A41) + (A14.*A21.*A43) - (A41.*A23.*A14)- (A43.*A24.*A11) - (A44.*A21.*A13) );
C33 =   ( (A11.*A22.*A44) + (A12.*A24.*A41) + (A14.*A21.*A42) - (A41.*A22.*A14)- (A42.*A24.*A11) - (A44.*A21.*A12) );
clearvars A44
C34 =  -( (A11.*A22.*A43) + (A12.*A23.*A41) + (A13.*A21.*A42) - (A41.*A22.*A13)- (A42.*A23.*A11) - (A43.*A21.*A12) );
clearvars A42 A43
C41 =  -( (A12.*A23.*A34) + (A13.*A24.*A32) + (A14.*A22.*A33) - (A32.*A23.*A14)- (A33.*A24.*A12) - (A34.*A22.*A13) );
C42 =   ( (A11.*A23.*A34) + (A13.*A24.*A31) + (A14.*A21.*A33) - (A31.*A23.*A14)- (A33.*A24.*A11) - (A34.*A21.*A13) );
C43 =  -( (A11.*A22.*A34) + (A12.*A24.*A31) + (A14.*A21.*A32) - (A31.*A22.*A14)- (A32.*A24.*A11) - (A34.*A21.*A12) );
clearvars A14 A24 A34
C44 =   ( (A11.*A22.*A33) + (A12.*A23.*A31) + (A13.*A21.*A32) - (A31.*A22.*A13)- (A32.*A23.*A11) - (A33.*A21.*A12) );
clearvars A12 A13   A22 A23    A32 A33

detA = 1./(A11.*C11 + A21.*C21 + A31.*C31 + A41.*C41);
clearvars A11 A21 A31 A41

iA11 = C11.*detA ; clearvars C11 ; iA21 = C12.*detA ; clearvars C12 ; iA31 = C13.*detA ;clearvars C13 ; iA41 = C14.*detA ; clearvars C14 ;
iA12 = C21.*detA ; clearvars C21 ; iA22 = C22.*detA ; clearvars C22 ; iA32 = C23.*detA ;clearvars C23 ; iA42 = C24.*detA ; clearvars C24 ;
iA13 = C31.*detA ; clearvars C31 ; iA23 = C32.*detA ; clearvars C32 ; iA33 = C33.*detA ;clearvars C33 ; iA43 = C34.*detA ; clearvars C34 ;
iA14 = C41.*detA ; clearvars C41 ; iA24 = C42.*detA ; clearvars C42 ; iA34 = C43.*detA ;clearvars C34 ; iA44 = C44.*detA ; clearvars C44 ;
clearvars detA

waitbar(1,WB,'Define Parameters');
close(WB);

%% ---------------------------------------_Iterate deconvolution algorithm_---------------------------------------

WB = waitbar(0,{['Iteration ',num2str(0),' of ',num2str(Iter), ' finished!'],[num2str(0),'%']});
for iter=1:Iter
   doResBal = ~mod(iter,round(10^(round(log10(iter)*10)/10))) || iter<10 || iter==Iter;  % Performs residual balancing logarithmically spaced 10 times per magnitude

   % x/t updates

   v0    = z0    - u0  ;
   vp    = zp    - up  ;
   v1x   = z1x   - u1x ;
   v1y   = z1y   - u1y ;
   v1z   = z1z   - u1z ;
   v2x   = z2x   - u2x ;
   v2y   = z2y   - u2y ;
   v2z   = z2z   - u2z ;
   v2xy  = z2xy  - u2xy;
   v2xz  = z2xz  - u2xz;
   v2yz  = z2yz  - u2yz;

   xnum1 = gamma_0.*At.*fftn(v0 ,SizeImg) + gamma_p.*fftn(vp ,SizeImg) + gamma.*fftn(Dt(v1x ,2) ,SizeImg) + gamma.*fftn(Dt(v1y ,1),SizeImg) + gamma.*fftn(Dt(v1z ,3),SizeImg);
   clearvars v0 vp
   xnum2 =                          - gamma  .*fftn(v1x,SizeImg) + eta  .*fftn(D( v2x ,2) ,SizeImg) + eta  .*fftn(D( v2xy,1),SizeImg) + eta  .*fftn(D( v2xz,3),SizeImg);
   clearvars v1x v2x
   xnum3 =                          - gamma  .*fftn(v1y,SizeImg) + eta  .*fftn(D( v2xy,2) ,SizeImg) + eta  .*fftn(D( v2y ,1),SizeImg) + eta  .*fftn(D( v2yz,3),SizeImg);
```

```
clearvars v1y v2xy v2y
xnum4 =                          - gamma  .*fftn(v1z,SizeImg) + eta  .*fftn(D( v2xz,2) ,SizeImg) + eta  .*fftn(D( v2yz,1),SizeImg) + eta  .*fftn(D( v2z ,3),SizeImg);
clearvars v1z v2xz v2yz v2z

if doResBal
   x_old  = x;
   T1_old = T1;
   T2_old = T2;
   T3_old = T3;
end

x    = iA11.*xnum1 + iA12.*xnum2 + iA13.*xnum3 + iA14.*xnum4;
T1   = iA21.*xnum1 + iA22.*xnum2 + iA23.*xnum3 + iA24.*xnum4;
T2   = iA31.*xnum1 + iA32.*xnum2 + iA33.*xnum3 + iA34.*xnum4;
T3   = iA41.*xnum1 + iA42.*xnum2 + iA43.*xnum3 + iA44.*xnum4;
clearvars xnum1 xnum2 xnum3 xnum4

x    = ifftn(x ,SizeImg);
T1   = ifftn(T1,SizeImg);
T2   = ifftn(T2,SizeImg);
T3   = ifftn(T3,SizeImg);

x    = sign(real(x )).*abs(x );
T1   = sign(real(T1)).*abs(T1);
T2   = sign(real(T2)).*abs(T2);
T3   = sign(real(T3)).*abs(T3);

if doResBal
   x_old  = x  -  x_old;
   T1_old = T1 - T1_old;
   T2_old = T2 - T2_old;
   T3_old = T3 - T3_old;
end

% z_0 update
Ax      = ifftn(A.*fftn(x,SizeImg),SizeImg);
Ax      = sign(real(Ax)).*abs(Ax);
v0      = Ax + u0;
if doResBal
   z0_old = z0;
end
z0       = RMPG(EELSData,z0,v0,gamma_0,Norm,SubtrBack,Gain,ReadVAR,OrigLength,1);
u0       = v0 - z0;
clearvars v0
if doResBal
   Atz0     = ifftn(At.*fftn(z0 - z0_old,SizeImg),SizeImg);
   clearvars z0_old
   Atz0     = sign(real(Atz0)).*abs(Atz0);
   S0       = -gamma_0.*Atz0;
   clearvars Atz0

   Atu0     = ifftn(At.*fftn(u0,SizeImg),SizeImg);
   Atu0     = sign(real(Atu0)).*abs(Atu0);
   S0norm   =  gamma_0.*Atu0;
   clearvars Atu0

   R0       = sqrt(mean((Ax - z0).^2,'all'));
   R0norm   = sqrt(max(mean(Ax.^2,'all'),mean(z0.^2,'all')));
   Rnorm0   = R0/R0norm;
   clearvars R0 R0norm
end
clearvars Ax

% z_p update
vp   = x  + up;
if doResBal
   zp_old = zp;
end

zp   = max(vp,0);
up   = vp - zp;
clearvars vp
if doResBal
   Sp     = -gamma_p.*(zp - zp_old);
   clearvars zp_old
   Spnorm =  gamma_p.*up;

   Rp     = sqrt(mean((x - zp).^2,'all'));
   Rpnorm = sqrt(max(mean(x.^2,'all'),mean( zp.^2,'all')));
   Rnormp = Rp./Rpnorm;
   clearvars Rp Rpnorm
end

% z_1 update
Dx   = D(x,2);
v1x  = Dx - T1 + u1x;

Dy   = D(x,1);
v1y  = Dy - T2 + u1y;

Dz   = D(x,3 );
v1z  = Dz - T3 + u1z;

vnorm = sqrt((lambda_1xy.*v1x).^2 + (lambda_1xy.*v1y).^2 + (lambda_1z.*v1z).^2);

if doResBal
```

```
    z1x_old = z1x;
end
z1x   = wBST(v1x,vnorm,lambda_1xy,gamma);
u1x   = v1x - z1x;
clearvars v1x
if doResBal
    z1x_old   =          z1x       - z1x_old   ;
    S         = -gamma.*Dt(T1_old    + z1x_old,2);
    S1norm    =  gamma.*Dt(u1x                ,2);

    S1a       =  gamma.*(D(-x_old,2) + z1x_old  );
    clearvars z1x_old
    S1anorm   =  gamma.*u1x;

    R         = mean((Dx - z1x - T1).^2,'all');
    R1norm    = mean((Dx       - T1).^2,'all');
    R2norm    = mean((     z1x     ).^2,'all');
end
clearvars Dx

if doResBal
    z1y_old = z1y;
end
z1y   = wBST(v1y,vnorm,lambda_1xy,gamma);
u1y   = v1y - z1y;
clearvars v1y
if doResBal
    z1y_old   =            z1y       - z1y_old    ;
    S         = S - gamma.*Dt(T2_old    + z1y_old ,1);
    S2norm    =     gamma.*Dt(u1y                 ,1);

    S2a       =     gamma.*(D(-x_old,1) + z1y_old   );
    clearvars z1y_old
    S2anorm   =     gamma.*u1y;

    R         = R      + mean((Dy - z1y - T2).^2,'all');
    R1norm    = R1norm + mean((Dy       - T2).^2,'all');
    R2norm    = R2norm + mean((     z1y     ).^2,'all');
end
clearvars Dy

if doResBal
    z1z_old = z1z;
end
z1z   = wBST(v1z,vnorm,lambda_1z,gamma);
clearvars vnorm
u1z   = v1z - z1z;
clearvars v1z
if doResBal
    z1z_old   =            z1z       - z1z_old    ;
    S         = S - gamma.*Dt(T3_old    + z1z_old ,3);
    S3norm    =     gamma.*Dt(u1z                 ,3);

    S3a       =     gamma.*(D(-x_old,3) + z1z_old   );
    clearvars x_old z1z_old
    S3anorm   =     gamma.*u1z;

    SN0       =  max(mean( S0norm.^2                  ,'all'),mean((Spnorm + S1norm + S2norm + S3norm - Sp - S ).^2,'all'));
    SNp       =  max(mean( Spnorm.^2                  ,'all'),mean((S0norm + S1norm + S2norm + S3norm - S0 - S ).^2,'all'));
    SN        =  max(mean((S1norm + S2norm + S3norm).^2,'all'),mean((S0norm + Spnorm                   - S0 - Sp).^2,'all'));
    clearvars S0norm Spnorm S1norm S2norm S3norm

    Snorm0    = sqrt(mean(S0.^2,'all')/SN0);
    clearvars S0 SN0
    Snormp    = sqrt(mean(Sp.^2,'all')/SNp);
    clearvars Sp SNp
    S         = sqrt(mean(S.^2,'all') + mean(S1a.^2,'all') + mean(S2a.^2,'all') + mean(S3a.^2,'all'));

    R         = sqrt(R      + mean((Dz - z1z - T3).^2,'all'));
    R1norm    =      R1norm + mean((Dz       - T3).^2,'all') ;
    R2norm    =      R2norm + mean((     z1z     ).^2,'all') ;

    RN        = sqrt(max(R1norm,R2norm));
    clearvars R1norm R2norm

    Rnorm     = R/RN;
    clearvars R RN
end
clearvars Dz

% z_2 update
Htx  = Dt(T1,2);
v2x  = Htx  + u2x;

Htxy = Dt(T1,1) + Dt(T2,2);
v2xy = Htxy + u2xy;

Hty  = Dt(T2,1);
v2y  = Hty  + u2y;

Htxz = Dt(T1,3) + Dt(T3,2);
v2xz = Htxz + u2xz;

Htyz = Dt(T2,3) + Dt(T3,1);
v2yz = Htyz + u2yz;
```

```
Htz  = Dt(T3,3);
v2z  = Htz  + u2z;

vnorm = sqrt((lambda_2xy.*v2x).^2 + (lambda_2xy.*v2xy).^2 + (lambda_2xy.*v2y).^2 + (lambda_2xyz.*v2xz).^2 + (lambda_2xyz.*v2yz).^2 + (lambda_2z.*v2z).^2);

if doResBal
   z2x_old = z2x;
end
z2x  = wBST(v2x,vnorm,lambda_2xy,eta);
u2x  = v2x  - z2x ;
clearvars v2x
if doResBal
   s1       = - eta.*D(z2x - z2x_old,2);
   clearvars z2x_old
   s1norm   =   eta.*D(u2x          ,2);

   r        = mean((Htx - z2x).^2,'all');
   r1norm   = mean((Htx      ).^2,'all');
   r2norm   = mean((      z2x).^2,'all');
end
clearvars Htx

if doResBal
   z2xy_old = z2xy;
end
z2xy = wBST(v2xy,vnorm,lambda_2xy,eta);
u2xy = v2xy - z2xy;
clearvars v2xy
if doResBal
   z2xy_old  =                    z2xy      - z2xy_old    ;
   s1       = s1     - eta.*D(Dt(-T2_old,2) + z2xy_old ,1);
   s1norm   = s1norm + eta.*D(                u2xy    , 1);

   s2       =        - eta.*D(Dt(-T1_old,1) + z2xy_old ,2);
   clearvars z2xy_old
   s2norm   =          eta.*D(                u2xy    , 2);

   r        = r      + mean((Htxy - z2xy).^2,'all');
   r1norm   = r1norm + mean((Htxy       ).^2,'all');
   r2norm   = r2norm + mean((       z2xy).^2,'all');
end
clearvars Htxy

if doResBal
   z2y_old = z2y ;
end
z2y  = wBST(v2y,vnorm,lambda_2xy,eta);
u2y  = v2y  - z2y ;
clearvars v2y
if doResBal
   s2       = s2     - eta.*(D(z2y - z2y_old,1));
   clearvars z2y_old
   s2norm   = s2norm + eta.*(D(      u2y    ,1));

   r        = r      + mean((Hty - z2y).^2,'all');
   r1norm   = r1norm + mean((Hty      ).^2,'all');
   r2norm   = r2norm + mean((      z2y).^2,'all');
end
clearvars Hty

if doResBal
   z2xz_old = z2xz;
end
z2xz = wBST(v2xz,vnorm,lambda_2xyz,eta);
u2xz = v2xz - z2xz;
clearvars v2xz
if doResBal
   z2xz_old  =                    z2xz      - z2xz_old    ;
   s1       = s1     - eta.*D(Dt(-T3_old,2) + z2xz_old ,3);
   s1norm   = s1norm + eta.*D(   u2xz                 , 3);
   s        =          mean(s1.^2,'all');

   sn       =      max(mean((S1anorm - S1a).^2,'all') ,  mean(s1norm.^2 ,'all'));
   clearvars S1a
   SN       = SN + max(mean((s1norm  - s1 ).^2,'all') ,  mean(S1anorm.^2,'all'));
   clearvars S1anorm s1 s1norm

   s3       =        - eta.*D(Dt(-T1_old,3) + z2xz_old ,2);
   s3norm   =          eta.*D(                u2xz    , 2);

   r        = r      + mean((Htxz - z2xz).^2,'all');
   r1norm   = r1norm + mean((Htxz       ).^2,'all');
   r2norm   = r2norm + mean((       z2xz).^2,'all');
end
clearvars Htxz

if doResBal
   z2yz_old = z2yz;
end
z2yz = wBST(v2yz,vnorm,lambda_2xyz,eta);
u2yz = v2yz - z2yz;
clearvars v2yz
if doResBal
   z2yz_old  =                    z2yz      - z2yz_old    ;
   s2       = s2     - eta.*D(Dt(-T3_old,1) + z2yz_old ,3);
   s2norm   = s2norm + eta.*D(                u2yz    , 3);
```

```
    s        = s      + mean(s2.^2,'all');

    sn       = sn + max(mean((S2anorm - S2a).^2,'all') ,  mean(s2norm.^2 ,'all'));
    clearvars S2a
    SN       = SN + max(mean((s2norm  - s2 ).^2,'all') ,  mean(S2anorm.^2,'all'));
    clearvars S2anorm s2 s2norm

    s3       = s3     - eta.*D( Dt(-T2_old,3) + z2yz_old ,1);
    s3norm   = s3norm + eta.*D(                u2yz     ,1);

    r        = r      + mean((Htyz - z2yz).^2,'all');
    r1norm   = r1norm + mean((Htyz       ).^2,'all');
    r2norm   = r2norm + mean((       z2yz).^2,'all');
end
clearvars Htyz

if doResBal
    z2z_old = z2z;
end
z2z  = wBST(v2z,vnorm,lambda_2z,eta);
u2z  = v2z  - z2z ;
clearvars v2z vnorm
if doResBal
    s3       = s3     - eta.*D(z2z - z2z_old,3);
    clearvars z2z_old
    s3norm   = s3norm + eta.*D(u2z          ,3);
    s        = sqrt(s + mean(s3.^2,'all'));

    sn       = sqrt(sn + max(mean((S3anorm - S3a).^2,'all') ,  mean(s3norm.^2 ,'all')));
    clearvars  S3a
    SN       = sqrt(SN + max(mean((s3norm  - s3 ).^2,'all') ,  mean(S3anorm.^2,'all')));
    clearvars S3anorm s3 s3norm

    snorm    = s/sn;
    clearvars s sn
    Snorm    = S/SN;
    clearvars S SN

    r        = sqrt(r      + mean((Htz - z2z).^2,'all'));
    r1norm   =      r1norm + mean((Htz      ).^2,'all');
    r2norm   =      r2norm + mean((      z2z).^2,'all');
    rn       = sqrt(max(r1norm,r2norm));
    clearvars r1norm r2norm
    rnorm    = r/rn;
    clearvars r rn
end
clearvars Htz

if doResBal
    % Applies the residual balancing to the penalty parameters gamma_0 (z0 residuals), gamma_p (z_p residuals), gamma (z1 residuals) and eta (z2 residuals)

    % gamma_0 update
    tau_gamma_0 = sqrt(Rnorm0/Snorm0);

    if isnan(tau_gamma_0) || tau_gamma_0==0 || tau_gamma_0==inf
        if gamma_0 > 1
            tau_gamma_0 = lim^(-1);
        elseif gamma_0 < 1
            tau_gamma_0 = lim^( 1);
        else
            tau_gamma_0 = 1;
        end
    end

    tau_gamma_0 = max(min(tau_gamma_0,10^(Lim)/gamma_0),10^(-Lim)/gamma_0);
    gamma_0     = gamma_0.*tau_gamma_0;
    u0          = u0     ./tau_gamma_0;                          % all u variables must be rescaled inversely

    % gamma_p update
    tau_gamma_p = sqrt(Rnormp/Snormp);

    if isnan(tau_gamma_p) || tau_gamma_p==0 || tau_gamma_p==inf
        if gamma_p > 1
            tau_gamma_p = lim^(-1);
        elseif gamma_p < 1
            tau_gamma_p = lim^( 1);
        else
            tau_gamma_p = 1;
        end
    end
    tau_gamma_p = max(min(tau_gamma_p,10^(Lim)/gamma_p),10^(-Lim)/gamma_p);
    gamma_p     = gamma_p.*tau_gamma_p;
    up          = up     ./tau_gamma_p;                          % all u variables must be rescaled inversely

    % gamma update
    tau_gamma = sqrt(Rnorm/Snorm);

    if isnan(tau_gamma) || tau_gamma==0 || tau_gamma==inf
        if gamma > 1
            tau_gamma = lim^(-1);
        elseif gamma < 1
            tau_gamma = lim^( 1);
        else
            tau_gamma = 1;
        end
    end
```

```
        tau_gamma = max(min(tau_gamma,10^(Lim)/gamma),10^(-Lim)/gamma);
        gamma     = gamma.*tau_gamma;
        u1x       = u1x  ./tau_gamma;                          % all u variables must be rescaled inversely
        u1y       = u1y  ./tau_gamma;
        u1z       = u1z  ./tau_gamma;

        % eta update
        tau_eta = sqrt(rnorm/snorm);

        if isnan(tau_eta) || tau_eta==0 || tau_eta==inf
           if eta > 1
              tau_eta = lim^(-1);
           elseif eta < 1
              tau_eta = lim^( 1);
           else
              tau_eta = 1;
           end
        end
        tau_eta = max(min(tau_eta,10^(Lim)/eta),10^(-Lim)/eta);
        eta     = eta .*tau_eta;
        u2x     = u2x ./tau_eta;                             % all u variables must be rescaled inversely
        u2xy    = u2xy./tau_eta;
        u2y     = u2y ./tau_eta;
        u2xz    = u2xz./tau_eta;
        u2yz    = u2yz./tau_eta;
        u2z     = u2z ./tau_eta;

        % Update denominator for x/t update
        if tau_gamma_0 ~=1 && tau_gamma_p ~=1 && tau_gamma ~=1 && tau_eta~=1
           A11 = gamma_0.*AtA + gamma_p + gamma.*DtD; A12 =        - gamma     .*dtx ; A13 =        - gamma   .*dty ; A14 =        - gamma   .*dtz ;
           A21 =                        - gamma.*dx ; A22 =  gamma + eta  .*DtD     ; A23 =          eta.*dy .*dtx ; A24 =          eta.*dz .*dtx ;
           A31 =                        - gamma.*dy ; A32 =          eta  .*dx .*dty ; A33 =  gamma + eta.*DtD     ; A34 =          eta.*dz .*dty ;
           A41 =                        - gamma.*dz ; A42 =          eta  .*dx .*dtz ; A43 =          eta.*dy .*dtz ; A44 =  gamma + eta.*DtD     ;


           C11 =   ( (A22.*A33.*A44) + (A23.*A34.*A42) + (A24.*A32.*A43) - (A42.*A33.*A24)- (A43.*A34.*A22) - (A44.*A32.*A23) );
           C12 =  -( (A21.*A33.*A44) + (A23.*A34.*A41) + (A24.*A31.*A43) - (A41.*A33.*A24)- (A43.*A34.*A21) - (A44.*A31.*A23) );
           C13 =   ( (A21.*A32.*A44) + (A22.*A34.*A41) + (A24.*A31.*A42) - (A41.*A32.*A24)- (A42.*A34.*A21) - (A44.*A31.*A22) );
           C14 =  -( (A21.*A32.*A43) + (A22.*A33.*A41) + (A23.*A31.*A42) - (A41.*A32.*A23)- (A42.*A33.*A21) - (A43.*A31.*A22) );

           C21 =  -( (A12.*A33.*A44) + (A13.*A34.*A42) + (A14.*A32.*A43) - (A42.*A33.*A14)- (A43.*A34.*A12) - (A44.*A32.*A13) );
           C22 =   ( (A11.*A33.*A44) + (A13.*A34.*A41) + (A14.*A31.*A43) - (A41.*A33.*A14)- (A43.*A34.*A11) - (A44.*A31.*A13) );
           C23 =  -( (A11.*A32.*A44) + (A12.*A34.*A41) + (A14.*A31.*A42) - (A41.*A32.*A14)- (A42.*A34.*A11) - (A44.*A31.*A12) );
           C24 =   ( (A11.*A32.*A43) + (A12.*A33.*A41) + (A13.*A31.*A42) - (A41.*A32.*A13)- (A42.*A33.*A11) - (A43.*A31.*A12) );

           C31 =   ( (A12.*A23.*A44) + (A13.*A24.*A42) + (A14.*A22.*A43) - (A42.*A23.*A14)- (A43.*A24.*A12) - (A44.*A22.*A13) );
           C32 =  -( (A11.*A23.*A44) + (A13.*A24.*A41) + (A14.*A21.*A43) - (A41.*A23.*A14)- (A43.*A24.*A11) - (A44.*A21.*A13) );
           C33 =   ( (A11.*A22.*A44) + (A12.*A24.*A41) + (A14.*A21.*A42) - (A41.*A22.*A14)- (A42.*A24.*A11) - (A44.*A21.*A12) );
           clearvars A44
           C34 =  -( (A11.*A22.*A43) + (A12.*A23.*A41) + (A13.*A21.*A42) - (A41.*A22.*A13)- (A42.*A23.*A11) - (A43.*A21.*A12) );
           clearvars A42 A43
           C41 =  -( (A12.*A23.*A34) + (A13.*A24.*A32) + (A14.*A22.*A33) - (A32.*A23.*A14)- (A33.*A24.*A12) - (A34.*A22.*A13) );
           C42 =   ( (A11.*A23.*A34) + (A13.*A24.*A31) + (A14.*A21.*A33) - (A31.*A23.*A14)- (A33.*A24.*A11) - (A34.*A21.*A13) );
           C43 =  -( (A11.*A22.*A34) + (A12.*A24.*A31) + (A14.*A21.*A32) - (A31.*A22.*A14)- (A32.*A24.*A11) - (A34.*A21.*A12) );
           clearvars A14 A24 A34
           C44 =   ( (A11.*A22.*A33) + (A12.*A23.*A31) + (A13.*A21.*A32) - (A31.*A22.*A13)- (A32.*A23.*A11) - (A33.*A21.*A12) );
           clearvars A12 A13   A22 A23    A32 A33

           detA = 1./(A11.*C11 + A21.*C21 + A31.*C31 + A41.*C41);
           clearvars A11 A21 A31 A41

           iA11 = C11.*detA ; clearvars C11 ; iA21 = C12.*detA ; clearvars C12 ; iA31 = C13.*detA ;clearvars C13 ; iA41 = C14.*detA ; clearvars C14 ;
           iA12 = C21.*detA ; clearvars C21 ; iA22 = C22.*detA ; clearvars C22 ; iA32 = C23.*detA ;clearvars C23 ; iA42 = C24.*detA ; clearvars C24 ;
           iA13 = C31.*detA ; clearvars C31 ; iA23 = C32.*detA ; clearvars C32 ; iA33 = C33.*detA ;clearvars C33 ; iA43 = C34.*detA ; clearvars C34 ;
           iA14 = C41.*detA ; clearvars C41 ; iA24 = C42.*detA ; clearvars C42 ; iA34 = C43.*detA ;clearvars C34 ; iA44 = C44.*detA ; clearvars C44 ;
           clearvars detA
        end
     end
     waitbar(round(iter/Iter,3),WB,{['Iteration ',num2str(iter),' of ',num2str(Iter), ' finished!'],[num2str(round(iter/Iter*100,2)),'%']});

end
DecResult = max(x./Mean,0);                                  % divide by mean intensity to get overall loss probabilities
close(WB);

clearvars -except DecResult
end

function z0 = RMPG(Image,z0,v0,gamma_0,N,ZLP,a,VAR,OrgLength,NewtIter)
% restoring mixed Poisson-Gaussian noise (RMPG).
% Restores the deconv. estimate to the original state: by blurring the
% deconv result, adding the subtracted bacground and by undoing the
% normalization. Then, it is comared to the measurement data.

z0(z0<0) = 0;
for I=1:NewtIter
    Est      = N.*z0  + ZLP;
    Noise    = a.*Est + VAR;
    dz       =          N.*(Est-Image)   ./(Noise)    -    a.*N   .*(Est-Image).^2./(2.*Noise.^2) + a.*N./(2.*Noise)                          - gamma_0.*(v0-z0);
    dz2      =  a.^2.*N.^2.*(Est-Image).^2./(Noise.^3) - 2.*a.*N.^2.*(Est-Image)   ./(   Noise.^2) + N.^2./(   Noise) - a.^2.*N.^2./(2.*Noise.^2) + gamma_0        ;

    z0       = z0 - dz./dz2;
    z0(z0<0) = 0;
end
z0(:,:,OrgLength+1:end) = v0(:,:,OrgLength+1:end);
clearvars -except z0
end
```

```
function z_i = wBST(v_i,vnorm,lambda,gamma)
% weighted block soft thresholding operator

k             = lambda.^2./gamma;
z_i           = zeros(size(v_i));
z_i(vnorm>=k) = v_i(vnorm>=k)- k .* v_i(vnorm>=k)./vnorm(vnorm>=k);
clearvars -except z_i
end

function Grad = D(x,dim)
% forward derivative

Grad        = x - circshift(x,+1,dim);
clearvars -except Grad
end

function Grad = Dt(x,dim)
% backward derivative

Grad        = x - circshift(x,-1,dim);
clearvars -except Grad
end

function Padding = EELSPadding(EELSData,ZLPPos,DetectorPSF,Gain,ReadVAR,Phi,isInterp)


%% ----------------------------_Create Padding_----------------------------
% Padding is created using the right side of the ZLP of the EELS data.

ReadStd    = sqrt(ReadVAR);

% Select ZLP for padding
ZLPInd1    = ZLPPos(1,1);
ZLPInd2    = ZLPPos(1,2);
Padding    = EELSData(:,:,ZLPInd1:ZLPInd2);

% Normalize padding to height of 1
pad        = reshape(Padding,[size(Padding,1)*size(Padding,2),size(Padding,3)]);
pad        = mean(pad,1);
pad        = pad./max(pad,[],2);

%Adjust detector PSF for the noise
PSFFactor  = DetectorPSF./max(DetectorPSF,[],2);
SizeDiff   = (size(PSFFactor,2) - size(pad,2)+1)/2;
PSFFactor  = PSFFactor(1,ceil(SizeDiff):end-floor(SizeDiff));
PSFFactor  = ifftshift(PSFFactor)./sum(PSFFactor,2);
PSFFactor  = ifft(fft(PSFFactor,[],2).*fft(pad,[],2),[],2);
PSFFactor  = max(PSFFactor,[],2)^(-1);

% get start and end values of the EELS data
StartPoint = mean(EELSData(:,:,1:5),3);
EndPoint   = mean(EELSData(:,:,end-5:end),3);                    % sets the endpoint as mean value of the last 5 points

% Adjust padding to the start and end points of the EELS data
Padding    = reshape(Padding,[size(Padding,1)*size(Padding,2),size(Padding,3)]);
Padding    = mean(Padding,1);

[~,Ind]    = max(Padding,[],2);
Padding    = Padding-min(Padding,[],2);
Padding    = Padding./max(Padding,[],2);


Padding    = reshape(Padding,[1,1,size(Padding,2)]);
Padding    = repmat(Padding,[size(EELSData,1),size(EELSData,2)]);
Padding    = Padding.*repmat((EndPoint-StartPoint).*PSFFactor,[1,1,size(Padding,3)])+repmat(StartPoint,[1,1,size(Padding,3)]);

%% ----------------------------_Blend in Padding_----------------------------
% To blend in the padding, we add the same noises as are foud in the regular data
% This also helps to easily calculate the mean noise level of the data for
% the ADMM-TGV algo

% Poisson distr. signal noise
Padding     = Padding./(Gain).*10^(-12);
Padding     = imnoise(Padding,'poisson');
Padding     = Padding.*10^(12).*(Gain);

% Correlations in the signal noise
SizeDiff    = (size(DetectorPSF,2) - size(Padding,3)+1)/2;
DetectorPSF = DetectorPSF(1,ceil(SizeDiff):end-floor(SizeDiff));
DetectorPSF = ifftshift(DetectorPSF)./sum(DetectorPSF,2);
DetectorPSF = reshape(DetectorPSF,[1,1,size(DetectorPSF,2)]);
DetectorPSF = repmat(DetectorPSF,[size(Padding,1),size(Padding,2),1]);

Padding     = ifft(fft(Padding,[],3).*fft(DetectorPSF,[],3),[],3);
Padding     = sign(real(Padding)).*abs(Padding);
Padding     = Padding(:,:,Ind:end);

% Gaussian distr. read-out noise of the detector
ReadNoise   = randn((size(Padding))).*ReadStd;

% Correlations in the detector noise due to possible interpolation of the data (energy realignment)
if isInterp
    PearsInterp          = zeros([1,size(Padding,3)]);
    PearsInterp(1,1:2)   = [2/3,1/6];
    PearsInterp(1,end)   = 1/6;
```

```
    PSFInter            = ifft(sqrt(abs(fft(PearsInterp,[],2))),[],2);
    PSFInter(PSFInter<0) = 0;
    PSFInter            = PSFInter./sum(PSFInter,'all');
    PSFInter            = reshape(PSFInter,[1,1,size(Padding,3)]);
    PSFInter            = repmat(PSFInter,[size(Padding,1),size(Padding,2),1]);
    ReadNoise             = ifft(fft(ReadNoise,[],3).*fft(PSFInter,[],3),[],3);
    ReadNoise             = sign(real(ReadNoise)).*abs(ReadNoise);

    ReadBack            = randn((size(Padding(1,1,:)))).*ReadStd./(sqrt(size(Padding,1)*size(Padding,2))).*sqrt(Phi);
    ReadBack            = ifft(fft(ReadBack,[],3).*fft(PSFInter(1,1,:),[],3),[],3);
    ReadBack            = sign(real(ReadBack)).*abs(ReadBack);
    ReadBack            = repmat(ReadBack,[size(Padding,1),size(Padding,2),1]);
end

Padding     = Padding + ReadNoise + ReadBack;


clearvars -except Padding
end

function SubtrBack = BackPadding(SubtrBack,EELSData,DetectorPSF,ZLPPos)
%% ----------------------------_Create Padding_----------------------------
% Padding is created using the right side of the ZLP of the EELS data.

% Select ZLP for padding
ZLPInd1     = ZLPPos(1,1);
ZLPInd2     = ZLPPos(1,2);
Padding     = EELSData(:,:,ZLPInd1:ZLPInd2);


padding     = mean(reshape(Padding,[size(Padding,1)*size(Padding,2),size(Padding,3)]),1);
[~,Ind]     = max(padding,[],2);
PaddingSize = ZLPInd2 - ZLPInd1 + 1 - Ind + 1;
TotalSize   = size(SubtrBack,3) + PaddingSize;
Diff        = size(EELSData,3) - TotalSize;

if Diff<0
    SubtrBack = SubtrBack(:,:,1:end+Diff);
end

% Normalize padding to height of 1
pad         = reshape(Padding,[size(Padding,1)*size(Padding,2),size(Padding,3)]);
pad         = mean(pad,1);
pad         = pad./max(pad,[],2);

%Adjust detector PSF for the noise
PSFFactor   = DetectorPSF./max(DetectorPSF,[],2);
SizeDiff    = (size(PSFFactor,2) - size(pad,2)+1)/2;
PSFFactor   = PSFFactor(1,ceil(SizeDiff):end-floor(SizeDiff));
PSFFactor   = ifftshift(PSFFactor)./sum(PSFFactor,2);
PSFFactor   = ifft(fft(PSFFactor,[],2).*fft(pad,[],2),[],2);
PSFFactor   = max(PSFFactor,[],2)^(-1);

% get start and end values of the EELS data
StartPoint  = mean(SubtrBack(:,:,1:5),3);
EndPoint    = mean(SubtrBack(:,:,end-5:end),3);                 % sets the endpoint as mean value of the last 5 points

% Adjust padding to the start and end points of the background data
Padding     = reshape(Padding,[size(Padding,1)*size(Padding,2),size(Padding,3)]);
[~,Ind]     = max(mean(Padding,1),[],2);
Padding     = mean(Padding,1);
Padding     = Padding-min(Padding,[],2);
Padding     = Padding./max(Padding,[],2);

Padding     = reshape(Padding,[1,1,size(Padding,2)]);
Padding     = repmat(Padding,[size(SubtrBack,1),size(SubtrBack,2)]);
Padding     = Padding.*repmat((EndPoint-StartPoint).*PSFFactor,[1,1,size(Padding,3)])+repmat(StartPoint,[1,1,size(Padding,3)]);

SizeDiff    = (size(DetectorPSF,2) - size(Padding,3)+1)/2;
DetectorPSF = DetectorPSF(1,ceil(SizeDiff):end-floor(SizeDiff));
DetectorPSF = ifftshift(DetectorPSF)./sum(DetectorPSF,2);
DetectorPSF = reshape(DetectorPSF,[1,1,size(DetectorPSF,2)]);
DetectorPSF = repmat(DetectorPSF,[size(Padding,1),size(Padding,2),1]);

Padding     = ifft(fft(Padding,[],3).*fft(DetectorPSF,[],3),[],3);
Padding     = sign(real(Padding)).*abs(Padding);
Padding     = Padding(:,:,Ind:end);

if Diff>0
   Padd2    = ones([size(Padding,1),size(Padding,2),Diff]).*EndPoint;
   Padding  = cat(3,Padd2,Padding);
end

SubtrBack   = cat(3,SubtrBack,Padding);

clearvars -except SubtrBack
end
```

Danksagung

Zum Ende dieser Thesis möchte ich meinen Dank all denjenigen aussprechen, die mich mit viel Rat und Tat durch meine Doktorandenzeit begleitet haben.
Besonders möchte ich mich bei Prof. Lindner bedanken, der mir in Paderborn eine spannende Perspektive bot, meine wissenschaftliche Arbeit an einem TEM fortzusetzen, und mich als Doktorand annahm.
Diese Arbeit war ursprünglich komplett als experimental-physikalische Arbeit angedacht und hat über die Corona-Zeit einen immer mehr statistisch-theoretischen Einschlag genommen. Lieber Jörg, vielen Dank, dass Du Dich zusammen mit mir durch den gesamten Formelwulst durchgearbeitet hast. Vielen Dank, dass Du mich bei diesem Vorhaben meiner Promotion nach bestem Wissen und Gewissen unterstützt hast, auch wenn die Formeln lang und länger wurden. Niemand liest sich freiwillig 100+ Seiten Formelwerk durch und doch haben wir eine recht umfassende Theorie über Rauschstatistik auf die Beine gestellt – und das als Experimentalphysiker! Dass Du Dir mein Detektorrauschen so verständnisvoll über mehrere Jahre hinweg angehört hast, ohne müde zu werden jedes Detail zu hinterfragen, dafür gebührt Dir mein größter Dank.
Weiterhin möchte ich mich auch bei dem Zweitkorrektor dieser Dissertation, Herrn Prof. Schindlmayr, bedanken, der sich ebenso durch die Rauschstatistiken durcharbeiten und sich zudem in die Thematik der Elektronenmikroskopie sowie der Elektronenenergieverlustspektroskopie im Speziellen einarbeiten musste.
Ich möchte mich bei Julius Bürger bedanken, der mich mit riesigem Fachwissen und viel Geduld in die Arbeit am TEM eingewiesen hat. Ohne Dich, lieber Julius, wäre die experimentelle Evaluation der Formeln völlig unmöglich gewesen. Danken möchte ich Dir insbesondere auch für das Korrekturlesen von Papern und der Dissertation. Vielen Dank, für die schöne Zeit im "Programmieroffice"; für die vielen lustigen Geschichten, die wir beim Korrigieren von Protokollen und Klausuren geteilt haben; für die intensiven Fachgespräche, bei denen die Tafeln vollgeschrieben wurden; für die kleineren Exkurse in viel zu scharfem koreanischen Essen und nicht zuletzt für die Kaffeepausen und Feierabendbiere.
Einen großen Teil meiner Zeit im Chemie- und Aufdampflabor habe ich mit Philipp Hodges verbracht. Lieber Philipp, vielen Dank, dass Du Dir die Zeit genommen hast, die so langwierigen Aufdampfprozesse der Platin-Gold-Janusstrukturen zu begleiten. Für die ganzen gemeinsamen Vorbereitungen und die Umbauten an der Aufdampfanlage, die die Herstellung der Strukturen erst ermöglicht haben, möchte ich mich bei Dir besonders bedanken; für den Frust, wenn wieder irgendwas schiefgelaufen ist und das Vakuum furchtbar wurde und für die Heurekamomente, wenn es nach mehrmaligem Auf- und Zuschrauben endlich doch funktionierte. Rückblickend war es doch eine schöne Zeit, in der wir vieles zusammen gelernt (und schnell geleert) haben. Vielen Dank auch Dir fürs oftmals wohlverdiente Feierabendbier.
Bedanken möchte ich mich bei Alexander Stratmann, der mir die Rakeltechnik beigebracht hat, die zur Erzeugung der Nanokugelmasken unabdingbar ist, und bei meinem TEOS-Spezialisten, Colin Wessel, der mir in seiner Bachelorarbeit ein einfaches Verfahren ausgearbeitet hat, mit dem sich Nanokugelmasken kontrolliert verschließen ließen.

Ferner möchte ich mich bei Daniel Kool und Harikrishnan Venugopal bedanken, deren AFM-Messungen wesentlich zu meinem Verständnis des Strukturwachstums beim Nanokugel-Lithograhieverfahren beigetragen haben.
Vielen Dank den Laboringenieuren Werner Sievers, Yannik Lang und Julian Sulikowski für ihre unermüdliche Arbeit, die Geräte in Schuss zu halten, und die schnelle Unterstützung, wenn etwas mal so gar nicht funktionieren wollte. Vielen Dank auch Dir, lieber Dennis Briese für das professionelle Verkabeln der Aufdampfanlagenelektronik.
Vielen Dank der Frühstücksrunde für das Zerstreuen der Gedanken jeden Mittwochmorgen und die vielen interessanten Fachsimpeleien über Gott und die Welt.
Bei meinen beiden Corps, bei meinen Vandalen und Sachsen, bedanke ich mich für so manche bierseelige Abende, die mir halfen von der ständigen Grübelei zuweilen loszukommen, um den Abstand zu gewinnen, den ich brauchte, um neu über Ansätze nachzudenken. Vielen Dank für die stete Motivation und die richtigen Motivatoren – und viel mehr noch für all den Unfug nebenher. Allgemein möchte ich mich bei euch für die herrliche Zerstreuung während meiner Studienzeit bedanken – ihr habt mir diese wertvolle Zeit so besonders und unvergesslich gemacht. Vivat!

Abschließend möchte ich mich bei meiner Familie für all die Unterstützung bedanken, die ich in der gesamten Zeit der Academia erhalten habe, ohne Euch wäre dieses komplette Unterfangen völlig undenkbar gewesen. Vielen Dank, dass Ihr mein ganzes Gefachsimpel ertragen habt; Verständnis hattet, wenn ich mal wieder Simulationen über mein Smartphone starten musste oder nur halb zuhörte, weil ich mal wieder über Physik nachgedenken musste. Lieber Malte, vielen Dank für das Korrekturlesen der Dissertation!

Vor allem aber bei Dir, liebe Tessa, möchte ich für die vielen Abende und Nächte um Entschuldigung bitten, an denen ich nur vor dem Computer saß; für die vielen Tage, an denen ich kaum ansprechbar war, weil ich nur die Physik im Kopf und nur einen Kopf für Physik hatte. Vielen Dank, dass Du mich so toll in all dieser Zeit unterstützt hast und immer an mich geglaubt hast, auch wenn ich im Peer review noch eine weitere Runde drehen musste. Ich liebe Dich!

Mutti, Vati und meine liebe Tessa, vielen Dank für Alles – Euch widme ich diese Dissertation.

Selbständigkeitserklärung

Ich versichere hiermit an Eides statt, dass ich die vorliegende Arbeit selbstständig angefertigt und ohne fremde Hilfe verfasst habe, keine außer den von mir angegebenen Hilfsmitteln und Quellen dazu verwendet habe und die den benutzten Werken inhaltlich und wörtlich entnommenen Stellen als solche kenntlich gemacht habe.
Um die sprachliche Qualität des Manuskripts zu verbessern, habe ich in dieser Thesis das Large Language Model "*Llama 3.1 405B*" und den DeepL-Write-Assistenten ausschließlich zu diesem genannten Zwecke genutzt. Hierbei habe ich insbesondere darauf geachtet, dass sowohl der ursprüngliche Sinn und Inhalt meiner Arbeit erhalten bleibt als auch die Integrität der in ihr enthaltenen Aussagen und Schlüsse gewahrt wird.

Gröbenzell, 15.07.2025